Diaphragm Performance in Steel Frame Structures Under Lateral Loading

A thesis submitted in partial fulfilment of the requirements for the Degree

of Doctor of Philosophy

in

The Department of Civil and Natural Resources Engineering

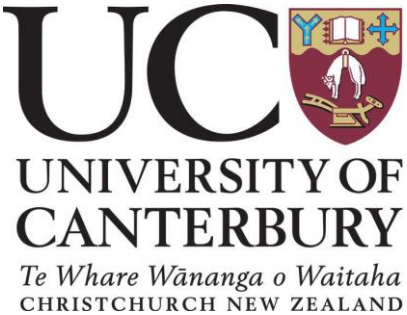

University of Canterbury

By

Saeid Alizadeh

University of Canterbury

Christchurch, New Zealand

2018

Abstract

Significant advances have been made over recent years in the design of vertical lateral force resisting (VLFR) systems such as frames and walls in buildings subject to earthquake loading. However, the in-plane seismic performance of floor diaphragms and connections of such diaphragms to the VLFR elements has received relatively little attention. This is despite the fact that the diaphragms are essential for maintaining building integrity and good frame performance. In this research, a number of diaphragm in-plane design issues are investigated.

In this study, building, diaphragm and connection model numerical analyses are conducted to better understand the behaviour of composite concrete-steel floor diaphragms for steel buildings under seismic loading, and to improve the diaphragm design process. The work conducted relates to diaphragm in-plane modelling, the performance and design of gravity beam-end connections, shear stud behaviour under lateral loading, diaphragm buckling, and assessing the demands on the building/ diaphragm for design. Key findings of this work are given below.

A new diamond truss method was proposed and calibrated to model diaphragm in-plane stiffness and strength. This method provides benefits, compared to the previously used diagonal truss method, such as: easy incorporation of local diaphragm details; reduced mesh sensitivity; clear load paths; better diaphragm in-plane stiffness estimation; and more reasonable beam-column connection axial and shear stud demands.

A method to assess gravity beam web side plate (WSP) connection axial strength is proposed. This strength is required to resist beam axial demands imposed by in-plane diaphragm forces and it considers beam dimensions, cope length, packing effect, and shear forces.

The performance of beam shear studs groups subjected to horizontal demands from in-plane diaphragm forces was shown to be sensitive to gravity loading. As the shear studs yielded

under lateral loading, beam composite action was lost. A method to assess shear stud group lateral force resistance, considering the possibility of shear stud fracture, was developed.

Methods were developed to assess the composite diaphragm buckling strengths due to in-plane loading considering initial out-of-plane deformation. From the analyses conducted it was found that the diaphragm buckling modes are not likely to govern the in-plane strength in conventional buildings with typical minimum diaphragm topping thicknesses.

Current methods to estimate building diaphragm in-plane demands were assessed, and a new "Diaphragm Equivalent Static Analysis" (DESA) method was proposed. This method has similar accuracy to some previous methods has more general and easier application.

Finally, findings from all parts of the study are combined to develop a step-by-step design procedure considering the possibility of gap or no gap conditions between the slab and columns. The procedure was then applied in a design example and confirmed by time-history analysis.

Acknowledgements

I would like to express my deepest gratitude to my senior supervisor Associate Professor Gregory MacRae for the continuous support of my PhD study, for his patience, motivation, enthusiasm, and immense knowledge. His guidance helped me in all the time of research and writing of this thesis. I wish to sincerely thank my co-supervisor Professor Des Bull for his support, guidance and offering valuable comments throughout this project. I also would like to thank Associate Professor Charles Clifton whose involvement was extremely helpful.

I gratefully acknowledge the financial support of this study provided by the University of Canterbury Doctoral scholarship. I am thankful to all my fellow postgraduate and undergraduate students for their help, advice and friendship over my time at the University.

I would like to express my appreciation to Professor Robert Tremblay and Professor Keh-Chyuan Tsai for their time and reviewing this thesis.

Finally, but by no means least, I would like to give special thanks to my family for your support and encouragement. To my parents, Nader Alizadeh and Roya Bateni, my brother Navid and my wife Shima, thank you so much for always being there with unwavering love, encouragement and patience through my numerous years at University.

Table of Contents

List of Figures

List of Tables

1 Introduction

Floor diaphragms are structural elements that play a key role in providing the building's integrity. They resist gravity loads, transfer such loads to the vertical gravity force resisting (VGFR) system, provide lateral support to vertical elements, resist horizontal forces from a number of sources (including from exterior walls and cladding, inertia, transfer effects, and inclined columns), and transfer these to vertical lateral force resisting (VLFR) systems.

Despite the crucial roles of the diaphragm in structures, there has been relatively little attention paid to diaphragm in-plane performance and design. This may be because diaphragms are different in shape from building to building, and sometimes they are complex to analyse and design. As a result, rigorous design for in-plane forces is often not conducted.

A robust diaphragm design could be performed using three major steps as follows:

1. **Obtaining diaphragm lateral forces**

   Diaphragm strength, stiffness and detailing requirements are related to the diaphragm in-plane demands. For designing the structural elements, structural engineers have often used Equivalent Static Analysis (ESA) together with other requirements. Such approaches are used because of their simplicity to obtain satisfactory results in many cases, based on comparison with field and experimental studies, as well as indications of behaviour from more advanced methods (e.g. Nonlinear Time History analysis). While the simplified lateral force methods have been developed for, and are accepted in designing structural elements, such as beams and columns, different methods are required to obtain diaphragm in-plane demands. This is because even for the elastic response, the dynamic floor demands are different from that of the ESA, and therefore other effects determining the required floor diaphragm strength. As a result, some simplified methods have been proposed by different researchers to obtain diaphragm

global in-plane demands. However, none of them is widely accepted, and each has advantages and disadvantages.

2. Diaphragm analysis and modelling technique

In practice, the elastic analysis is commonly used by engineers to perform structural analysis and design. In order to analyse a 3D building to assess its likely seismic performance, decisions need to be made about the in-plane modelling characteristic of the floor diaphragm. The assumptions made regarding the diaphragm in-plane stiffness affect the forces and displacements in both the diaphragm and the vertical lateral force resisting (VLFR) system of the structure. Furthermore, a modelling method is required to obtain the load path through diaphragm so that it can be detailed appropriately. For this to be used by designers, it should be compatible with commonly available analysis software packages. A number of truss modelling methods exist, and are included in some design guidelines. However, these generally lack a robust basis.

3. Diaphragm strength calculation and load path to VLFR system

Floor diaphragms in most steel structures consist of composite (cold-formed steel decking with concrete and reinforcing bar) slabs because of high construction speed, low costs (as there is no need for other formwork), and lighter weight (reducing the sizes of other frame elements and foundation). Despite these benefits, thin composite slabs may be flexible both out-of-plane and in-plane. The out-of-plane flexibility may increase the chance of diaphragm instability under imposed lateral forces.

Meanwhile, during earthquake events, in-plane diaphragm forces need to be transferred to the structural frames. Generally, force transfer directly from the diaphragm into the column cannot always be considered as a reliable load path since a gap may open between the diaphragm and vertical lateral force resisting element (e.g. column). Therefore, the diaphragm in-plane forces should transfer into the steel beam through

friction and mechanical attachments (e.g. shear studs), along with the beam and to the connection, and from the connection into the column. As a result there are forces on the shear studs, in the beam, and beam-column connection which are often not considered directly in traditional diaphragm design resulting in the possibility of failure.

The above discussion shows that there is a need to address the issues above to achieve a robust diaphragm design procedure that engineers can use with confidence.

1.1 Objective and scope

This project aims to address the need above by seeking answers to the following questions:

1) What are the floor diaphragm in-plane issues?
2) How can diaphragm modelling be undertaken in a simple way that will provide sufficient accuracy, and provide information in a form that is useful to designers?
3) How can the axial compression/tension force capacity of WSP connection be estimated?
4) What are the effects of lateral forces on composite action and how should the number of shear studs be considered in the design of traditional and low damage structures?
5) What are the possible buckling modes in composite floor diaphragms and how should these be considered in design?
6) How can likely diaphragm in-plane demands be estimated using a simple lateral force method which is better than the other methods proposed?
7) How can standard diaphragm design/assessment processes be modified and applied while explicitly considering diaphragm stiffness and strength, shear stud behaviour, and beam system axial strength?

1.2 Preface

Chapter 2 presents an overview of diaphragm in-plane design issues related to steel frame structures. These include methods to estimate diaphragm imposed forces, diaphragm in-plane demands, slab analysis methods, gapping issue, and load transfer mechanism from diaphragm to the VLFR system of the structure. This chapter seeks to answer Question 1.

Chapter 3 presents a diaphragm in-plane modelling method using truss elements. Here a new truss modelling pattern called the "Diamond shape" model is proposed. The diamond shape model is compared with the diagonal shape model in terms of accuracy in assessing beam axial forces and shear stud demands. Also, different truss element methods, using a combination of compression/tension, compression-only and tension-only members are investigated and compared in terms of obtaining in-plane stiffness and internal load path. This chapter seeks to answer Question 2.

Chapter 4 investigates the axial behaviour of web-side-plate (WSP) connections considering the effects of different boundary conditions, connection geometry and initial loading condition. A method is proposed to estimate the axial compressive strength of WSP connections. The proposed method is verified against a number of FE models. This chapter seeks to answer Question 3.

Chapter 5 investigates the effects of slab lateral forces on composite beams subjected to gravity loads. A method is proposed to estimate the lateral force resistance of shear studs placed on a composite/non-composite beam considering gravity load effects. Some recommendations are provided to design composite beams that are part of the diaphragm load path to VLFR systems in both traditional and low damage structures. This chapter seeks to answer Question 4.

Chapter 6 presents diaphragm buckling strength under in-plane forces. Three buckling modes are considered which include 1) inter-rib local buckling, 2) intra-panel diaphragm

buckling and 3) intra-bay diaphragm buckling. All these buckling modes are investigated before and after concrete crack formation. In addition, the effects of gravity loads on the diaphragm buckling loads are studied. This chapter seeks to answer Question 5.

Chapter 7 proposes a diaphragm force method to obtain diaphragm in-plane demands. This method is based on the equal displacement assumption considering elastic ESA lateral forces. The accuracy of the proposed method is compared to the available diaphragm force methods such as ESA, pESA, pushover and NLTH analyses. This chapter seeks to answer Question 6.

Chapter 8 presents steps for diaphragm design based on the findings from the earlier chapters. These are illustrated with a design example. Some parameter studies show the significance of different parameters, including the effect of gapping between the diaphragm and the column. The demands obtained from the design methods are compared with the results of time history analysis. This chapter seeks to answer Question 7.

Chapter 9 presents the overall conclusions from the research and discusses possible future work.

2 An Overview of In-plane Diaphragm Considerations for Steel Buildings in Seismic Zones

2.1 Introduction

Significant advances have been made over recent years in the design of Vertical Lateral Force Resisting (VLFR) systems such as frames and walls in buildings subject to earthquake loading. However, the in-plane seismic performance of floor diaphragms, and connections of such diaphragms to the VLFR elements, has received relatively little attention. This is despite the fact that their integrity is essential for robust building performance. This was shown in the recent February 2011 Canterbury earthquake, where several buildings exhibited diaphragm distress and damage. In particular, one concrete building, the CTV building collapsed killing some 115 persons, and the inadequate diaphragm connection to the lift shaft/stair core was considered to be one of the major causes (Canterbury Earthquakes Royal Commission, 2012).

Standards do consider diaphragm in-plane stiffness, and generally categorise diaphragms as either ‘rigid’ or ‘flexible’ for subsequent analysis. The majority of multi-storey buildings with concrete floors are characterised as having rigid diaphragms. While standards require load paths to be followed, specific efforts to perform this are not always undertaken. This is because (i) reasonable methods to do this are still under development and detailed guidance is not incorporated in standards, and (ii) while commonly used building design software can allow flexible shell/plate diaphragm modelling, or truss analysis, most engineers use the rigid diaphragm option which makes it difficult to obtain diaphragm forces.

In the 1980s, precast floor diaphragm became popular for concrete buildings. This generally consisted of precast beams with timber in-fills and a concrete topping, or hollow core units with a concrete topping. These floor diaphragms often comprised a thin lightly reinforced topping slab on precast units. Since the 1990s, thinner composite floors, consisting

of concrete on cold-formed corrugated steel decking, all supported on a grid-work of steel beams, have increased in dominance. This decking was originally designed to span 3.5m, but different decking profiles, with un-propped spans up to 5.5m and propped spans up to 8.5m, together with simple design tools, were developed in the late 1990s. Such composite slabs are economical as there is no need for other formwork. There is a high construction speed, and the light weight reduces the sizes of other frame elements and foundations. These were implemented in several buildings around New Zealand before the Christchurch earthquake sequence. They are most suitable for steel buildings where through-deck welding is used to connect decking to the beams and place shear studs (Bruneau and MacRae, 2017).

For the reasons listed above it may be seen that it is necessary to understand diaphragm in-plane behaviour so that guidelines can be developed which will ensure robust and desirable diaphragm performance during strong earthquake shaking.

This Chapter seeks to overview diaphragm in-plane issues to progress the understanding of behaviour for an appropriate design. As part of this, answers are sought to the following questions:

1) What are the floor diaphragm in-plane issues?
2) How can seismic demands on diaphragms be obtained?
3) What are the mechanisms by which in-plane forces enter the diaphragms?
4) How can diaphragm internal forces be evaluated?
5) Is it beneficial to provide a gap between the concrete diaphragm and the column?
6) How can diaphragm forces be transferred to VLFR systems?

2.2 Floor diaphragm issues

2.2.1 Rigid diaphragm assumption

Diaphragm in-plane stiffness in a structure can vary between being fully rigid and fully flexible depending on the relative stiffness of the diaphragm and VLFR system. For simplicity, many standards consider that a diaphragm can be treated as being either "fully rigid", or "not rigid" (e.g. "semi-rigid"), which is often termed flexible. Most diaphragms in multi-storey buildings with concrete floors are considered to be rigid, and the building as a whole is generally analysed with software that incorporates the rigid-diaphragm assumption. Such software commonly does not make it easy for designers to consider how load paths should be followed, so separate analyses are required to obtain the likely forces within the diaphragm and the axial forces in the beams. Furthermore, there is currently no accepted consensus about the best way to perform such analyse, and various methods have only recently been proposed.

Several studies have been conducted to investigate the influence of diaphragm flexibility on building dynamic response. In 1961 the validity of the rigid-floor assumption was questioned by Blume et al. (1961). Goldberg and Herness (1965) investigated the dynamic properties of multi-storey buildings considering floor and wall deformations using generalized slope deflection equations. Analyses of a ten storey building with a 1:8 plan aspect ratio indicated that the first two mode shapes and frequencies were similar for both flexible and rigid diaphragm assumptions. While, higher modes showed considerable bending forces and floor deformations. Such higher modes are generally overlooked when floor deformation is neglected as a result of the rigid diaphragm assumption.

Shepherd and Donald (1967) investigated the influence of floor flexibility on structure modal properties. They found that neglect of in-plane floor flexibility did not significantly change the computed dynamic properties.

Nakashima et al. (1981) investigated the effects of RC floor slab diaphragms on building response. A building with a 1:6 plan aspect ratio was analysed under earthquake loading. It was found that diaphragm flexibility did not significantly alter the structure fundamental period or total base shear. However, the rigid diaphragm assumption caused significant changes in base shear distribution between the lateral load resisting systems.

Jain and Jennings (1985) presented an analytical model for dynamic analysis of one and two storey structures with flexible diaphragms spanning between end walls. For a two storey building with a 1:5 plan aspect ratio, the first two modes, which were dominated by floor or roof in-plane deformations, made the largest contributions to the total base shear.

Celebi et al. (1989) observed mid-span floor acceleration magnifications of a single story gymnasium building during the 1984 Morgan Hill earthquake. Although the plan aspect ratio of the building was about 1:1.25, the recorded acceleration amplifications of 4.2 and 5.0 in N-S and E-W directions respectively were attributed to being due to diaphragm flexibility.

Kunnath et al. (1991) found that for reinforced concrete buildings with narrow rectangular plans and end walls as shown in Figure 2-1, when floor flexibility and inelasticity were considered the rigid diaphragm assumption led to non-conservative estimations of strength and ductility demands on interior frames. The demands increased with increasing numbers of longitudinal spans and decreasing numbers of stories.

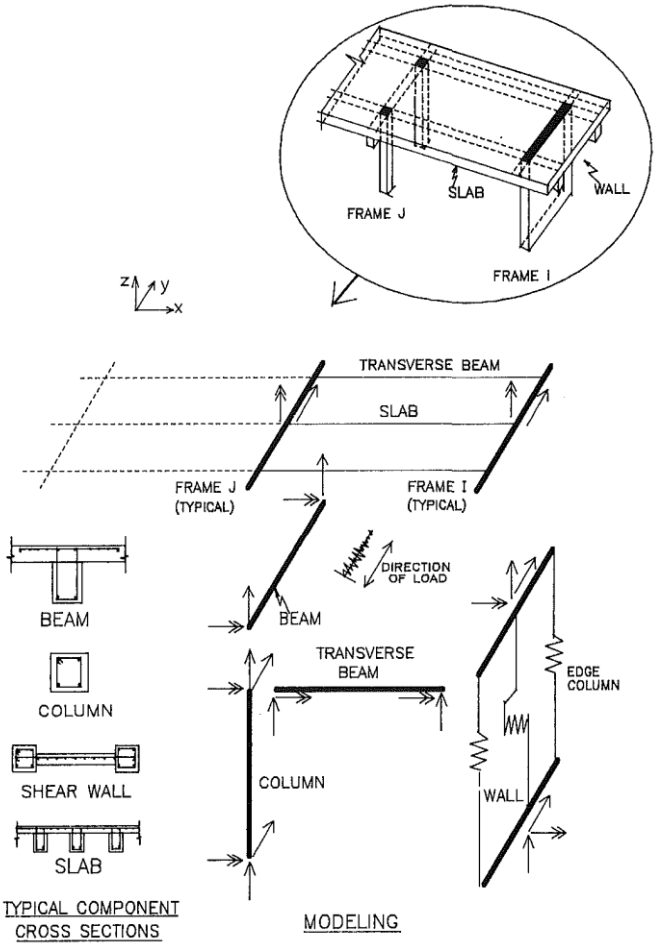

Figure 2-1. Component modelling scheme showing degrees of freedom (Kunnath et al. 1991)

Similar studies by Suto and Asayama (1988), Aktan and Nelson (1988), Yang and Liu (1988), Moon and Lee (1992), Saffarini and Qudaimat (1992), Dolce et al. (1994), Colunga and Abrams (1996), Tremblay and Stiemer (1996), Masi et al. (1997), Ju and Lin (1999), Fleischman et al. (2002), Barron and Hueste (2004), Kim and White (2004), Basu and Jain (2004), Lee et al. (2007), Hadianfard and Sedaghat (2012) and Humar and Popovski (2013) reached similar conclusions.

Sadashiva et al. (2012) studied diaphragm flexibility effects on symmetrical structures using elastic and inelastic time history analysis and proposed a methodology for quantifying diaphragm flexibility effects in symmetrical structures considering different deformation types, different vertical lateral force resisting element configurations and different structural heights. Figure 2-2 shows examples of structural configurations considered. The results

indicated that the fundamental natural period of structures increases with increasing diaphragm flexibility. This effect is more significant in one storey structures and reduces with increasing structure height.

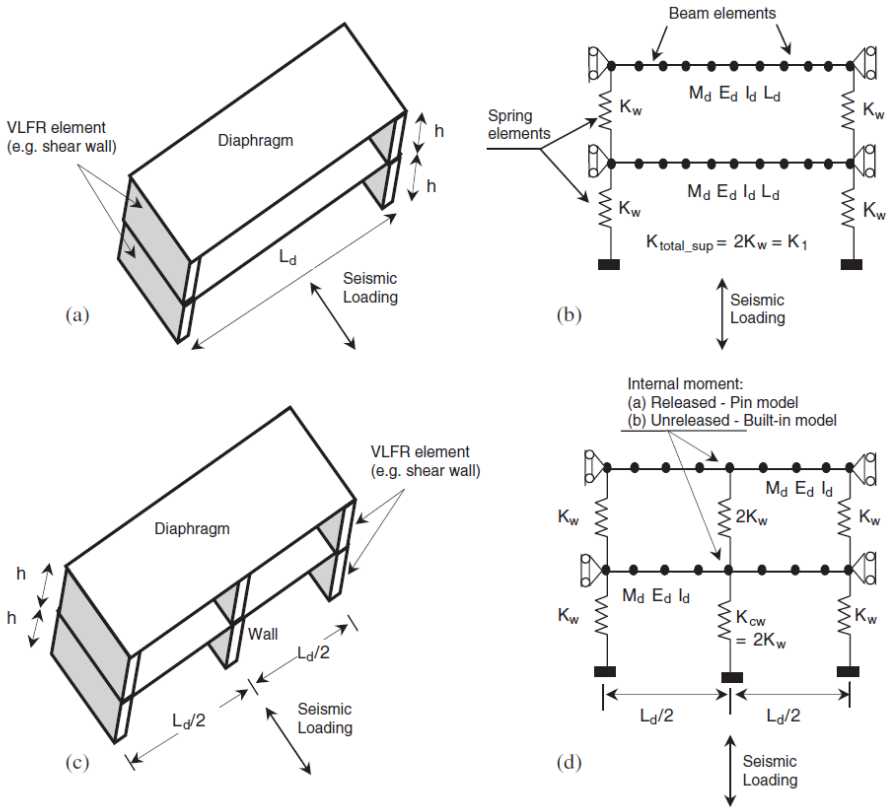

Figure 2-2. Example of structural configurations used for floor flexibility effects (Sadashiva et al. 2012)

Moroder (2016) studied the dynamic behaviour of multi-storey post-tensioned timber frame and wall structures using non-linear time history analyses considering diaphragm flexibility. The parameters investigated include number of storeys, diaphragm flexibility and hysteretic damping. Based on the analyses performed, the fundamental period of stiff structures was found to be more sensitive to diaphragm flexibility than it was for flexible structures. The influence of higher modes was most significant for shear and moment distributions in frame structures with four or more storeys and wall structures with six or more storeys.

Based on the literature above, overestimating the diaphragm stiffness (e.g. rigid diaphragm) may have the following consequences:

1) Structural periods may be underestimated resulting in higher acceleration and lower displacement estimates.
2) Underestimation of demands on components not designated as being part of the seismic force-resistance system. This includes:
   a) Gravity frames located at the position of highest drift, as shown in Figure 2-3, where demands may be underestimated by the rigid diaphragm assumption. This may lead to non-ductile diaphragm failure or structural instability due to high drift demands in the gravity system (Fleischman et al. 2002).
   b) Elements such as slab-column and slab-wall connections, and non-structural elements such as cladding attachments (Moehle et al. 2010).
3) The floor rigidity assumption affects lateral force distributions between VLFR systems.

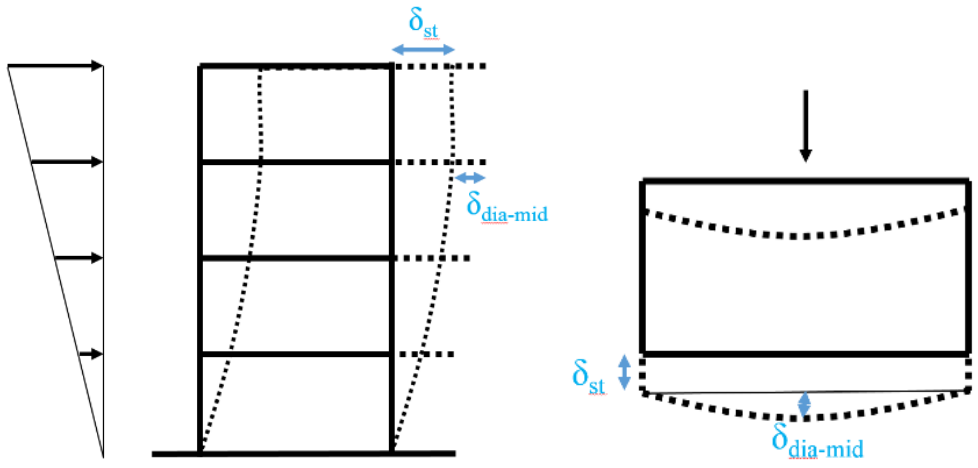

Figure 2-3. Diaphragm flexibility effect (Fleischman et al. 2002)

2.2.2 Neglecting the beam axial force in beam and connection design

Beams in moment-frames are often considered to carry only bending and shear with the slab transferring inertia and other lateral forces to the VLFR system through compression

bearing of the slab on the column faces. However, since slab inertia forces act in the same direction as the frame sways, the column moves away from the slab at location "A" shown in Figure 2-4, and a gap between the slab and column opens. Because of this, slab inertia forces cannot go directly from the slab into the column. Instead, the forces must move into the steel beam through friction and mechanical transfer using studs (MacRae and Clifton, 2015a). These axial forces must pass through the beam plastic hinge regions and through the connections at the beam ends. Consideration of such forces should be part of the design procedure. It seldom seems to be incorporated in practice. Also, if there is no construction gap between the slab and column then, as the column sways, the column bears against the concrete slab on the far side of the column as shown on the right hand of the column in Figure 2-4. This increases the forces that the slab must transfer into the beam, and which the beam must transfer back to the columns, often through the plastic hinge regions and connections. These beam axial forces may decrease the structure's lateral strength and deformation capacity.

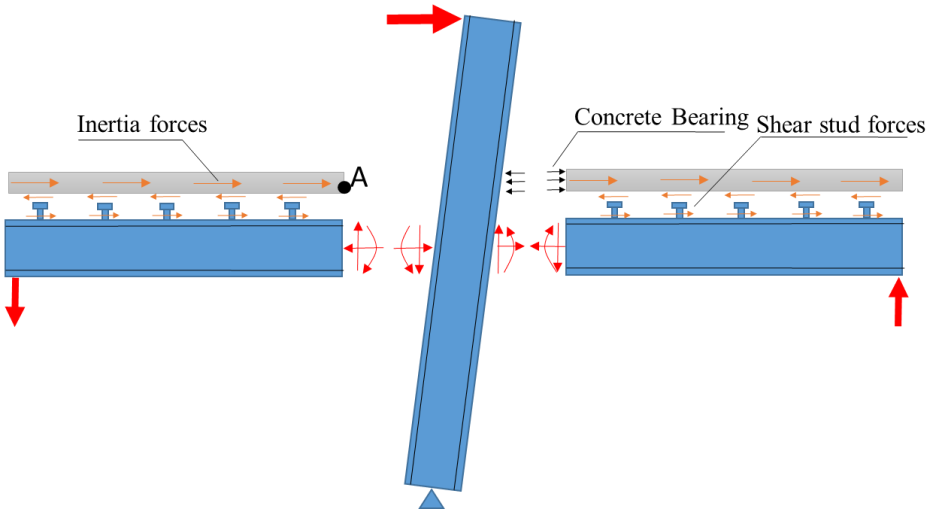

Figure 2-4. Beam axial forces (MacRae and Clifton, 2015a)

2.2.3 Acceptable floor slab thickness

The minimum thickness of concrete required on top of the steel decking (i.e. the topping) is specified in different building standards and design guides. This may be governed by fire

insulation, shear stud, acoustic insulation, seismic or in-service vibration considerations. ANSI/SDI (2011) and NZS3101 (2006) both require that the minimum concrete thickness on top of the steel deck shall not be less than 50 mm. The background to this dimension is not clear.

The ANSI/SDI (2011) states that "the concrete thickness above the top of the steel deck shall not be less than 2 inches (50mm), nor that required by any applicable fire-resistance rating requirements". The Canadian steel design standard (CSA C. S16-14) requires 65mm effective thickness, which effective thickness is defined as overall slab thickness minus the height of the steel decking corrugation. The same minimum slab thickness, 50mm, on top of the steel deck is specified in NZS3404 (2007) Clause 13.3.2.2.1(e). However, another limitation specified in Clause 13.3.2.3(e) relates to the minimum concrete cover required on top of the shear studs which is based on the concrete cover criteria for different environmental conditions from NZS3101 (2006). This has a minimum value of 20 mm for indoor condition and intended minimum life of 50 years, which makes the total minimum topping thickness equal to 40+20=60 mm. The topping thickness is above the top of the steel decking, rather than above the depth of the main trough, as some decking profiles have a significant height above the main trough depth (e.g. ComFlor 80).

Out-of-plane global, or local, buckling due to slab in-plane forces, together with any initial out-of-plane forces/deformations, is not explicitly considered in design standards such as NZS3404 (2007). These buckling, and the related crushing, modes may limit the ability of the slab to reliably carry diaphragm in-plane transfer forces during earthquake shaking as shown in Figure 2-5. The diaphragm buckling is investigated in Chapter 6 in detail.

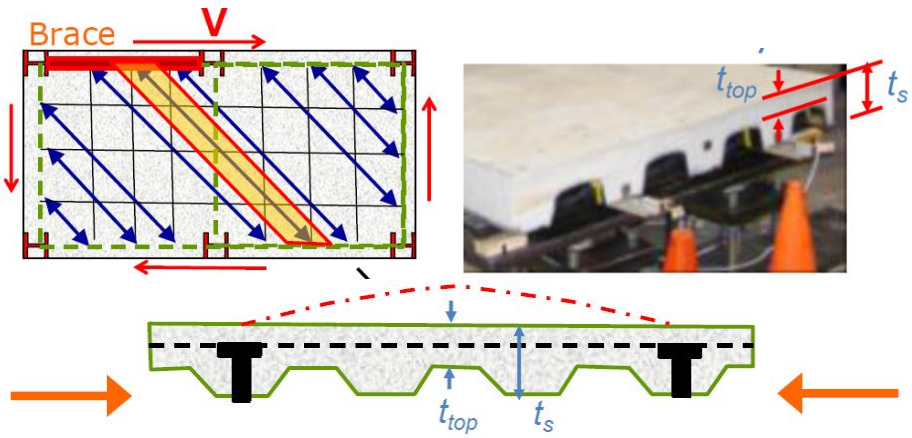

Figure 2-5. Diaphragm buckling due to large in-plane imposed forces (MacRae and Bull, 2015)

2.2.4 Elongation in composite beam elements

During earthquake events, "beam growth" occurs in reinforced and pre-stressed concrete moment frame structures. This is because concrete beams are generally designed for tensile failure modes involving reinforcement yielding rather than concrete crushing. This means cracks develop under inelastic demands and these cracks are not fully closed on load reversal. Crack widths can increase with subsequent loading cycles and causes beam elongation which can push columns apart causing additional demands on the structural frame and damage and loss of support to precast floor systems.

In steel structures, with no construction gap, the neutral axes in the beams on different sides of the column will be both in slab when the slab is strong in tension, as shown in Figure 2-6a. However, when the slab is weak in tension, the neutral axes are at different heights as shown in Figure 2-6b. Due to flexure on the right-hand side, the neutral axis is at the beam centre. That on the left-hand side of the beam may be in the slab. This would imply more tension yielding at the centre of the beam than compression yielding and some net elongation. This elongation would be expected to be much less than that of a concrete beam where cracks/gaps open at both ends of the beam.

Beam elongation measurements by MacRae et al. (2013) on some steel beam-column-slab subassemblies showed that the beams tend to shorten as a result of buckling of the beam

and spalling of the concrete at the slab/column interface. The residual shortening, measured as the shortening at zero column drift, was less than 2mm during cycles up to about 3.5% drift. This would probably not be significant for a typical structural beam, but subassemblies showing gap opening characteristics such as those with reinforced concrete beams, can place much greater demands on the diaphragm (SESOC 2011).

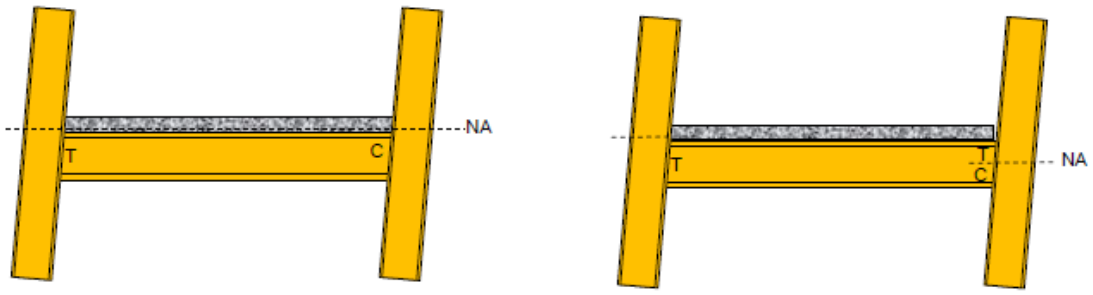

a) Strong slab around column b) Weak slab around column

Figure 2-6. Steel beam elongation (MacRae et al. 2013)

2.2.5 Load path concept in diaphragms

Although the load path concept is emphasized in undergraduate structural classes around the world, it is not generally considered in diaphragm design. One reason may be that there is currently no generally accepted procedure for evaluating diaphragm forces during an earthquake event. Some methods to estimate diaphragm forces are discussed in Section 2.3.

In addition, even if the diaphragm-imposed forces are evaluated realistically, an appropriate method is needed to analyse the floor diaphragm in a rational and suitable manner for a design office. Several methods have been proposed by researchers in this regard. These are mostly for pre-cast and cast in-situ concrete floors and they might need some modification for diaphragms using cold-formed decking.

2.2.6 Slab effects on subassembly strength and degradation

For floor slabs on steel beams, shear studs are generally provided to make a steel-concrete composite member which is considered to have greater strength and stiffness than

the steel beam alone under gravity loads. Also, in the case of lateral loading, the beam is generally considered to have an increase in stiffness and strength along its length as a result of the composite action. However, the current NZ design approach (NZS3404, 2007) states that under lateral seismic loading:

1) The strength at the end of the beam should be that due to the non-composite steel beam alone. (This is because the effect of the slab is not considered to be reliable.)
2) For determining the beam over-strength effects to compute column demands, the slab effect should be explicitly considered (if the slab is in contact with the column) and methods to do this are specified. This over-strength requirement is unique to NZS3404 (2007).

MacRae et al. (2013) recommend that when:

1) Slabs are cast against the column and where no special detailing is provided to confine the concrete at the member ends, then NZS3404 (2007) method should be followed.
2) Slabs which are not cast against the column, but which are isolated/separated by means of a gap placed between the concrete and the column, slab effects should not be considered on the flexural strengths at the end of the beam for either beam design, or beam over-strength calculation. However, there are concerns that making a gap in the slab may increase beam axial forces and decrease the flexural resistance available of beam ends. Gapping issues are discussed in Section 2.6 in more detail.
3) Slabs that are full depth for a significant distance from the column face, and where special detailing is provided to effectively confine the slab concrete at the

beam-ends against the column, then the slab effect may be considered both for beam strength design and for over-strength design.

2.3 Methods to estimate diaphragm in-plane forces

In order to conduct a realistic analysis of floor diaphragms, global force demands affecting the diaphragms are required. Procedures for estimating floor diaphragm imposed forces for design must:

1) Be simple enough to be used in design offices,
2) Be compatible with the commonly used elastic 3D software,
3) Indicate likely magnitude of demands.

The following methods have been proposed:

2.3.1 Full-3D non-linear time history analysis (NLTH)

This method evaluates the nonlinear response of a structure, including the diaphragm, to given ground motion, or suite of records. To do this, it requires the diaphragm to be modelled as an assemblage of elements and members with appropriate boundary conditions and member properties, not just modelled using a rigid diaphragm option. Although this method presents the closest results to the exact solution for any given ground motion, it is difficult to implement it appropriately in a conventional design. This is because it requires considerable technical knowledge and information about the nonlinear behaviour of different structural elements.

2.3.2 Method proposed by Sabelli et al. 2011

Sabelli et al. (2011) suggested conducting a number of frame analyses to capture the likely combination of transfer and inertial effects. *N* different analyses are needed in each direction for a frame with *N* levels. In the equivalent static analysis method, floor forces

reduced for ductility are applied at each level, but greater forces, corresponding to the acceleration expected of the diaphragm, are applied at the level of diaphragm considered. The diaphragm acceleration may be found using response spectrum analysis. The force distributions are shown in Figure 2-7. A significant issue is that the determination of these diaphragm specific forces requires judgement from the user to extract meaningful information from the response spectrum analysis. Because forces lose their sign during modal combination process and they are not in equilibrium.

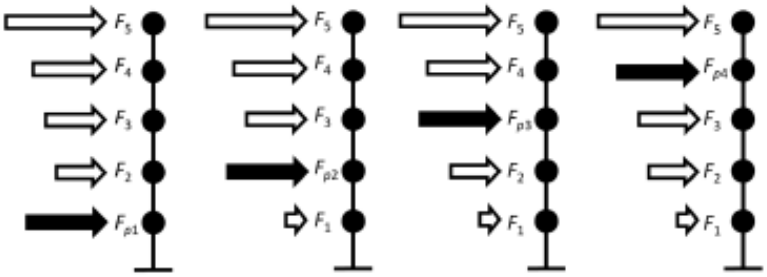

Figure 2-7. Force distribution for considering transfer and inertial forces at each storey (Sabelli et al. 2011)

2.3.3 Equivalent Static Analysis (ESA) and Over-strength ESA (OESA)

The Equivalent Static Analysis (ESA), and the other methods below, are applied to an elastic model of the structure such as those commonly considered in design.

The ESA method is based on the assumption that the first mode dominates the building deformation and all the structure mass participates in this mode. Although this method can be used for obtaining frame and wall design forces in some cases, it underestimates diaphragm in-plane demands especially in lower stories (Bull, 1997, Nakaki, 2000, and Fleischman et al. 2002).

The ΦESA method is the ESA scaled by the building's over-strength factor. It better estimates floor diaphragm forces, but the floor diaphragm forces near the base of the structure may be underestimated.

An alternative method by Tiong and Lyes (2014), applies the over-strength force distribution to the frame, but making sure that the forces at the level considered are no less than those resulting from the anticipated in the Parts and Components section of the loading standard. This method has similarities to that of Sabelli et al. (2011) but it is more conservative. This approach is more suitable for diaphragms that do not act as transfer diaphragm which means the inertia forces govern the design criteria.

2.3.4 pseudo Equivalent Static Analysis (pESA)

The pseudo Equivalent Static Analysis (pESA) method (Bull, 1997 and Gardiner, 2011) modifies the ESA method to account for:

1) Increased forces in the lower levels of structure, and
2) Over-strength actions, which develop in the lateral force resisting systems.

Both inertia and transfer force effects result from the analysis with one lateral force distribution. Figure 2-8 illustrates the ESA, in the blue line, and pESA forces, in the yellow line.

The pESA is only recommended for structures up to about nine stories in height because for taller (longer period) structures, the forces associated with the peak ground acceleration unrealistically dominate the floor in-plane demands at all periods.

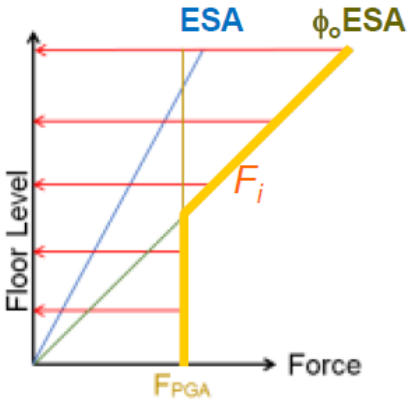

Figure 2-8. Schematic force distributions of ESA and pESA (MacRae and Bull, 2015)

2.3.5 Parts and Components method (P&C)

The "Parts and Components" method is a force-based design approach, which is used for design of "parts" or "components" of a structure. These forces are considered to be applied at every level independently and not together with those at other levels. In this case, inertial effects on the diaphragm are obtained, the transfer forces due to the deformations of the other stories are not considered. On the other hand, if these forces are applied simultaneously to the whole structure, the demands are likely to be overestimated, because the peak floor accelerations at different floors do not occur at the same time.

This method is applicable to floors in structures where the transfer forces are not significant. If the seismic resisting systems acting in the same direction of loading are different, or if they change location in plan, then the P&C method does not take into account the actions from transfer diaphragm effects.

A variation of this method is proposed by Cowie et al. (2014) where the floor height coefficient (C_{Hi}) is considered equal to 1.6 instead of using Clause 8.3 of NZS1170.5 (2004).

2.3.6 Pushover analysis

Pushover is a nonlinear-static analysis method where a structure is subjected to gravity loading and a monotonic displacement-controlled lateral load pattern. The lateral forces are increased until either the total capacity of the structure is exceeded, or a predetermined displacement of the structure is reached. A variation of the pushover method is adaptive pushover method that was developed to mitigate the uncertainties related to the lateral force pattern. In this method, the lateral loading pattern is updated at each loading step according to the structure lateral deformation and structure stiffness matrix.

The results of this method may be sensitive to the selected loading pattern and target displacement. Pushover analysis may underestimate storey drifts at lower levels (Fenwick

and Davidson 1991, 1997). Also, the maximum diaphragm force may not occur at the maximum lateral displacement of the structure as shown in Appendix A.

2.3.7 Modal response spectrum method

Modal response spectrum method (RSA) is a linear-dynamic statistical analysis method which measures the contribution from each vibration mode to indicate the likely maximum seismic response of an elastic structure. The modal response spectrum analysis is generally used when the higher mode effects are considered to be significant. Modal response spectrum analysis accounts for higher mode effects. However, its results cannot directly be used for diaphragm analysis and need engineering judgment. The design actions lose their sign through the modal combination process and are not in equilibrium.

2.3.8 Discussion on methods to estimate diaphragm forces

As described above, several methods exist for evaluating diaphragm in-plane demands. These range from advanced methods, like the use of nonlinear time history analysis, to simple methods, like ESA. Amongst the simple methods that are used with elastic frame analysis there is no correct method for estimation of diaphragm in-plane demands. The following points are noted:

1) For elastic multi-story buildings, peak floor forces are greater from those implied from methods used to obtain peak shears at each level for elastically responding structures due to the way individual storey higher mode accelerations need to be combined. Therefore, scaling the ESA method forces to the elastic level does not strictly estimate the likely peak elastic floor forces at that particular level.
2) Many studies have been conducted to estimate peak floor accelerations at specific floor levels. These differ markedly between researchers because they depend on

the structural framing type, the records used, and the analysis assumptions. (E.g. Dantanarayana et al., 2012).

3) Demands based solely on peak accelerations considered on a floor diaphragm at one level by itself are not generally appropriate for use in design because associated inertial forces are not generally large. (They can generally be carried by a low number of shear studs). Transfer, bearing and compatibility forces can cause much larger diaphragm demands.
4) The duration of the peak force/acceleration demand may significantly affect the structural response. For example, if high force/acceleration demands occur only briefly, causing a small inelastic displacement, then its effect may be minor. Designing for the peak values may therefore be conservative (MacRae and Bull, 2015, Bruere and Colley, 2015).

Methods to estimate diaphragm in-plane forces are discussed and investigated in Chapter 7 in more detail.

2.4 Slab in-plane demands

In Section 2.3, the total in-plane demands on the diaphragm at any level for frame analysis were described. Here, more specific details about how force gets into a diaphragm are discussed.

2.4.1 Inertia forces

In steel frame structures, concrete diaphragms comprise a significant portion of the building mass. Therefore, higher inertia forces may be imposed on the floor diaphragm and consequently on the connections between the diaphragm and the steel frame. Diaphragms are expected to remain elastic, or almost so, during seismic shaking, while other elements are expected to dissipate the seismic energy.

Inertia forces of floor slabs are often considered to be transferred to the steel frame through compression of the slab on the column faces. However, as was shown in Figure 2-4, since slab inertia forces act in the same direction as the frame sways, a partial gap opens at location “A”. Therefore, slab inertia forces cannot directly transfer into the columns. Instead, the forces must move into the steel beams through friction and mechanical transfer using shear studs, along the beam causing axial force, through the beam plastic hinge and connection into the columns (MacRae and Clifton, 2015b).

Figure 2-9 shows two cases of transferring the inertia forces from the slab to the frames. Jensen (2004) conducted finite element analyses of a floor slab assumed to be restrained at the columns as shown in Figure 2-9a. This was assumed to be representative of a column in a reinforced concrete frame. Here, it is assumed that the slab bears onto the column and inertia forces are directly transferred to the column, so compression struts are formed in the slab with the beams acting as tension ties. The forces tend to be carried by the nearest columns. Beams between the columns are assumed to carry forces perpendicular to the direction of loading to balance the diagonal strut forces. Figure 2-9b shows the situation in steel frame structures where the gap occurs between the slab and column, so the inertial forces are transferred to the steel frame not at the column location, but through shear studs along the beam length. The beam then carries these forces through axial tension/compression to the column. It may be seen that tension ties are needed within the slab perpendicular to the direction of loading to balance the diagonal strut forces.

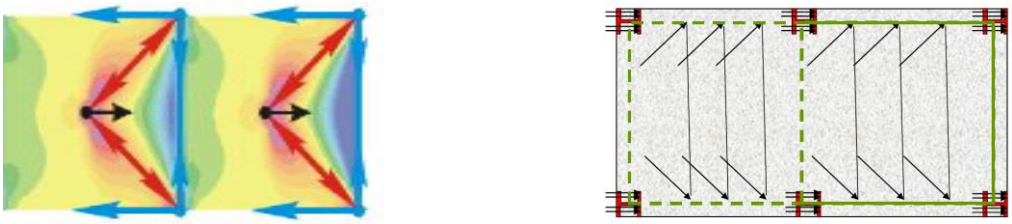

a) Slab bears on columns (Jensen, 2004)

b) Actual case in steel structures (MacRae and Bull, 2015)

Figure 2-9. Inertia forces in floor diaphragm

2.4.2 Transfer forces

Transfer forces are diaphragm in-plane shear forces, which occur as a result of deformation incompatibility of different VLFR systems such as moment frames and RC walls wanting to move different amounts at different levels under the applied lateral forces. The classic illustration of transfer forces is shown in Figure 2-10 (Paulay and Priestley, 1992). Here the wall and frame want to move together at the base, and apart near the top. This causes compression and tension in the links between these two VLFR systems. These links represent the diaphragms, which must carry these forces as in-plane diaphragm transfer forces.

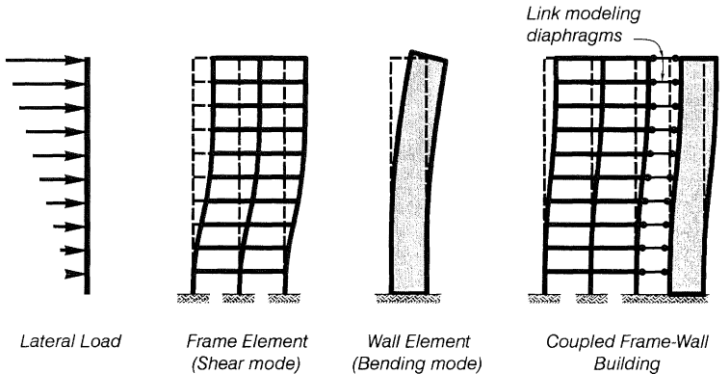

Figure 2-10. Transfer forces due to deformation incompatibility (Paulay and Priestley, 1992)

While transfer forces are generally illustrated as being an issue for multi-storey structures, they can also affect single storey structures. This is shown in Appendix A where:

1) The magnitude of the transfer force can depend on the strength and stiffness of the VLFR elements, and
2) The peak transfer force demands do not necessarily occur at the peak floor lateral displacement.

In multi-storey structures the magnitude of transfer forces in diaphragms may be significantly increased where there are discontinuities in plan location of the VLFR elements, generating the need to transfer forces between the two displaced VLFR systems above and below. A common discontinuity in plan in the vertical elements is at a podium slab.

It has been suggested that transfer forces in multi-storey frames may be reduced by detailing column splices as pins as shown in Figure 2-11 (MacRae and Bull, 2015). However, making all columns in the building effectively continuous provides additional redundancy and helps with frame self-centring, both desirable features that may be reduced if the splices are designed as pins.

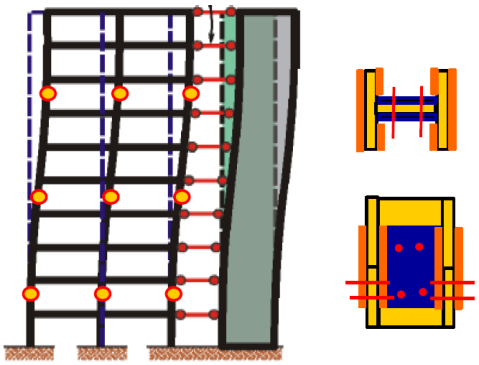

Figure 2-11. Decreasing transfer forces by detailing column splices as pins (MacRae and Bull, 2015)

Overall, the magnitude of transfer forces may be limited by the following:

1) The shear stud strength
2) Beam/connection axial strength
3) Concrete diaphragm compression/ tension /shear capacity, and
4) A column mechanism, such as that shown in Figure 2-12. It is indicated as being a possibility in studies by Haselton and Deierlein, (2007) on building collapse

under very severe motions. It is recognized that this is not a desirable mechanism for overall frame performance.

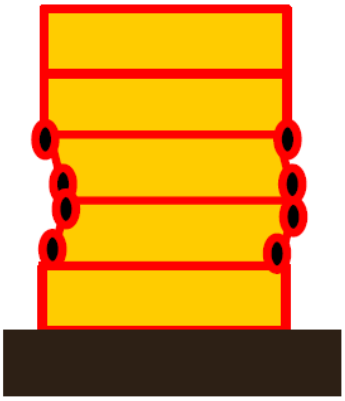

Figure 2-12. Column mechanism (Haselton and Deierlein, 2007)

Where beams in the gravity system are used to transfer diaphragm forces into the seismic resisting system, such as shown in Figure 2-13a, the gravity beams form collectors (both tension and compression) and must be designed appropriately. To carry these forces, an additional plate may be required above the beam at the connection of the beam to the column as shown in Figure 2-13b. Recent studies by Weir and Clarke (2016) have indicated that the axial strength of an eccentric shear cleat connection may be less than one-half of that of a yielding connection with no cleat eccentricity for a typical connection.

The slab must also be strong enough to reliably carry the transfer forces illustrated in Figure 2-13a without buckling or crushing. Studies, similar to that initiated by Luo et al. (2015), are therefore required to evaluate slab performance for design (Figure 2-14).

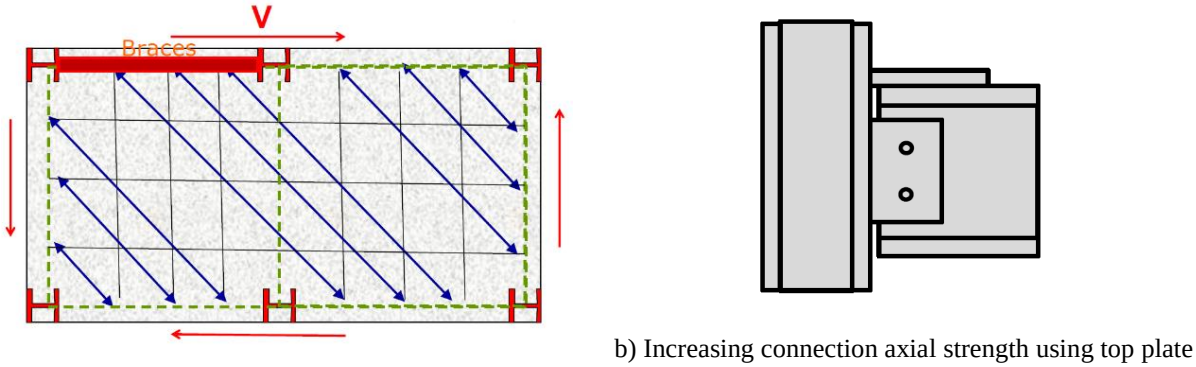

a) Transfer forces

b) Increasing connection axial strength using top plate detail

Figure 2-13. Transfer force effect example (MacRae and Bull, 2015)

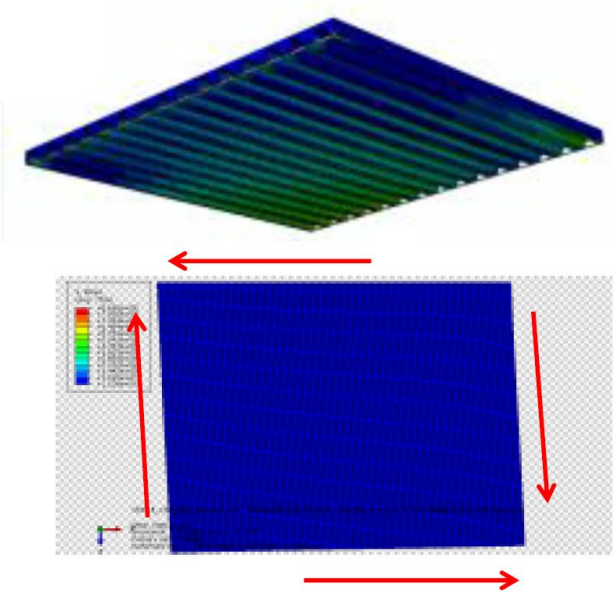

Figure 2-14. Numerical study on slab performance (Luo et al., 2015)

2.4.3 Slab bearing forces

If there is no construction gap between the slab and column, then as the column sways, it bears against the concrete slab on the far side of the column from point "A" in Figure 2-4 (MacRae and Clifton, 2015b). This causes an extra bearing force on the slab. This force must be transferred through the slab, shear studs, beam, and back to the column.

The magnitude of slab bearing forces is a function of concrete compressive strength, number and strength of shear studs, and force transferring mechanisms into the column. Force limiting mechanisms depend on parameters such as shear key types between column

flanges, beam/connection strength, and concrete confinement as discussed by Chaudhari et al. (2015) and MacRae and Bull (2015). If confinement of the top surface of the concrete slab is not provided beside the column, the slab can spall due to bearing during the large deformations. Other mechanisms of slab strength loss, such as shear key fracture, and longitudinal splitting, can also occur (Chaudhari et al. 2015, MacRae et al. 2013 and Hobbs et al. 2013).

Disadvantages of allowing the concrete slab to bear against the column include the following:

1) Bearing of the concrete against the column increases the beam moment input into the column, $M_{p,beam}$. This is typically about 30% for typical members and it requires larger column sizes (MacRae and Bull, 2015).
2) Since it is difficult to confine the concrete slab properly, after spalling of the concrete occurs, the composite beam strength, $M_{p,beam}$, degrades to that of the bare steel beam alone, $M_{p,bare\ beam}$, as shown in Figure 2-15 (Chaudhari et al. 2015).
3) Once spalling of the concrete occurs in one direction, the strength of the subassembly in different directions changes increasing the likelihood of deformations ratcheting in one direction only (MacRae and Bull, 2015).
4) The composite action increases the beam axial forces, which act through the connection and beam plastic hinge (MacRae and Bull, 2015). Some beam growth effects are also possible.

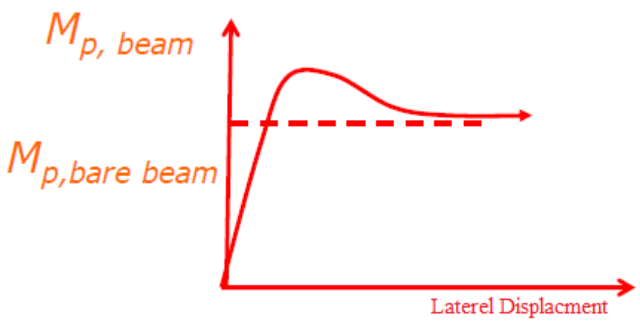

Figure 2-15. $M_{p,beam}$ composite degrades to $M_{p,bare\ beam}$ due to lack of confinement (Chaudhari et al., 2015)

In order to avoid these effects, there have been efforts to more economically design frames with slabs. These include:

1) Designing the slab around the column to limit strength degradation during large deformations by special detailing around the column (MacRae et al. 2013 and Chaudhari et al. 2015).
2) Providing a gap between the column and the slab as shown in Figure 2-16 to avoid bearing effects. This gapping issue is discussed further in Section 2.6.

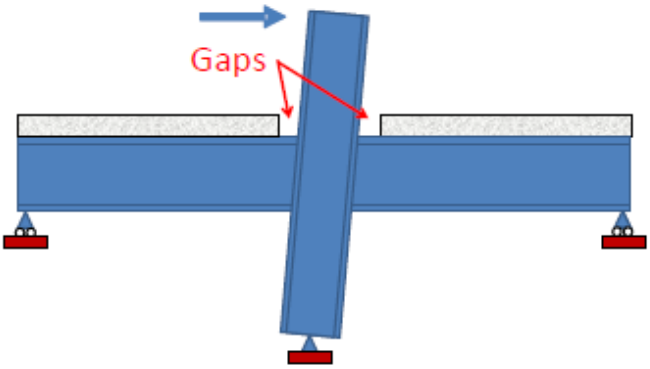

Figure 2-16. Intentional gap between the column and the slab (MacRae and Bull, 2015)

2.4.4 Compatibility forces

When neutral axes of beams on either side of the column are at different heights due to the composite action of slab as shown in Figure 2-6b, the distance between beam-ends tends to increase, causing slab (compression) forces and beam (tension) forces (MacRae and

Clifton, 2015b). This elongation would be expected to be much less than that of a concrete beam where cracks/gaps open at both ends of the beam (MacRae et al. 2013) but it should be taken into account in analysis because it can impose extra forces on column as well as on beam plastic hinge region and beam-column connection. As shown in Figure 2-17, the slab effect on moment-resisting structural systems can be modelled (Umarani and MacRae, 2007 and Ahmed et al., 2013), but it is not considered in most analyses.

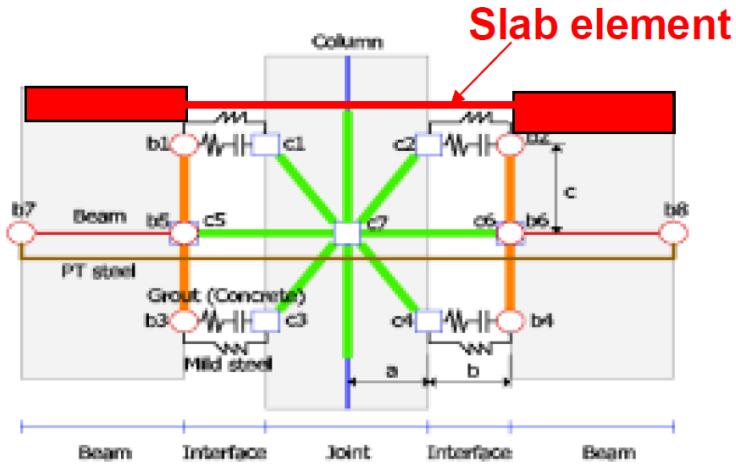

Figure 2-17. Modelling the composite action effect (Umarani and MacRae, 2007 and Ahmed et al., 2013)

2.4.5 Forces due to interaction with other elements

As floor diaphragms tie structural elements together, they interact with other elements. This interaction may impose various forces on the diaphragms. Inclined columns, as shown in Figure 2-18, can develop diaphragm in-plane tension and compression forces due to gravity and overturning actions (Moehle et al. 2010 and Scarry, 2014). These forces should be taken into account in diaphragm design.

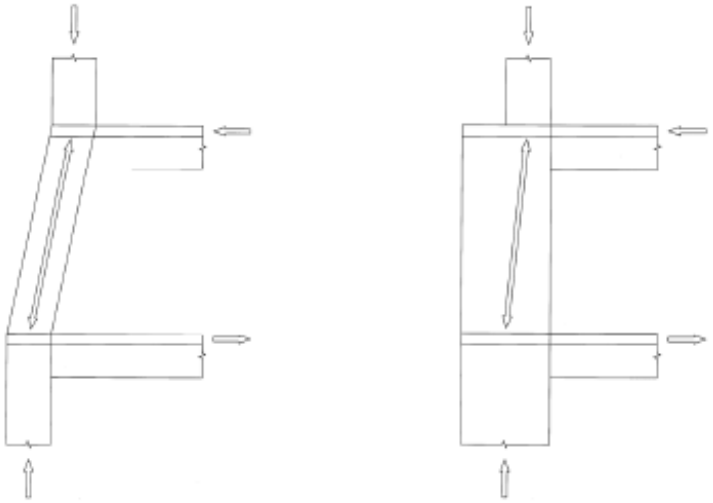

Figure 2-18. Diaphragm forces due to sloped column (Scarry, 2014)

Ramps and sloping diaphragms are another sources of interaction forces. The effect of ramps can be more significant especially where they connect different stories of a structure and story shear can migrate out of the vertical elements of the seismic force resisting system through the ramp in the form of shear or axial forces (Moehle et al., 2010). This effect should be considered in analyses and modelling the structure. It is particularly important in car parking structures if the lower end of the ramp cannot slide.

2.5 Slab analysis

After evaluating the global diaphragm lateral forces using the methods described in Section 2.3, separate diaphragm analysis is required to determine the load paths and diaphragm internal forces for design purposes. The forces on the diaphragm are obtained from the difference in shear above and below each vertical element passing through the floor system. These, together with the applied inertia forces at the diaphragm, result in a floor system that is in equilibrium, and the different components can be designed (Fenwick et al. 2012). Slab analysis methods include ‘detailed Finite Element Method (FEM)’, ‘Deep Beam’, and ‘Truss model’. These methods vary in the level of complexity and accuracy.

2.5.1 Detailed finite element method analysis

The finite element method is one of the most widely accepted numerical solutions for exploring engineering problems. Modelling a diaphragm using FEM (include shell or solid elements) can be beneficial for evaluating the transfer forces among vertical lateral load resistance elements and inertia forces, especially for irregular diaphragms in shape and around large openings in the floor plan as well as the impact of ramps in parking garages (Moehle et al., 2010).

When using a finite element model, the continuous nature of the floor diaphragm is considered. This advantage helps to capture the stresses around the floor openings. Also zones where stress concentrations may be expected to occur are readily identified (Gardiner, 2011). In spite of this,

1) FEM programs are often expensive, difficult to use and require significant pre and post-processing times for each analysis (Scarry, 2014), and
2) stresses and strains do not relate directly to design and it may be difficult to estimate how much reinforcing steel is required in specific locations.

2.5.2 Deep Beam

The ‘Deep Beam’ method is appreciated because of its simplicity. It considers the diaphragm as a deep beam with a distributed load. The approximation of a deep beam method is only appropriate in regular floor plans. Figure 2-19 illustrates the deep beam design analogy of a typical floor diaphragm.

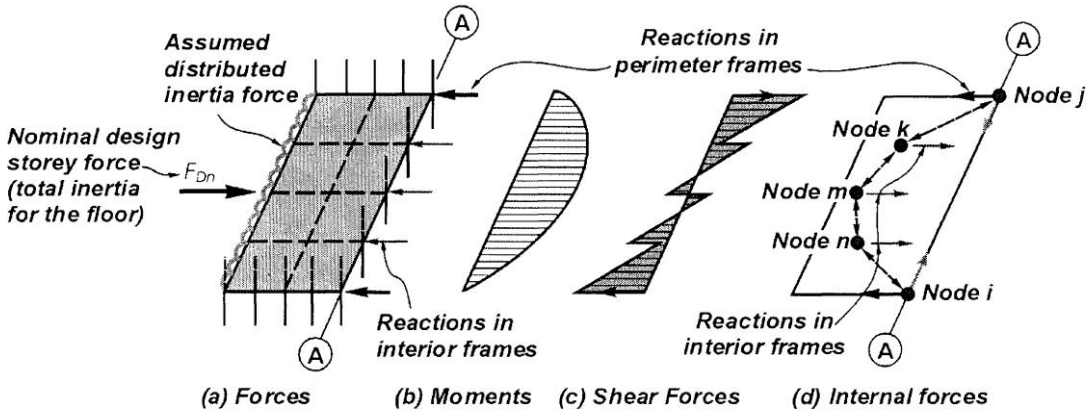

Figure 2-19. Graphical representation of a beam analogy (NZCS, Technical Report No. 15, 1994)

This method provides adequate demand for buildings with regular geometries and two lines of continuous vertical elements as support of floor slabs. In floor slabs with more than two supports (VLFR elements), the equivalent beam on springs model, which is more complex, may be appropriate to determine diaphragm demands (Moehle et al. 2010). Figure 2-20 shows a typical equivalent beam on springs model. This method is usually used for one storey buildings because the stiffness of springs can be calculated easily, while for multi-storey buildings, computer models are needed.

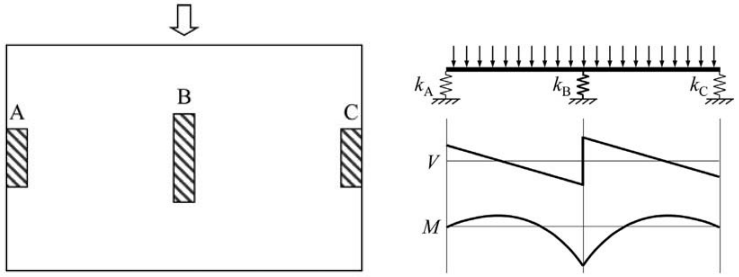

Figure 2-20. Typical deep beam on springs model (Moehle et al., 2010)

In buildings with more complex configurations of VLFR elements, another approach is to use the distribution of diaphragm inertial forces to vertical elements from a computer model and then implement the corrected equivalent beam model to determine the diaphragm demands (Moehle et al. 2010).

2.5.3 Truss model

Diaphragms can be modelled and analysed by creating an elastic framework of truss elements. The idea of replacing the continuous material of an elastic body with a framework of truss elements according to a definite pattern and suitable element properties was introduced by Hrennikoff (1941).

Hrennikoff proposed the framework method for solving two-dimensional stress problems, bending of plates, bending of cylindrical shells and also the general case of three-dimensional stress. This method is based on replacing continuous material of an elastic body with a definite pattern of one-dimensional truss elements. It can be shown that if the size of the truss unit pattern be small enough, the results of the framework method are the same as the exact differential equation solution. Hrennikoff investigated various framework patterns that some of them are shown in Figure 2-21.

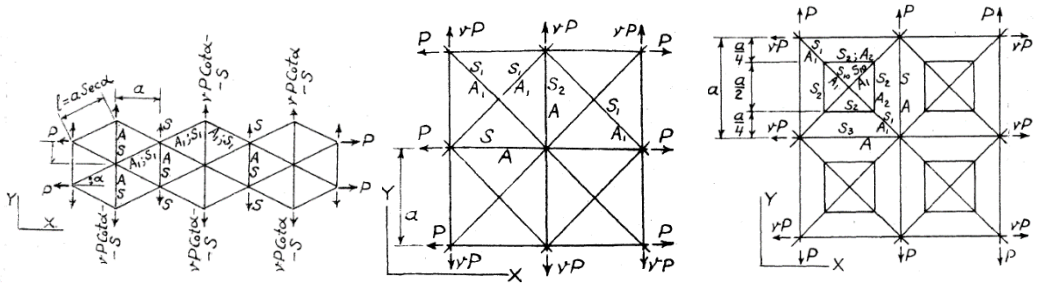

Figure 2-21. Patterns of truss elements investigated by Hrennikoff (1941)

Gardiner (2011) used the lattice element which is based on the Hrenikoff (1941) lattice analogy for modelling and analysing diaphragms. Hrenikoff provides the strut effective widths of 0.53 times *a* and orthogonal elements effective widths of 0.75 times *a* (*a* is truss mesh unit dimension for a square shape), for material with a Poison's ratio of 0.33, where the compression struts go between corners in both directions.

Holmes Consulting Group (2014) prepared a practice note about modelling and analysing diaphragms using truss elements based on Hrenikoff (1941). It is suggested in order

to get higher accuracy, truss mesh unit size should be reduced, while maintaining the square format for the following situations:

a) around the nodes where vertical elements would be connected to the floor plate,

b) around floor penetrations like stairs or lifts,

c) at re-entrant corners, and

d) around collectors.

Scarry (2014), proposed a modification on Hrenikoff (1941) method to consider the diagonal elements carry compression only and orthogonal elements carry both tension and compression. Figure 2-22 shows a diaphragm modelled using truss elements with compression-only pairs of diagonals to allow for strut action.

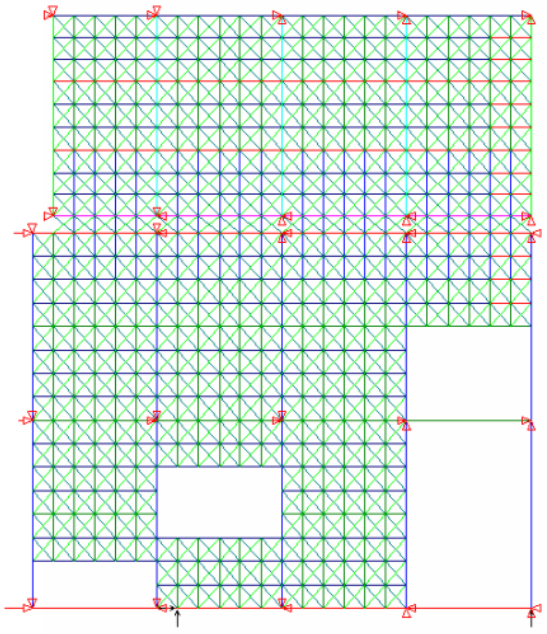

Figure 2-22. Truss model assigned to a typical floor diaphragm (Holmes Consulting Group 2014)

Another advantage of using the truss model is that multiple load cases can be analysed by one model and the struts and ties can be identified more easily. Stress concentration zones around openings and at re-entrant corners can be captured. Also, in this method, complex diaphragms consisting of vertical steps (three-dimensional diaphragms), can be modelled by employing beam elements and rigid links (Scarry, 2014).

2.5.4 Strut-and-Tie

The truss model with compression-only diagonal members and compression/tension orthogonal members may be called 'Strut-and-Tie' model. The 'Strut-and-Tie' approach has also been advocated for diaphragm analysis (Bull 1997, Gardiner 2011, Bull 2004 and Bull 2014). Clause 13.3.9 of NZS3101 (2006) states that "the strength design of diaphragms for shear shall be based upon strut-and-tie models". This can be used for general floor plan layouts with irregularities, such as openings in the diaphragm. In the strut-and-tie method, compression struts and tension ties are placed throughout the floor slab to develop a truss system of admissible force paths (Gardiner, 2011). One of the good examples of representing strut-and-tie in different problems is published by Schlaich et al. (1987).

In the references above, compression struts representing the diaphragm stiffness have been placed between column-to-beam, or beam-to-beam, nodes. In a building with an orthogonal plan, the steel (beams or reinforcing) run in the orthogonal directions.

An alternative, recently proposed by MacRae and Bull (2015) places the nodes at the centres of the beams. This nodal position represents the centroid of the shear studs on top of the beam. It may be regarded as an effective shear stud for the beam. Actual shear studs will be spread out along the beam. Compression struts representing the concrete strut effects run diagonally between these nodes. Tension ties, representing the steel, run perpendicular to the beam. This approach has some advantages compared to the previous approach which includes:

a) Axial forces in (and parallel to) the beam can be obtained directly from the analysis.
b) The number of studs required can be easily obtained from the difference in axial force along the beam either side of the central node.

c) The tension steel required as reinforcing bars in the slab is easily obtained from the force in this tension element perpendicular to the beam. This can be distributed to the shear studs acting along the beam.

This modelling method is discussed in Chapter 3 in more detail.

2.6 Gapping issues

Based on the current NZ design approach (NZS3404, 2007), structural steel beams are designed for earthquake-induced forces without considering the slab effect. This is because the slab is unconfined and beam composite strength degrades to the bare beam strength due to concrete failure as discussed with regard to Figure 2-15. Columns and connections are required to be designed to resist beam over-strength actions considering the slab effects. The NZ standard therefore considers the most conservative scenario by (a) ignoring the strength increase from the slab in design of the beam to resist the seismic loads in a force-based design, and (b) considering its influence when determining the over-strength actions at the column and joint from the inelastically responding composite beam. With an unconfined slab this may be appropriate as the slab strength is not dependable due to the possibilities of spalling and shear key fracture, as described in Section 2.4.3.

To consider the slab strength for design at the expected peak displacement, the slab should not degrade in strength and should therefore be well confined as shown in Figure 2-23. MacRae et al. (2013) have suggested special detailing for concrete slab around the column such that the slab be able to sustain its strength at higher drifts. Some economical ways of providing this detailing have been described by Chaudhari et al. (2015). Figure 2-23 illustrates some examples of detailing to confine the slab.

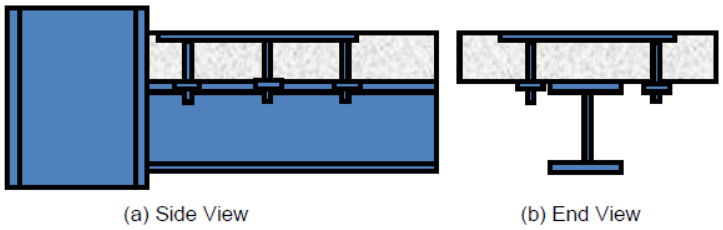

a) Slab confinement with a plate

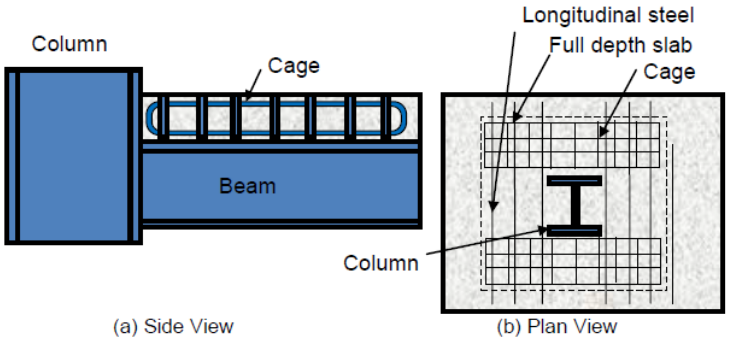

b) Slab confinement with a reinforcing cage

Figure 2-23. Details for providing slab confinement (MacRae et al. 2013)

Another approach is to not consider the slab strength either for the beam design or for over-strength. This may be conducted by isolating the column, and the elements connected to it, from the slab (MacRae and Clifton, 2015a). The slab can be separated from the column using a fire-proof material or a diamond gap cut all around the column may provide gapping as shown in Figure 2-24. It should be noted that gapping around the column involves isolating column and attachments, e.g. haunches, endplates, endplate bolts etc. as shown in Figure 2-25.

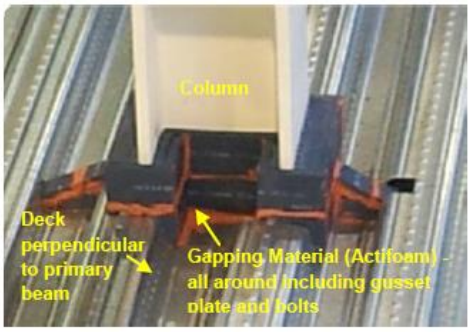

a) Gap around the column (Chaudhari et al. 2015)

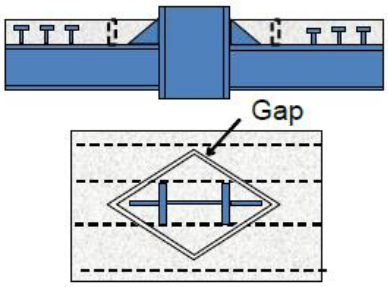

b) Gap within the slab (MacRae and Clifton, 2015b)

Figure 2-24. Gapping around column

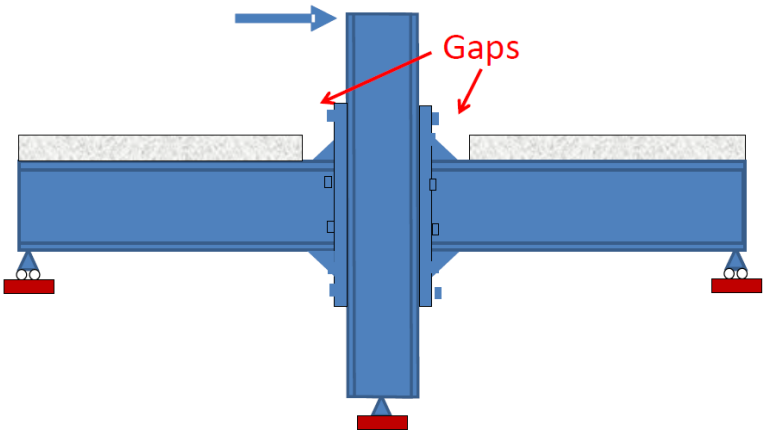

Figure 2-25. Isolating column and attachments (MacRae and Bull, 2015)

Chaudhari et al. (2015) indicate that gapping around column can provide good performance. It also decreases bearing and compatibility stresses which:

1) Eliminates the slab effect on beam over-strength, resulting in smaller columns.
2) Reduces slab damage and strength degradation.
3) Has the possibility of reducing ratcheting where the structure tends to yield predominantly in one direction because the same strength is in each direction of loading (MacRae and Clifton, 2015b).
4) Decreases beam/connection axial forces.

The disadvantages of gapping may be the following:

1) Increasing the chance of column instability by twisting due to having no slab to restrain it, such instability has been seen in columns with beams tested with reduced beam sections by Chi and Uang (2002). Details such as those shown in Figure 2-26 may reduce the propensity for such twist.
2) The initial stiffness and strength of the structure decrease (in the first cycle) so the period increases and the structure is likely to have greater displacements (MacRae and Clifton, 2015b).
3) Gap installation costs may be significant (MacRae and Bull, 2015).

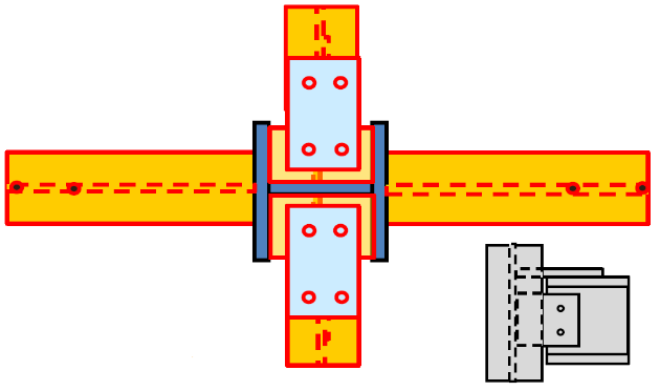

Figure 2-26. Limiting column twisting in gapped slabs (MacRae and Bull, 2015)

Whether or not gaps are provided between the slab and column, diaphragm forces are likely to be transferred to the column through axial force in the beam. For beam axial forces greater than about $0.2Af_y$ the lateral resistance of the frame may decrease, where A and f_y are beam cross-section area and yielding stress respectively. It has therefore been suggested that design should be conducted to ensure the beam axial force is less than this value (MacRae and Bull, 2015).

2.7 Load transfer from diaphragm to frame

Many buildings have a limited number of seismic frames, which are designed to carry horizontal forces from the diaphragms to the foundation. Two options to transfer this horizontal force are discussed below.

2.7.1 Designing diaphragms to transfer horizontal force only through the seismic frame beams

In this case, forces on the diaphragm, including inertial and transfer forces, are transferred to the seismic beam via shear studs on the beam. In general, transfer of forces directly from the diaphragm into the column should not be used as it is not a reliable load path because:

1) A gap opens between the slab and column face, as discussed in Section 2.2.2 and Figure 2-4, since slab inertia forces act in the same direction as the frame sways. Slab inertia forces therefore cannot go directly into the column.
2) The slab is not generally confined and it may break down under the first cycle of displacement so it cannot transfer subsequent load to the column.

For this mechanism, with force only considered to be transferred into the seismic frame(s):

a) Sufficient shear studs should only be placed on the seismic beam and all force transfer should occur here.
b) The ability of diaphragms on the gravity beams to transfer horizontal force should be limited by:
    i. ensuring that there are no shear studs on the gravity beams,
    ii. reducing friction on the top of these gravity beams, or

iii. minimising the possibility of interaction between the slab and the gravity columns (possibly by providing a seismic gap), as any force there would need to be transferred through the beams as an axial force.

c) A strut-and-tie mechanism needs to be developed. Schlaich et al. (1987) have shown that the pattern is typically like that in Figure 2-27. Here the compression struts become inclined at a distance of about $L/2$ from the beam carrying the lateral force, where L is the frame width as shown in Figure 2-27. The change in orientation of compression forces at this location causes extra forces perpendicular to the direction of earthquake shaking that need to be considered in design. Here Beams 1, 2, 3 and 4 are gravity beams, and all the forces from the diaphragm must be transferred through the composite seismic beams 5 and 6, in the braced seismic bays. The strut-and-tie mechanism involves:

i. Providing sufficient shear studs in Beams 5 and 6 to transfer expected forces.

ii. Providing sufficient transverse tie steel to balance the forces. The steel decking is not always considered to be continuous so it cannot be relied on to carry these tension forces even if it is spanning in the appropriate direction.

iii. Ensuring that the beam, and its connections, can transfer the axial forces induced into the columns, while still carrying the other forces expected for them to fulfil their purpose as part of the seismic frame.

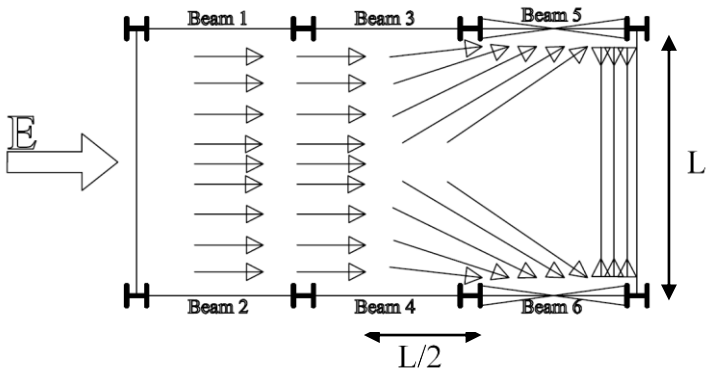

Figure 2-27. Typical floor plan with braced frames if shear studs are only provided on beam 5 and 6

The advantage of this method is that very small horizontal force on the gravity beams is expected, so beam axial tension/compression does not need to be considered. The gravity beams and their connections can be designed for vertical forces only. In this case, a simple shear connection from the gravity beams to the column, such as that shown in Figure 2-28, may be appropriate.

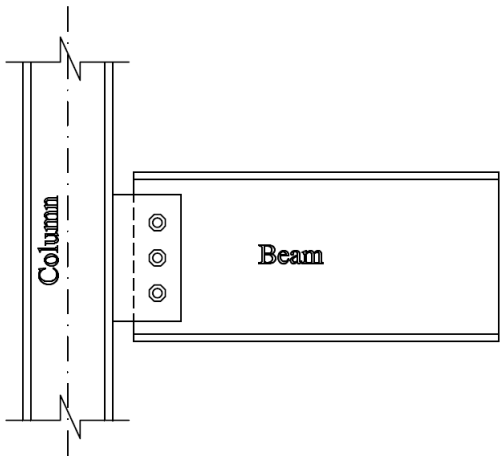

Figure 2-28. Typical cleat connection for gravity frames

2.7.2 Designing diaphragms to transfer horizontal force also through beams outside the seismic frame

When the composite action of the gravity beams is desired, these beams and their connections need to be designed for the expected forces. In this case, strut-and-tie mechanism with reinforcing steel perpendicular to all beams is required.

Apart from designing the beam itself for axial force, in conjunction with other imposed forces, appropriate connection design is also required. Some ways of detailing the connection include:

1) Using a bolted end plate connection at the beam end, or
2) Placing a top flange plate on the beam as shown in Figure 2-26.

If design is conducted assuming the seismic beams carry all horizontal forces from the diaphragms (including those from inertial and transfer effects), yet shear connectors are placed on the gravity beams, forces in the gravity beam connections may be greater than their capacities, and this may result in connection failure (Weir and Clarke, 2016). The deformation of these eccentric cleat connections are subject to, and is limited by, the deformations of the diaphragm on the seismic frame beams. In some cases this displacement compatibility limits the demands on the gravity beam end connections.

2.8 Conclusions

In-plane design considerations for floor diaphragms in steel buildings were described. It was shown that:

1) A number of issues that are not generally explicitly considered in current standards or current design, were described. These included: (a) diaphragm rigidity/flexibility considerations, (b) beam/connection axial forces, (c) thin diaphragm buckling, (d) elongation issues in composite beams, (d) load paths within a diaphragm to the supports, and (f) slab effects on subassembly strength and degradation.
2) A number of methods proposed to estimate forces on a building to evaluate global diaphragm in-plane demands were described. These vary in complexity and rationality. While no one method has been accepted as being appropriate for design using commonly available design software, it is beneficial to select one

distribution of forces which can capture the likely inertial and transfer effects considering over-strength.

3) Five types of diaphragm in-plane forces were discussed: (i) inertia forces, (ii) transfer forces, (iii) slab bearing, (iv) compatibility, and (v) interaction with other elements. It was shown that because of the way frames move, diaphragm inertial forces cannot generally be transferred directly from the slab into the columns, so appropriate consideration of the shear studs, and axial forces in the beam and end connections are required. Transfer forces are affected by the distributions of stiffness and strength not only over the building height, but also within one storey. Slab bearing and compatibility forces are affected by any gap provided between the concrete slab and column.
4) The strut-and-tie method was considered the most general and appropriate means of obtaining forces for design. Nodes placed at the beam centres to allow beam axial demands, shear stud demands and reinforcing steel demands to be captured directly. The automated strut-and-tie method also considers diaphragm flexibility.
5) Providing a gap in the slab around a column can reduce beam over-strength forces but the possibility of column twisting should be considered in design.
6) The number of bays over which force is transferred from the diaphragm to the frame should be considered explicitly in design.

References

[1] Ahmed S. M., Umarani C. and MacRae G. A. (2013). "Slab Effects on Building Seismic Performance: State of The Art", Journal of Structural Engineering, 40 (2): 136-141.

[2] Aktan A. E. and Nelson G. E. (1988). "Problems in predicting seismic responses of RC buildings", Journal of Structural Engineering, 114(9): 2036-2056.

[3] ANSI/SDI (2011). American National Standards Institute/Steel Deck Institute, C-2011 Standard for Composite Steel Floor Deck-Slabs.

[4] Barron J. M. and Hueste M. B. D. (2004). "Diaphragm effects in rectangular reinforced concrete buildings", Structural Journal, 101(5): 615-624.

[5] Basu D. and Jain S. K. (2004). "Seismic analysis of asymmetric buildings with flexible floor diaphragms", Journal of structural engineering, 130(8): 1169-1176.

[6] Blume J. A., Sharpe R. L. and Elsesser E. (1961). "A structural dynamic investigation of fifteen school buildings subjected to simulated earthquake motion". Division of Agriculture, Sacramento, Calif.

[7] Bruere R. J. and Davies-Colley M. (2015). "Effect of Reducing Maximum Response on Concrete Floor Diaphragms", Final Year Projects, Dept. of Civil and Natural Resources Engineering, University of Canterbury. Project supervisors: MacRae G. A. and Bull D. K.

[8] Bruneau M. and MacRae G. (2017). "Reconstructing Christchurch: A Seismic Shift in Building Structural Systems", Quake Centre, University of Canterbury.

[9] Bull D. (1997). "Diaphragms, Seismic Design of Reinforced Concrete Structures", Technical Report No. 20, New Zealand Concrete Society.

[10] Bull D. K. (2004). "Understanding the Complexities of Designing diaphragms in Buildings for Earthquakes", Bulletin of the New Zealand Society for Earthquake Engineering, 37 (2): 70-88.

[11] Bull D. K. (2014). "Module-2 ENCI429:2014 [PowerPoint slides]". University of Canterbury, Christchurch, New Zealand.

[12] Canterbury Earthquakes Royal Commission (2012): Final Report Volume 1.

[13] Celebi M., Bongiovanni G., Safak E. and Brady A. G. (1989). "Seismic response of a large-span roof diaphragm", Earthquake Spectra, 5(2): 337-350.

[14] Chaudhari T. D., MacRae G. A., Bull D., Chase G., Hicks S., Clifton G. C. and Hobbs M. (2015). "Composite Slab Effects on Beam–Column Subassembly Seismic Performance", 8th International Conference on Behavior of Steel Structures in Seismic Areas, Shanghai, China.

[15] Chi B. and Uang C. M. (2002). "Cyclic Response and Design Recommendations of Reduced Beam Section Moment Connections with Deep Columns", J. Struct. Engrg., ASCE, 128(4): 464-473

[16] Clifton G. C. (2015). "Determination of Diaphragm Actions and Distribution into the Frames; section 9.4 of the Civil 714 Multistorey Building Design Steel Notes", University of Auckland, Auckland, New Zealand.

[17] Cowie K. A., Fussell A. J., Clifton G. C., MacRae G. A. and Hicks S. J. (2014). "Seismic Design of Composite Metal Deck and Concrete-Filled Diaphragms–A Discussion Paper", NZSEE Conference.

[18] CSA, C. (2014). S16-14. Design of Steel Structures, Canadian Standards Association, Toronto, ON.

[19] Dantanarayana H. N., MacRae G. A., Dhakal R. P., Yeow T. Z. & Uma S. R. (2012) "Quantifying Building Engineering Demand Parameters in Seismic Events", 14 World Conference on Earthquake Engineering, Lisbon, Portugal, August 2012. Paper number 3424.

[20] Dolce M., Lorusso V. D. and Masi A. (1994). "Seismic response of building structures with flexible inelastic diaphragm", Structural Design of Tall Buildings 3(2): 87-106.

[21] Fenwick R., Bull D. and Gardiner D. (2012). "Assessment of Hollow-Core Floors for Seismic Performance", Research Report 2010-02, Department of Civil and Natural Resource Engineering, University of Canterbury, Christchurch, New Zealand.

[22] Fenwick R. C. and Davidson B. J. (1991). "The Seismic Response of Multi-storey Buildings", Department of Civil Engineering, University of Auckland. Report number 495.

[23] Fenwick R. C. and Davidson B. J. (1997). "P-delta Actions and the Loadings Code" SESOC 10(1): 58-62.

[24] Fleischman R. B., Farrow K. T. and Eastman K. (2002). "Seismic performance of perimeter lateral-system structures with highly flexible diaphragms". Earthquake Spectra, 18(2), 251-286.

[25] Gardiner D. R. (2011). "Design Recommendations and Methods for Reinforced Concrete Floor Diaphragms Subjected to Seismic Forces", PhD Thesis, University of Canterbury.

[26] Goldberg J. E. and Herness E. (1965). "Vibration of Multistory Buildings Considering Floor and Wall Deformations", Bulletin of the Seismological Society of America. 55(1): 181-200.

[27] Hadianfard M. A. and Sedaghat S. (2013). "Investigation of joist floor diaphragm flexibility on inelastic behavior of steel braced structures", Scientia Iranica, 20(3): 445-453.

[28] Haselton C. B. and Deierlein G. G. (2007). "Assessing Seismic Collapse Safety of Modern Reinforced Concrete Moment Frame Buildings", Report No. 156, Department of Civil and Environmental Engineering, Stanford University.

[29] Hobbs M., MacRae G. A., Bull D., Gunasekaran U., Leon R. and Clifton G. C. (2013). "Slab Column Interaction - Significant Or Not?", Steel Innovations Conference, Christchurch, New Zealand.

[30] Holmes Consulting Group, Practice Note No. 8.1, Version No. 1, (2014). "Modelling Diaphragm Force Distributions - Simple Grillage Method" by Bull DK and Galloway B.

[31] Hrennikoff A. (1941). "Solution of problems of elasticity by the framework method", Journal of applied mechanics, 8 (4):169-75.

[32] Humar J. and Popovski M. (2013). :Seismic response of single-storey buildings with flexible diaphragms", Canadian Journal of Civil Engineering, 40(9): 875-886.

[33] Jain S. K., Jennings P. C. (1985). "Analytical models for low-rise buildings with flexible floor diaphragms" Journal of Earthquake Engineering and Structural Dynamics, 13(2):225-241.

[34] Jensen J. (2004). "Diaphragm Action Issues in a Jointed Precast Concrete System", A final year project report submitted in partial fulfilment of the requirements for the degree of Bachelor of Engineering, Department of Civil Engineering, University of Canterbury, New Zealand.

[35] Ju S. H. and Lin M. C. (1999). "Building analyses comparisons assuming rigid or flexible floors", Journal of Structural Engineering ASCE, 125: 25-31.

[36] Kim S. C. and White D. W. (2004). "Linear static analysis of low-rise buildings with flexible diaphragms using the structural separation method", Engineering Structures, 26(1): 83-93.

[37] Kunnath S. K., Panahshahi N., Reinhorn A. M. (1991). "Seismic response of RC buildings with inelastic floor diaphragms", Journal of Structural Engineering, 117(4): 1218-1237.

[38] Lee H. J., Aschheim M. A. and Kuchma D. (2007). "Interstory drift estimates for low-rise flexible diaphragm structures", Engineering structures, 29(7): 1375-1397.

[39] Luo F., Gholamhoseini A. and MacRae G. A. (2015). "Analytical Study of Seismic Behaviour of Composite Slabs", Steel Innovations Conference, Auckland, New Zealand.

[40] MacRae G. A. and Bull D. (2015). "Diaphragm Design, ENEQ650: Seismic Design of Steel and Composite Structures", Postgraduate Class notes, University of Canterbury, 2015.

[41] MacRae G. A. and Clifton G. C. (2015a). "NZ Research on Steel Structures in Seismic Areas", 8th International Conference on Behavior of Steel Structures in Seismic Areas, Shanghai, China.

[42] MacRae G. A. and Clifton G. C. (2015b). "Research on Seismic Performance of Steel Structures", Steel Innovations Conference, Auckland, New Zealand.

[43] MacRae G. A., Hobbs M., Bull D., Chaudhari T., Leon R., Clifton G. C. and Chase C. (2013). "Slab Effects on Beam-Column Subassemblies – Beam Strength and Elongation Issues", Composite Construction VII Conf., Palm Cove, Queensland, Australia.

[44] Masi A., Dolce M. and Caterina F. (1997). "Seismic response of irregular multi-storey buildings with flexible inelastic diaphragms", Structural Design of Tall Buildings, 6(2): 99-124.

[45] Moehle J. P., Hooper J. D., Kelly D. J. and Meyer T. R. (2010). "Seismic Design of Cast-in-Place Concrete Diaphragms, Chords, and Collectors", NEHRP Seismic Design Technical Brief No. 3.

[46] Moon S. K. and Lee D. G. (1994). "Effects of in plane floor slab flexibility on the seismic behaviour of building structures", Engineering Structures, 16(2): 129-144.

[47] Moroder D. (2016) "Floor diaphragms in multi-storey timber buildings" PhD Thesis, University of Canterbury.

[48] Nakaki S. D. (2000). "Design Guidelines for Precast and Cast-in-place Concrete Diaphragms", Technical Report. E. P. Fellowship, Earthquake Research Institute.

[49] Nakashima M., Huang T. and Lu L. W. (1981). "Effect of diaphragm flexibility on seismic response of building structures", 1983 National Science Foundation Washington, DC 20550 October 30, 1981 Professor Ti Huang Fritz Engineering Laboratory Lehigh University Bethlehem, PA 18015.

[50] NZCS (1994). Revisions to the New Zealand Standard for the design of concrete structures: NZS 3101, Technical report No. 15, New Zealand concrete society.

[51] NZS 3101 (2006). Concrete structures standard. Standards New Zealand, Wellington, NZ.

[52] NZS 3404 (2007). Steel Structures Standard. Standards New Zealand, Wellington, New Zealand. Including Amendments 1 and 2, 2001/2007.

[53] NZS 1170.5 (2004). Structural Design Actions-Part, 5. Standards New Zealand, Wellington, New Zealand. Including Amendment 1, 2016.

[54] Paulay T. and Priestley M. J. N. (1992). "Seismic Design of Reinforced Concrete and Masonary Buildings", John Wiley and Sons, New York.

[55] Sabelli R., Sabol T. A. and Easterling W. S. (2011). "Seismic Design of Composite Steel Deck and Concrete-filled Diaphragms A Guide for Practicing Engineers", NEHRP Seismic Design Technical Brief No. 5.

[56] Sadashiva V. K., MacRae G. A., Deam B. L. and Spooner M. S. (2012). "Quantifying the seismic response of structures with flexible diaphragms", Earthquake Engineering & Structural Dynamics, 41(10): 1365-1389.

[57] Saffarini H. S. and Qudaimat M. M. (1992). "In-plane floor deformations in RC structures", Journal of Structural Engineering 118(11): 3089-3102.

[58] Scarry J. M. (2014). "Floor diaphragms – Seismic bulwark or Achilles' heel", NZSEE Conference Paper Number O19.

[59] Scarry J. M. (2015). "Floor Diaphragms and a Truss Method for Their Analysis", Bulletin of the New Zealand Society for Earthquake Engineering, 48 (1).

[60] Schlaich J., Schäfer K. and Jennewein M. (1987). "Toward a consistent design of structural concrete", PCI Journal, 6;32(3):74-150.

[61] SESOC (2011). Design of Conventional Structural Systems Following the Canterbury Earthquakes: Structural Engineering Society of New Zealand, ENG.SESOC.0016.1, Version No. 4:21.

[62] Shepherd R. and Donald R. A. H. (1967). "The Influence of In-Plane Floor Flexibility on the Normal Mode Properties of Buildings" J. Sound VS. 5(I): 29-36.

[63] Suto F. and Asayama S. (1988). "Experimental considerations on earthquake behaviours of a large long strip-type of actual structure", In Proc. 9th World Conf. on Earthquake Engineering, 503-508.

[64] Tena-Colunga A., Abrams D. P. (1996). "Seismic Behavior of Structures with Flexible Diaphragms", J. Struct. Eng., 122(4): 439-445

[65] Tiong D. and Lyes D. (2014). "Minimum Slab Thickness for Composite Floor Diaphragms", Final Year Project Report, Supervised by MacRae, Bull and Cowie, Dept. of Civil and Natural Resources Engineering, University of Canterbury.

[66] Tremblay R. and Stiemer S. F. (1996). "Seismic behavior of single-storey steel structures with a flexible roof diaphragm", Canadian Journal of civil engineering, 23(1): 49-62.

[67] Umarani C. and MacRae G. A. (2007). "A New Concept For Consideration Of Slab Effects On Building Seismic Performance", Journal of Structural Engineering, Structural Engineering Research Centre, Chennai, India, 34 (1): 25–32.

[68] Weir C. and Clarke H. (2016). "Eccentric cleat connection", Undergraduate Final Year Project Report, Supervised by Scarry JM and MacRae GA, Dept. of Civil and Natural Resources Engineering, University of Canterbury.

[69] Yang C. and Liu D. (1988). "The effect of stiffness degradation of shear wall and floor horizontal deformation on the frame-shear wall buildings", In Proc. 9th World Conf. on Earthquake Engineering, 17-22.

3 Floor Diaphragm In-Plane Modelling Using Truss Elements

3.1 Introduction

In order to analyse a 3D building to assess its likely seismic performance, decisions need to be made about the in-plane modelling characteristic of the floor diaphragm. Many standards categorise diaphragms as being either 'rigid' or 'flexible'. However, in reality, diaphragms have a quantifiable stiffness. This stiffness depends on whether the diaphragm is cracked or not. The assumption made regarding diaphragm in-plane stiffness may affect the forces and displacements in both the diaphragm and the vertical lateral force resisting (VLFR) system of the structure.

To obtain realistic structural response/behaviour a realistic diaphragm in-plane stiffness is required. Furthermore, the stiffness effect must be able to simply be used in available structural analysis software packages.

It should be noted that diaphragm stiffness can be modelled in most common building analysis software using shell/plate elements. However, this is not often performed as the rigid diaphragm assumption is simpler to use. Also, post-processing the outputs to obtain useful design parameters, such as the concrete strut compression force or the steel tie tension force may be difficult.

In this study a number of truss element modelling methods are proposed and investigated as to their suitability for use in structural design/assessment. This is achieved by seeking answers to the following questions:

1) How have diaphragms been modelled/analysed for design in the past?
2) How can diaphragm modelling be undertaken using truss elements?

3) Do diagonal or diamond truss element modelling methods provide the greatest accuracy?
4) What element stiffness values are required for general rectangular truss model with different aspect ratio?
5) Which truss models are best in design?
6) What is the effect of diaphragm elastic stiffness assumptions on simple structures considering earthquake shaking?

3.2 Literature review

Diaphragm in-plane stiffness can vary between being fully rigid and fully flexible. For simplicity, many standards (e.g. ASCE7-10 and NZS1170.5, 2004) consider that a diaphragm can be treated as being fully rigid or flexible. Some FEM software (e.g. ETABS and SAP2000, 2013) exists which allows diaphragm flexibility to be considered; however, most engineers consider concrete floor diaphragms in multi-storey buildings to be rigid. Using the rigid diaphragm assumption does not make it easy for designers to consider how load paths should be followed, so separate analyses are required to find the likely in-plane forces within the diaphragm and the axial forces in the beams. Diaphragms can be modelled using shell elements, but interpreting stress contours to find the required amount of reinforcing is not direct. Strut-and-ties can also be used, but these are not generally placed within the structure to obtain the desired engineering parameters, and it is not clear what stiffness and strength are appropriate.

Several modelling techniques have been used by previous researchers to take into account the diaphragm flexibility in a structure. In the three-dimensional analysis, diaphragms have generally been modelled using shell elements (Barron and Hueste 2004, Saffarini and Qudaimat 1992, Ju and Lin 1999 and Tena-Colunga and Abrams 1996) or beam

elements (Jain and Jennings 1985, Tremblay and Stiemer 1996, Lee et al. 2007 and Sadashiva et al. 2012).

3.2.1 Different slab analysis methods

In order to design the floor diaphragms, an appropriate method is needed to analyse the floor diaphragm and also be suitable for a design office. Several methods have been proposed by researchers in this regard which these methods vary in the level of complexity and accuracy. Slab analysis methods include:

1) Detailed Finite Element Method (FEM)
2) Deep Beam
3) Truss Method

- **Detailed Finite Element Method (FEM)**

Modelling a diaphragm using FEM software can be beneficial for evaluating the transfer forces among vertical lateral force resistance elements as well as inertia forces. Particularly for irregular diaphragms in shape and around large openings in the floor plan. Despite this, FEM programs are often expensive, difficult to use and require significant process and post-processing times for each analysis, also stresses and strains do not relate directly to design, and it may be difficult to estimate how much reinforcing steel is required in specific locations.

- **Deep Beam**

The 'Deep Beam' technique (e.g. Naeim and Boppana, 2001 and Sabelli et al., 2011) is a simple method for regular floor plans. It considers the diaphragm as a beam with a distributed load. The approximation of the deep beam method is only appropriate in regular floor plans.

- **Truss Method**

Buildings with complex floor plans can be modelled and analysed by creating a framework of truss elements. The idea of replacing the continuous material of an elastic body with a framework of truss elements according to a definite pattern and suitable element properties was introduced by Hrennikoff (1941). In the truss model all actions including global shear, bending and axial demands, are resisted by strut-and-tie action. The truss model evaluates internal floor forces by linear finite element method using simple truss elements instead of triangular or rectangular shell elements (Scarry, 2014).

Hrennikoff (1941) proposed the framework method for solving two-dimensional stress problems such as flat and cylindrical shells. This method is based on replacing continuous material of an elastic body with a definite pattern of one-dimensional truss elements. Hrennikoff investigated various framework patterns shown in Figure 3-1.

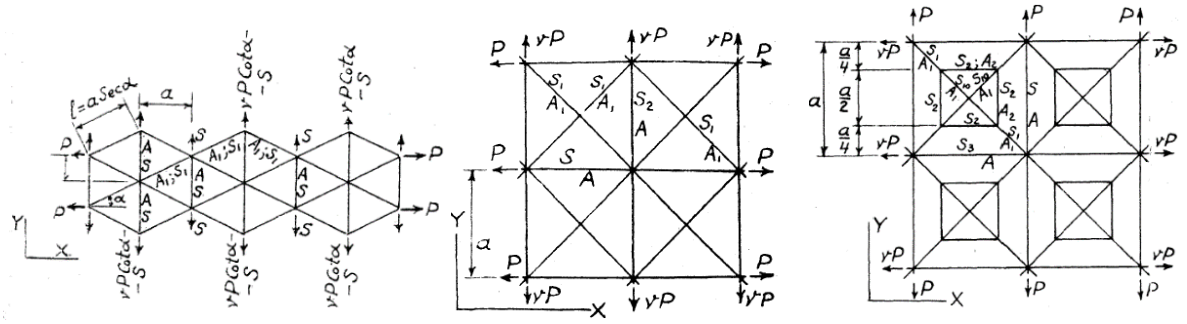

Figure 3-1. Patterns of truss elements investigated (Hrennikoff, 1941)

To obtain properties of the framework elements, the necessary and sufficient condition is equality in deformability of continuum body and the framework under all possible loading conditions. Characteristics of truss framework that should be determined include the cross-section area of truss elements and the angle between them.

Gardiner (2011) used the truss model which is based on the Hrennikoff (1941) truss model for modelling and analysing diaphragms. She studied the effect of considering concrete tensile strength in modelling and found that it could change the internal diaphragm

load paths in comparison with the compression-only concrete assumption. For example, forces in the most largely loaded elements changed as much as 40%. Holmes Consulting Group (2014) prepared a practice note about modelling and analysing diaphragms using truss elements based on the Hrennikoff truss framework pattern. This practice note also is being referred to in part C of the "Seismic Assessment of Existing Buildings, 2017" guideline for modelling/analysing of floor diaphragms. Moroder (2016) proposed enhancements for applying the truss model to timber diaphragms.

The advantage of using the truss model is that multiple load cases can be analysed using one model and the struts and ties can be identified more easily. Stress concentration zones around openings and at re-entrant corners can be captured. Moreover, the analysis results could be more directly used for design or assessment of concrete compression struts and tension reinforcements (ties).

The truss model with compression-only diagonal members and compression/tension orthogonal members may be called 'Strut-and-Tie' model. One of the good examples of representing strut-and-tie in different problems is published by Schlaich et al. (1987). This method can be used easily for general floor plan layouts with different irregularities such as openings in diaphragm. In the strut-and-tie method, compression struts and tension ties are placed throughout the floor slab to develop a truss system of acceptable force paths. It provides information that is more useful for a designer than the deep beam method. Figure 3-2 shows the implementation of the strut-and-tie method in a simple diaphragm for inertia and transfer forces.

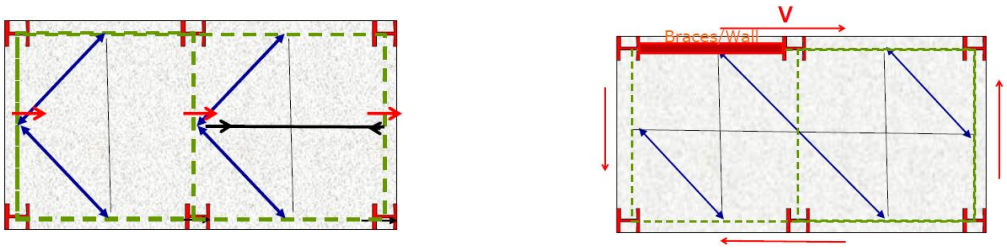

a) Inertial forces

b) Transfer forces

Figure 3-2. Strut-and-tie solution in a typical diaphragm (MacRae and Bull, 2015)

3.2.2 Hrennikoff diagonal model

Figure 3-3 shows three general loading conditions that were used for determining the framework properties in Hrennikoff studies. The plate is assumed to continue in both directions and only two truss mesh units in each direction are shown in this Figure. In the first loading condition, Figure 3-3a, the plate is loaded uniformly with normal load per unit length P in the X-direction and νP (υ is Poisson's ratio of the plate material) in the Y-direction. The second loading condition, Figure 3-3b, is achieved by changing the X and Y-directions. The third loading condition, Figure 3-3c, includes uniform tangential loading per unit length P, applied to the plate edges in the X and Y-directions. The right hand side of each Figure shows the square truss mesh unit where diagonal members are at 45°.

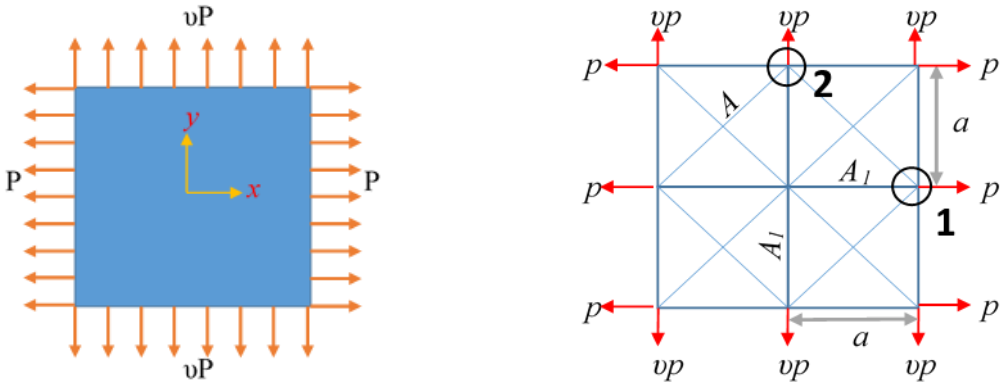

a) Plate and truss framework subjected to normal force per unit length, P, in the X-direction and νP in the Y-direction

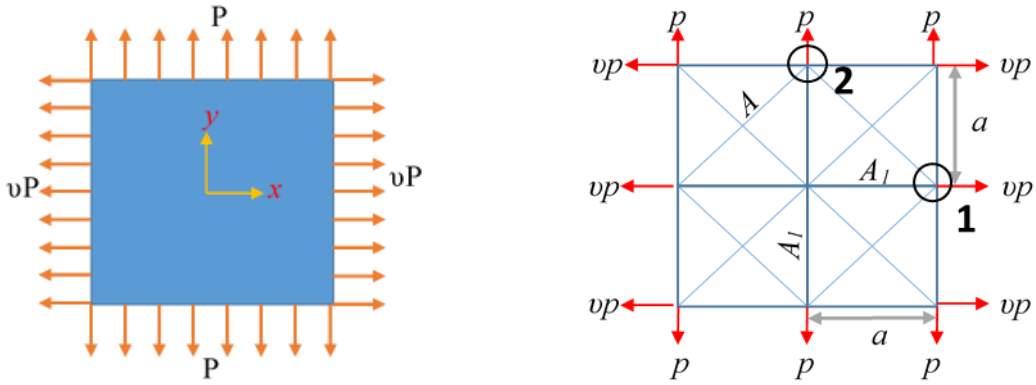

b) Plate and truss framework subjected to normal force per unit length, P, in the Y-direction and νP in the X-direction

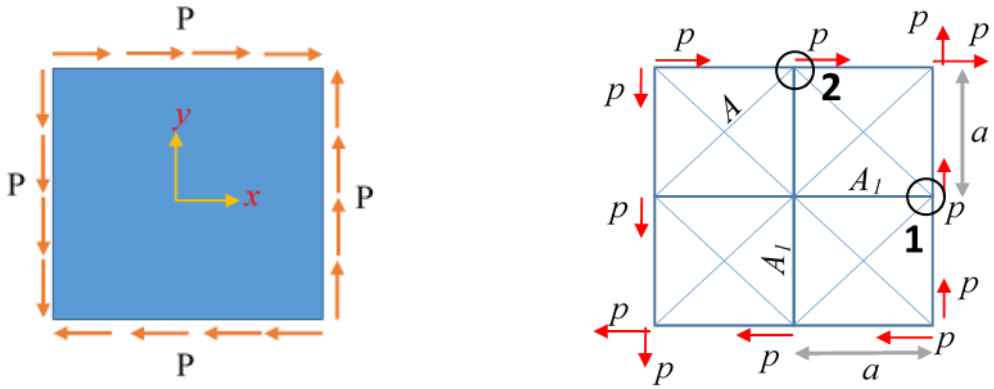

c) Plate and truss framework subjected to pure shear force per unit length, P

Figure 3-3. General loading conditions for determining truss framework properties, p is the normal edge force to each element where $p = Pa$, truss framework continues in both directions

Strains in the truss framework for each case in Figure 3-3 can be calculated based on the applied forces, p, truss element stiffnesses, Eta, and the configuration represented by the angle α. Then the framework strains are equated to the corresponding strains in the plate member ε_x, ε_y and γ_{xy} loaded the same way.

Based on solid mechanics (e.g. Timoshenko and Goodier, 1970), the axial strains in the X and Y-directions, ε_x and ε_y for the first case of loading (Figure 3-3a), can be obtained as follows for a plate member.

$$\varepsilon_x = \frac{p(1-\nu^2)}{Eta} \qquad \text{Eq. (3-1)}$$

$$\varepsilon_y = 0 \qquad \text{Eq. (3-2)}$$

Here p is the normal edge force to each element ($p = Pa$) and E and ν are the elastic modulus and Poisson's ratio of plate material respectively. The horizontal and vertical dimensions of each square truss mesh unit and the plate thickness are denoted as a and t respectively. The same equations are applicable to the second case by changing the X and Y-directions.

Shear deformation of the plate subjected to tangential force can be obtained using Eq. (3-3) (e.g. Timoshenko and Goodier, 1970).

$$\gamma_{xy} = \frac{2(1+\nu)p}{Eta} \qquad \text{Eq. (3-3)}$$

By equating the truss framework and the plate strains, Eqs. (3-1 to 3-3), the truss element characteristics can be obtained. Figure 3-4 presents an enlarged view of Figure 3-3a with more details. The equations used for finding the truss element characteristics are presented in the following.

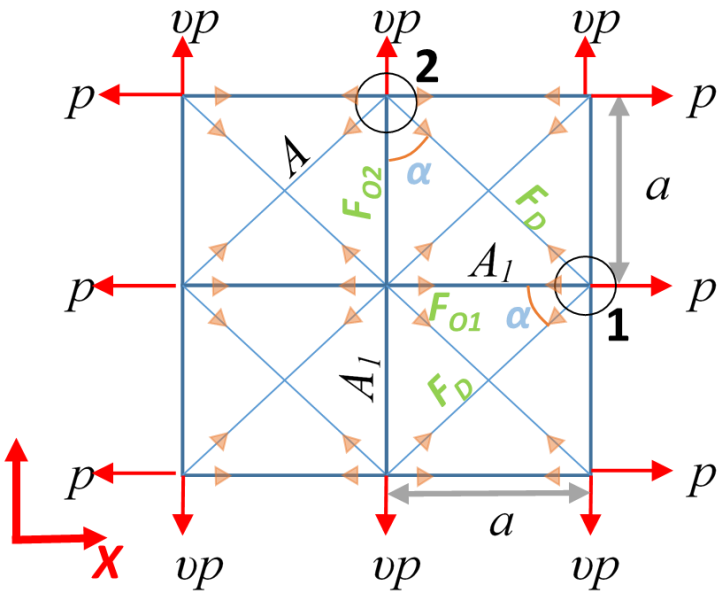

Figure 3-4. Truss framework subjected to normal force p in the X-direction and νp in the Y-direction

Force equilibrium in the X-direction at Point 1 shown in Figure 3-4, gives:

$$F_{O1} + 2F_D \cos\alpha - p = 0 \qquad \text{Eq. (3-3a)}$$

Where F_{O1} is the internal force of orthogonal member in the X-direction and F_D is the diagonal member internal force. Writing the force equilibrium in the Y-direction at Point 2 also gives:

$$F_{O2} + 2F_D \cos\alpha - \nu p = 0 \qquad \text{Eq. (3-3b)}$$

It is known that the lateral deformation (deformation in the Y-direction, Eq. (3-2)) is zero due to applied νp in this direction. Therefore $F_{O2} = 0$ and by substituting this in the force equilibrium in the Y-direction, Eq. (3-3b), the diagonal member force can be obtained:

$$F_D = \frac{\nu p}{2\cos\alpha} \qquad \text{Eq. (3-3c)}$$

Considering the truss framework units are square ($\alpha = 45°$), by substituting F_D into the force equilibrium in the X-direction, Eq. (3-3a), the orthogonal member force (F_{O1}) can be obtained as:

$$F_{O1} = p(1 - \nu)$$

The X-direction axial strain of the orthogonal truss member, which needs to be equal to the axial strain of the corresponding plate member, can be calculated using:

$$\varepsilon_x = \frac{p(1-\nu)}{EA_1}$$

By equating the axial strain of the plate given in Eq. (3-1) and the truss element axial strain above, the cross-section area of the orthogonal truss element member can be found:

$$A_1 = {at}/{(1+\nu)} \qquad \text{Eq. (3-4)}$$

By changing the loading condition to normal force p in Y-direction and νp in X-direction, the same result can be obtained for the orthogonal member in the Y-direction.

In case of tangential (shear) forces applied to the truss framework as shown in Figure 3-3c, all orthogonal members are unstressed due to the symmetry in the truss pattern.

However, all the diagonal members are stressed with equal tension and compression values. Force equilibrium in the Y-direction at Point 1 gives:

$$2F_D \sin\alpha - p = 0$$

Considering the units in the truss framework are square ($\alpha = 45°$), the diagonal member internal force subjected to shear stresses is:

$$|F_D| = \frac{p}{\sqrt{2}} \qquad \text{Eq. (3-4a)}$$

Similarly, the force equilibrium in the X-direction at Point 1 in Figure 3-3c shows that the orthogonal member internal force is zero.

$$F_D \cos\alpha - F_D \cos\alpha + F_{O1} = 0$$

$$F_{O1} = 0$$

The axial deformation (change in length) of the diagonal truss members is equal to:

$$\delta = \frac{pa\sqrt{2}}{\sqrt{2}EA}$$

$$\delta = \frac{pa}{EA} \qquad \text{Eq. (3-4b)}$$

Which transform the square pattern into a parallelogram as shown in Figure 3-5.

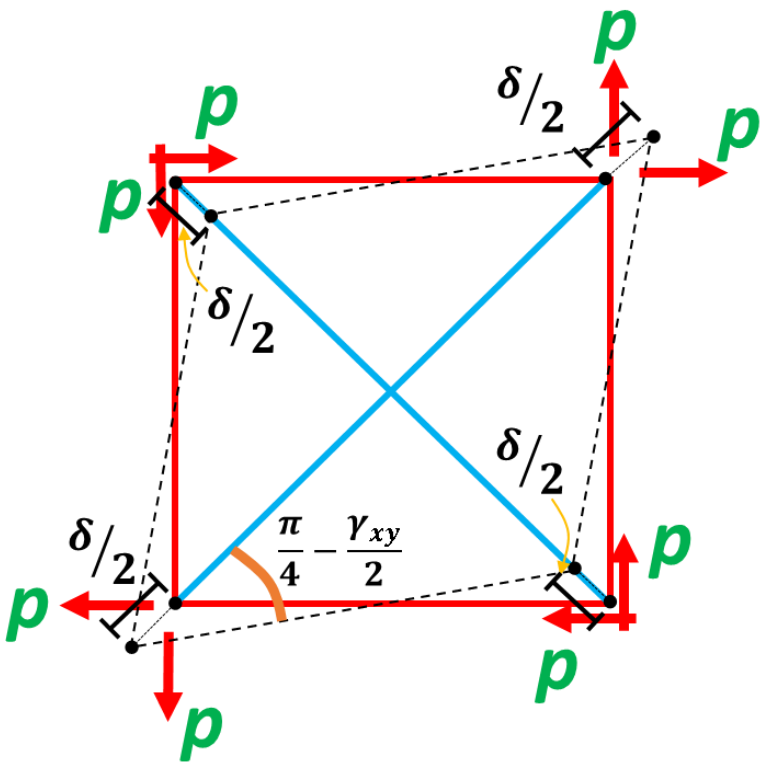

Figure 3-5. Square pattern deformed shape subjected to shear stress

As shown in Figure 3-5, the shear strain in the framework, γ_{xy}, can be calculated from:

$$\tan\left(\frac{\pi}{4}+\frac{\gamma_{xy}}{2}\right)=\frac{\frac{a}{\sqrt{2}}-\frac{\delta}{2}}{\frac{a}{\sqrt{2}}+\frac{\delta}{2}}$$

$$=\frac{1-\frac{\delta}{a\sqrt{2}}}{1+\frac{\delta}{a\sqrt{2}}} \qquad \text{Eq. (3-4c)}$$

Also, from the mathematical rule of trigonometric addition formulas (e.g. Abramowitz and Stegun, 1965) and assuming small deformations which, $\tan(\gamma)\cong\gamma$,

$$\tan\left(\frac{\pi}{4}+\frac{\gamma_{xy}}{2}\right)=\frac{\tan\frac{\pi}{4}-\tan\frac{\gamma_{xy}}{2}}{1+\tan\frac{\pi}{4}\tan\frac{\gamma_{xy}}{2}}$$

$$=\frac{1-\frac{\gamma_{xy}}{2}}{1+\frac{\gamma_{xy}}{2}}$$

By equating the above equation with Eq. (3-4c) and substituting Eq. (3-4b), the shear strain, γ_{xy}, can be obtained as:

$$\gamma_{xy} = \frac{p\sqrt{2}}{EA}$$ Eq. (3-4d)

By equating the plate and truss framework shear strains, using Eq. (3-3) and Eq. (3-4d), the diagonal truss element cross-section area can be obtained:

$$A = \frac{at}{\sqrt{2}(1+\nu)}$$ Eq. (3-5)

Poisson's ratio, ν, should be found to satisfy the deformation compatibility equation. Figure 3-6 shows the framework deformation in the X-direction subjected to normal force, p, in the X-direction and νp in the Y-direction.

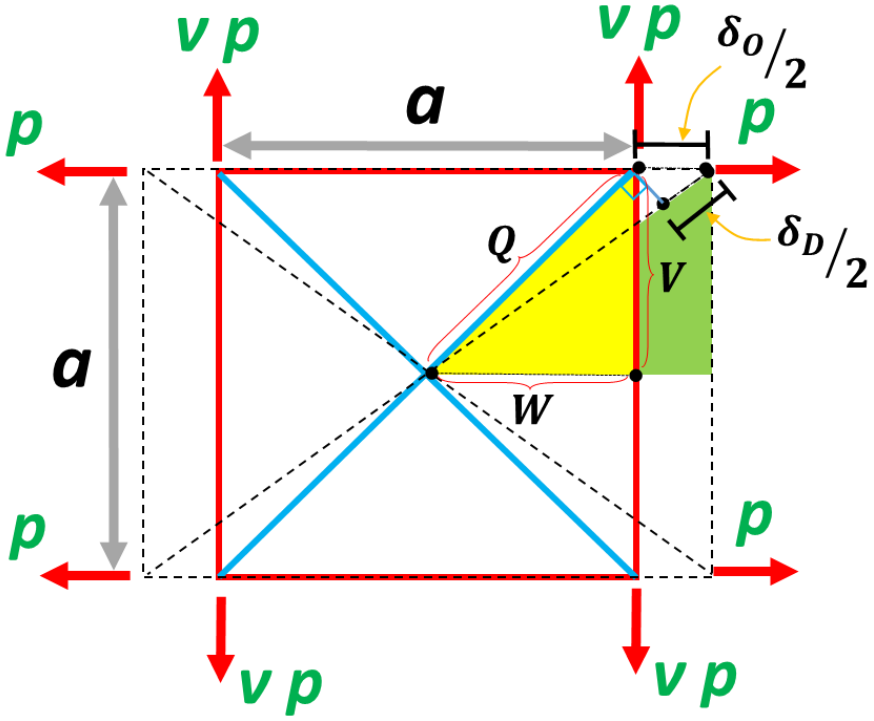

Figure 3-6. Framework deformation in the X-direction subjected to normal force p in the X-direction and νp in the Y-direction

The deformation compatibility could be simply found by writing the relationship between the orthogonal and diagonal member deformations as:

$$\frac{\delta_D}{2} = \frac{\delta_O}{2}\cos 45$$ Eq. (3-5a)

The truss element axial deformations are denoted by δ_D and δ_O for diagonal and orthogonal members respectively.

Considering the truss element axial forces obtained using equilibrium in the X-direction, Eq. (3-3a), and truss member cross-section areas given in Eqs. (3-4 and 3-5), δ_D and δ_O may be calculated as:

$$\delta_D = \frac{vp\sqrt{2}(1+v)}{Et}$$

$$\delta_O = \frac{p(1-v^2)}{Et}$$

Substituting these axial deformations into Eq. (3-5a), gives:

$$\frac{vp\sqrt{2}(1+v)}{Et} = \frac{p(1-v^2)}{\sqrt{2}Et}$$

From which $v = \frac{1}{3}$ results.

Considering the Poisson's ratio $v = \frac{1}{3}$, the cross-section area of the orthogonal and the diagonal members are obtained using Eqs. (3-4 and 3-5) respectively as:

$A_1 = 0.75at$ (Orthogonal member)

$A = 0.53at$ (Diagonal member)

Where a is the dimension of the framework pattern and t is the plate thickness.

3.3 Truss element modelling

3.3.1 Diamond ⟐ shape model

In steel frame structures with composite floor system, shear studs on the top of any beam can be represented by one effective stud at the centre of the beam span (MacRae and Bull, 2015). In this configuration, axial forces parallel to the beam are resisted by the beam, tension force demands perpendicular to the beam can be resisted by reinforcing steel placed in the slab, and compression forces at different angles to the beam axis are resisted by the concrete. This approach also gives axial forces in the beams which also must be considered in design (MacRae and Clifton, 2015). A diamond ⟐ shape model for this purpose is proposed below.

This model can be achieved by putting nodes at the centre of the beams (or at the shear stud locations) to be able to capture beam axial forces more effectively and also be able to capture shear stud demands. This framework pattern is shown in Figure 3-7. Similar to the diagonal model, the cross-section area of members can be derived by equating framework deformations with elastic strains of the plate. It is noted that in this modelling method boundary elements, as shown in Figure 3-7 with dashed lines, are required to provide overall stability for the truss framework. These boundary elements may represent beams, walls or any other element that can restraint diaphragm boundaries.

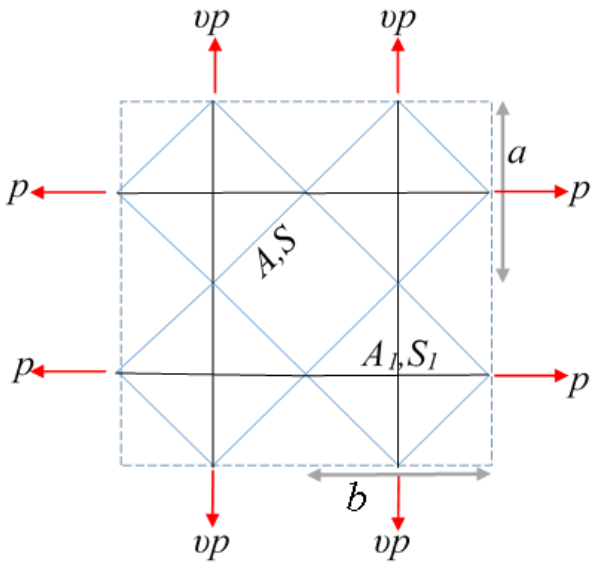

Figure 3-7. Diamond shape model

Using the same method as obtaining the cross-section areas of the diagonal ☒ model, the cross-section areas of diamond truss elements can be calculated. As shown in Appendix B, $A_1 = 0.75at$ (orthogonal members) and $A = 0.53\ at$ (diagonal members) are calculated for a square truss mesh unit (with $a = b$), where a is the dimension of framework pattern and t is the plate thickness.

If a non-square truss mesh unit be considered, by solving the equilibrium and compatibility equations, the Poisson's ratio for the framework is related to the truss mesh unit dimensions as:

$$\nu = \frac{ab}{a^2+b^2+ab} \qquad \text{Eq. (3-6)}$$

Where a and b are the framework pattern dimensions in Figure 3-7.

Therefore for modelling a concrete material with Poisson's ratio equal to 0.2, the framework aspect ratio (a/b) should be 3.73. Although this is correct mathematically, this value is not practical in modelling and more importantly by taking this value as truss modelling aspect ratio, the cross-section area of the orthogonal truss element results in a negative value that does not have physical meaning.

3.3.2 Comparison of the diagonal ☒ and diamond ⟐ models

The diagonal (Hrennikoff, 1941) and the diamond models are compared in this section. Here all elements are considered to carry both tension and compression forces. The comparison is made in terms of mesh sensitivity and beam axial and shear stud force results.

3.3.2.1 Mesh sensitivity

Mesh sensitivity for the diamond ⟐ and the diagonal ☒ truss models is investigated both using closed-form solutions and also some numerical examples.

- ***Closed form assessment***

Consider the plate in Figure 3-8 subjected to axial force only. Based on the mechanics of material, the axial strain in the plate member can be easily found using Eq. (3-7).

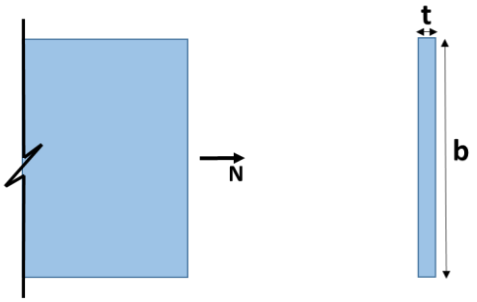

a) Plan b) Cross-section

Figure 3-8. A plate member under axial force

$$\varepsilon_x = \frac{N}{Etb} \qquad \text{Eq. (3-7)}$$

Where N is the applied axial force, t and b are thickness and width of the plate section and E is the plate elastic modulus. Here, the same plate member is modelled using the diagonal ☒ and the diamond ⌖ truss models and the axial strain is calculated. Figure 3-9a and b show the models schematically. In both models, the axial strain of the truss mesh unit is equal to the axial strain of member T_1 as shown in Figure 3-9. This can easily be found by analysing one unit of the truss model.

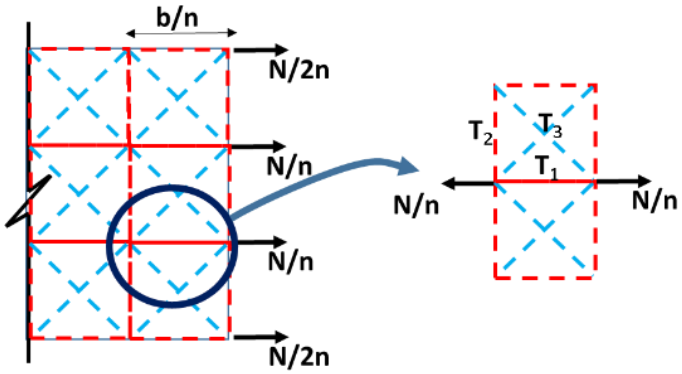

a) Diagonal ☒ truss model of a plate member

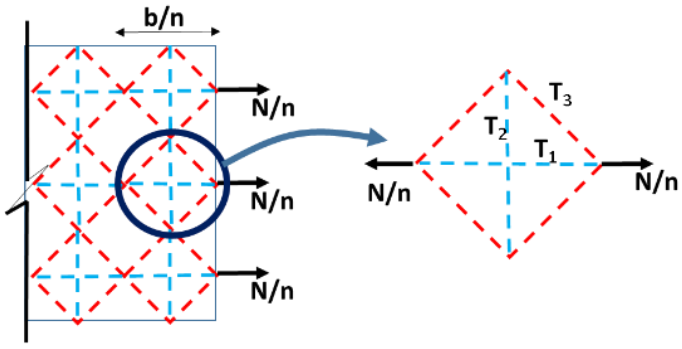

b) Diamond ⌖ truss model of a plate member

Figure 3-9. Diagonal ☒ and diamond ⌖ truss models subjected to an axial tension force

Considering the cross-section area of the elements obtained in Section 3.2.2 and the axial force of member T_1 in the diamond ⌖ and the diagonal ☒ models, the axial strain can be obtained. The axial force of member T_1 is $F_1 = \frac{3N}{4n}$ for both the diagonal ☒ and the diamond

⟐ models. Where n is the number of elements in plate width. Element/model axial strain in both truss models is equal to:

$$\varepsilon_x = \frac{3N/(4n)}{3Ebt/(4n)} = \frac{N}{Etb}$$

Note that in the diagonal ⊠ model, the stiffness of boundary elements are half the internal elements. Also, it may be seen that if there were no diagonal members, then $F_1 = N/n$. The fact that T_1 is only 75% of this value indicates that the diagonals carry 25% of the force.

The calculated strain shows that the axial deformation in both models is independent of the number of elements and it results in the same axial deformations as plate member. In the case of biaxial loading, when the Poisson's ratio of the plate is equal to 0.33, similar results are obtained.

For truss models subjected to shear force as shown in Figure 3-10, shear deformations can also be obtained without error for materials with a Poisson's ratio equal to 0.33. The shear strain of the plate can be easily obtained using Eq. (3-8).

$$\gamma_{xy} = \frac{2(1+\nu)N}{Etb} = 2.66\frac{N}{Etb} \qquad \text{Eq. (3-8)}$$

In both models, there are $2n$ diagonal members that resist shear forces; the stiffness of each of these members in the direction of applied force is equal to $\frac{EA}{L}\cos^2\theta$. Here A and L are the cross-section area and length of diagonal members respectively, and θ is the angle between the diagonal member and the direction of applied force (here $\theta = 45^\circ$). By substituting A, L and θ, the stiffness of diagonal element is equal to $\frac{3Et}{16}$ for the diagonal ⊠ model and $\frac{3Et}{8}$ for the diamond ⟐ model. Therefore, the shear strains, γ_{xy}, in both models can be obtained.

For the diagonal ⊠ model this is calculated as:

$$\gamma_{xy} = \frac{(\frac{N}{2n} \times \frac{16}{3Et})}{b/n} = \frac{8N}{3Etb} = 2.66\frac{N}{Etb}$$

For the diamond ⌖ model this is calculated as:

$$\gamma_{xy} = \frac{(\frac{N}{2n} \times \frac{8}{3Et})}{\frac{1}{2} \times b/n} = \frac{8N}{3Etb} = 2.66\frac{N}{Etb}$$

It is obvious from shear strain equations that both models can capture shear deformations independent of the number of elements.

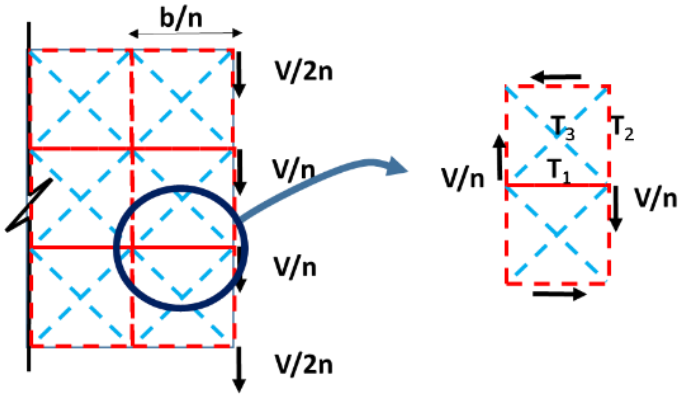

a) Diagonal ☒ truss model of a plate member

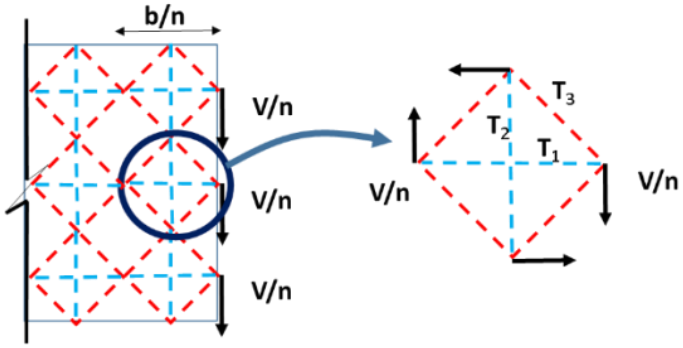

b) Diamond ⌖ truss model of a plate member

Figure 3-10. Diagonal ☒ and diamond ⌖ truss models under shear forces

In the case of bending moments, the error is related to finding the moment of inertia of the plate cross-section. For truss models, the moment of inertia can be obtained from Eq. (3-9) where A_k is the equivalent cross-section area of diagonal and orthogonal elements at each

node of a section and y_k is the distance of each elements to the section neutral axis. The equation that is used to calculate I, depends on whether the number of elements, n, is even or odd.

$$I = \int_A y^2 dA = \sum_{k=1}^{n} A_k y_k^2 \qquad \text{Eq. (3-9)}$$

For the diagonal ☒ model when the number of elements is even:

$$I = 2\sum_{k=1}^{(n/2)-1} A_k y_k^2 + \frac{b^3 t}{4n} = 2\sum_{k=1}^{(n/2)-1} \frac{bt}{n}\left(\frac{kb}{n}\right)^2 + \frac{b^3 t}{4n} = 2\frac{b^3 t}{n^3}\sum_{k=1}^{(n/2)-1} k^2 + \frac{b^3 t}{4n}$$

For the diagonal ☒ model when the number of elements is odd:

$$I = 2\sum_{k=1}^{(n-1)/2} A_k y_k^2 + \frac{b^3 t}{4n} = 2\sum_{k=1}^{(n-1)/2} \frac{bt}{n}\left(\frac{(2k-1)b}{2n}\right)^2 + \frac{b^3 t}{4n}$$

$$= \frac{b^3 t}{2n^3}\sum_{k=1}^{(n-1)/2} (2k-1)^2 + \frac{b^3 t}{4n}$$

For the diamond ⌖ model when the number of elements is even:

$$I = 2\sum_{k=1}^{n/2} A_k y_k^2 = 2\sum_{k=1}^{n/2} \frac{bt}{n}\left(\frac{(2k-1)b}{2n}\right)^2 = \frac{b^3 t}{2n^3}\sum_{k=1}^{n/2} (2k-1)^2$$

For the diamond ⌖ model when the number of elements is odd:

$$I = 2\sum_{k=1}^{(n-1)/2} A_k y_k^2 = 2\sum_{k=1}^{(n-1)/2} \frac{bt}{n}\left(\frac{kb}{n}\right)^2 = 2\frac{b^3 t}{n^3}\sum_{k=1}^{(n-1)/2} k^2$$

Using Faulhaber's formula for sum of the power series, the above equations can be simplified as below:

For the diagonal ☒ model when the number of elements is even:

$$I = 2\frac{b^3 t}{n^3}\sum_{k=1}^{(n/2)-1} k^2 + \frac{b^3 t}{4n} = 2\frac{b^3 t}{n^3}\left(\frac{\left(\frac{n}{2}-1\right)^3}{3} + \frac{\left(\frac{n}{2}-1\right)^2}{2} + \frac{\left(\frac{n}{2}-1\right)}{6}\right) + \frac{b^3 t}{4n} \qquad \text{Eq. (3-10)}$$

For the diagonal ☒ model when the number of elements is odd:

$$I = \frac{b^3 t}{2n^3}\sum_{k=1}^{(n-1)/2}(2k-1)^2 + \frac{b^3 t}{4n} = \frac{b^3 t}{2n^3}\left[4\left(\frac{\left(\frac{n-1}{2}\right)^3}{3} + \frac{\left(\frac{n-1}{2}\right)^2}{2} + \frac{\left(\frac{n-1}{2}\right)}{6}\right) - 4\left(\frac{\left(\frac{n-1}{2}\right)^2}{2} + \frac{\left(\frac{n-1}{2}\right)}{2}\right) + \frac{n-1}{2}\right] + \frac{b^3 t}{4n} \quad \text{Eq. (3-11)}$$

For the diamond ⌖ model when the number of elements is even:

$$I = \frac{b^3 t}{2n^3}\sum_{k=1}^{n/2}(2k-1)^2 = \frac{b^3 t}{2n^3}\left[4\left(\frac{\left(\frac{n}{2}\right)^3}{3} + \frac{\left(\frac{n}{2}\right)^2}{2} + \frac{\left(\frac{n}{2}\right)}{6}\right) - 4\left(\frac{\left(\frac{n}{2}\right)^2}{2} + \frac{\left(\frac{n}{2}\right)}{2}\right) + \frac{n}{2}\right] \quad \text{Eq. (3-12)}$$

For the diamond ⌖ model when the number of elements is odd:

$$I = 2\frac{b^3 t}{n^3}\sum_{k=1}^{(n-1)/2} k^2 = 2\frac{b^3 t}{n^3}\left(\frac{\left(\frac{n-1}{2}\right)^3}{3} + \frac{\left(\frac{n-1}{2}\right)^2}{2} + \frac{\left(\frac{n-1}{2}\right)}{6}\right) \quad \text{Eq. (3-13)}$$

Based on the above equations, the moment of inertia of the truss models is dependent on the number of elements. For instance, for the diagonal ☒ model with three elements, the moment of inertia is 1.22 times the actual plate moment of inertia. For the diamond ⌖ model with three elements, the moment of inertia is 0.889 times the actual plate moment of inertia. Figure 3-11 shows the moment of inertia of the truss models with a different number of elements from Eqs. (3-10) to (3-13) divided by that of the plate moment of inertia as well as some specific numerical results. Based on the analytical and numerical results, the diamond ⌖ model is less sensitive to a number of elements than the diagonal ☒ model, but the diamond ⌖ model underestimates *I*, while the diagonal ☒ model overestimates it.

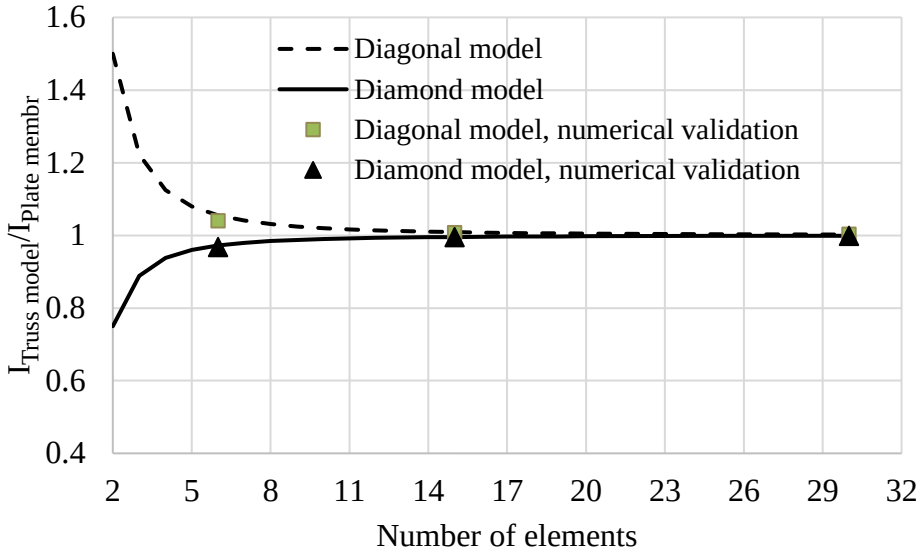

Figure 3-11. The trend of change in moment of inertia of the truss models with an increasing number of elements

- ***Numerical validation***

In order to validate the results of the analytical mesh sensitivity study, a short numerical study is conducted with different mesh sizes varying between 100mm and 500mm for a 9m tall cantilever plate beam. The beam width and thickness are 3000mm and 300mm respectively. A 1000 kN lateral force is applied at the top of the beam and the material is considered to be concrete with an elastic modulus of 27GPa. The deformed shapes and lateral displacements are shown in Figure 3-12 and Table 3-1, respectively. The expected behaviour is calculated based on the formulation provided by Timoshenko (1940), Eq. (3-13a). This Equation is for a cantilever beam that the cross-section is prevented from warping at the support and is loaded at the other end. Based on Eq. (3-13a) the expected deformation at the top of the cantilever plate beam is 14.33 mm.

$$\delta = \frac{PL^3}{3EI}\left[1 + 0.71\left(\frac{h}{L}\right)^2 - 0.10\left(\frac{h}{L}\right)^3\right] \qquad \text{Eq. (3-13a)}$$

Where P is the applied force, E and I are the elastic modulus and moment of inertia of the cantilever plate beam. Section height and beam length are denoted by h and L respectively. Note that Poisson's ratio is considered 0.3 for obtaining this equation.

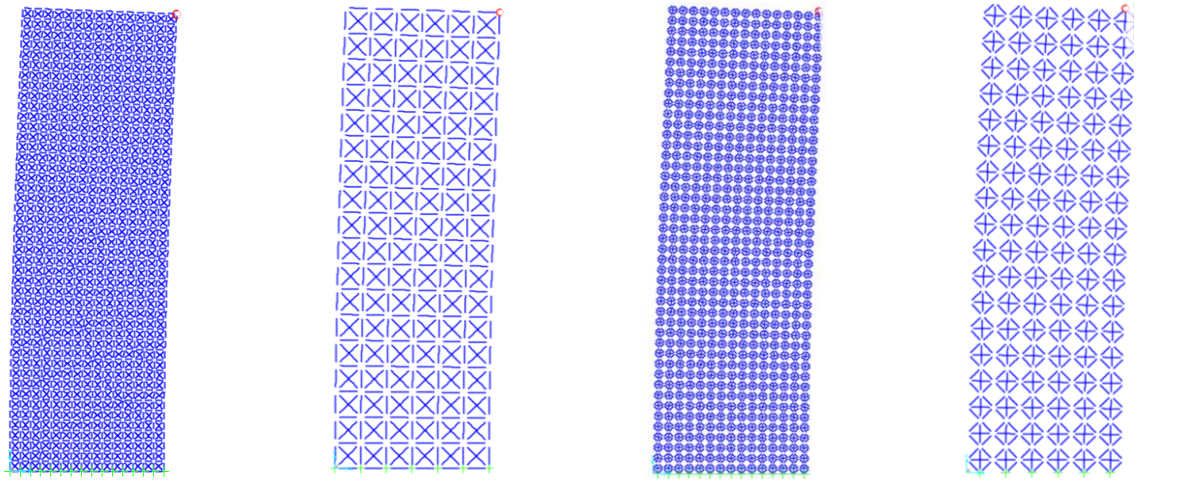

a) Diagonal ☒ model, 200mm mesh size | b) Diagonal ☒ model, 500mm mesh size | c) Diamond ⌖ model, 200mm mesh size | d) Diamond ⌖ model, 500mm mesh size

Figure 3-12. Comparison of diagonal ☒ and diamond ⌖ truss models

Table 3-1. Mesh size effect on cantilever plate beam lateral deformation

Mesh size (number of elements)	Deformation (mm)	
	Diagonal ☒ model	**Diamond ⌖ model**
500mm (18×6)	13.77	14.81
200mm (45×15)	14.22	14.40
100mm (90×30)	14.29	14.35
The lateral displacement from hand calculation is 14.33 mm		

The results indicate that the stiffness of the diagonal ☒ model decreases with finer mesh size while for the diamond ⌖ model the stiffness increases with a finer mesh and converge to the expected value. This is because in the diagonal ☒ model the actual width of the truss model is greater than the actual wall width due to the cross-section area of orthogonal boundary members and by decreasing the mesh size, the width of the plate in truss model reaches to the actual size. The stiffness ratio of cantilever beam plate models to the hand calculation is also plotted in Figure 3-11 which show good agreement with the closed-form assessment.

3.3.2.2 Beam axial forces and shear stud demands

- ***Beam axial and shear stud forces concept***

Beams in structural frames are often considered to carry bending and shear forces. However, during an earthquake event, inertia and transfer forces act on the diaphragm need to be transferred to the structural frames. Some mechanisms contribute to transferring these forces to the structural frame. It is often assumed that the slab transfers the lateral forces to the column through compression on the column face. While, in frame structures, since slab inertia forces act in the same direction as the frame sways, due to the beam-column joint rotation, a gap opens at location "A", shown in Figure 3-13. Because of this, slab inertia forces cannot go directly into the column. Instead, the forces must transfer into the steel beam through friction and mechanical attachments (shear studs) (MacRae and Clifton, 2015); this situation imposes axial forces to beam plastic hinge regions and connections at the beam ends that may need to be considered in design procedure. Also, if there is no construction gap between the slab and column, as the column sways, it bears against the concrete slab on the far side of the column causing a slab-interaction effect that increases the forces that the slab must transfer into the beam, and the beam must transfer it back to the columns. Axial forces in the beams may decrease the structure's lateral strength and deformation capacity.

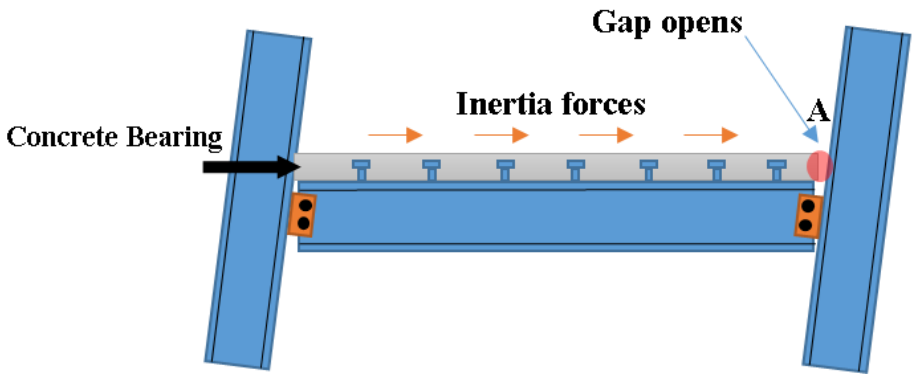

Figure 3-13. Slab-column interaction, a gap opens at Point A due to joint rotation

Overall, it should be noted that whether a gap opens or not, part of diaphragm forces will be transferred to the column or vertical lateral force resisting system through the beams because the diaphragm is not fully rigid.

- ***Beam axial and shear stud forces in truss modelling***

In truss element modelling, the beam axial forces and shear stud demands may be obtained directly from the analysis. However, the pattern of truss framework used for truss modelling can affect the results and the analysis assumptions. Therefore extra care should be made for selecting an appropriate truss model. In this study, differences between the diamond and the diagonal truss modelling methods are described.

Generally, the beam axial forces can be obtained if the rigid diaphragm assumption is not considered in the structural analysis, for shell, solid, or truss element modelling. However, the results from each of these modelling techniques are different and mainly represents a certain situation. For instance, if the diaphragm is modelled using shell or solid elements, part of the diaphragm forces is transferred directly to the column because the corner elements of the diaphragm are connected to the column nodes. This situation represents a full contact between the diaphragm and the column. Experimental tests that had been done by Chaudhari et al. (2015) showed that even when the slab is not isolated from the column, a gap opens between the slab and column in the moment frame structure and the slab forces cannot be transferred to the column directly.

Therefore, diaphragm forces need to be transferred into the steel beam through mechanical attachments, e.g. shear studs. This can be achieved using the diamond truss model directly because the diagonal members which represent the concrete struts are not connected to the beam-column joints. Consequently, the strut compression force transfers to VLFR system through beam axial forces as shown in Figure 3-14a. This means that in the case of truss modelling using the diamond ⟐ pattern, the slab is totally isolated. However, in

the diagonal truss element method, struts are connected to the beam-column joints and part of the slab forces transfers directly to the column as shown in Figure 3-14b. This results in lower beam axial and shear stud demands.

Therefore, using the diamond ⟐ model gives more reasonable results in terms of the beam axial forces for designing the beams and beam-column connections. On the other hand, the truss modelling nodes could be placed at the shear stud locations to directly record the shear stud demands. Similar results may be obtained using the diagonal ☒ truss element modelling or shell element modelling by removing the corner elements that are connected to the column nodes. However, it may decrease the total diaphragm in-plane stiffness based on the selected mesh size.

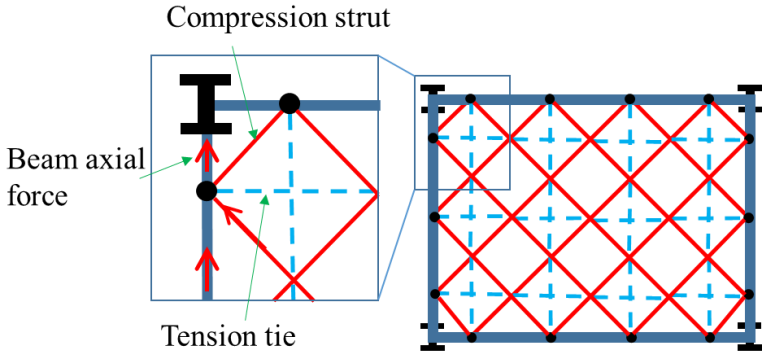

a) Diamond model

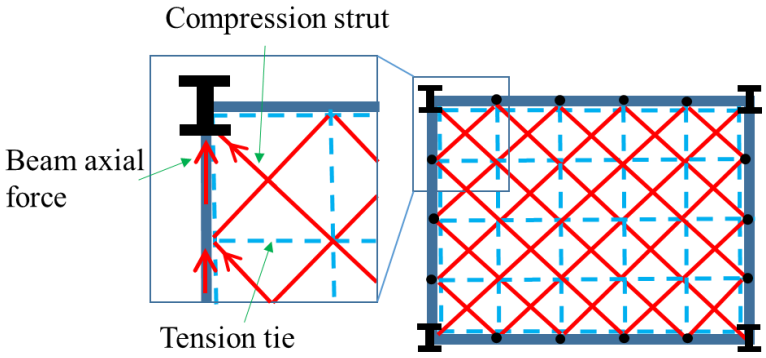

b) Diagonal model

Figure 3-14. Strut placed at the corner truss mesh unit

In addition to the strut locations, it should be noted that in the diagonal truss element modelling, the orthogonal members are required to be placed at the beam locations to complete the square framework pattern as shown in Figure 3-14b. These orthogonal elements also carry some portion of the beam axial and shear stud demands directly to the column which is not realistic due to gap opens, or due to an initial physical gap being placed around the column.

A one-storey two-bay braced frame, with the dimensions shown in Figure 3-15, is considered to investigate the beam axial and shear stud forces using both truss element modelling methods. In this model, it is assumed that a gap is provided around the column and there is no slab-column interaction. Also, a detailed elastic FEM model was created using ABAQUS software to compare the results with truss element modelling. The truss models were created using SAP2000 (2015) software. The simulated structure is designed using New Zealand building standards (e.g. NZS1170.5 2004 and NZS3404 2007) and the elastic ESA method is used to find the diaphragm imposed forces for performing the following analysis.

The lateral inertia force was distributed to truss element nodes based on the tributary area of each node. This was conducted in the detailed FEM, ABAQUS, model by defining a uniform horizontal surface traction force.

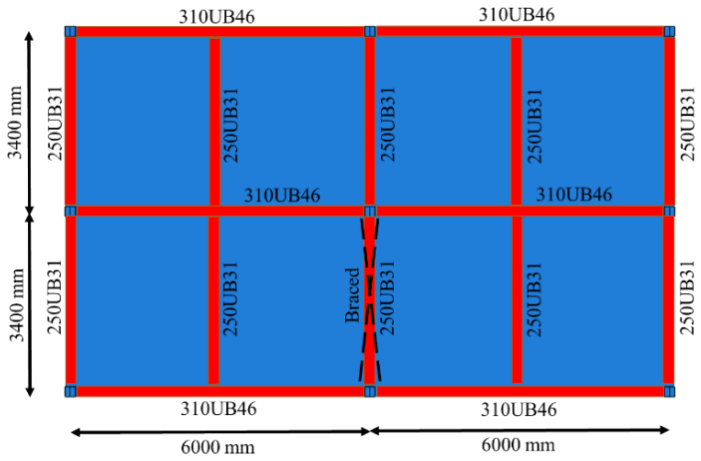

a) Floor plan dimensions and beam sections

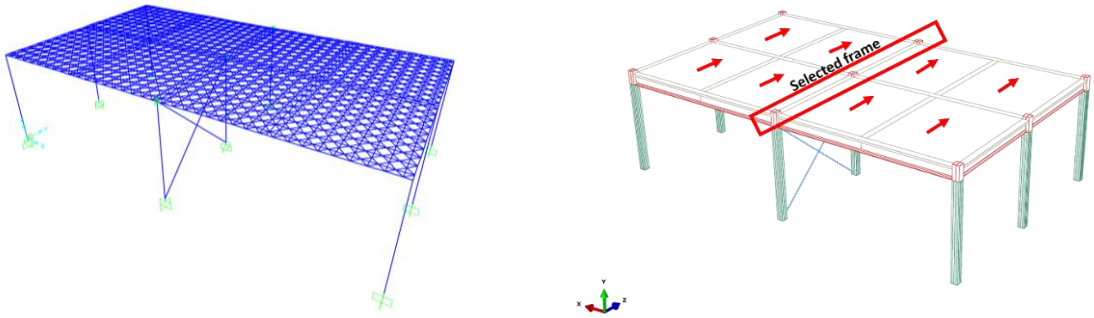

b) SAP2000 model

c) ABAQUS model

Figure 3-15. Model considered for investigating the beam axial and shear stud forces

Figure 3-16 shows the beam axial force diagram for the beam located in the middle of the simulated diaphragm. In the detailed FEM model physical gap has been provided between the slab and column to prevent the slab forces being transferred to the column directly and slab bearing forces to occur on the other side of the beam. As can be seen, the diamond ⟐ model indicate similar results to the detailed FEM model, the maximum difference in the peak values at the beams ends is less than 10%. The overall behaviour of the diagonal ☒ model is similar to the diamond ⟐ model, while, the peak beam axial forces in the diagonal ☒ model is considerably lower (about 35%). This is because, in the diagonal ☒ model, the slab is connected to the column and part of the diaphragm force transfers to the column directly as was shown in Figure 3-14.

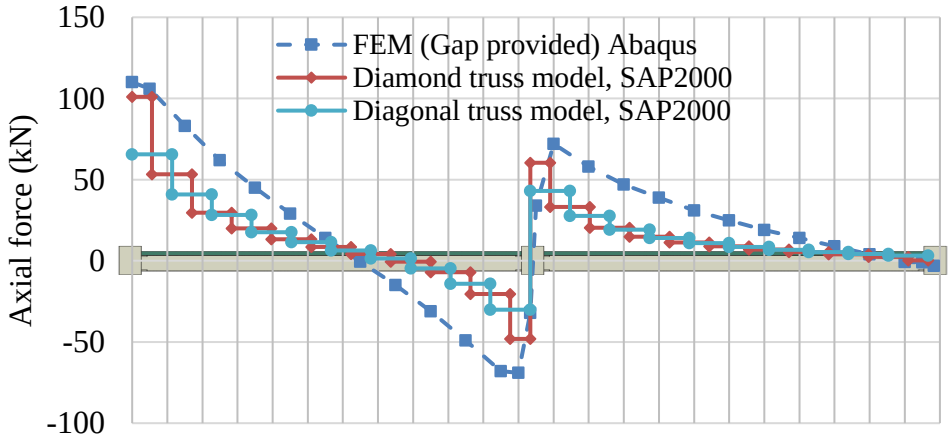

a) Beam axial force diagram

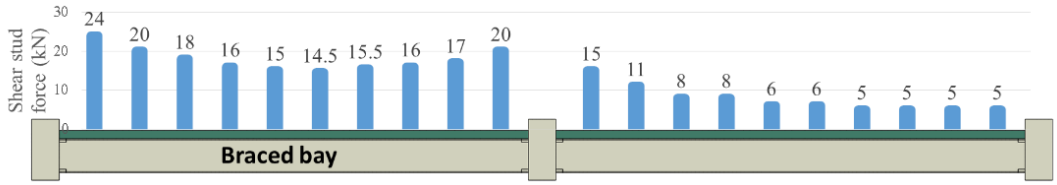

b) Shear stud forces in the shell/solid element model (ABAQUS), Average for left beam 17.6kN, right beam 7.4kN

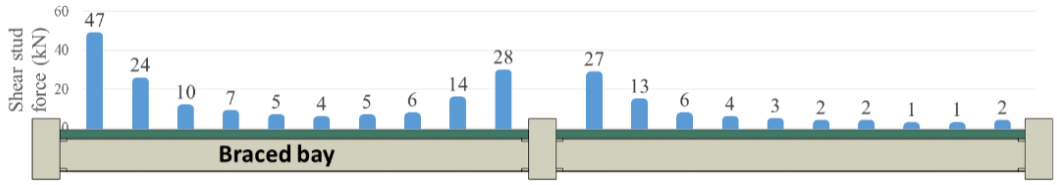

c) Shear stud forces (SAP2000) in the diamond ⟡ model, Average for left beam 15kN, right beam 6 kN

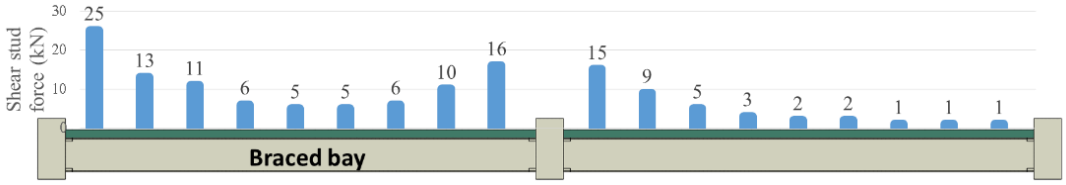

d) Shear stud forces (SAP2000) in the diagonal ☒ model, Average for left beam 10.5kN, right beam 4.4kN

Figure 3-16. Beam axial and shear stud forces in elastic models

Regarding shear stud demands, the trend of changing the shear forces in all models are similar. However, the average forces in the diamond ⟡ and the diagonal ☒ models are 15% and 50% lower than the detailed FEM model respectively.

3.4 Truss element modelling with different element aspect ratio

In Section 3.3.2, it has been shown that truss element modelling can effectively obtain diaphragm in-plane stiffness, and beam axial and shear stud forces. All of the examples used in this study consist of one or two bays structures, where it is possible to use a large number of truss elements to model diaphragm. For instance, the mesh size in the studied model

shown in Figure 3-15 was considered to be 300mm. However, in a real structure with several bays and storeys, it is not practical to create a fine mesh model and investigate the load path through the diaphragm. Therefore, it may be beneficial to model every bay with a limited number of elements (based on the diaphragm aspect ratio and geometry) considering an acceptable error in results.

Most floor plans consist of a number of bays with different aspect ratio due to architectural or geometry limitations. Therefore, the cross-section area of truss elements considering non-square units needs to be derived. Figure 3-17 shows a non-square truss framework.

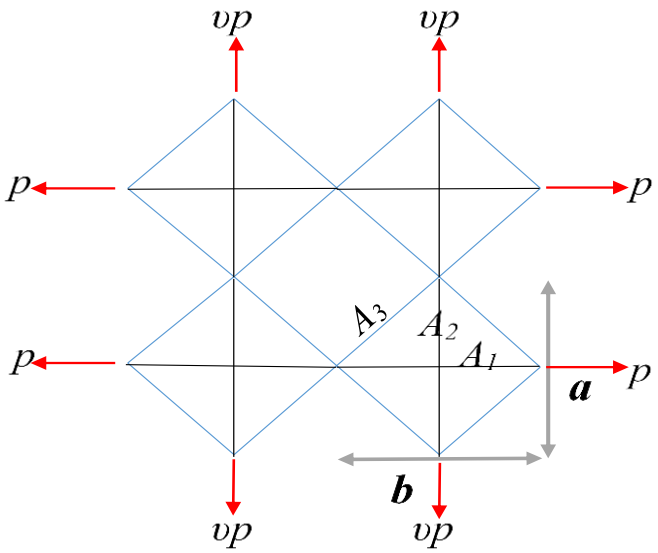

Figure 3-17. Non-square truss framework

Using the same method that was discussed in Section 3.2.2, the cross-section areas of the non-square truss framework can be found as follows according to Appendix C.

$$A_1=at\frac{\left(1-\frac{\nu b^2}{a^2}\right)}{1-\nu^2} \qquad \text{Eq. (3-14)}$$

$$A_2=bt\frac{\left(1-\frac{\nu a^2}{b^2}\right)}{1-\nu^2} \qquad \text{Eq. (3-15)}$$

$$A_3=\frac{\sqrt{a^2+b^2}\left(a^2+b^2\right)}{4ab(1+\nu)}t \qquad \text{Eq. (3-16)}$$

Where a and b are the dimensions of the framework pattern, t is the plate thickness and ν is Poisson's ratio of the plate material. It can be shown that in the case of the square mesh unite and $\nu = 1/3$, truss element cross-section areas are $A_1 = 0.75at$, $A_2 = 0.75at$ and $A_3 = 0.53at$.

- Beam axial and shear stud forces

The studied model in Section 3.3.2.2 is regenerated using one truss element between steel beams by putting the nodes at the centre of the beams as shown in Figure 3-18. In this example, the lateral load is distributed based on the tributary area of each node.

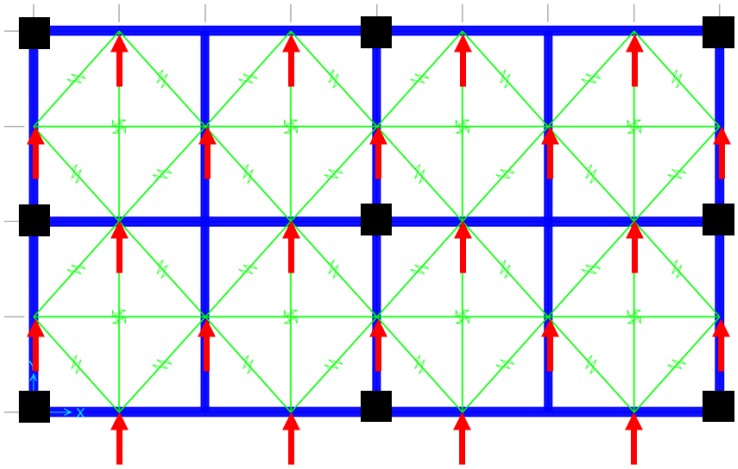

Figure 3-18. Putting nodes at the centre of the beams

The beam axial forces for the beam at the middle bay is plotted in Figure 3-19. As can be seen, the peak beam axial force values show less than 20% difference from the fine mesh truss model.

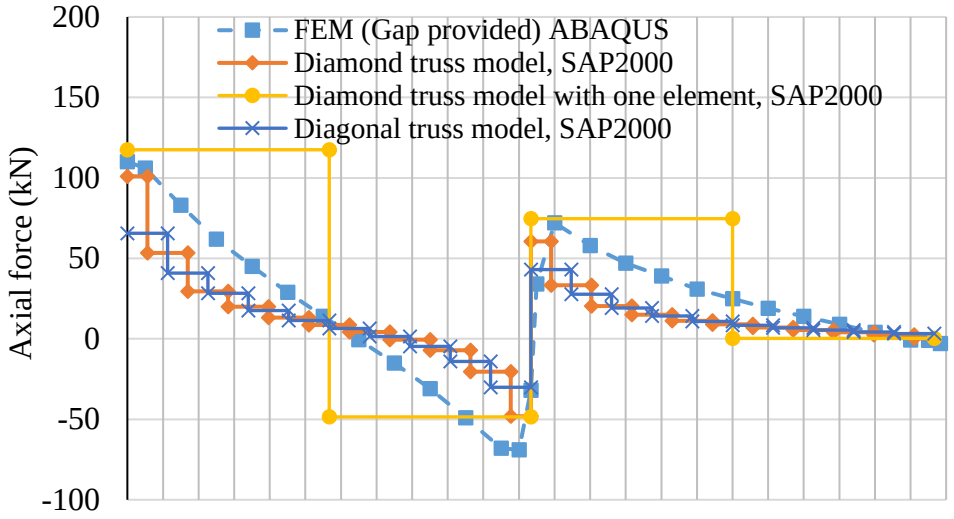

a) Beam axial force diagram

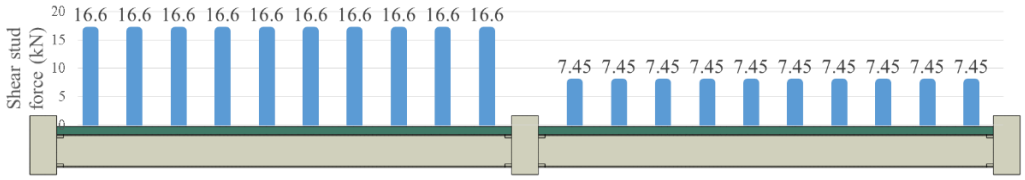

b) Average shear stud forces of single truss element model

Figure 3-19. Beam axial and shear stud force in single truss element model

Also, the average shear stud forces in this model was obtained by dividing the total shear force by the number of shear studs. The computed shear stud force was about 5% lower at the left beam and about 1% higher at the right beam compared with the detailed FEM model of Figure 3-16.

In most real structures even if the floor plan is rectangular, there are openings with various sizes in different locations for stairs, lifts, mechanical or electrical ducts. Therefore using a small number of large elements may be unsuitable for diaphragm modelling to obtain the likely load path through the diaphragm or in-plane deformations. However, it can be used for estimating the maxima of beam axial force at the beam ends, and average shear stud demands.

3.5 Different truss element modelling types

The concept of truss modelling method and both diagonal and diamond models were introduced in the previous sections. Generally, the truss method first was developed considering the elastic behaviour of a plate member, and it was assumed that all truss elements can carry tension and compression forces to satisfy the equilibrium and compatibility equations. However, for modelling a diaphragm consist of concrete material, the tension behaviour of the concrete (cracking) should be taken into account to achieve more realistic results. Therefore, different modelling techniques are introduced and compared here to find out the best method for modelling concrete diaphragms in design. The modelling methods considered on a square truss mesh unit include the following.

Model 1. Elastic truss modelling

Model 2. Compression-only diagonal members with elastic orthogonal members (compression and tension)

Model 3. Compression-only diagonal members with considering reinforcements as orthogonal members (concrete compression, tension reinforcement)

Model 4. Compression-only diagonal members with tension-only orthogonal members

Model 5. Compression-only diagonal members with elastic orthogonal members (based on "The Seismic Assessment of Existing Buildings" Section C5 recommendations)

Model 6. Truss modelling considering nonlinear properties of the concrete and reinforcements

Note that, as it was shown the diamond model has advantages over the diagonal model such as i) it has less mesh sensitivity, ii) provides more reasonable beam axial force and shear stud demands and iii) considers gap around the column, all the different truss modelling types are investigated using the diamond model in the following sections.

3.5.1 Elastic truss modelling (all members carry both tension and compression)

This method was described comprehensively in Section 3.2.2. It was shown that this method gives accurate results for materials with Poisson's ratio $\nu = 0.33$ and considering a sufficient number of elements. The orthogonal and diagonal member cross-section areas are $A_1 = 0.75at$ and $A = 0.53\,at$ respectively. Where a is the dimension of the framework pattern and t is the plate thickness.

3.5.2 Compression-only diagonal members with compression/tension orthogonal members

The elastic truss model can effectively model the shell element behaviour. However, it does not provide good information about the actual strut compression forces and tension tie forces because the diagonal members are assumed to carry both tension and compression forces. Therefore, the truss element method with compression-only diagonal members (which represents concrete struts) may be used for finding more realistic load paths through the diaphragm.

Considering that the diagonal members act in compression only (strut) and the orthogonal members act in both compression and tension, the tension and compression behaviour of the truss model will be different. Which means the truss model subjected to orthogonal compression forces in one direction acts like an elastic plate because all the elements are contributing in load carrying mechanism. While in tension the truss model works independently in perpendicular directions and the longitudinal and transverse deformations are not related to the Poisson's ratio. Thus, for calculating the truss element cross-section areas three loading conditions considered, include 1) uniaxial tension, 2) uniaxial compression and, 3) pure shear as shown in Figure 3-20.

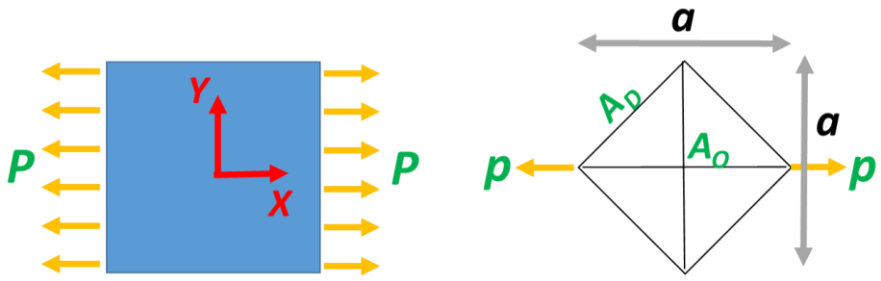

a) Normal tension force per unit length, P in the X-direction

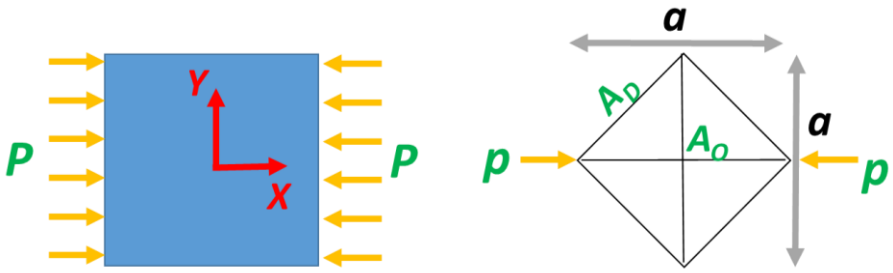

b) Normal compression force per unit length, P in the X-direction

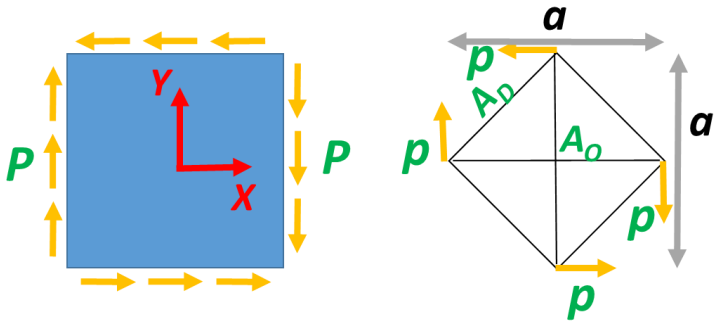

c) Pure shear force per unit length, P

Figure 3-20. General loading conditions for determining framework properties, p is the normal edge force to each element where $p = Pa$

Similar to the method discussed in Section 3.2.2, using equilibrium and compatibility conditions the cross-section area of the truss elements can be obtained as shown below. Note that these areas are different from those assuming all fully elastic elements as described by Hrennikoff (1941). The truss element strains are obtained in terms of element cross-section area and the angle between them. Then the framework strains are equated to the

corresponding strains in the plate member ε_x and ε_y with the same loading condition. Based on solid mechanics, the plate strain in the X-direction, ε_x, for the first case of loading is

$$\varepsilon_x = \frac{P}{Et} \quad \text{Eq. (3-17)}$$

Where P is uniform force per unit length, E is the elastic modulus of the plate material and t is the plate thickness.

As it was mentioned in the previous paragraph, when tension is applied in one direction there is no deformation in the orthogonal direction in this method because the diagonal members work in compression only. Therefore, the cross-section area of orthogonal members in tension, A_{OT}, could simply be found by equating the strains in the plate and the truss element subjected to tension forces only. Note that the cross-section areas of orthogonal members in tension, A_{OT}, and compression, A_{OC}, may not be equal necessarily.

The tensile strain in the truss element can be found using:

$$\varepsilon_x = \frac{Pa}{EA_{OT}} \quad \text{Eq. (3-18)}$$

By equating Eq. (3-17) and Eq. (3-18), A_{OT} can be found as

$$A_{OT} = at \quad \text{Eq. (3-19)}$$

The shear deformation of the plate subjected to a tangential load, γ_{xy}, can be calculated using Eq. (3-3) for an elastic plate member as shown in Figure 3-20c.

$$\gamma_{xy} = \frac{2(1+\nu)P}{Et} \quad \text{Eq. (3-3)}$$

Similar to the elastic truss element model in Section 3.2.2, by equating the framework shear strain with the plate shear strain, the cross-section area of the compressive diagonal member, A_D, can be found as:

$$A_D = \frac{\sqrt{2}at}{(1+\nu)} \quad \text{Eq. (3-20)}$$

To find the cross-section area of the orthogonal member in compression, A_{OC}, deformation compatibility and force equilibrium should be satisfied simultaneously.

Based on the force equilibrium in the X and Y-directions:

$$F_{OC} + 2F_D \cos 45 = p \quad \text{Eq. (3-21)}$$

$$2F_D \cos 45 = F_{OT} \quad \text{Eq. (3-22)}$$

Where F_D, F_{OT} and F_{OC} are diagonal member compression force, orthogonal member tension and compression forces respectively.

Substituting Eq. (3-22) into Eq. (3-21) gives:

$$F_{OC} + F_{OT} = p$$

Figure 3-21 shows the deformation of the truss unit subjected to an axial compression force, p. It can be seen that the axial deformation δ_x is equal to the lateral expansion δ_y plus the component from the axial contraction in the diagonal members that is denoted by δ_D.

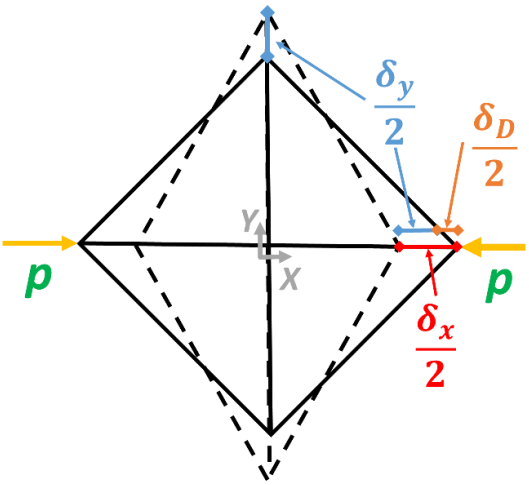

Figure 3-21. Deformation of the truss unit under axial compression

Considering the relationship between the diagonal and orthogonal member deformations, δ_D and δ_x, and substituting the diagonal cross-section area, A_D from Eq. (3-20) and orthogonal tension cross-section area, A_{OT} from Eq. (3-19), the orthogonal compression cross-section area, A_{OC}, can be found which is discussed below in detail.

Based on the deformation compatibility, shown in Figure 3-21, which δ_x is the axial deformation of the truss element under axial compression force and δ_y is the transverse deformation:

$$\delta_x = \delta_y + \delta_D \qquad \text{Eq. (3-23)}$$

Substituting Eqs. (3-17, 3-19 and 3-20) into Eq. (3-23) gives

$$\frac{p}{2Et} = \frac{F_{OT}a}{2Eta} + \frac{F_D\left(\frac{\sqrt{2}a}{2}\right)(1+\nu)}{\left(\frac{\sqrt{2}}{2}\right)\sqrt{2}Eta} \qquad \text{Eq. (3-24)}$$

Considering Eq. (3-24) and Eq. (3-22), the axial force in the diagonal member, F_D, can be obtained as:

$$F_D = \frac{p}{\sqrt{2}(2+\nu)}$$

Also, the axial tension force in the vertical orthogonal member, F_{OT}, is

$$F_{OT} = \frac{p}{(2+\nu)}$$

And using Eq. (3-21)

$$F_{OC} = \frac{p(1+\nu)}{(2+\nu)} \qquad \text{Eq. (3-25)}$$

The compression cross-section area of the orthogonal members, A_{OC}, may simply be found using the axial strain Eq. (3-17) and the truss member axial force, F_{OC} of Eq. (3-25) as:

$$\frac{F_{OC}}{EA_{OC}} = \frac{p}{Eta}$$

Substituting F_{OC} from Eq. (3-25) gives

$$A_{OC} = \frac{at(1+\nu)}{(2+\nu)} \qquad \text{Eq. (3-26)}$$

Based on the Poisson's ratio definition:

$$\nu = \frac{\delta_y}{\delta_x}$$

By substituting the axial deformations δ_y and δ_x in the above equation, it can be found that

$$\delta_y = \frac{p}{(2+\nu)Eat}$$

$$\delta_x = \frac{p}{Eat}$$

$$\nu = \frac{\frac{p}{(2+\nu)Eat}}{\frac{p}{Eat}}$$

$$\nu = \frac{1}{2+\nu} \qquad \text{Eq. (3-26a)}$$

By solving Eq. (3-26a), $\nu = 0.414$. That is, this framework with compression-only diagonal members is only accurate for material with Poisson's ratio, ν, equal to 0.414. Considering this Poisson's ratio, the truss element cross-section areas are equal to:

$$A_D = at$$

$$A_{OT} = at$$

$$A_{OC} = 0.585at$$

These values show that orthogonal members in tension should have the same width as the truss mesh unit, $A_{OT} = at$, because diagonal members cannot act in tension and participate in force carrying mechanism. But in compression some part of the axial compression force can be carried by the diagonal members and therefore smaller orthogonal cross-section in compression, $A_{OC} = 0.585at$, is required to achieve the same axial strain as the plate member.

3.5.3 Compression-only diagonal members with reinforcement tension/concrete compression orthogonal members

In this case it is assumed that all the tension forces are carried by slab reinforcements in a fully cracked situation. Therefore the tension cross-sectional area of the orthogonal members, A_{OT}, is equal to the steel reinforcement area, A_s, within the element width as:

$$A_{OT} = A_s \qquad \text{Eq. (3-27)}$$

Similar to the Section 3.5.2, since the diagonal members are in compression only, the tensile deformations in perpendicular directions are independent.

The shear deformation of the plate, γ_{xy}, subjected to tangential force, p, as shown in Figure 3-20c, can be found using Eq. (3-3) similar to the elastic plate member.

$$\gamma_{xy} = \frac{2(1+\nu)p}{Eta} \qquad \text{Eq. (3-3)}$$

By equating the framework shear strain obtained in Section 3.2.2 Eqs. (3-4 and 3-5) with the plate shear strain, γ_{xy}, the cross-section area of the diagonal member, A_D, is

$$A_D = \frac{\sqrt{2}at}{(1+\nu)} \qquad \text{Eq. (3-20)}$$

To find the compression cross-section area of the orthogonal member, A_{OC}, the deformation compatibility and force equilibrium conditions should be satisfied. Based on the force equilibrium in the X and Y-directions:

$$F_{OC} + 2F_D \cos 45 = p \qquad \text{Eq. (3-21)}$$

$$2F_D \cos 45 = F_{OT} \qquad \text{Eq. (3-22)}$$

Where F_D, F_{OT} and F_{OC} are diagonal member compression force, orthogonal member tension and compression forces respectively.

Substituting Eq. (3-22) into Eq. (3-21) gives:

$$F_{OC} + F_{OT} = p$$

Similar to the previous modelling method in Section 3.5.2, the deformation of the truss unit under an axial compression force, p, is shown in Figure 3-21. It can be seen that the axial deformation δ_x is equal to the lateral expansion δ_y plus the contribution from the axial contraction in the diagonal members that is denoted by δ_D. Considering the relationship between the diagonal and orthogonal member deformations (δ_D, δ_x and δ_y) and substituting the diagonal cross-section area, A_C, and orthogonal tension cross-section (reinforcement cross-section area), A_{OT}, the orthogonal compression cross-section area, A_{OC}, can be obtained as is discussed below.

The plate axial compression strain equals to

$$\varepsilon_x = \frac{P}{Et} \qquad \text{Eq. (3-17)}$$

Based on the deformation compatibility, where δ_x is the axial deformation of the truss element under axial compression and δ_y is the transverse deformation as shown in Figure 3-21.

$$\delta_x = \delta_y + \delta_D \qquad \text{Eq. (3-23)}$$

Substituting Eqs. (3-17, 3-27 and 3-20) into Eq. (3-23) gives

$$\frac{p}{2Et} = \frac{F_{OT}a}{2E_sA_s} + \frac{F_D\left(\frac{\sqrt{2}a}{2}\right)(1+\nu)}{\left(\frac{\sqrt{2}}{2}\right)\sqrt{2}Eta} \qquad \text{Eq. (3-28)}$$

Where E_s and A_s are the elastic modulus and area of the reinforcements placed within each element. Considering Eq. (3-28) and Eq. (3-22) the axial force in the diagonal member can be found as

$$F_D = \frac{p}{2Et\left(\frac{a}{\sqrt{2}E_sA_s} + \frac{(1+\nu)}{\sqrt{2}Et}\right)} \qquad \text{Eq. (3-29)}$$

Substituting Eq. (3-29) into Eq. (3-21) gives

$$F_{OC} = p\left(1 - \frac{\sqrt{2}}{2Et\left(\frac{\sqrt{2}}{2E_st\rho} + \frac{(1+\nu)}{\sqrt{2}Et}\right)}\right) \qquad \text{Eq. (3-30)}$$

Where ρ is the reinforcement ratio $\frac{A_s}{at} = \frac{A_{OT}}{at}$.

The compression cross-section area of the orthogonal members, A_{OC}, can simply be found using the axial strain Eq. (3-17) and the orthogonal member axial force, F_{OC} (Eq. 3-30) as:

$$A_{OC} = at\left(1 - \frac{\sqrt{2}}{2Et\left(\frac{\sqrt{2}}{2E_S t\rho} + \frac{(1+\nu)}{\sqrt{2}Et}\right)}\right) \qquad \text{Eq. (3-30)}$$

This equation shows that the cross-section area of the orthogonal member in compression, A_{OC}, is dependent on the reinforcement ratio provided in the slab, ρ, and hence on A_{OT}.

Based on the Poisson's ratio, ν, definition

$$\nu = \frac{\delta_y}{\delta_x}$$

By substituting the axial deformations in the above equation, it can be found that the Poisson's ratio is related to the reinforcement ratio.

$$\nu = \frac{1}{1+\frac{(1+\nu)E_S\rho}{E}} \qquad \text{Eq. (3-30a)}$$

or

$$\rho = \frac{E(1-\nu)}{\nu(1+\nu)E_S}$$

Figure 3-22 plots the Poisson's ratio (ν) versus the reinforcement ratio (ρ). Note that this Figure is plotted considering $\frac{E_S}{E} = 9$, where E_s and E are the elastic modulii of reinforcements and concrete respectively.

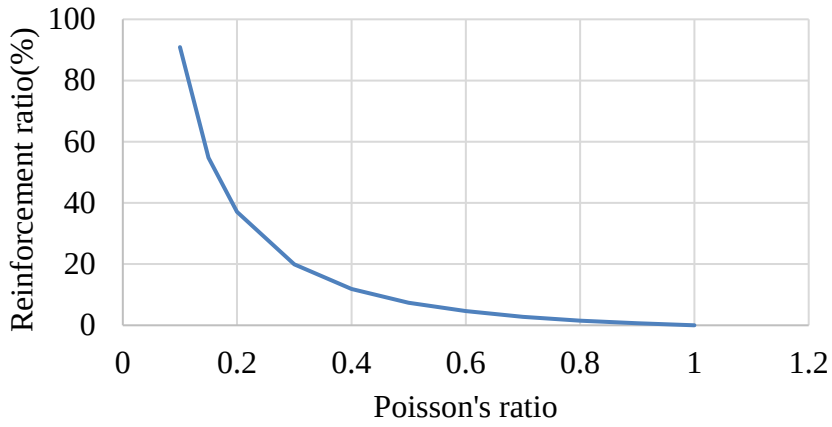

Figure 3-22. Poisson's ratio (ν) versus reinforcement ratio (ρ) for compression-only diagonal-reinforcement tension orthogonal member

This plot shows that increasing the reinforcement ratio decreases the Poisson's ratio of the truss model. Which is because more reinforcement in the slab decreases the lateral deformations. Also, it is noted that for reinforcement ratio less than 7.4% the Poisson's ratio becomes more than 0.5.

Figure 3-23 plots the A_{OC} and A_D versus reinforcement ratio (ρ).

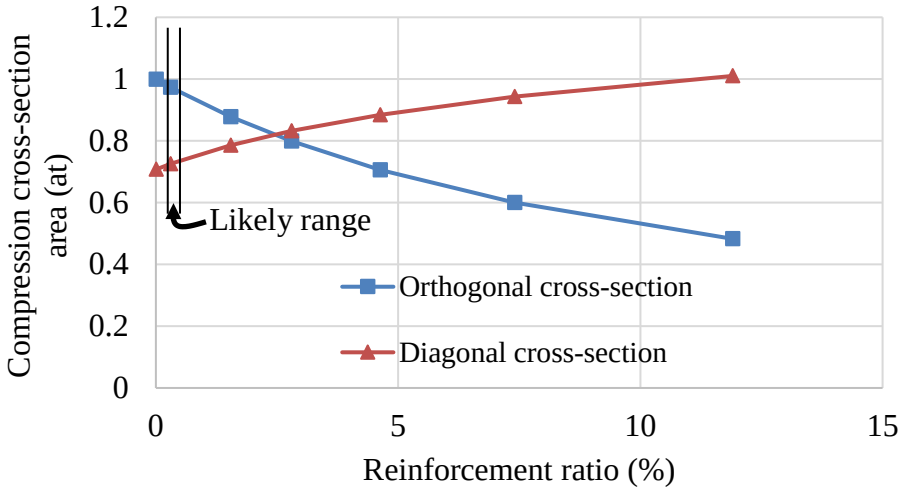

Figure 3-23. Orthogonal and diagonal compression cross-section areas, A_{OC} and A_D, versus reinforcement ratio (ρ) for compression-only diagonal-reinforcement tension orthogonal member

According to the plots in Figure 3-23, there is no specific value for diagonal and orthogonal cross-section areas in compression, A_D and A_{OC}, to be applicable for all situations.

These cross-section areas vary depending on the amount of reinforcement, A_s or A_{OT}, provided in slab.

Considering the fact that the reinforcement ratio in steel deck composite slabs usually is between 0.2% to 0.4% according to AS/NZS2327 (2017) Table 2.2.1, the truss element cross-sectional areas may be taken as that based on a 0.3% reinforcement ratio without significant error, as shown in Figure 3-23, as:

$$A_D = 0.725at$$

$$A_{OT} = A_s$$

$$A_{OC} = 0.97at$$

These values show that orthogonal members in tension should have the same area as slab reinforcement, $A_{OT} = A_s$. This is because it was assumed all tension forces will be carried by reinforcement and diagonal members cannot act in tension and participate in the force-carrying mechanism. In compression, some part of the axial compression force can be carried by the diagonal members, however, this is limited by the amount of reinforcement provided in the orthogonal member as shown in Figure 3-21. Therefore, a larger orthogonal cross-section in compression, $A_{OC} = 0.97at$, is required compare to "compression-only diagonal members with compression/tension orthogonal members truss model" to achieve the same axial strain as a plate member.

Note that 0.2% to 0.4% reinforcement ratios result in Poisson's ratio about 0.95 according to Eq. (3-30a). Although this value is impossible considering elastic material behaviour, the error associated with this will be checked later.

3.5.3.1 Tension stiffening considerations

When a reinforced concrete member is loaded in tension, the axial stress-elongation diagram of the member shows that the concrete contributes to carrying tension forces even

after severe cracking has developed. This effect which increases the stiffness of bare steel reinforcements in tension is called *tension-stiffening*.

The tension stiffening mechanism is shown in Figure 3-24. This shows a prism loaded in tension and the stress distribution of concrete and reinforcement along the specimen length. At cracks, the entire force is transferred across the reinforcement. Between the cracks, axial tension force transfers from steel to concrete through bond stress and the force is carried by both steel and concrete. The total applied force is equal to the sum of the force in the reinforcement and the force in the concrete at any section. At the cracked locations, stress in concrete is assumed to be zero.

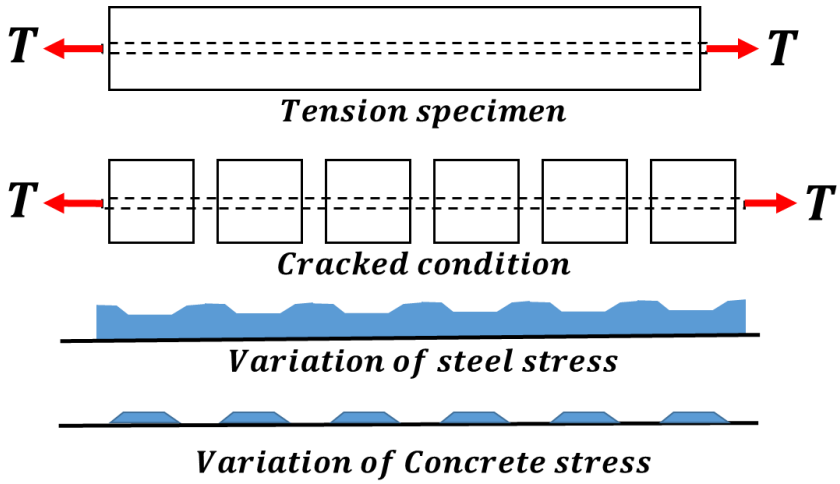

Figure 3-24. Tension-stiffening mechanism

Figure 3-25 presents a schematic stress-strain behaviour of a reinforced concrete member in tension. It shows that the axial tension stiffness of the reinforced concrete decreases by increasing the axial tension strain to reach the bare steel stiffness. Therefore the axial stiffness of the member is a function of the axial strain.

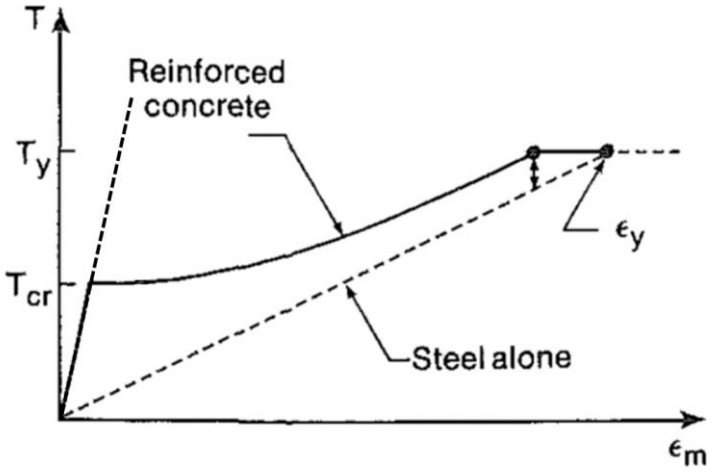

Figure 3-25. Axial stress-strain behaviour of a reinforced concrete member

To consider the tension-stiffening effect in the truss modelling method, the cross-sectional area of the orthogonal member in tension, A_{OT}, should be modified using a try and error procedure knowing the likely tensile behaviour of the reinforced concrete member as shown in Figure 3-25. To conduct this modelling, an arbitrary cross-sectional area in between the reinforcement, A_s, and the concrete, A_{OT}, cross-sectional areas should be selected. Using the analysis results, the assumed tension cross-sectional area for the orthogonal members may be corrected according to the strain of the orthogonal members.

In this study, the tension-stiffening effects are not considered because:

1. The try and error method is not practical in design and also the level of tension force in orthogonal members is different for each truss mesh unit. Therefore, each truss mesh unit should have a unique cross-section area depending on the tension forces.
2. The tension-stiffening effects depend on various parameters (Massicotte et al. 1990, Moehle 2015 and Carreira and Chu 1986) such as:
    a) Bond properties between the reinforcement and the concrete
    b) Level of the imposed tension forces
    c) Reinforcement ratio of the member

d) Loading strain rate

e) The thickness of the concrete cover

f) Effective tension area of the concrete surrounding the tension reinforcement

In this study, the upper and lower bounds of the concrete slab in-plane stiffnesses are investigated considering the compression-only diagonal members with compression/tension orthogonal members model described in Section 3.5.2 and the compression-only diagonal members with reinforcement tension/concrete compression orthogonal members model described in Section 3.5.3.

3.5.4 Compression-only diagonal member, tension-only orthogonal member

Another potential method for truss element modelling is to consider compression-only diagonal members and tension-only orthogonal members. This method seems to be easier to use because diagonal members act in compression only and orthogonal members in tension-only. Therefore the results may be easier to interpret for designer. However, this method does not satisfy compatibility equations as is discussed in the following.

Similar to the previous methods, the shear deformation of the plate subjected to tangential force can be calculated using Eq. (3-3) similar to the elastic plate member.

By equating the framework shear strain with the plate shear strain, the cross-section area of the diagonal member can be found from Eq. (3-20).

Based on the force equilibrium in the X and Y-directions:

$$2F_D \cos 45 = p \qquad \text{Eq. (3-31)}$$

$$2F_D \cos 45 = F_{OT} \qquad \text{Eq. (3-32)}$$

Therefore,

$$F_{OT} = p$$

Where F_D and F_{OT} are the diagonal member compression force and the orthogonal member tension force respectively.

The tension cross-section area of the orthogonal member, A_{OT}, can simply be found by equating the strain in the plate and the truss element. The tensile strain in the truss element can be found using:

$$\varepsilon_x = \frac{p}{EA_{OT}} \qquad \text{Eq. (3-33)}$$

Where A_{OT} is the cross-section area of the orthogonal member in tension. By equating Eq. (3-17) and Eq. (3-33), A_{OT} is found.

$$A_{OT} = at$$

Using deformation compatibility equation, Eq. (3-28) and substituting Eq. (3-20) and A_{OT}:

$$\delta_x = \delta_y + \delta_D$$

$$\frac{p}{2Eta} = \frac{p}{2Eat} + \frac{F_D\left(\frac{\sqrt{2}a}{2}\right)(1+\nu)}{\left(\frac{\sqrt{2}}{2}\right)\sqrt{2}Eta}$$

Which means

$$\frac{F_D\left(\frac{\sqrt{2}a}{2}\right)(1+\nu)}{\left(\frac{\sqrt{2}}{2}\right)\sqrt{2}Eta} = 0$$

The force in the diagonal member cannot be zero due to the force equilibrium, Eq. (3-31), therefore, A_D needs to be infinitely large. This is in contradictory with A_D found using the shear deformation equation in Eq. (3-20). This modelling method cannot satisfy deformation compatibility, and cannot be considered as a possible truss modelling method.

3.5.5 Compression-only diagonal members with compression/tension orthogonal members (based on "The Seismic Assessment of Existing Buildings (2017)" Section C5 recommendations)

In "The Seismic Assessment of Existing Buildings (2017)" guideline, it is suggested that for buildings that are essentially rectangular with a relatively uniform distribution of vertical lateral force-resisting systems across the plan of the building, and have no significant change of plan with height, simple hand-drawn strut-and-tie solutions can be used. However, buildings with significant asymmetry in the location of lateral force-resisting elements (distribution across the building plan, termination up the height of the building, varying stiffness and/or strength between vertical elements) may require more sophisticated analysis.

For these irregular types of structures, the truss model is recommended to obtain diaphragm design actions based on the practice note prepared by Holmes Consulting Group, (2015). This document was prepared based on Hrennikoff's (1941) study. The effective width of truss elements was recommended for orthogonal and diagonal members equal to 0.75×grid spacing and 0.53×grid spacing respectively. Note that the diagonal members carry compression forces only. This assumption contradicts Hrennikoff's (1941) study assumptions which assume all elements carry compression and tension forces.

Also, this guideline provides some recommendations regarding the effective thickness of the truss elements. For in situ slabs and flat slabs, the combined thickness of the topping and units (if present) parallel and transverse to the units (if present) was considered. And for steel profile composite floors it is suggested that, the average of the flange and web cross-section areas for elements parallel to the webs. The thickness of the flange for truss members transverse to the webs was also suggested.

The Holmes Practice Note (Holmes, 2015) was prepared based on the diagonal modelling method of Hrennikoff (1941). A modification to the framework was included in

the Practice Note to account for anticipated diaphragm damages/deterioration such as floor to beam separation due to beam elongation in concrete structures or column separation from slab due to the beam-column rotation as discussed in Section 3.3.2.2. It was also recommended to remove the diagonal strut to the corner column in the corner element because these compression struts may not be able to transfer the axial force to the VLFR system as shown in Figure 3-26.

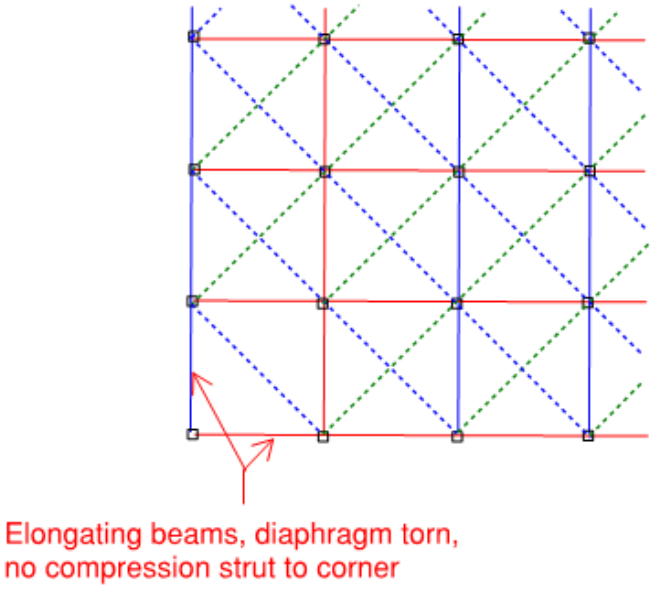

Figure 3-26. Recommended truss modelling at corner columns to account for anticipated diaphragm damage/deterioration (Holmes, 2015)

Note that the cross-section areas that are mentioned in Holmes (2015) Practice Note were developed for the diagonal truss element model. However, they can equally be used for diamond truss modelling because in the elastic truss element models the cross-section areas of the diagonal and the diamond models are the same.

3.5.6 Nonlinear truss element modelling

Nonlinear truss element method may also be employed for modelling a diaphragm. This allows the nonlinear behaviour of the reinforcement and concrete material to be considered. If the tensile strength of the concrete material is ignored (for simplicity), then the truss model

has compression-only diagonal members and orthogonal members that carry tension represents the reinforcement and compression represents the concrete as mentioned in Section 3.5.3. Considering the same method used in Section 3.5.3, the cross-section area of the orthogonal and diagonal members are equal to:

$$A_D = 0.725at$$

$$A_{OT} = A_s$$

$$A_{OC} = 0.97at$$

Note that as shown in Section 3.5.3, using a cross-section reinforcement ratio of 0.3% is reasonable for the range of reinforcement ratio likely in practice.

3.5.7 Comparison of different truss element modelling techniques

In order to compare the truss modelling methods, the cantilever beam-plate shown in Figure 3-27 is modelled with the different techniques. The results are compared in terms of global stiffness and internal forces on specific plate elements. Table 3-2 firstly summarises the modelling methods and cross-section properties of each truss element. The diamond truss framework is used without beam members.

Table 3-2. Cross-section properties of truss element modelling methods

Model	Model description	Diagonal member		Orthogonal member	
		Compression	Tension	Compression	Tension
1	Truss elastic	$0.53\,at$	$0.53\,at$	$0.75at$	$0.75at$
		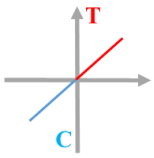		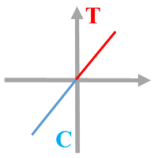	
2	Diagonal Compression-only-1 (elastic)	at	0	$0.585at$	at
		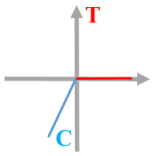		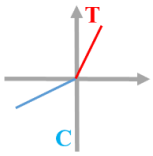	
3	Diagonal Compression-only-2 (cracked)	$0.725at$	0	$0.97at$	A_s
		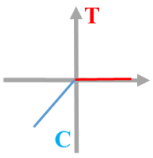		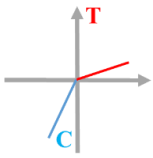	
4	Diagonal Compression-only, Orthogonal tension-only	$0.949at$	0	0	at
		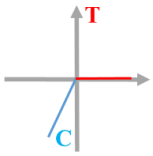		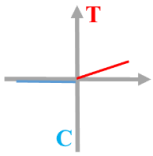	
5	Diagonal Compression-only "seismic assessment guideline"	$0.53\,at$	0	$0.75at$	$0.75at$
		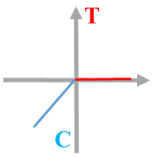		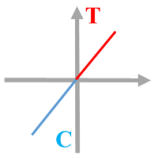	
6	Shell elastic	-		-	
7	Nonlinear truss	$0.725at$	0	$0.97at$	A_s
		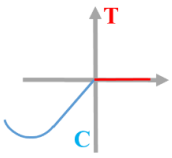		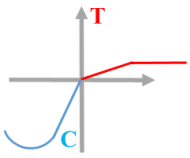	
8	Nonlinear FEM	-		-	

- **Stiffness investigation**

Aspect ratios, L/w, of 1, 2, 4, and 10 are investigated and the stiffnesses of Model 1-6 are presented in Table 3-2. Figure 3-27 shows the geometry of the investigated model where w is equal to 1.5m and L is changing with aspect ratio. Shear force is applied at the far end of

the diaphragm and the other end is fixed. The cantilever beam-plate is considered to be reinforced with φ8@250mm mesh which is equal to 0.33% reinforcement ratio. The concrete elastic modulus, Poisson's ratio and the reinforcements elastic modulus are considered 32 GPa, 0.2 and 200 GPa respectively. The slab topping thickness is 50mm. Note that the truss mesh unit dimension in all the models is equal to 250mm.

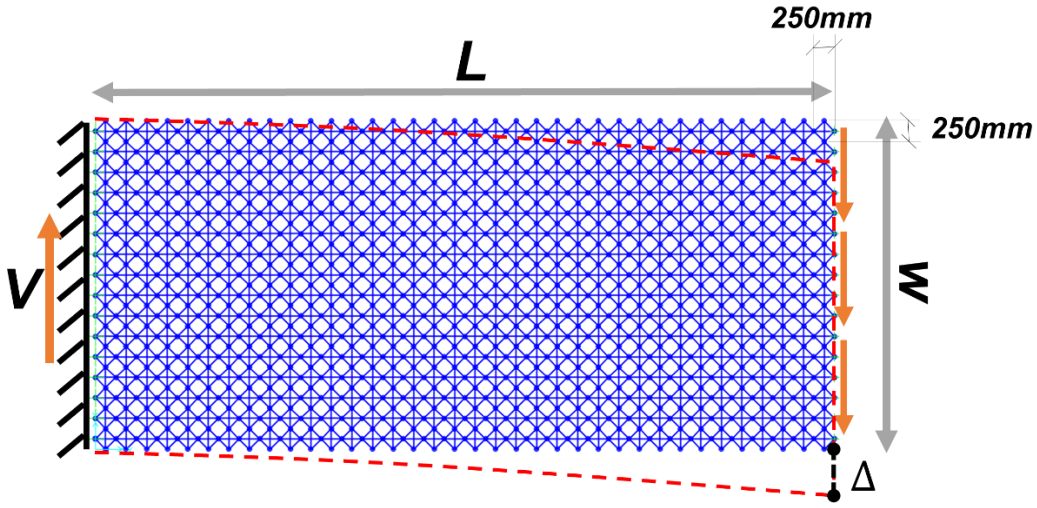

Figure 3-27. Cantilever beam-plate considered for comparing truss element modelling techniques

Table 3-3 summarises the stiffness of all models. Also the results are plotted in Figure 3-28. In this Figure, the stiffness of each model is normalised by the stiffness of Model 6, shell elastic, which is considered as the most accurate elastic (non-cracking) solution.

Model 1, truss elastic, gives the closest result to the shell element in terms of stiffness. However, in this model diagonal members act in both compression and tension making it difficult to directly obtain compression strut and tension tie demands. The reason for the difference between the shell (Model 6) and elastic truss model (Model 1) is different Poisson's ratio and the number of elements used for modelling. The difference due to different Poisson's ratio is higher at lower aspect ratios and as the beam length increases the effect of Poisson's ratios decreases. The required Poisson's ratio is 0.33 to match the results as described in Section 3.2.2, however, a Poisson's ratio of 0.2 for concrete is used in Model 6.

Table 3-3. Stiffness of investigated modelling techniques for different aspect ratios

	Stiffness (kN/mm)					
Aspect ratio (L/w)	Model 1, Truss elastic	Model 2, Diagonal Compression -only-1 (elastic)	Model 3, Diagonal Compression -only-2 (cracked)	Model 4, Diagonal Compression -only, Orthogonal tension-only	Model 5, Diagonal Compression -only "seismic assessment guideline"	Model 6, Shell elastic
1	260.41	187.05	13.44	155.28	123.76	299.94
2	48.73	40.63	2.80	28.37	30.69	52.19
4	6.93	6.35	0.47	4.05	5.22	7.22
10	0.46	0.44	0.036	0.27	0.38	0.47

Model 2, diagonal compression-only elastic, presents a good stiffness especially for large aspect ratios. Also its results are easier to investigate and obtain design parameters. Model 3, diagonal compression-only cracked, is suitable for considering cracking in the diaphragm. Note that this model does not consider the tension-stiffening effects, therefore it may represent the lower bond in-plane stiffness of a cracked diaphragm. This model is similar to Model 2, diagonal compression-only elastic, and its results can easily be used for design. Model 4, diagonal compression-only, orthogonal tension-only, underestimated the beam stiffness by up to 45% and also shows independent behaviour with respect to aspect ratio. Model 5, shows the same trend as Model 2, diagonal compression-only elastic, while it underestimated the stiffness by up to 60% for aspect ratio one and it reached to nearly 20% for aspect ratio 10 and larger.

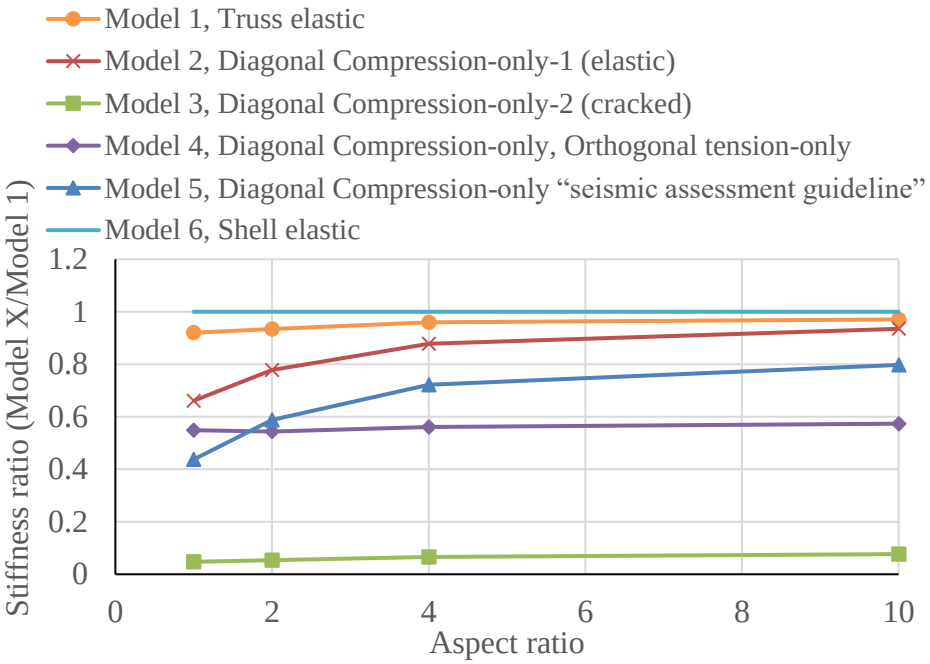

Figure 3-28. Stiffness ratio of different modelling methods respect to Model 6

Models 2, 3 and 5 that are compression-only diagonal members, showed sensitivity to aspect ratio. This is because these models have larger deformations under shear force as the applied shear forces need to be carried by one diagonal member only. The other diagonal member is in tension and therefore carries no force. The net result is an axial force in the orthogonal members as shown in Figure 3-29a. While in the elastic truss model subjected to shear forces the orthogonal member force is zero as shown in Figure 3-29b. Therefore with increasing the model aspect ratio the share of bending deformation increases and the share of shear deformation decreases causing the plots in Figure 3-28 tend to converge to a certain value at larger aspect ratios.

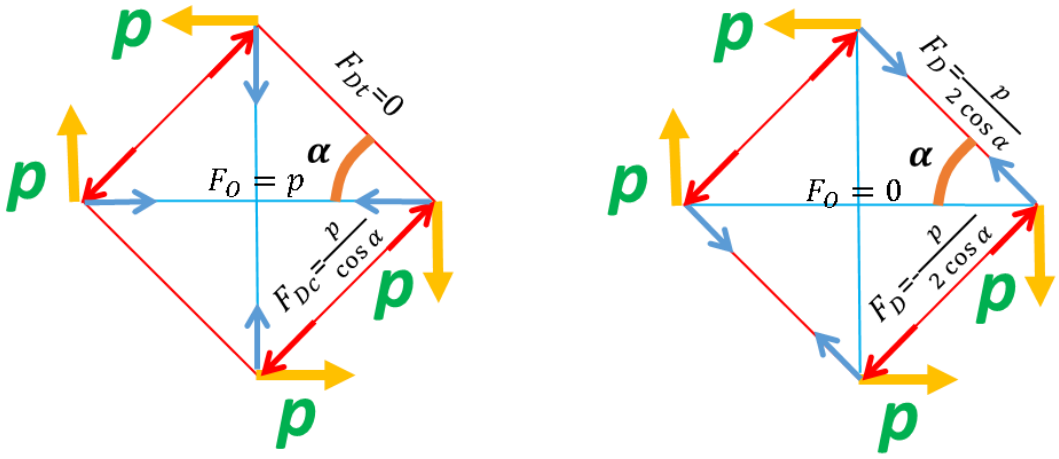

a) Compression-only diagonal member model b) Elastic truss model

Figure 3-29. Orthogonal member axial force due to applied shear force

- **Investigating element forces in truss models**

The stiffness study showed that Model 2, diagonal compression-only elastic, gives good results in terms of stiffness and also because of using compression-only diagonal members, its results can directly be used for design. Also, Model 3, diagonal compression-only cracked, presented the same situation considering the fully cracked in-plane stiffness of the concrete diaphragm. In this Section, the truss element internal forces which represent the load path through the diaphragm are studied. Figure 3-30 shows the investigated truss model with an aspect ratio of 4.0. Compression and tension forces in two horizontal orthogonal members and one diagonal member of different truss modelling types are presented in Table 3-4. In addition, two support reactions are also recorded to make a comparison with the elastic shell and nonlinear FEM model. Here, F_{Ot} and F_{Oc} are orthogonal member tension and compression forces respectively. The diagonal member compression force is denoted by F_{Dc}, and the support compression and tension reactions are denoted by F_{Rc} and F_{Rt} respectively.

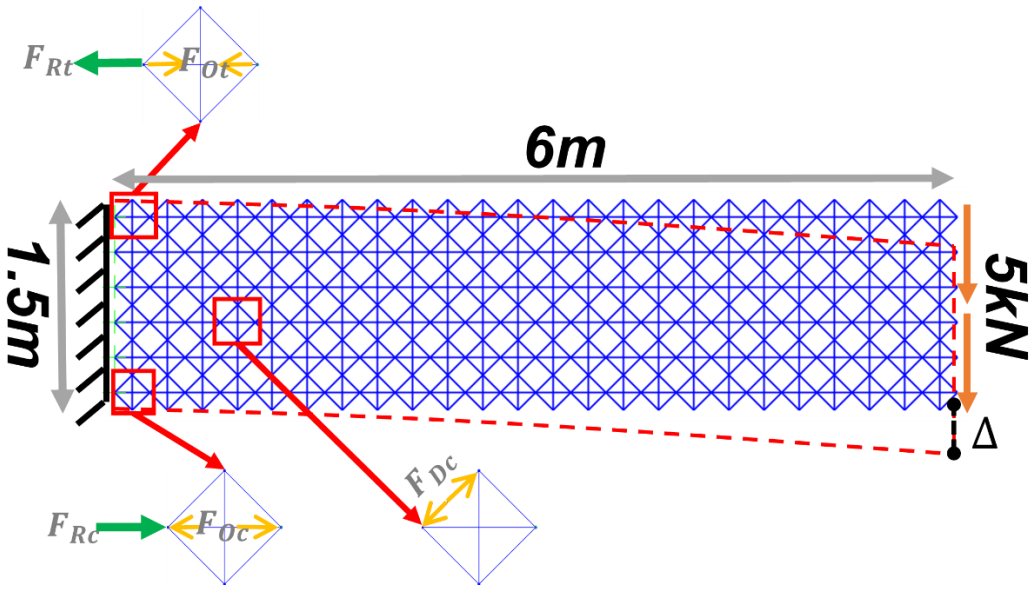

Figure 3-30. Truss model with aspect ratio 4 considered to investigate internal truss element forces

Table 3-4. Truss element forces and support reactions

#	**Model description**	F_{Ot}(kN)	F_{Oc}(kN)	F_{Dc}(kN)	F_{Rt}(kN)	F_{Rc}(kN)
1	Truss elastic	12.70	12.70	1.41	17.90	17.90
2	Diagonal Compression-only-1(elastic)	14.40	11.50	2.15	14.47	21.80
3	Diagonal Compression-only-2 (cracked)	10.06	28.80	1.86	10.05	33.10
4	Diagonal Compression-only, Orthogonal tension-only	17.79	0.00	4.19	17.80	18.60
5	Diagonal Compression-only "seismic assessment guideline"	13.80	15.60	2.00	13.84	22.57
6	Shell elastic	--	--	1.35	18.60	18.60
7	Nonlinear truss	10.07	28.60	1.90	10.07	32.90
8	Nonlinear FEM	--	--	0.90	9.92	32.50

The truss element forces in Model 1 are similar to the elastic shell element model (Model 6) as it was expected. The internal element forces of Model 3 show good agreement with Models 7 and 8, which means the fully cracked elastic model (Model 3) is able to estimate compression and tension demands reasonably considering concrete cracking. The internal

truss element forces of Model 4 do not provide any useful information about the load path as the axial compression force of the orthogonal member is zero, and all the force is transferred to the supports through diagonal members. Models 2 and 5 show similar results with a small variation in orthogonal member compression force which is due to the difference in diagonal member cross-section areas.

In conclusion, considering both stiffness and simplicity in internal truss element forces, Model 2 is suitable for elastic diaphragm modelling and Model 3 can be effectively be used for considering cracked stiffness of the diaphragm.

- **Comparison of nonlinear truss model and detailed FEM model**

The nonlinear truss model, Model 7, is compared to the nonlinear solid element and beam element FE models. The comparison is made in terms of overall behaviour, initial stiffness and the ultimate strength. The nonlinear solid FEM modelling was conducted using ABAQUS. The ABAQUS model consists of detailed FEM model using 3D solid elements for concrete and one-dimensional truss elements for the reinforcement. An additional beam model was created in OpenSees software with distributed plasticity fibre sections to consider the nonlinear behaviour of the concrete and reinforcement.

The FIB model code for concrete structures (2010) is used to obtain the stress-strain relation for short-term loading of concrete in compression. The stress-strain relation of concrete is shown in Figure 3-31, considering 33MPa concrete strength, 32 GPa elastic modulus and 0.0035 ultimate strain.

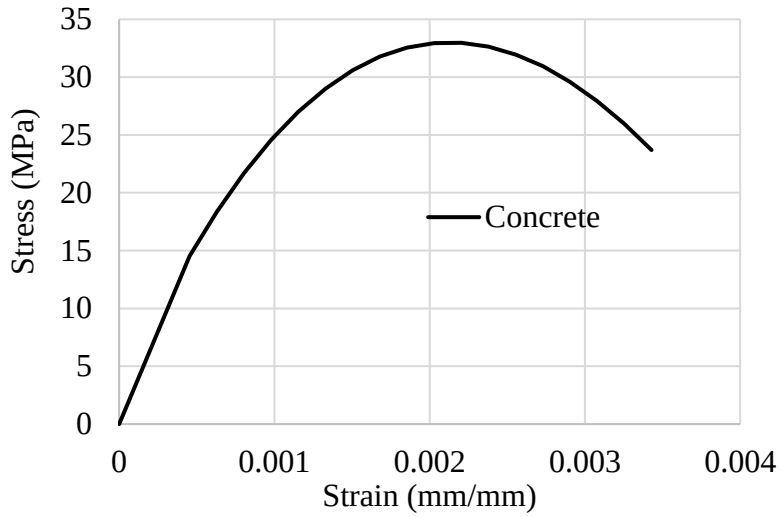

Figure 3-31. Stress-strain relations for short-term loading of concrete in compression based on FIB model code, (2010)

A bilinear material is used for modelling reinforcement steel considering 0.01% strength hardening for better numerical convergence. The reinforcement yield stress of $F_y = 300MPa$ is used in this study as shown in Figure 3-32.

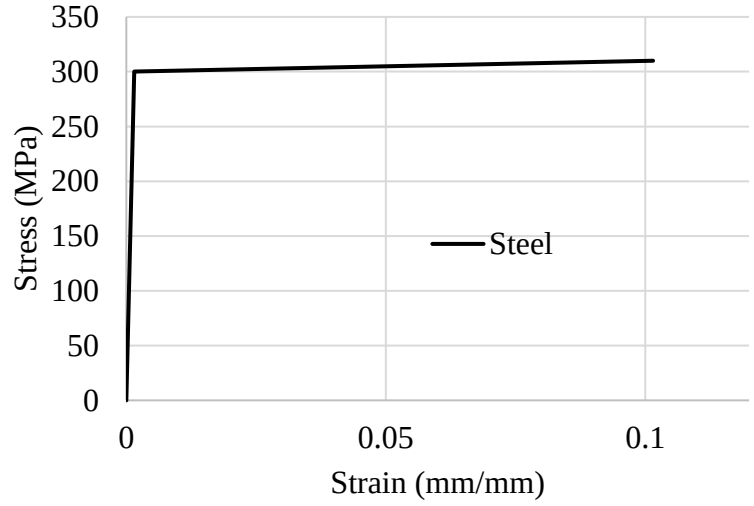

Figure 3-32. Stress-strain relations for reinforcement steel

"Concrete damaged plasticity" material is used for modelling concrete in ABAQUS software. This material model assumes that the two main concrete failure mechanisms are tensile cracking and compressive crushing of the concrete material. Note that the tensile behaviour of concrete is not considered in the OpenSees beam model while the "concrete

damaged plasticity" material in the ABAQUS solid elements considers $0.01f_c'$ as the minimum tensile strength of concrete as the default value. The reinforcing bars were modelled using the ABAQUS "plastic" model with isotropic hardening with the von-Mises yield criterion.

For creating the truss element model, SAP2000 (2015) software is used. Nonlinear link elements were used for modelling the orthogonal and diagonal elements. These can provide similar behaviour to the truss elements for elastic deformation, but also allow non-linear properties to be considered. Since the link elements have zero length, modifications for the cross-section properties and element length needs to be considered. Figure 3-33 shows the force-displacement curves of orthogonal and diagonal elements. This Figure shows the diagonal member is stiffer than the orthogonal member, which is due to different length and cross-section areas of these elements.

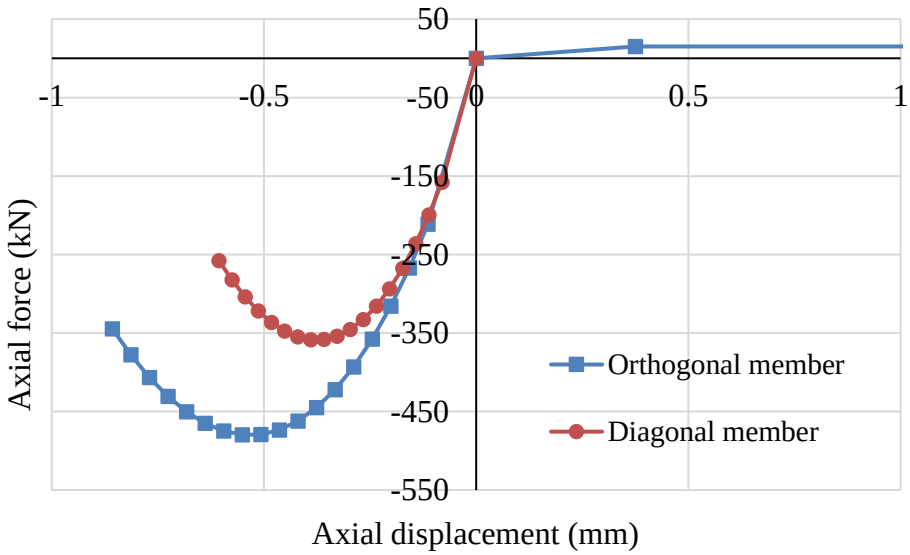

Figure 3-33. Link properties for nonlinear truss modelling in SAP2000

Note that concrete tension behaviour cannot be considered in the truss element model. This is because when concrete cracks, the properties of the orthogonal (tension and compression) and diagonal (compression) elements should change from Model 1 to Model 3

listed in Table 3-4. However, due to the limitation of SAP2000 software, this was not able to be performed within the analysis.

Since the material properties are nonlinear, the displacement-control analysis is chosen for better convergence. The edge of the model was pushed to 100mm and reaction forces were recorded. Results of FEM models (ABAQUS and OpenSees) and truss element modelling are shown in Figure 3-34.

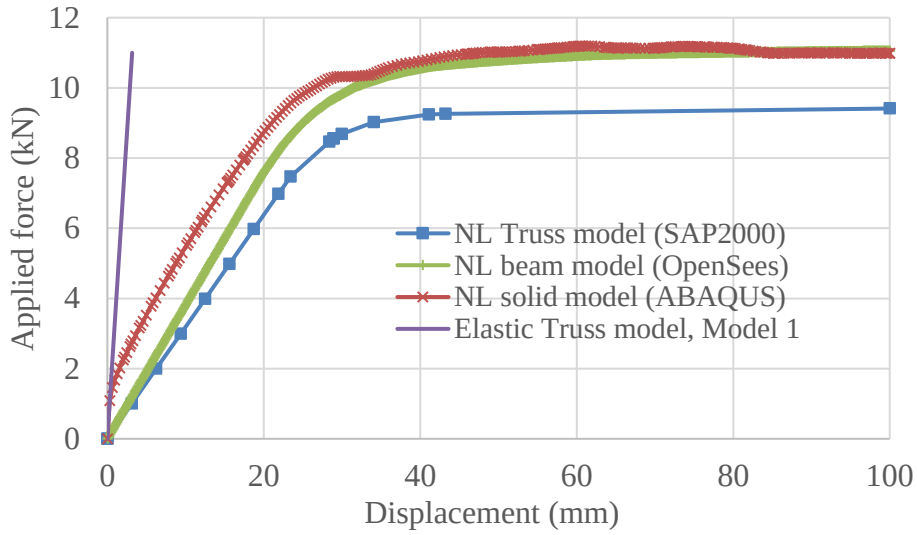

a) Force-displacement plots

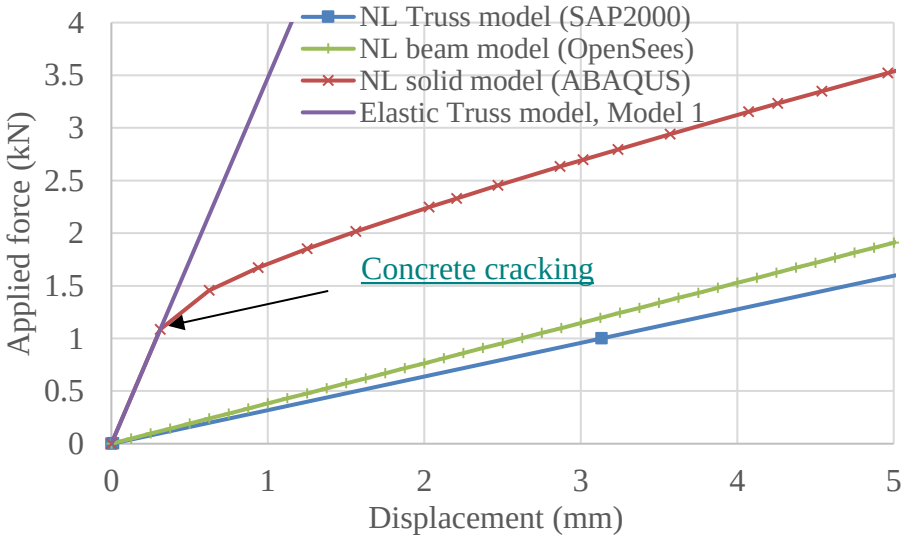

b) Enlarged view of Figure (a)

Figure 3-34. Force-displacement results of FEM models and nonlinear truss element modelling

As can be seen, the overall behaviour of all three models is similar. The total difference in the ultimate strength is about 15% which is due to a smaller lever arm in the truss model. The stiffness of all three models is similar with small differences. The beam model (OpenSees) indicates larger stiffness, because the distributed plasticity fibre element cannot capture shear deformations. The loading stiffness of the ABAQUS model is nearly equal to the elastic model, Model 1, which represents the pre-cracking stiffness of the model.

3.6 Effect of truss element modelling error on structure behaviour

Based on the mathematical equations and considering different mesh size, aspect ratios and Poisson's ratios mentioned in Section 3.3, it was shown that the elastic stiffness of an elastic diaphragm can be obtained using a reasonable number of truss elements with less than 10% error. Here, the question is, how much does this error can affect the overall response of a structure?

This section aims to obtain the effect of possible errors in determining diaphragm flexibility in total structure behaviour. In this study, the results and methods from the study that was conducted by Sadashiva et al. (2012) are used.

Sadashiva et al. (2012) studied the diaphragm flexibility effects on symmetrical structures using elastic and inelastic time history analysis and proposed a method for quantifying diaphragm flexibility effects in symmetrical structures considering different deformation types, different vertical lateral force resisting element configurations, and different structural heights. They studied symmetric one-bay and two-bay structures as shown in Figure 3-35, with a different number of storeys. Time-history analyses were employed for both rigid and flexible diaphragms using 20 SAC (SEAOC-ATC-CUREE) LA earthquake ground motion records with probabilities of exceedance of 10% in 50 years. In their research, the soil-foundation interaction and foundation flexibility effects were ignored. In each time

history analysis, the peak value of frame and diaphragm displacement were recorded. Peak lateral displacement value of the rigid diaphragm model $\delta_{Total-rig}$, total in-plane displacement at diaphragm mid-span $\delta_{Total-flx}$ and diaphragm mid-span displacement δ_{d-flx} are used to define static flexibility ratio as:

$$\gamma_s = \frac{\delta_{d-flx}}{\delta_{Total-flx} - \delta_{d-flx}}$$

Which is zero for rigid diaphragms and greater than zero for flexible diaphragms. Also $\delta_{total-ratio}$ was defined to investigate the effect of diaphragm flexibility in increasing the total structure drift.

$$\delta_{total-ratio} = \frac{\delta_{Total-flx}}{\delta_{Total-rig}}$$

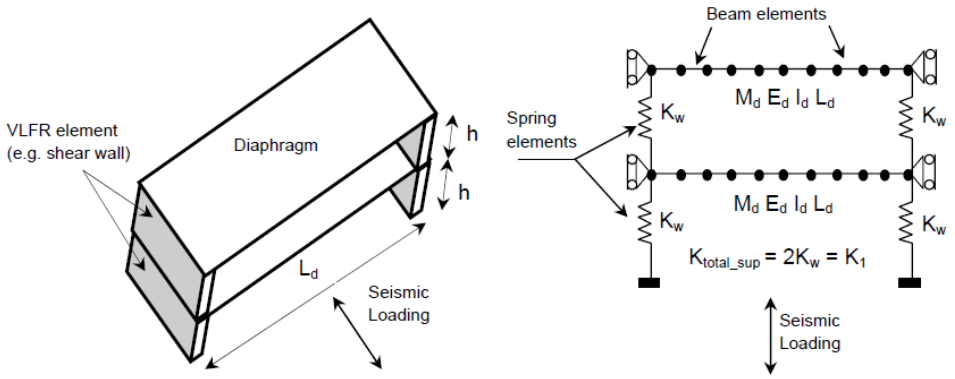

Figure 3-35. Schematic view of single-bay two-storey structure and the analytical model (Sadashiva et al., 2012)

Figure 3-36 shows the recorded peak values of time-history analysis for one and three-story buildings with a fundamental period of 0.3s (this fundamental period is calculated based on rigid diaphragm assumption). As can be seen, a 10% increase/decrease in diaphragm flexibility, γ_s, (shown with dotted and dashed lines) causes a total diaphragm displacement, $\delta_{total-ratio}$, increase/decrease for the one-story structure up to 7%. This effect decreased by increasing the number of storeys, so that in the three-story building, a 10% difference in diaphragm flexibility, γ_s, changed the $\delta_{total-ratio}$ by only 2%.

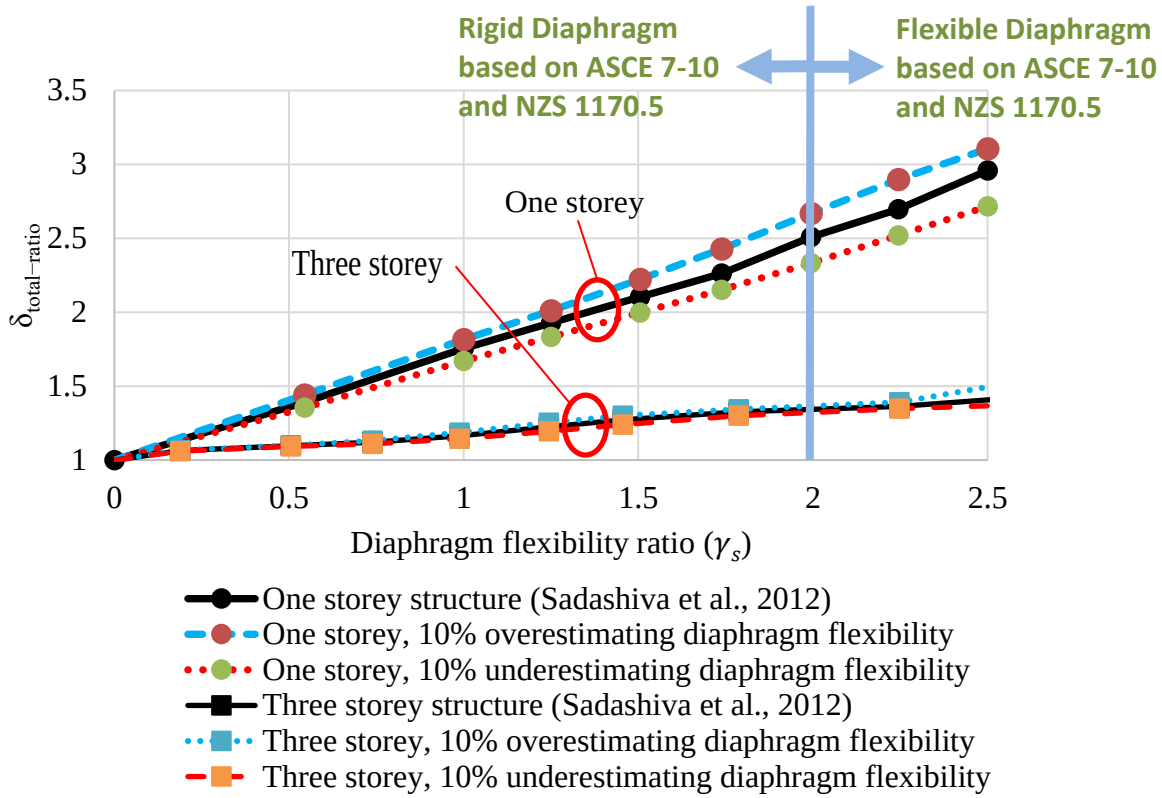

Figure 3-36. Possible change in total structure response considering 10% difference in estimating diaphragm flexibility in one and three storey structures studied

As it can be seen in Figure 3-36, the absolute value of error increased with increasing diaphragm flexibility ratio, γ_s. Increasing γ_s implies that the ratio of diaphragm stiffness to the frame stiffness increases. Based on this it is possible that in a structure, yielding of VLFR systems during earthquake events which decreases the frame stiffness, hence γ_s decreases (as $\delta_{Total-flx}$ increases) so the $\delta_{total-ratio}$ decreases indicating that the diaphragm flexibility effect becomes less.

3.7 Conclusions

In this Chapter, a number of truss modelling methods were evaluated to determine their suitability for use in design. This includes a new diamond model truss framework which was proposed. Differences between the performance of the diamond model and the well-established Hrennikoff diagonal model were evaluated. Also, different possible truss element

modelling methods were studied. Comparisons of elastic stiffness and internal forces from these models were made. The models studied included:

1. Elastic truss.
2. Diagonal compression-only truss members with compression/tension orthogonal members. Here the concrete is assumed to be un-cracked.
3. Diagonal compression-only truss members considering reinforcement as orthogonal members, with concrete compression and, tension reinforcement. Here the concrete is assumed to be cracked.
4. Diagonal compression-only truss members with tension-only orthogonal members.
5. Diagonal compression-only truss members with compression/tension orthogonal members based on "The Seismic Assessment of Existing Buildings" Section C5 recommendations (2017) which follows Holmes Practice Note, (2014).
6. Nonlinear truss considering likely properties of the steel and concrete material.

In this study it was found that:

1) While building diaphragms have often been considered to be rigid in-plane during analysis, there are some cases where flexibility have also been directly considered. In these cases modelling has been conducted using plate/shell elements, beam elements, truss elements and deep beam approaches. While the truss models are most suitable for design, little work has been conducted to obtain stiffness parameters for these truss models.
2) Cross-section properties of truss elements of a square truss mesh unit were obtained using two conditions:
    i. by equating the strains of the truss framework with the corresponding plate strains and

ii. satisfying deformation compatibility condition within each truss mesh unit.

Contrary to existing truss model where diagonal elements are placed between the far corner nodes of the truss mesh units, it is proposed that nodes be placed at the centres of beams and diagonal (concrete) as well as orthogonal (steel and/or concrete) elements interact there. This is advantageous for design allowing beam axial demands, shear stud demands, and reinforcing steel demands to be obtained directly. This gives a diamond (⌖) shape truss mesh unit as opposed to the diagonal (☒) one used previously.

3) For elastic truss models where all elements have the same stiffness in tension and compression, the error in estimating diaphragm deformations was reduced to less than 10% for the diaphragm alone when a sufficient number of element were used. However, the diamond ⌖ configuration was more accurate requiring fewer elements to obtain the same accuracy. For example, for 3 elements in the direction of loading, the deformation error was 22% for the diagonal ☒ model but 11% for the diamond ⌖ model. In addition, using the diamond ⌖ model gives more realistic results in terms of the beam axial forces and shear stud demands.

4) Truss element cross-section areas and stiffnesses were obtained for elastic rectangular truss frameworks with different aspect ratio to match the analytical solutions. It was noted that for realistic concrete slabs, the aspect ratio required was inconsistent for use in design, and some elements were required to have negative stiffnesses.

5) Different possible diamond truss models, placed in a framework to represent a diaphragm, were compared with shell elastic and nonlinear solid element FEM models in terms of their in-plane stiffness and internal forces. Based on the analyses conducted, Truss Model 2 with diagonal compression-only and orthogonal compression/tension elements (representing un-cracked diaphragm properties), and Truss Model 3 with diagonal compression-only and orthogonal reinforcement tension/concrete compression

members (representing cracked diaphragm properties) satisfied the criteria of providing simple outputs usable for design and reasonable accuracy. They were recommended for use in design. Note that the tension-stiffening effect was not considered in Truss Model 3 in this study. It was assumed Truss Model 3 may conservatively estimate the lower bond in-plane stiffness of the diaphragm considering concrete cracking.

6) For analyses conducted of a one-storey and a three storey structure, a 10% increase in diaphragm flexibility caused 7% and 2% increase in total structural displacement at the diaphragm levels respectively.

References

[1] Abramowitz, M., & Stegun, I. A. (1965). Handbook of mathematical functions: with formulas, graphs, and mathematical tables (Vol. 55). Courier Corporation.

[2] ASCE/SEI 7-10 Minimum Design Loads For Buildings and Other Structures, American Society of Civil Engineers, 2010.

[3] Barron, J. M., & Hueste, M. B. D. (2004). Diaphragm effects in rectangular reinforced concrete buildings. Structural Journal, 101(5), 615-624.

[4] Bull, D. K. (1997). Diaphragms, Seismic Design of Reinforced Concrete Structures. Technical Report No. 20, New Zealand Concrete Society.

[5] Bull, D. K. (2004). Understanding the complexities of designing diaphragms in buildings for earthquakes. Bulletin of the New Zealand Society for Earthquake Engineering, 37(2), 70-88.

[6] Canterbury Earthquakes Royal Commission (2012): Final Report Volume 1.

[7] Carreira, D. J., & Chu, K. H. (1986, January). Stress-strain relationship for reinforced concrete in tension. In Journal Proceedings (Vol. 83, No. 1, pp. 21-28).

[8] Chaudhari, T. D., MacRae, G. A., Bull, D. K., Chase, G., Hicks, S., Clifton, G. C., & Hobbs, M. (2015, July). Composite slab effects on beam-column subassembly seismic performance. In NZSEE Conference.

[9] Code, M. (2010). Fib model code for concrete structures 2010. Document Competence Center Siegmar Kästl eK, Germany.

[10] CSI Analysis Reference Manual. (2013). CSI Analysis Reference Manual for SAP2000®, ETABS®, SAFE® and CSiBridge®.

[11] Gardiner, D. R. (2011). Design recommendations and methods for reinforced concrete floor diaphragms subjected to seismic forces.

[12] Holmes Consulting Group, Practice Note No. 8.1, Version No. 1, (2014). Modelling Diaphragm Force Distributions - Simple Grillage Method. by Bull DK and Galloway B.

[13] Hrennikoff, A. (1941). Solution of problems of elasticity by the framework method. Journal of applied mechanics, 8 (4):169-75.

[14] Jain, S. K., & Jennings, P. C. (1985). Analytical models for low-rise buildings with flexible floor diaphragms. Earthquake engineering & structural dynamics, 13(2), 225-241.

[15] Ju, S. H., & Lin, M. C. (1999). Building analyses comparisons assuming rigid or flexible floors. Journal of Structural Engineering (ASCE), 125, 25-31.

[16] Lee, H. J., Aschheim, M. A., & Kuchma, D. (2007). Interstory drift estimates for low-rise flexible diaphragm structures. Engineering structures, 29(7), 1375-1397.

[17] MacRae, G. A., & Clifton, G. C. (2015, September). Research on seismic performance of steel structures. In Proc of Steel Innovations 2015 Conference. Auckland, New Zealand (Vol. 3, No. 4).

[18] MacRae, G. A. & Bull, D. K. (2015). Diaphragm Design, ENEQ650: Seismic Design of Steel and Composite Structures. Postgraduate Class notes, University of Canterbury.

[19] Massicotte, B., Elwi, A. E., & MacGregor, J. G. (1990). Tension-stiffening model for planar reinforced concrete members. Journal of Structural Engineering, 116(11), 3039-3058.

[20] Moehle, J. P. (2015). Seismic design of reinforced concrete buildings (pp. 230-235). New York: McGraw-Hill Education.

[21] Moroder, D. (2016). Floor diaphragms in multi-storey timber buildings.

[22] Naeim, F., & Boppana, R. R. (2001). Seismic Design of Floor Diaphragms. In The Seismic Design Handbook (pp. 373-407). Springer, Boston, MA.

[23] Sabelli, R., Sabol, T. A., & Easterling, W. S. (2011). Seismic design of composite steel deck and concrete-filled diaphragms. NEHRP Seismic Design Technical Brief No, 5.

[24] Sadashiva, V. K., MacRae, G. A., Deam, B. L., & Spooner, M. S. (2012). Quantifying the seismic response of structures with flexible diaphragms. Earthquake Engineering & Structural Dynamics, 41(10), 1365-1389.

[25] Saffarini, H. S., & Qudaimat, M. M. (1992). In-plane floor deformations in RC structures. Journal of Structural Engineering, 118(11), 3089-3102.

[26] Scarry, J. M. (2014). Floor diaphragms–Seismic bulwark or Achilles' heel. In NZSEE Conference.

[27] Schlaich, J., Schäfer, K., & Jennewein, M. (1987). Toward a consistent design of structural concrete. PCI journal, 32(3), 74-150.

[28] NZS 1170.5 (2004). Structural Design Actions-Part, 5. Standards New Zealand, Wellington, New Zealand. Including Amendment 1, 2016.

[29] AS/NZS 2327 (2017). Composite structures - Composite steel-concrete construction in buildings. Standards New Zealand, Wellington, New Zealand.

[30] NZS 3404 (2007). Steel Structures Standard. Standards New Zealand, Wellington, New Zealand. Including Amendments 1 and 2, 2001/2007.

[31] Tena-Colunga, A., & Abrams, D. P. (1996). Seismic behavior of structures with flexible diaphragms. Journal of Structural Engineering, 122(4), 439-445.

[32] The Seismic Assessment of Existing Buildings, Technical Guidelines for Engineering Assessments, (2017).

[33] Timoshenko, S. (1940). Strength of materials Part 1. D. Van Nostrand Co., Inc.

[34] Timoshenko, S. P., & Goodier, J. N. (1970). Theory of Elasticity, (216).

[35] Tremblay, R., & Stiemer, S. F. (1996). Seismic behavior of single-storey steel structures with a flexible roof diaphragm. Canadian journal of civil engineering, 23(1), 49-62.

4 Web-Side-Plate Connection Axial Strength

4.1 Introduction

Buildings in many western countries are generally designed with different frames carrying lateral force, than those carrying gravity force. Many research has been conducted on the lateral force resistance frames, but less has been done on the gravity frames which need to maintain their integrity as they follow through the lateral deformation of the lateral force resistance frames. The evaluations that have been conducted on gravity frames have generally been undertaken on gravity frame subassemblies, (columns, beams and connections) to evaluate their flexural behaviour.

It has recently been shown (Alizadeh et al. 2017) that significant horizontal forces may occur in slabs of buildings, especially during earthquake shaking. Which, these are often not able to be transferred directly from the slab to the column, because a gap can occur between the slab and column due to frame lateral movements. As a result, the slab forces must be transferred through the shear studs to the beam and from the beam to the column.

Simple/pinned beam-end shear connections are usually used at the ends of gravity beams. In such beams, the beam-end is usually assumed to carry shear forces only as part of a gravity load system and the connection is designed for the shear force and a moment due to the shear force eccentricity. However, during earthquake shaking, significant horizontal forces may be transferred to the beam from the floor diaphragm, column-slab interaction and also interaction with other structural elements. These forces must be transferred through beam axial force to the vertical lateral force resisting elements of the structure. Since these forces are not usually considered directly in beam and beam-column design, there is a possibility of connection failure and collapse.

There are several types of beam-column connections in gravity frames of steel structures as shown in Figure 4-1, such as i) double-angle, ii) shear end plate, iii) unstiffened seated, iv) stiffened seated, v) web-side-plate (WSP), vi) single angle and, vii) tee connections. WSP connections are widely used due to low construction costs and simplicity of fabrication. These connections usually take the form of a single plate welded to the support element (column or girder) and bolted to the web at the beam-end. WSP connection also known as shear tab in the United States or fin plate in other countries (Australia, Japan, and United Kingdom).

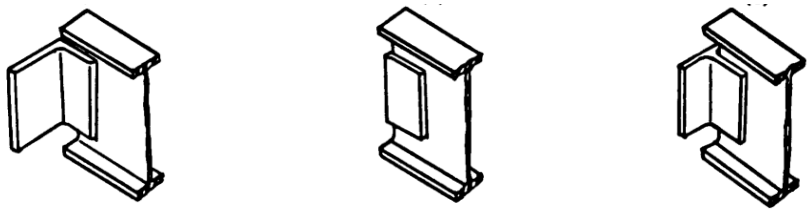

a) Double angle connection b) Single plate connection c) Tee connection

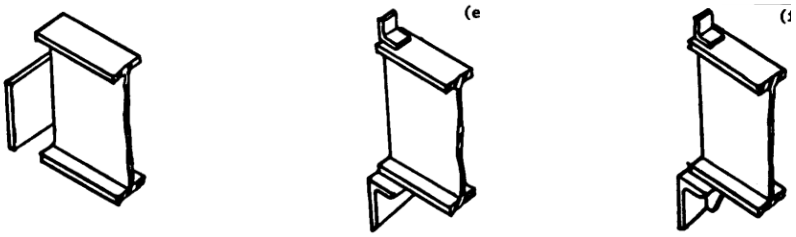

d) Shear end plate e) Seated beam f) Stiffed seated beam

Figure 4-1. Simple beam-column connection types (Astaneh, 1989b)

Unfortunately, a method to determine the axial tension/compression capacity of the most common simple beam-column connection in gravity frames, the WSP connection, is not available.

This research aims to answer the following questions:

1) What causes beam axial forces during earthquake shaking?
2) What studies have been conducted in the past regarding WSP shear or axial behaviour?

3) How are the deformations and mechanisms of a typical WSP connection perform under compression/tension axial force?
4) Which parameters axial force capacity of WSP connections most sensitive to?
5) How can the axial compression/tension force capacity of WSP connection be estimated?

4.2 Beam axial force

Diaphragm in-plane demands include i) inertia forces, ii) transfer forces, iii) compatibility forces, iv) slab bearing forces and, v) interaction with other elements. These are described in detail in Chapter 2. These diaphragm in-plane forces need to be transferred to the ground through vertical lateral force resisting (VLFR) system of the structure. The axial forces generated in a beam as a part of the load transfer mechanism are different depending on whether a gap is provided between the slab and the column or not.

4.2.1 Gap not provided around column

In traditional construction, the concrete slab is cast up to the column face and no gap exists. It is often assumed that the slab transfers the lateral forces to the column through compression on the column face. While, in frame structures, since slab inertia forces act in the same direction as the frame sways, due to the beam-column joint rotation, a gap opens at location "A", shown in Figure 4-2. Because of this, slab forces cannot go directly into the column. Instead, the forces transfer into the steel beam through friction and mechanical attachments (e.g. shear studs) (MacRae and Clifton, 2015); this situation imposes axial forces to beam plastic hinge regions (assuming rigid end connection) and connections at the beam-ends that may need to be considered in design procedure. Also, when there is no construction gap between the slab and column, as the column sways, it bears against the concrete slab on the far side of the column

causing a slab-interaction effect that increases the forces that the slab must transfer into the beam, and the beam must transfer it back to the columns.

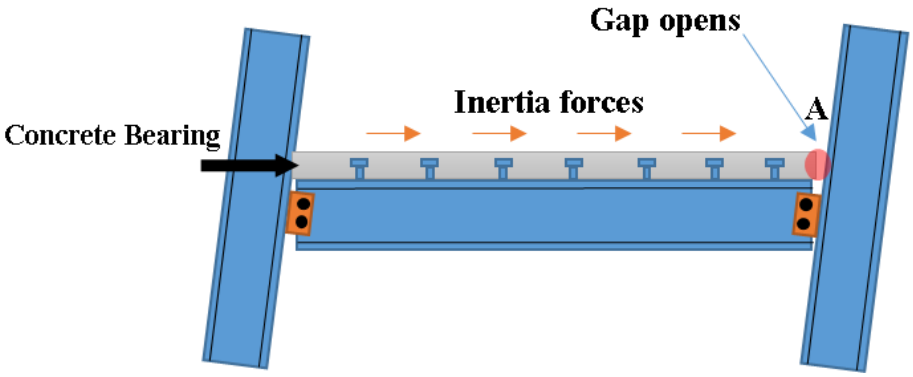

Figure 4-2. Slab-column interaction, a gap opens at Point A due to joint rotation

Furthermore, the load path through slab bearing is not reliable due to concrete crushing, which may occur in high-stress locations during earthquake events. Therefore, it is more reliable to consider diaphragm forces mainly should be transferred to the columns through beams.

4.2.2 Gap provided around column

In order to minimize column-slab interaction, and the moment imposed on the column when the beam yields, gaps have been placed between the column and slab as shown in Figure 4-3. Some ways of providing gap around column and proper filling material have been described by Chaudhari et al. (2015).

In this case, the only load path for transferring diaphragm in-plane forces to the VLFR system of the structure is through beams which causes beam axial forces.

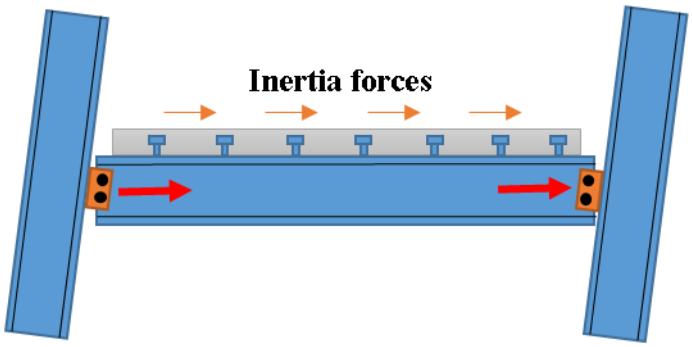

Figure 4-3. Beam-column connection axial force when a gap is provided around the column

It should be noted that whether a gap is provided or not, part of diaphragm in-plane forces is transferred to the column or VLFR system through the beams. This is because the diaphragm is not entirely rigid in reality.

4.3 Literature review

4.3.1 Past studies

The shear force resistance mechanism in WSP connections is complicated because the applied shear force should be transferred from the beam web through the bolts and cleat plate to the support member. Many parameters may affect the connection behaviour. Many researchers have investigated the behaviour of this type of connection over the past few decades and a number of design methods have been proposed for calculating shear strength of WSP connections.

Lipson (1968) investigated the behaviour of single angle and single plate connections as an alternative to double angle connections in shear. Three different shear connections consist of bolted-bolted angle connections, welded-bolted angle connections, and welded-bolted plate connections were studied. The aims of this research were to study the shear behaviour of these connections, maximum rotation, failure limit states and, whether the connections could be classified as simply-supported under the AISC Design Specification (1963). It was found that

welded-bolted plates could be classified as "flexible" according to the AISC Design Specification (1963).

Caccavale (1975) investigated the strength and ductility of WSP connections using the FE method. This study showed that the ductility of WSP connection is because of the plate distortion at the bolts and not from shear deformation of the bolt itself.

Hormby (1981) conducted an experimental study on WSP connections bolted using A307 and A325 bolts. Connections with A307 bolts were tested with slotted holes and connections with A325 bolts were tested in both round and slotted holes. It was shown that A307 bolts require a bolt diameter to plate thickness ratio, D/t, of at least four to assure ductile behaviour and they are not practical in WSP connections with round holes. Also A325 bolts tightened up to the bolt proof load behaved essentially the same in round or slotted holes.

Richard et al. (1982) studied A325 and A490 bolts with A36 ($F_y = 250\ MPa$) plates to achieve ductile connection behaviour. They found that this can be achieved when the diameter of the bolt to plate (or web) thickness ratio (D/t) is greater than 2.0 for A325 and 1.5 for A490 bolts. Also, edge distance to prevent bolt tear-out failure mode was required to be at least twice the bolt diameter.

Astaneh et al. (1989a) investigated the shear resistance and the rotational ductility of WSP connections by testing five full-scale specimens, with an increasing number of bolts. All specimens had a single vertical row of bolts. In order to achieve realistic loading, the likely relationship between the shear force and the connection rotational demand was required. To obtain this relationship, Astaneh (1989b) defined the shear-rotation behaviour of simply supported beams considering different steel beam cross-sections and span lengths. Figure 4-4 shows the resulting tri-linear shear-rotation behaviour used for loading the tested specimens. This plot accounts for both the elastic and the inelastic shear behaviour of WSP connections.

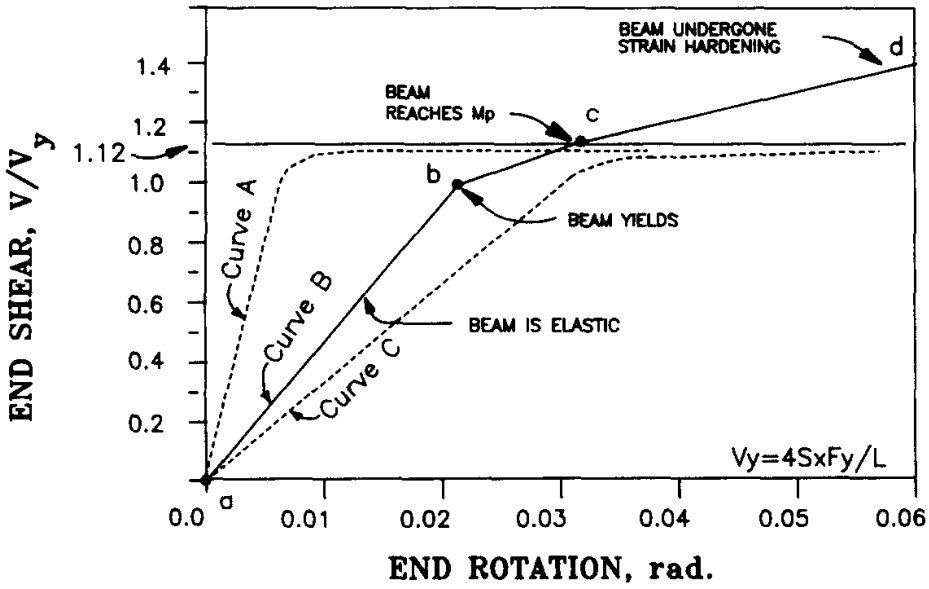

Figure 4-4. Proposed shear-rotation relationship for simple beams (Astaneh, 1989b)

Astaneh et al. (1989c) proposed design equations considering the ultimate limit state hierarchy, as shown in Figure 4-5, such that ductile failure modes (e.g. shear plate yielding) occur before brittle failure modes such as bolt and weld fracture. It was found that WSP connections can undergo a large level of rotation (e.g. 0.04-0.05 rad) and they may be considered as pinned connections.

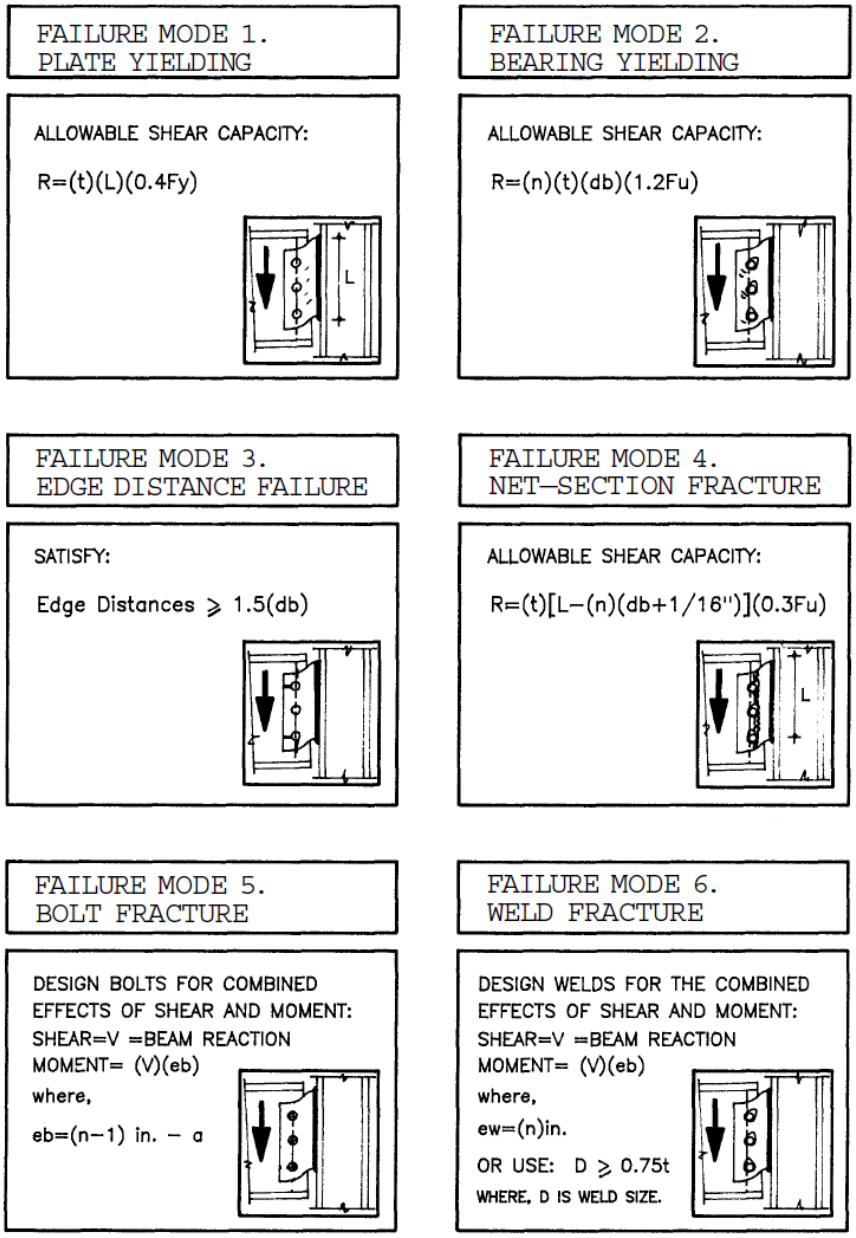

Figure 4-5. Failure limit states of WSP connections (Astaneh, 1989a)

WSP connections that support floor slabs, may have an axial force acting on the connection due to the composite action. The presence of the concrete slab in a composite member causes the neutral axis to move toward the concrete slab. In this situation the steel beam is more in tension in positive moment regions and compression in negative moment regions. Due to the concrete cracking in the negative moment regions the amount of slab reinforcement controls the amount of the beam axial compression force. This compression axial force transfers directly to the connection. This force, due to gravity loads only, is shown in Figure 4-6. This effect first

was investigated by Ren (1995) in beam-column connections. Ahmed et al. (1997) studied WSP and shear angle connections considering the axial force due to composite effect and proposed a method to consider this effect in design.

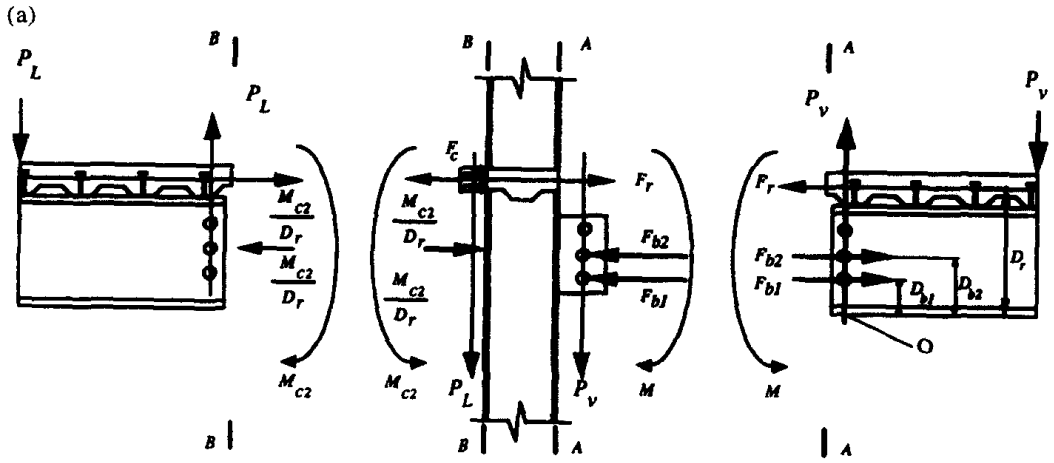

Figure 4-6. Free body diagram of connection under gravity load considering composite action (Ren, 1995)

Patrick et al. (2002) also studied this effect on WSP connections. They used the test setup, shown in Figure 4-7 that enabled them to eliminate most parts of the connection and only study the behaviour of the connection region. They tested 50 specimens considering plate thickness, steel grade and different bolt group arrangements.

In the above-mentioned investigations, the axial behaviour of WSP connections due to the composite effect was investigated. However, beam axial forces due to earthquake shakings were not considered.

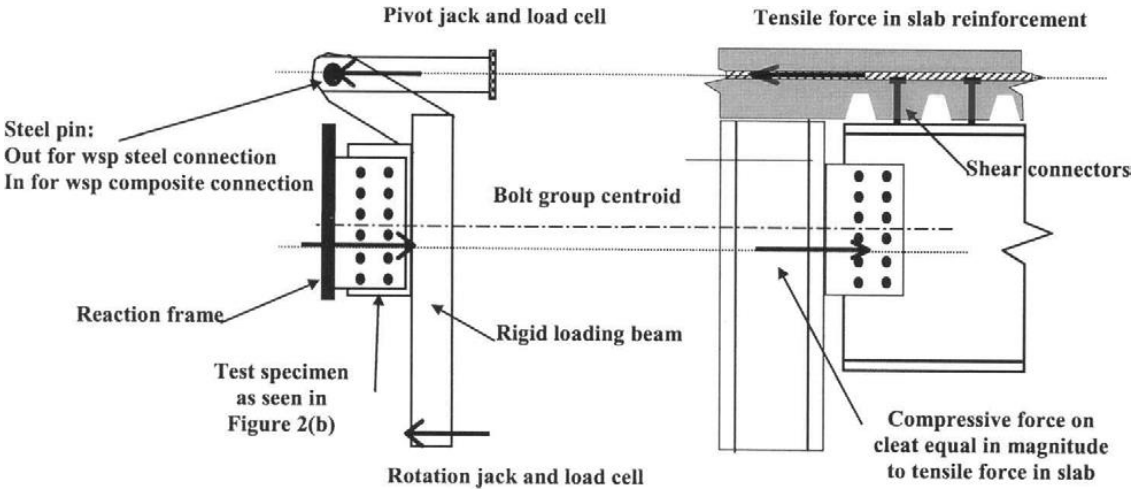

Figure 4-7. Test setup (Patrick et al., 2002)

Sherman and Ghorbanpoor (2002) conducted an experimental study to develop a design procedure and explore failure modes unique to the extended WSP configuration with 31 full-scale specimens. In the extended WSP configuration the distance between bolt-line to weld-line on the cleat plate is greater than 89mm according to AISC manual (2011). Figure 4-8 shows typical unstiffened extended WSP connections. The design equations to evaluate force eccentricity in the extended WSP connections proposed by Sherman and Ghorbanpoor (2002), were adopted by the AISC 13th Edition Manual (2005) and later editions as an alternative method.

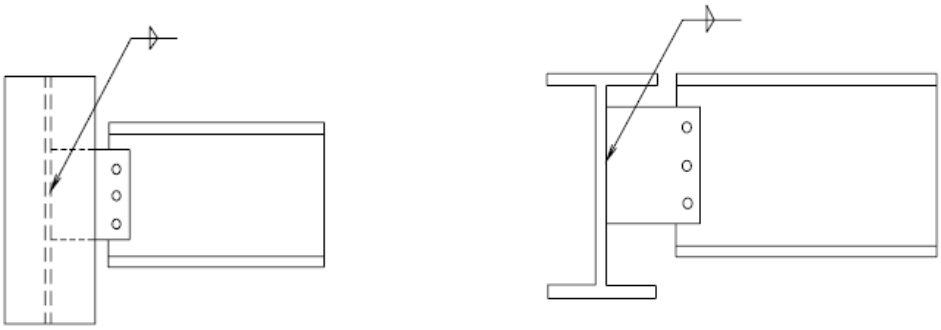

a) Beam-column b) Beam-beam

Figure 4-8. Unstiffened extended WSP connections (Sherman and Ghorbanpoor, 2002)

Many other researchers such as Ashakul (2004), Creech (2005), Rahman et al. (2007), Mahamid et al. (2007), Marosi (2011), Suleiman (2013), D'Aronco (2014), Ashakul and Khampa (2014), Abou-zidan and Liu (2015) and Koia et al. (2018) investigated the WSP connection performance to improve the methods for obtaining the shear strength and increasing the connection rotational ductility.

Weir and Clarke (2016) investigated the axial force capacity of WSP connections using the FE models. They used ABAQUS software to model connections considering 310UB40 beam grade 300 and different boundary conditions with and without copping. Figure 4-9 shows the geometry of un-coped, single-coped, and double-coped beams connected to the cleat plate. Restraints were applied at the centreline of the members (although it is shown differently in Figure 4-9). Shear and axial forces were not considered in their study. They found that failure occurred through local buckling of the beam web and plastic hinge formation in the cleat plate. In the un-coped case, the flanges stiffened the web, resulted in a complex yield line pattern, and increased the axial capacity. Also it was shown that connection eccentricity of 6mm reduced the connection's compressive axial strength up to 70% in the studied case. An empirical hand method to assess beam strength was proposed, but it was not generalized to other beam sections.

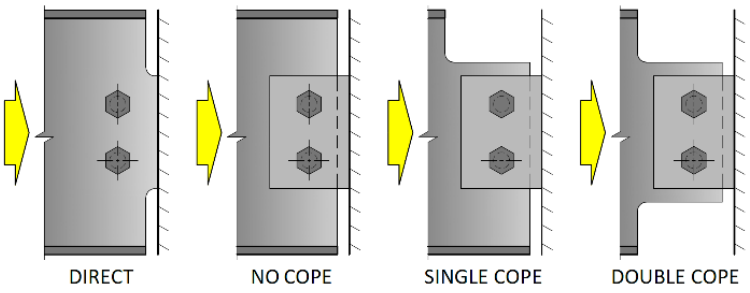

a) Geometry of connections

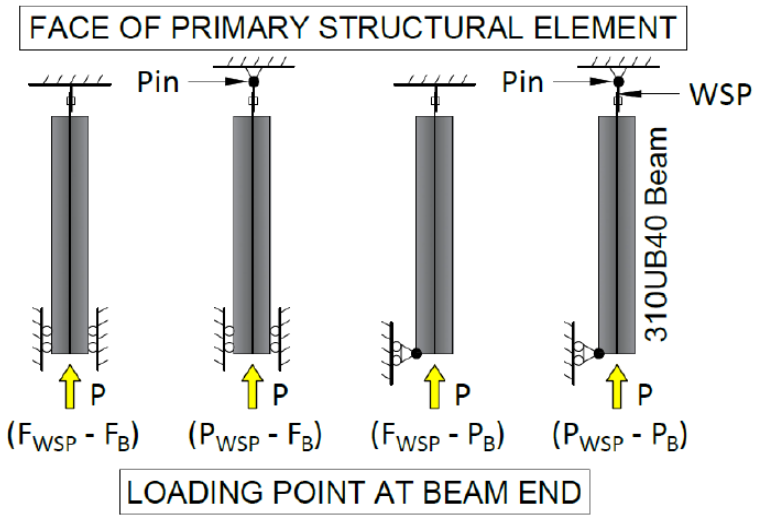

b) Boundary conditions

Figure 4-9. FEM models (Weir and Clarke, 2016)

Thomas et al. (2017) performed experimental studies on extended WSP connections under the combination of shear, axial force and rotation, as shown in Figure 4-10, to define the shear capacity of WSP connections under a particular axial force. They tested 23 full-scale extended WSP connections. The studied parameters include i) stabilizer plates, ii) plate thickness, iii) plate height, and iv) number of bolt lines. The test procedure consisted of three stages. Firstly, a rotation up to 0.03 rad was applied to connections. Then the axial force was applied up to the target level. Finally, the vertical shear force was applied until the connection failure. Horizontal forces in these tests varied from about $0.1F_yA_{beam}$ in compression to $0.04F_yA_{beam}$ in tension. Results indicated that the connections tend to be ductile, and the shear capacities of the connections without stiffeners and without axial force were greater than those predicted by available design provisions.

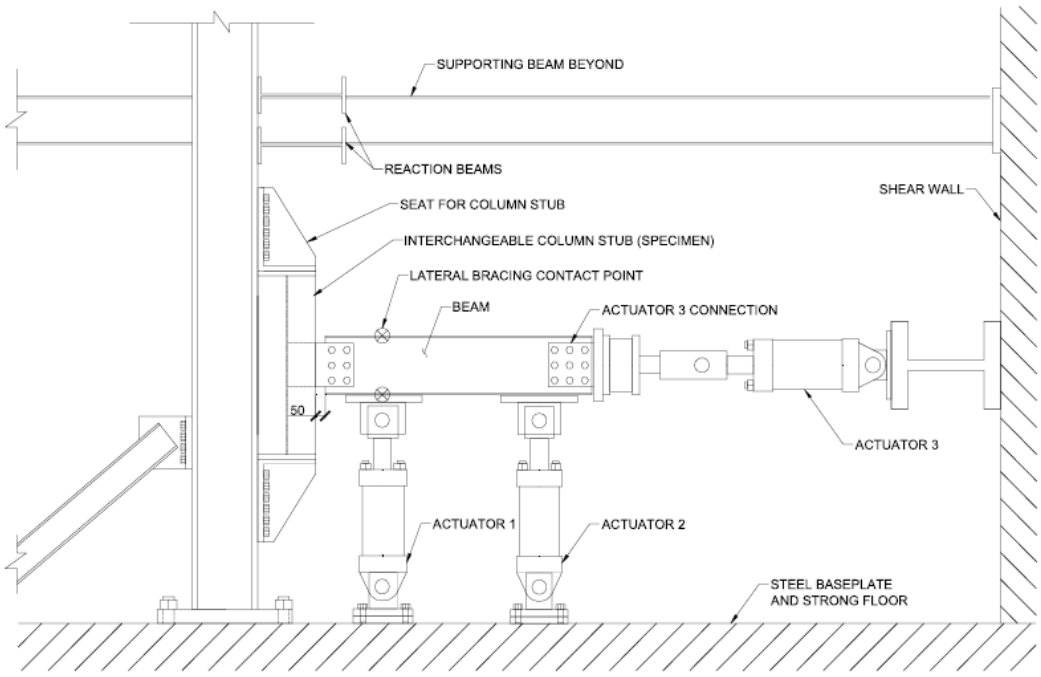

Figure 4-10. Test setup (Thomas et al., 2017)

4.3.2 WSP connection design for gravity loads

Here, the design considerations of the 14th edition of AISC steel construction manual (2011) and New Zealand design procedure (HERA R4-100 2003) are described.

4.3.2.1 AISC steel construction manual (2011)

14th Edition of AISC steel construction manual (2011) includes detailed provisions for designing WSP connections referred to as "single plate connections". This design guide categorizes the WSP connections into two groups based on the distance between the bolt-line to the weld-line, a. A conventional WSP connection refers to the group where the distance "a" is less than or equal to 89mm. an extended WSP connection refers to the group where the distance "a" is greater than 89mm.

For both of these connections, fillet welds are to be sized at $5/8$ of the plate thickness and design recommendations are equally applicable to plate and beam web material with $Fy = 250MPa\ or\ 344\ MPa$. The design procedure is valid for bolts that are snug-tightened, or pre-

tensioned/slip-critical. Specific considerations for each type of WSP connection are described below.

1. Conventional WSP connection

Conventional WSP connections are limited to a single vertical row of two to 12 bolts, as shown in Figure 4-11. In this connection type, bolts and plate capacities are required to be checked considering an eccentricity, e. The eccentricity should be chosen based on the number of bolts, n, and the type of bolt-holes as shown in Table 4-1, where STD and SSLT are standard holes and short-slotted holes respectively. Also minimum horizontal edge distance should be greater than or equal to $2d$ (d is the bolt diameter). In this design guide, maximum plate and beam web thicknesses are specified to ensure ductile behaviour.

Table 4-1. Design values for conventional single-plate shear connections (AISC steel construction Manual 2011)

Design Values for Conventional WSP Connections			
n	Hole Type	e	Maximum t_p or t_w (in)
2 to 5	SSLT	$a/2$	None
	STD	$a/2$	$d/2 + 1/16$
6 to 12	SSLT	$a/2$	$d/2 + 1/16$
	STD	a	$d/2 - 1/16$

Design considerations for this type of WSP connection include:

i. The bolts must be designed for required shear with the in-plane eccentricity, e, as shown in Figure 4-11, which is given in Table 4-1.

ii. The beam web must be designed for bolt bearing and block shear.

iii. The cleat plate must be designed for the required shear with the in-plane eccentricity, e (given in Table 4-1), both in the net and gross sections.

iv. Plate buckling is not required to be controlled explicitly for the conventional WSP connection.

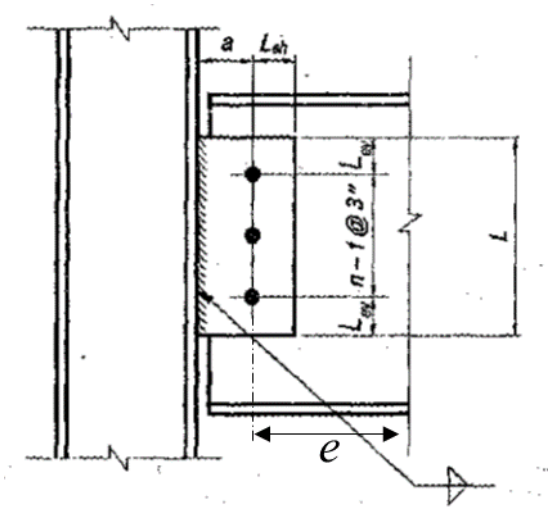

Figure 4-11. Conventional WSP connection (AISC steel construction Manual 2011)

2. Extended WSP connection

The design method of extended WSP connections is applicable for "a" distances greater than 89mm and/or multiple vertical bolt rows as shown in Figure 4-12. In this case the number of bolts is not limited.

Design considerations for this type of connections include:

i. The bolts must be designed for required shear with the in-plane eccentricity e, defined as the distance from the support to the centroid of the bolt group, as shown in Figure 4-12.

ii. Maximum plate thickness must be checked such that the moment strength of the plate does not exceed that of the bolt group.

iii. The cleat plate must be designed for the limit states of shear yielding, rupture, block shear and shear and flexural failure.

iv. Buckling of the cleat plate over the unsupported length must be considered.

v. The supported beam should be braced laterally.

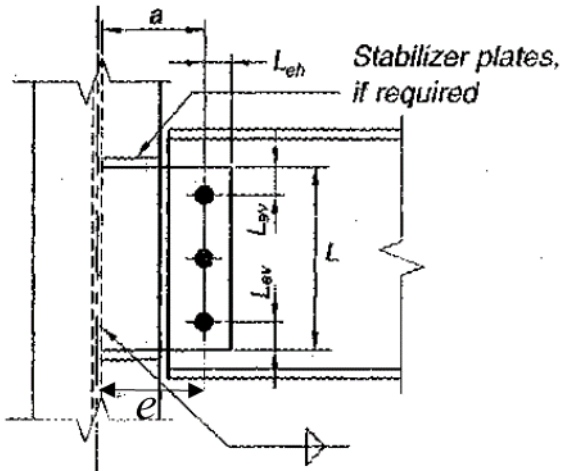

a) Extended WSP connection with stabilizer plates

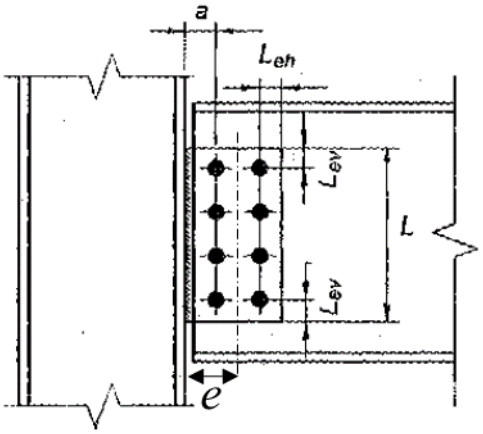

b) Extended WSP connection with two vertical bolt rows

Figure 4-12. Extended WSP connection (AISC steel construction Manual 2011)

4.3.2.2 New Zealand design procedure (HERA R4-100, 2003)

New Zealand Heavy Engineering Research Association (HERA R4-100, 2003) has published a design guide for different types of structural connections, which also includes specifications for WSP connection. In this design guide the effect of structure drift is also considered.

Design considerations for this type of connections include:

i. In the beam-column connections, in addition to factored gravity shear forces, seismic drift induced shear forces should be considered.

ii. The bolts must be checked for required shear with an eccentricity equal to the bolt-line to the weld-line distance.

iii. The cleat plate gross and net sections must be designed for shear, flexure and shear-flexure limit states.

iv. For the single coped beams, the gross cross-section must be checked for shear, flexure, shear-flexure and block shear limit states. (note that block shear is not considered in the NZS3404 (2007) standard)

v. For the double coped beams, the gross and net cross-sections must be checked for shear, flexure, shear-flexure and block shear limit states.

vi. WSP connections must be able to sustain gravity loads and also be ductile enough to accommodate seismic drift induced rotations up to 0.03 rad. To prevent the possibility of bolt shear failure under extreme seismic drift rotations the cleat plate thickness is limited to half the bolt diameter. Also, the flexural capacity of the bolt group must be greater than the flexural capacities of the beam web and the cleat plate. The tension capacity of the weld between the cleat plate and the support member shall not be less than the ultimate tension capacity of the cleat plate to ensure weld fracture mechanism does not govern the connection ultimate capacity.

4.4 Axial behaviour of WSP connection

In this section, the behaviour of WSP connections subjected to axial force is investigated using FEM. Different parameters that may affect the axial behaviour of WSP connections are studied. ABAQUS software is employed for numerical investigations. The geometry of the studied models, assumptions, boundary conditions and the investigated parameters are described in the following.

4.4.1 Geometry of selected model and analysis assumptions

Figure 4-13 shows the geometry of the selected steel beams for numerical simulations. To study different beam sizes three beam spans (three, six and nine meters long) are considered. The tributary area of each beam for calculating gravity loads is assumed 5m. Dead and live loads are assumed 5kPa and 3kPa respectively. A composite slab with a total height of 140mm is considered on top of the steel beams so that the composite slab ribs are perpendicular to the beam direction as shown in Figure 4-13b. For calculating the beam moment capacity and stiffness, 50% composite action is considered as per typical beams (NZS3404, 2007).

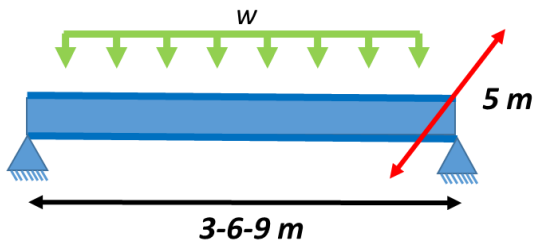

a) Beam lengths and tributary area

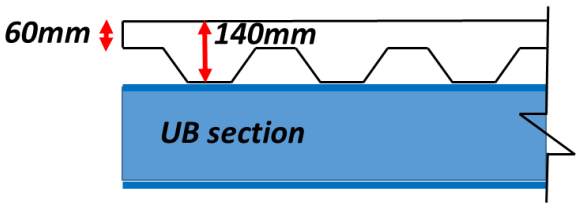

b) Composite slab orientation

Figure 4-13. Geometry of selected beams

4.4.1.1 Boundary conditions

To simulate the boundary conditions, the entire beam including the compression and tension sides are modelled. This allows both compression and tension behaviour of the WSP connections to be investigated and compared simultaneously.

The boundary conditions of the base model are shown in Figure 4-14 schematically. The base model is considered to have single shear studs at 300mm spacing on the steel beam top flange. The beam top flange is restraint laterally at the shear stud locations, and the axial force is applied to these locations as well. It is assumed that the beam is connected to a stiff column at its ends. Therefore, in models, cleat plates are supported by a rigid plate to reduce the computational costs. All other parameters, which may affect the boundary conditions, are described in the parametric study section.

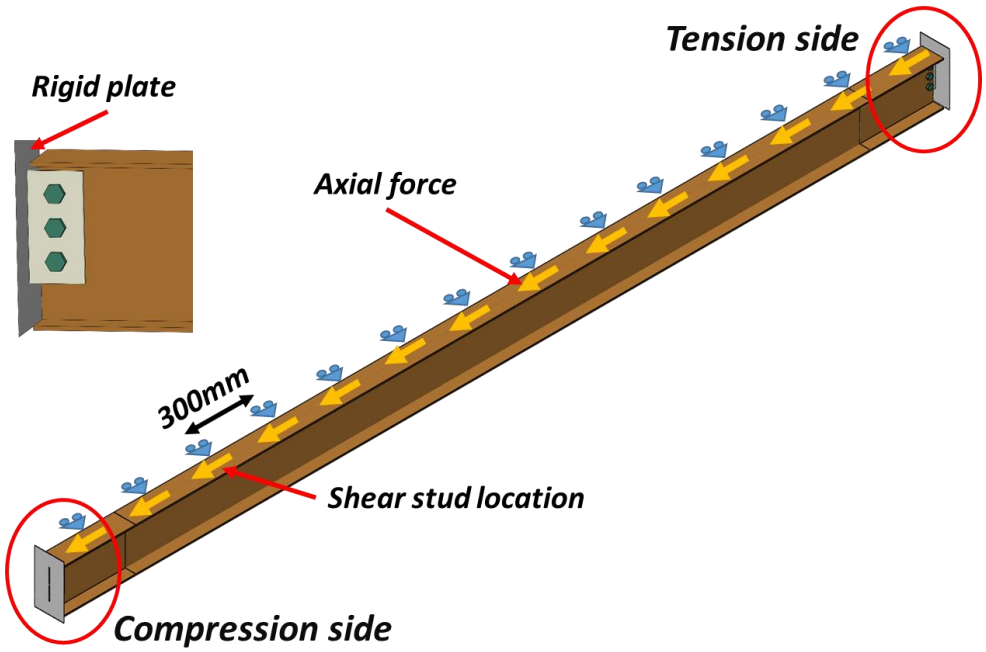

Figure 4-14. Boundary conditions for the base model

It is assumed that a gap is provided between the column and the slab, such that the force transfer is not possible through slab bearing and all the beam axial forces need to be transferred to the support through the WSP connections.

4.4.1.2 Connection design

"Structural steelwork connection guide" (SCNZ report 14.1, 2007) published by SCNZ is used in this research to design WSP connections under gravity loads. Details of the base model connection are shown in Figure 4-15.

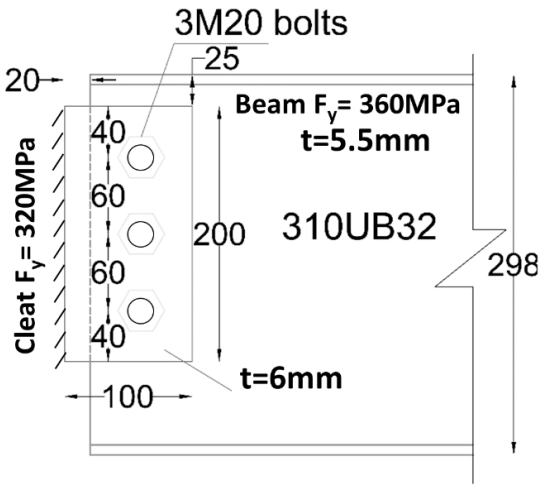

Figure 4-15. Base-model connection details (all dimensions in mm)

4.4.2 FEM modelling

The FE models are first verified with the experimental results of Astaneh et al. (1988) and Sherman and Ghorbanpoor (2002). Then the verified models are used to perform the simulations of the WSP connections under axial force.

Element selection, material properties and mesh sensitivity study are described in Appendix D. The modelling method, assumptions and the results of verification with Astaneh et al. (1988) and Sherman and Ghorbanpoor (2002) studies are described in Appendices E and F respectively.

4.4.2.1 Model geometry

Similar assumptions and FEM modelling techniques that were used for verifying the FE models are employed for the parametric models. Three different universal beams, UB, sections with various cleat plate heights, different beam flange coping conditions, and boundary conditions are investigated. For the base model a 6-meter long beam using 310UB32 steel section is selected.

4.4.2.2 Material properties

Elastic-perfectly plastic stress-strain relationship is used to model the high-strength bolt material, and a bilinear stress-strain relationship with 1% strain hardening is used for the steel beam and cleat plates. These stress-strain relationships had been used by Mahamid et al. (2007) for FEM modelling of WSP connections. The elastic modulus and Poisson's ratio of the steel material are considered 200GPa and 0.3 respectively. Table 4-2 shows the engineering stress of the material used for modelling.

Table 4-2. Material tensile properties

Member	***Yield strength (MPa)***	***Ultimate strength (MPa)***	***Strain hardening (%)***
Cleat plate	*320*	*440*	*1%*
Beam	*360*	*480*	*1%*
Bolt	*830*	*830*	*0*

4.4.2.3 Interactions

Similar to the verified models, the interaction between contact surfaces are considered using "surface-to-surface" interaction option available in ABAQUS software. To define the "surface-to-surface" interaction, "hard" contact with allowing separation is used for normal contact behaviour. To define "Tangential behaviour", "Penalty" friction formulation with a friction coefficient of 0.3 is used. The contact surfaces for the base model are shown in Figure 4-16.

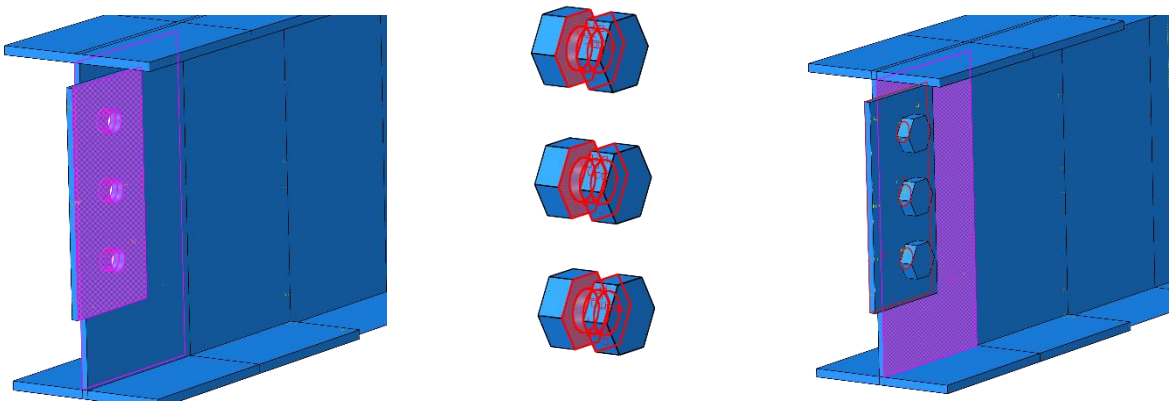

a) Cleat plate and beam web surfaces in contact with bolts

b) Bolts surfaces in contact with cleat plate and beam web

c) Contact surface between beam web and cleat plate

Figure 4-16. Interaction surfaces between bolt, cleat plate and beam

4.4.2.4 Bolt pre-tensioning

Bolt pre-tensioning needs to be considered in simulation to get more realistic results. The base model was simulated without bolt pre-tension. The effect of bolt pre-tension (proof loading) is also investigated in the parametric study section.

4.4.2.5 Meshing

According to the mesh sensitivity study presented in Appendix D, 5 mm mesh size is used for modelling the cleat plate and the beam web close to the connection. Finer mesh size, 2mm, is used for modelling curved surfaces such as bolts and bolt-holes. It should be noted that four

layers of elements are used along the thickness of the beam web and the cleat plate to obtain the interaction between the bolts and the plates. Three dimensional 8-node reduced integration solid elements, (which are called C3D8R in ABAQUS element library) are used for modelling the cleat plate, bolts and part of the steel beam. Also, two dimensional 4-node reduced integration shell elements, (which are called S4R in ABAQUS element library) are used for modelling the middle part of the steel beam far from the connections. It was found that this area does not experience high-stress levels and modelling with shell elements may not affect the results. These elements are used for reducing the computational costs and analysis time. Figure 4-17 shows the meshing on different parts of the base model.

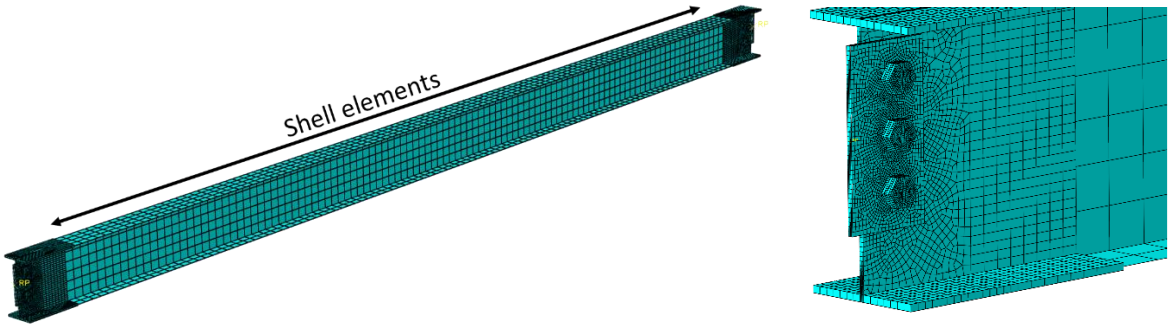

a) Overall model view b) Connection zone

Figure 4-17. Base model meshing

4.4.2.6 Axial compression and tension behaviour of the base model

Axial force versus axial deformation for both tension and compression sides of the base model are plotted in Figure 4-18a. The axial force is obtained through recording reaction forces of the rigid plate (support), and the axial deformation is recorded from a selected node on the beam top flange at 300 mm from the beam-end as shown in Figure 4-18b.

As can be seen in Figure 4-18a, the axial compression strength of the WSP connection is lower than its axial tensile strength. This behaviour was expected due to the innate out-of-plane (OOP) eccentricity of this type of connection and also the cleat plate slenderness. The axial force OOP eccentricity imposes additional moment to the cleat plate and the beam web.

Furthermore, the connection eccentricity results in P-Δ effect and the cleat plate buckles at lower axial forces. The axial force of the tension side increases until it reaches the first controlling limit state which in this case was beam web tear-out failure.

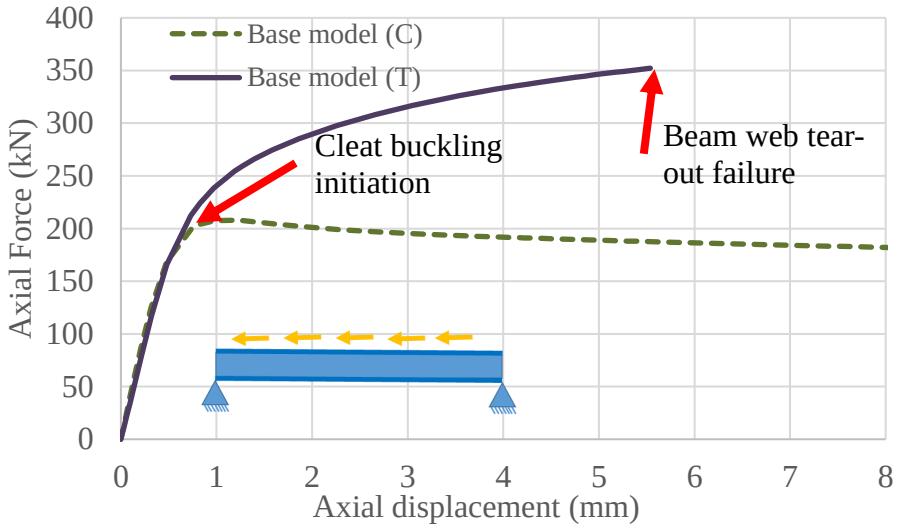

a) Axial force-displacement plot of both tension and compression sides

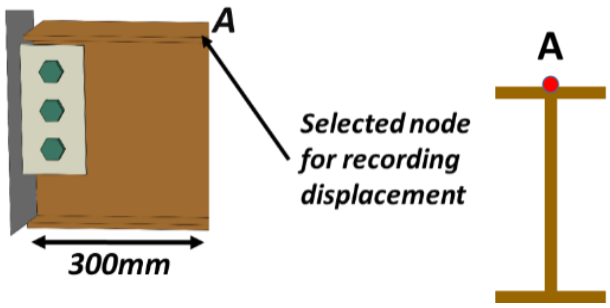

b) Selected node for obtaining axial deformation

Figure 4-18. WSP axial force behaviour

In the following Sections, the failure modes and deformed shapes of the base model are discussed.

- ***Compression behaviour***

Figure 4-19 and Figure 4-20 show the connection deformed shape under axial compression force at the initiation of the cleat plate buckling, 0.8mm axial deformation, and at the ultimate deformation, 8 mm, respectively.

The behaviour of the WSP connection under the axial loading of Figure 4-14 on the compression side is shown in Figure 4-18a. It indicates an elastic part at the beginning of loading. Then the cleat plate starts to yield due to the combination of the axial force and corresponding moment. The cleat plate yielding decreases the stiffness and increases the lateral deformations which lead the cleat plate to buckle and experience large lateral deformations as shown in Figure 4-20.

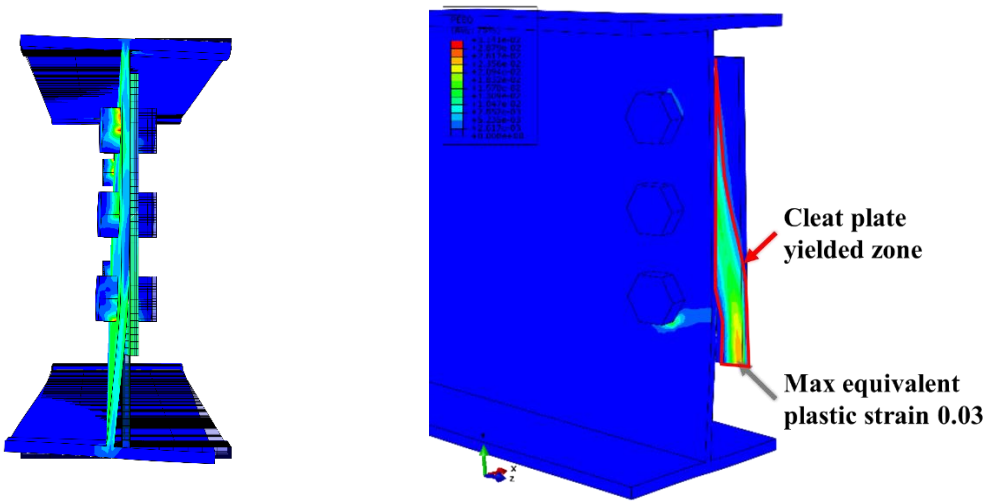

a) Deformed and un-deformed shape of WSP connection on compression side of beam

b) Equivalent plastic strains

Figure 4-19. Starting point of cleat buckling at 0.8 mm axial compression deformation

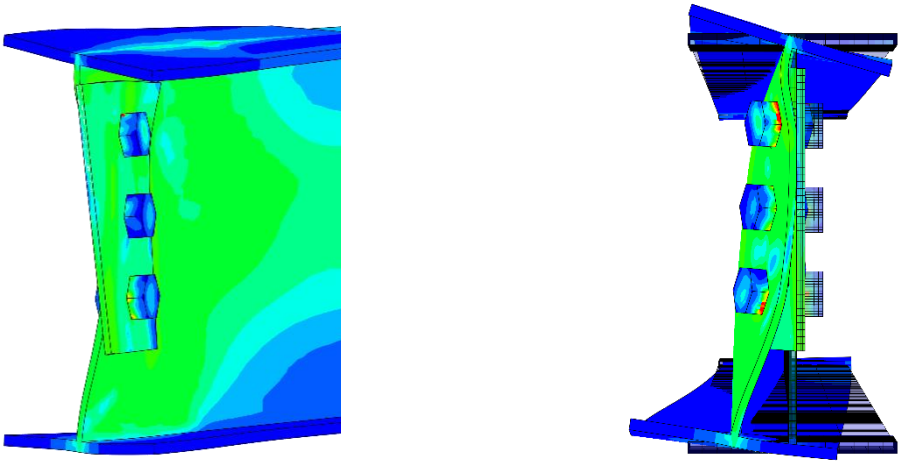

a) 3D view of the model

b) Front view (deformed and un-deformed shape)

Figure 4-20. Deformed shape of WSP connection under compression force at 8mm axial deformation

In the base model, lateral support was not provided for the beam bottom flange and the top flange was restrained laterally at the shear stud points. Although the presence of composite slab on the top flange can provide some level of torsional restraint for the beam top flange, lack of torsional restraint can lead to lower strength and more conservative results. In this model it was assumed that the top flange is not restrained torsionally.

Figure 4-20 shows that the pattern of cleat buckling is complex and its final deformed shape depends on various parameters. Some of these parameters are investigated in Section 4.6.

Investigating the base model for finding the failure modes showed that the bolts did not experience large deformations and significant yielding. The equivalent plastic strain of the bolts at 8 mm axial deformation was obtained lower than 0.004 which means bolt shear failure did not occur. This is shown in Figure 4-21a and b, where the bolts section cut is presented. The cleat plate and the beam web equivalent plastic strains of Figure 4-21c and d were as large as 0.027 and the deformed shape indicated that out-of-plane plastic hinge occurred at both the cleat plate and in the beam web. The plastic hinges were formed after the peak strength was reached at a displacement of 0.8mm according to Figure 4-18a.

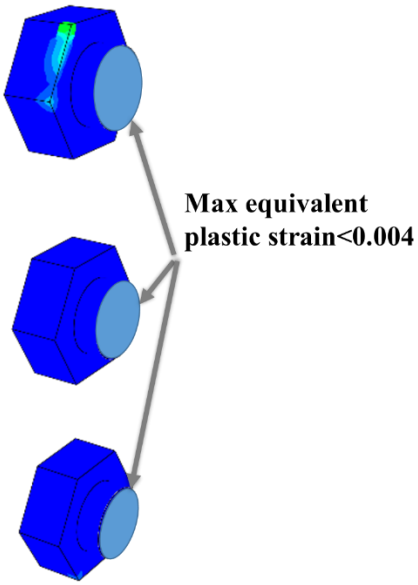

a) Bolts equivalent plastic strain

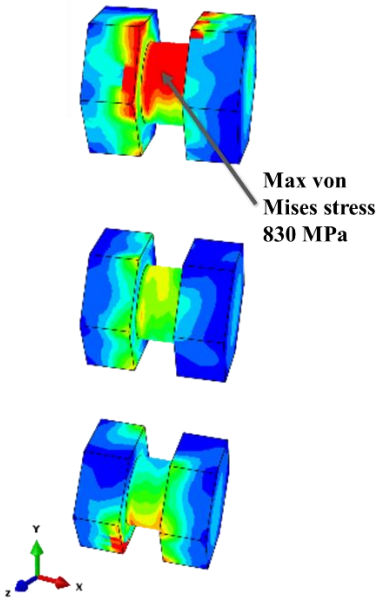

b) Bolts von Mises stress

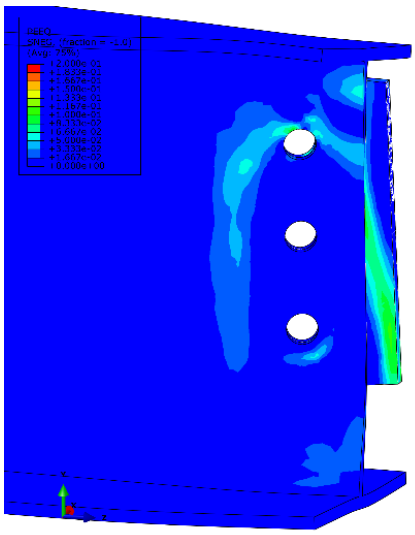

c) Equivalent plastic strain of cleat plate and beam web (front view)

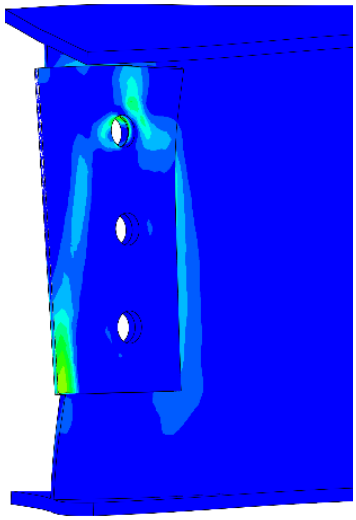

d) Equivalent plastic strain of cleat plate and beam web (back view)

Figure 4-21. Stress and equivalent plastic strain of bolts, cleat plate and beam web at 8mm axial deformation under compression

- ***Tension behaviour***

Tension force-displacement of the WSP connection is plotted in Figure 4-18a. It shows a stable behaviour which the tension force increases up to the point that the weakest element

fails. Here, investigating the FEM results of the base model indicated that the bolts did not experience large plastic strains. The maximum equivalent plastic strain was limited to 0.004 as shown in Figure 4-22.

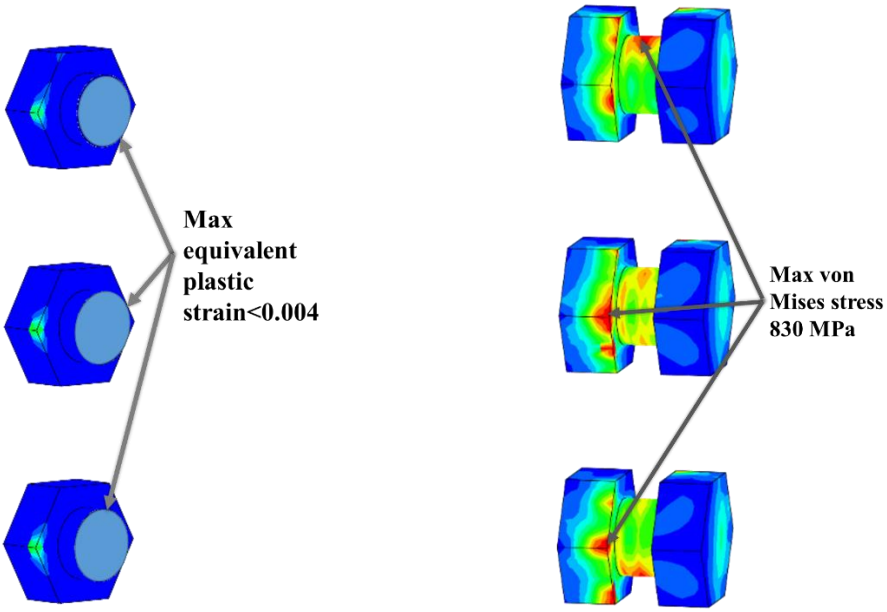

a) Equivalent plastic strain of bolts

b) von Mises stresses of bolts

Figure 4-22. Stress and equivalent plastic strain of bolts at 5.5mm axial deformation under tension

Since the fracture of materials is not defined in the FE models in this study, the equivalent plastic strain is used as a tool to judge failure initiation in each element. When the equivalent plastic strain reaches 0.2 in steel material, it is assumed it starts to fracture, and this point is considered as a failure point. The strain value of 0.2 is considered as lower bound elongation of steel material in accordance with AS/NZS3697 (2016). Also, this value can be used for the bolt material based on the test results provided by Kulak et al. (2001).

The equivalent plastic strain in the cleat plate and the beam web indicated that bolt tear-out failure controlled the ultimate tensile strength of the base model. Figure 4-23 shows the regions near the bolt holes in the cleat plate and the beam web that started to fracture with tension on the effective net area.

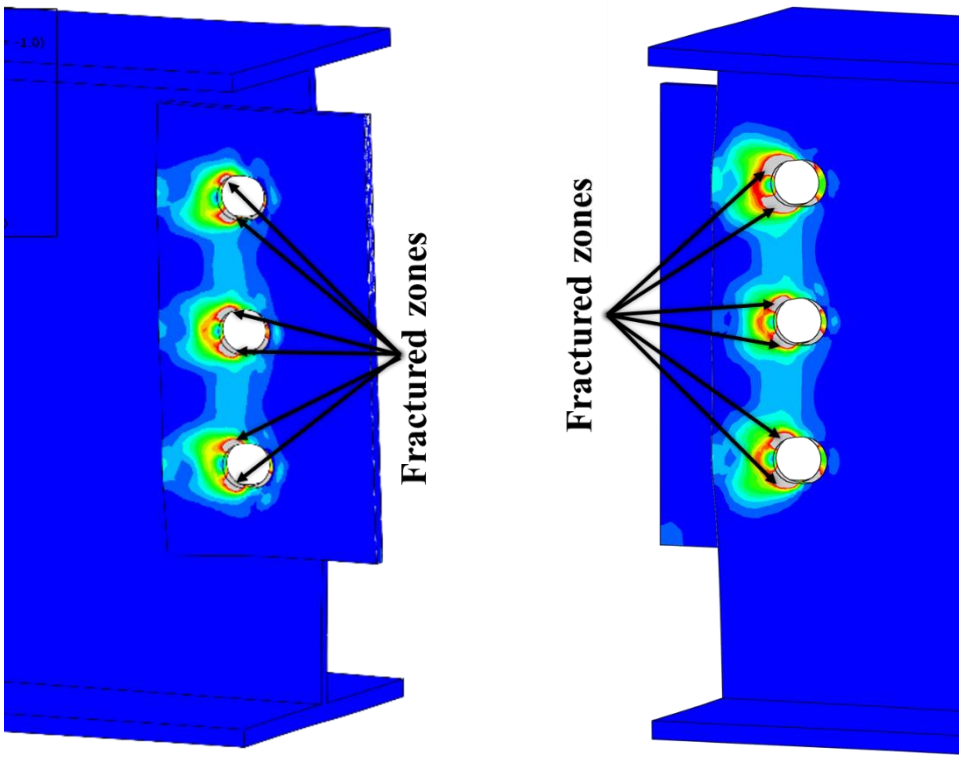

a) Material failure zones at the cleat plate b) Material failure zones at the beam web

Figure 4-23. Equivalent plastic strains of cleat plate and beam web at 5.5 mm axial deformation under tension

4.5 Parameters affecting the axial behaviour of WSP connections

Many parameters may affect the axial behaviour of WSP connections. When the axial compression force is applied to the WSP connection, the load transfer mechanism is more complicated than the tension force behaviour due to stability issues.

Parameters affecting the axial behaviour and ultimate strength of the WSP connections may be categorised in the following groups:

1) Boundary conditions
2) Connection geometry
3) Initial loading conditions

Each of these parameters is described in the following section.

4.5.1 Boundary conditions

Various boundary conditions that may affect the axial performance of WSP connections include:

i) Beam lateral restraints, such as secondary beams. Beam lateral restraint can decrease the beam effective length which may increase the connection axial compression strength.

ii) Top flange lateral restraint due to using shear connectors to connect the slab to the beam. The beam-slab connection can restrain the beam top flange laterally. This may increase the WSP axial compression strength.

iii) Direction of the composite slab ribs on the beam. Composite slab direction can affect the torsional rigidity of the beam top flange as shown in Figure 4-24. Providing torsional restraint for the beam top flange may increase the axial compression strength of the WSP connection by decreasing beam web lateral deformations. If the connection between the composite slab and the beam top flange is considered fully rigid, then the ribs orientation can affect the top flange torsional stiffness. As shown in Figure 4-24, when the ribs are perpendicular to the beam longitudinal direction, Figure 4-24b, the beam top flange is more restrained than when the ribs are parallel to the beam, Figure 4-24a.

a) Ribs parallel to beam direction b) Ribs perpendicular to beam direction

Figure 4-24. Effect of steel deck rib direction on top flange torsional stiffness

iv) Cleat plate support condition. The cleat plate support condition may also affect the WSP axial compression strength by changing the cleat effective length factor. For example in connection type A shown in Figure 4-25, the cleat plate is connected to the column flange which is relatively stiffer than the cleat plate and provides more end-restraint, even though the

rotational stiffness of the column about its vertical axis is finite. However, in Connection types B and C the cleat plates are connected to the column/beam web which is relatively more flexible than Connection type A. Based on the relative stiffness of the cleat plate and the supporting element, the connection of cleat plate to the supporting element may be considered as rigid, pinned or in-between.

v) Packing effect. Packing effect represents the imperfection when the cleat plate and the beam web do not align perfectly. The construction tolerances can increase the WSP connection OOP eccentricity. This results in larger in-plane moments and decreases the WSP axial strength. The allowable construction tolerances at the beam-end connections could be found in different building standards. According to Clause 15.3.5 of NZS3404 (2007) and Table F3.4 of AS/NZS5131 (2016), the allowable construction tolerance of beam web position at the connections should be within ±3mm.

4.5.2 Connection geometry

Cleat plate length and beam flange coping conditions also can affect the axial strength of WSP connections. As it was mentioned in Section 4.3.2.1, AISC steel construction Manual (2011) considers WSP connections with bolt line to weld line distance less than or equal to 89mm as normal or conventional WSP connections and longer cleat plates are called extended WSP connections. Cleat buckling is more likely in the extended WSP connections under axial compression force. As presented in Figure 4-25b, Connection A has a normal length cleat plate without beam flange coping. Connection B, Figure 4-25c, has a normal length cleat plate with a double coped beam. Connection C, Figure 4-25d, has a normal length cleat and may be single or double coped depending on the connected and supporting beam heights. In connection D, Figure 4-25e, the extended cleat plate is used to avoid beam flange coping.

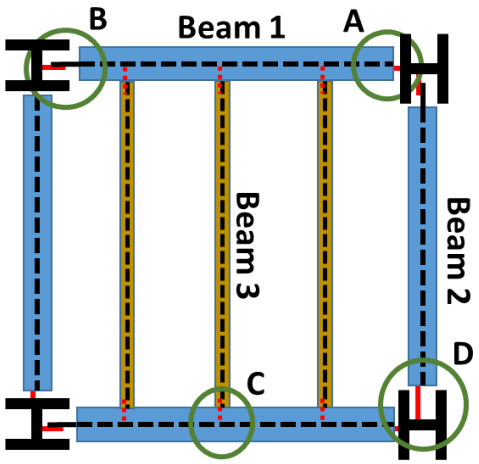

a) Typical steel structure floor plan for different WSP connections

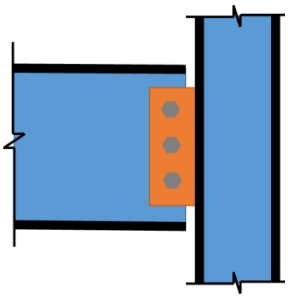

b) Connection A, conventional WSP

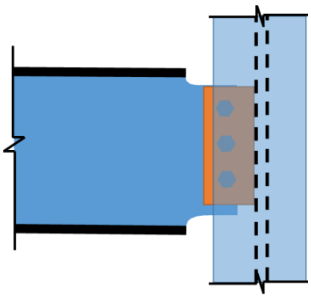

c) Connection B, conventional WSP

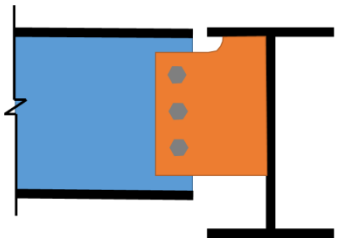

d) Connection C, extended WSP

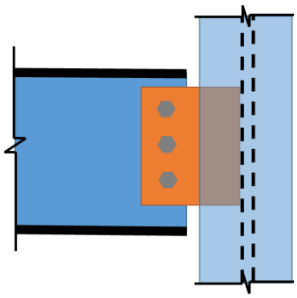

e) Connection D, extended WSP

Figure 4-25. Typical steel structure floor plan with different types of WSP connections

The size and thickness of the cleat plate, height and thickness of the beam web and the number of bolts can also affect the axial behaviour of WSP connections. However, these parameters usually are limited to some pre-defined values in design guides to prevent brittle failure modes under shear forces. For example, the cleat thickness is limited to half the bolt diameter to facilitate bearing yielding of the bolt holes rather than bolt shear failure in both

AISC steel construction manual (2011) and New Zealand design procedure (HERA R4-100 2003) as described in Sections 4.3.2.1 and 4.3.2.2 respectively.

4.5.3 Initial loading condition

Initial gravity loading may exist on a WSP connection at the time that beam axial force is imposed to the beam. This can affect the axial behaviour and ultimate strength of the WSP connection. Beam gravity loads can impose shear force, V_G, at the bolt centroid, and a moment, M_G. This will cause a rotation, θ_G, at the beam-end as shown on the left hand side of Figure 4-26a. During an earthquake event, these shear force and rotation may be increased or decreased because of the earthquake vertical excitation. The rotation, shear force and moment due to the earthquake vertical excitation are respectively denoted by θ_{EV}, V_{EV} and M_{EV} in Figure 4-26.

Furthermore, beam axial forces mainly occur due to lateral loading events. Lateral forces acting on the structure cause lateral deformations and inter-storey drifts. These drifts impose additional rotation and moments to the connections. The beam-column rotation due to inter-storey drift is shown on the right-hand side of Figure 4-26a denoted by θ_E. Depending on the relative direction of the beam axial force and the inter-storey drift, shown in Figure 4-26a and b, the drift rotation may decrease or increase the effect of gravity loads on the compression side of the beam.

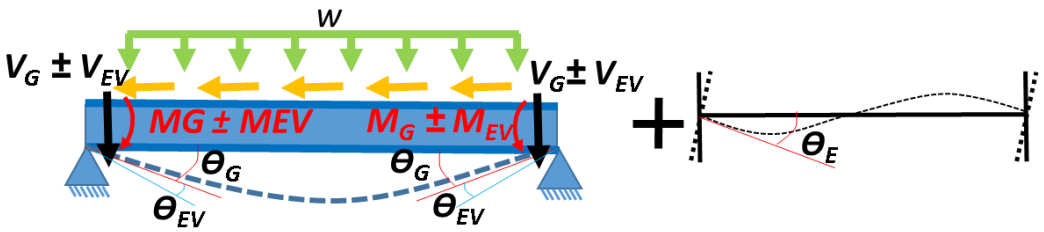

a) Drift increases the WSP rotation on the compression side and decreases on the tension side

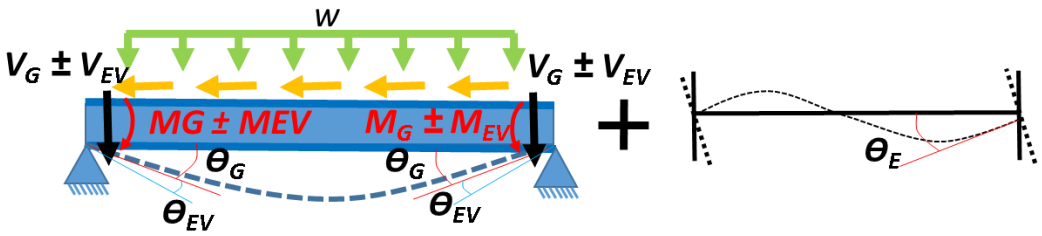

b) Drift increases the WSP rotation on the tension side and decreases on the compression side

Figure 4-26. Initial conditions due to gravity load and storey drift

Considering that the beam axial force can occur in the gravity beams of steel buildings, the axial capacity of WSP connections is required to be quantified to ensure robust load path for design.

4.6 Parametric study

As it was discussed in Section 4.5, various parameters can affect the axial behaviour of WSP connections. In this section some of the affecting parameters are investigated. Parameters that are studied include:

1) Boundary conditions including

i. Beam lateral restraint along the length

As it was mentioned in Section 4.4.2.6, cleat buckling can be a possible failure mode of the WSP connections under axial compression force. Therefore, providing lateral support for the beam may increase the axial compression capacity of the WSP connection by preventing buckling or decreasing the effective length.

The beam top flange usually is laterally supported due to the presence of floor slab and mechanical attachments such as shear studs. However, the beam web and bottom flange may be free to move out-of-plane as shown in Figure 4-27a. Lateral restraint for beam web and bottom flange can be provided by the secondary beams like beam 3 shown in Figure 4-27b. In this section, the effect of distance between the secondary beams is investigated considering 2m

and 3m spacing between the secondary beams. The results are compared to the base model which does not have any lateral support.

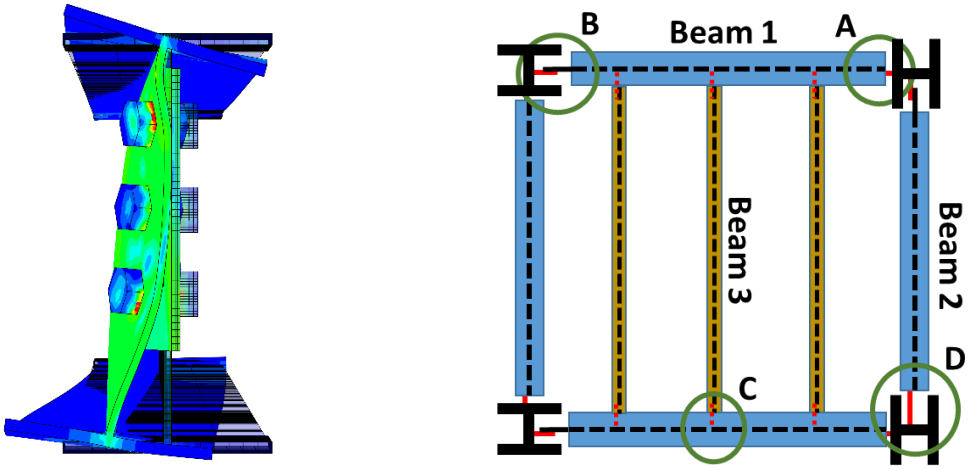

a) Lateral deformation of beam bottom flange subjected to the compressive axial force

b) Schematic floor plan of a steel structure

Figure 4-27. Lateral support for beam bottom flange

ii. Beam top flange torsional restraint

Top flange torsional restraint is another boundary condition that may increase the axial compression capacity of WSP connection. Generally, several parameters that may influence top flange torsional stiffness include: (i) direction of composite slab ribs on the beam as shown in Figure 4-28, (ii) shear connector type such as shear stud or other shear connectors, e.g. channel sections, and (iii) pattern of shear stud locations on the beam top flange.

a) Composite slab parallel to the beam direction

b) Composite slab perpendicular to the beam direction

Figure 4-28. Effect of composite slab direction on top flange torsional stiffness

It is expected that top flange torsional restraint increases the axial compression strength by increasing the cleat-buckling capacity and decreasing the out-of-plane deformations of the beam web. Here, this parameter is investigated by comparing two models with and without top flange torsional restraint.

i. Packing effect representing the imperfection when the cleat plate and the beam web do not align perfectly

The allowable construction tolerances at the beam-end connections could be found in different building standards. According to Clause 15.3.5 of NZS3404 (2007) and Table F3.4 of AS/NZS5131 (2016), the allowable construction tolerance of beam web position at the connections should be within ±3mm.

In this study, the base model is selected to investigate the packing effect on the axial capacity of the WSP connection. Here, the construction tolerance is modelled by putting a filler plate with different thicknesses ranging from one to 5mm between the beam web and the cleat plate as shown in Figure 4-29. This method is used to avoid increasing the complexity of models instead of modelling a twisted or skewed cleat plate.

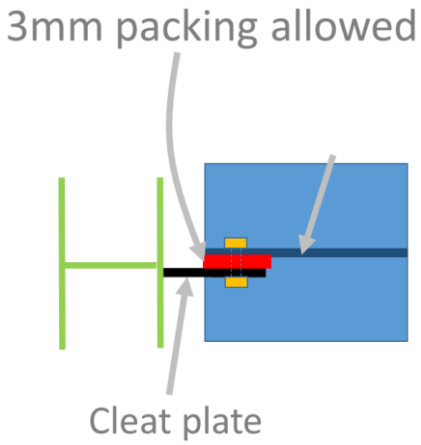

Figure 4-29. Schematic view of models with the filler plate

2) Connection geometry, including

i. Cleat plate located on one side or opposite sides at beam-ends

Cleat plates at both beam-end connections can be placed at one side or opposite sides of the beam web. When the cleat plates are placed at the different sides of the beam web, the imposed in-plane moment to the beam due to axial force eccentricity is in the opposite direction as shown in Figure 4-30a. In this case, the moment at the tension side may increase the beam out of plane deformation and consequently decrease the axial compression strength of the connection. On the contrary, when the cleat plates are on the same side of the beam, the imposed moments are in the same direction, Figure 4-30b. In this case, double curvature deformation of the beam may help to reduce the unrestraint length of the beam and increase the axial force carrying capacity of connection at the compression side.

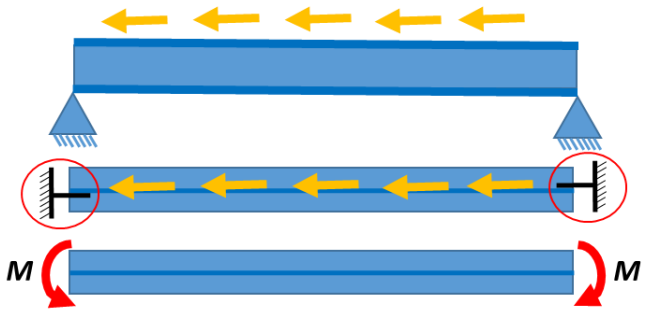

a) Cleat plates at different sides

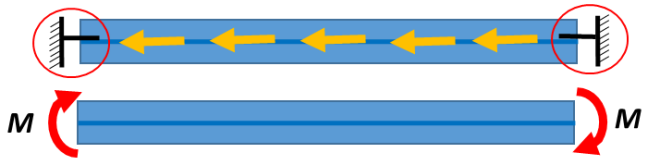

b) Cleat plates at the same sides

Figure 4-30. Location of cleat plates at the beam-ends

ii. Cleat plate height ranging from 0.5 to 0.8 times of beam height

Cleat plate dimension can directly affect the axial behaviour of WSP connection. Cleat plate length and the distance between bolt-line and weld-line, can directly affect the ultimate axial compression capacity of the connection. In design guidelines, there is a limitation for bolt-line to weld-line distance, and this length cannot be increased more than a specified

amount. Cleat plate height can also affect the ultimate capacity of the WSP connection. Three plate heights 150mm, 200mm and 250mm with 2, 3 and 4 bolts respectively, are modelled and analysed.

iii. Beam flange coping effects

In some cases such as a beam to beam connection or beam to column web connection (connections B and C shown in Figure 4-25a) because of constructability considerations, beam flanges need to be coped. In this situation, the effect of beam flanges on providing lateral restraint for the beam web and the cleat plate decreases. This cause lower axial compression force capacity. Here, the behaviour of WSP connections with coped and un-coped beams are compared, and the behaviour of coped beam-column connections with different cope lengths is studied.

iv. Cope length effects

Beam flange cope length is usually governed by the geometry of supporting member, but due to the plate buckling considerations, cope length cannot be more than a specified value that is related to the beam web thickness and height. By increasing the cope length, the effect of beam flange on restraining the beam web and cleat plate decreases and consequently the ultimate capacity of the connection reduces.

3) Initial loading conditions including

i. Gravity loads causing a beam shear up to 60% of the WSP capacity

During an earthquake event, a combination of gravity loads and beam axial forces act on the beam and the beam-column connection. Gravity loads on a simply supported beam impose a shear force and rotation to the beam-column connection. The amount of shear can simply be calculated using equilibrium equation. However, the amount of beam-end rotation relates to several parameters such as connection rigidity, gravity load distribution on the beam, and level of beam composite action.

As it was mentioned in Section 4.4.1, steel beams in this research are designed using 5kPa dead load, G, and 3kPa live load, Q. The critical load combination for beam design under gravity loads based on AS/NZS1170.0 (2002) may be 1.5Q+1.2G, which is equal to 10.5kPa. The load combination considering the combination factor given in AS/NZS1170.0 (2002) Table 4.1 for the amount of gravity loads during earthquake is 0.4Q+G, which is equal to 6.2kPa. Therefore, the ratio of the imposed gravity loads at the time of earthquake event to the factored design loads is equal to 0.6 in this case. This value is used in this study to impose different levels of shear force to the WSP connections and investigate their axial behaviour.

Steel beams are designed with considering 50% composite action. In the FEM modelling the concrete slab was not modelled for simplicity. Consequently, the steel beam in the FE models has less flexural stiffness than a corresponding composite beam with 50% composite action. When the serviceability loads are applied to the bare beam in the FE models, it causes the same shear force at the connection. However, the rotation may be more than the composite beam due to lower stiffness. To overcome this problem, part of the gravity load which is equal to $gravity\ load \times \frac{I_{bare\ beam}}{I_{composite\ beam}}$ is applied as distributed uniform load on the beam and the rest are imposed to the beam-ends as concentrated loads to avoid increasing the beam-ends rotation. Here, $I_{bare\ beam}$ and $I_{composite\ beam}$ are moments of inertia of the bare beam and the composite beam with 50% composite action respectively. Figure 4-31 shows the gravity loading in FEM models schematically.

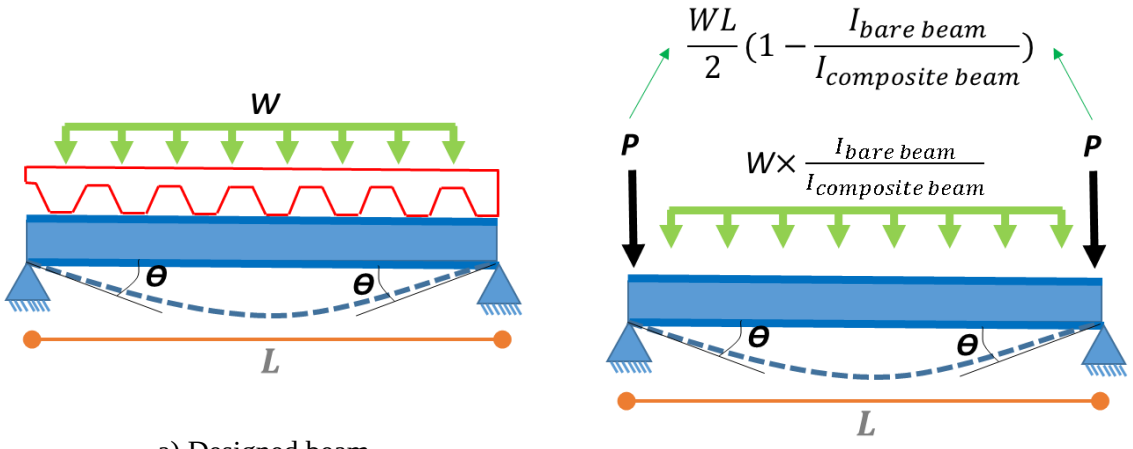

a) Designed beam

b) FE modelling method

Figure 4-31. Beam gravity loading

ii. Bolt pre-loading from zero to 100% of the proof load

Another parameter that may affect WSP connection axial behaviour is the bolt tightening level. Although in most construction projects, snug-tightened bolts are used in the WSP connections, here a short study is conducted to investigate the effect of bolt proof loading on the WSP axial behaviour.

ABAQUS software provides a method for applying bolt pre-tension force by using "bolt-load" option in the software "load" module. Using this feature, a certain amount of pre-tension load can be applied to the bolts. The amount of bolt pre-tension load or the bolt length can be chosen to remain the same in all the following analysis steps. When the bolt length is chosen to remain constant, the bolt behaves with its mechanical properties plus existing pre-tension force; this option is used in the FE simulations of this study.

iii. Lateral storey drift

As it was described in Section 4.5.3, structure drifts impose additional rotation and bending moment to the beam-column connections. In the structural steel-work connections guide (SCNZ report 14.1, 2007) design procedure, the imposed moments due to the drift rotations are also considered to prevent connection failure during lateral drifts. Also a gap is required to

be provided between the beam-end and column to ensure beam does not touch the column during lateral movements.

Beam axial force and the storey drift may act in the same direction or the opposite direction as shown in Figure 4-32. Here the effect of additional rotation due to the structure inter-storey drift is investigated in both possible directions. Also, to simulate a more realistic situation, a gravity load corresponding to $0.5V_y$ of the cleat plate is applied to all models as an initial condition.

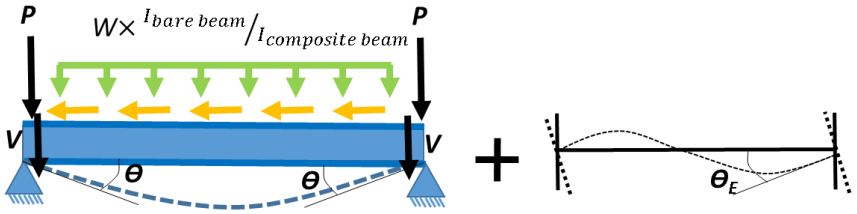

a) Positive storey drift

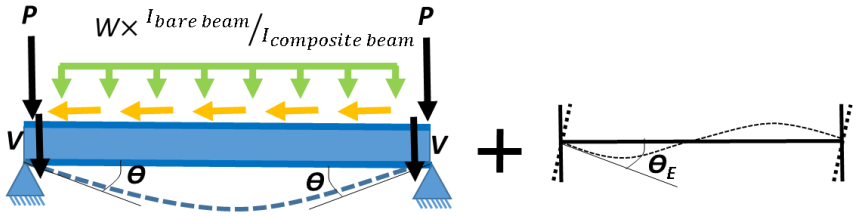

b) Negative storey drift

Figure 4-32. Beam axial force and structure lateral drift

4.6.1 Parametric matrix

In this study, thirty-one models are investigated to obtain the effect of each parameter on the axial behaviour of WSP connections. Table 4-3 summarises the models detail and the parameters investigated. Letter "C" in the model number is used for coped beam models.

Table 4-3. FEM models detail

	Lateral bracing	*Gravity load, V*	*Θ Earthquake*	*Number of bolts*	*Beam section*	*Description*	*Section*
1 (Base model)	---	---	---	3 Bolts	310UB32		
2	---	V/V_y*=0.15	---	3 Bolts	310UB32		4.6.2.1
3	---	V/V_y*=0.3	---	3 Bolts	310UB32		4.6.2.1
4	---	V/V_y*=0.5	---	3 Bolts	310UB32		4.6.2.1
5	---	V/V_y*=0.6	---	3 Bolts	310UB32		4.6.2.1
6	---	---	---	3 Bolts	310UB32	Bolts proof loaded	4.6.2.2
7	at 2000 mm	---	---	3 Bolts	310UB32		4.6.2.3
8	at 3000 mm	---	---	3 Bolts	310UB32		4.6.2.3
9	---	V/V_y*=0.5	+0.5% drift	3 Bolts	310UB32		4.6.2.4
10	---	V/V_y*=0.5	-0.5% drift	3 Bolts	310UB32		4.6.2.4
11	---	V/V_y*=0.5	+1.0% drift	3 Bolts	310UB32		4.6.2.4
12	---	V/V_y*=0.5	-1.0% drift	3 Bolts	310UB32		4.6.2.4
13	---	V/V_y*=0.5	+2.0% drift	3 Bolts	310UB32		4.6.2.4
14	---	V/V_y*=0.5	-2.0% drift	3 Bolts	310UB32		4.6.2.4
15	---	---	---	3 Bolts	310UB32	Cleat plates located at different sides of beam	4.6.2.5
16	---	---	---	2 Bolts	310UB32		4.6.2.6 4.6.3.1
17	---	---	---	4 Bolts	310UB32		4.6.2.6 4.6.3.1
18	---	---	---	3 Bolts	310UB32	Top flange is restraint laterally and torsionally	4.6.2.7
19	---	V/V_y*=0.5	---	2 Bolts	310UB32		4.6.2.1
20	---	V/V_y*=0.5	---	4 Bolts	310UB32		4.6.2.1
21	---	---	---	3 Bolts	310UB32	1mm packing	4.6.3.3
22	---	---	---	3 Bolts	310UB32	2mm packing	4.6.3.3
23	---	---	---	3 Bolts	310UB32	3mm packing	4.6.3.3
24	---	---	---	3 Bolts	310UB32	4mm packing	4.6.3.3
25	---	---	---	3 Bolts	310UB32	5mm packing	4.6.3.3
26C	---	---	---	2 Bolts	310UB32	, Cope length=100mm	4.6.3.1

27C	---	---	---	3 Bolts	310UB32	Cope length=100mm	4.6.3.1 4.6.3.2
28C	---	---	---	4 Bolts	310UB32	Cope length=100mm	4.6.3.1
29C	---	---	---	3 Bolts	310UB32	Cope length=200mm	4.6.3.2
30C	---	---	---	3 Bolts	310UB32	Cope length=150mm	4.6.3.2
31C	---	---	---	3 Bolts	310UB32	Cope length=75mm	4.6.3.2
V_y: shear strength of cleat plate gross section							

4.6.2 Un-coped beams

4.6.2.1 Gravity loads

Figure 4-33 presents the results of the base model subjected to four different level of shear forces (gravity load). In this Figure V_y is the shear strength of cleat gross section, $0.6f_y t_c h$, where t_c and h are the cleat thickness and height respectively. As it is expected, the compressive axial force capacity decreased with increasing the shear force. Similar results are observed in Figure 4-34, for different cleat heights when the applied shear force of about 50% of the cleat gross section shear strength was imposed to the connections. From these analysis, it was found that the gravity load reduced the connection compressive axial strength by up to 15% when the applied shear force is about 0.6 times the yield shear strength of the cleat plate compared to the connections without gravity loads.

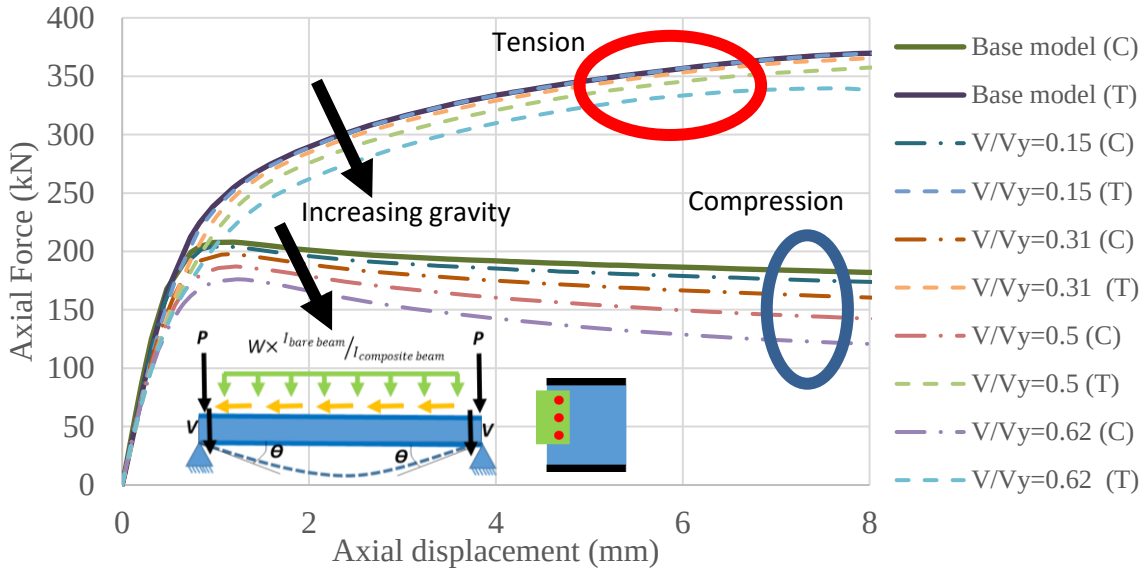

Figure 4-33. WSP axial behaviour under different levels of shear forces

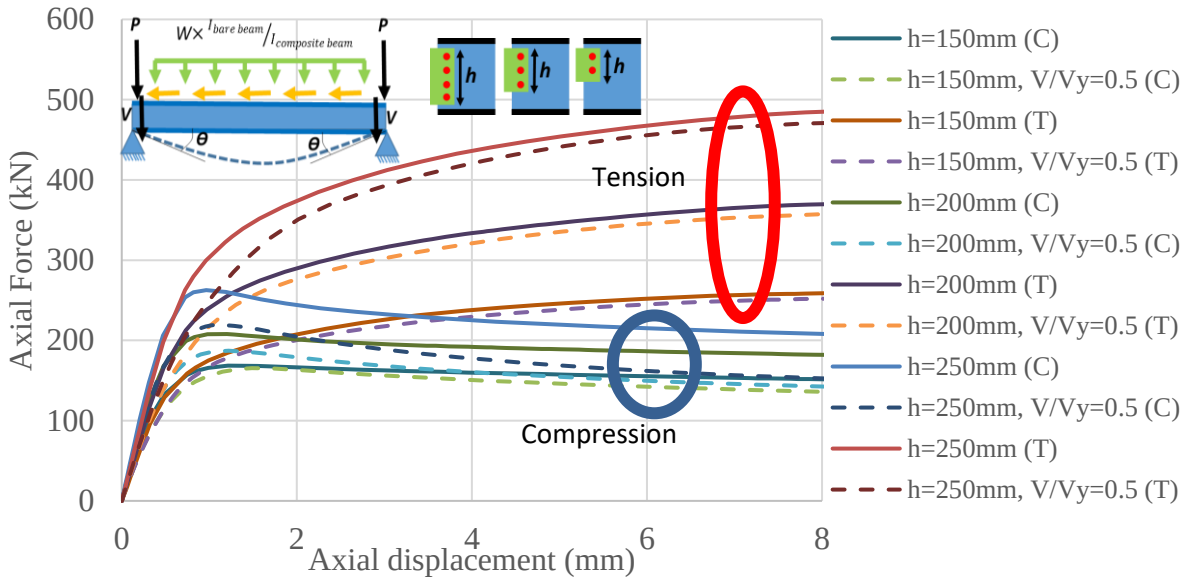

Figure 4-34. WSP axial behaviour with different cleat height under shear forces

4.6.2.2 Bolt pre-tensioning

Figure 4-35 shows the base model, with snug-tightened bolts and proof-loaded bolts. As can be seen in this Figure, in both models the ultimate tension and compression capacities were similar with less than 3% difference at the ultimate axial strength. However, the only noticeable difference in their axial force-displacement behaviours was a slight increase in the initial stiffness of the proof-loaded model.

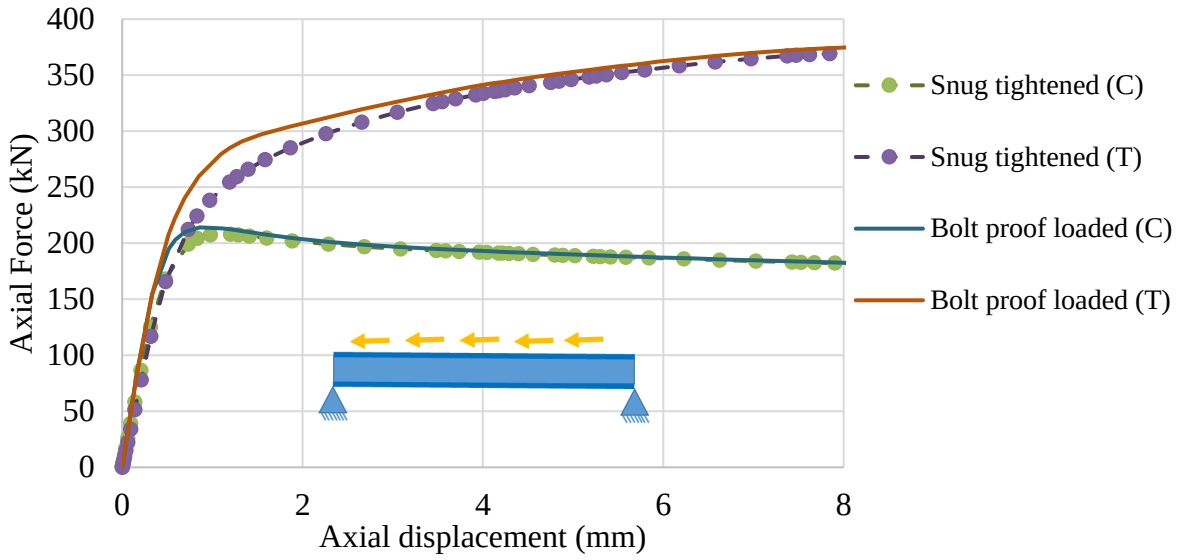

Figure 4-35. Effect of bolt tightening level, base model with snug-tightened and proof-loaded bolts

4.6.2.3 Beam lateral restraint

Figure 4-36 shows the effects of providing the lateral bracing at the mid-point and third points along the beam length which restrains the section against twist. Lateral movement is already restrained at the shear stud locations on the top flange. It may be seen that restraining the beam twist by providing lateral bracing did not alter the tensile strength and the compression strength increased by less than 4%. This indicates that the connection was not affected much by the beam lateral restraint away from the ends. Other parameters such as bottom flange dimensions and cleat plate height, also may affect the WSP compressive strength when the lateral support is provided, but investigating these parameters is not in the scope of this research.

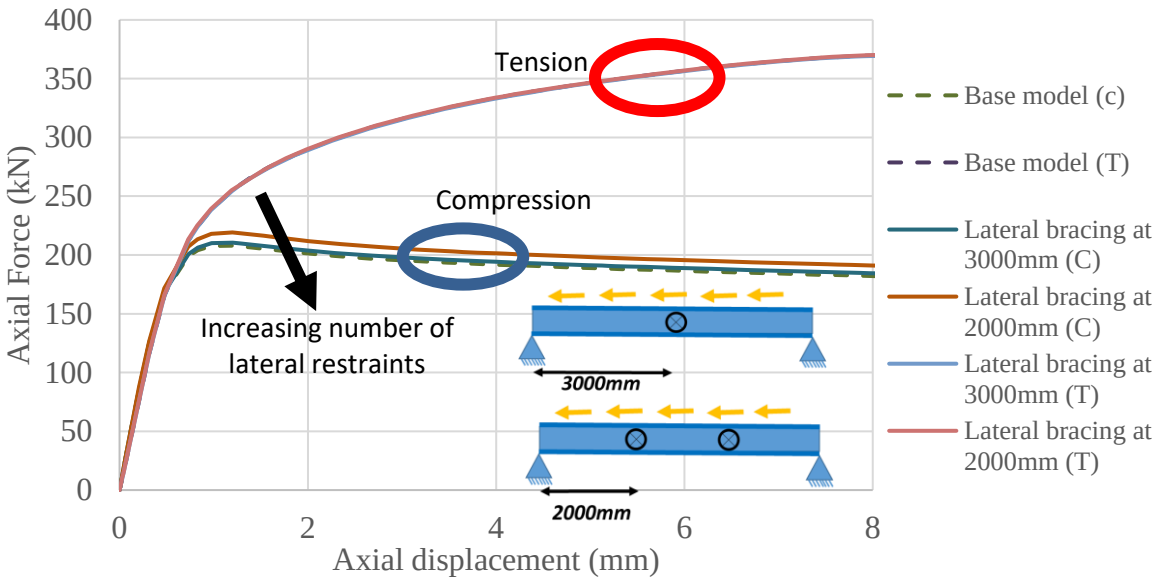

Figure 4-36. Lateral bracing of beam web and bottom flange

4.6.2.4 Lateral drift effect

Figure 4-37 plots the axial force behaviour of the studied WSP connections under different levels of inter-storey drift. In the positive storey drifts, beam-end rotation due to the inter-storey drift decreases the beam-end rotation due to gravity loads on the compression side and for the negative storey drifts it increases the beam-end rotation on the compression side.

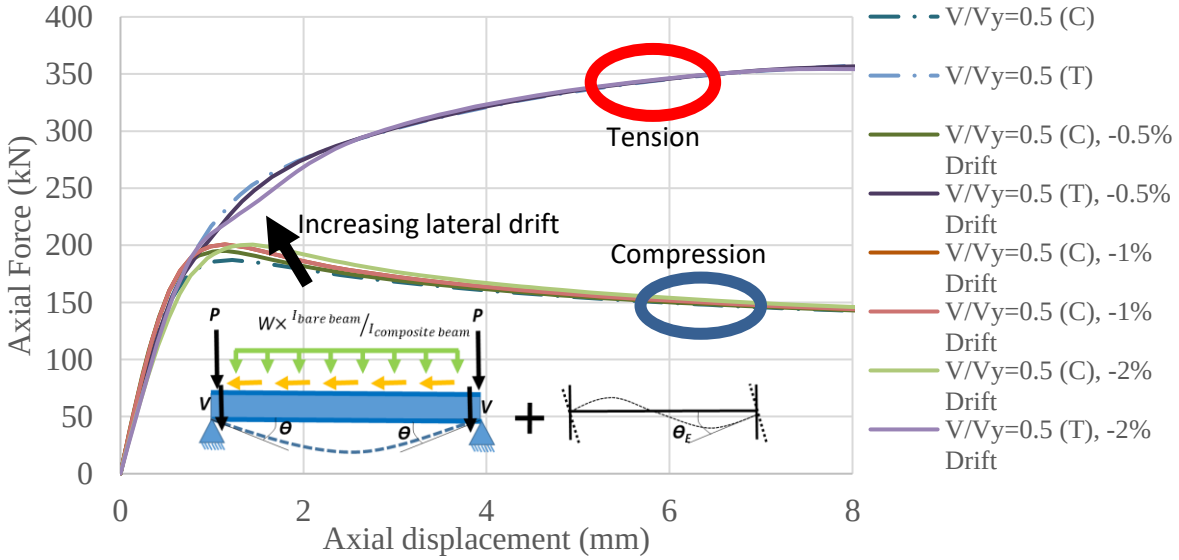

a) Axial force and storey drift in the same direction

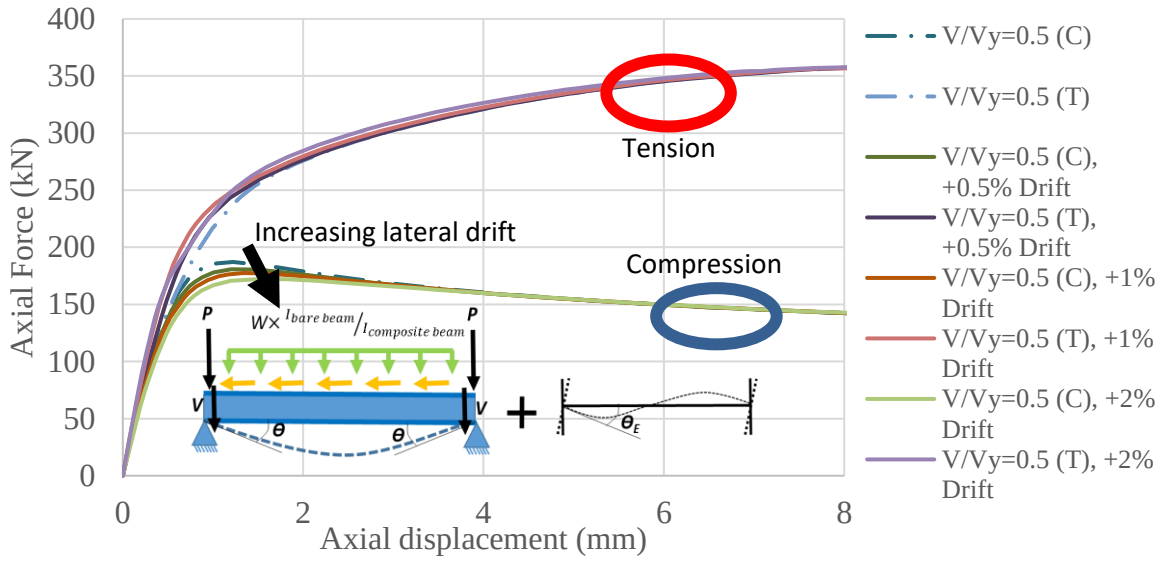

b) Axial force and storey drift in the opposite direction

Figure 4-37. Axial behaviour of WSP connections under different levels of inter-storey drift

Based on the results plotted in Figure 4-37, when the lateral drift decreased the rotation due to gravity loads on the compression side (Figure 4-37a), connection compressive capacity showed an increasing trend. On the contrary, when the lateral drift increased the effect of gravity loads (Figure 4-37b), connection compressive capacity showed a decreasing trend with increasing the storey drift level. Also, it was found that additional rotation did not have a noticeable effect on the tension behaviour of WSP connections.

Overall, the increase or decrease of ultimate capacity of the studied connections under axial compression force was measured less than ±8% for 2% drift angle.

4.6.2.5 Cleat plate location on beam sides

Figure 4-38 plots axial force-displacement of both conditions for the base model. The results showed that the effect of placing cleat plates at different sides of the beam was less than 1% for the studied case. It should be noted that the beam length and the ratio of the cleat plate stiffness to the beam weak axis stiffness may also affect this behaviour.

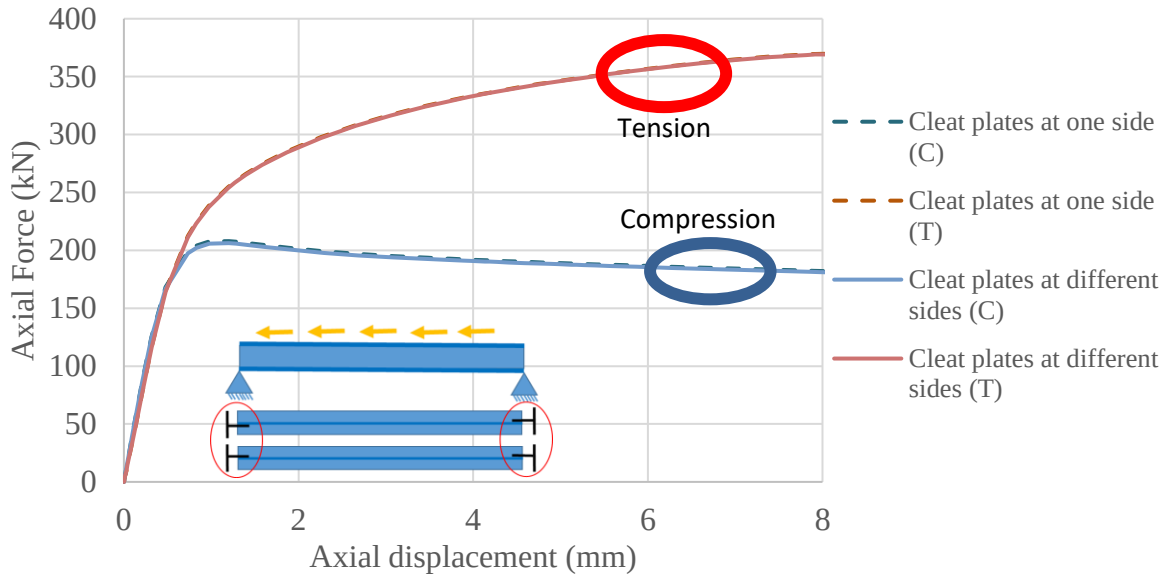

Figure 4-38. Axial behaviour of WSP connections with cleat plates located at different sides and the same side

4.6.2.6 Effect of cleat plate height

Figure 4-39 plots the tension and compression force-displacement of models with different cleat plate heights. The plots indicate that the compression and tension capacities of the WSP connection increased with increasing the cleat plate height. The ultimate tension and compression capacities versus cleat plate heights are shown in Figure 4-40. This plot shows that tensile strength more increased than compression capacity by increasing the cleat plate height. This is because the compression capacity of the cleat plate is more affected by the boundary conditions.

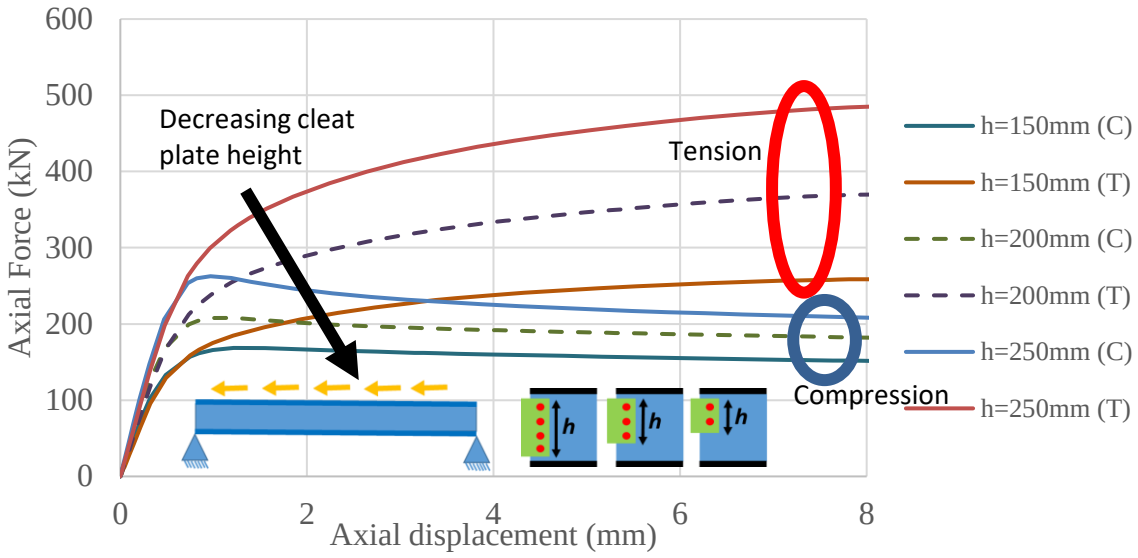

Figure 4-39. Effect of cleat plate height on WSP axial behaviour

In these models, the distance between the cleat plate and the beam top flange, which is restraint laterally, is constant and the cleat plate height is increased toward the bottom flange which is free laterally. Part of the cleat plate closer to the bottom flange has less effect on the axial compression capacity of the connection due to lack of lateral support. Note that in the studied cases beam top flanges are restrained, and bottom flanges are free laterally similar to the base model.

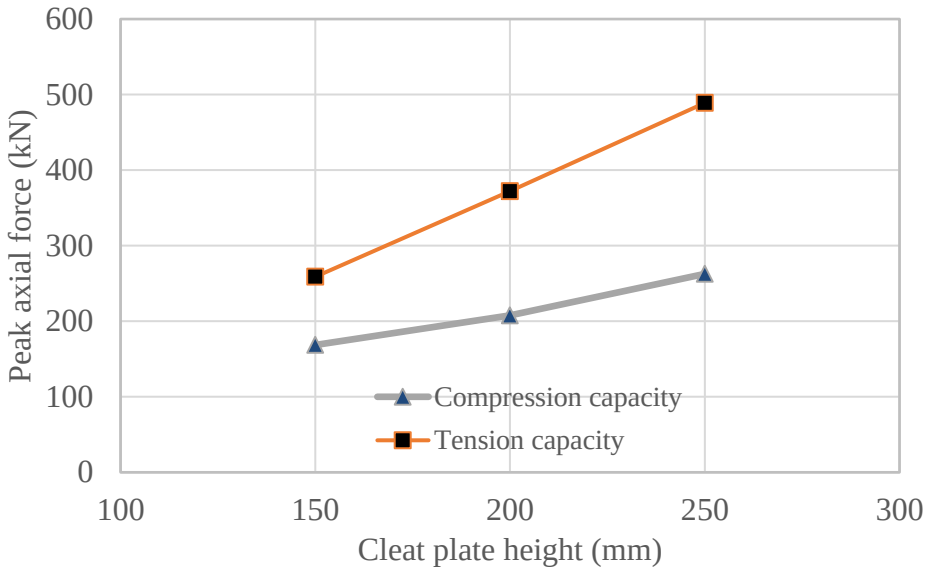

Figure 4-40. Ultimate tension and compression capacities versus cleat plate height

4.6.2.7 Top flange torsional restraint

Figure 4-41 shows the deformed shape patterns of the compression side of both models at 8mm axial deformation. As can be seen from this Figure, torsional restraint of the beam top flange can effectively decrease the bottom flange lateral deformations.

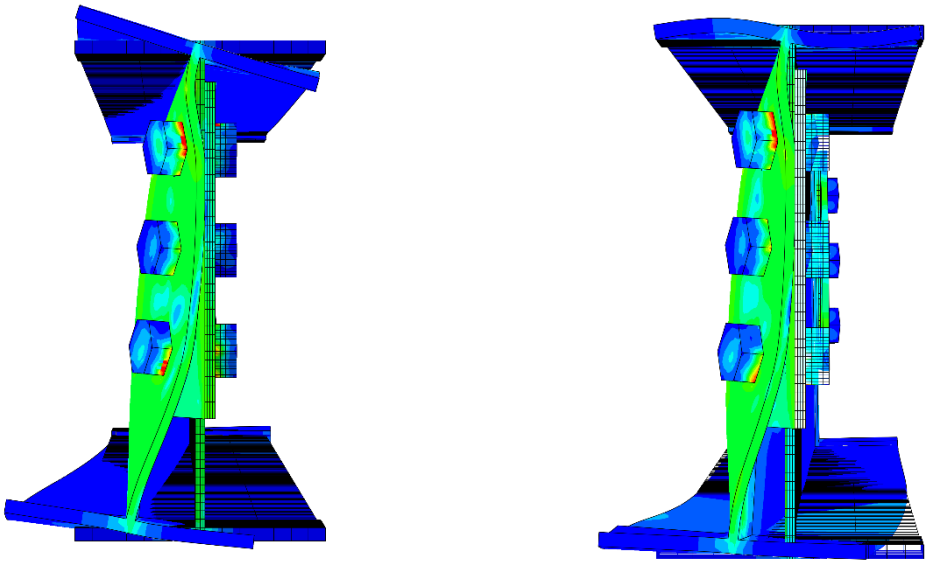

(a) Top flange unrestraint (b) Top flange restraint

Figure 4-41. Deformed shape of beam-end at the compression side with and without beam top flange torsional restraint

Axial force-displacements of the studied models are plotted in Figure 4-42. The tension behaviour did not show any change, while the compression capacity was increased by about 14% in the top flange torsionally restrained model.

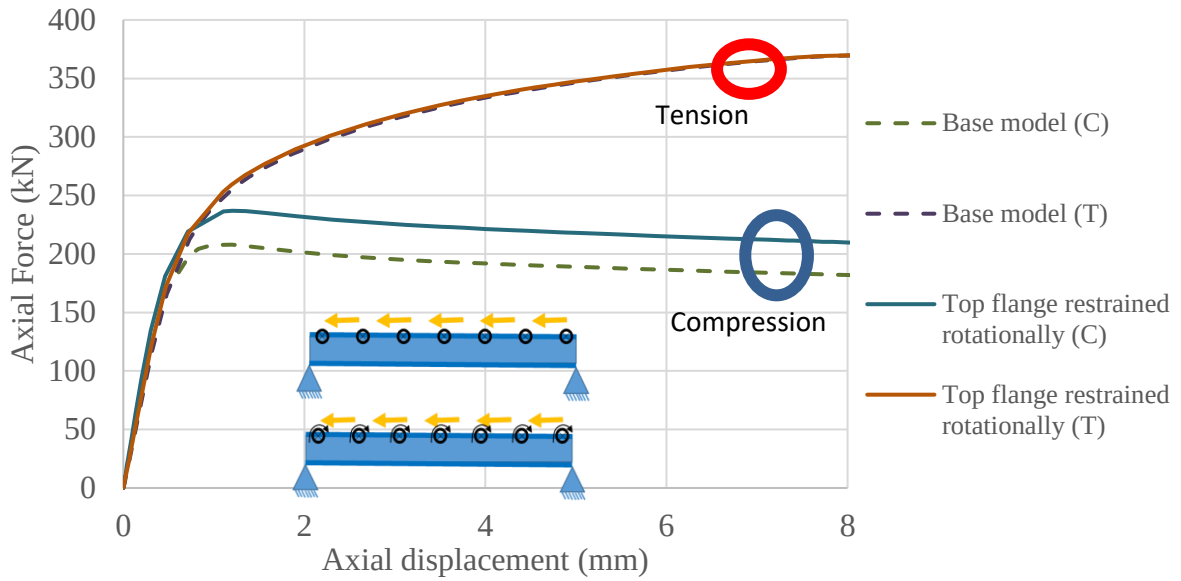

Figure 4-42. Effect of beam top flange torsional restraint

Evaluating the realistic level of torsional restraint can be very complicated and may depend on various parameters such as relative stiffness of the slab to the beam top flange, the beam web thickness and also, the shear connectors' stiffness. Therefore, in this study it is considered that the top flange is free to twist for all other models to obtain more conservative axial compression capacity.

4.6.3 Double-coped beams

4.6.3.1 Coping effect

Figure 4-43 shows the axial behaviour of the coped and un-coped connections with different cleat plate heights. In these models, cope length is considered equal to 100mm.

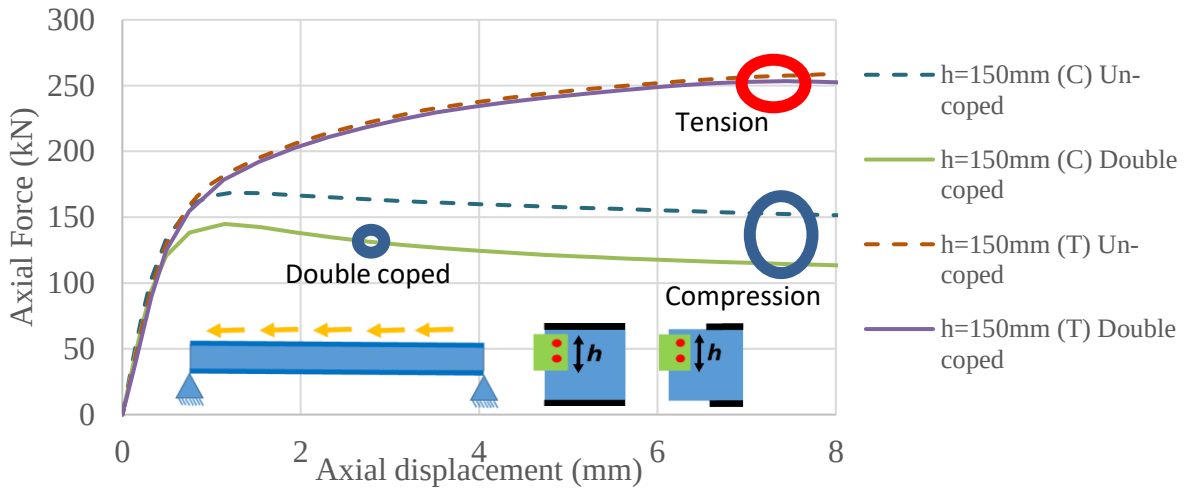

a) Two bolts connection

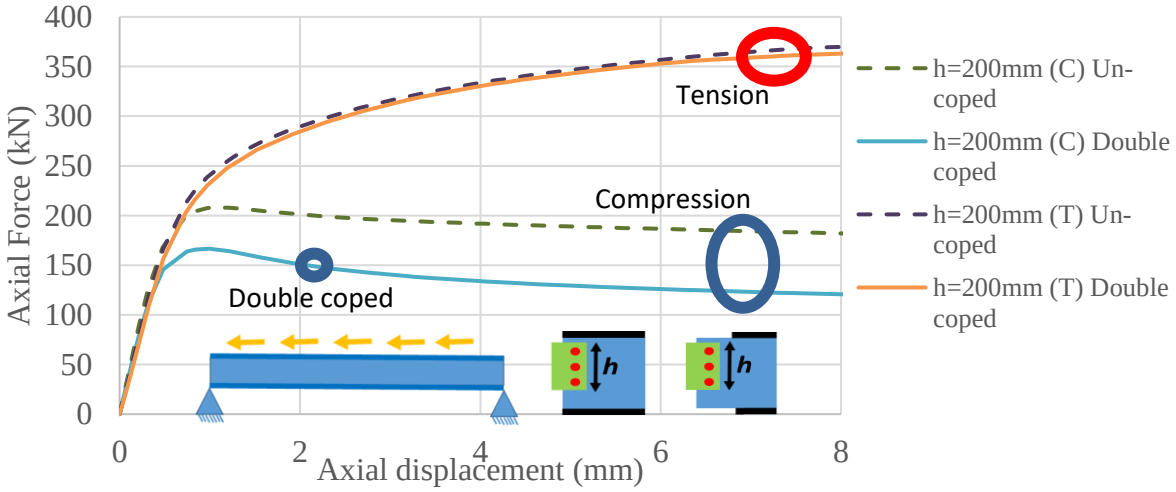

b) Three bolts connection

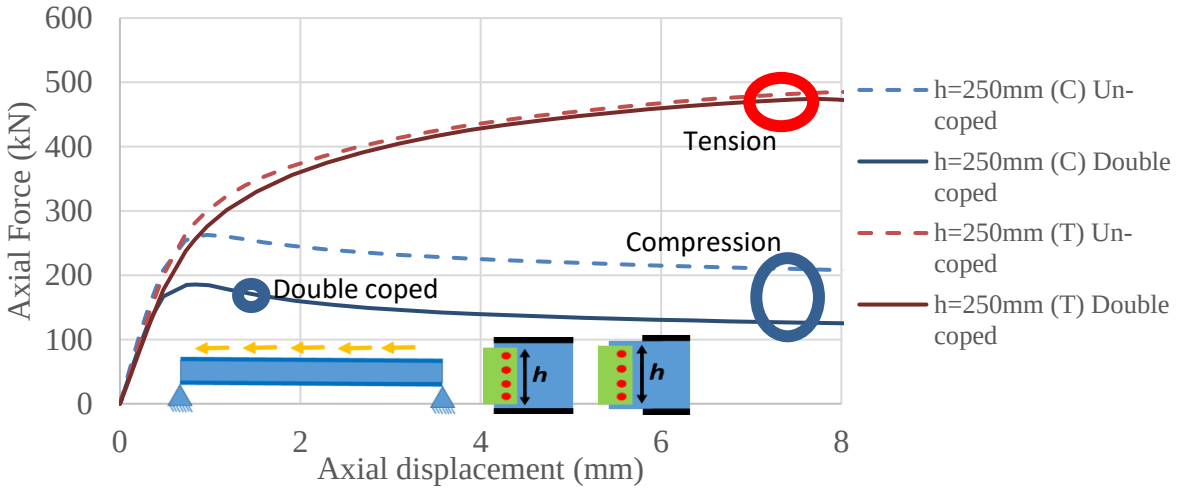

c) Four bolts connection

Figure 4-43. Beam flange coping effect on the axial behaviour of WSP connection

Based on the results, the tensile capacity of the studied models decreased by about 2% because of the reduction in the beam web cross-section area. However, the axial behaviour of compression side experienced a more decline, such that, 2, 3 and 4 bolts connections experienced 16%, 24% and 48% reduction in the ultimate capacity.

4.6.3.2 Cope length effect

Figure 4-44 plots the axial force-displacement behaviour of four models with different cope lengths. The results indicated that increasing the cope length does not affect the tensile capacity of the WSP connections. However, the connection compression capacity is directly related to the cope length.

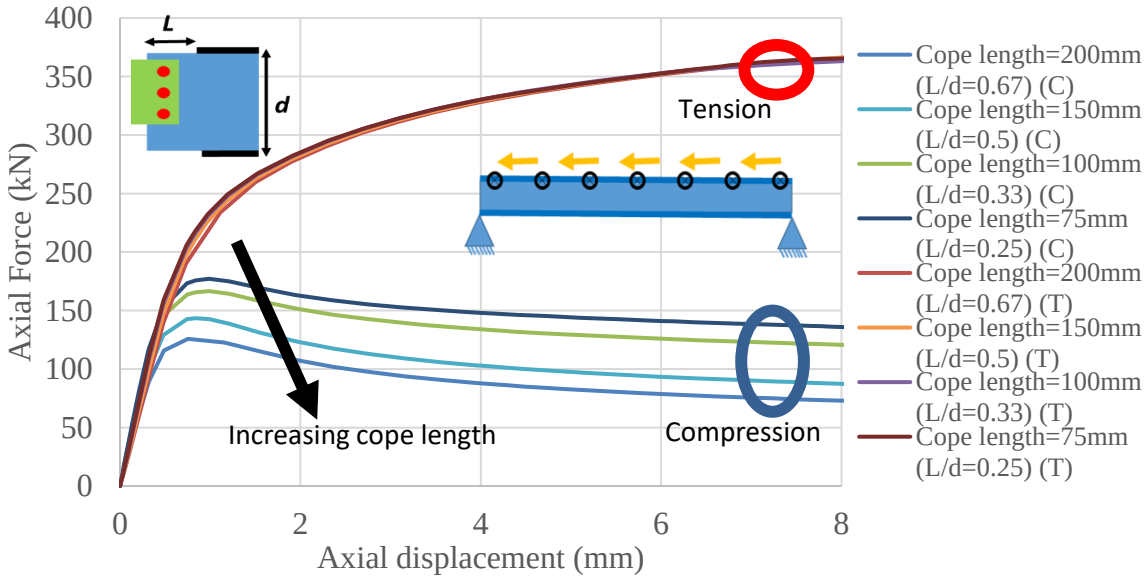

Figure 4-44. Behaviour of models with different cope lengths

Figure 4-45 plots the peak compression forces versus the cope length to beam height ratio. Results indicate that axial compression strength decreased linearly with increasing the cope length.

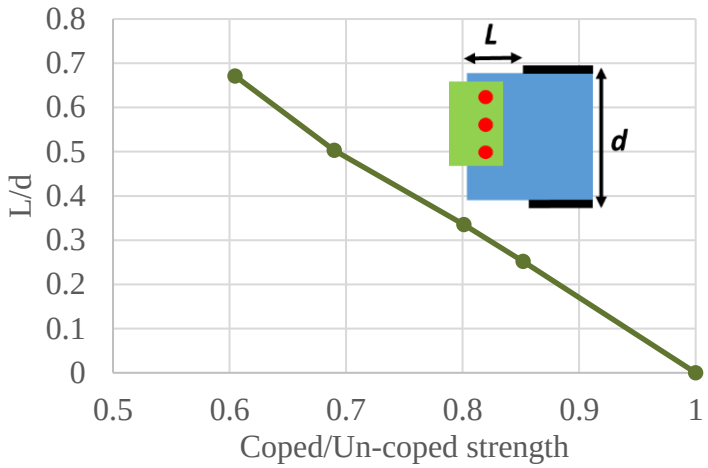

Figure 4-45. Peak compression force of the studied models versus the cope length to beam height ratio, cleat plate height=200mm

4.6.3.3 Packing effect

The axial force-displacement results of the WSP connections with different filler plates are plotted in Figure 4-46. The results indicate that 3mm eccentricity in the studied connection caused more than 25% decrease in the axial compression strength of the WSP connection. Increasing the axial force eccentricity in the compression side increase the imposed moment and cause cleat buckling to occur at lower axial forces.

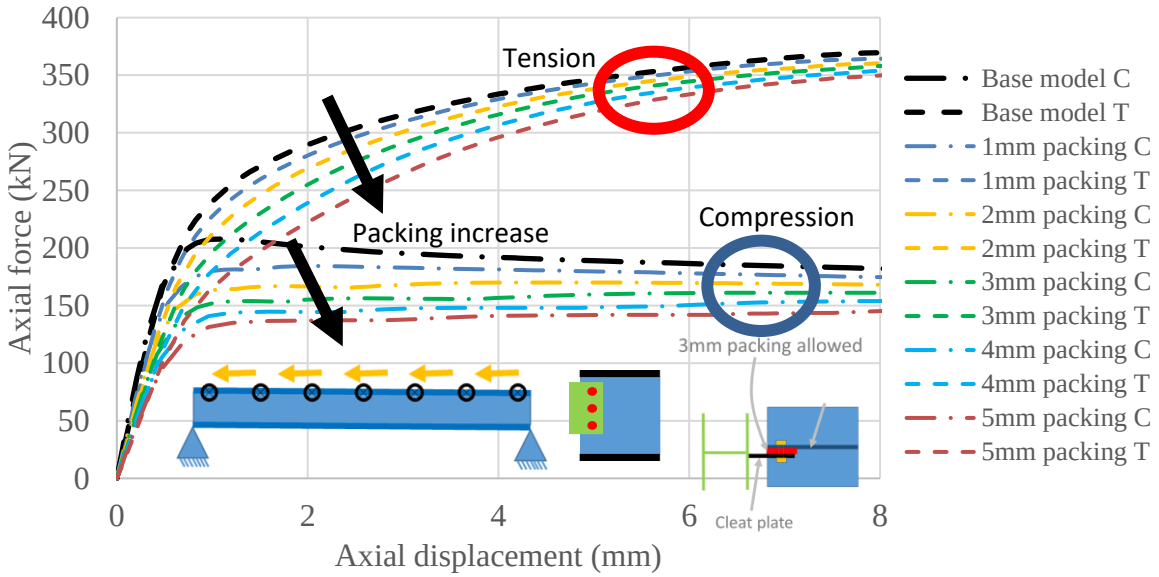

Figure 4-46. Axial force-displacement plots of WSP connection with different filler plate thicknesses

Based on the results, the ultimate tensile strength of the WSP connection changed by about 7% due to increasing the load eccentricity up to 3mm. This is because of increase in the imposed moment to the connection due to axial force eccentricity. These results emphasize the importance of considering the additional eccentricity due to the packing effect in calculating WSP connection axial strength.

4.7 Estimating axial strength of WSP connections

In this section, the axial force carrying mechanism of WSP connections is investigated and a method for estimating the axial force capacity is proposed. The proposed method is based on the material mechanic principles and it is verified with FEM results. Note that the proposed method is required to be verified by experimental tests which is out of the scope of this research.

4.7.1 Behaviour of laterally restraint and free WSP connections

The cleat plate and the beam web in WSP connections act as a beam-column member under axial force because of the connection out-of-plane eccentricity. Generally, the out-of-plane stiffness of the cleat plate is considerably lower than the steel beam; therefore, the cleat plate performance may govern the overall behaviour of the connection.

The behaviour of WSP connection under the axial compression force may vary from a simple to a complicated behaviour based on the boundary conditions and the beam flange coping. For instance, when both beam flanges are coped and the beam is not restrained laterally, the behaviour can be predicted using column equations available in building standards (e.g. NZS3404, 2007). However, when the beam is restrained laterally, the deformed shape and buckling pattern become complicated and different parameters may affect the connection capacity.

Here, the behaviour of two connection types are studied,

1. The WSP connection that the beam flanges are coped and the beam is not restrained laterally
2. The WSP connection that the beam flanges are not coped and the top flange is restrained laterally

The first is simple, so methods described are easily understood. The second is perhaps more realistic for beams used in buildings. Together they can be considered to be bounds on the behaviour of some typical beams.

Figure 4-47 shows the coped beam connected to the cleat plate and the axial force-deformation plot of the connection. The behaviour of this connection is defined in three stages.

i. Elastic part, which the connection does not experience any inelastic deformations. Typically this is about up to 0.3-0.4mm axial deformation.
ii. The second part is from the first yield to the formation of plastic hinges in the cleat and the beam web. First yielding may occur either in the cleat or the beam web depending on their relative stiffness and cross-sectional properties.
iii. In the third part, plastic hinges are formed and the strength of the connection decreases due to large lateral deformations and the P-Δ effect.

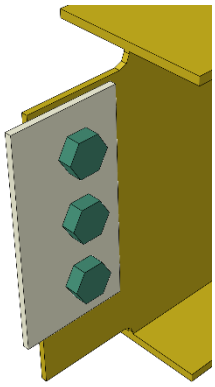

a) 3-bolts connection with coped flanges

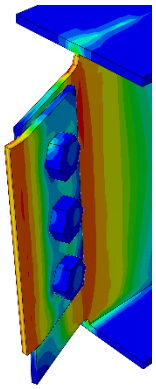

b) Deformed shape of the FE model at 4mm axial deformation

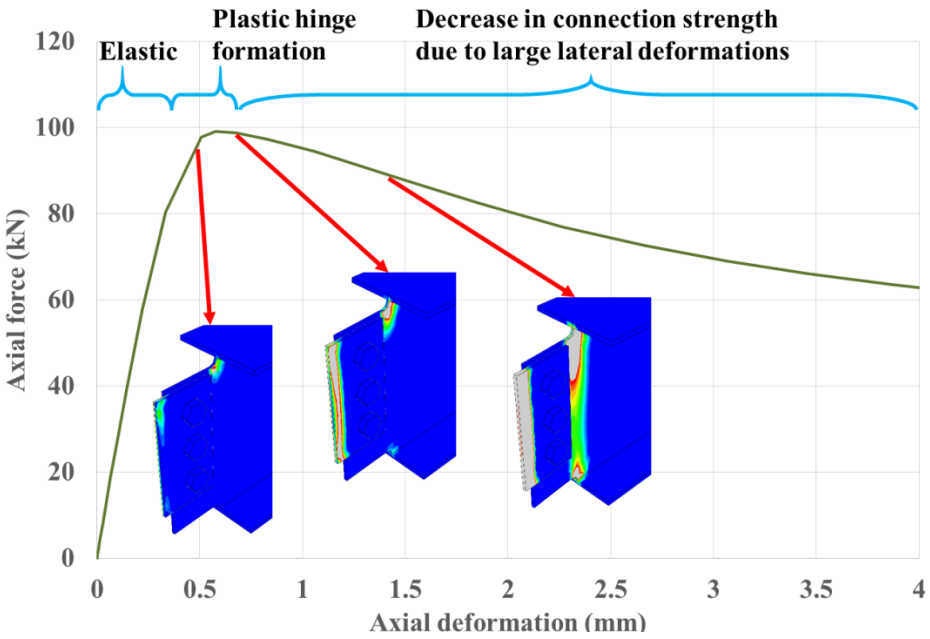

c) Axial force-deformation plot and loading stages

Figure 4-47. Axial behaviour of a double coped, laterally unrestrained connection

In case of the uncoped beam and the presence of lateral restraints on the beam top flange, the force carrying mechanism becomes more complicated than the double coped laterally free connection. Figure 4-48 shows a WSP connection where the top flange is restrained laterally without beam flange coping. Overall, the force carrying stages are similar to the connection in Figure 4-47, but the stresses are not uniformly distributed:

i. In the first part of the axial compression loading (up to about 0.4mm axial deformation) the connection is elastic.

ii. By increasing the axial deformation, some part of the cleat that is far from the beam top flange, experience large lateral deformations and start to yield. By increasing the axial force, more regions yield and plastic hinges form in the cleat plate and the beam web. The difference between this connection and the coped-unrestrained one is that in the coped-unrestrained connection the plastic hinge forms quickly after the first yield but in this connection plastic hinge forms at larger axial deformations due to non-uniform stress distribution.

iii. In the third stage, similar to the previous model, the plastic hinges are formed and the connection strength decreases due to large lateral deformations.

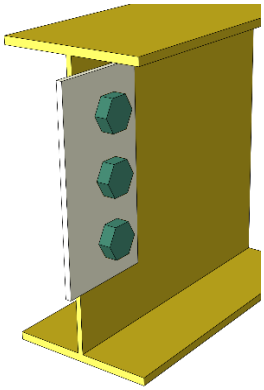

a) 3-bolts connection without beam flange coping

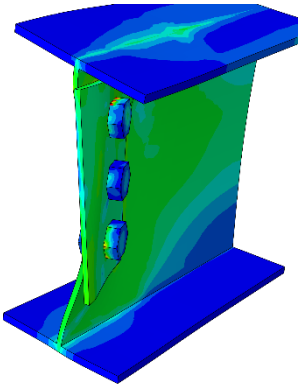

a) Deformed shape of the FE model at 4mm axial deformation

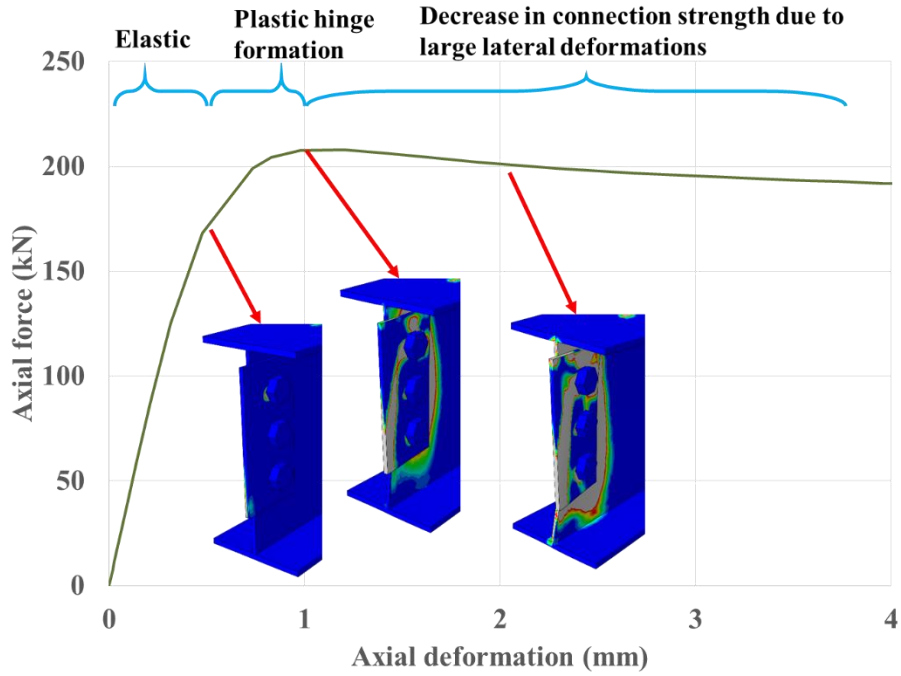

c) Axial force-deformation plot and loading stages

Figure 4-48. Axial behaviour of uncoped laterally restrained top flange connection

As can be seen from these models, the axial force carrying mechanism of WSP connections may considerably vary based on the boundary conditions and the geometry of the connection.

Methods to estimate the axial compression capacity of three WSP connection configurations are investigated in this study including:

1. Double coped, laterally unrestrained connection
2. Un-coped, top flange restrained laterally
3. Double coped, top flange restrained laterally

4.7.2 Method of estimating WSP axial compression strength

4.7.2.1 Basic concepts

Building standards have different approaches for finding the capacity of a structural element under specific loading condition. For instance, in NZS3404 (2007) building standard, the capacity of a structural element is calculated based on the section considerations and the member considerations separately. While, in AISC 360-16, the member and section considerations are considered together. In this study, it is tried to use simple equations and consider both the section and member capacities together.

The issue of estimating the axial compression capacity of a WSP connection is the method of considering the interaction between the axial force and the corresponding bending moment. The simplest equation to consider the interaction of the axial force and bending moment is presented in Eq. (4-1). This equation is a conservative way of considering axial force-bending moment interaction. Although, the effect of buckling of the member can be considered to obtain the cleat compression strength, P_u, the effect of secondary moments due to lateral deformations of the element is not considered in this equation. The secondary moments are more important in slender beam-column elements because of larger lateral deformations. In Eq. (4-1), P is the applied axial force, P_u is the ultimate strength of a centrally loaded column (considering buckling). The applied moment due to axial force eccentricity and the moment capacity of the member (without axial force) are donated by M_0 and M_u respectively.

$$\frac{P}{P_u} + \frac{M_0}{M_u} \leq 1 \qquad \text{Eq. (4-1)}$$

Johnston (1976) recommended modification for Eq. (4-1) to account for secondary moments given in Eq. (4-2). Here, the term $(\frac{1}{1-P/P_{cr}})$ is the moment magnification factor for considering secondary moments caused by the combined action of the axial force and lateral deformations produced by the primary moment. The Euler critical buckling force, P_{cr}, can be calculated using $\frac{\pi^2 EI}{(kL)^2}$, where E, I and kL are the elastic modulus, moment of inertia and the effective length of the member respectively.

$$\frac{P}{P_u} + \frac{M_0}{M_u(1-P/P_{cr})} \leq 1 \qquad \text{Eq. (4-2)}$$

Most design standards (e.g. AISC-360-16) use this equation with some modifications. In this study, Eq. (4-2) is used to calculate the axial capacity of WSP connections.

4.7.2.2 Double coped, laterally unrestrained connection

- ***Considering cleat plate only***

In the first step, it is assumed that only the cleat plate governs the overall behaviour of the WSP connection. Therefore, an axial force is applied to the cleat plate alone with an OOP eccentricity equal to half the cleat and beam web thicknesses. Here, the results of the studied model in Section 4.7.1 are used to verify the calculated strength using Eq. (4-2).

Figure 4-49a shows the dimensions and material properties of the studied connection. The axially loaded cleat plate acts similar to a beam-column member as shown in Figure 4-49b. It should be noted that the beam web must be checked to make sure the cleat axial strength is not larger than the beam web axial strength.

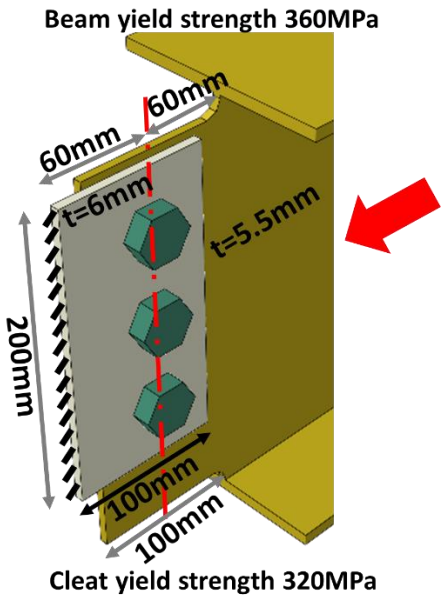

a) Dimensions and material properties of the model

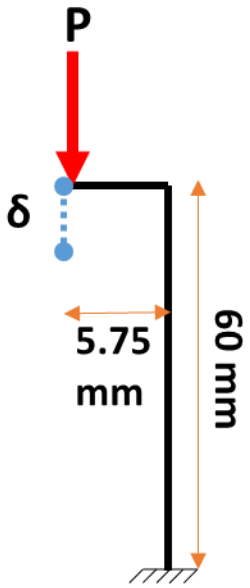

b) Considering cleat plate alone

Figure 4-49. Geometry of eccentrically loaded cleat

To estimate the cleat ultimate axial strength, the cleat moment capacity, M_u should be calculated using the fully plastic moment capacity of the cross-section ($S \times F_y$). The effective length factor, k, in this case is equal to 2 based on the geometry of the cleat which is fully fixed at one end and is laterally free at the other end. In the next sections the effective length factor is discussed in detail for different cases.

A simple FEM model using beam elements (similar to Figure 4-49b) is created to study the nonlinear behaviour of eccentrically loaded cleat only and compare the results with the estimated capacity. Figure 4-50 shows the axial force-deformation plots of the eccentrically loaded cleat and FEM results of the WSP connection shown in Figure 4-49a.

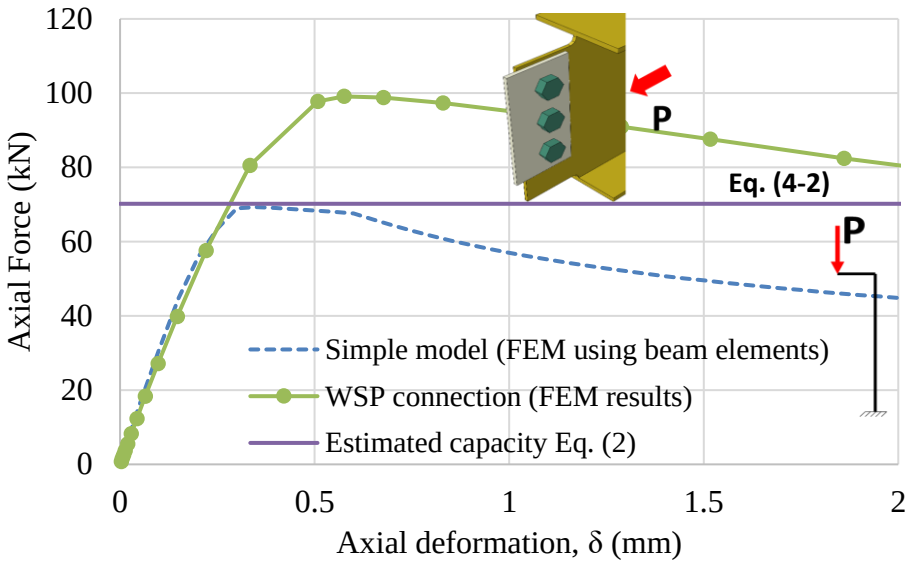

Figure 4-50. Axial force-deformation plots of the eccentrically loaded cleat and general FEM model shown in Figure 4-49a

Figure 4-50 shows that Eq. (4-2) may be used to calculate the axial force carrying capacity of an eccentrically loaded cleat. However, the simple model strength, using the configuration showed in Figure 4-49b which is of the cleat alone, is about 30% lower than the strength of the WSP connection from the model in Figure 4-49a in this case. Therefore, considering the cleat only may provide conservative results.

- ***Considering cleat plate and beam web***

If the beam web effect is considered, the model showed in Figure 4-49b changes to the model presented in Figure 4-51. In this case, the imposed moment due to the axial force eccentricity is distributed between the cleat plate and the beam web. Thus, the axial force capacity of the cleat increases.

The rotational stiffness of the beam web is represented by a rotational spring at the cleat plate end for simplicity. There are some parameters that need to be obtained before proceeding to calculate the WSP axial capacity of this case, such as:

i. Boundary and support conditions of the beam web end,

ii. Beam web effective length contributing in the rotational stiffness of the spring shown in Figure 4-51c, and

iii. The cleat plate effective length factor considering the beam web

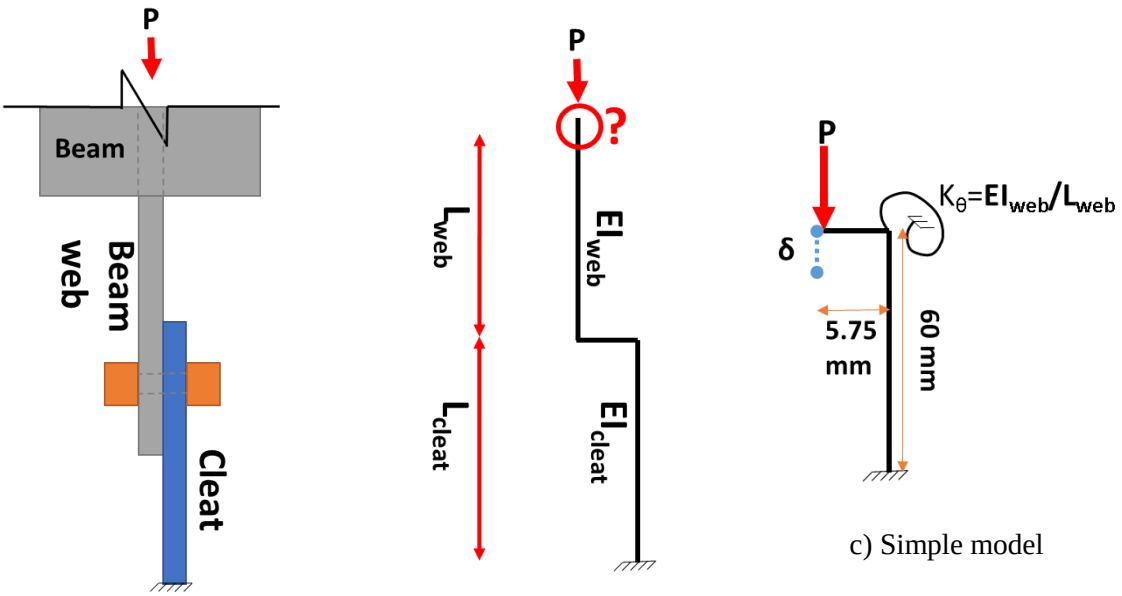

a) Realistic model

b) Equivalent model

c) Simple model

Figure 4-51. Geometry of unrestrained-coped connection

a) Boundary and support conditions

Figure 4-52 shows a schematic view of the beam and connection deformed shape under axial compression force. As it was mentioned, it is assumed that the beam is not supported laterally in this case. Two possible deformed shapes can be considered for this model as:

1. When the lateral stiffness of the connection is relatively low compared to lateral stiffness of the beam member, Mode 1, as shown in Figure 4-52a is likely to occur.
2. When the beam member is relatively stiff compared to the connection region, the lateral deformation may be concentrated in the connection area (either in the beam web or the cleat plate) and Mode 2, as shown in Figure 4-52b, may occur.

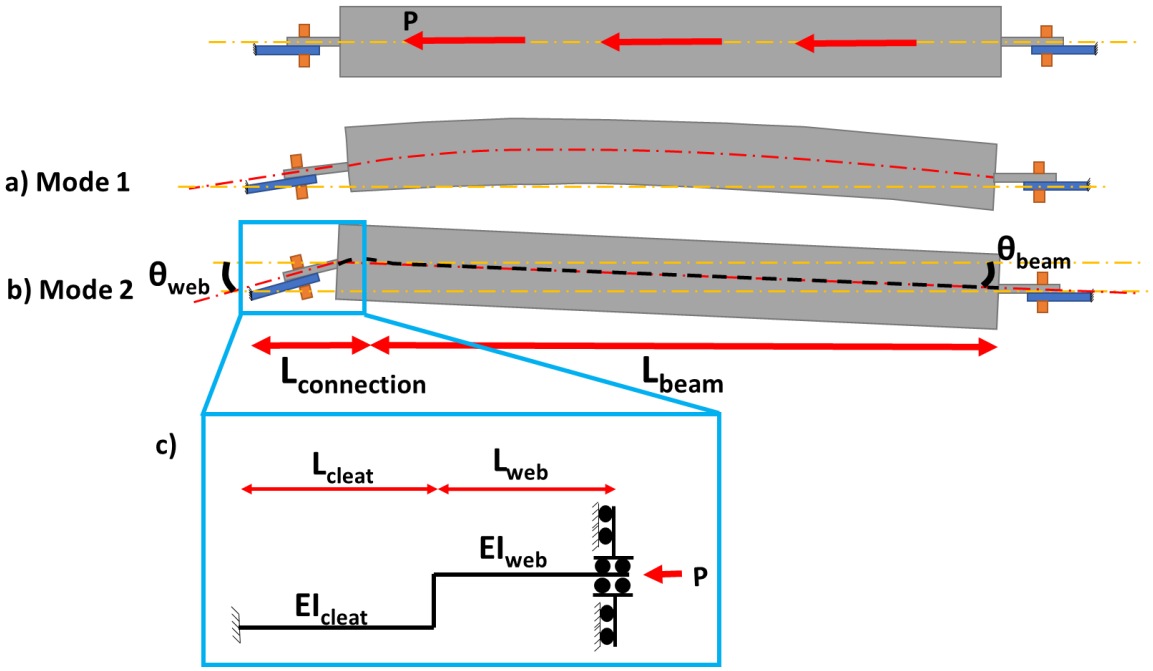

Figure 4-52. Schematic deformed shape of beam and connection under axial compression force

In connections with coped beam flanges, connection stiffness is usually controlled by the cleat plate and/or the beam web stiffnesses. Since the connection stiffness is lower than the lateral stiffness of the beam member, Mode 2 of deformation shown in Figure 4-52 is more likely to occur in most cases.

When Mode 2 is governing the deformed shape of an axially loaded beam member, it can be assumed that the beam web rotation is much larger than the beam rotation, $\theta_{web} >> \theta_{beam}$, for a specific lateral displacement. This is because the beam length is normally much longer than the connection length. Assuming that $\theta_{web} >> \theta_{beam}$, the beam-web end connection may be taken as a fixed support where rotation is not allowed but it is free to translate in the out-of-plane direction, as shown in Figure 4-52c.

b) Beam web contributing length, L_{web}

Figure 4-53 shows the von Mises stress field of the beam web of the studied model in Section 4.7.1 at the peak axial force. It can be seen that at the beam web mid-height, part of the beam web beyond the coped area experiences stress and out-of-plane deformation. In the design model, the beam web stiffness needs to be represented by one rotational spring.

Therefore the equivalent beam web length contributing to rotational stiffness should be obtained.

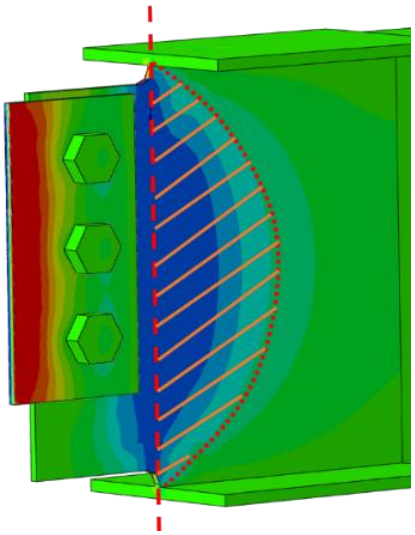

Figure 4-53. Part of the beam web beyond the coped area that contributes to beam web stiffness, stress field recorded at 0.5mm axial deformation

Beam local deformations are because of the beam web flexibility. While beam global deformations are the result of beam lateral movements due to the web moments. Figure 4-54a-c show both local and global deformations schematically. The local, global and the total (global+local) rotations of the 6m long 310UB32 beam subjected to a web moment are plotted in Figure 4-54d. These plots are normalised to the total rotation. Here, the effect of global rotation is about 4% of the total rotation.

The effect of global rotations, θ_g, is neglected in this study because:

i. in real structures, secondary beams are usually connected to the primary beams and provide lateral support which decreases the global deformation of the primary beam,

ii. in some other cases, the beam top flange is restrained laterally because of connection to the composite slab, which helps to reduce the lateral movements of the beam

iii. the beam weak-axis flexural stiffness is much higher than that of the beam web alone, therefore when the moment is applied to the beam web, the beam web local rotation is expected to be larger than the global beam-end rotation.

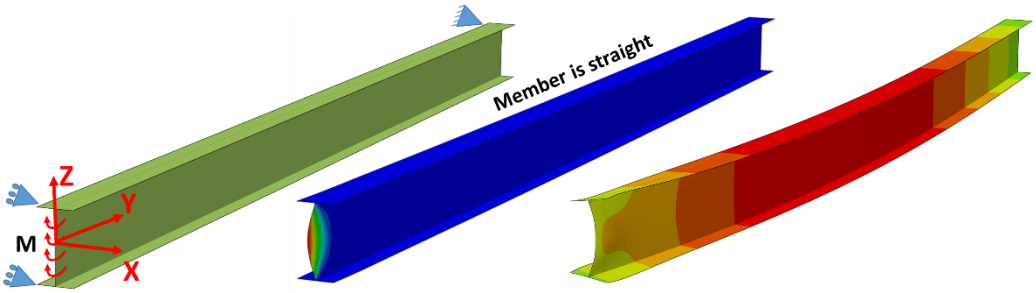

a) Model geometry b) Local deformation c) Total deformation

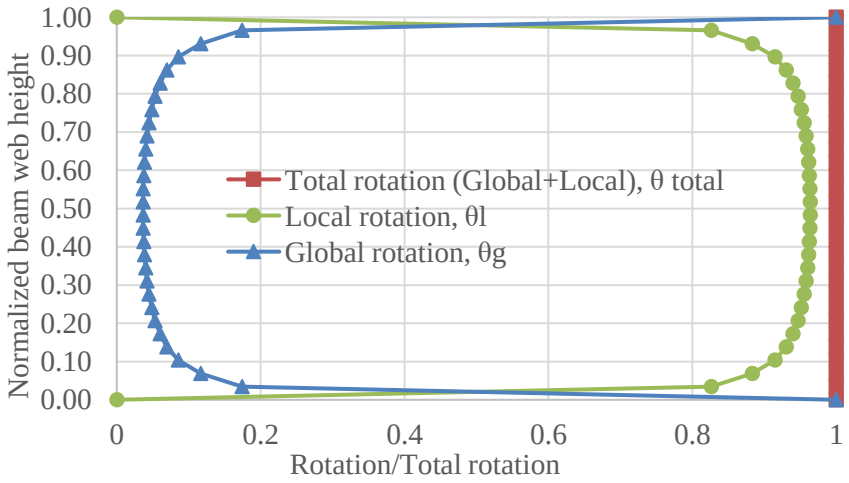

d) Rotation over beam height, $\theta_{total} = \theta_l + \theta_g$

Figure 4-54. Beam rotations

To obtain the beam web contributing length, a simple plate model with ideal boundary conditions is created as shown in Figure 4-55. Here, a long plate member with the aspect ratio of 10 is selected to represent a beam web. The plate is fixed at three edges and a uniform moment is applied at the free left-hand side. The plate rotation on the free side is recorded. This rotation is equal to the local rotation, θ_l, because the fixed edges cannot move in the out-of-plane directions (i.e. $\theta_g = 0$ and $\theta_{total} = \theta_l$).

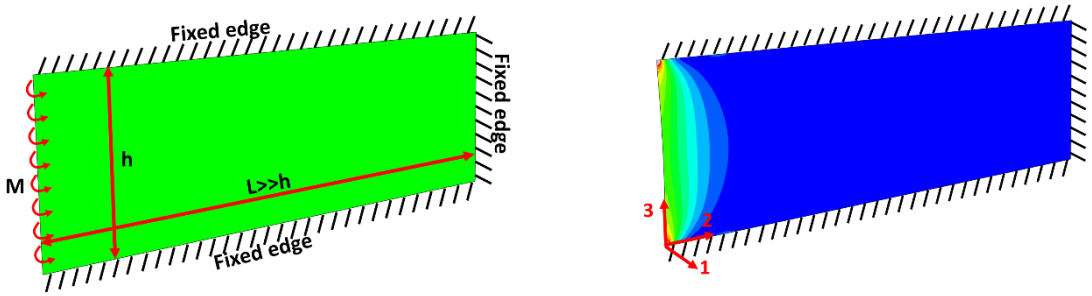

a) Model geometry b) Model deformed shape

Figure 4-55. Simple plate model for finding the equivalent length of beam web

The beam web is divided into virtual strips. Based on the recorded rotations at the end of the plate and the imposed moment magnitude, equivalent strip length is calculated for each strip. Figure 4-56a shows the calculated strip lengths of the plate model schematically. The strip length at the plate mid-height is about 0.25 of the plate height.

For calculating the WSP connection strength, the beam web needs to be considered as one beam-column element connected to the cleat plate. Therefore, the average of the parabolic function is derived using integration over the beam web height and the result is shown in Figure 4-56b schematically. The average is appropriate since stiffness is a function of EI/L. The beam web effective length that can be used for the beam web rotational spring is equal to the average of all the strip lengths which is about $h/5$ (h is beam web height) plus the coped length.

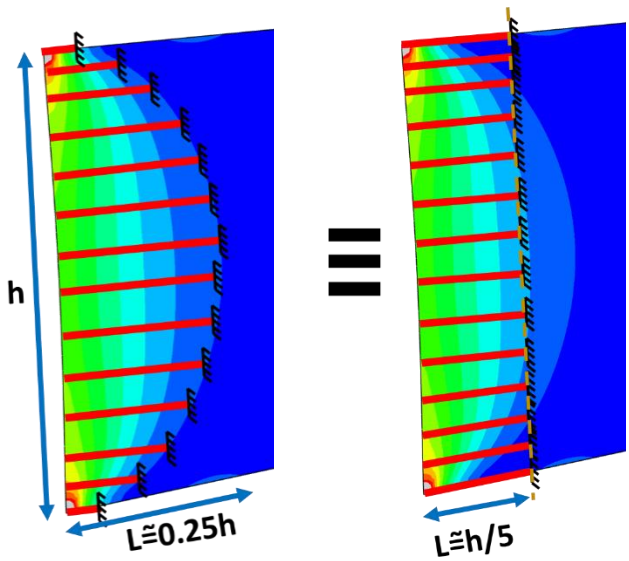

a) Actual strips lengths b) Average of strips lengths

Figure 4-56. Equivalent length of beam web

c) Cleat effective length factor (k_c)

The cleat plate effective length factor, k_c is required for calculating the critical buckling load, P_{cr}, of the cleat plate. In Section 4.7.2.2 where the cleat plate only was considered for calculating the axial capacity of the WSP connection, the effective length factor for the cleat plate was considered 2. However, the presence of the beam web and different boundary conditions can affect the cleat effective length factor. In this section, the cleat plate effective length factor, k_c, is discussed and equations for estimating k_c are proposed.

- **Case 1: Pinned connection**

It can conservatively be assumed that the cleat plate and the beam are connected with a pin connection for simplicity, as shown in Figure 4-57. Although this case is not realistic, it can provide a good understanding of why the effective length factor increases or even decreases when the cleat is connected to another element. Also, this case can provide an upper bound for k_c. Here, it is assumed that the beam does not buckle under axial forces due to lower slenderness than the cleat plate. Since the beam element is pinned to the cleat and has a roller support at the far end, it can just transfer axial forces similar to a truss member. Applying an axial force to the cleat plate through another element, beam, can impose a lateral force which is the horizontal component of the axial force, as shown in Figure 4-57b. This lateral force leads the cleat to buckle at lower axial forces.

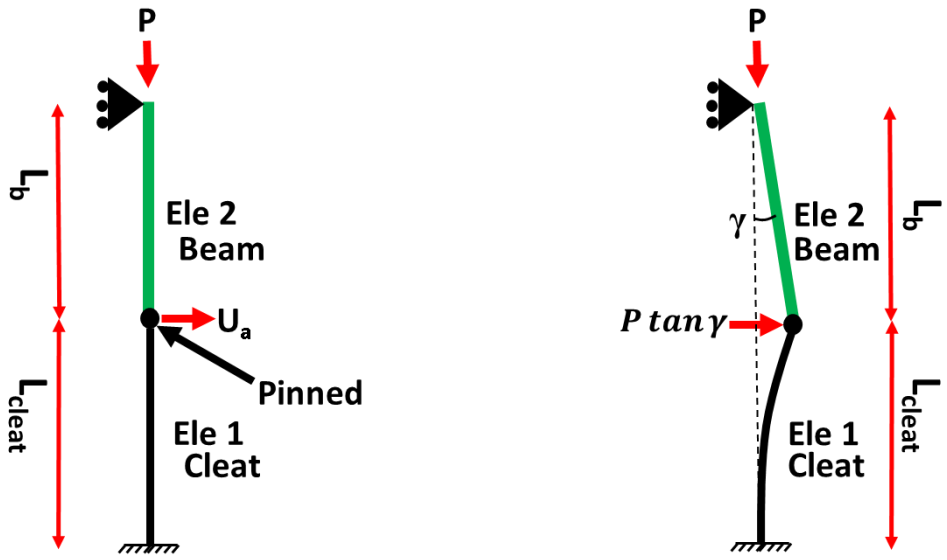

a) Simplified model b) Model deformation and horizontal force

Figure 4-57. Cleat and beam pinned together

In order to find the effective length factor, one method is using stability functions. The stability function is the general stiffness matrix of an element that also considers the effect of axial force. If the axial force is considered equal to zero, the stability function becomes equal to the beam stiffness matrix. The stability function of the cleat plate shown in Figure 4-57a is presented in Eq. (4-3).

$$K_{cleat} = \frac{EI_c}{L_c}\begin{bmatrix} f_c/L_c^2 & g_c/L_c \\ g_c/L_c & s_c \end{bmatrix} \quad \text{Eq. (4-3)}$$

The horizontal component of the axial force is equal to $P \times tan\,\gamma$ and for small angles, $tan\,\gamma$ can be approximated by $\frac{U_a}{L_b}$. Using this approximation the lateral force can be combined with the stability function which gives the stability function for the whole system (Eq. (4-4)).

$$K_{total} = \frac{EI_c}{L_c}\begin{bmatrix} f_c/L_c^2 - (P/L_b)\frac{L_c}{EI_c} & g_c/L_c \\ g_c/L_c & s_c \end{bmatrix} \quad \text{Eq. (4-4)}$$

Where,

$$s = \frac{\emptyset_c(\sin\emptyset_c - \emptyset_c\cos\emptyset_c)}{2(1-\cos\emptyset_c)-\emptyset_c\sin\emptyset_c} \quad \text{Eq. (4-5)}$$

$$r = \frac{{\emptyset_c}^2 - \emptyset_c\sin\emptyset_c}{2(1-\cos\emptyset_c)-\emptyset_c\sin\emptyset_c} \quad \text{Eq. (4-6)}$$

$$f_c = 2(s+r) - {\emptyset_c}^2 \quad \text{Eq. (4-7)}$$

$$g_c = s + r \quad \text{Eq. (4-8)}$$

$$\emptyset_c = \sqrt{\frac{PL_c^2}{EI_c}} \quad \text{Eq. (4-9)}$$

$$k_c = \frac{\pi}{\emptyset_c} \quad \text{Eq. (4-10)}$$

When the determinant of the stability function matrix, Eq. (4-4), is equal to zero, $det[K_{total}] = 0$, it means the inverse of this matrix does not exist and the system is unstable. The applied force at this stage is equal to the critical buckling load. By solving the determinant equation ($det[K_{total}] = 0$), $\emptyset_c$ can be obtained and then using Eq. (4-10), k_c can simply be calculated.

MatLab software was employed to calculate k_c for different beam to cleat length ratios. The effect of different length ratios is plotted in Figure 4-58. The calculated effective length factor, k_c, is verified with FEM models and the results are presented in Appendix G.

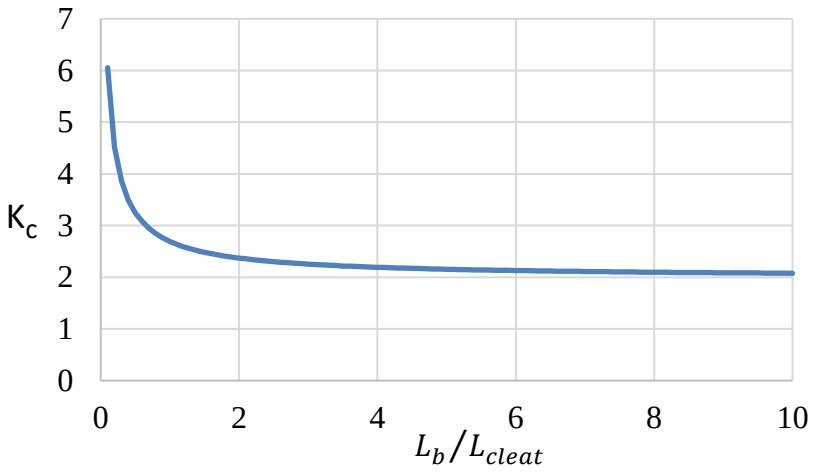

Figure 4-58. Cleat effective length factor with different beam to cleat length ratios

This plot shows that k_c has large values when the beam length is smaller than the cleat length and it gradually decreases to reach to 2 with large beam to cleat plate length ratios. This is because as the beam length increases the horizontal force component decreases and the cleat behaves similar to a cantilever column.

The above results can also be obtained by solving the determinate equation using the first order approximations (Taylor series) of the stability function parameters (s,r,f and g). Equation (4-12) presents a closed form solution for k_c.

$$\emptyset_c = \sqrt{\frac{156\alpha - 24\sqrt{(31\alpha^2 + 55\alpha + 25)} + 120}{9\alpha + 8}} \quad \text{Eq. (4-11)}$$

$$\emptyset_c \cong \sqrt{\frac{3\alpha}{\frac{9}{8}\alpha + 1}} \quad \text{Eq. (4-12)}$$

Where,

$$\alpha = \frac{L_b}{L_{cleat}} \quad \text{Eq. (4-13)}$$

$$k_c = \frac{\pi}{\emptyset_c} \quad \text{Eq. (4-14)}$$

- **Case 1: Fixed connection**

Another approach for determining the cleat plate effective length factor, is to consider the beam web flexibility and its effect on the cleat buckling load. The configuration shown in Figure 4-59 is considered for obtaining k_c, which is the same as Figure 4-51 without the axial force eccentricity. It should be noted that the moment due to the axial force eccentricity does not affect the stiffness matrix and the effective length factor, k_c.

It is assumed that the cleat plate is fixed at one end and connected to the beam web at the other end. The boundary condition assumptions for the beam web element is based on the deformed shape observed in the FE models, in accordance with Section 4.7.2.2.a. The length of the beam web element should be taken as the equivalent beam web length that was obtained in Section 4.7.2.2.b to be consistent.

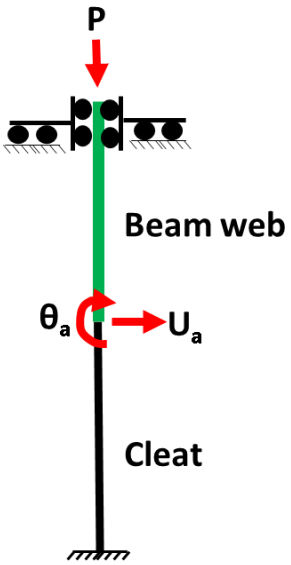

Figure 4-59. Model considered for calculating cleat effective length factor

Equations (4-15) and (4-16) present the stability functions of the cleat and the beam web members.

$$K_{cleat} = \frac{EI_c}{L_c}\begin{bmatrix} f_c/L_c^2 & g_c/L_c \\ g_c/L_c & s_c \end{bmatrix} \quad \text{Eq. (4-15)}$$

$$K_{web} = \frac{EI_w}{L_w}\begin{bmatrix} 0 & 0 \\ 0 & s_w - g_w^2/f_w \end{bmatrix} \quad \text{Eq. (4-16)}$$

The total stiffness matrix is obtained by assembling the stiffness matrices of each member at node "a" shown in Figure 4-59. Equation (4-17) shows the total stiffness matrix for the system. The parameters that are used in this matrix are similar to the previous case, Eqs. (4-5 to 4-11).

$$K_{total} = \begin{bmatrix} \frac{EI_c}{L_c} \times f_c/L_c^2 & \frac{EI_c}{L_c} \times g_c/L_c \\ \frac{EI_c}{L_c} \times g_c/L_c & \frac{EI_c}{L_c} \times s_c + \frac{EI_w}{L_w} \times (s_w - g_w^2/f_w) \end{bmatrix} \quad \text{Eq. (4-17)}$$

By solving the determinate equation of the total stiffness matrix, $det[K_{total}] = 0$, critical axial force can be obtained. MatLab software is used to calculate k_c for different stiffness and length ratios. To show the effect of different length and stiffness ratios together the results are

plotted in a 3D plot as shown in Figure 4-60. The calculated effective length factor, k_c, is verified with FEM models and the results are presented in Appendix G.

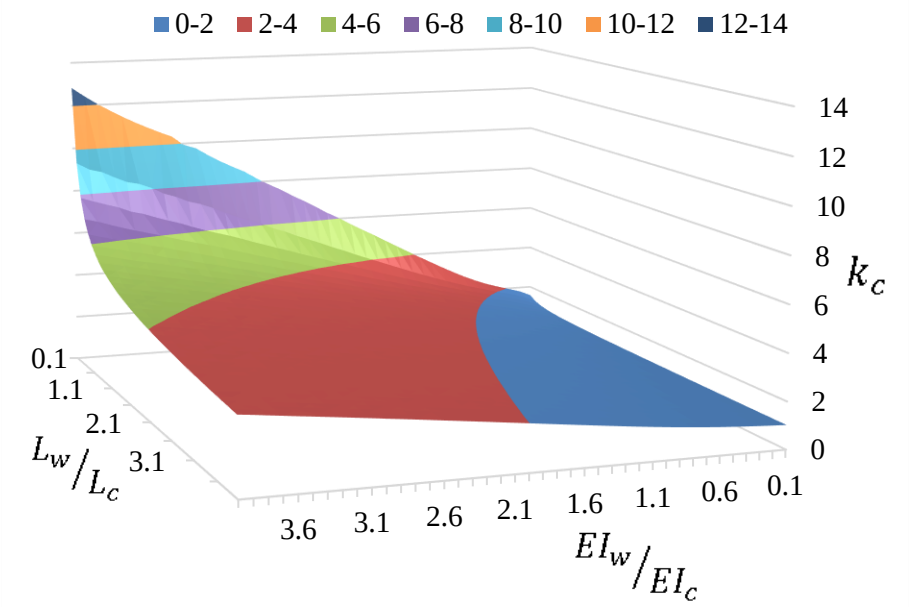

Figure 4-60. 3D plot indicating k_c for cleat member with different length and stiffness ratios

To show the cleat plate effective length factor, k_c, for a range of stiffness, the results are non-dimensionalised in terms of $(\frac{EI}{L^2})_{cleat}/(\frac{EI}{L^2})_{web}$ shown in Figure 4-61. These plots are provided for a range of different length ratios and each ratio is plotted separately. Figure 4-61b shows an enlarged view of Figure 4-61a, for stiffness ratios up to 2.

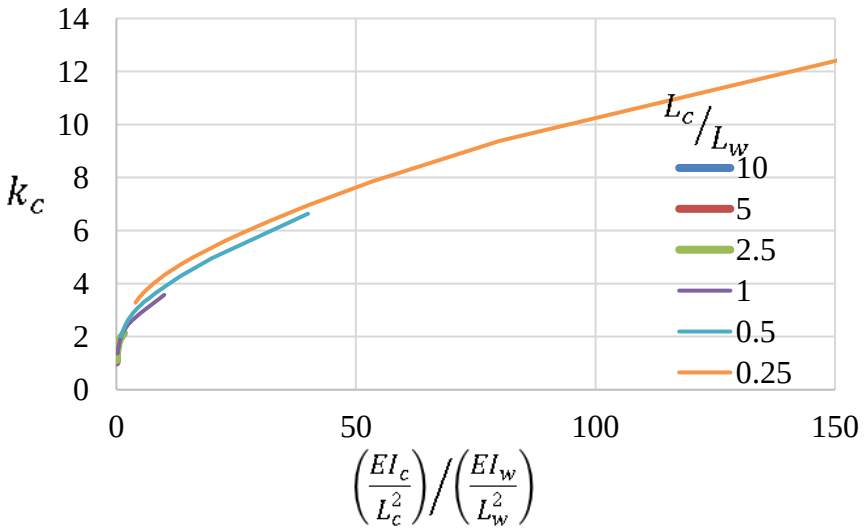

a) Cleat effective length factor

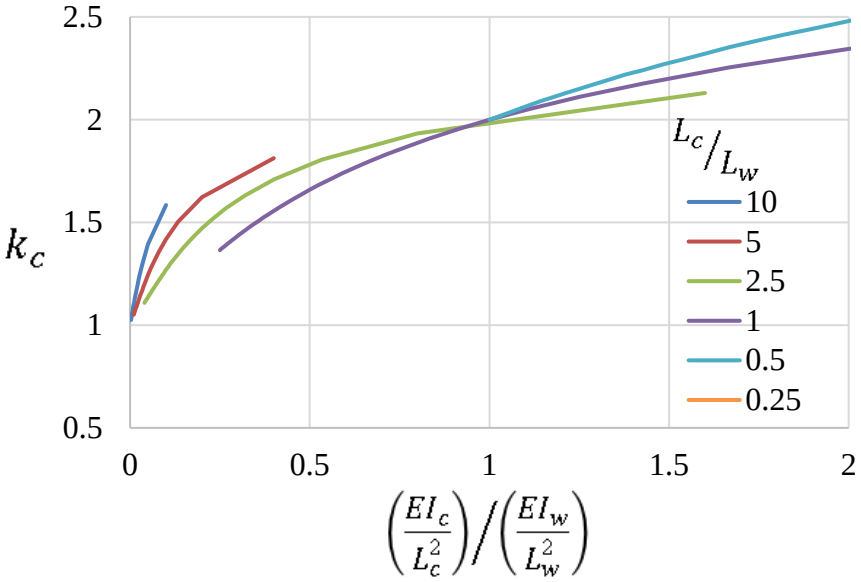

b) An enlarged view of Figure a

Figure 4-61. Effective length factor, k_c, for cleat member with different length and stiffness ratios

The plots shown in Figure 4-61 indicate that k_c starts at 1 and increases as the stiffness of the cleat increases. Also, it can be seen that k_c is a function of the cleat to the beam web length ratio. Here, the effective length factor is calculated for $\frac{\mathrm{EI}_w}{\mathrm{EI}_c}$ and $\frac{\mathrm{L}_w}{\mathrm{L}_c}$ ranging between 0.1 to 4, therefore, plots for $\frac{\mathrm{L}_c}{\mathrm{L}_w}$ equal to 10 and 5, end at lower values in terms of $\left[\left(\frac{\mathrm{EI}}{L^2}\right)_{cleat}/\left(\frac{\mathrm{EI}}{L^2}\right)_{web}\right]$.

Figure 4-62 plots the cleat plate effective length factor in terms of the square root of $\left(\left(\frac{\mathrm{EI}}{L^2}\right)_{cleat}/\left(\frac{\mathrm{EI}}{L^2}\right)_{web}\right)$, for all range of length and stiffness ratios. The results show nearly a linear trend. This may be beneficial for finding a simple equation to estimate k_c for design.

In this study, the upper bound of the k_c results is estimated by a bilinear function as the following:

$$\boldsymbol{k_c} = \begin{cases} 1.05 \times \sqrt{\frac{EI_c}{EI_w}} \times \frac{L_w}{L_c} + 1.2 & for \ \sqrt{\frac{EI_c}{EI_w}} \times \frac{L_w}{L_c} < 2 \\ 0.9 \times \sqrt{\frac{EI_c}{EI_w}} \times \frac{L_w}{L_c} + 1.5 & for \ \sqrt{\frac{EI_c}{EI_w}} \times \frac{L_w}{L_c} \geq 2 \end{cases} \qquad \text{Eq. (4-18)}$$

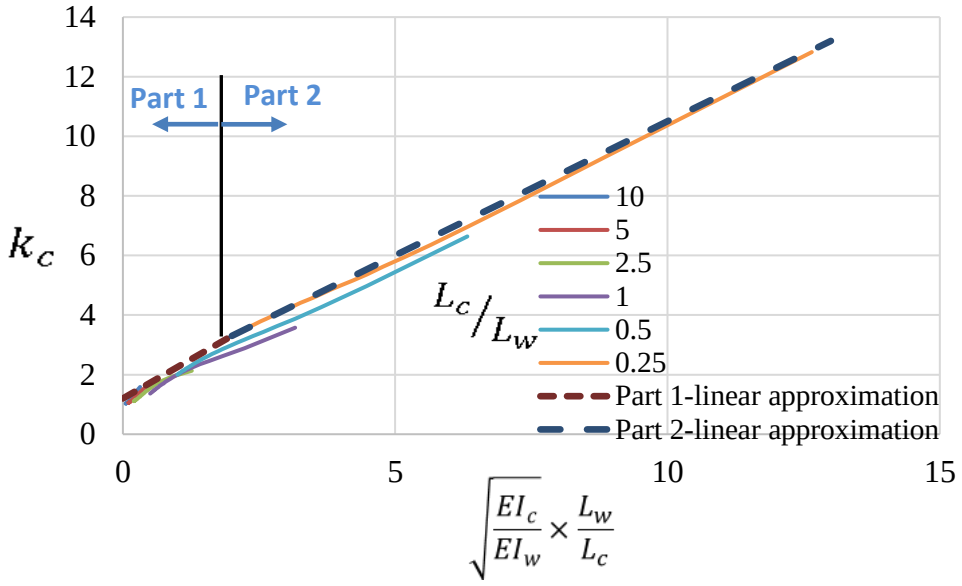

Figure 4-62. Effective length factor k_c and linear approximation plots

As discussed in Section 4.5.1, the end of the cleat is not fully rigid, so k_c may be greater than that calculated here.

d) Effective beam web height contributing in WSP axial strength (h_{we})

Another parameter that is required for obtaining the capacity of the axially loaded WSP connection is the effective beam web height. The effective beam web height is part of the beam web that contributes to supporting axial force and bending moment. In this study, it is suggested to use the minimum beam web height or 1.5 times the cleat height. This value is achieved based on observations of the studied FEM models. Figure 4-63 shows the von Mises stresses of a 2-bolt and 3-bolt WSP connections under axial compression force at 0.5mm axial deformation. The effective beam web height is shown in this Figure for these connections.

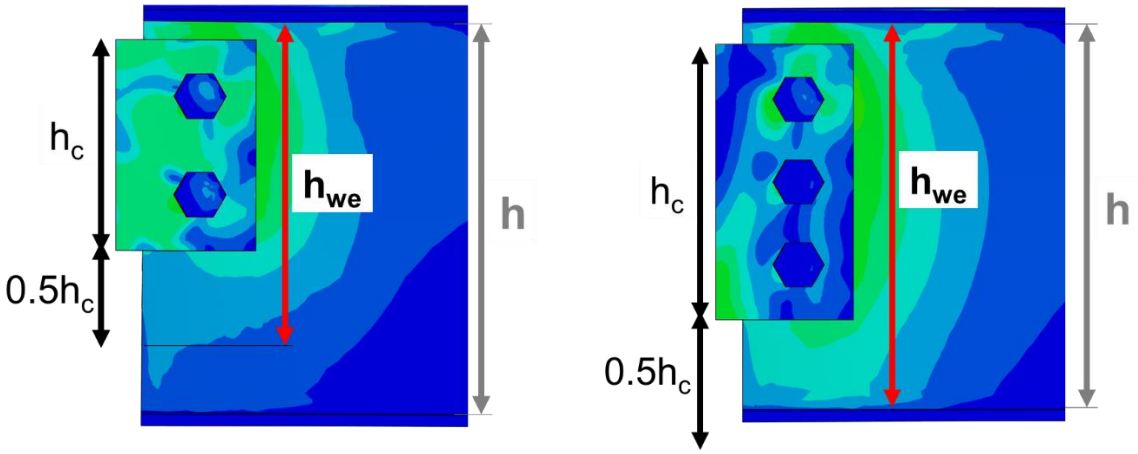

a) 2-bolt WSP connection

b) 3-bolt WSP connection

Figure 4-63. von Mises stresses of a 2-bolt and 3-bolt WSP connections under axial compression force at 0.5mm axial deformation, showing $\boldsymbol{h_{we}}$

Based on SCNZ report 14.1(2007), the cleat plate height cannot be less than 0.45 times the beam height. Therefore, the effective beam web height can be between 0.675 to 1 times the beam height minus beam flange thicknesses or coped area.

e) Cleat plate and beam web axial capacity estimation

As it was discussed in Section 4.7.2.2, Eq. (4-2) can be used to obtain the cleat plate axial strength alone. However, in the case of considering the beam web effect, this equation needs to be modified. This is because the imposed moment due to axial force OOP eccentricity distributes between the cleat plate and the beam web based on their stiffness. So, the applied moment, M_0, in the Eq. (4-2) is multiplied by a modification factor, α, in Eq. (4-19). This modification factor is the ratio of the cleat stiffness to the sum of the cleat plate and the beam web stiffnesses. Note that P_u and M_u are calculated based on NZS3404 (2007). For calculating P_u, $\alpha_b = 0.5$ is considered.

$$\frac{P}{P_u} + \frac{\alpha \times M_0}{M_u(1-P/P_{cr})} \leq 1 \qquad \text{Eq. (4-19)}$$

Where,

$$\alpha = \left(\frac{{}^{I_{cleat}}/_{L_{cleat}}}{{}^{I_{cleat}}/_{L_{cleat}} + {}^{I_{web}}/_{L_{web}}} \right) \quad \text{Eq. (4-20)}$$

In this equation, L_{web} is based on the recommended value in Sections 4.7.2.2.b, and P_{cr} is calculated using the effective length factor, $\boldsymbol{k_c}$, provided in Section 4.7.2.2.c.

A simple beam model using the beam elements is created to check the accuracy of the assumptions such as the boundary condition and the beam web contributing length. The results of the simple model and the corresponding full 3D FEM model are compared as shown in Figure 4-64.

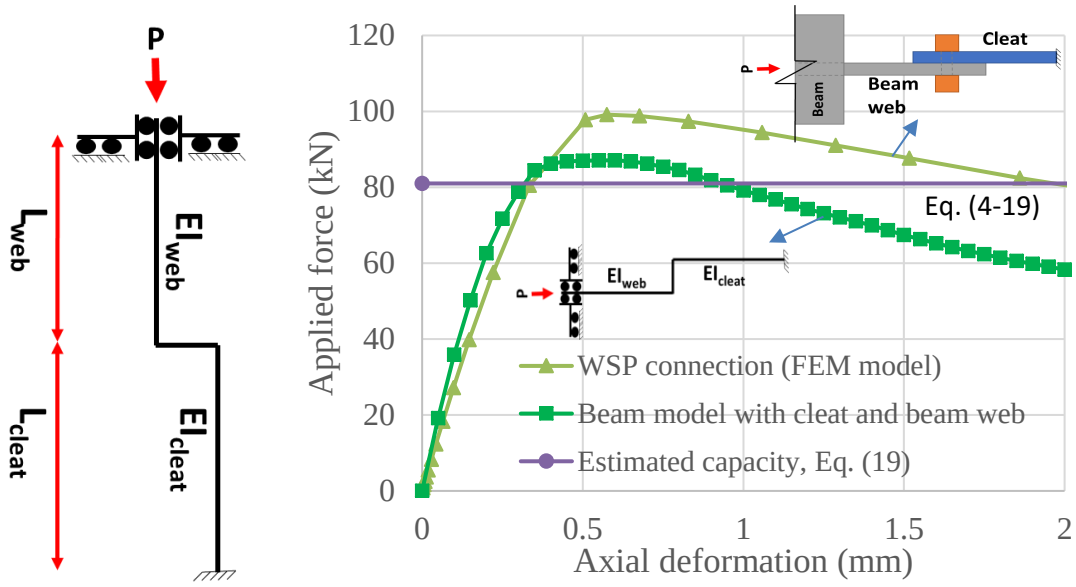

a) Simplified FE model b) Results of general FE model, simple model and calculated capacity

Figure 4-64. Considering the effect of beam web in estimating WSP connection axial strength

As can be seen in Figure 4-64b, the simple beam element model and the general FE model show similar behaviour. The ultimate strength of the simple model is about 12% lower than the general FEM model. The difference between the elastic stiffness of both models is due to using perfect boundary conditions in the simple FE model, while in the general FE model the stiffness of the beam flange and the bolts are also contributing in the overall behaviour and cause lower stiffness. At the post-peak zone, the simple model shows lower strength, which is due to the

difference between the location of the plastic hinge in the beam web of the simple model in comparison with the general FE model.

The ultimate strength of the connection is obtained using Eq. (4-19) and is plotted in Figure 4-64b. The result of the proposed method underestimated the ultimate strength of the simple beam model and the general FE model by about 7% and 18% respectively.

It should be noted that the beam web also needs to be checked with the same procedure to make sure that the beam web is able to sustain this level of axial force and bending moment.

4.7.2.3 Uncoped, beam top flange restrained laterally

The overall behaviour of WSP connection under axial compression force with laterally restrained top flange was described in Section 4.7.1. This boundary condition is more common in residential and office buildings due to the presence of a composite slab on the beam. The slab is usually connected to the beam top flange through shear studs to take advantage of the composite action and also transferring lateral forces to VLFR system of the structure.

Since the behaviour of WSP connection with laterally restrained top flange is more complicated, it cannot be simply modelled as two beam-column members representing the beam web and the cleat plate similar to the laterally unrestrained WSP connection described in Section 4.7.2.2. This is because the presence of lateral support for the beam top flange prevents part of the cleat plate near the top flange to experience large lateral deformations. Also part of the bending moment due to the axial force OOP eccentricity transfers to the beam top flange.

Based on the observations of the FE models, it was found that the idea of effective width can be employed for estimating the axial capacity of WSP connections when the top flange is retrained laterally. In this method, part of the beam web near the beam top flange is identified as the effective restrained height. And part of the cleat plate height that lays in this area is considered as column member without axial force eccentricity, as shown in Figure 4-65. The rest of the cleat height is considered similar to the laterally unrestrained WSP connection that

was explained in Section 4.7.2.2. Total connection capacity is equal to the sum of these two simplified models, $P_1 + P_2$.

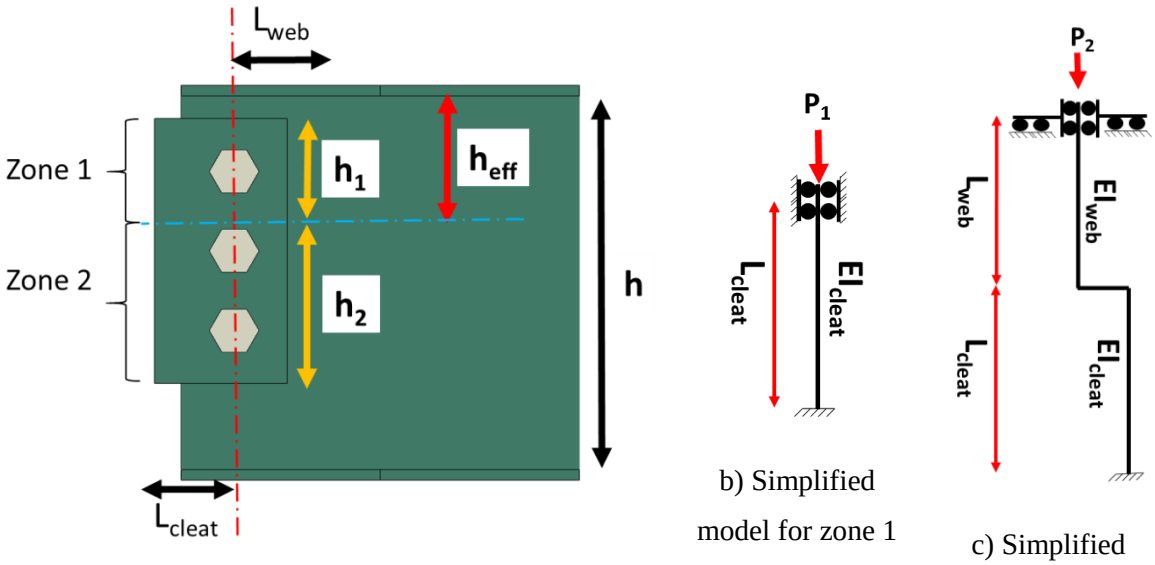

a) Effective height of beam web

b) Simplified model for zone 1

c) Simplified model for zone 2

Figure 4-65. WSP connection with top flange restrained laterally

In this case the beam web effective length could be taken equal to $h/5$ similar to the laterally unrestrained WSP condition, which h is the beam web clear height.

- ***Beam web effective height***

The effective height/width concept is a semi-empirical method for estimating the ultimate strength of plates subjected to axial compression forces. Stress distribution after plate buckling is not uniform and most of the applied force is carried by regions of the plate in the vicinity of restrained edges. For example when a plate is under uniform axial force longitudinally, and the other two edges parallel to the loading direction are restrained from out of plane movement or rotation, most of the axial force may be carried by regions of the plate near the edges as shown in Figure 4-66a (Ziemian, 2010).

The effective height/width concept assumes that the maximum edge stress acts uniformly over parts of the plate that do not experience large out-of-plane deformations. Figure 4-66b

shows the true and simplified stress distributions for a plate member under axial compression force based on the effective width concept.

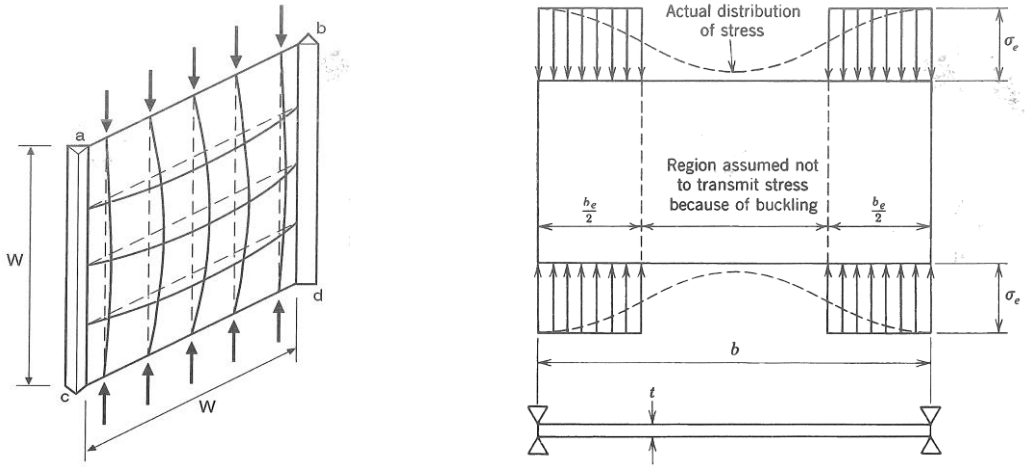

a) Buckling shape b) Actual and simplified stress distributions

Figure 4-66. Plate under axial force (Ziemian 2010)

The effective width concept has been using in many design standards (e.g. AISC 360-16 and NZS3404, 2007) for designing structural members having plates with b/t ratios greater than a specified limit. In this study, the specifications of NZS3404 (2007) are used for obtaining the effective height of the beam web for calculating the axial force capacity of WSP connections.

In NZS3404 (2007) Clause 6.2.4, the effective height/width, b_e, for a flat plate members can be calculated as follow:

$$b_e = \min \begin{cases} b\left(\frac{\lambda_{ey}}{\lambda_e}\right) \\ b \end{cases} \quad \text{Eq. (4-21)}$$

Where,

$$\lambda_e = \frac{b}{t}\sqrt{\left(\frac{f_y\,(MPa)}{250}\right)} \quad \text{Eq. (4-22)}$$

In these equations, b is the beam web height, t is the beam web thickness and λ_{ey} is the element yield slenderness limit. Using Table 6.2.4 of NZS3404 (2007), λ_{ey} can be taken equal

to 16 for hot rolled plate that is supported at one end. The "supported at one end" category is selected because only the beam top flange is restrained laterally. If in some cases both flanges are restrained, then λ_{ey} can be taken equal to 45 and half the effective length should be placed near the top flange and half near the bottom flange.

Figure 4-67 shows the axial behaviour of a WSP connection with a restrained top flange and the estimated axial capacity using the calculated effective height.

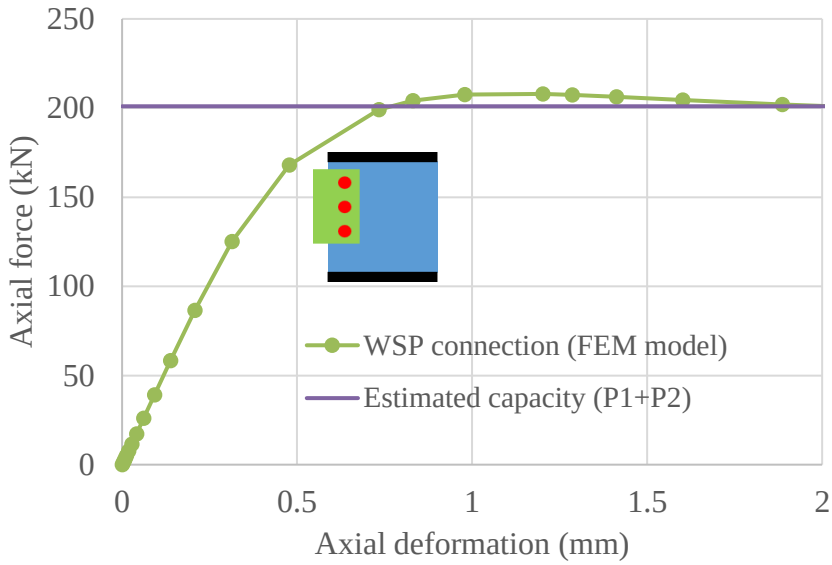

Figure 4-67. Axial behaviour of WSP connection with restrained top flange and the estimated axial capacity

This plot shows that the proposed method underestimated the axial strength of the studied WSP connection with less than 4% in this case.

4.7.2.4 Double coped, top flange restrained laterally

The double-coped laterally unrestrained and the no-cope laterally restrained conditions were investigated in Sections 4.7.2.2 and 4.7.2.3. Another boundary condition for WSP connection that may frequently be used in construction is a double-coped connection with the beam top flange laterally restrained. The behaviour of double-coped WSP connection with different cope lengths was studied in Section 4.6.2.2. It was shown that the cope length does not affect the tensile strength of the WSP connections. However, the compression capacity was

directly related to the cope length, such that the axial strength decreased linearly with increasing the cope length, as shown in Figure 4-45.

The cope length is usually governed by the support geometry and the beam web buckling considerations. Cope length cannot be more than a certain value that is related to the beam web thickness and height. A limitation on the cope length was provided by Steel Construction Institute & British Constructional Steelwork Association (2002) which applies to the beams restrained against lateral torsional buckling, as follows:

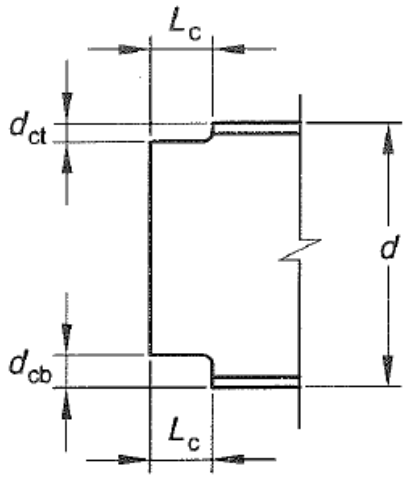

Figure 4-68. Double coped I-shape member

$$d_{ct}, d_{cb} \leq 0.20d \qquad \text{Eq. (4-23)}$$

$$L_c \leq d \quad for \quad \frac{d}{t_{wb}} \leq \frac{900}{\sqrt{f_{yw}}} \qquad \text{Eq. (4-24)}$$

$$L_c \leq \frac{730\times10^6 d}{\sqrt{f_{yw}^3\left(\frac{d}{t_{wb}}\right)^3}} \quad for \quad \frac{d}{t_{wb}} > \frac{900}{\sqrt{f_{yw}}} \qquad \text{Eq. (4-25)}$$

Where, t_{wb} is the beam web thickness and f_{yw} is the beam web yield stress.

The method of estimating the axial capacity of this type of connection is similar to the uncoped laterally restrained top flange connections with only one modification. By increasing the cope length, the distance between the beam flange, which is restrained laterally, and bolt-line increases. Therefore the effect of lateral restraint of the beam top flange on increasing the

connection strength decreases. Based on Figure 4-45, the relationship between increasing the cope length and decline in WSP axial strength is approximately a linear function. Based on the results of the analysed FEM models, Equation (4-26), is proposed to obtain the effective width of the beam web for double-coped connection and laterally restrained top flange.

$$\frac{b_{ec}}{b_e} = 1 - 0.5\frac{L_c}{d} \qquad \text{Eq. (4-26)}$$

Where, b_{ec} is the effective height of the beam web of the coped member, b_e should be calculated using Eq. (4-21) and L_c and d are the coped length and the beam height respectively as shown in Figure 4-68.

4.7.2.5 Effect of gravity loads on the axial strength of WSP connections

WSP connections subjected to the pure axial compression force were studied in Sections 4.7.2.1-4.7.2.4 and a method for estimating the axial compression capacity was developed. In real structures, the WSP connections are generally designed for supporting vertical loads in gravity frames. Therefore, in an earthquake event the connections may experience a combination of gravity and axial forces.

Figure 4-69 shows the forces acting on the cleat plate and the beam web due to the shear and the axial compression force. It is noted that the torsional moment (M_1) due to gravity load OOP eccentricity is not illustrated in this Figure. It was shown that Eq. (4-19) can estimate the axial force capacity in situations that only M_3 and P exist. In this section the proposed method is developed to account for the interaction of the axial force and gravity loads considering $P - M_2 - M_3$ interaction and vertical shear force effects.

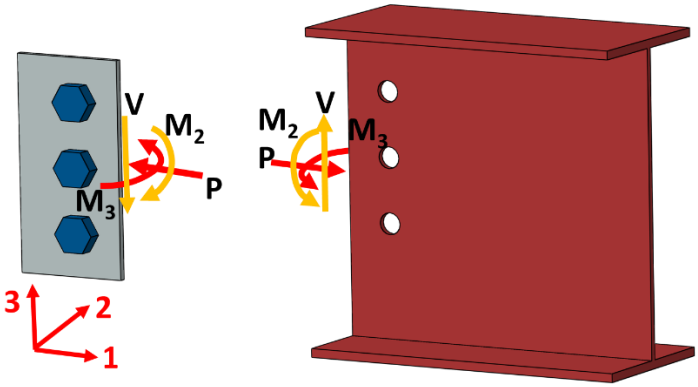

Figure 4-69. Shear and axial forces acting on cleat plate and beam web

The applied gravity loads on a simply supported beam, impose shear force and moment to the beam-column connection. In "Structural steelwork connection guide" (SCNZ report 14.1, 2007), the effect of this moment due to connection rigidity is ignored for calculating the shear strength of the connection and the cleat plate is only required to be designed for the moment produced by the shear force acting on the bolt line as was mentioned in Section 4.3.2.2.

Many research studies have been conducted to obtain the interaction relationship between the axial force, bending moment and the shear force on a steel section. Neal (1961) proposed an interaction relationship Eq. (4-27) for a fully plastic steel section. This equation gives an approximation for all values of P, V, and M. This relationship is exact for $V = 0$, and the divergence never exceeds 5% over the full range of values of P, V, and M.

$$\frac{M}{M_u} + \left(\frac{P}{P_u}\right)^2 + \frac{\left(\frac{V}{V_v}\right)^4}{\left(1-\left(\frac{P}{P_u}\right)^2\right)} = 1 \qquad \text{Eq. (4-27)}$$

It should be noted that this equation only considers the section properties, and the member characteristic such as global or local buckling modes and out-of-straightness are not included in this equation.

In this study, equations provided in NZS3404 (2007) are employed to account for the interaction of shear force and the corresponding bending moment due to gravity loads on WSP connections. This is because to provide consistency between the developed method and the

standard design equations and also, to achieve more conservative results. The more exact interaction relationships such as Eq. (4-27) may provide a more accurate result, however, in the absence of experimental tests, it is suggested to use the more conservative approach.

Based on Section 8.4.2 of NZS3404 (2007), the effect of the bending moment, M_2, can simply add to Eq. (4-19). To obtain the effect of secondary moments, the applied moment should be increase by a factor of $\frac{1}{1-P/P_{cr}}$. However, the P_{cr} for the strong axis of the cleat plate results in large value and the factor $\frac{1}{1-P/P_{cr}}$ becomes close to 1. Therefore, Eq. (4-19) may be rewritten as:

$$\frac{P}{P_u}+\frac{\alpha\times M_3}{M_{u3}(1-P/P_{cr})}+\frac{M_2}{M_{u2}}\leq 1 \qquad \text{Eq. (4-28)}$$

For considering the shear force interaction with other force components, the simplified shear-moment interaction relationship, Eq. (4-29), according to Clause 5.12.2 of NZS3404 (2007) can be used. This equation considers the interaction of M_2-V. It can be seen that for the shear force values up to $0.6V_v$ (V_v is the shear strength of the cleat plate), the effect of shear force can be ignored.

$$\begin{cases}\frac{V}{V_v}+\frac{1.6M_{u2}}{\emptyset M_s}\leq 2.2 \quad for \quad V\geq 0.6V_v\\ M_{u2}=\emptyset M_s \quad for \quad V<0.6V_v\end{cases} \qquad \text{Eq. (4-29)}$$

Where, V_v is the nominal shear capacity of the cleat plate and M_s is the nominal section moment capacity of the cleat gross cross-section about strong axis. The value of M_{u2} in Eq. (4-28) should be updated using this equation to consider the shear force effect on the axial capacity of WSP connection.

Simply supported beams are usually designed for critical gravity load combination which is $1.5Q+1.2G$ according to AS/NZS1170.0 (2002). In this load combination, Q is live load and G is dead load. The reduced load combination that is considered acting on the structure at the time of earthquake event is $\psi Q+G$. The factor ψ accounts for reducing live loads based

on the functionality of the structure. For a wide range of building types, except for storage or other buildings with a high level of live loads, $\psi = 0.3$ may be used. Based on these load combinations and considering different values for dead and live load, the ratio of the reduced gravity load to the ultimate design load combination can be obtained. This ratio is plotted versus different live load to dead load ratios in Figure 4-70. This plot shows the average value for the ratio of reduced gravity load to the ultimate design load combination is about 0.5. Therefore, if as a worst case scenario it is assumed that the shear strength of the cleat plate or the beam web governs the shear strength of the connection, in most cases the applied gravity loads on the connection may be about $0.5V_V$. Thus, in most conventional cases, the shear force may not have a significant effect on the WSP axial capacity. It is noted that the shear strength of the cleat plate is usually larger than the connection shear capacity due to other failure modes.

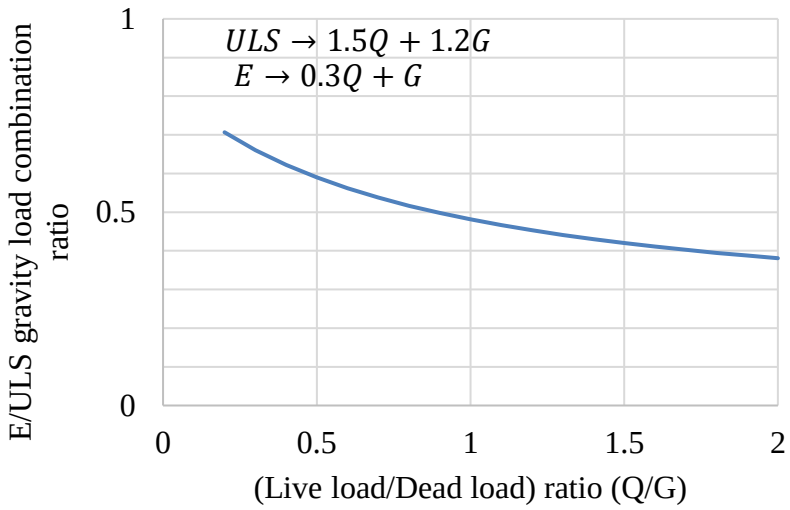

Figure 4-70. Ratio of reduced gravity load combination to ultimate load combination versus different live load to dead load ratio

4.7.3 WSP axial tension strength

Based on the FEM models that were studied in this research, it was found that the tension force-displacement of the WSP connections shows a stable behaviour so that tension force increases up to the point that weakest element starts to yield or fail.

4.7.3.1 Tension strength of WSP connection

The tension behaviour of WSP connections is more predictable than the compression behaviour, because it does not involve nonlinear geometry issues like buckling. However, all the possible tension failure modes need to be checked to obtain the controlling failure mechanism. The tension failure modes may be different based on the copping situation of the beam-end. For a WSP connection without copping the limit states include:

i. Cleat plate weld fracture,
ii. Bolt shear failure,
iii. Cleat plate net section fracture,
iv. Cleat plate yielding,
v. Cleat plate bearing yielding,
vi. Cleat plate tear-out failure,
vii. Beam web bearing yielding,
viii. Beam web tear-out failure,
ix. Beam web block shear failure.

If the beam flanges are coped the following limit states also need to be checked.

x. Beam web net section fracture
xi. Beam web yielding

Equations for calculation all these limit states are available in the literature and they can easily be obtained from different building standards.

Here, all of the above-mentioned limit states are calculated for the base model and are shown in Figure 4-71. The tensile force-displacement of WSP connection is plotted up to the point that equivalent plastic strain in the first element reached to 0.20. In calculating these limit states the reduction factors are not considered as they are being compared with the FEM model with known material strength.

The beam web block shear is the lowest predicted failure mode that was not observed in the FEM model. This may be because of the bilinear stress-strain relationship of the steel material that was used in the FE model. Alternatively, it may be due to the fact that the block shear formulations are conservative in the standards. The second lowest calculated failure mode is beam web tear-out failure which was observed in the FE model as the main failure mode.

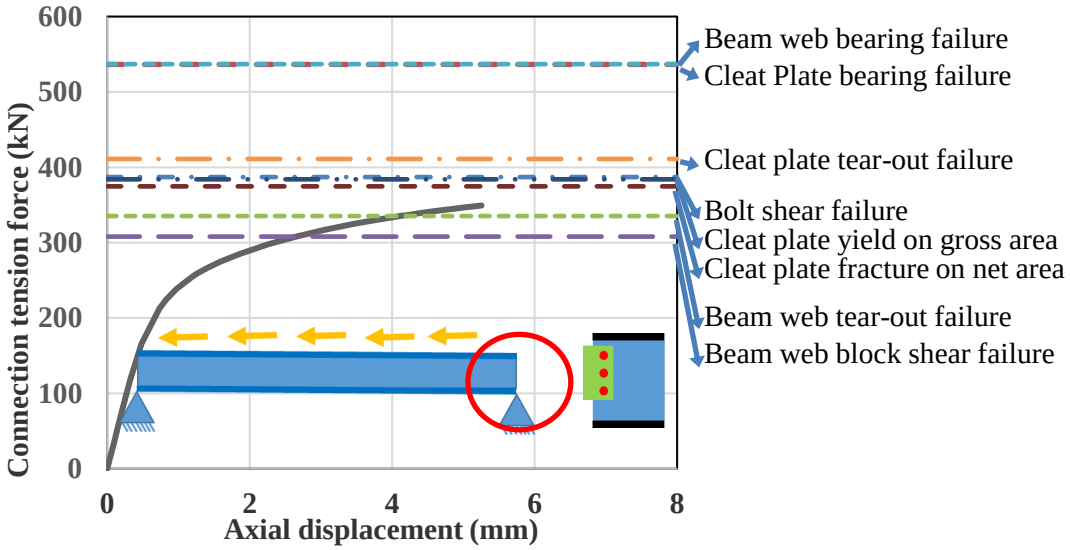

Figure 4-71. Tension behaviour of base model and calculated tensile strengths

Based on this plot, calculating the tensile strength of WSP connections using the above limit states and considering relevant strength reduction factors may be appropriate in design.

4.7.4 Verification of the proposed method against FEM models

The proposed method for calculating the axial compression strength of WSP connection is verified by comparing the results of thirty-four FEM models considering

i. different beam sections,

ii. cleat plate sizes,

iii. number of bolts and

iv. different level of shear forces.

The tensile strength of connections that were recorded in the FEM analysis are also compared with calculated tensile strength considering all the tension limit states. Table 4-4 presents details of FEM models, obtained and calculated strengths.

Three types of boundary conditions are studied in these models which include:

i. double coped beam with unrestrained beam top flange, "coped-TF free"

ii. double coped beam with restrained beam top flange, "coped-TF fix"

iii. Un-coped beam with restrained beam top flange, "No cope-TF fix"

Table 4-4. FEM model details, obtained and calculated strengths

	Connection type	Beam section	Cleat plate size (mm)	Cope length (mm)	Beam length (m)	Applied shear load on the connection (kN)	Calculated connection shear capacity (kN) (SCNZ report 14.1,2007)	Recorded tension strength inFEM analysis (kN)	Recorded compression strength inFEM analysis (kN)	Tension strength (tension limit states) (kN)	Compression strength (proposed method) (kN)
1	Coped-TF* free	180UB16	130×100×6	80	3	38	66.4	182.3	62.2898	164	32
2	Coped-TF free	310UB32	150×100×6	120	6	59	110.8	241.4	66.2566	218	30.3
3	Coped-TF free	310UB32	250×100×6	120	6	115	208.5	433.5	76.7782	414	50.5
4	Coped-TF free	610UB101	340×100×6	250	10	163	293.7	534.7	181.85	463	92.9
5	Coped-TF fix	180UB16	130×100×6	80	3	38	66.4	185.3	103.059	164	81
6	Coped-TF fix	180UB16	130×100×6	120	3	29	47.4	185.0	77.6153	165	64
7	Coped-TF fix	310UB32	150×100×6	100	6	--	110.8	240.4	144.878	218	125.8
8	Coped-TF fix	310UB32	150×100×6	100	6	78	110.8	231.9	134.856	218	113.7
9	Coped-TF fix	310UB32	200×100×6	74.5	6	--	172.8	351.0	177.1	308	155
10	Coped-TF fix	310UB32	200×100×6	100	6	--	172.8	350.1	166.549	308	141
11	Coped-TF fix	310UB32	200×100×6	100	6	104	172.8	333.1	137.889	308	128
12	Coped-TF fix	310UB32	200×100×6	120	6	92	172.8	338.7	122.588	308	122
13	Coped-TF fix	310UB32	200×100×6	150	6	92	172.8	339.2	114.605	308	111.5
14	Coped-TF fix	310UB32	200×100×6	150	6	--	172.8	351.3	143.419	308	120.5
15	Coped-TF fix	310UB32	200×100×6	200	6	--	76	355.7	125.743	308	102.7
16	Coped-TF fix	310UB32	250×100×6	100	6	--	216	458.1	185.513	414	155.5
17	Coped-TF fix	310UB32	250×100×6	100	6	132	216	448.1	130.065	414	141.7
18	Coped-TF fix	610UB101	340×100×6	250	10	159	293.7	537.4	347.052	463	236
19	Coped-TF fix	610UB101	340×100×6	350	10	159	293.7	535.9	338.66	463	202.7
20	No cope-TF fix	180UB16	130×100×6	--	3	--	77.7	190.8	154.113	165	128.5

21	No cope-TF fix	180UB16	130×100×6	--	3	41	77.7	189.2	150.527	165	115.2
22	No cope-TF fix	310UB32	150×100×6	--	6	--	110.8	244.0	168.547	218	161
23	No cope-TF fix	310UB32	150×100×6	--	6	77	110.8	237.2	165.414	218	144.2
24	No cope-TF fix	310UB32	150×100×6	--	6	57	110.8	238.9	168.961	218	149
25	No cope-TF fix	310UB32	200×100×6	--	6	--	172.8	352.2	207.922	308	186
26	No cope-TF fix	310UB32	200×100×6	--	6	34	172.8	349.8	204.523	308	179
27	No cope-TF fix	310UB32	200×100×6	--	6	69	172.8	349.1	197.65	308	172.8
28	No cope-TF fix	310UB32	250×100×6	--	6	--	216	454.0	262.614	414	210
29	No cope-TF fix	310UB32	250×100×6	--	6	109	216	447.9	226.882	414	192.4
30	No cope-TF fix	310UB32	250×100×6	--	6	129	216	442.1	219.443	414	189
31	No cope-TF fix	610UB101	340×100×6	--	10	--	293.7	554.2	496.084	463	371
32	No cope-TF fix	610UB101	340×100×6	--	10	165	293.7	540.2	486.505	463	347.5
33	No cope-TF fix	610UB101	500×100×6	--	10	--	432	863.8	705.266	740	476
34	No cope-TF fix	610UB101	500×100×6	--	10	239	432	802.1	642.539	740	449.4

TF→ Top Flange
Note: the tension capacity of connections are obtained without strength reduction factors to be compared with FE results

The recorded and calculated tension and compression strengths of FEM models are plotted in Figure 4-72. The average ratio of the calculated compression strength to the recorded strength of FEM analysis is about 80.1% with a standard deviation of 13.7%. For the tension side, the average ratio of the calculated tensile strength to the recorded strength from FEM analysis is about 89.3% with a standard deviation of 2.8%. Based on the results, the proposed method indicates good agreement with the FEM models for estimating axial compression strength of WSP connections. However, there is a need for an experimental investigation to verify this method.

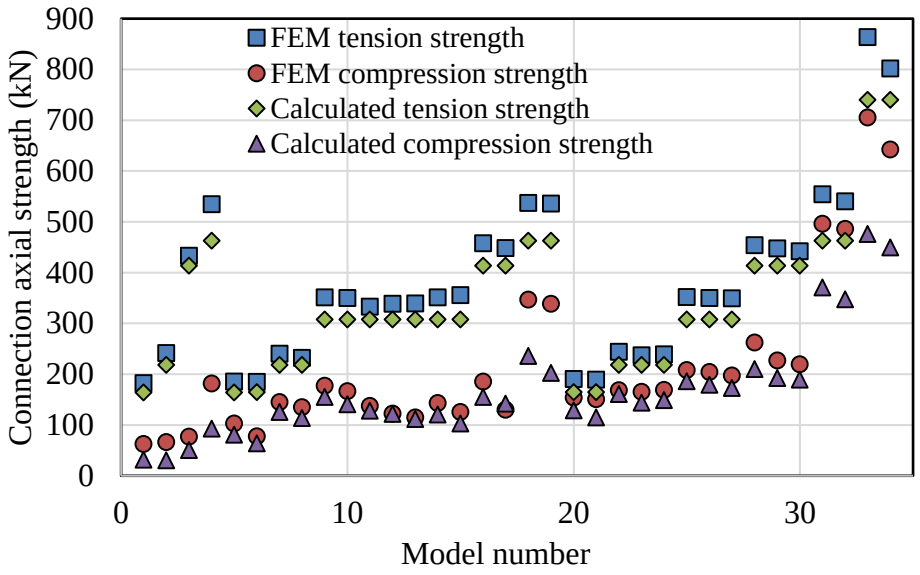

a) Connection tension and compression strengths calculated using the developed method and FEM

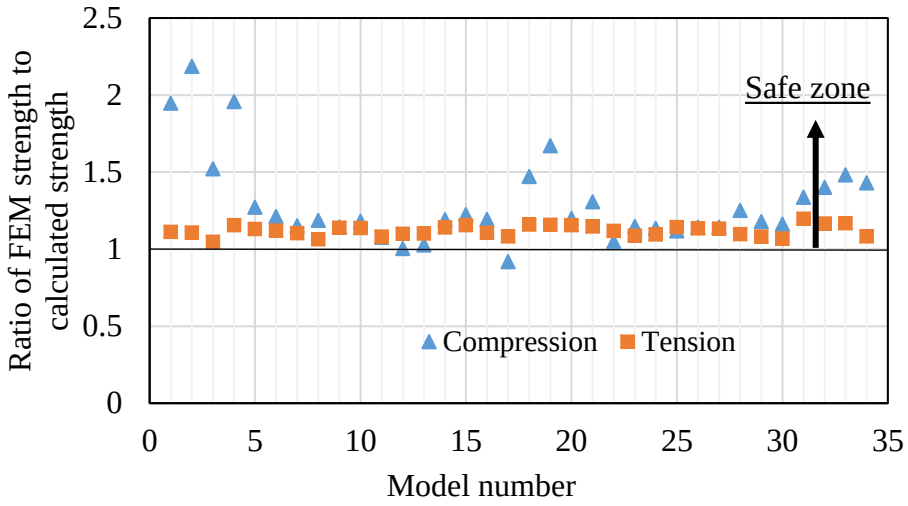

b) Ratio of FEM strength to calculated axial strength

Figure 4-72. Connections recorded strength and calculated strength

Note that the packing effect was not considered in the FE models as well as out-of-straightness and residual stresses in the members. Therefore, in this study it is recommended to use strength reduction factor of $\phi = 0.75$ for WSP axial compression capacity to account for packing effect and other parameters that were not possible to be considered in the FEM

analysis explicitly. An experimental study is required to achieve more accurate results and confirm the findings of this study which is out of the scope of this research.

4.8 Conclusion

In this chapter, the axial behaviour of WSP connections was investigated and a method to assess the axial compressive strength of WSP connections considering the gravity loads effect was proposed. The main findings of this study include:

1) Diaphragm in-plane forces need to be transferred to the ground through VLFR system of the structure. Structural beams as a part of the load path transfer the diaphragm in-plane forces to VLFR system. The axial forces generated in a beam as a part of the load transfer mechanism may depend on whether a gap is provided between the slab and the column or not.
2) Based on the literature, many research studies have been conducted to investigate the shear force and rotation capacity of the WSP connections since the 1960s. The results of these studies were employed by different building standards to calculate the shear strength of WSP connections. However, the axial behaviour of this type of connection was only investigated by few researchers focusing on connection axial forces due to the beam composite action.
3) From the analysis conducted in this study, it was found that the axial compression capacity of a WSP connection is lower than the axial tensile capacity because of the axial force eccentricity, the cleat plate slenderness, and P-Δ effect. The axial force eccentricity imposes additional moment to the cleat plate and the beam web, and initiates the cleat buckling at lower axial forces compared to a centrally loaded cleat plate. For the connection subjected to the axial tension force, axial force increases to reach the first controlling failure limit state.

4) A number of parameters that can affect the axial behaviour of WSP connections are investigated, the results found include:

   i. Beam lateral restraint at the mid-point and third points along the beam length did not alter the tensile strength and the compression strength increased by less than 4% in the studied case.

   ii. Top flange torsional restraint did not change the tensile strength of the WSP connection. However, the compression capacity increased by about 14% for the studied case compared to the unrestrained beam.

   v. The effect of cleat plate location on only one side or opposite sides at beam-ends was less than 1% for the studied case.

   vi. Compression and tension capacities of the WSP connection increased with increasing cleat plate height. The ultimate tension and compression capacities showed that the tensile strength more increased than compression capacity by increasing the cleat plate height.

   vii. For the models studied, the tensile capacity decreased by about 2% because of the reduction in the beam web cross-section area due to copping. The compression behaviour experienced a significant reduction, so that, the 2, 3 and 4 bolts connections experienced 16%, 24% and 48% reduction in the ultimate compression capacity.

   viii. Cope length did not significantly affect the tensile capacity of the WSP connection. However, the connection compression capacity decreased with increasing the cope length. For the range of cases studied the axial compression strength decreased linearly with increasing the cope length.

   iv. Gravity loads causing a beam shear force up to 60% of cleat plate shear yield strength reduced the connection compressive axial strength by up to 15%.

v. It was found that for connections with both snug-tightened and proof loaded bolts the ultimate tension and compression capacities were almost the same with less than 3% difference at the ultimate axial strength.

vi. Based on the results of the studied cases, column lateral drift increased or decreased the ultimate capacity of the studied connections under axial compression by less than ±8% for a 2% drift angle. Also, it was found that additional rotation did not affect the tension behaviour of WSP connections.

vii. Considering 3mm eccentricity in the studied connection caused up to 25% decrease in the axial compression strength and the ultimate tensile strength of the WSP connection changed by about 7% due to increasing the load eccentricity up to 3mm.

5) For the proposed method to calculate WSP axial compression strength, it was found that considering the cleat plate alone may result in a conservative estimate of compression strength. Therefore, the effect of the beam web and different boundary conditions should be considered. The proposed method covers the connections with the following conditions:

    1. Double coped, laterally unrestrained connection
    2. Un-coped, top flange restrained laterally
    3. Double coped, top flange restrained laterally

The axial compression strengths obtained using the proposed method were compared with thirty-four models considering different parameters. The average ratio of calculated compression strength to the strength obtained from FEM analysis was 80.1% with standard deviation of 13.7% and for tension side, the average ratio of calculated tension strength to the strength obtained from FEM analysis was about 89.3% with standard deviation of 2.8%. Note that some parameters considered in the analytical strength calculation approach were not considered in the numerical models. These included: residual stress

effect and out-of-straightness effect. To consider these and also possible packing effect in design it is therefore suggested that the calculated compression capacity be multiplied by a strength reduction factor of $\phi = 0.75$. However, further experimental investigation is required.

4.9 Summary of the proposed method

In this section a summary of the proposed method for estimating axial strength of WSP connections is presented. Figure 4-73 shows elevation and section views of a typical WSP connection.

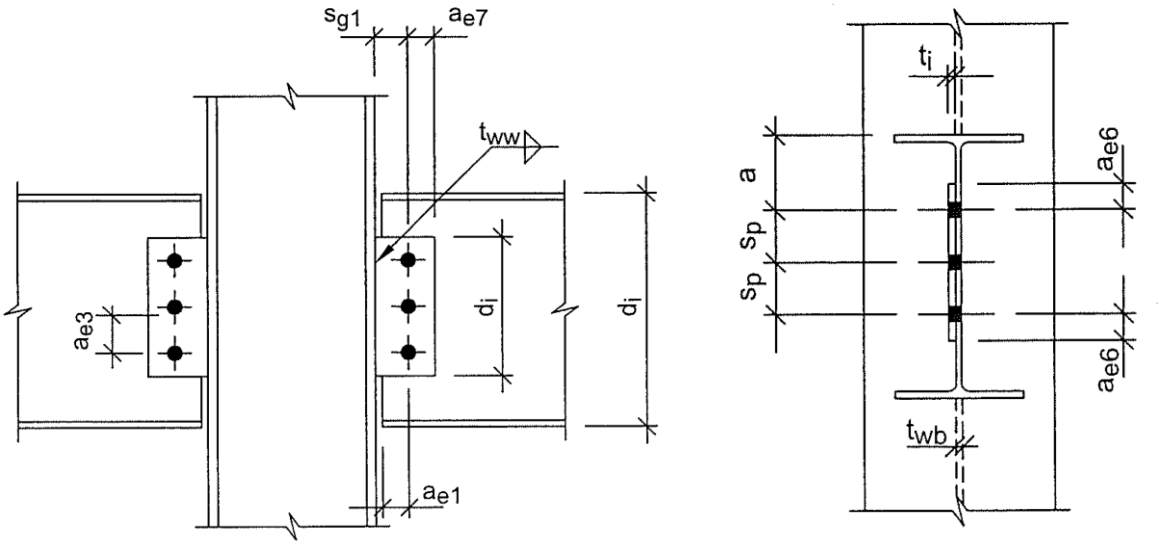

a) Elevation b) Section view

Figure 4-73. Elevation and section of typical WSP connection

4.9.1 Case one, beam top flange not restrained laterally

4.9.1.1 Checking the cleat plate

1) Obtain effective length of the beam web (L_w)

$$\begin{cases} L_w = \frac{h_w}{5} + L_{cope} - a_{e1} \ \rightarrow for\ coped\ beam \\ L_w = \frac{h_w}{5} \ \rightarrow for\ un-coped\ beam \end{cases}$$

Note: a_{e1} is the distance between the beam-end and bolt line as shown in Figure 4-73.

2) Obtain contributing height of the beam web, $h_{we} = min[h_w, 1.5h_c]$

3) Calculate effective length factor for the cleat plate

$$\begin{cases} k_c = 1.05\frac{L_w}{L_c}\sqrt{\frac{EI_c}{EI_w}} + 1.2 \;\; \rightarrow for \; \frac{L_w}{L_c}\sqrt{\frac{EI_c}{EI_w}} < 2 \\ k_c = 0.9\frac{L_w}{L_c}\sqrt{\frac{EI_c}{EI_w}} + 1.5 \;\; \rightarrow for \; \frac{L_w}{L_c}\sqrt{\frac{EI_c}{EI_w}} \geq 2 \end{cases}$$

Note: I_w is calculated based on the effective beam web height (h_{we})

4) Calculate elastic buckling load for the cleat plate, $P_{cr} = \frac{\pi^2 EI_c}{(k_c L_c)^2}$

5) Obtain P_u for the cleat plate based on Section 6 of NZS3404 (2007) considering $\alpha_b = 0.5$

6) Obtain M_{u3} (plastic moment) of the cleat plate about weak axis

7) Calculate moment participation factor, $\alpha = \left(\frac{I_c/L_c}{I_c/L_c + I_w/L_w}\right)$

8) Calculate e (axial load eccentricity) using $e = \frac{t_c + t_w}{2}$

9) Obtain M_{u2} (plastic moment) of the cleat plate about strong axis

- Note: the plastic moment of the cleat plate about strong axis should be modified using shear-moment interaction

$$\begin{cases} \frac{V}{V_v} + \frac{1.6M_{u2}}{\emptyset M_{s2}} \leq 2.2 \quad for \;\; V \geq 0.6V_v \\ M_{u2} = \emptyset M_{s2} \quad for \;\; V < 0.6V_v \end{cases}$$

10) Calculate the cleat plate capacity (P_c) using

$$\frac{P_c}{P_u} + \frac{\alpha \times P_c \times e}{M_{u3}(1 - P/P_{cr})} + \frac{M_2}{M_{u2}} \leq 1$$

4.9.1.2 Checking the beam web:

The process of checking the beam web is similar to calculating the cleat plate axial strength. Only the effective length factor and moment participation factors are different for the beam web as follow:

$$k_w = k_c \frac{L_c}{L_w}\sqrt{\frac{EI_w}{EI_c}}$$

$$\alpha = \left(\frac{{I_w}/{L_w}}{{I_c}/{L_c} + {I_w}/{L_w}} \right)$$

$$\frac{P_w}{P_u} + \frac{\alpha \times P_w \times e}{M_{u3}(1 - P/P_{cr})} + \frac{M_2}{M_{u2}} \leq 1$$

- WSP compression strength is equal to minimum of $\{P_w, P_c\}$.

4.9.2 Case two, beam top flange restrained laterally

4.9.2.1 Checking the cleat plate

1) Obtain h_{eff} based on Clause 6.2.4 of NZS3404 (2007)

$$h_{eff} = 16 t_w \sqrt{\frac{250}{f_{yw}}} \leq h_w$$

- Note: if the beam top flange is retrained and the beam is coped, the h_{eff} should be modified using:

$$\frac{h_{ec}}{h_e} = 1 - 0.5 \frac{L_c}{d}$$

2) Calculate h_1 and h_2

$$h_1 = h_{eff} + t_f - a + a_{e6}$$

$$h_2 = h_c - h_1$$

Note: a_{e6} is the vertical edge distance at top of the cleat plate

3) Calculate cleat axial capacity at zone 1 (P_{c1}) shown in Figure 4-65

$$P_{c1} = h_1 t_c f_{yc}$$

4) Calculate P_2, this stage is the same as the case one, while the h_c should be substituted by h_2

4.1) Obtain effective length of the beam web (L_w)

$$\begin{cases} L_w = \frac{h_w}{5} + L_{cope} - a_{e1} \ \rightarrow for\ coped\ beam \\ L_w = \frac{h_w}{5} \ \rightarrow for\ un-coped\ beam \end{cases}$$

4.2) Obtain contributing height of the beam web, $h_{we} = min[h_w, 1.5h_2]$

4.3) Calculate effective length factor for the cleat plate

$$\begin{cases} k_c = 1.05\frac{L_w}{L_c}\sqrt{\frac{EI_{c2}}{EI_w}} + 1.2 \;\; \rightarrow for \; \frac{L_w}{L_c}\sqrt{\frac{EI_{c2}}{EI_w}} < 2 \\ k_c = 0.9\frac{L_w}{L_c}\sqrt{\frac{EI_{c2}}{EI_w}} + 1.5 \;\; \rightarrow for \; \frac{L_w}{L_c}\sqrt{\frac{EI_{c2}}{EI_w}} \geq 2 \end{cases}$$

- Note: I_w is calculated based on effective beam web height (h_{we}) and I_{c2} is calculated using h_2

4.4) Calculate elastic buckling force for the cleat plate, $P_{cr} = \frac{\pi^2 EI_{c2}}{(k_c L_c)^2}$

4.5) Obtain P_u for the cleat plate based on Section 6 of NZS3404 (2007) considering $\alpha_b = 0.5$

4.6) Obtain M_{u3} (plastic moment) of the cleat plate about weak axis (using h_2)

4.7) Calculate moment participation factor, $\alpha = \left(\frac{I_{c2}/L_c}{I_{c2}/L_c + I_w/L_w}\right)$

4.8) Calculate e (axial load eccentricity) using $e = \frac{t_c + t_w}{2}$

4.9) Finding M_{u2} (plastic moment) of the cleat plate about strong axis

- Note: the plastic moment of cleat plate about strong axis should be modified using shear-moment interaction

$$\begin{cases} \frac{V}{V_v} + \frac{1.6M_{u2}}{\emptyset M_{s2}} \leq 2.2 \quad for \;\; V \geq 0.6V_v \\ M_{u2} = \emptyset M_{s2} \quad for \;\; V < 0.6V_v \end{cases}$$

4.10) Calculate the cleat plate capacity at zone 2 (P_{c2}) shown in Figure 4-65

$$\frac{P_{c2}}{P_u} + \frac{\alpha \times P_{c2} \times e}{M_{u3}(1 - P/P_{cr})} + \frac{M_2}{M_{u2}} \leq 1$$

5) Calculate total cleat capacity

$$P_c = P_{c1} + P_{c2}$$

4.9.2.2 Checking the beam web:

1) Calculate beam web strength at zone 1 (P_{w1})

$$P_{w1} = (h_{eff} - h_2)t_w f_{yw}$$

The process for calculating P_{w2} is similar to the cleat axial strength calculation and the effective length and moment participation factors are different in this case as follows:

$$k_w = k_c \frac{L_c}{L_w}\sqrt{\frac{EI_w}{EI_{c2}}}$$

$$\alpha = \left(\frac{{I_w}/{L_w}}{{I_{c2}}/{L_c} + {I_w}/{L_w}}\right)$$

$$\frac{P_{w2}}{P_u} + \frac{\alpha \times P_{w2} \times e}{M_{u3}(1 - P/P_{cr})} + \frac{M_2}{M_{u2}} \leq 1$$

$$P_w = P_{w1} + P_{w2}$$

- ❖ WSP compression nominal strength is equal to minimum of $\{P_w, P_c\}$
- ❖ Here it is suggested that the calculated compression capacity be multiplied by a strength reduction factor of $\phi = 0.75$.

An example of WSP axial strength calculation is provided in Appendix M.

References

[1] ABAQUS, analysis user's guide, version 6.14, Dassault systemes solidworks corp, Waltham, Massachusetts, 2014.

[2] Abou-zidan, A., & Liu, Y. (2015). Numerical study of unstiffened extended shear tab connections. Journal of Constructional Steel Research, 107, 70-80.

[3] Ahmed, B., Li, T. Q., & Nethercot, D. A. (1997). Design of composite finplate and angle cleated connections. Journal of Constructional Steel Research, 41(1), 1-29.

[4] AISC (1963). Manual of Steel Construction, 6th Edition. American Institute of Steel Construction. Chicago, IL.

[5] AISC (2010). Specification for structural steel buildings (ANSI/AISC 360-10). American Institute of Steel Construction, Chicago-Illinois.

[6] AISC (2016). Specification for structural steel buildings (ANSI/AISC 360-16). American Institute of Steel Construction, Chicago-Illinois.

[7] AISC, L. (2001). Manual of steel construction, load and resistance factor design.

[8] Alizadeh, S., MacRae, G. A., Bull, D., & Clifton, G. C. (2017). In-Plane Diaphragm Issues for Steel Buildings in Seismic Zones. In 16th World Conference on Earthquake, 16WCEE.

[9] American Institute of Steel Construction. (2005). Steel construction manual.

[10] AS/NZS 1170.0 (2002), Structural design actions-Part 0: General principles.

[11] AS/NZS 3679.1 (2016), Structural steel - Part 1: Hot-rolled bars and sections

[12] AS/NZS 5131 (2016), Structural steelwork - Fabrication and erection.

[13] Ashakul, A. (2004). Finite element analysis of single plate shear connections (Doctoral dissertation, Virginia Tech).

[14] Ashakul, A., & Khampa, K. (2014). Effect of plate properties on shear strength of bolt group in single plate connection. Steel and Composite Structures, 16(6), 611-637.

[15] Astaneh, A. (1989a). New concepts in design of single plate shear connections. In Proc., National Steel Construction Conf (pp. 3-1).

[16] Astaneh, A. (1989b). Demand and supply of ductility in steel shear connections. Journal of Constructional Steel Research, 14(1), 1-19.

[17] Astaneh, A., Call, S. M., & McMULLIN, K. M. (1989c). Design of single plate shear connections. Engineering Journal, 26(1), 21-32.

[18] Astaneh, A., McMULLIN, K. M. & Call, S. M. (1988). Design of single plate framing connections," Report No. UCB/SEMM-88/12 to the American Institute of Steel Construction. University of California at Berkeley.

[19] Caccavale, S. E. (1975). Ductility of single plate framing connections.

[20] Chaudhari TD, MacRae GA, Bull D, Chase G, Hicks S, Clifton GC and Hobbs M (2015). "Composite Slab Effects on Beam–Column Subassembly Seismic Performance", 8th International Conference on Behavior of Steel Structures in Seismic Areas, Shanghai, China.

[21] Creech, D. D. (2005). Behavior of single plate shear connections with rigid and flexible supports.

[22] D'Aronco, M. (2013). Behaviour of double and triple vertical rows of bolts shear tab connections and weld retrofits(Doctoral dissertation, École Polytechnique de Montréal).

[23] Goodrich, W. S. (2005). Behavior of extended shear tabs in stiffened beam-to-column web connections.

[24] Hormby, D. E. (1981). Design of single plate framing connections.

[25] Hyland, C., Cowie, K., & Clifton, C. (2008). Structural Steelwork Connections Guide: Design Procedures, SCNZ 14.1 2007. Steel Construction New Zealand (Inc), Manukau City.

[26] Johnston, B. G. (1976). Guide to stability design criteria for metal structures.

[27] Kulak, G. L., Fisher, J. W., & Struik, J. H. (2001). Guide to Design Criteria for Bolted and Riveted Joints Second Edition.

[28] Lipson, S. L. (1968, February). Single-angle and single-plate beam framing connections. In Canadian Structural Engineering Conference, Toronto, Ontario (pp. 141-162).

[29] Mahamid, M., Rahman, A. D. E. E. B., & Ghorbanpoor, A. (2007). The Analyses of Extended Shear Tab Steel Connections Part II: Stiffened Connections. ENGINEERING JOURNAL-AMERICAN INSTITUTE OF STEEL CONSTRUCTION, 44(2), 133.

[30] Manual of Steel Construction, 14th Edition, American Institute of Steel Construction, Chicago: AISC, 2011.

[31] Marosi, M. (2011). Behaviour of single and double row bolted shear tab connections and weld retrofits. In Masters Abstracts International (Vol. 50, No. 02).

[32] Neal, B. G. (1961). The effect of shear and normal forces on the fully plastic moment of a beam of rectangular cross section. Journal of Applied Mechanics, 28(2), 269-274.

[33] Needham, J., Koia, R., Alizadeh, S., Scarry, J. and MacRae, G.A. (2018). Beam Shear Connections. Steel Structures in Seismic Areas (STESSA) Conference, Christchurch, 14-16 February 2018.

[34] New Zealand Heavy Engineering Research Association, structural steelwork connections guide, design procedures. HERA R4-100 2003.

[35] NZS 3404 (2007). Steel Structures Standard. Standards New Zealand, Wellington, New Zealand. Including Amendments 1 and 2, 2001/2007.

[36] Patrick, M., Berry, P. A., & Wheeler, A. T. (2002). -Web-side-plate framing connections in both steel and composite construction. In Advances in Building Technology (pp. 199-206).

[37] Rahman, A., Mahamid, M., Amro, A., & Ghorbanpoor, A. L. (2007). The analyses of extended shear tab steel connections-Part I: The unstiffened connections. ENGINEERING JOURNAL-AMERICAN INSTITUTE OF STEEL CONSTRUCTION INC, 44(2), 117-132.

[38] Ren, P. (1995). Numerical modelling and experimental analysis of steel beam-to-column connections allowing for the influence of reinforced-concrete slabs (No. THESIS_LIB). EPFL.

[39] Richard, R. M., Gillett, P. E., Kriegh, J. D., & Lewis, B. A. (1980). The analysis and design of single plate framing connections. Engineering Journal, 17(2).

[40] Sherman, D. R., & Ghorbanpoor, A. (2002). Design of Extended Shear Tabs," Final report for the American Institute of Steel Construction. October, University of Wisconsin, Milwaukee, Wisconsin.

[41] Steel Construction Institute (Great Britain) & British Constructional Steelwork Association (2002). Joints in steel construction: simple connections. Steel Construction Institute, Ascot

[42] Suleiman, M. F. (2013). Non-Linear Finite Element Analysis of Extended Shear Tab Connections (Doctoral dissertation, University of Cincinnati).

[43] Thomas, K., Driver, R. G., Oosterhof, S. A., & Callele, L. (2017, May). Full-scale Tests of Stabilized and Unstabilized Extended Single-plate Connections. In Structures (Vol. 10, pp. 49-58). Elsevier.

[44] Weir, C., & Clarke, H. (2016). Web Side Plate Connections under Axial Load. Final Year Projects, Dept. of Civil and Natural Resources Engineering, University of Canterbury.

[45] Ziemian, R. D. (Ed.). (2010). Guide to stability design criteria for metal structures. John Wiley & Sons.

5 Shear Studs Considerations

5.1 Introduction

Composite beams typically consist of a steel beam with a concrete slab on top of the beam. Composite action increases the beam stiffness and strength. Therefore, smaller beam section sizes can be used compared to the non-composite situation. Composite beams are commonly used in steel structures.

Composite action is developed between the concrete slab and the steel beam through the use of mechanical attachments which transfer longitudinal shear between the concrete slab and the steel beam. There are different types of mechanical attachments such as bar connectors, angle connectors, channel connectors and steel headed-studs, also referred to as shear studs. The most widely used type of shear connector is the shear stud. The advantages of the shear stud connectors include i) rapid welding process, ii) little obstruction to reinforcement in the concrete slab and, iii) equal strength and stiffness in shear in all directions normal to the longitudinal axis of the stud (Johnson, 2008).

Equations for determining composite beam strength and stiffness to carry gravity loads are provided by different building standards (e.g. AISC/ANSI 360-16 and NZS3404, 2007). The flexural strength of a composite beam is normally derived from standard rigid-plastic equilibrium analyses of the forces across the beam section.

During earthquake events, in-plane diaphragm forces due to inertia, transfer, compatibility, slab bearing and interaction with other structural elements need to be transferred to the structural frames (Alizadeh et al. 2017). In general, force transfer directly from the diaphragm into the column should not be used as it is not a reliable load path. This is because if a gap is provided around the column during construction, as shown in Figure 5-1a, the diaphragm forces need to be transferred to the VLFR system of the structure through the beam axial forces.

However, even if there is no construction gap around the column, since the slab inertia forces act in the same direction as the frame sways, due to the beam-column joint rotation, a gap opens at location "A", shown in Figure 5-1c. Because of this, the slab forces cannot transfer directly into the column through slab bearing. Instead, the diaphragm in-plane forces transfer into the steel beam through friction and mechanical attachments (e.g. shear studs) and from the beam to the column (MacRae and Clifton, 2015).

In addition, when there is no construction gap between the slab and column, as the column sways, it bears against the concrete slab on the far end of the beam. This is the left side of the beam, at location "B", in Figure 5-1c. This slab bearing force is likely to increase the slab forces that must transfer into the beam using shear studs, and the beam must transfer it back to the columns.

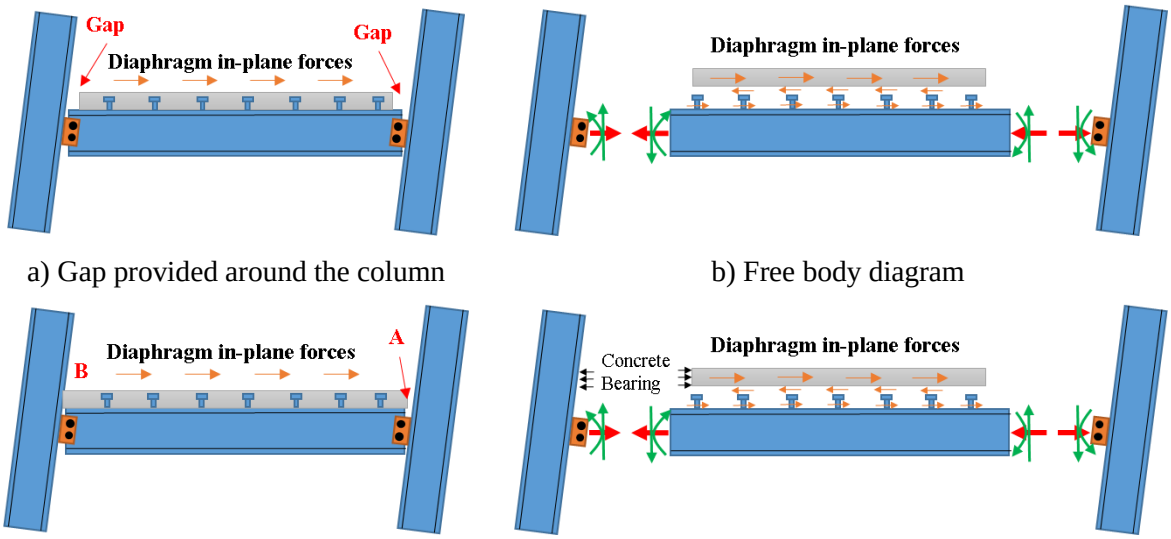

a) Gap provided around the column

b) Free body diagram

c) No gap provided

d) Free body diagram

Figure 5-1. Gapped and non-gapped slab-column details

Note that when there is no construction gap around the column and a gap is opened due to the frame lateral drifts at point "A"; slab lateral movements (because of the shear stud and beam-column flexibility) may close the gap and form a load path through the slab bearing. However, the existence of this load path depends on the relative displacement of the slab to the beam/column, and even after contact is made, the load path is not reliable due to concrete

crushing. Therefore, it is more reliable and conservative for shear stud design to consider forces transferred from the diaphragm to the beam through shear studs.

In this study, the behaviour of composite beams subjected to lateral forces are investigated by answering the following questions:

1) What design recommendations exist for shear studs subject to lateral forces in combination with gravity loads?
2) What are the effects of lateral forces on composite action and beam vertical deflection?
3) How should the number of shear studs be considered in design of traditional structures?
4) If undesirable effects of lateral force on beam behaviour are to be mitigated, how should this be done?

5.2 Literature review

A summary of the available provisions/recommendations to design beams subject to lateral force in combination with the gravity loads are presented. Also, a brief review of the research works and building standards relevant to the monotonic and cyclic force-slip behaviour of shear studs is conducted.

5.2.1 Available provision/recommendations to design shear studs for lateral forces in combination with gravity loads

There are few documents in the literature that consider the lateral force resistance of shear studs on a composite beam. Mullett (1998) states that it is not normally necessary to provide additional shear connectors to carry diaphragm in-plane forces except close to points of local transfer of shear forces such as adjacent to VLFR systems.

- **Composite beams**

Burmeister and William (2008) state that for the beams that are designed as composite members to carry gravity loads, additional shear studs to transfer the superimposed horizontal forces into the beam may not be required. This is because:

1) The quantity of shear studs used for a composite beam is usually determined based on an ultimate gravity load combination, such as $1.2G + 1.5Q$ based on NZS 1170.0 (2002). However, at the time that the lateral forces are imposed the reduced gravity loads include the dead load, G, and a part of the live load, Q, act on the beam. The load combination for this situation is provided by loading standards. In NZS1170.0 (2002) this is $G + \psi_E Q$ where $\psi_E = 0.3$ for most buildings (except storage and structures with installed heavy machinery). Under the reduced gravity load combinations, the shear studs will be under-used and thus have additional capacity available to transfer the diaphragm in-plane forces.
2) The interaction of the shear flow from the different loading conditions is additive for some studs but opposite for others. The distribution of horizontal shear from the beam flexure is assumed to flow in two directions from the point of the maximum moment to the point of zero moments as shown in Figure 5-2.

Based on Burmeister and William (2008) study, when the shear studs have sufficient ductility to distribute the horizontal shears evenly along the beam, the composite beam can transfer the horizontal shear due to lateral forces equal to the sum of the strengths of all the shear studs on the beam regardless of the gravity load demand on the shear studs. Similar provisions were given in AISC/ANSI 360-16.

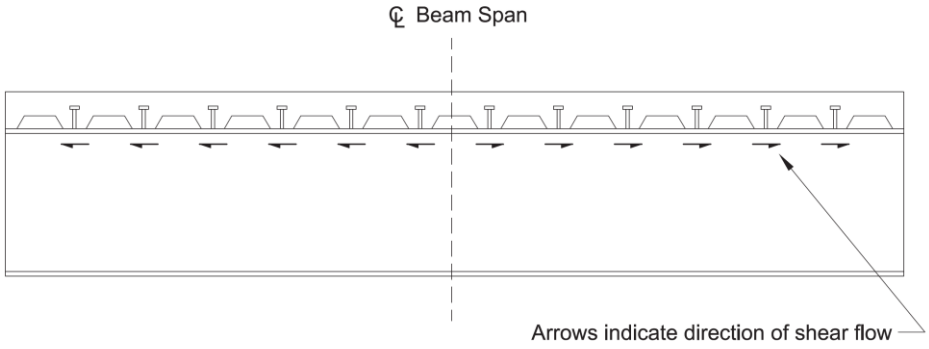

(a) Shear flow due to gravity loads only

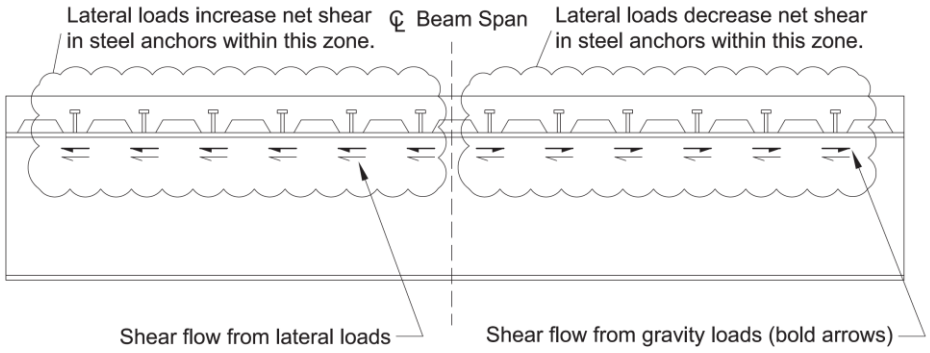

(b) Shear flow due to gravity and lateral loads in combination

Figure 5-2. Shear flow at collector beam (AISC/ANSI 360-16)

Based on Cowie et al. (2014) the number of shear studs required should be computed as that needed to develop composite action to resist the gravity loads from the $1.0G + 1.0Q$ load combination in addition to the number of shear studs required for lateral forces. Using $1.0Q$ in this combination instead of $\psi_E Q$ is in accordance with the requirements of Clause 12.10.2.2 NZS 3404 (2007) to prevent uniaxial beam hinging (shakedown) in moment resisting frames. Although this recommendation is for beams in moment resisting frames, it may be applied to any beam forming a key component of the diaphragm force transfer system (Cowie et al., 2014).

- **Non-composite beams**

Burmeister and William (2008) state that in the non-composite beams, that the shear studs are only placed to transfer lateral forces, shear studs still will be subjected to horizontal shears due to flexural effects from gravity loads. In order to ensure the shear studs are not overloaded

under the gravity loads, it was recommended that all beams have enough shear studs to achieve a minimum of 25% partial composite action. This provides some lateral force resistance. When fewer shear studs than this are provided, large slips may occur in the shear studs under gravity loads limiting the ability of the beam to function as intended under lateral forces. Similar provisions were given in AISC/ANSI 360-16.

Other research (e.g. Cowie et al., 2014 and Sabelli et al., 2011) also endorsed the provisions given in AISC/ANSI 360-10 which are similar to AISC/ANSI 360-16.

NZS 3404 (2007) provides equations for determining the ultimate composite beam strength and stiffness for supporting gravity loads. However, there is only one clause in this standard regarding the seismic design of composite floor slabs. Clause 13.2.3.2 of NZS 3404 (2007) states that the actions induced in shear connectors by seismic-induced diaphragm effects shall be added to any design actions from the composite action using appropriate design load combinations from loading standard. There is no further information about how many shear studs contribute to lateral force resistance or the appropriate method for combining these actions.

Some provisions (Clause 8.3.2) are also provided in AS/NZS 2327 (2017) about considering the stiffness of composite members on the frame lateral stiffness. However, there is no guidance about considering the interaction of gravity loads and lateral forces on composite beams.

5.2.2 Force-slip behaviour of shear studs

Behaviour of steel-concrete composite beams under gravity loads, lateral forces or combination of these forces, highly depends on the shear connector stiffness, force-slip relationship and ductility. In the following, the shear behaviour of shear studs as the most widely used shear connectors is described.

Three parameters that are considered as the main characteristics of shear studs in this study include:

i. Ultimate slip capacity of a ductile shear stud

ii. Force-slip relationship of shear stud

iii. Cyclic behaviour of shear stud

5.2.2.1 Ultimate slip capacity of a ductile shear stud

Shear connectors (e.g. shear studs) in a composite beam experience a level of shear slip under the imposed gravity loads. The amount of this slip depends on the shear stud stiffness, strength, the composite action level and also the imposed gravity loads. The slip is higher in partially composite beams because a lower number of shear studs are provided to carry steel-concrete interface shear forces in comparison with a fully composite beam. The shear stud ductility is an important parameter to avoid unexpected failure under gravity load.

Meanwhile, shear studs in a composite beam subjected to the combination of gravity and lateral forces require more ductility to accommodate deformations than those due to lateral forces alone. This situation will be discussed in more detail in Section 5.3.

The minimum ultimate slip, S_u, to consider a shear stud as a ductile shear connector is 6mm based on Eurocode 4 (2004). The same limitation is also given in AS/NZS 2327 (2017) Clause 3.6.1.1. Figure 5-3 presents a schematic force-slip behaviour of shear studs from a push-out test indicating S_u.

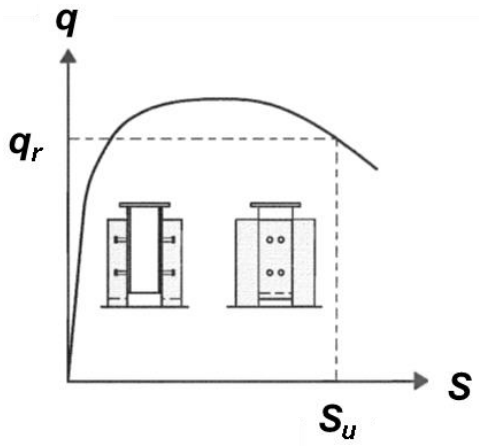

Figure 5-3. Schematic force-slip of shear stud (Eurocode 4, 2004)

Johnson and Molenstra (1991) conducted an extensive study on shear stud behaviour in partially composite beams. They used the result of available shear stud tests at the time to obtain the ultimate slip capacity of shear studs. Based on their study, the ultimate slip, S_u, of shear studs with 13mm, 16mm and 22mm diameter can be considered $4mm$, $6mm$ and $8.5mm$ respectively. The ultimate slip capacity of 19mm diameter shear studs is $S_u = 7.25mm$ by linear interpolation between 16mm and 22mm shear studs.

5.2.2.2 Shear stud force-slip relationship

The shear strength of an individual shear stud depends on the shear stud diameter, the materials properties, the concrete slab properties, the orientation of the steel decking, the position of the stud within the ribs, and the number of studs. Some force-slip relationships for shear studs are available in the literature. The force-slip curves are usually obtained using monotonic push-out tests on shear studs.

Johnson and Molenstra (1991) proposed an empirical equation to represent the force-slip, $q - S$, relationship of shear studs, using the shear stud ultimate strength, q_r.

$$q = q_r\left(1 - e^{-\beta S}\right)^{\alpha} \qquad \text{Eq. (5-1)}$$

In this equation, α and β are empirical values that in this study are considered equal to 0.989 and 1.535 respectively. These values are based on Johnson and Molenstra (1991) results

for 19mm shear studs. Shear stud strength, q_r, can be calculated using equations provided in different building standards e.g. NZS3404 (2007), Eurocode 4 (2004), AS/NZS 2327 (2017) and AISC/ANSI 360-16 (2016).

5.2.2.3 Cyclic behaviour of shear stud

The horizontal shear flow of shear studs due to the beam bending is in opposite directions from the point of the maximum moment to the point of zero moments as was shown in Figure 5-2. When lateral forces are applied to the slab, the interaction of the shear flow and lateral forces is additive for some studs but opposite for the others. Therefore some studs experience unloading and with increasing the imposed lateral force some may be reloaded in the opposite direction compared to their initial force. Because of this, cyclic behaviour of shear studs plays a key role in identifying the lateral force behaviour of composite beams.

Most of the research studies in the literature have focused on the monotonic behaviour of the shear studs. This is because the gravity load capacity and stiffness of composite beams were mostly in the interest of researchers. The cyclic loading-unloading behaviour of shear studs was also investigated to obtain the fatigue behaviour of shear connectors in the bridge construction by some researchers (e.g. Slutter and Fisher, 1966 and Gattesco and Giuriani, 1996) as shown in Figure 5-4.

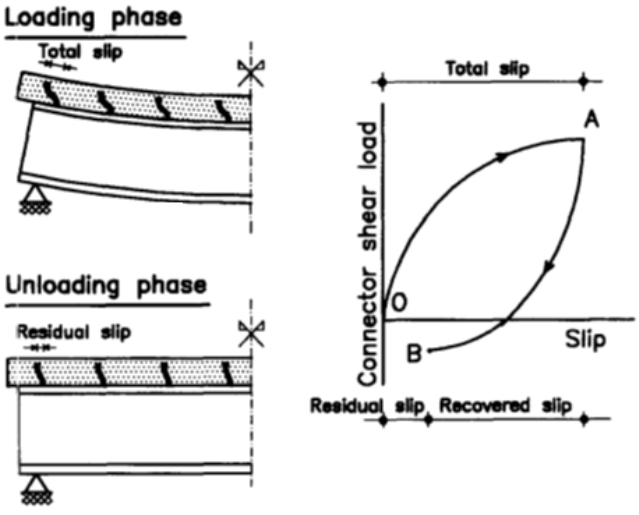

Figure 5-4. Shear stud behaviour subjected to loading and unloading (Gattesco and Giuriani, 1996)

The behaviour of shear studs subjected to fully reversed cyclic loading was investigated by Oehlers and Coughlan (1986), Nakajima et al. (2003) and Civjan and Singh (2003). Figure 5-5 shows an example of force-slip hysteresis curve for shear studs.

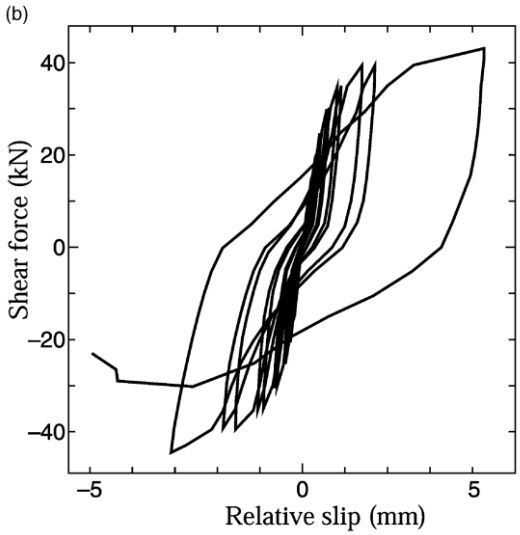

Figure 5-5. Shear stud behaviour subjected to fully reversed cyclic loading, 13mm diameter shear stud (Nakajima et al., 2003)

Based on these studies, for stable hysteresis behaviour, it would be expected that the shear studs reach the same absolute force due to the same slip in the opposite direction. This assumption is used in this study to obtain the gravity and lateral force interaction behaviour of composite beams.

5.3 Effects of slab lateral force on composite beams subject to gravity loading

5.3.1 Combination of gravity loads and lateral forces on composite beams

As it was described in Section 5.1, transferring diaphragm in-plane forces to the structural frames during earthquake events imposes additional shear force on the shear connectors placed on the beams. These shear connectors may primarily be placed on the beam to provide composite action under gravity loading, or may have been designed considering lateral force.

It is noted that lateral forces may also be transferred through friction between the slab and the steel beam. This is described in Section 5.5.2 in more detail.

The total number of shear studs determines the level of composite action. In the fully composite beam, there are enough shear studs between the maximum bending moment and zero moment location to develop the full flexural strength of the composite beam. To decrease construction costs the number of shear studs can be reduced, which makes the beam partially composite. The composite action percentage can be expressed as the ratio of the total shear resistance of the shear studs provided to the limiting shear force that is the minimum of tensile yielding of the steel beam or the compression capacity of the concrete slab.

Figure 5-6a shows the shear flow at the steel beam and concrete slab interface schematically. In this Figure, a uniform distributed gravity load is considered on the beam. The horizontal shear at the steel beam-concrete slab interface from the beam flexure is assumed to flow in opposite directions from the point of the maximum moment to the point of zero moments. The magnitude of shear forces also increases from the point of the maximum moment to the point of zero moments. Shear force demand of the shear studs is shown in Figure 5-6b schematically. In this Figure the sum of all shear stud forces is zero, $\sum F_i^L + \sum F_i^R = 0$.

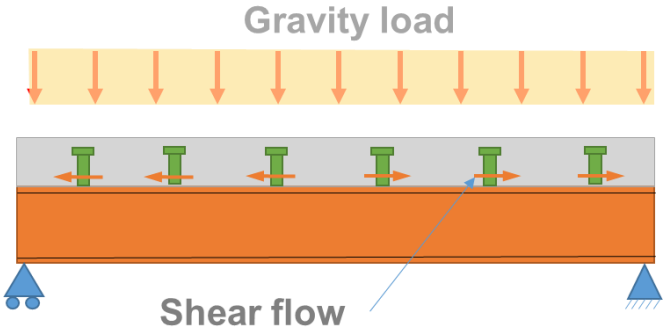

a) Shear flow at steel beam-concrete slab interface

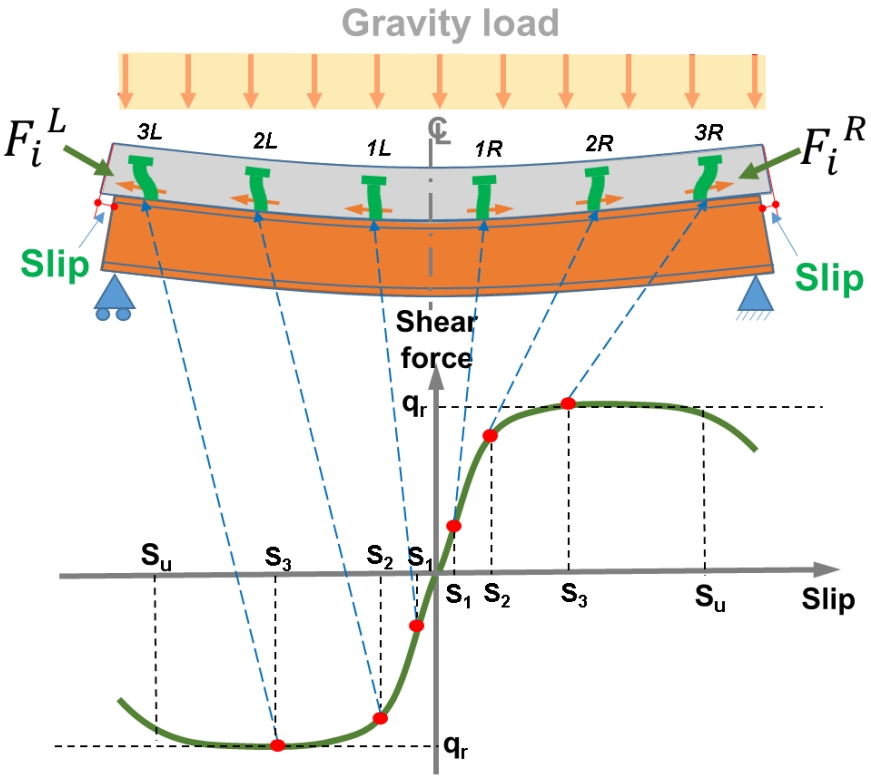

b) Shear stud demands subjected to gravity load

Figure 5-6. Schematic view of a composite beam subjected to gravity loads

When the slab is subjected to an in-plane force, P, additional shear force is imposed on the shear studs as shown in Figure 5-7. The interaction of the shear flow from gravity loads with shear forces from diaphragm in-plane forces is additive for some studs and the opposite for the others as shown in Figure 5-7. This is consistent with Figure 5-2. The shear studs on the additive side experience additional shear force and slip. However, the shear studs on the opposite side experience unloading. In this case the sum of all shear stud forces is equal to the lateral imposed force, $\sum F_i^L + \sum F_i^R = P$.

With increasing the lateral imposed force, P, left hand to the right, the slab moves to the right and the shear studs on the left hand side of the beam unload. For example, shear stud 3L has a new displacement δ to the right, and a reduced force as shown by the point 3L'. Shear studs on the right hand side of the beam also move approximately the same displacement, δ, to the right. Often this does not result in a significant change in force (e.g. stud 3R has a similar

demand to that in its translocated position 3R'), but its deformation demand is increased. If the displacement demand is too large, fracture and strength loss may occur.

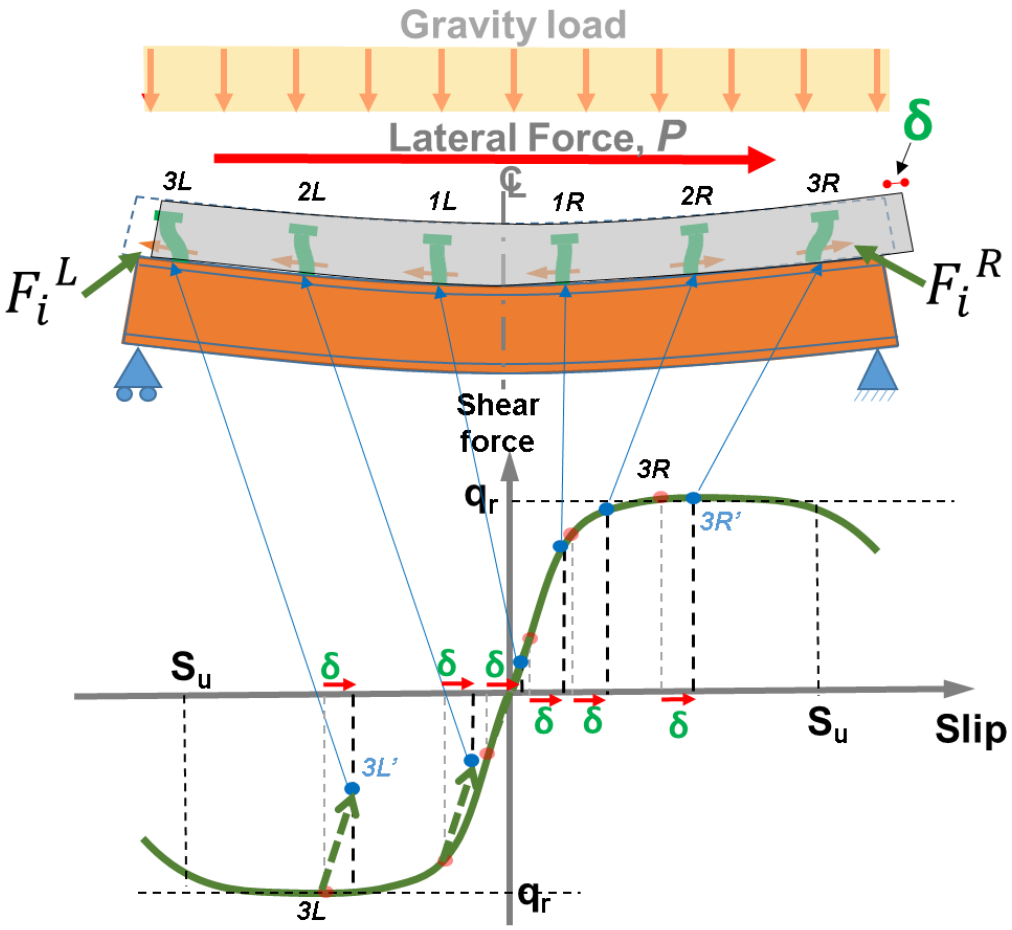

Figure 5-7. Schematic view of a composite beam subjected to a combination of gravity loads and lateral forces

5.3.2 Total lateral force resistance of shear studs on a beam

Figure 5-8 shows the step by step lateral force resistance behaviour of shear studs on a beam schematically.

i. Initially, in Step 1, the composite beam is subjected to gravity loads only and lateral force is zero, $\sum F_i = 0$.

ii. In Step 2, a small lateral force is imposed which increases the shear stud force/slip on the additive side of the beam and unloads the shear studs on the opposite side.

The sum of the shear stud forces is equal to the lateral force, $\sum F_i = P$. In this step, some shear studs on the additive side are yielded.

iii. By increasing the lateral force in Step 3, more shear studs yield and the shear stud at the far end of the beam on the additive side reaches to fracture slip limit. In this step some of the shear studs on the opposite side still experiencing unloading or early levels of loading depending on the shear stud slip under gravity loads. After this step the lateral force cannot be increased because shear studs have displacements greater than that corresponding to their peak strength.

iv. At step four of loading with increasing the lateral slip, the lateral force resistance of shear studs decreases due fracture in some shear studs on the additive side.

For a composite beam without gravity load, the ultimate lateral force resistance of shear studs is equal to the sum of the shear capacity of each stud. This is because all shear studs experience a similar level of slip at each step of loading. However, in the presence of gravity loads, the total lateral force resistance of shear studs may not reach the sum of the ultimate capacity of all shear studs. This is because of the shear force and slip that are imposed on the shear studs due to the gravity load. On the additive side of the beam some studs may fracture before some shear studs on the opposite side reach their ultimate capacity. Therefore the maximum lateral force resistance of all shear studs is related to the shear stud slip under gravity load.

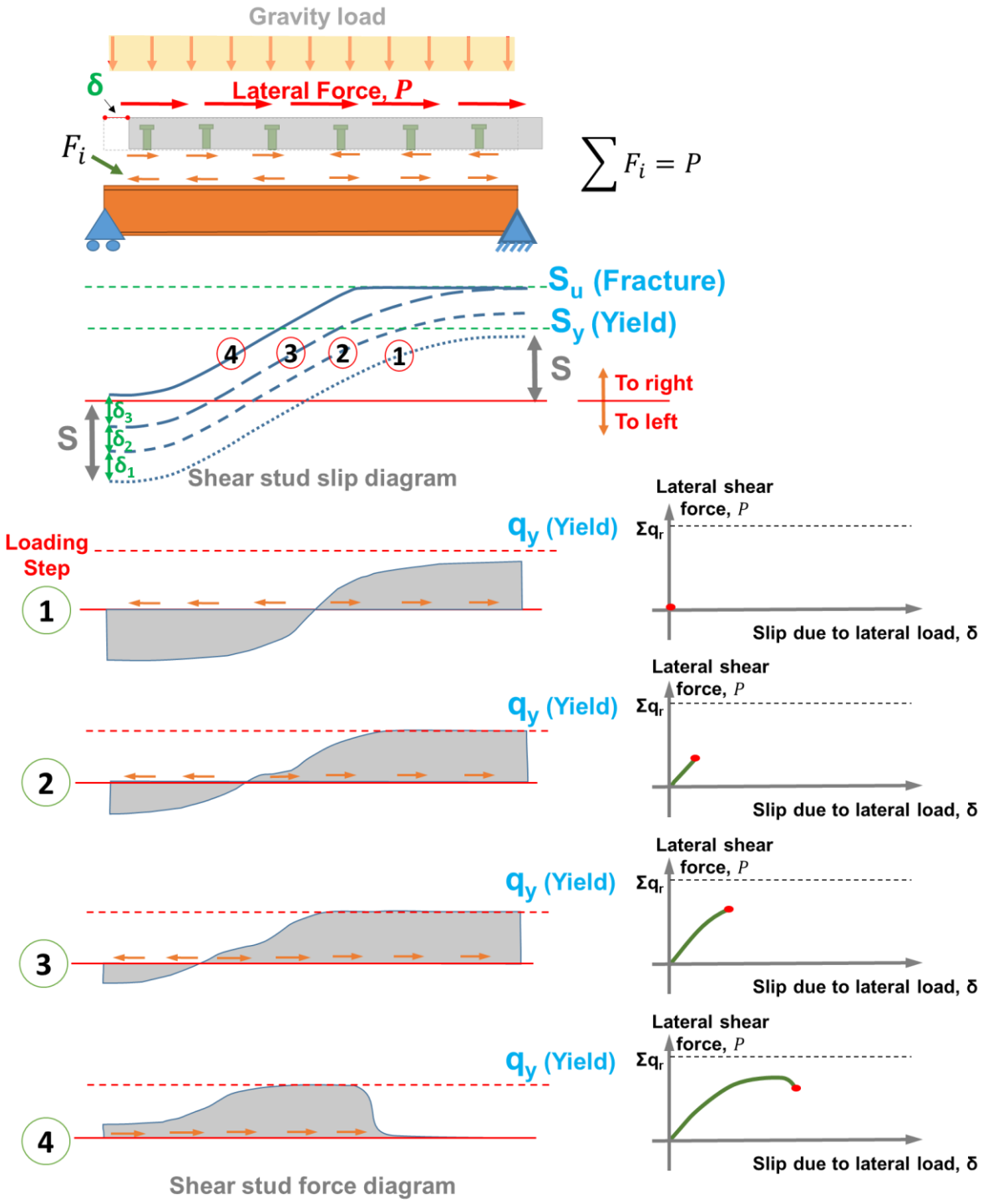

Figure 5-8. Schematic view of lateral force resistance mechanism of shear studs on a beam

- **FEM model example**

A FEM model can be used to show the behaviour of shear studs on a composite beam subjected to gravity loads and lateral forces. The model consists of a six-meter-long composite beam, using steel beam section $360UB50.7$ and $1500 \times 150mm$ cross-section concrete slab

as shown in Figure 5-9. The yield stress and elastic modulus of the steel material were considered to be $340MPa$ and $200GPa$ respectively and the compressive strength and elastic modulus of the concrete material were considered $30MPa$ and $25GPa$ respectively.

A schematic view of the model is presented in Figure 5-9. Shear studs are provided to achieve 50% composite action. The analysis is performed in two steps. First, the gravity load is applied, and then the lateral force is imposed on the slab using displacement control analysis.

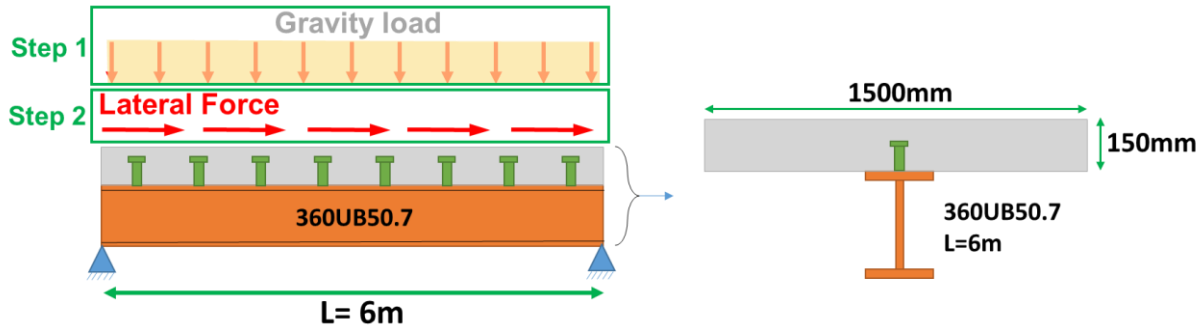

Figure 5-9. Schematic view of model

To obtain an appropriate gravity load for the first step of loading (Gravity load), the strength and stiffness of the composite beam shown in Figure 5-9 were calculated using the equations provided in Clause C13.1.2.6 of NZS3404 (2007). Both strength and stiffness (maximum recommended vertical deflection) criteria were considered to obtain a reasonable gravity load for analysis. Two different uniformly distributed loads were considered for the composite beam considering partial composite action of 50%:

i. The load corresponding to the composite beam strength, M_{pb}, $94kN/m$

ii. The second related to the maximum recommended vertical deflection, $L/300$, $328kN/m$. Since this value is about three time the beam capacity, it was not considered further.

The final gravity load selected for use in the step one of analysis was taken as 0.6 times the gravity load corresponding to the ultimate composite beam strength, M_{pb}, $(= 0.6 \times 94 = 55\ kN/m)$.

To model the composite beam subjected to gravity and lateral forces SAP2000 software (2015) is used. Figure 5-10 shows the modelling method used in this study. The beam and concrete elements are placed at the centre of the steel beam and the concrete slab respectively. Nonlinear link elements are used to model shear stud connections between the concrete slab and the steel beam. The shear stud nonlinear links are connected to the concrete slab and the steel beam elements using rigid links as shown in Figure 5-10. In this model, the flexural stiffness of the concrete slab is ignored due to concrete cracking.

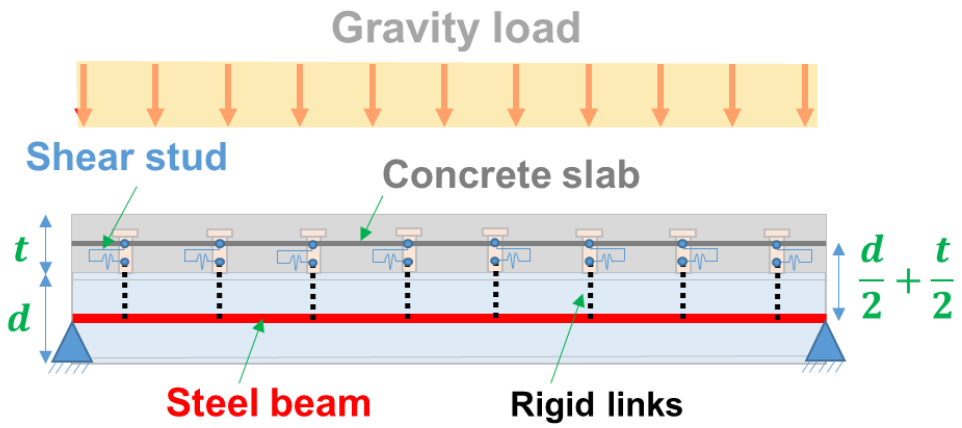

Figure 5-10. Composite beam modelling method

As mentioned in Section 5.2.2.2, Johnson and Molenstra (1991) proposed an equation for the shear force-slip behaviour of shear studs, Eq. (5-1). In this study, the shear force-slip behaviour of shear studs is idealised as shown in Figure 5-11. The idealisation is performed to obtain the same energy using elastic-perfectly plastic behaviour. Considering S_{max} and S_e are the ultimate slip and yield slip of a shear stud respectively, the yield slip can be obtained in Eqs (5-2) and (5-3) equal to $S_e = 1.3mm$. where, $\beta = 1.535$ and $S_{max} = 7.2mm$ in this study.

$$\frac{S_e q_r}{2} + q_r(S_{max} - S_e) = \int_0^{S_{max}} q_r\left(1 - e^{-\beta S}\right) dS \qquad \text{Eq. (5-2)}$$

$$S_e = \frac{2}{\beta}\left(1 - e^{-\beta S_{max}}\right) \qquad \text{Eq. (5-3)}$$

After $7.2mm$ slip, S_{max}, the shear stud strength is decreased to $0.1q_r$ at $8mm$ slip to help numerical convergence.

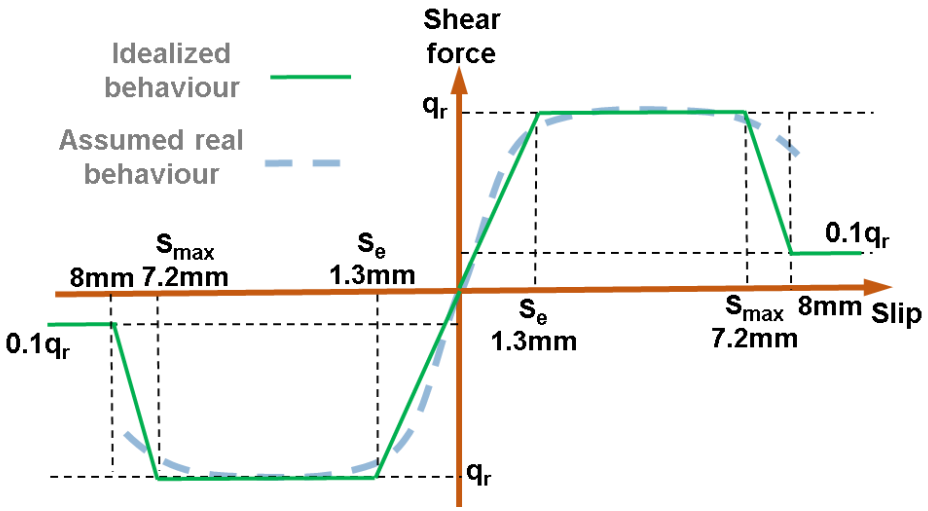

Figure 5-11. Idealized shear stud behaviour

Figure 5-12 shows the lateral force-slip behaviour of the model with and without gravity loads. As can be seen, in the absence of the gravity load, the total lateral force resistance of shear studs is equal to the sum of all shear stud strengths. However, in the presence of the gravity load, $55kN/m$, the ultimate lateral force resistance is decreased up to 18% in this case. The stiffness is also decreases because some shear studs experience unloading and some others yield at early stages of lateral loading.

Note that the maximum shear stud slip under gravity load was obtained 0.98mm in this model.

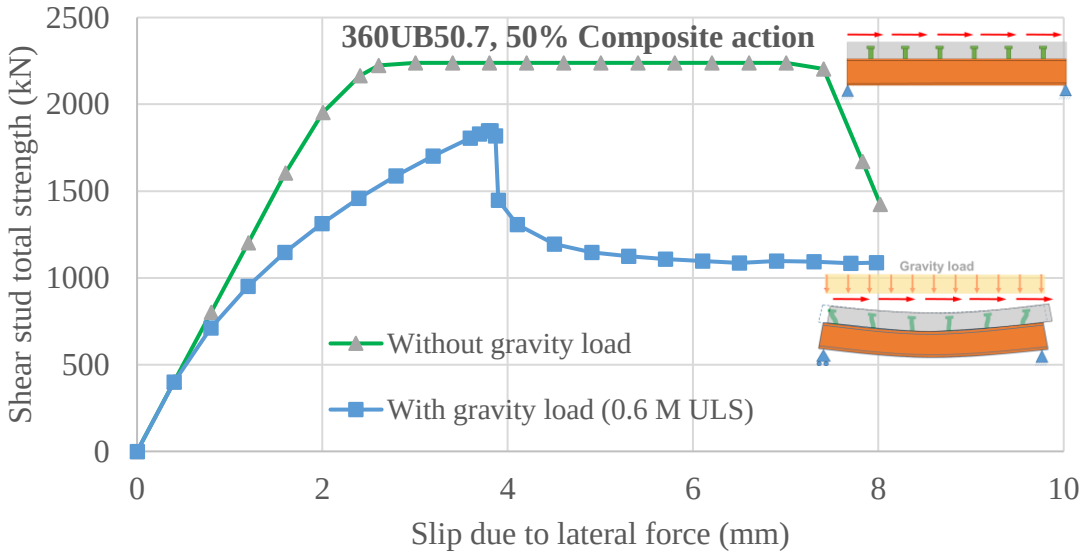

Figure 5-12. Lateral force-slip behaviour of model with 360UB50.7 beam section

5.3.3 Effective shear stud zone

Based on the lateral load carrying behaviour of shear studs on a beam described in Section 5.3.2, the total lateral force resistance of all shear studs is related to the level of shear stud slip under gravity loads and the fracture slip capacity of the shear studs. Increasing the gravity load or decreasing the composite action level may increase the interface shear force for the critical shear studs and/or slip of shear studs under gravity load.

Assume a situation that the strength capacity of all shear studs on a beam shown in Figure 5-13 is required to carry lateral forces. Considering the hysteresis behaviour of shear studs mentioned in Figure 5-5, the shear stud $3L$ on the left hand side of the beam, needs to experience lateral deformation $\delta = 2S_3$ to the right to reach a similar strength in the reversed direction. Similarly, after $\delta = 2S_3$ lateral slip, shear stud $3R$ on the right hand side of the beam experiences $S_3 + 2S_3 = 3S_3$ slip. This is based on the assumption that the diaphragm is stiffer than shear studs and axial deformation of the concrete slab is negligible in comparison with the lateral slip.

After imposing gravity load and lateral forces, if the maximum slip of the shear stud $3R$ on the right hand side of the beam is less than the ultimate slip capacity, S_u, it can still carry lateral forces when the shear stud $3L$ reaches its ultimate strength. This means the maximum slip of shear stud $3R$ under gravity load should be:

$$3S_3 < S_u \qquad \text{Eq. (5-4)}$$

Alternatively,

$$S_3 < {}^{S_u}/_{3} \qquad \text{Eq. (5-5)}$$

Otherwise, it fails before other shear studs on the opposite side reach their ultimate capacity, as was shown in Figure 5-8 Step 4.

Based on the above discussion, shear studs that experience slip larger than $S_u/3$ under gravity load should be excluded from calculating the total lateral force resistance of shear studs on a composite beam. Figure 5-13 shows the region of the beam that shear studs can carry lateral forces referred to as "effective shear stud zone". Note that due to the cyclic nature of the lateral deformations, shear studs with slip larger than $S_u/3$ are excluded from both sides of the beam.

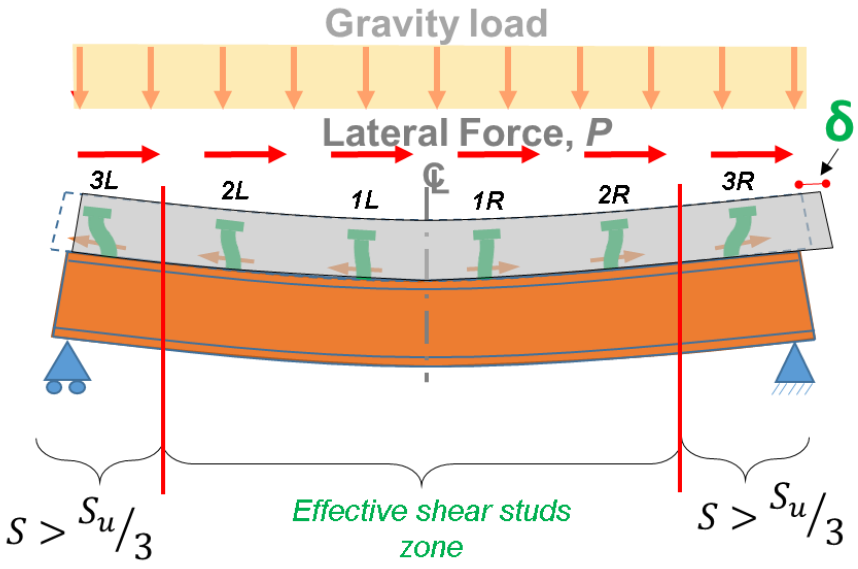

Figure 5-13. Effective shear studs in lateral force carrying mechanism

As it was mentioned in Section 5.2.2.1, the minimum slip limit for categorizing a shear stud as a ductile shear connector is 6mm under monotonic loading according to Eurocode 4 (2004) and Clause 3.6.1.1 of AS/NZS 2327 (2017). Johnson and Molenstra (1991) showed that the ultimate slip capacity of 19mm diameter shear studs under monotonic loading could be considered $S_{um} = 7.25mm$. Note that the maximum shear stud slip capacity was mainly obtained using monotonic test results in the literature. However, shear studs on the composite beams may be under cyclic loading and the ultimate slip limit may be lower than those of monotonic loading, $S_u \leq S_{um}$. In this study $S_u = S_{um}$ is considered due to lack of information about ultimate shear stud slip limit under reversed cyclic loading.

5.3.4 Composite action-lateral force interaction

The composite action between the steel beam and the concrete slab forms by transferring shear forces due to flexural moments at the steel-concrete interface. This causes axial compression forces in the concrete slab and tension forces in the steel beam as shown in Figure 5-14. The resultant moment of these compression and tension forces increase the beam strength compared to that of the steel beam alone.

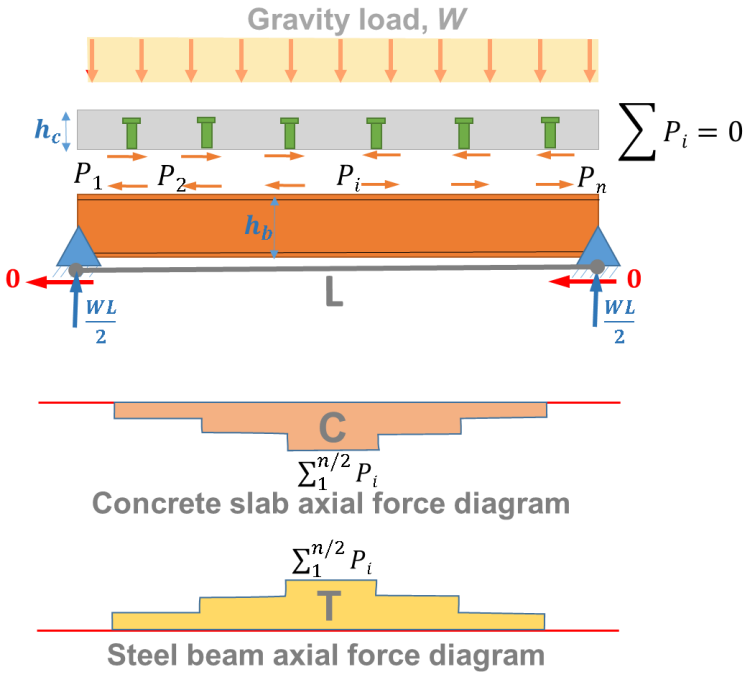

Figure 5-14. Axial force diagram of steel beam and concrete slab due to composite action

When the concrete slab is subjected to lateral forces as was explained in Section 5.3.1 the shear studs on the additive side of the beam experience loading while the others experience unloading and change in the force direction. Assume that the behaviour of all shear studs is elastic without any yielding. Therefore, the applied lateral force may increase or decrease the shear forces of the shear studs uniformly. This imposes additional axial forces to the steel beam and the concrete slab as shown in Figure 5-15.

As can be seen in Figure 5-15b-ii, the axial force diagram of the concrete slab is not changed due to lateral loading from that under gravity loading only as shown in Figure 5-15a-ii. While the axial force diagram of the steel beam is changed due to lateral forces (compare

Figure 5-15a-iii and b-iii). Decomposing the beam axial force diagram in Figure 5-15b-iv shows that it is the sum of axial forces due to composite action (gravity load) and lateral forces. Therefore the elastic assumption of shear stud behaviour leads to addition of the beam shear stud forces and maintaining the composite action between the concrete slab and the steel beam regardless of the level of imposed lateral force. The composite action effect shown in Figure 5-15b-ii and b-iv-α is the same as that in Figure 5-15a-ii and a-iii for concrete and steel respectively. The peak beam axial demands in Figure 5-15b-iii due to lateral force can increase or decrease depending on the sharing of force at the reactions.

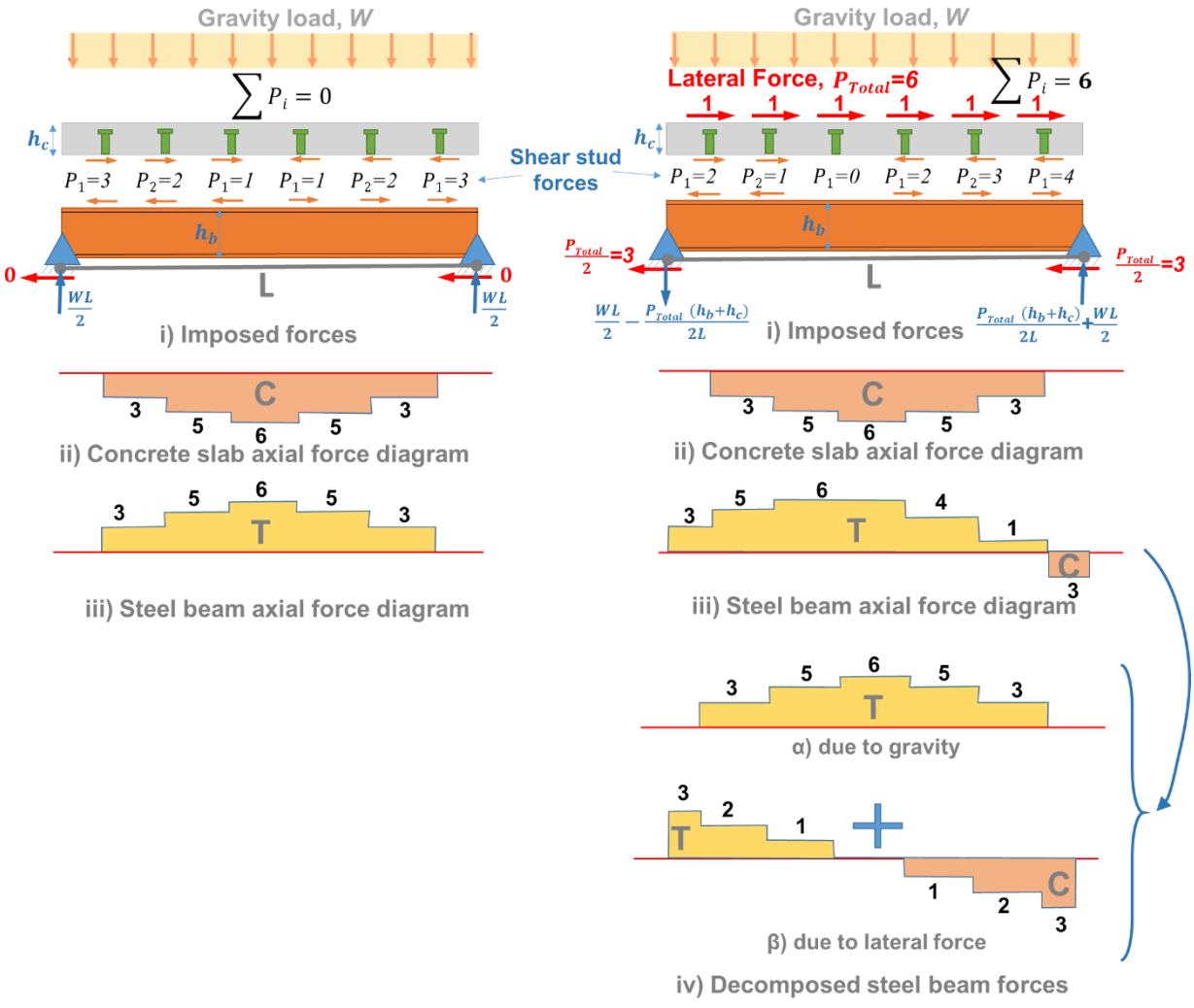

a) Composite beam subjected to gravity load

b) Composite beam subjected to gravity load and lateral forces

Figure 5-15. Axial force diagram of steel beam and concrete slab due to composite action and lateral forces assuming elastic shear studs

For yielding studs, such as those with the characteristics in Figure 5-11, lateral forces can cause different member axial forces, depending on the gravity load magnitude, composite action level, total beam height and lateral force level. When some shear studs yield, the gravity-induced axial forces and the lateral force induced axial forces can no longer be computed separately and added together to obtain the total force as interaction occurs. Figure 5-16 presents a situation that all shear studs are yielded in the same direction under lateral force and they all have the same shear force. Here, with the horizontal forces applied at the shear stud locations, each shear stud resists the horizontal force applied causing no net axial force in the concrete slab and axial force in the steel beam relates to the applied horizontal forces. Here, the applied gravity load has no effect on the concrete or steel beam axial forces and the composite beam has effectively lost its composite action to resist gravity loads.

Because composite action is lost, the flexural stiffness of the composite beam reduces to the sum of that from the bare steel beam alone plus that from the concrete slab alone. Since the concrete slab stiffness is small and the concrete cracks, the flexural stiffness to resist vertical loading is that from the steel beam alone. The maximum beam deflection may be computed considering the flexural stiffness of the steel beam alone.

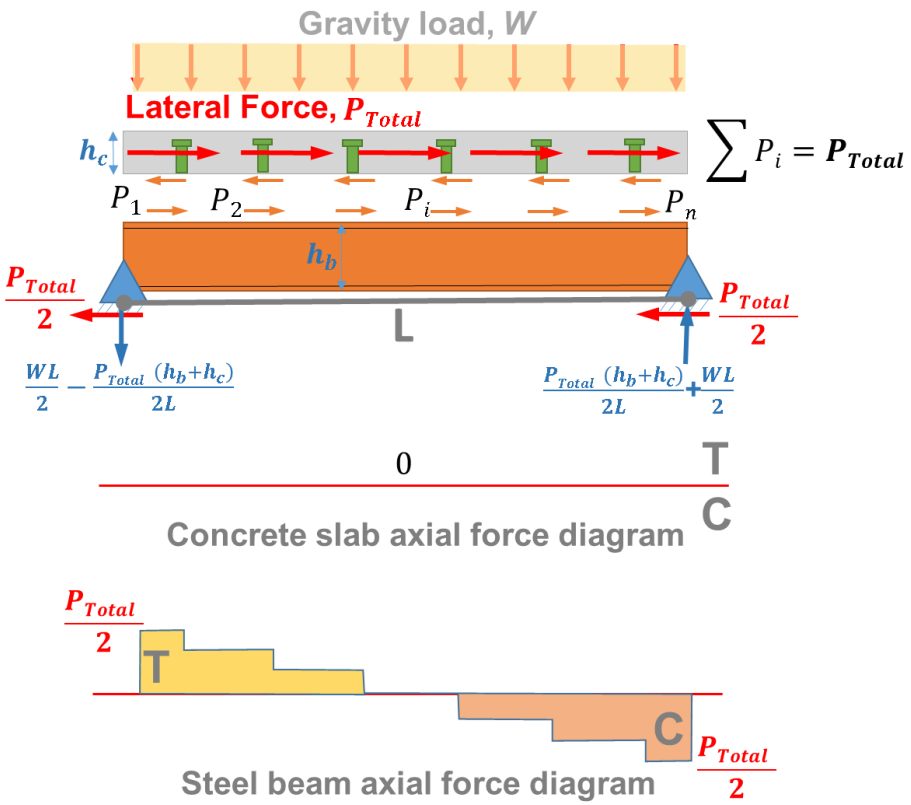

Figure 5-16. Axial force diagram of steel beam and concrete slab due to composite action and lateral forces considering the nonlinear behaviour of shear studs

An interesting consequence of this redistribution of shear stud forces due to shear stud yield is that the likelihood of failure of the critical shear studs (i.e. those at the beam end subject to deformation in the same direction from gravity and lateral forces) is greater than that if shear stud deformations were computed from either of these causes alone and then added. This is because the shear studs slip under gravity loads directly relates to the vertical deflection of the beam. Thus the loss of composite action which causes an increase of beam vertical deflecting increases the shear stud slips under gravity loads. This can be understood considering the beam in Figure 5-17a where under gravity loads alone shear stud "A" is subject to a shear slip, S, as shown in Figure 5-17a-iii. When lateral force is imposed, then shear stud "A" will undergo further deformation, δ, to the right as P_{Total} is applied to the right. When some or all of shear studs yield under lateral force, then shear stud "A" will undergoes further deformation, Δ, due

to loss of composite action and increase of beam vertical deflection as shown in Figure 5-17b-iii.

Considering the combination of lateral force and gravity loads, by increasing the lateral force, the shear slip demand of shear studs increases due to:

1) Lateral forces
2) Loss of composite action and increase of shear stud slip under gravity loads

These cause some shear studs to reach their maximum slip capacity before that sum of the initial shear stud slip under gravity load only, S, (composite beam) and the lateral deformation, δ, reach the ultimate slip capacity of the shear stud.

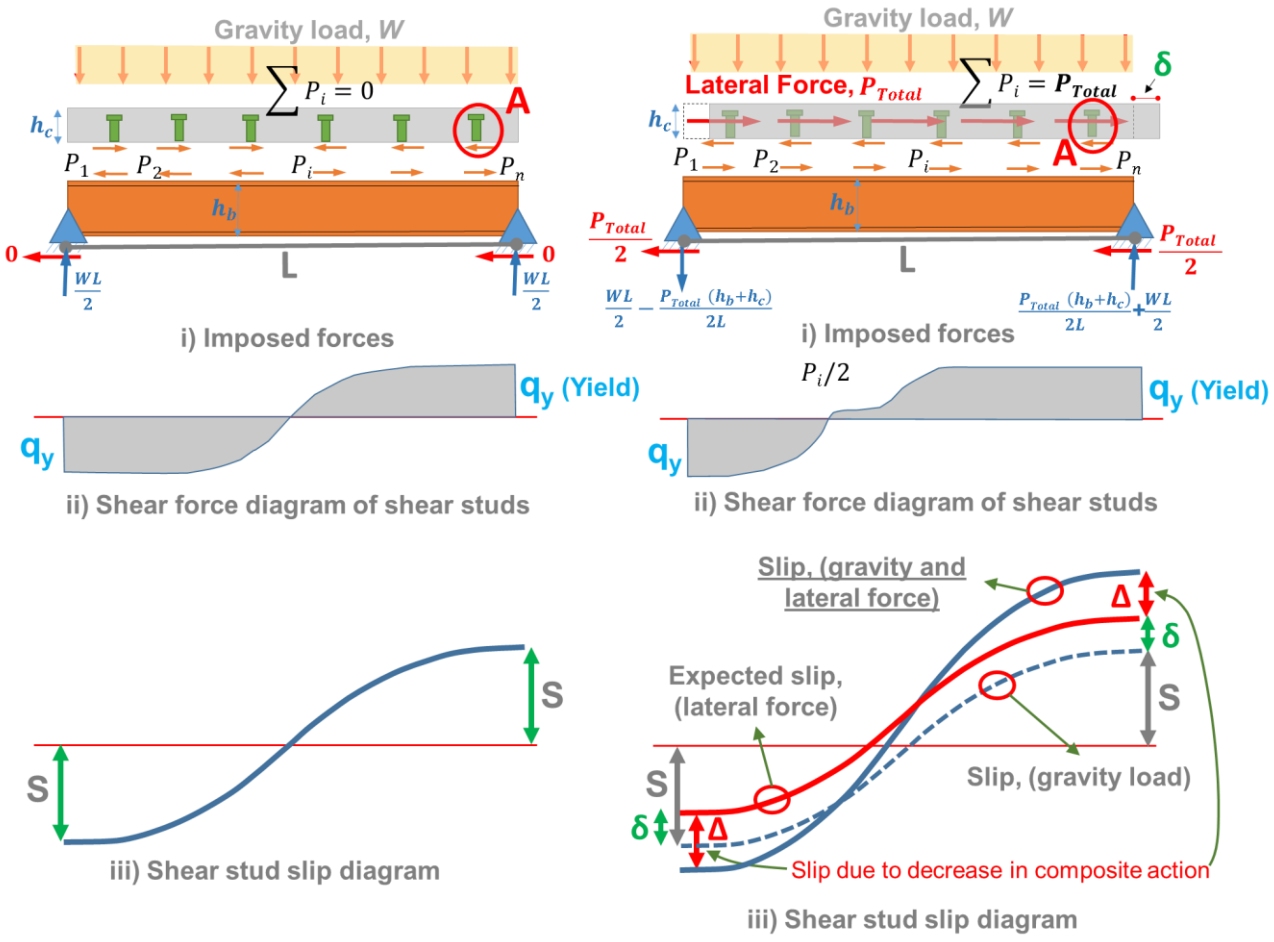

a) Gravity load alone b) Lateral + gravity load

Figure 5-17. Addition shear slip imposed to shear studs due to loss of composite action

For example, shear slips of the shear stud A, shown in Figure 5-17, under gravity loads considering 100% composite action and without composite action are $S = 1.4mm$ and $S + \Delta = 3.5mm$ respectively. The maximum slip capacity of this 19mm shear stud, S_u, is assumed to be $6mm$. After imposing lateral forces and without considering the loss of composite action effects, it is expected that the shear stud A can sustain $6 - 1.4 = 4.6mm$ before failure. However, because of loss of composite action due to yielding of some or all of shear studs, this shear stud reaches to fracture after $6 - 3.5 = 2.5mm$ lateral deformation.

- **FEM model example**

The FEM model used in Section 5.3.3 and Figure 5-9 for the 6m long beam is considered here to investigate the effect of lateral forces in decreasing the composite action. Vertical deflection of the composite beam mid-point under $55kN/m$ gravity load (causing 0.6 M_{ULS} from $1.2G + 1.5Q$) is obtained from the FEM model equal to $16.2mm$, shown in Figure 5-18a. After imposing lateral force, the vertical deflection at the mid-point at the peak lateral force resistance ($3.9mm$ lateral deformation as shown in Figure 5-12) increases from 16.2mm to $29.6mm$ as shown in Figure 5-18b. This shows that after imposing lateral force, composite action decreased and in this case the vertical deflection of the mid-point of the beam increase by about 82%.

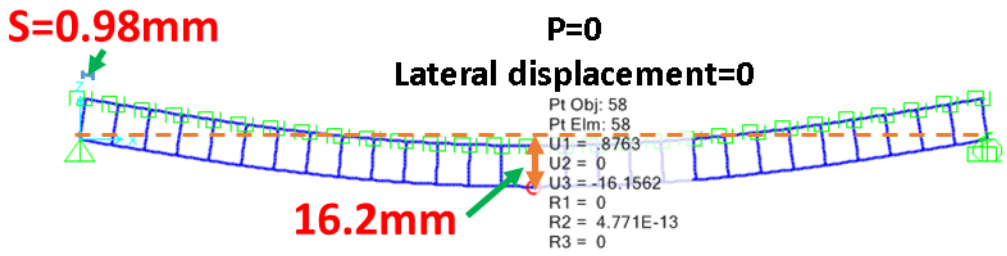

a) Vertical deflection due to gravity loads only

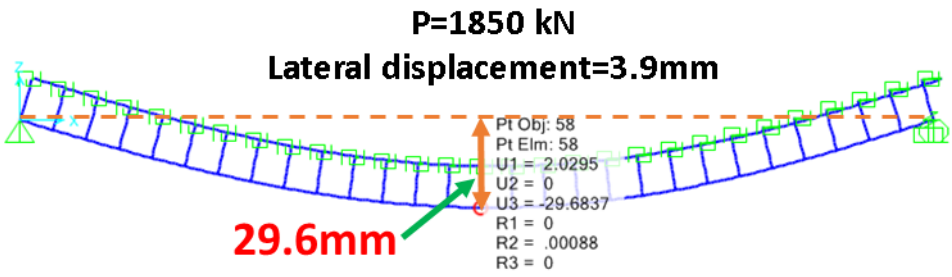

b) Vertical deflection at the peak lateral force resistance of shear studs

Figure 5-18. Vertical deflection of the model studied

Another effect of a decrease in composite action is an increase in the slip of shear studs under gravity load that was shown in Figure 5-17. In this model, the maximum shear stud slip at the beam ends was $0.98mm$ under gravity load only as shown in Figure 5-18a. Therefore considering an ultimate shear stud slip of $7.2mm$ and without considering the loss of composite action, it is expected that at $(7.2 - 0.98 =)6.22mm$ lateral displacement the lateral force resistance start decreasing due to the failure of shear studs at the far end of the beam. However, Figure 5-12 shows that the maximum lateral force resistance occurs at $3.9mm$. This is due to the fact that after imposing lateral force, composite action decreases gradually which increases the shear stud slip under gravity loads. This finding is consistent with the schematic slip diagram shown in Figure 5-17.

5.3.5 Composite beam vertical deflection subjected to lateral force

Beam vertical deflection is usually considered in design to prevent large deformations which may cause damage in non-structural elements or sensitive equipment that may be installed in special buildings.

In Section 5.3.4 it was shown that lateral force may decrease or eliminate the composite action. It was shown in Figure 5-16, when all shear studs yield, the beam vertical deflection becomes equal to the vertical deflection of the bare steel beam under gravity loads. This means the resisting moment provided in the steel beam due to the composite action (as shown in Stage 1 of lateral loading in Figure 5-19) eliminates when the direction and magnitude of all shear

stud forces are similar, as shown in Stage 3 of lateral loading in Figure 5-19. Further increasing lateral forces may cause failure in some shear studs on the additive (right hand) side of the beam. Failure of a number of shear studs changes the lateral force diagram imposed on the beam as shown in Stage 4 of lateral loading in Figure 5-19. This non-uniform reduction in the shear stud forces imposes additional moment to the beam adding the effect of gravity loads.

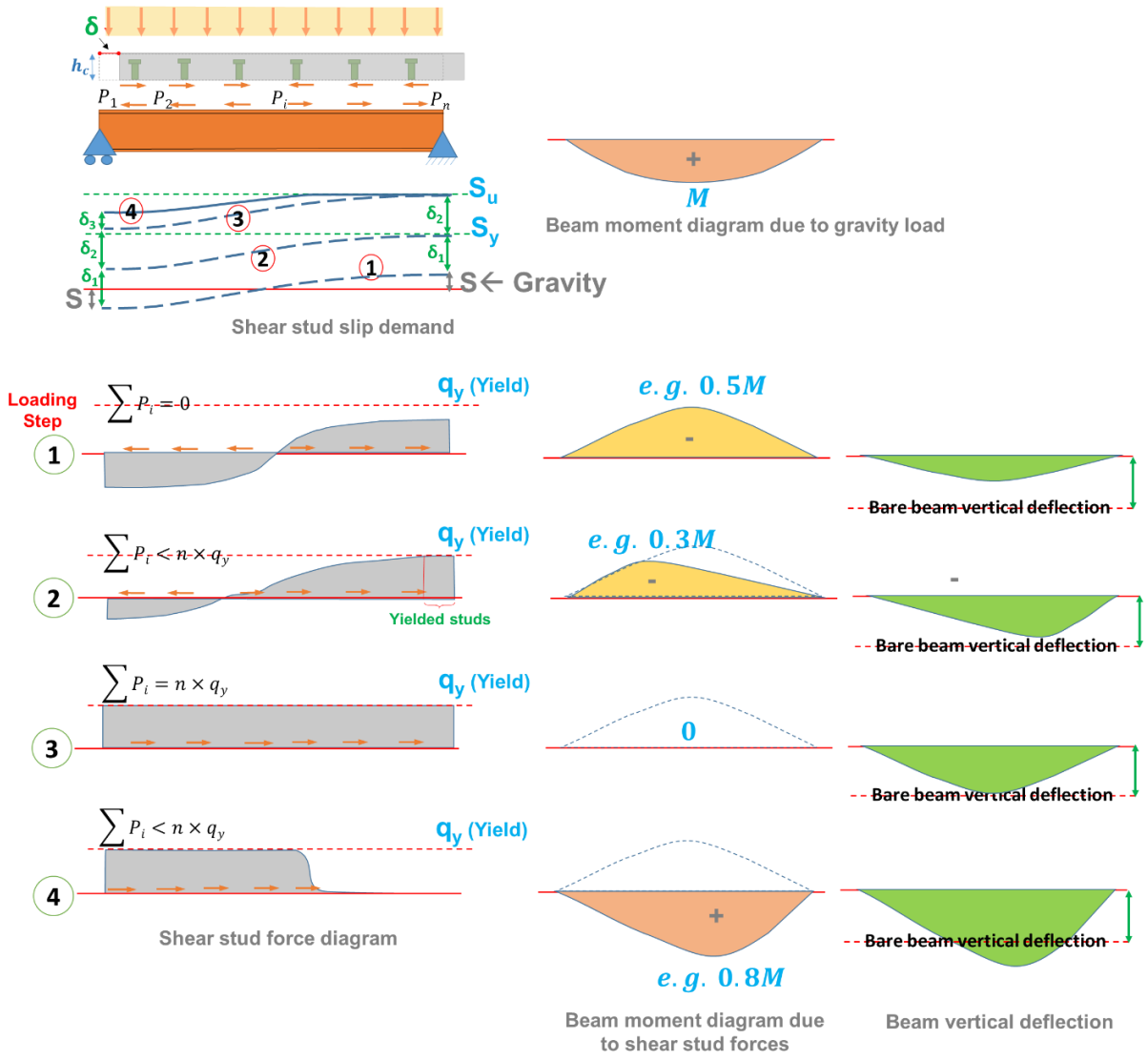

Figure 5-19. Increase in beam vertical deflection due to shear stud fracture

This may increase the vertical deflection of the composite beam more than the bare steel beam deflection under gravity loads.

- **FEM model example**

Vertical deflection of the beam mid-point of the studied model in Section 5.3.2 (Figure 5-9) is plotted against the lateral deformation of the concrete slab in Figure 5-20b. These results are obtained from the same analysis as those in Figure 5-12 which is replotted in Figure 5-20a for more convenience. This plot shows that with increasing the lateral deformation, composite action decreases and vertical deflection increases. At point 2, with $3.9mm$ lateral deformation the shear studs on the beam reached the maximum lateral force resistance, the vertical deflection of the beam mid-point obtained $29.6mm$.

The maximum elastic vertical deflection of the bare steel beam can be calculated $37.6mm$ for this case under $55kN/m$ gravity load. This vertical deflection is shown in Figure 5-19. Here, the vertical deflection of the beam increased further than the vertical deflection of the bare steel beam (0% composite action) by up to 46% at 8mm lateral deformation. This is consistent with the above explanations and Figure 5-19.

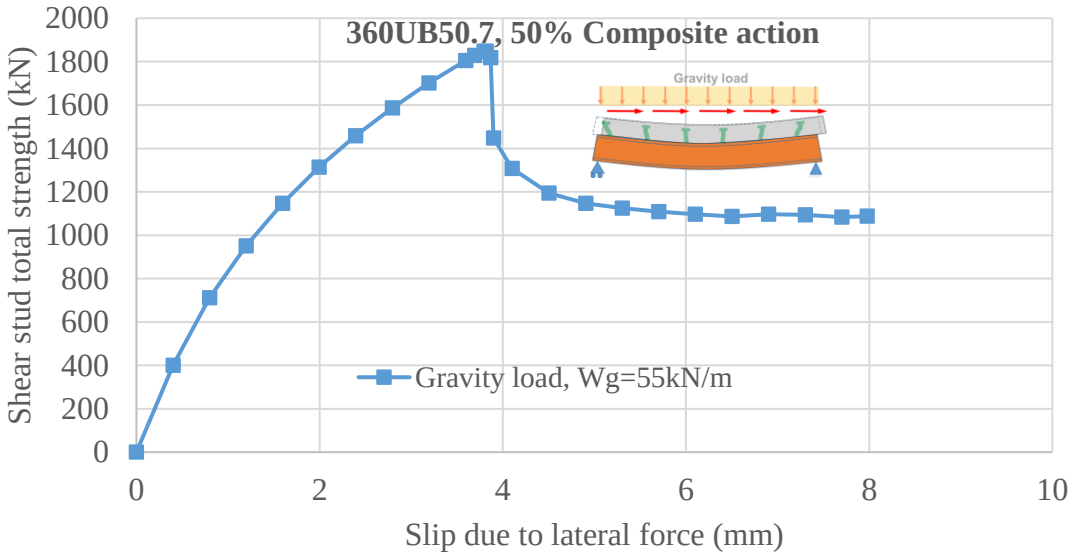

a) Lateral force-slip behaviour of FE model

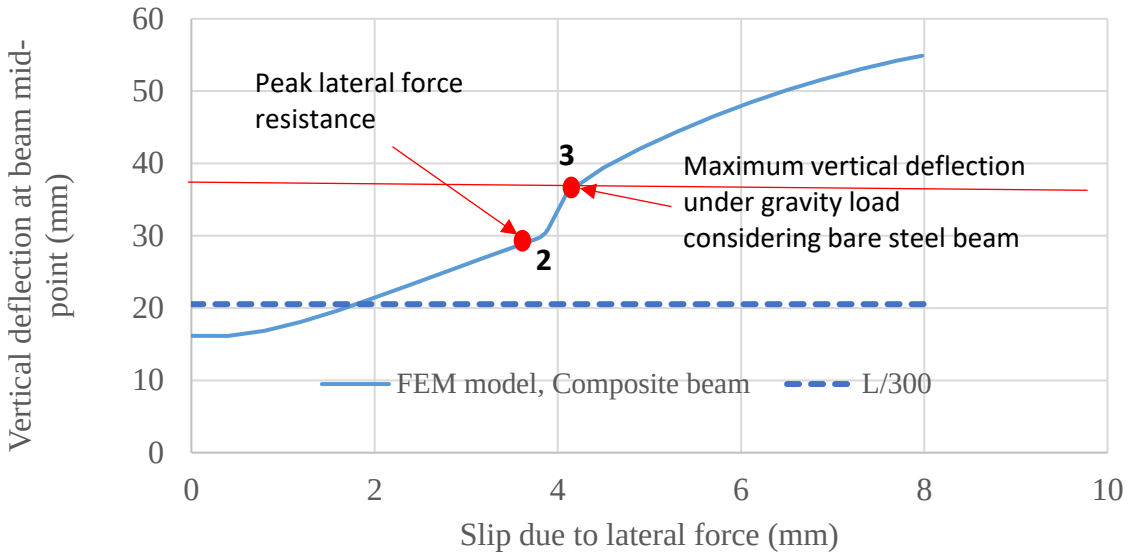

b) Beam mid-point vertical deflection

Figure 5-20. Vertical deflection of beam mid-point versus lateral deformation of the concrete slab

5.4 Estimation of required number of shear studs on beam for lateral loading considering beam gravity effects

In this section a method is proposed to obtain the total lateral force resistance of the shear studs when the beam is subject to the combination of gravity and lateral forces.

In Section 5.3.3 it was shown that the total number of shear studs that can contribute to the lateral force resistance is related to the shear stud behaviour and the level of maximum slip, S, that the shear studs experience under gravity loads. This can be achieved by excluding the shear studs that experience larger slip than the cyclic shear stud slip limit, $S_u/3$, under gravity loads. Therefore, shear stud slip under gravity load is required to obtain the number of shear studs on the beam contributing in lateral force resistance.

In Section 5.3.4 it was shown that imposing lateral force to the concrete slab can decrease or eliminate the composite action effects depending on the number of yielded shear studs. Therefore, for calculating shear stud slip demands under gravity loads, shear stud slip due to loss of composite action, Δ, as shown in Figure 5-17, should be considered. Generally, calculating the level of composite action loss is a complex problem because:

i. Yield/fracture of shear studs occurs on one side of the beam (where the slip due to gravity load and lateral force are additive), and

ii. The shear stud behaviour is nonlinear

Here, it is conservatively assumed that at peak lateral force resistance, all composite action is lost. Therefore, the non-composite beam properties are used to calculate the steel beam-concrete interface slip.

5.4.1 Shear stud slip calculation

Calculating the shear stud slip in a composite beam is a complex problem and it requires consideration of equilibrium and compatibility conditions simultaneously. This may be conducted using either differential equations or numerical solutions. The closed form solution to calculate the shear stud slip considering totally elastic shear studs was provided by Johnson (2008). Considering the nonlinear behaviour of shear studs increases the complexity and requires to solve a second order nonlinear differential equation or a system of linear differential equations. Appendix H presents a closed-form solution for calculating the shear stud slip in composite beams considering the nonlinear behaviour of shear studs. In this analytical solution, the shear stud behaviour is idealised with an elastic-perfectly plastic behaviour.

Two construction conditions, propped and unpropped, can be considered for calculating the shear stud slip. For a propped composite beam, both the steel beam and the concrete slab contribute in carrying gravity loads from the point that the props are removed. In an unpropped composite beam, the bare steel beam carries the gravity load of the steel beam and the concrete slab or any other gravity loads that are imposed before concrete hardening. After concrete hardening, shear forces can be transferred between the steel beam and the concrete slab to form the composite action and carry additional gravity loads compositely. The shear stud slips for both propped and unpropped beams are investigated in the following.

5.4.1.1 Propped composite beam

The shear slip value at the beam-slab interface at every point of the beam is equal to the sum of the elongation of the bottom fibre of the slab cross-section, $\varepsilon_c(x)$, and contraction of the top fiber of the beam cross-section, $\varepsilon_b(x)$, over the length. For calculating the elongation and contraction of the concrete and the steel members, the beam moment equation, $M(x)$, is required. In this study, it is assumed that the beam is subjected to uniformly distributed gravity load, W.

Bending moment demand of the beam shown in Figure 5-21 at every point along the beam length, $M(x)$, can be obtained using:

$$M(x) = \frac{W}{2}\left[L\left(\frac{L}{2} - x\right) - \left(\frac{L}{2} - x\right)^2\right] \qquad \text{Eq. (5-6)}$$

$$= -\frac{Wx^2}{2} + \frac{WL^2}{8}$$

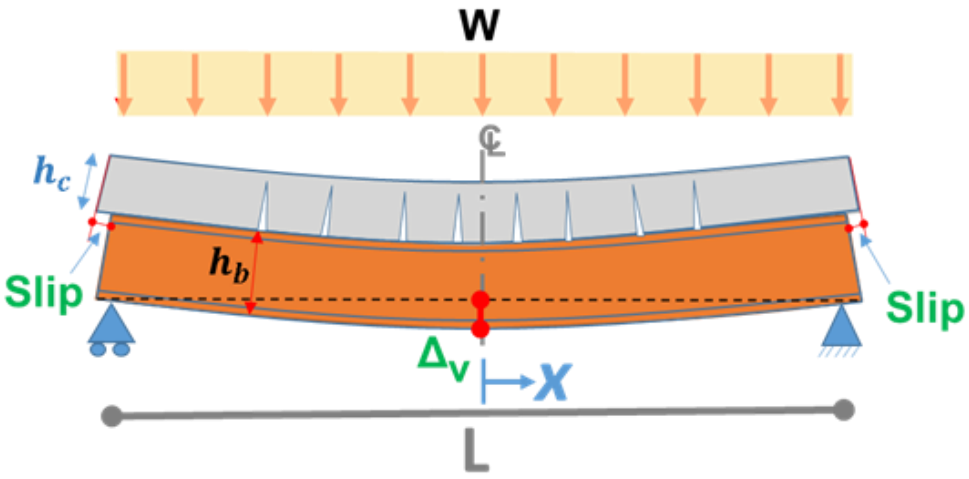

Figure 5-21. Schematic view of composite beam subjected to gravity loads

Solid mechanics relationships can be used to calculate the strain at the top fibre of the steel beam in the composite beam cross-section, $\varepsilon_b(x)$. The steel beam total height, moment of inertia and elastic modulus are denoted by h_b, I and E respectively. Here, it is assumed that all moment is carried by the steel beam (non-composite beam).

$$\varepsilon_b(x) = \frac{M(x)h_b}{2EI} \qquad \text{Eq. (5-7)}$$

The flexural stiffness of the concrete is ignored due to the concrete cracking. To calculate the elongation of the bottom fibre of the slab cross-section, $\varepsilon_c(x)$, it is assumed that the concrete slab curvature is equal to the steel beam curvature. The strain, $\varepsilon_c(x)$, does not occur in the concrete because of the concrete cracks. Instead, this represents an average strain at the level of the bottom of the concrete.

$$\varepsilon_c(x) = \frac{M(x)h_c}{EI} \qquad \text{Eq. (5-8)}$$

Where h_c is the concrete slab thickness. Note that if a steel decking composite floor was used, the total slab height is equal to the rib height and the topping.

Total slip, $S(x)$, at every point of the beam is equal to the integration of the sum of $\varepsilon_b(x)$ and $\varepsilon_c(x)$ from the maximum moment location to the point of interest. It is zero at the center of the beam where $x = 0$. Here, d is equal to $2h_c + h_b$. Substituting Eq. (5-6) into Eq. (5-10) and knowing $S(x) = 0$ where $x = 0$ gives:

$$S(x) = \int_0^x \varepsilon_c(x) + \varepsilon_b(x)\, dx \qquad \text{Eq. (5-9)}$$

$$S(x) = \int_0^x \frac{M(x)d}{2EI} dx \qquad \text{Eq. (5-10)}$$

$$= \frac{d}{2EI}\left[-\frac{Wx^3}{6} + \frac{WxL^2}{8}\right] + C$$

$$S(x) = \frac{Wd}{4EI}\left[\frac{L^3}{12} - \left(\frac{x+L}{3}\right)\left(\frac{L}{2} - x\right)^2\right] \qquad \text{Eq. (5-11)}$$

The maximum slip occurs at $x = \pm\frac{L}{2}$ which equals to:

$$S_{max} = \frac{WdL^3}{48EI} \qquad \text{Eq. (5-12)}$$

The vertical deflection, Δ_v, of a simply supported general beam under gravity load, W, may be obtained as:

$$\Delta_v = \frac{5WL^4}{384EI} \qquad \text{Eq. (5-13)}$$

Substituting Eq. (5-13) into Eq. (5-12), maximum shear stud slip, S_{max}, can be obtained in terms of the vertical beam deflection, Δ_v:

$$S_{max} = 1.6\frac{\Delta_v d}{L} \quad \text{Eq. (5-14)}$$

Note that Δ_v should be calculated using the bare steel beam stiffness without considering composite action.

In Equations (5-5 to 5-13), W is considered as the total available dead load and the live load at the time that lateral force is imposed. This gravity load level can be used for calculating the maximum slip for a propped beam which all the imposed gravity loads contribute in the beam-slab interface slip.

5.4.1.2 Unpropped composite beam

For an unpropped composite beam, parts of the dead load which usually are the self-weight of the concrete slab and the steel beam are carried by the bare steel beam. Shear stud deformations and slip at beam-slab interface occur after concrete hardening. Thus the gravity load of the unpropped condition, $W_{unpropped}$, can be obtained by reducing the concrete slab self-weight. i.e. $W_{unpropped} = W - W_{self\ weight\ of\ steel\ and\ concrete}$.

Similarly, for an unpropped case, the beam deflection, Δ, may be obtained as:

$$\Delta_v = \frac{5(W_{unpropped})L^4}{384EI} \quad \text{Eq. (5-15)}$$

The maximum shear stud slip, S_{max}, can be obtained similar to the propped composite beam using Eq. (5-14).

5.4.2 Obtaining effective shear stud zone

To calculate the lateral force resistance of shear studs on a beam, shear studs that are expected to experience shear slip larger than their ultimate shear slip capacity should be excluded. This may be achieved by using the maximum shear stud slip, S_{max}, derived for both

propped and unpropped beams in Sections 5.4.1.1 and 5.4.1.2, and the effective shear stud zone discussed in Section 5.3.3. For obtaining the effective shear stud zone on a beam, shear studs that experience cyclic slip larger than $S_u/3$ under gravity loads should be excluded.

Using Eq. (5-11), the magnitude of shear stud slip at any point on the beam length can be obtained considering uniform distributed gravity load. Figure 5-22 plots the normalised slip versus normalised beam length using Eq. (5-11). This plot shows the trend of change in the shear stud slip demand along the beam length.

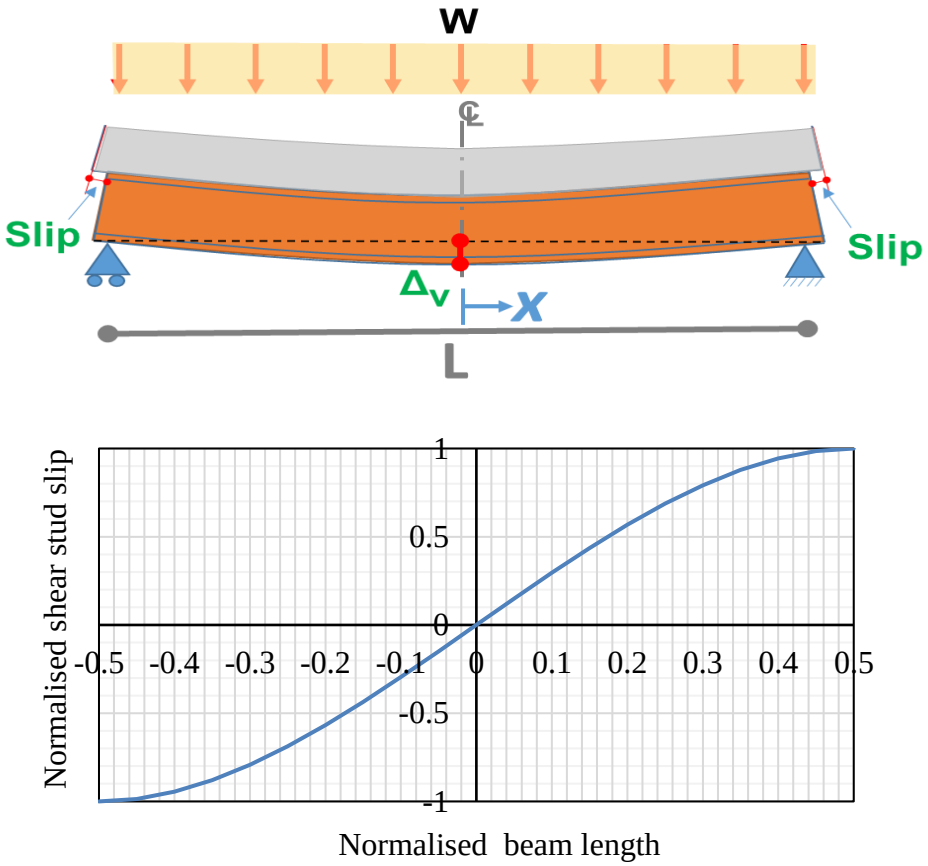

Figure 5-22. Normalised slip versus normalised beam length

Using this plot, parts of the beam that experience larger slips than the specified limit can be obtained. Alternatively, shear studs that are required to carry lateral forces, should be placed within the region that the shear stud slip under gravity loads is lower than $S_u/3$.

For example, if the maximum allowable cyclic slip, $S_u/_3$, is assumed 2.4mm and the maximum slip demand, Eq. (5-14), is calculated 3mm, then using Figure 5-23, it can be found that $0.6L$ (i.e. from $-0.3L$ to $+0.3L$) of the middle part of the beam experience lower slip than 2.4mm. The number of shear studs placed within this zone can be used for carrying lateral force. Note that due to the cyclic nature of the lateral forces, shear studs with slips larger than $S_u/_3$ are excluded from both sides of the beam. If more shear resistance is required, more shear studs need to be placed at the effective shear stud zone.

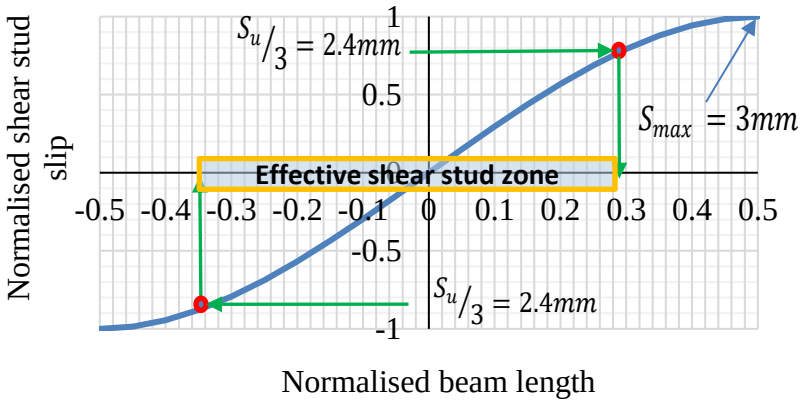

Figure 5-23. An example for calculating effective shear stud zone

A designer can select an appropriate shear connector deformation limit and the amount of gravity load, W, at the time of the earthquake event to calculate bare steel beam vertical deflection, Δ_v. The gravity load, W, may also include vertical earthquake excitation and account for the propped and unpropped conditions.

5.5 Case study

In this section thirty-three FE models including non-composite, partially-composite and fully-composite beams with different span lengths and section heights are studied. This study investigates:

i. Parameters, such as composite level and total beam height, on the lateral force-gravity load interaction

ii. The accuracy of the proposed method to calculate the lateral force resistance of shear studs on a composite beam

iii. The vertical deflection of the beam mid-point

5.5.1 Models geometry and material properties

Three steel beam sections; 180UB22.2, 360UB50.7 and 610UB125, are considered for modelling 4m, 6m and 10m long span beams respectively. The spacing between the beams is assumed 2000mm. The dimensions of the concrete slabs on top of each steel beam section are shown in Figure 5-24. The effective width of each beam is determined considering the beam span according to NZS3404 (2007) Clause 13.4.2.1. Here, it is given as:

$$b_{eff} = min\begin{cases} Beam\ spacing \\ Span/4 \end{cases} \qquad \text{Eq. (5-16)}$$

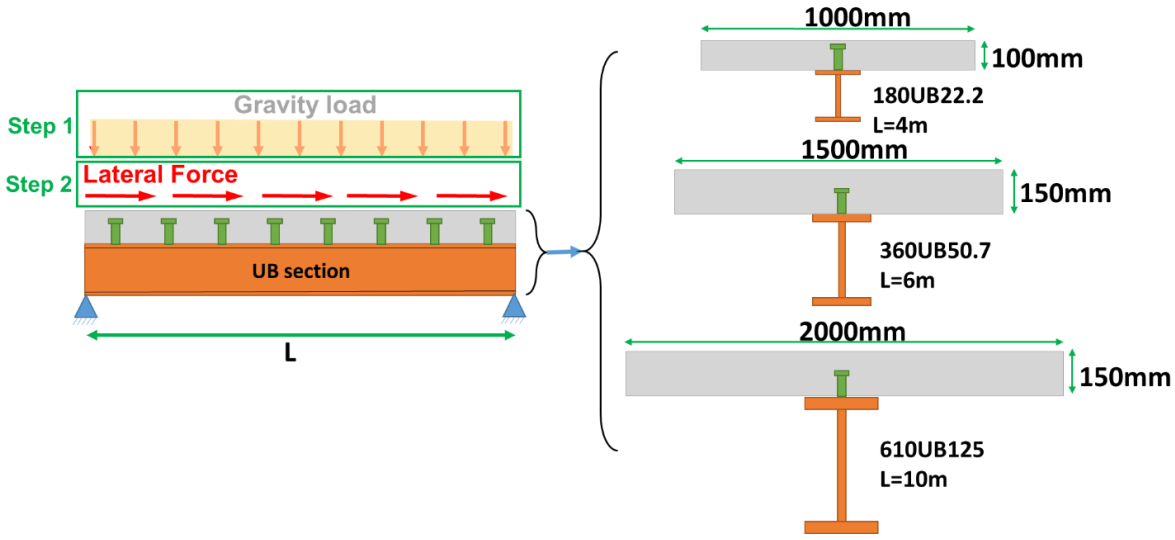

Figure 5-24. Schematic view of the studied models

The yield stress, F_y, and elastic modulus, E_s, of the steel material are considered to be $340MPa$ and $200GPa$ respectively. The compressive strength, f_c', and elastic modulus, E_c, of concrete are considered $30MPa$ and $25GPa$ respectively. In the models the concrete and the steel materials are considered elastic up to their yield point while yielding is allowed in the shear studs using the idealized shear stud behaviour shown in Figure 5-11.

5.5.2 Loading and analysis assumptions

In these analyses all the beams are considered simply supported for carrying gravity loads. The analyses are performed in two steps. First, the gravity load is applied. In this step, one end of the beam has a pinned support and the other end has a roller connection. This is because the steel beam may experience some elongation due to composite action and with this support configuration the elongation is allowed without any axial force reaction. The steel beam axial elongation under gravity loads in Model 11 with 180UB, 360UB and 610UB beam sections was obtained 1.5mm, 2.5mm and 3.4mm respectively. In the second step, after imposing the gravity loads the roller support changes to the pinned support to carry lateral forces. Then the lateral force is imposed on the concrete slab using the displacement-control analysis.

The strength and stiffness of all the studied beams shown in Figure 5-24 were calculated using equations provided in NZS3404 (2007) to obtain an appropriate gravity load for the step one of the analyses. The uniformly distributed gravity load corresponding to both the beam strength and the beam stiffness (maximum recommended vertical deflection, $L/300$) were considered to obtain a reasonable gravity load for analysis. The gravity load was calculated equal to the minimum of 0.6 times the gravity load corresponding to the composite beam strength, M_{pb}, (representing reduced gravity load at the time of earthquake) and the gravity load correspond to the vertical deflection limit, Eq. (5-17). All models with different composite actions are analysed with and without the gravity loads to compare the lateral force carrying behaviour considering the interaction with the gravity loads.

$$W_g = min\begin{cases} W\ causing\ \Delta = L/300 \\ W\ causing\ 0.6M_p \end{cases} \qquad \text{Eq. (5-17)}$$

Four composite action levels considered in this study were 10%, 25%, 50% and 100%. Models with 10% composite action represent a condition that the beam is not designed as a composite member and the shear studs are placed to carry lateral forces only. Models with 25%

composite action are considered to investigate the design recommendations provided by AISC/ANSI 360-16. Where this value of 25% was recommended as a minimum composite action as described in Section 5.2.1.

Friction between the concrete slab and the steel beam is not considered in these models and it is assumed its effect may be negligible. For example, consider a composite beam with a dead load of G=5kPa and live load of Q=3kPa with 5m tributary area and load combination of G+0.3Q, will provide 5.9×5=29.9 kN/m gravity load acting on the beam. Assuming friction coefficient of μ=0.3 between the steel beam and concrete slab result in shear force transfer capacity of 0.3×29.9=8.85 kN/m. Assuming maximum longitudinal spacing of shear studs to be 400mm according to Clause 13.3.2.3 of NZS3404, the shear force transfer through friction over this length would be 8.85kN/m×0.4m=3.54kN. Comparing this value with the shear capacity of a 19mm shear stud in a 30MPa concrete which is about 80kN (per stud), shows that the shear force transfer through friction may be neglected. Note that shear stud strength has been obtained from tests which implicitly include the friction effect however, it was not explicitly considered in this study.

5.5.3 Modelling method

To model the composite beams SAP2000 software (2015) is used. Figure 5-25 shows the modelling method used in this study. The beam and concrete elements are placed at the centre line of the steel beam and the concrete slab respectively. In the slab chosen, the centre of the slab differed from the centre of elastic compressive part of the slab (considering concrete cracking) by up to 15mm. The difference in the maximum shear stud slip from the FE model and the closed form solution, described in Appendix H, was less than 10%.

Nonlinear link elements are used to model shear studs. The shear stud nonlinear links are connected to the concrete slab and the steel beam elements using rigid links as shown in Figure 5-25. In this model the flexural stiffness of the concrete slab is ignored due to concrete cracking.

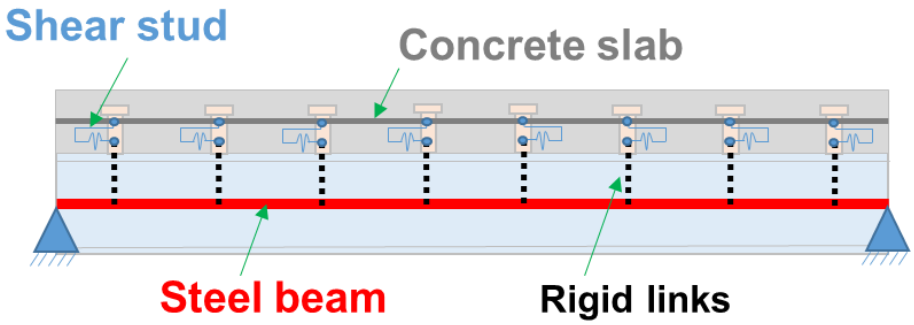

Figure 5-25. Method used for modelling composite beam

5.5.4 Results

Results of the analysed models are investigated in terms of i) lateral force-slip behaviour, ii) accuracy of the proposed method, and iii) vertical deflection of the beam mid-point.

5.5.4.1 Lateral force-slip behaviour

Figure 5-26 to Figure 5-29 show the lateral force-slip behaviour of the studied models with and without gravity load. As can be seen in these Figures, in the absence of gravity load (Models 1, 3, 6 and 9 with different beam sections), the total lateral force resistance of shear studs is equal to the sum of all shear stud strengths. However, in the presence of gravity loads (Models 2, 4, 5, 7, 8, 10 and 11 with different beam sections), the ultimate lateral force resistance is decreased in some cases and the overall stiffness is decreased in all the models.

From the analyses conducted it is found that increasing the level of gravity load, W_g, decreased the total lateral force resistance provided by the shear studs. This is because higher gravity load, W_g, leads to larger shear stud slip, S_{max}, as described in Section 5.3.2. The results are consistent with the explanations provided in that Section. Also, in the presence of gravity loads, increasing the beam total height decreased the lateral force resistance of the shear studs.

In the beams with low (10%) composite action and low gravity load, W_g, that the shear studs are provided to carry lateral forces only, it is found that the ultimate total lateral force resistance of shear studs for the beam section 180UB is equal to the sum of all shear stud strength as shown in Figure 5-26a. The 360UB model with 10% composite action showed a

similar behaviour, as shown in Figure 5-26b. However, the lateral force-slip plot for 180UB model shows more ductile behaviour than for the 360UB model. In the model with the 610UB steel section with a 10% composite action, the lateral force resistance of the shear studs was about 18% lower than the sum of all shear stud strengths. This is because increasing the total beam height increases the shear slip at the concrete slab-steel beam interface. This was shown in Eq. (5-14) where the shear stud slip has a linear correlation with the total beam height in a non-composite beam. Calculated values of S_{max} were 1.48mm, 2.76mm and 4.06mm for the 180UB, 360UB and 610UB beams respectively. Note that here d is considered equal to $h_c + h_b$ to be consistence with the FE models because the concrete cracking was not considered in these models.

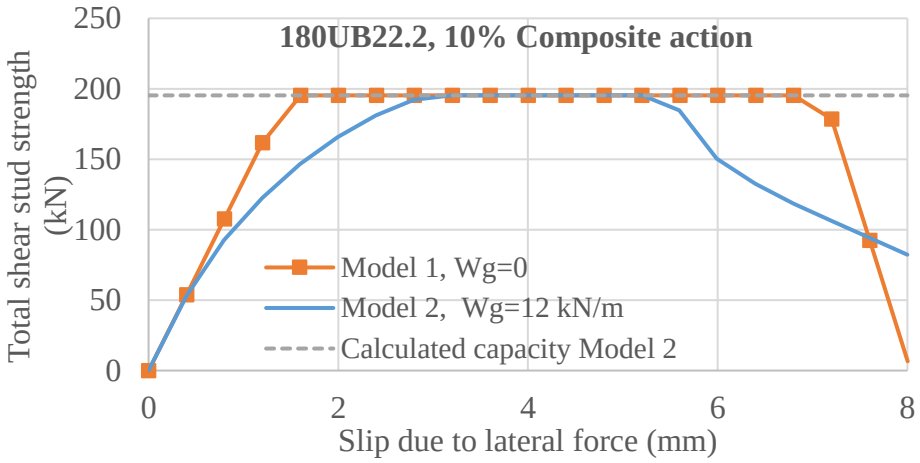

a) 10% composite action, 180UB22.2

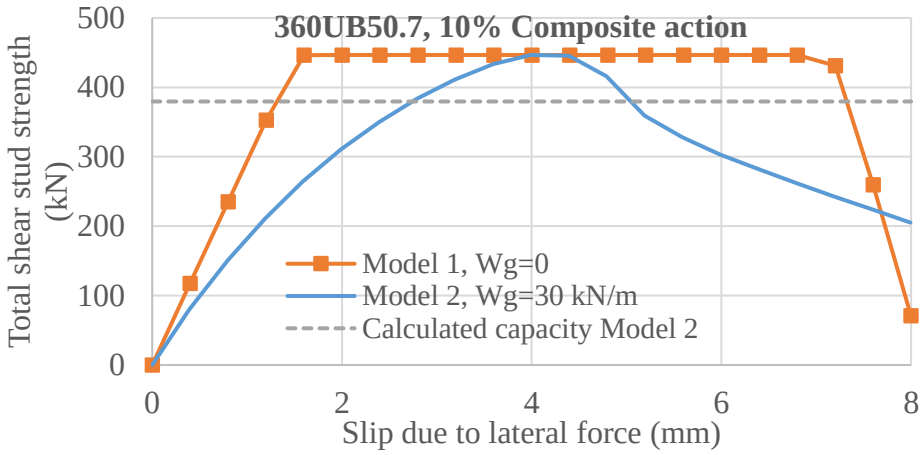

b) 10% composite action, 360UB50.7

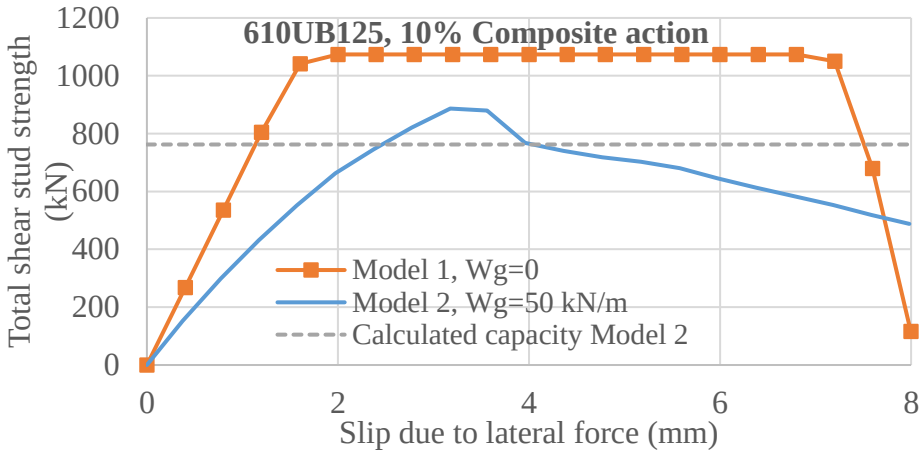

c) 10% composite action, 610UB125

Figure 5-26. Lateral force-slip of non-composite beams

Considering the beam vertical deflection limit of $L/300$ and assuming the shear stud slip limit of $2.4mm$ ($= {}^{S_u}/_{3}$ as discussed in Section 5.3.3), the maximum beam total height of a non-composite beam at which all shear studs can be used to provide lateral force resistance, to prevent all shear studs from fracture, is found using Eq. (5-14).

$$1.6\frac{\Delta_v d}{L} \leq 2.4mm \qquad \text{Eq. (5-18)}$$

Substituting $\Delta_v = L/300$ gives

$$d \leq 450mm \qquad \text{Eq. (5-19)}$$

Eq. (5-19) shows that in a non-composite beam, with total beam height lower than 450mm, all shear studs can be considered for lateral force resistance. The total height of models with 180UB, 360UB and 610UB beam sections including the concrete slab thicknesses are equal to 279mm, 506mm and 762mm respectively. This equation provides consistent results with FEM models where all shear studs of 180UB beam contributed in lateral force resistance for this low (10%) level of composite action. In 360UB model some shear studs fractured after reaching to the ultimate strength and in 610UB the ultimate strength was lower than the sum of all shear stud strengths.

The results of partially composite beams with 25% composite action show similar trends to the non-composite beams. Again, lateral force resistance decreases with increasing the total beam depth. The behaviour of the 610UB composite beam with 25% composite action is shown in Figure 5-27c. This Figure indicates that the total lateral force resistance of shear studs on the 25% partially composite beam is lower than the sum of all shear stud strength. In Model 4, shown in Figure 5-27c, which is considered as bare steel beam and 25% composite action is provided only to carry lateral forces, the total lateral force resistance of shear studs is lower than the sum of all shear stud strength. Therefore, providing 25% composite action cannot ensure that the shear studs do not experience large slips under the gravity loads. Based on these results it is recommended to calculate the lateral force resistance of shear studs even though more composite action than the required level was provided.

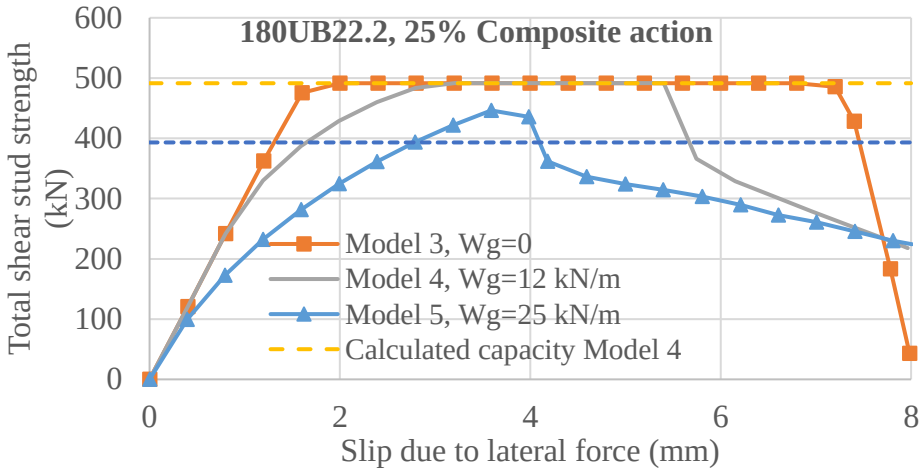

a) 25% composite action, 180UB22.2

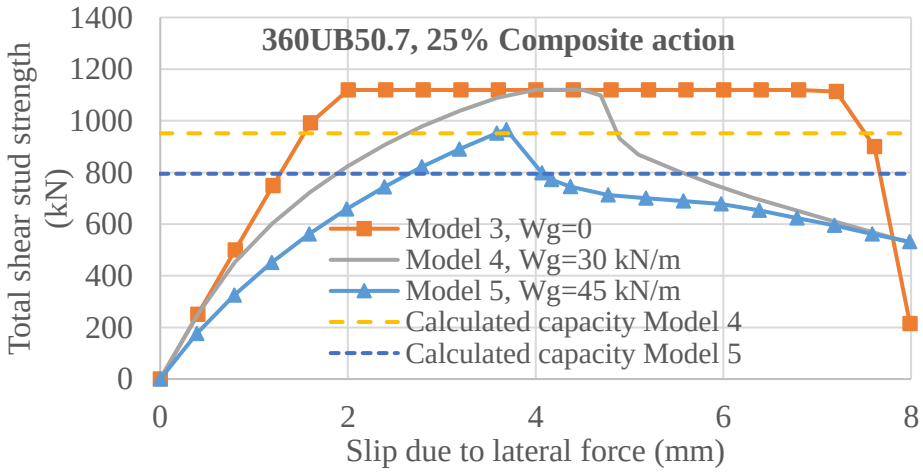

b) 25% composite action, 360UB50.7

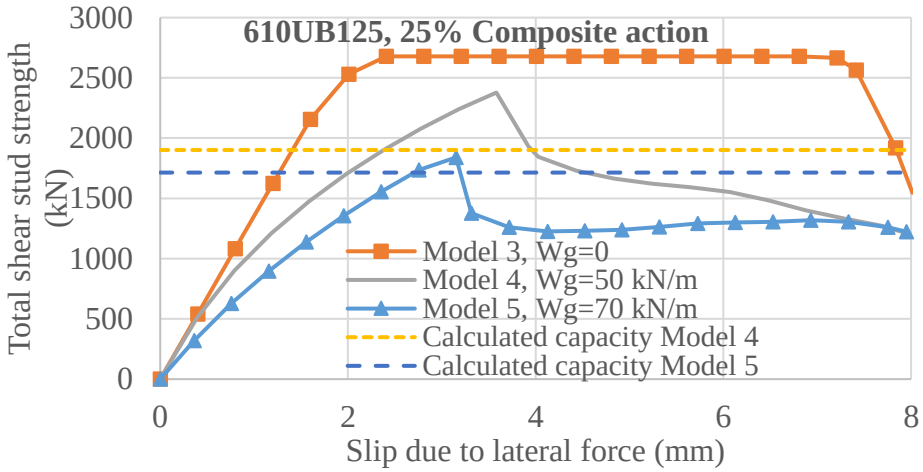

c) 25% composite action, 610UB125

Figure 5-27. Lateral force-slip of models with 25% composite actions

Similar results as 25% composite action were found for 50% partially composite beams and fully composite beams as shown in Figure 5-28 and Figure 5-29.

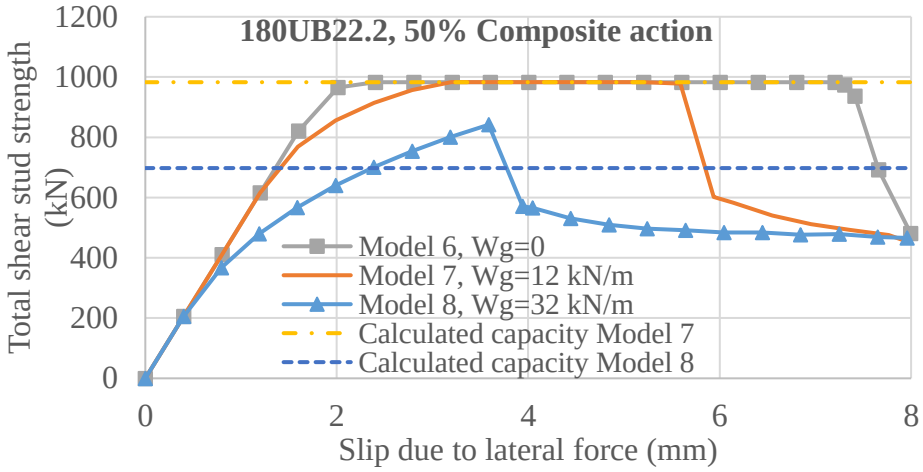

a) 50% composite action, 180UB22.2

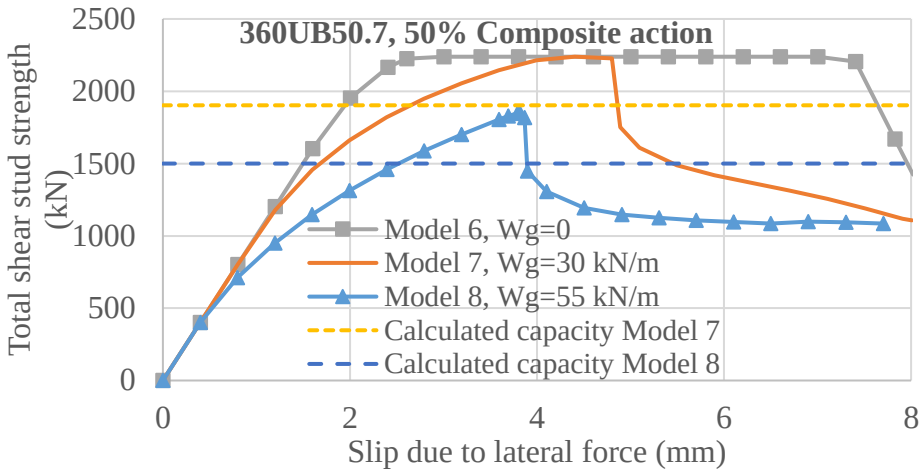

b) 50% composite action, 360UB50.7

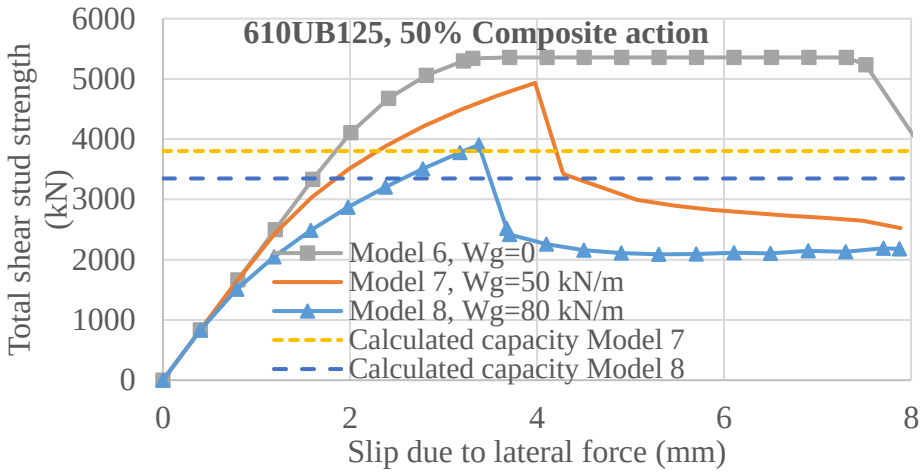

c) 50% composite action, 610UB125

Figure 5-28. Lateral force-slip of models with 50% composite actions

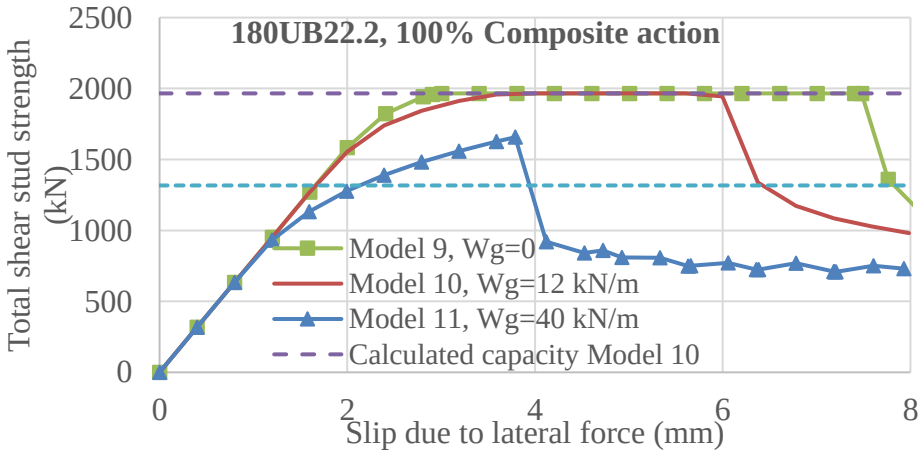

a) 100% composite action, 180UB22.2

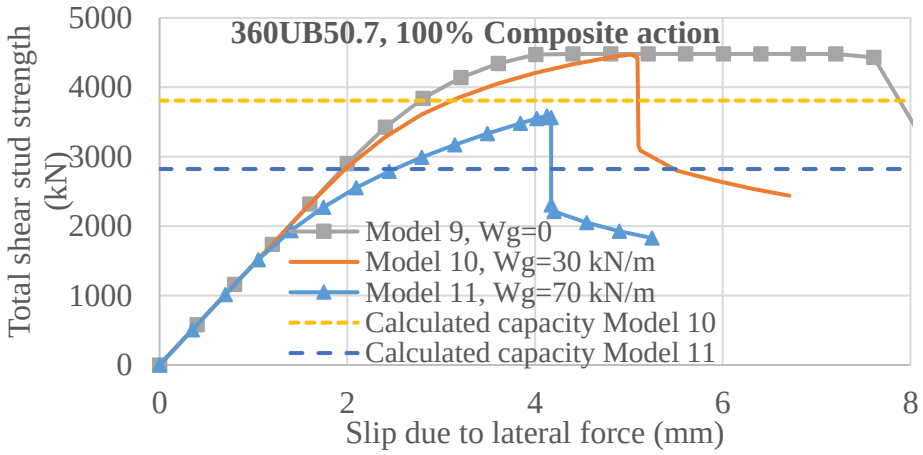

b) 100% composite action, 360UB50.7

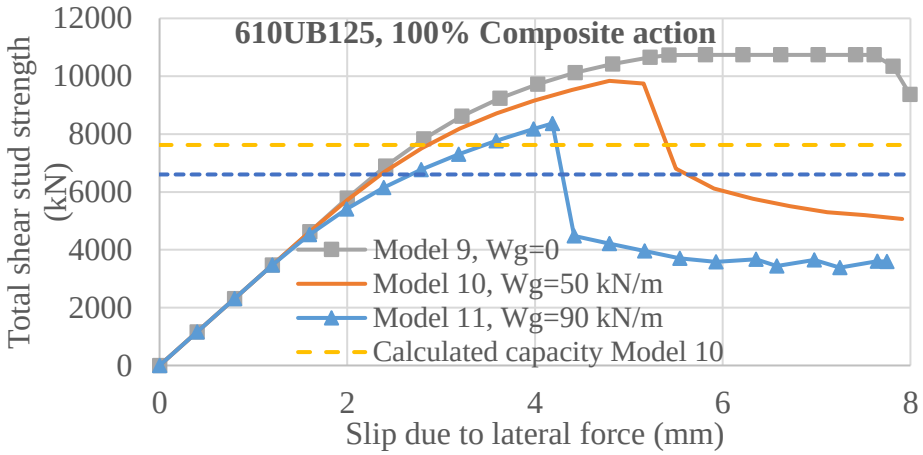

c) 100% composite action, 610UB125

Figure 5-29. Lateral force-slip of models with 100% composite actions

The behaviour of the FEM models are summarised in Table 5-1 to Table 5-3 in terms of

1. maximum shear stud slip under gravity load at the beam ends, S,
2. vertical deflection of the beam mid-point under gravity load, Δ_g, and
3. vertical deflection of the beam mid-point at the peak lateral force, Δ_{Hmax}.

Also the beam mid-point vertical deflection of the bare steel beam is calculated to compare with the composite beam vertical deflection, Δ_{gb}.

Table 5-1. Summary of vertical deflection and shear stud slip of 180UB section models

180UB22.2, L=4m											
Composite action	10%		25%			50%			100%		
Model number	1	2	3	4	5	6	7	8	9	10	11
Gravity load (kN/m), W_g	0	12*	0	12	25*	0	12	32*	0	12	40*

Maximum slip under gravity (mm), S	0	0.97	0	0.57	1.19	0	0.35	0.9	0	0.18	0.6
Gravity deflection (mm), Δ_g	0	9	0	6.7	14	0	5.3	14.3	0	4.4	14.7
Deflection at peak lateral force (mm), Δ_{Pmax}	0	13.3	0	13.4	27.5	0	13.4	28.5	0	14	29.7
Deflection bare steel beam (mm), Δ_{gb}	0	13.3	0	13.3	27.7	0	13.3	35.5	0	13.3	44.5
* W_g=Min { W causing 0.6 M_{pb} and W causing L/300 deflection}											

Table 5-2. Summary of vertical deflection and shear stud slip of 360UB section models

360UB50.7, L=6m											
Composite action	10%		25%			50%			100%		
Model number	1	2	3	4	5	6	7	8	9	10	11
Gravity load (kN/m), $\boldsymbol{W_g}$	0	30*	0	30	45*	0	30	55*	0	30	70*
Maximum slip under gravity (mm), $\boldsymbol{S}$	0	1.64	0	0.91	1.41	0	0.54	0.98	0	0.29	0.68
Gravity deflection (mm), Δ_g	0	14.4	0	10.7	16.2	0	8.8	16.2	0	7.5	17.5
Deflection at peak lateral force (mm), Δ_{Pmax}	0	20.5	0	20.5	31.1	0	20.8	29.7	0	20.3	31.1
Deflection bare steel beam (mm), Δ_{gb}	0	20.5	0	20.5	30.7	0	20.5	37.6	0	20.5	47.8
* $\mathbf{W_g}$=Min { **W** causing 0.6 $\mathbf{M_{pb}}$ and **W** causing L/300 deflection}											

Table 5-3. Summary of vertical deflection and shear stud slip of 610UB section models

610UB125, L=10m											
Composite action	10%		25%			50%			100%		
Model number	1	2	3	4	5	6	7	8	9	10	11
Gravity load (kN/m), $\boldsymbol{W_g}$	0	50*	0	50	70*	0	50	80*	0	50	90*
Maximum slip under gravity (mm), $\boldsymbol{S}$	0	2.46	0	1.07	1.75	0	0.6	0.96	0	0.31	0.74
Gravity deflection (mm), Δ_g	0	25.3	0	18.9	27.3	0	16.6	26.6	0	15.2	27.4
Deflection at peak lateral force (mm), Δ_{Pmax}	0	31.9	0	30.6	39.4	0	29.4	39.2	0	26.9	39.3
Deflection bare steel beam (mm), Δ_{gb}	0	33.3	0	33.3	46.6	0	33.3	53.3	0	33.3	60
* $\mathbf{W_g}$=Min { **W** causing 0.6 $\mathbf{M_{pb}}$ and **W** causing L/300 deflection}											

The FEM shear stud slip under gravity loads increased with increasing the beam total height and the level of gravity load as shown in Table 5-1 to Table 5-3. While it decreased with increasing the composite action. These are consistent with Eq. (5-14).

Appendix H presents the closed form solution for calculating shear stud slips under gravity loads considering different composite action levels and nonlinear behaviour of shear studs. The shear stud slips of similar FE models were verified with the closed-form solution and it was

found that the difference between the slip calculated and obtained from the FEM models was less than 10% for the studied cases.

The results also show that at the peak lateral force, P_{max}, the beam mid-point vertical deflection, Δ_{Pmax}, increased in all models. However, in some models it reached to the bare steel beam deflection, Δ_{gb}, under the same gravity load. This means the composite action was completely eliminated. This occurred in the models that the peak lateral force resistance, P_{max}, reached to the sum of shear strengths of all shear studs, P_{total}. In other models that the lateral force resistance was lower than the total shear stud strengths, which means some shear studs failed before others reach to their ultimate strength, some level of composite action may still exist. Figure 5-30 plots the composite beam moment of inertia using the beam mid-point vertical deflection at the peak lateral force, $I_{beam\ at\ peak\ lateral\ force}$. This plot shows that the moment of inertia of the beam varies between the composite beam and the bare steel beam moment of inertia, closer to $I_{bare\ steel\ beam}$.

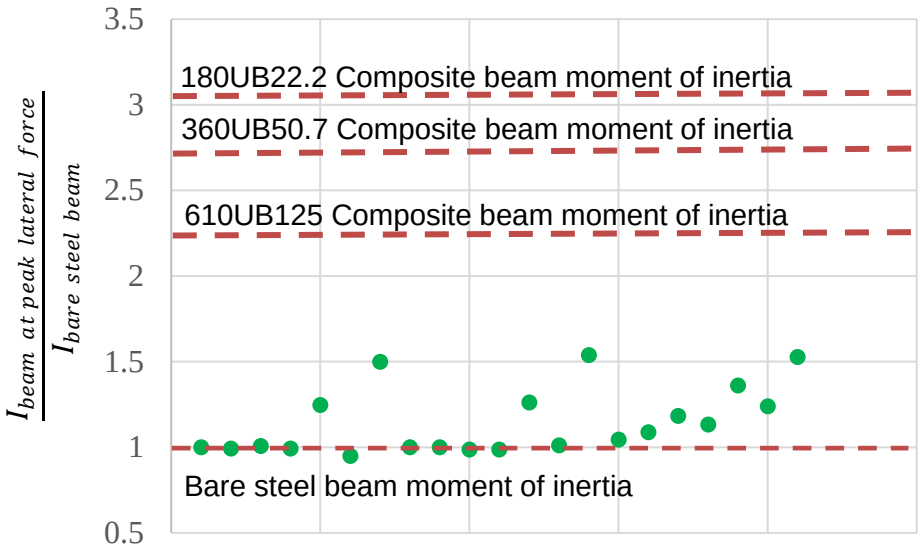

Figure 5-30. Composite beam moment of inertia at peak lateral force

Since the moment of inertia of the composite beam at the peak lateral force depends on different parameters and is hard to estimate. Here, it is recommended to use the bare steel beam moment of inertia for beams in buildings expected to be used after they have been subject to at

least one significant lateral load event and shear studs are required to transfer slab in-plane forces to the beams.

The increase in the beam vertical deflection should be observed after real earthquake events. However no literature indicating measurements of this effect was found.

Based on the behaviour of the composite beam subjected to lateral forces that was discussed in Section 5.3, and the findings of this case study, it is recommended that when all shear studs on a composite beam are required to carry lateral forces, the bare steel beam designed to carry unfactored gravity loads, $D + L$ to prevent collapse under gravity loads. This is because the composite action may be eliminated during the lateral loading. The load combination $D + L$ is selected instead of reduces serviceability load combination, $D + \psi L$, because:

i. The reduced load combination represents an average of imposed gravity forces on a wide range of structures and this level of force may be exceeded.

ii. Vertical earthquake excitation may also increase the beam vertical imposed forces

5.5.4.2 Proposed method strength verification

The method proposed in Section 5.4 is used here to calculate the lateral force resistance of the models studied. The calculated lateral force resistances are plotted in Figure 5-26 to Figure 5-29 for each model. Also the calculated (analytical) and FEM (numerical) lateral force resistances are presented in Table 5-4 to Table 5-6.

Table 5-4. Calculated lateral force resistance and the FEM results for models with 180UB section

180UB22.2, L=4m											
Composite action	10%		25%			50%			100%		
Model number	1	2	3	4	5	6	7	8	9	10	11
Sum of all shear stud strengths (kN), P_{total}	195	195	491	491	491	983	983	983	1966	1966	1966
Lateral force resistance, FEM models (kN), $P_{max,FE}$	195	195	491	491	446	983	983	842	1966	1966	1657

Calculated lateral force resistance (kN), $P_{max,Calc}$	195	195	491	491	393	983	983	698	1966	1966	1317
$\frac{P_{max,FE}}{P_{max,Calc}}$	1	1	1	1	1.13	1	1	1.20	1	1	1.26

Table 5-5. Calculated lateral force resistance and the FEM results for models with 360UB section

360UB50.7, L=6m											
Composite action	10%		25%			50%			100%		
Model number	1	2	3	4	5	6	7	8	9	10	11
Sum of all shear stud strengths (kN), P_{total}	447	447	1119	1119	1119	2239	2239	2239	4481	4481	4481
Lateral force resistance, FEM models (kN), $P_{max,FE}$	447	447	1119	1119	966	2239	2239	1848	4481	4473	3589
Calculated lateral force resistance (kN), $P_{max,Calc}$	447	380	1119	952	795	2239	1903	1500	4481	3809	2823
$\frac{P_{max,FE}}{P_{max,Calc}}$	1	1.18	1	1.18	1.22	1	1.18	1.23	1	1.18	1.27

Table 5-6. Calculated lateral force resistance and the FEM results for models with 610UB section

610UB125, L=10m											
Composite action	10%		25%			50%			100%		
Model number	1	2	3	4	5	6	7	8	9	10	11
Sum of all shear stud strengths (kN), P_{total}	1074	1074	2678	2678	2678	5356	5356	5356	10738	10738	10738
Lateral force resistance, FEM models (kN), $P_{max,FE}$	1074	887	2678	2378	1839	5356	4933	3905	10738	9916	8366
Calculated lateral force resistance (kN), $P_{max,Calc}$	1074	762	2678	1901	1714	5356	3803	3348	10738	7624	6604
$\frac{P_{max,FE}}{P_{max,Calc}}$	1	1.16	1	1.25	1.08	1	1.3	1.16	1	1.3	1.27

Here it is shown that the ratio of the FEM lateral force resistance of shear studs, $P_{max,FE}$, to the calculated strength using the proposed method, $P_{max,Calc}$, is between 1.0 to 1.25. Figure 5-31 plots the calculated lateral force resistance against the FEM results. It is noted that part of this difference between the calculated and the FEM strengths is because in the calculated

method the shear studs with slips larger than $S_u/3$ are excluded from both sides of the beam. However, in the FE models only one side of the beam experienced shear stud failure. This is because the lateral force was only applied in one direction monotonically.

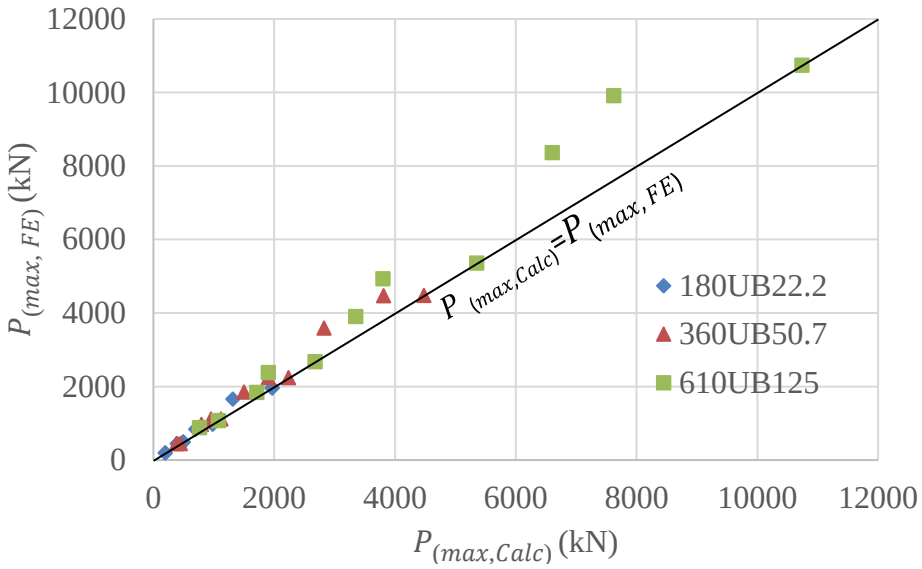

Figure 5-31. Calculated lateral force resistance compared with FEM results

5.5.4.3 Vertical deflection of beam mid-point

Increasing both the lateral force, and the concrete slab lateral displacement, increases the beam vertical deflection when shear studs start to yield or fracture. This effect was described in Sections 5.3.4 and 5.3.5 in detail.

Figure 5-32 shows the behaviour of the 180UB22.2 partially (50%) composite beam under a combination of gravity and lateral forces. The vertical deflection behaviour of the beam mid-point is described as follows:

- Zone 1: at this stage lateral force did not cause any yielding in the shear studs and they were in elastic range. As it was shown in Figure 5-15, when the shear studs are elastic, lateral force does not decrease composite action. In can be seen that the vertical deflection is equal to the initial gravity deflection at this zone.
- Zone 2: at this stage some shear studs on the additive side of the beam started to yield. Increasing the lateral force/displacement caused more shear studs to yield.

In this case, at $\delta = 3.2mm$ lateral slip, all shear studs yielded. As can be seen the vertical deflection gradually increased until it reached to the bare steel beam vertical deflection when all shear studs yielded. This was shown in Figure 5-19 Loading Step 3.

- Zone 3: at this stage all shear studs yielded and the beam vertical deflection was equal to the bare steel beam vertical deflection. Between lateral slips, $\delta = 3.2mm$ to $\delta = 5.6mm$ no increase in the vertical deflection was observed in this case.
- Zone 4: increasing lateral slip (more than 5.6mm in this case) caused some shear studs to reach their maximum slip capacity and fracture. This decreased the lateral force resistance. In this zone the beam vertical deflection increased more than bare steel beam deflection. This was shown in Figure 5-19 Loading Step 4.

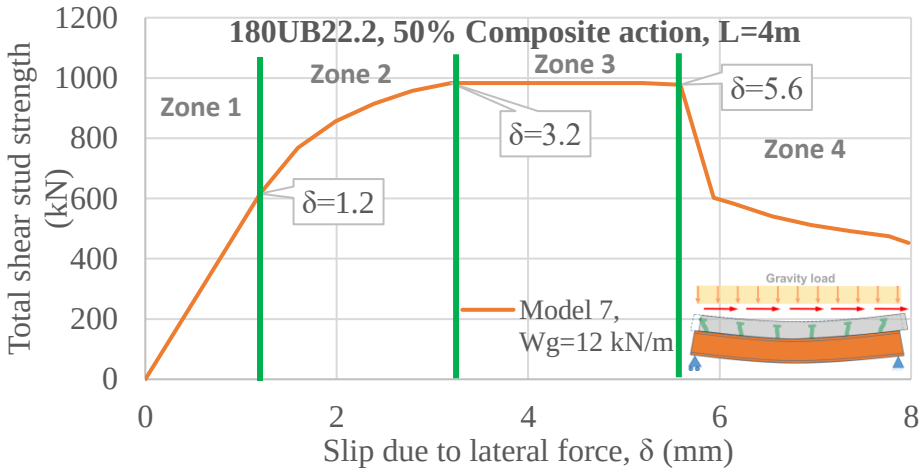

a) Lateral force-slip behaviour

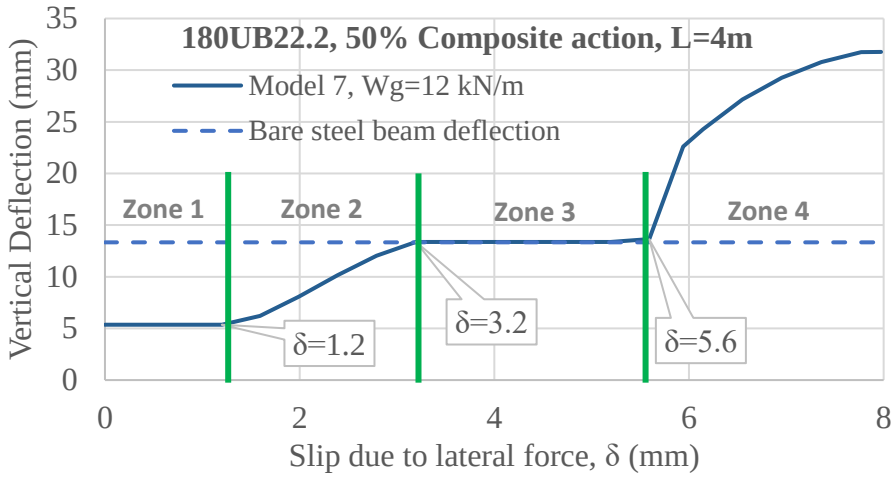

b)Vertical deflection- slip behaviour

Figure 5-32. Beam vertical deflection behaviour subject to lateral loading

The vertical deflection of the beam mid-point of all the studied FEM models is obtained and plotted in Figure 5-33. These show that the beam vertical deflection of a fully composite beam increased more in compared to a non-composite or partially composite beam. For example, the ratio of the beam mid-point vertical deflection at 6mm lateral deformation to the deflection under gravity load only of models with 360UB50.7 steel section are 3.2 and 2.4 for the fully (100%) composite and 25% partially composite beams respectively. This is because in a fully composite beam the stiffness reduction due to the imposed lateral force is higher than a partially composite beam. Also in a fully composite beam more shear studs are provided therefore failure of some shear studs at one side of the beam may impose larger moments to increase the beam vertical deflection as was shown in Figure 5-19 Loading Step 4.

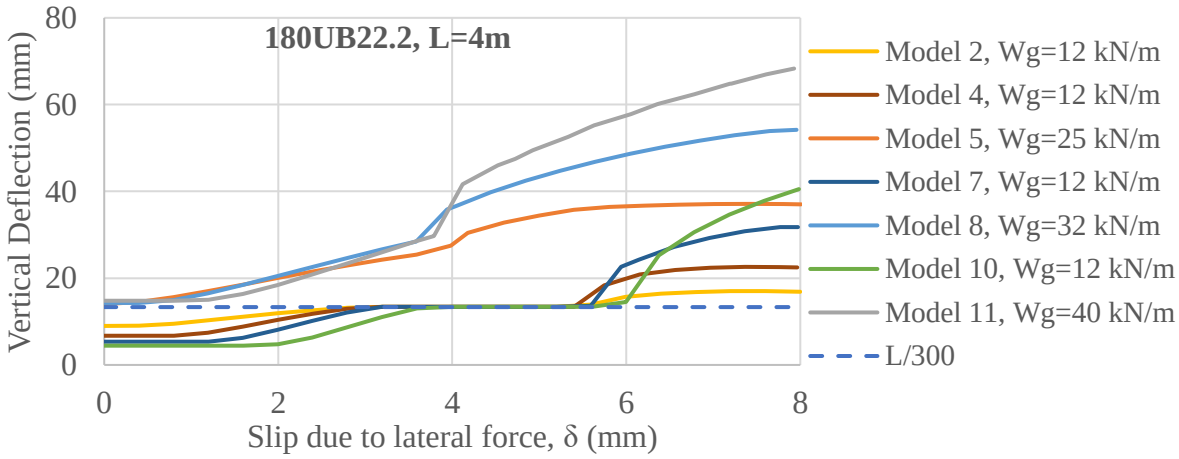

a) Models with 180UB steel beam section

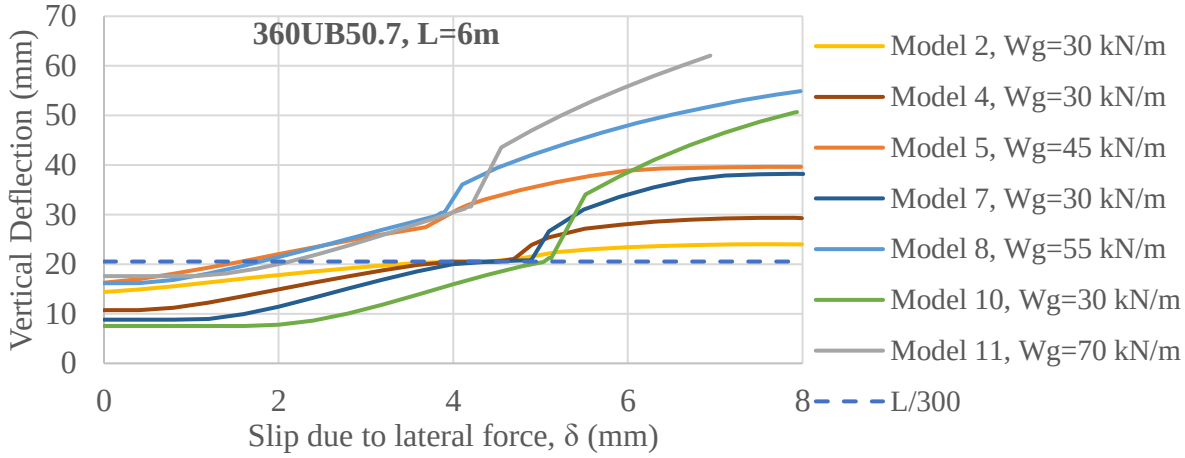

b) Models with 360UB steel beam section

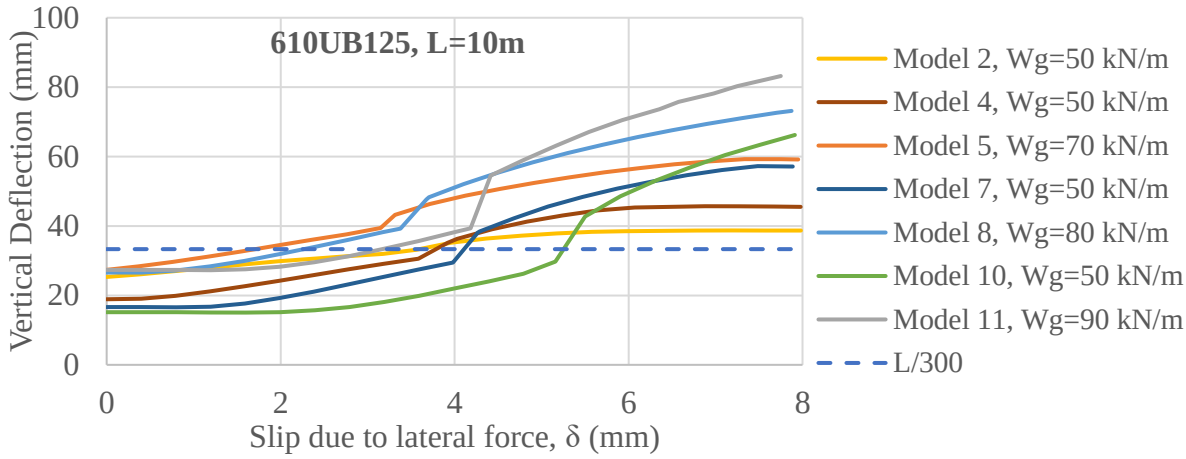

c) Models with 610UB steel beam section

Figure 5-33. Lateral slip-vertical deflection of beam mid-point of the studied models

5.6 Preventing large beam vertical deflections for low damage structures

The interaction of the lateral forces and composite action of composite beams were studied in Section 5.3. It was shown that with increasing the lateral imposed forces on the concrete slab, composite action gradually decreases. Considering a situation that all shear studs are required to transfer lateral forces, a large vertical deflection due to gravity loads may be expected due to loss of composite action. However, when the objective of structural design is the low-damage construction, structural components are required to be designed to avoid damage during the expected earthquake shaking level. This requires preventing the large beam

deflections. In this section recommendations are developed to limit damage to the composite beams subjected to lateral forces by controlling the beam vertical deflection.

Evaluating the amount of composite action lost due to lateral forces may be difficult using analytical methods because the loss depends on many parameters including the beam support conditions, lateral force distribution on the concrete slab, shear connector type, and shear connector cyclic behaviour. Therefore the numerical models are used. A 10% (for example) increase in the beam vertical deflection due to the imposed lateral forces is considered to be acceptable. The lateral force resistance corresponding to a 10% increase of vertical deflection, $P_{\Delta 10\%}$, for all models is given in Table 5-7.

Table 5-7. Ratio of the lateral force resistance corresponding to a 10% increase of the beam mid-point vertical deflection to peak FE lateral strength

	Composite action	10%	25%		50%		100%	
	Model number	2	4	5	7	8	10	11
180UB	Gravity load level (kN/m), W_g	12	12	25	12	32	12	40
	$P_{\Delta 10\%}/P_{max,FE}$	0.63	0.67	0.59	0.78	0.57	0.79	0.68
360UB	Gravity load level (kN/m), W_g	30	30	45	30	55	30	70
	$P_{\Delta 10\%}/P_{max,FE}$	0.47	0.54	0.44	0.65	0.51	0.64	0.71
610UB	Gravity load level (kN/m), W_g	50	50	70	50	80	50	90
	$P_{\Delta 10\%}/P_{max,FE}$	0.49	0.51	0.49	0.71	0.64	0.58	0.81

It may be seen that the ratio of the imposed lateral force at 10% increase in vertical deflection, $P_{\Delta 10\%}$, to the maximum numerical lateral force resistance, $P_{max,FE}$, is more than 0.5 in most cases considering a range of composite actions, gravity loads and beam sizes. Therefore if the imposed lateral force be limited to 50% of the ultimate total shear studs strength, $P_{max,FE}$, or alternatively the shear studs be designed for twice the expected lateral force, large vertical deflections may be avoided. This may prevent loss of composite action in the composite beams for low-damage construction. A designer is not able to compute $P_{max,FE}$ easily, therefore $P_{max,Calc}$ can be used which may provide more conservative results. In this case it is still

recommended that the bare steel beam be able to carry un-factored gravity loads, $D + L$, to prevent collapse under gravity loads in case of loss of composite action.

5.7 Conclusion

From studying the behaviour of composite and non-composite beams subjected to gravity loads and lateral forces, it was found that:

1) The literature indicates that very little consideration of lateral forces on shear studs has been undertaken. Based on the available literature, additional shear studs to transfer diaphragm horizontal forces into the beam may not be required in composite beams designed to carry gravity loads. This is because the quantity of shear studs used for a composite beam is usually determined based on an ultimate gravity load combination and the interaction of the shear flow from the gravity and lateral loading conditions is additive for some studs but opposite for others. Also for the beams that are designed as non-composite members under gravity loads, it is recommended that beams that transfer diaphragm in-plane forces have enough shear studs to achieve a minimum of 25% partial composite action, or else have sufficient capacity to resist $1.0G + 1.0Q$ non-composite to avoid large shear slips on shear studs under gravity load.
2) Considering the interaction of gravity loads and lateral forces on shear studs on a steel beam, it was shown that: (i) the maximum total lateral force resistance of shear studs depends on the level of shear stud slip under gravity load. So that in the absence of gravity load, the total lateral force resistance of shear studs is equal to the sum of all shear stud strengths. (ii) Yielding of the shear studs under a combination of gravity and lateral loads reduced or eliminated the shear flow at the steel beam-concrete slab interface and decreased composite action. This caused loss of composite action and increased the beam vertical deflection. (iii) Increasing the lateral force may cause

fracture in a number of shear studs and change the lateral force imposed on the steel beam top flange. This imposed additional moment to the beam and increased the effect of gravity loads. Therefore, the beam vertical deflection even more than the bare steel beam deflection under gravity loads was obtained.

3) A design method was developed to estimate the lateral force resistance of a beam shear stud group considering gravity forces and shear stud fracture. Numerical FEM studies indicated strengths in the range of 1.0-1.25 times that from the design method. Also the steel beam alone should be designed to carry un-factored gravity loads, $D + L$ to prevent collapse under gravity loads. This is because the composite action of the beams subject to lateral forces may be eliminated or decreased under lateral loading.

4) For composite beams in low damage structures, or structures where it is desired that the building be permitted to continue operation after at least one major earthquake, a maximum acceptable increase in vertical deflection of gravity beams was arbitrarily chosen to be 10%. To meet this limit, the ratio of slab lateral force demand applied to the shear studs in a bay should be less than 50% of the peak total resistance of these shear studs. This value is appropriate for the likely range of gravity loading, beam depth and level of composite action. Also the steel beam alone should be designed to carry un-factored gravity loads, $D + L$.

5.8 Summary of the proposed method for calculating lateral force resistance of shear studs

For both composite and non-composite beams that are subjected to lateral forces the total shear strength of shear studs may be calculated using the following method.

5.8.1 Calculating S_{max} for propped composite beams

The maximum shear stud slip, S_{max}, can be obtained for propped composite beams as:

$$S_{max} = 1.6\frac{\Delta_v d}{L}$$

Where

Δ_v: Vertical deflection of the bare steel beam mid-point under gravity loads ($\frac{5WL^4}{384EI}$)

d: $h_b + 2h_c$

L: Beam span

h_b: Steel beam total height

h_c: Concrete slab total height

Note that Δ_v should be calculated using the bare steel beam stiffness without considering composite action effects.

5.8.2 Calculating S_{max} for unpropped beams

The maximum shear stud slip, S_{max}, for unpropped beams can be obtained using the similar equation:

$$S_{max} = 1.6\frac{\Delta_v d}{L}$$

While Δ_v should be calculated using the reduced gravity load, $W_{un-propped}$, to decrease the effect of dead loads imposed before concrete hardening.

$$\Delta_v = \frac{5(W_{un-propped})L^4}{384EI}$$

Note 1: Δ_v should be calculated using the bare beam stiffness without considering composite action.

Note 2: earthquake vertical excitation can be included in the gravity load, W or $W_{un-propped}$.

5.8.3 Calculating lateral force resistance

5.8.3.1 Obtaining effective shear stud zone

For obtaining the effective shear stud zone the shear stud slip limit is required. Here the value of $S_u/_3$ is recommended for the shear stud slip limit. The maximum shear stud slip capacity, S_u, of a 19mm shear stud is about 7.2mm based on Johnson and Molenstra (1991) study.

The normalised slip versus normalised beam length plot is shown in Figure 5-34. For calculating the effective shear stud zone, the point on the horizontal axis corresponding to the value of $\frac{S_u}{3S_{max}}$ on the vertical axis should be obtained. This point represent the length of the beam from the beam center-line that the shear stud slips are lower than the shear stud slip limit.

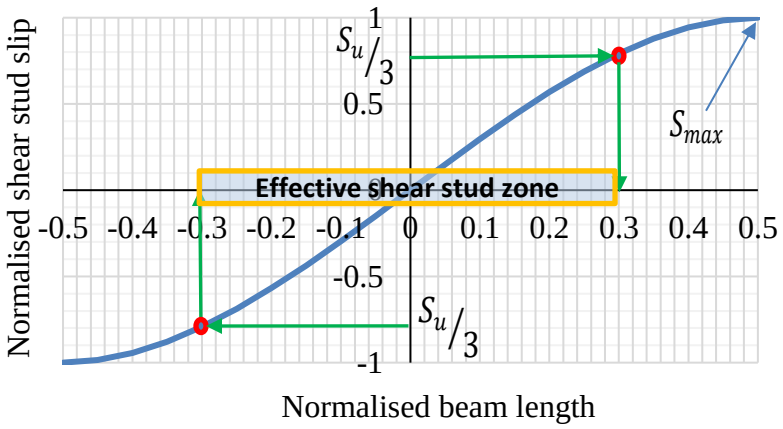

Figure 5-34. An example for calculating effective shear stud zone

5.8.3.2 Calculating lateral force resistance of shear studs

Lateral force resistance of the shear studs on a beam is equal to the sum of the strengths of all shear studs placed within the effective shear stud zone as shown in Figure 5-34.

5.8.4 Design considerations for composite beams in low-damage structures

To prevent vertical deflections more than 10% of the beam vertical deflection under gravity loads, it is recommended that the imposed lateral forces be limited to 50% of the

ultimate shear studs strength. Alternatively, the shear studs may be designed for twice the expected lateral force. In addition it is recommended that the bare steel beam be able to carry un-factored gravity loads, $D + L$ to prevent collapse under gravity loads.

References

[1] Alizadeh, S., MacRae, G. A., Bull, D., & Clifton, G. C. (2017). In-Plane Diaphragm Issues for Steel Buildings in Seismic Zones. In 16th World Conference on Earthquake, 16WCEE.

[2] ANSI, A. 360–10.(2010). Specification for structural steel buildings

[3] ANSI, A. 360–16.(2016). Specification for structural steel buildings

[4] AS/NZS 1170.0 (2002), Structural design actions-Part 0: General principles.

[5] AS/NZS 2327 (2017). Composite structures - Composite steel-concrete construction in buildings. Standards New Zealand, Wellington, New Zealand.

[6] Burmeister, S., & William, P. J. (2008). Horizontal floor diaphragm load effects on composite beam design, December 2008. Modern Steel Construction.

[7] EN, C. 1994. 1-1, (2004) Eurocode 4: Design of composite steel and concrete structures.

[8] Civjan, S. A., & Singh, P. (2003). Behavior of shear studs subjected to fully reversed cyclic loading. Journal of Structural Engineering, 129(11), 1466-1474.

[9] Cowie, K. A., Fussell, A. J., Clifton, G. C., MacRae, G. A., & Hicks, S. J. (2014, March). Seismic design of composite metal deck and concrete-filled diaphragms–A discussion paper. In NZSEE Conference.

[10] Gattesco, N., & Giuriani, E. (1996). Experimental study on stud shear connectors subjected to cyclic loading. Journal of Constructional Steel Research, 38(1), 1-21.

[11] Johnson, R. P. (2008). Composite structures of steel and concrete: beams, slabs, columns, and frames for buildings. John Wiley & Sons.

[12] Johnson, R. P., Molenstra, N., & EPPIB. (1991). Partial shear connection in composite beams for buildings. Proceedings of the Institution of Civil Engineers, 91(4), 679-704.

[13] MacRae G. A. and Clifton G. C. (2015). "Research on Seismic Performance of Steel Structures", Steel Innovations Conference, Auckland, New Zealand.

[14] Mullett, D. L. (1998). Composite floor systems. Blackwell Science.

[15] Nakajima, A., Saiki, I., Kokai, M., Doi, K., Takabayashi, Y., & Ooe, H. (2003). Cyclic shear force–slip behavior of studs under alternating and pulsating load condition. Engineering Structures, 25(5), 537-545.

[16] NZS 3404 (2007). Steel Structures Standard. Standards New Zealand, Wellington, New Zealand. Including Amendments 1 and 2, 2001/2007.

[17] Oehlers, D. J., & Coughlan, C. G. (1986). The shear stiffness of stud shear connections in composite beams. Journal of Constructional Steel Research, 6(4), 273-284.

[18] Sabelli, R., Sabol, T. A., & Easterling, W. S. (2011). Seismic design of composite steel deck and concrete-filled diaphragms. NEHRP Seismic Design Technical Brief No, 5.

[19] SAP2000, C. S. I. (2015). Structural Analysis Program. Berkeley, California.

[20] Slutter, R. G., & Fisher, J. W. (1966). Fatigue strength of shear connectors, December 1966, Reprint 315 (66-21).

6 Floor Diaphragm Buckling

6.1 Introduction

Floor diaphragms in most structures consist of a flat slab designed primarily to carry gravity forces. However, they also tie the vertical lateral force resisting systems of the structure together. During an earthquake event floor diaphragms experience various demands depending on the floor plan configuration, the location, stiffness, strength and deformation mode of the vertical lateral force resisting (VLFR) systems and many other parameters. It is generally assumed that the floor diaphragms will remain elastic during wind and earthquake shaking. However, in previous earthquakes, some inelastic behaviour, concrete damage and shear failures in diaphragms are reported (e.g. Henry et al. 2017).

In the 1980s, precast floor diaphragm became popular for concrete buildings. This generally consisted of precast beams with timber in-fills and a concrete topping, or hollow core units with a concrete topping. These floor diaphragms often comprised a thin lightly reinforced topping slab on precast units. Since the 1990s, thinner composite floors, consisting of concrete on cold-formed corrugated steel decking, all supported on a grid-work of steel beams, have increased in dominance. This decking was originally designed to span 3.5m, but different decking profiles, with un-propped spans up to 5.5m and propped spans up to 8.5m, together with simple design tools, were developed in the late 1990s. These were implemented in several buildings around New Zealand before the Christchurch earthquake sequence. They are most suitable for steel buildings where through-deck welding is used to connect decking to the beams and place shear studs (Bruneau and MacRae, 2017). Such composite slabs are economical as there is no need for other formwork, the construction speed is high, and the light weight reduces the sizes of other frame elements and foundations. Despite the benefits, thin composite slabs may be flexible both out-of-plane and in-plane. The out-of-plane flexibility may increase the

chance of diaphragm instability under imposed lateral forces. Although the diaphragm buckling has not been reported yet, there is a need for understanding the mechanics and nature of diaphragm buckling, especially with the increasing number of steel frame construction in recent years.

Many studies have been conducted to investigate shear resistance of composite floors subject to lateral forces in the literature. Bolluyt (1980) has prepared a list of composite diaphragm failures based on experimental studies as shown in Table 6-1. These composite floor failure modes under lateral force include:

i) Diagonal tension failure which occurs when the concrete stress reaches its tensile limit.

ii) Direct concrete shearing, which may occur along a line parallel to the deck corrugations and the ultimate strength depends on the shear strength of the concrete.

iii) Stability failure which may occur in the long span floors, and the presence of gravity loads may increase the chance of out-of-plane buckling.

iv) Localized failure when there is a non-uniform shear distribution in the diaphragm that causes regions of high stress (Bolluyt, 1980).

v) Decking/concrete interface, and diaphragm/edge member interface failures are also described.

Table 6-1. Diaphragm failure modes (Bolluyt, 1980)

1. Composite Diaphragm
    a. Shear strength
        1. Diagonal tension
        2. Parallel to deck corrugations
    b. Stability failure
    c. Localized failure
2. Deck/Concrete Interface
    a. Interfacial shear parallel to the corrugations
    b. Interfacial shear perpendicular to the corrugations
        1. Pop up (overriding)
        2. Deck fold-over
3. Diaphragm/Edge Member Interface
    a. Arc spot welds
        1. Shearing of weld
        2. Tearing and/or buckling of deck around weld
    b. Concrete rib
    c. Studs (or other shear connectors)
        1. Shearing of stud
        2. Shear failure of concrete around stud

The stability limit state is more complicated than the other failure modes and it has not been studied in the literature. This study aims to find out the importance of diaphragm buckling and to develop a method for calculating the buckling strength of composite floor diaphragms by answering the following questions:

1. What are the possible buckling modes in the composite floor diaphragms?
2. What is the critical buckling strength for each buckling mode?
3. How do gravity loads affect the ultimate buckling strength of a composite floor diaphragm?

6.2 Methodology and scope

In this study, three failure modes of the composite floor diaphragms which include 1) Inter-rib buckling (local buckling), 2) intra-panel buckling (between secondary beams) and 3) global

buckling (between primary beams) are investigated. Each of these buckling modes is studied before and after cracking of the concrete. These are referred to as the i) pre-cracking, and ii) post-cracking stages. In the pre-cracking stage, the concrete material is considered homogenous and elastic shear buckling strength of the diaphragm is investigated. In the second stage (post-cracking) it is considered that the struts and ties are formed in the concrete. Therefore, the buckling strength of the concrete strut is studied. Furthermore, the reduction in the buckling strength of the composite floor due to the presence of gravity forces is also investigated. Finally, a design procedure is provided to assess the diaphragm buckling for composite slabs.

Limitations of this study include:

1. The steel deck sheet is not considered in finding the composite floor in-plane stiffness.
2. Non-structural elements such as partitions that may affect the boundary conditions and buckling capacity are not considered.
3. It is assumed the concrete is homogenous before cracking. Creep and shrinkage cracks are not considered in finding the floor slab stiffness.
4. The boundary conditions are assumed to be simply supported because the concrete topping is lightly reinforced and after cracking it is not able to transfer bending moments.
5. It is assumed that the floor diaphragm in-plane forces are applied to the floor diaphragm boundaries without any eccentricity.

6.3 Typical composite floor details in steel frame structures

Figure 6-1 shows a floor plan layout of a typical steel frame structure which consists of a composite slab sitting on the gridwork of secondary beams. These secondary beams are supported by primary beams. The primary beams are connected to the vertical lateral force resisting (VLFR) systems or the gravity columns. The composite slab is usually connected to

both primary and secondary beams using shear studs. This increases the strength and stiffness of the beams by taking the advantages of composite action. The number of shear studs that transfer forces from the composite slab to the beams controls the level of composite action.

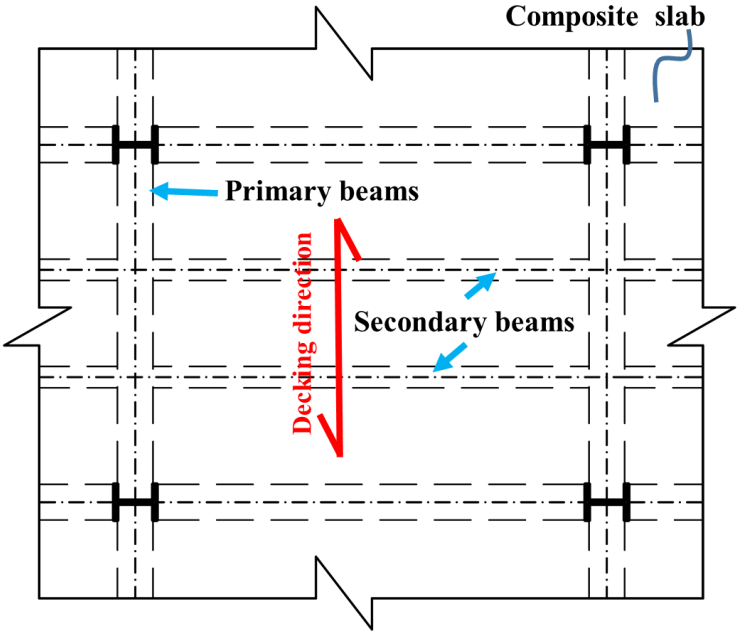

Figure 6-1. Typical floor plan layout showing composite floor

The steel decking sections/profiles vary between different manufacturers but the general floor layout is the same for all of them. Different steel decking section profiles are available, but the most common profiles used in New Zealand are shown in Figure 6-2. In general, the deeper the steel decking section, the further the span of the composite slab, and also the greater likelihood that propping is required for the long spans. The noticeable differences in the steel deck sections are i) the total steel deck height and ii) the distance required between secondary beams. Figure 6-2 shows the details of three steel deck sections known as "ComFlor" from S&T Stainless Ltd that are the most widely used in New Zealand.

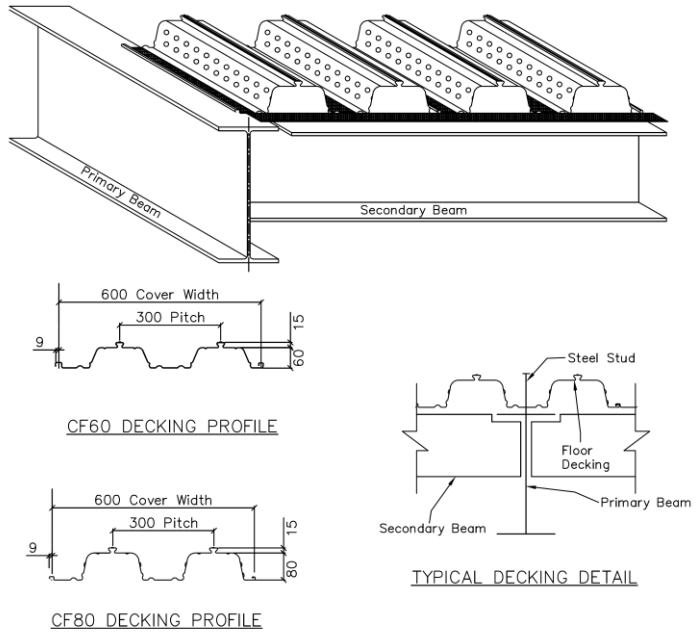

a) ComFlor 60 and 80 details

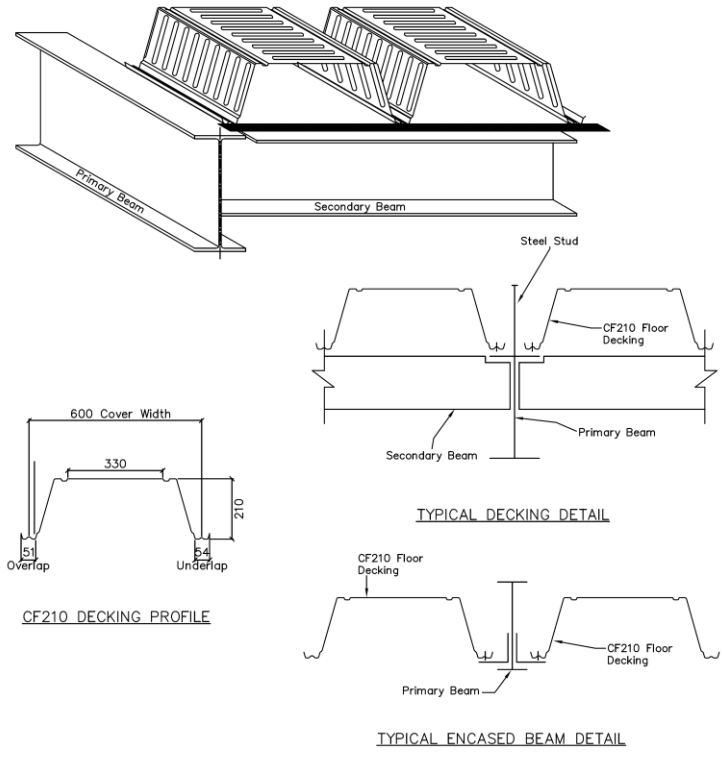

b) ComFlor 210 details

Figure 6-2. ComFlor 60, 80 and 210 section details (https://www.comflor.nz)

According to the ComFlor product guides provided by S&T Stainless Ltd, the ComFlor 60 is capable of supporting un-propped continuous spans up to 4.5 metres and propped spans up to 6.8 metres. ComFlor 80 can have un-propped continuous spans up to 5.3 metres and propped spans up to 7.1 metres. These large spans emphasize the importance of studying the diaphragm buckling considering the thin (as low as 50mm) concrete topping on the steel decking.

6.4 Diaphragm buckling modes

While the in-plane composite floor strength is governed by the modes listed in Table 6-1, one of the most difficult modes to assess is that of buckling. This is described in detail below.

When a plate element is subjected to compression, bending, shear or combination of these forces in its plane, the plate may buckle locally or globally before reaching the material yield stress. The plate buckling occurs by gradual distortion of the cross-section of the member. Therefore, contrary to the definition of buckling in columns, elastic plate members experience a gradual increase in strength as they buckle as shown in Figure 6-3. Other failure modes such as material yield and initial geometric imperfections may also control the strength.

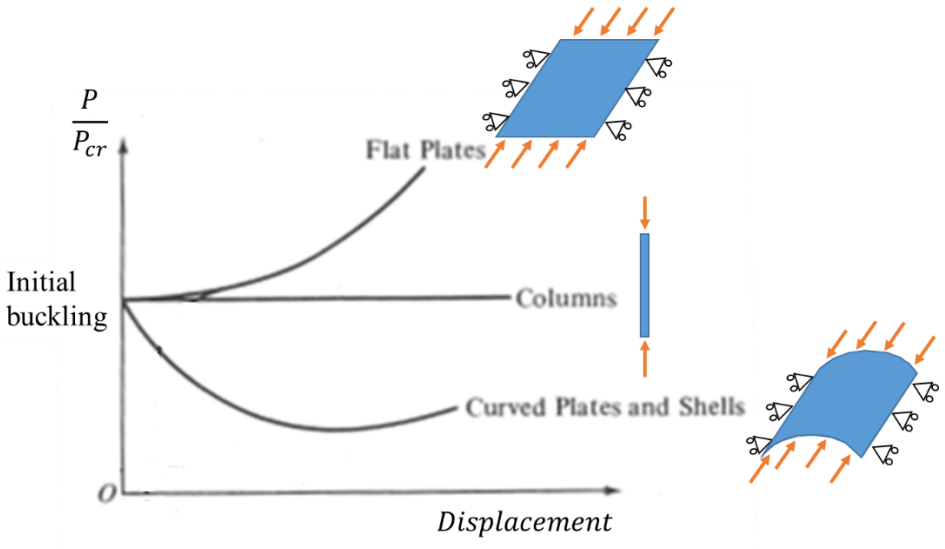

Figure 6-3. Post-buckling behaviour of elastic flat and curved plate (small deformation) (Szilard, 1974)

This buckling problem is more complicated in the case of the composite slabs due to the corrugated nature of the slab and also the secondary beams supporting the slab which act like stiffeners.

Based on the floor plan layout shown in Figure 6-1, three different buckling modes are considered.

1) Inter-rib (local) buckling which consists of buckling of concrete topping between the steel deck ribs.
2) Intra-panel buckling which can occur for the composite slab between the secondary beams.
3) Global (or intra-bay) buckling, which may occur for the composite floor located between the primary beams of the structure.

These buckling modes are shown in Figure 6-4 schematically. In the first mode, the slab between the ribs is assumed to have a uniform thickness. Therefore it could be assumed as a flat plate with a thickness equal to that of the topping for buckling investigations. While in the modes two and three, the corrugated nature of the composite slab and the presence of secondary beams significantly increase the buckling resistance of the topping.

Note that, in this study, the interaction between modes is assumed not to govern the behaviour.

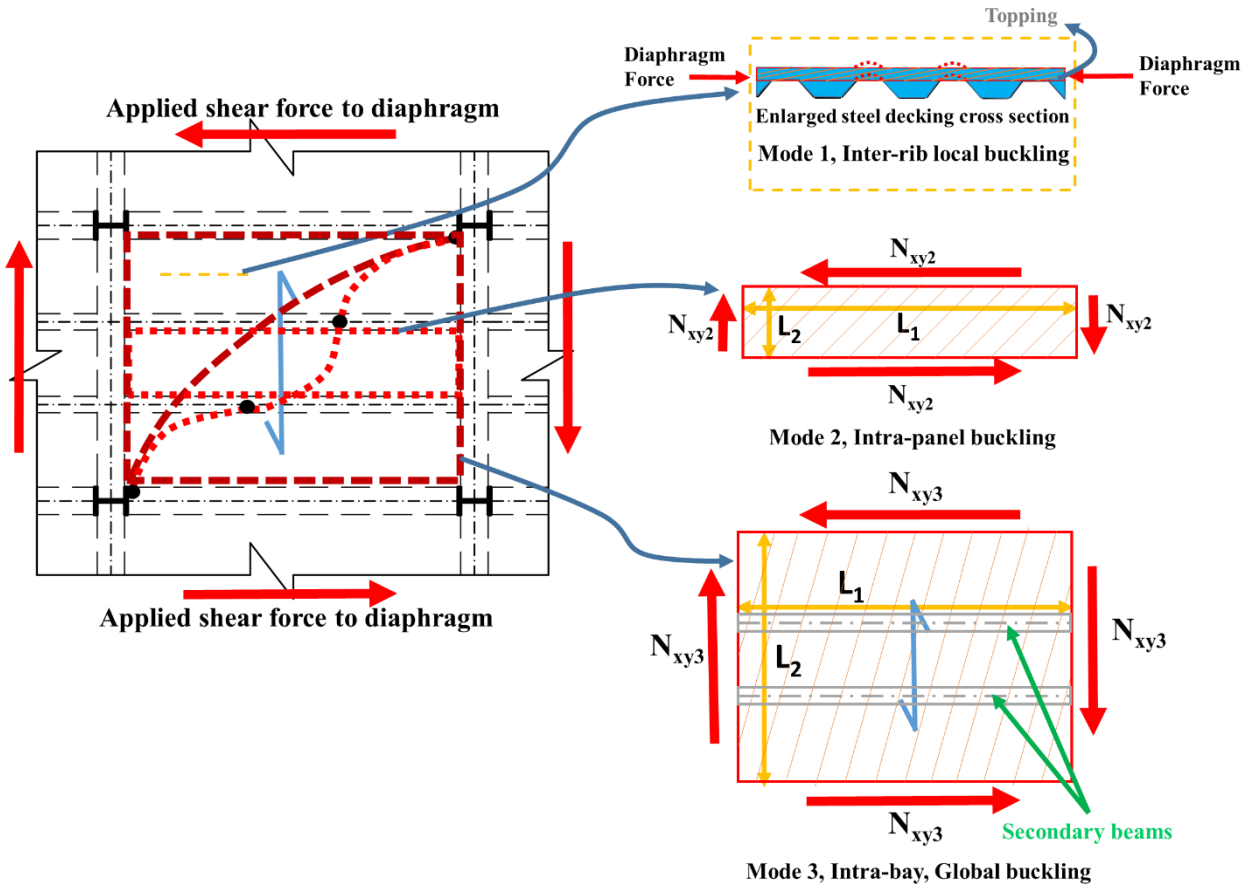

Figure 6-4. Diaphragm buckling modes

6.4.1 Buckling mode 1, inter-rib (local) buckling

Typical composite slabs consist of a corrugated steel sheet on to which concrete is poured. Therefore the concrete thickness of the ribs is equal to the steel deck depth plus the concrete topping. Between the ribs, the concrete thickness is just equal to the concrete topping as shown in Figure 6-5.

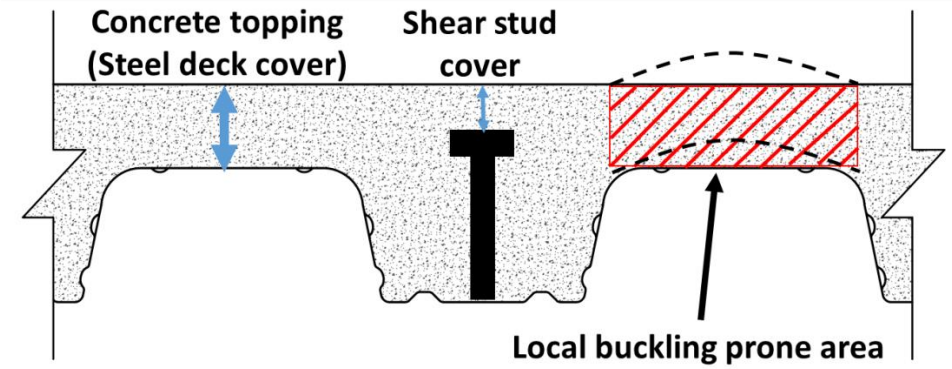

Figure 6-5. Typical steel deck section and local buckling

- **Minimum concrete topping thickness**

The minimum thickness of concrete required on top of the steel decking (i.e. the topping) is specified in different building codes and design guides. These recommendations seem to be arbitrary but they provide some floor integrity, some sound resistance and vibration control and some ability for the floor diaphragm to transfer lateral forces. Note that some of these benefits may be lost if conduit or other ducts are placed within this region. In addition specific fire and shear stud cover checks may be required.

ANSI/SDI (2011) states that "the concrete thickness above the top of the steel deck shall not be less than 2 inches (50mm), nor that required by any applicable fire-resistance rating requirements". The Canadian steel design standard (CSA C. S16-14) requires 65mm effective thickness, which effective thickness is defined as overall slab thickness minus the height of the steel decking corrugation.

The same minimum slab thickness, 50mm, on top of the steel deck is specified in NZS3404 (2007) Clause 13.3.2.2.1(e). However, another limitation specified in Clause 13.3.2.3(e) relates to the minimum concrete cover required on top of the shear studs which is based on the concrete cover criteria for different environmental conditions from NZS3101 (2006). This has a minimum value of 20 mm for indoor condition and intended minimum life of 50 years, which makes the total minimum topping thickness equal to 40+20=60 mm.

- **Effect of pre and post-cracking stages on inter-rib buckling**

Local buckling of the concrete topping can be investigated in pre and post-cracking stages of the concrete. This is because, the concrete may crack at low tension stresses, therefore the state of the pure shear can change to diagonal compression due to concrete strut formation after the cracking.

In this study, it is assumed that the major applied loads to the diaphragms are the form of shear that comes from "transfer" forces between different VLFR systems. These imposed shear forces are being carried by

(a) the diaphragm through shear stresses before crack formation in the concrete (which the concrete material can be assumed to be homogeneous), and

(b) after the crack formation in the concrete, the imposed shear forces are transferred by the compression struts and tension ties in the concrete.

Figure 6-6 shows the stress situations in a concrete topping element (between ribs). In this study, the pure shear condition and the combination of shear and axial stresses are investigated. It should be noted that other possible stress combinations can also be investigated using the buckling interaction formula.

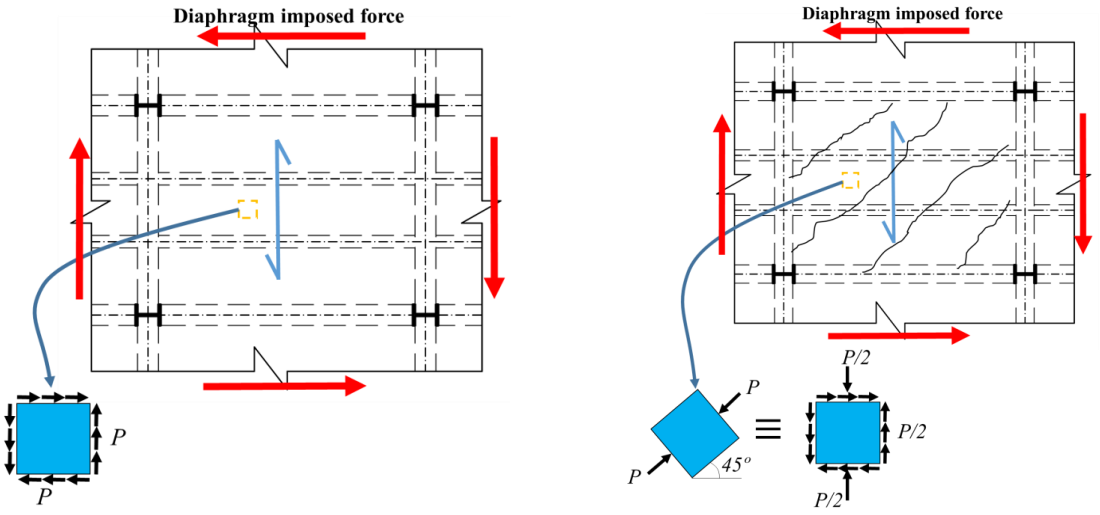

a) Concrete topping subjected to the pure shear stress (pre-cracking)

b) Concrete topping subjected to the shear and axial stress (post-cracking)

Figure 6-6. Stresses at inter-rib concrete element

6.4.1.1 Slab subjected to pure shear, pre-crack condition

Studying the buckling of plate members under axial, shear or combination of these stresses started in the early 1900s (Szilard, R., 1974). Eq. (6-1) presents the general governing differential equation of the plate elastic stability. With solving this differential equation for various boundary conditions and loading patterns, the critical buckling load can be obtained.

$$\frac{\partial^4 w}{\partial x^4} + 2\frac{\partial^4 w}{\partial x^2 \partial y^2} + \frac{\partial^4 w}{\partial y^4} = \frac{1}{D}\left(\bar{n}_x \frac{\partial^2 w}{\partial x^2} + 2\bar{n}_{xy}\frac{\partial^2 w}{\partial x\,\partial y} + \bar{n}_y \frac{\partial^2 w}{\partial y^2}\right) \qquad \text{Eq. (6-1)}$$

Where $\bar{n}_x$, $\bar{n}_y$ and $\bar{n}_{xy}$ are the in-plane axial and shear stresses applied at the boundaries of the middle surface of the plate. And D is the plate flexural stiffness. A schematic view of a general plate member subjected to edge forces is shown in Figure 6-7.

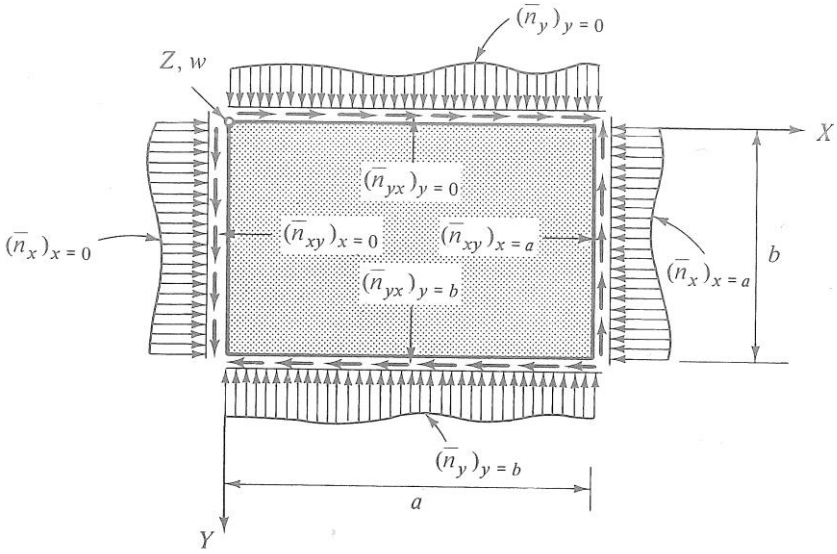

Figure 6-7. Rectangular plate member subjected to edge stresses (Szilard, 1974)

Considering the plate member in Figure 6-7 that is subjected to pure shear ($\bar{n}_x = \bar{n}_y = 0$) stress, the solution of the differential equation (Szilard, 1974) for the elastic critical shear stress (buckling stress) is expressed as Eq.(6-2):

$$N_{xy1} = k_s \frac{E\pi^2}{12(1-\nu^2)(b/t)^2} \qquad \text{Eq. (6-2)}$$

Where N_{xy1} is the elastic critical shear stress ($\bar{n}_{xy} = \bar{n}_{yx}$), b and t are the plate width and thickness respectively and E and ν are the elastic modulus and Poisson's ratio of the plate

material. The parameter k_s is the plate elastic buckling coefficient determined by a theoretical critical-load analysis. This parameter is a function of plate geometry and boundary conditions. The parameter k_s is plotted for three edge support conditions in Figure 6-8 (Ziemian, 2010). In this plot, the plate aspect ratio is used, considering that the plate width (b) used in Eq. (6-2) is shorter in length.

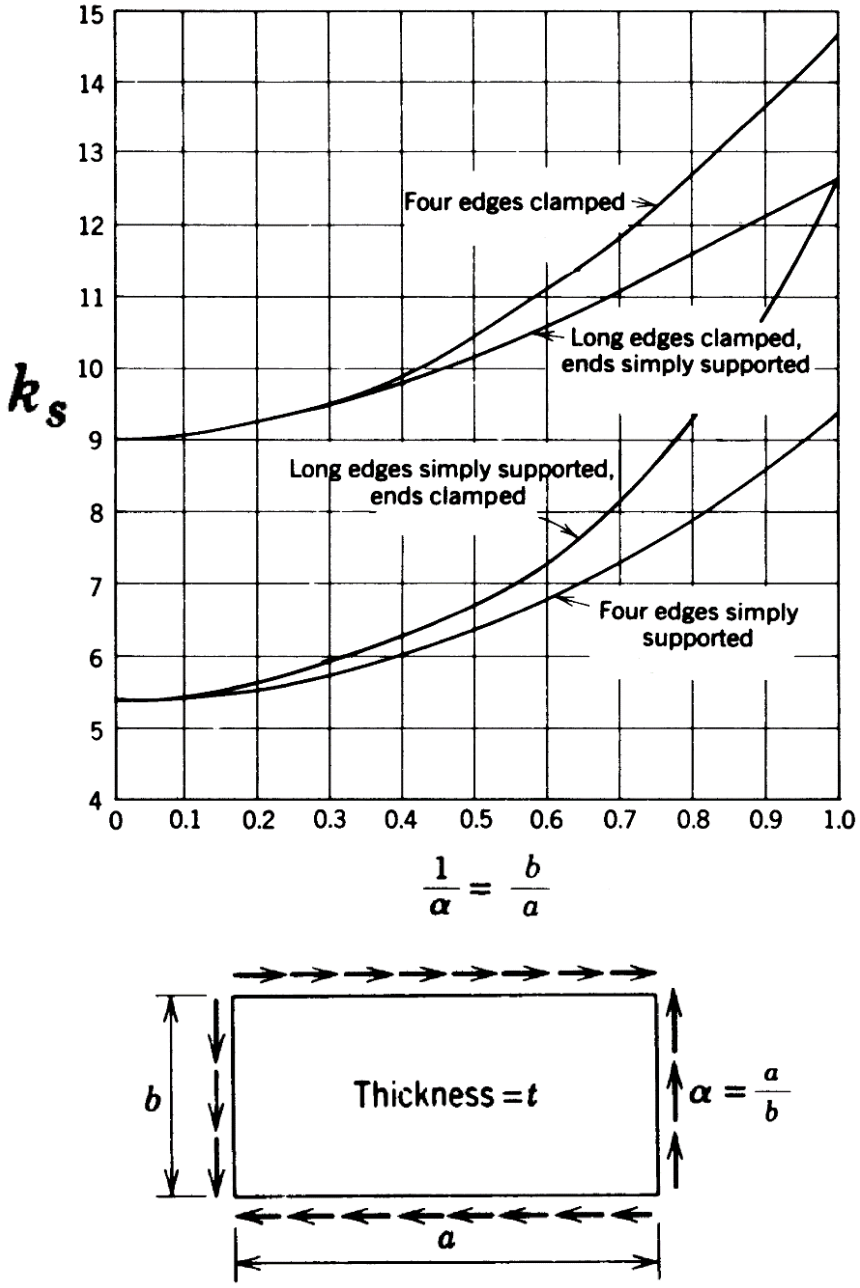

Figure 6-8. Plate buckling coefficient subjected to pure shear stress (Ziemian, 2010)

Based on the plots in Figure 6-8, the plate buckling coefficient (k_s) has the lowest value when the plate is infinitely long ($b/a = 0$) for all support conditions. The lowest value that can be used for k_s is equal to 5.4, where the plate is infinitely long and all four edges are simply supported. It increases by up to about 75% for a square plate ($b = a$).

- **Case study**

The elastic shear buckling of all three ComFlor sections, shown in Figure 6-2, is investigated here. Since the steel deck profiles usually have complex shapes for higher efficiency and construction considerations, in this study the cross-sections are simplified as shown in Figure 6-9.

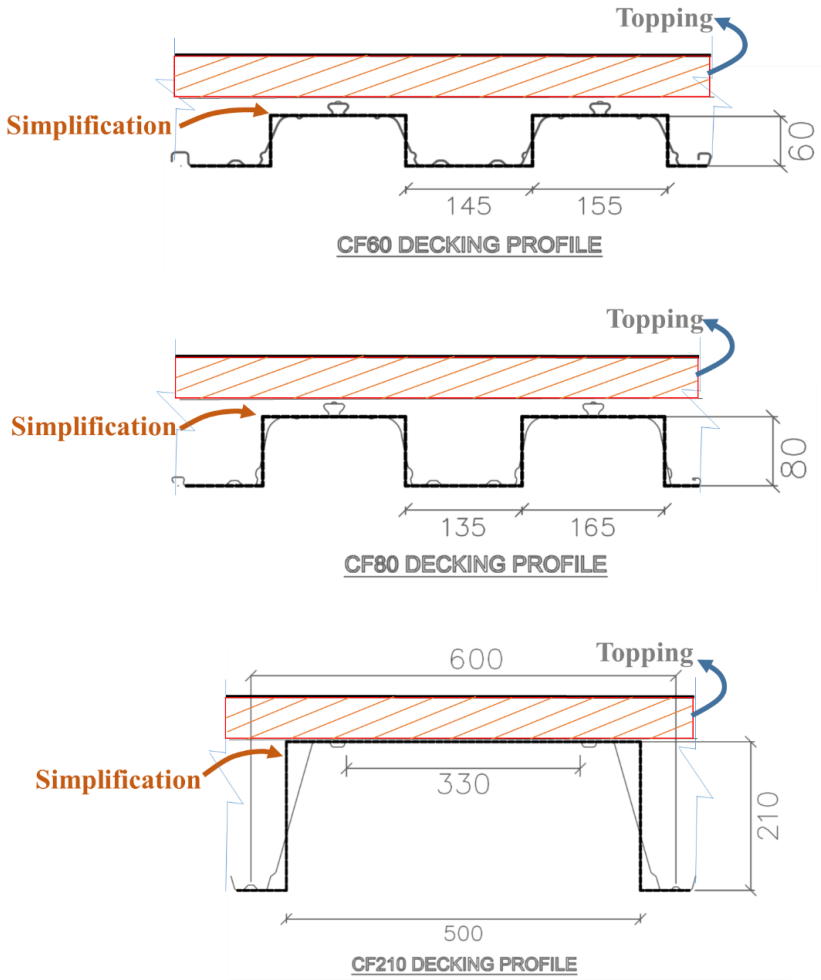

Figure 6-9. Simplified steel deck profiles cross-section

It is assumed that the concrete compressive strength is 30 MPa with an elastic modulus of 25 GPa. The concrete shear strength, τ_{max}, calculated based on NZS 3101 (2006) Clause 7.5.2,

as the minimum of $0.2f_c'$ ($= 0.2 \times 30\text{MPa} = 6\text{MPa}$) and 8 MPa. Table 6-2 presents a summary of the floor dimensions and concrete strength and stiffness.

Table 6-2. Steel decking dimensions

Decking type	b (distance between ribs)
ComFlor 60 (CF60)	155 mm
ComFlor 80 (CF80)	165 mm
ComFlor 210 (CF210)	500 mm

Figure 6-10 plots the elastic critical shear stress against the concrete topping thickness up to 100 mm considering the conservative assumption $k_s = 5.4$. Note that topping thickness is measured above the highest point of decking as shown in Figure 6-9. The results show that for 50 mm concrete topping, the elastic critical shear stresses are 12,075 MPa, 10,655 MPa and 1,160 MPa for ComFlor 60, 80 and 210 respectively. These values show that the elastic critical stresses are much larger than the shear strength of the concrete of 6 MPa, therefore, before buckling, the shear strength of the slab governs the behaviour.

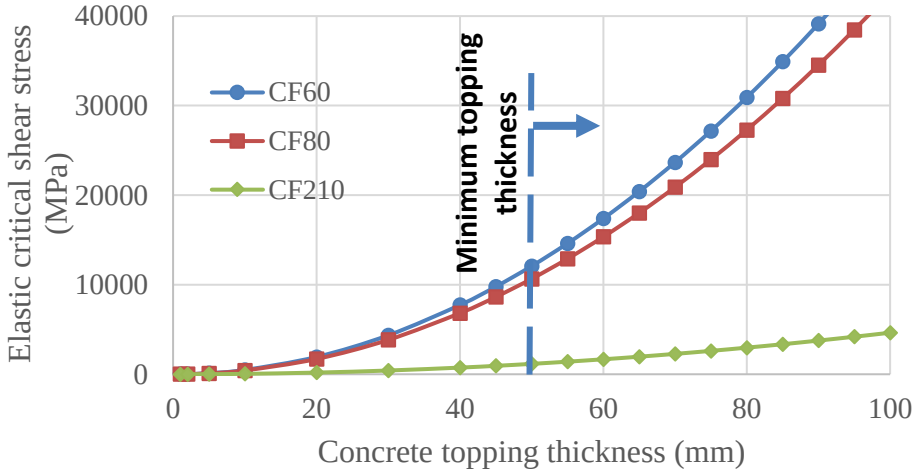

a) Elastic critical shear stress of ComFlor 60, 80 and 210 composite slabs subjected to pure shear

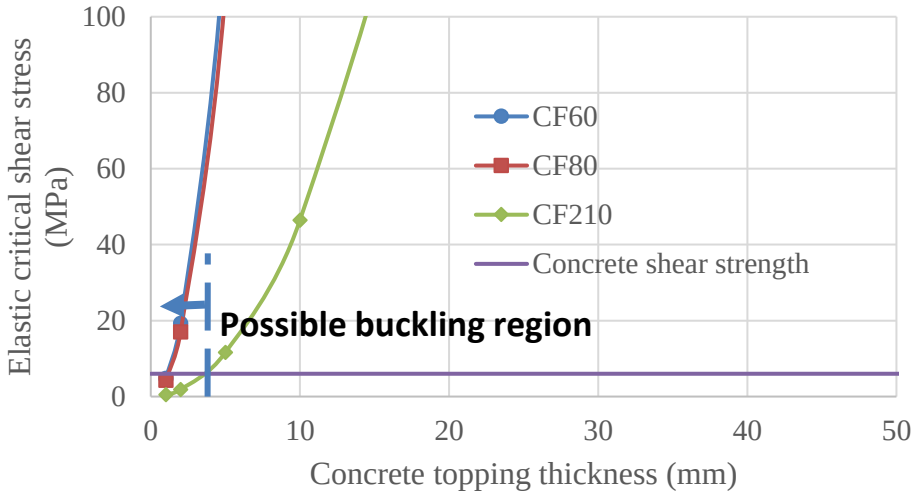

b) An enlarged view of Figure 6-10a

Figure 6-10. Elastic critical shear stress of ComFlor 60, 80 and 210 subjected to pure shear

Table 6-3. Elastic critical shear stress (MPa) of ComFlor 60, 80 and 210 subjected to pure shear

	CF60	**CF80**	**CF210**
Concrete topping thickness (mm)	**Critical shear stress (MPa)**		
1	4.83	4.26	0.46
2	19.32	17.05	1.86
5	120.75	106.56	11.6
50	12075.23	10655.92	1160.43
60	17388.34	15344.53	1671.02

Table 6-3 presents the values of elastic critical shear stress for selected thicknesses. The underlined values are lower than the shear strength of the concrete. The critical thickness is between 1 to 2 mm for ComFlor 60 and 80 and it is between 2 to 5 mm for ComFlor 210. It should be noted that the boundary conditions are considered simply supported and the plate is assumed infinitely long. Changing these assumptions to clamped edges or rectangular plate with lower aspect ratio result in higher elastic critical shear stress.

Considering the values in Table 6-3, it can be concluded that the elastic shear buckling stress is much larger than the concrete shear strength for minimum slab thickness (50 mm). Therefore the elastic shear buckling will not occur for the inter-rib section of the above-mentioned composite slabs.

6.4.1.2 Composite slab subjected to strut forces, (post-cracking condition)

As it was discussed in Chapter 3, (truss modelling) after concrete cracking compression struts form and the diaphragm imposed forces are transferred by strut and tie mechanism. In this situation, it could be assumed that in the compression strut zone (between cracks) the concrete material is still homogeneous. Based on this assumption, the concrete topping element (between ribs) experiences high axial forces in the direction of the concrete strut. For investigating the state of the concrete topping in this condition, the axial force is transformed to a combination of axial and shear stresses as shown in Figure 6-11. The maximum strut axial force could be found using truss element modelling described in Chapter 3.

The angle of the concrete strut may be any value between 0º and 90º for satisfying the equilibrium conditions based on the imposed forces to the diaphragm, floor plan dimensions and location of VLFR systems. In this study, because of using the strut forces from the truss modelling method, 45º angle for struts is assumed for simplicity.

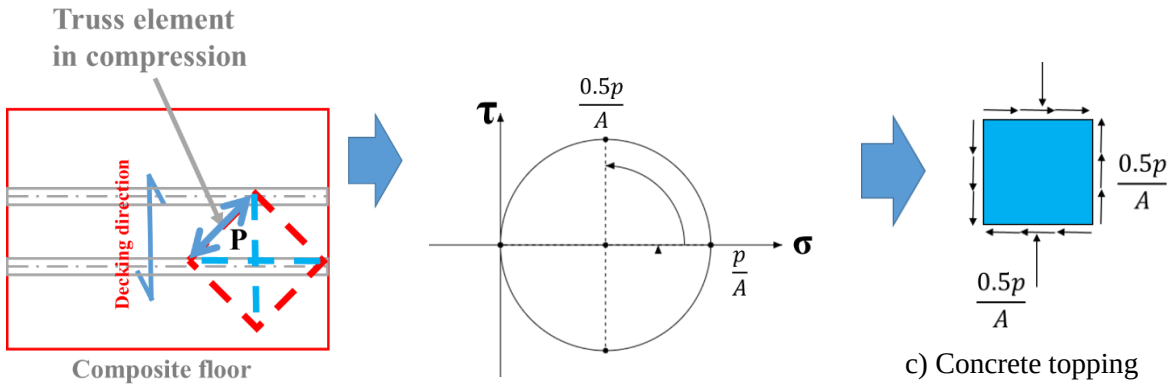

a) Axial force obtained from the truss element modelling

b) Mohr's circle

c) Concrete topping element between ribs

Figure 6-11. Transforming the axial force from truss element modelling to the axial and shear for the inter-rib element considering 45º angle between the strut and decking directions

Note that if the steel decking ribs be parallel or perpendicular to the concrete struts as shown in Figure 6-12, then only N_{cr} could be used as critical axial buckling stress.

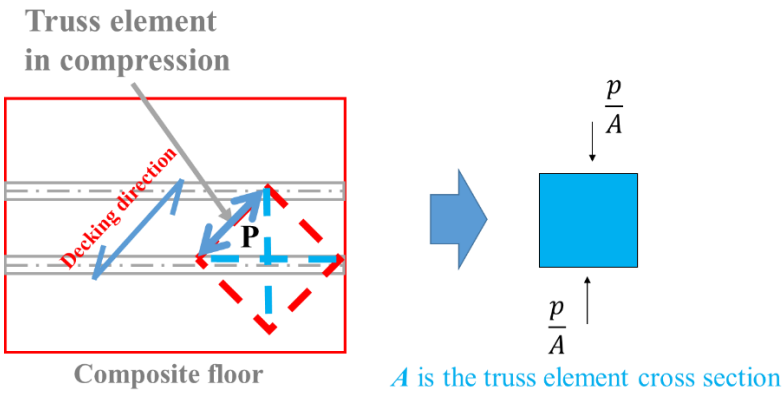

Figure 6-12. The axial force from truss element modelling used for the inter-rib element buckling considering the strut and decking directions are parallel

Considering the plate member subjected to axial stress, the solution of the general plate differential equation, Eq. (6-1), for elastic critical axial stress can be expressed as the following (Ziemian, 2010):

$$N_{cr} = k\frac{E\pi^2}{12(1-\nu^2)(b/t)^2} \qquad \text{Eq. (6-3)}$$

Where N_{cr} is the critical axial stress ($\bar{n}_x$), parameter k is the plate buckling coefficient determined by a theoretical critical-load analysis. This parameter is a function of the plate geometry and boundary conditions same as k_s. This parameter (k) is plotted against the plate aspect ratio for different edge support conditions in Figure 6-13. In this plot, the aspect ratio of the plate is used, considering the width of the plate (b) is perpendicular to the loading direction.

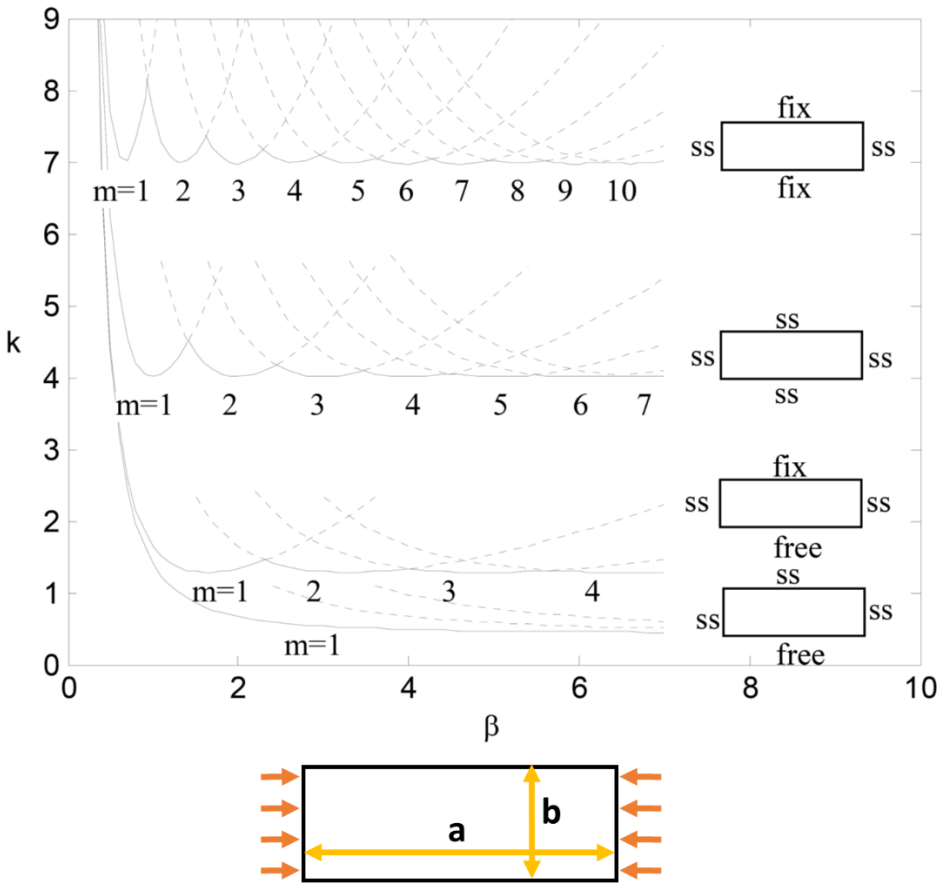

Figure 6-13. Plate buckling coefficient for plates under axial load, β=a/b, m=number of buckled half-waves along the length of the plate (Yu and Schafer, 2006)

Based on the plots in Figure 6-13, the lowest value of the plate buckling coefficient (k_{min}) when the plate is simply supported along all four edges is $k = 4$. This value can be increased by considering different aspect ratios. However, in this study, the lowest value is used to obtain conservative results.

On the other hand, in this case, both the shear and axial stresses are acting on the plate element simultaneously, therefore the interaction between shear and axial stresses need to be investigated. Iguchi (1938) suggested the following interaction formula:

$$\left(\frac{\partial_c}{N_{cr}}\right) + \left(\frac{\tau_c}{N_{xy1}}\right)^2 \leq 1 \qquad \text{Eq. (6-4)}$$

Where N_{cr} and N_{xy1} denote the critical axial and shear stress capacities, respectively, and ∂_c and τ_c represent the imposed axial and shear stress demands. Figure 6-14 plots the Eq. (6-4).

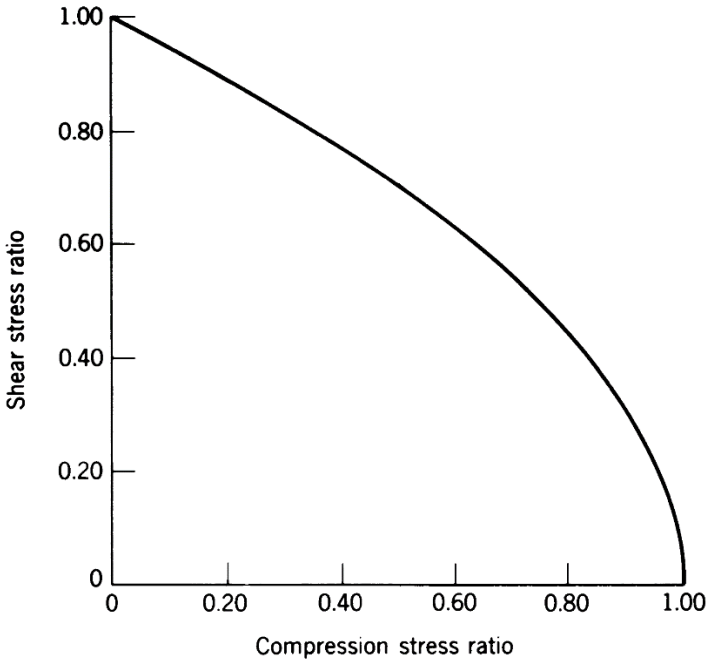

Figure 6-14. Interaction curve for buckling of flat plates subjected to uniform shear and compression (Ziemian, 2010)

- **Case study**

The elastic critical stress for three steel deck sections (ComFlor 60, 80 and 210) are investigated under the shear and compression stress. The assumptions for material properties and dimensions are the same as the previous section. It is considered that the plate buckling coefficient for the axial compression is $k = 4$ to obtain conservative results.

The imposed axial and shear stresses should be extracted from floor diaphragm analysis results, however, it is known that the shear stress cannot exceed the shear strength of concrete and also the axial compression stress is limited to concrete strut compression strength. In this section, the ultimate concrete strength in compression (strut strength) and shear are used as imposed forces to find out the possibility of inter-rib buckling mode.

The effective compressive strength of a concrete strut can be calculated based on Appendix A of NZS 3101 (2006) using the following equation:

$$f_{cu} = \beta_s \alpha_1 f_c' \qquad \text{Eq. (6-5)}$$

Where, β_s is equal to unity when the strut has the same width along its length. This parameter can get lower values based on the concrete type and geometry of the strut. Using $\beta_s = 1$ gives higher axial strength which turns to more conservative results in the case considered. The parameter α_1 accounts for equivalent rectangular concrete stress distribution which can be taken as 0.85 for concrete strengths up to 55 MPa.

The ultimate values of the shear and axial strengths are controlled by concrete failure mechanism under combined shear an axial stresses. Figure 6-15 shows the shear and axial stress interaction plot of concrete material which was found by Bresler and Pister (1958). Therefore the ultimate shear and axial compression that are acting simultaneously on the concrete plate are lower than the ultimate strength under uniaxial compression or pure shear conditions due to shear and axial stress interaction.

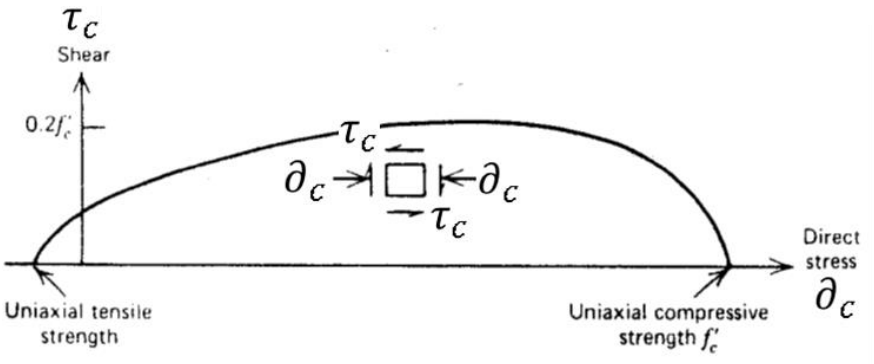

Figure 6-15. Shear and axial stress interaction plot (material capacity) (Bresler and Pister, 1958)

As a conservative assumption, the ultimate shear and axial compressive strengths of the concrete material are considered as imposed forces to the plate member without taking into account the material interaction failure.

The critical elastic buckling interaction values (demand to capacity ratio) using Eq. (6-4) are presented in Table 6-4 for selected concrete topping thicknesses.

Table 6-4. Interaction values for ComFlor 60, 80 and 210 subjected to shear and uniform compression (demand to capacity ratio)

	CF60	**CF80**	**CF210**
Concrete topping thickness (mm)	**Interaction values (DCR)**		
1	8.70	10.09	244.54
2	1.88	2.15	29.12
3	0.81	0.92	10.34
4	0.45	0.51	5.30
5	0.28	0.32	3.24
10	0.07	0.08	0.76
20	0.01	0.02	0.18
30	0.008	0.009	0.08
40	0.004	0.005	0.04
50	0.003	0.003	0.03
60	0.002	0.002	0.02
70	0.001	0.002	0.01
80	0.001	0.001	0.01
90	0.001	0.001	0.009
Note: $DCR = \left(\frac{\partial_c}{N_{cr}}\right) + \left(\frac{\tau_c}{N_{xy1}}\right)^2$ and $DCR < 1 \rightarrow safe\ zone$			

As it is shown in this Table, when DCR is less than unity means the buckling criteria does not govern. The critical thickness for ComFlor 60 and 80 is between 2 and 3 mm and it is about 9 mm for ComFlor 210. It should be noted that the boundary conditions are considered simply supported and the lowest buckling coefficient is used. Changing these assumptions to clamped edges or rectangular plate with lower aspect ratio result in lower DCR values.

Considering the values in Table 6-4, it can be concluded that the elastic buckling strength under a combination of axial and shear stresses is much larger than the concrete strength for minimum slab thickness (50 mm). Therefore, buckling will not occur for the inter-rib section of the above-mentioned floor slabs subjected to strut forces. Any other floor slab section with different cross-section and geometry can also be investigated using the presented equations.

6.4.2 Buckling mode 2, intra-panel buckling

Another buckling mode that may occur in the composite floor slabs is "intra-panel buckling". In this buckling mode, the composite slab in the panel between the secondary beams is considered to experience instability under the in-plane imposed forces and the secondary beams act as nodal lines for the panels.

The intra-panel buckling mode was also investigated in pre and post-cracking stages of the concrete. This is because, the concrete can crack at low tension stresses, therefore the state of the pure shear can change to diagonal compression due to concrete strut formation after the cracking. Figure 6-16 shows the intra-panel subjected to pure shear (pre-crack) and compression strut force (post-crack) conditions.

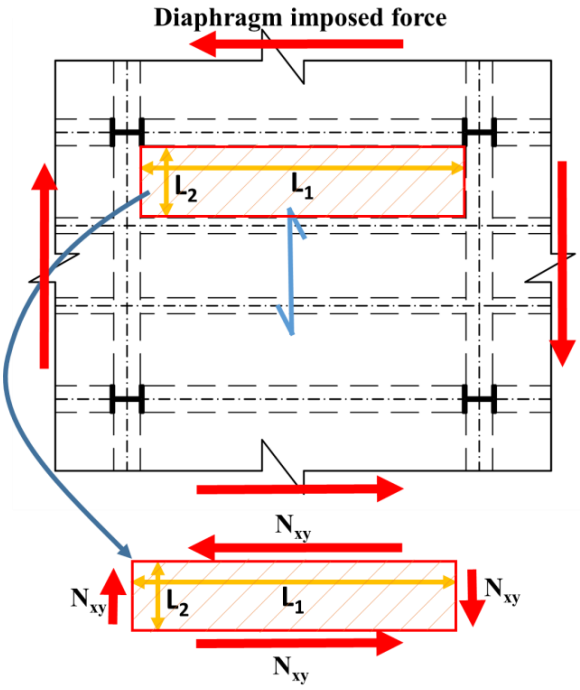

a) Intra-panel subject to pure shear, (pre-crack)

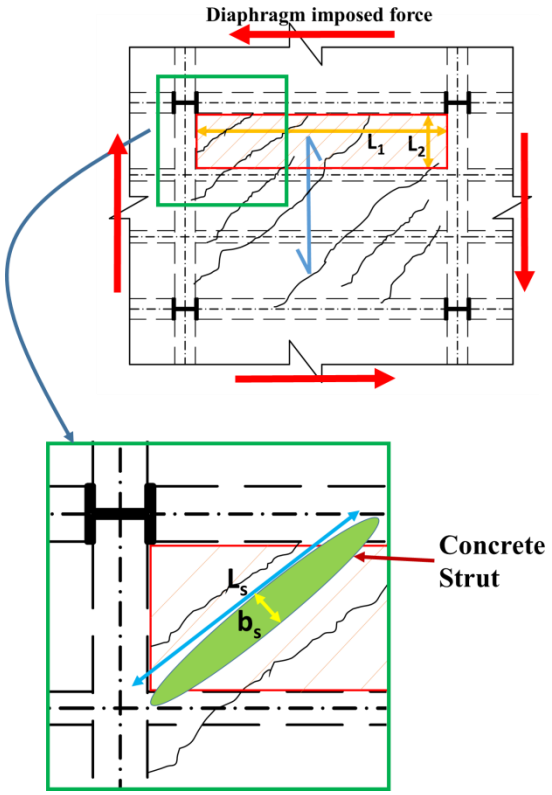

b) Intra-panel subject to diagonal strut forces, (post-crack)

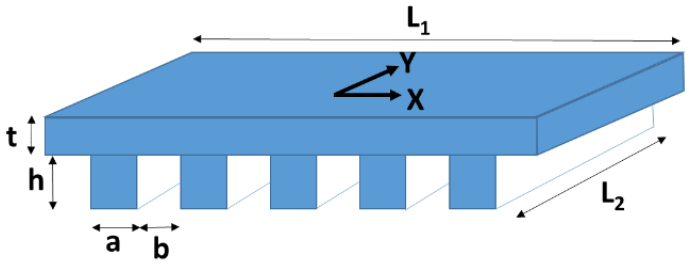

c) Intra-panel cross-section

Figure 6-16. Intra-panel loading conditions

The composite floor slab is not a flat plate member because of the ribs shown in Figure 6-16. The ribs stiffen the concrete topping. Therefore, this situation is more complicated than the buckling of a simple uniform plate.

There are two methods for finding the critical buckling loads of such stiffened plate member,

1) analytical approach and

2) FEM modelling.

It is obvious that using FEM would be easier and in some cases more precise because, in numerical investigations, imperfections, realistic boundary conditions and also residual stresses could be included in the model. However, the disadvantage of FEM modelling is that the numerical study is limited to a number of models and limited results. However, the analytical method is more difficult to obtain due to mathematical works, but the results are more general and the upper and lower limits could be investigated more easily. Using the analytical approach, a general method for investigating any other case could be developed. In this section, the critical buckling loads are investigated analytically and the results are verified with the FEM models.

Investigating the critical buckling load of the intra-panel subjected to non-uniform loads and different loading conditions is complicated. Also, the nature of imposed loads are not fully known, therefore in this study two loading scenarios are investigated include

1) the intra-panel subjected to uniform pure shear stress (pre-cracking) and

2) the intra-panel subjected to diagonal compression (strut force) after concrete cracking.

6.4.2.1 Intra-panel subjected to uniform shear stress (pre-cracking)

The critical buckling load of the intra-panel zone is investigated by studying the buckling behaviour of the *equivalent* orthotropic plate member. In the next sections, the method for finding an *equivalent* orthotropic plate and the critical buckling load of the orthotropic plate is discussed.

- ***Equivalent orthotropic plate***

The composite floor slab is like a plate member that is stiffened by ribs. Generally, the stiffened plate members have been used in civil, marine, aerospace and lots of other engineering fields. Steel bridges, ship and aeroplane structure are the examples of using stiffened plate elements. Since decreasing the structure weight was and is the most important parameter in design especially for marine and aerospace applications, the buckling phenomenon and stability was the main concern in these elements. Investigating the critical buckling load of stiffened plates was in the focus of researchers during the 1940s and 1950s (e.g. Wittrick 1954, Seide and Stein 1949, Seide 1953).

Generally, an *orthotropic* plate is defined as a plate member that has different elastic material properties in two perpendicular directions. The orthotropic plate theory has the same assumptions as the isotropic plate theory, include:

1. The plate material is homogenous and also continuous between outer surfaces of the plate.
2. The plate thickness is uniform and is small compared to the other plate dimensions.
3. The plate material is in accordance with Hooke’s law.
4. The plate deformations are small compared to plate thickness.

It should be considered that the composite slab differs in several aspects from an ideal orthotropic plate. The most important difference is that the composite slab is not continuous which means the material does not fill the space between outer plate surfaces (between ribs). Also, unlike the ideal orthotropic plate, the different rigidities in two perpendicular directions come from different geometric properties rather than from difference in material properties. Also, due to eccentric arrangements of ribs, the neutral surfaces for bending in two directions do not coincide (Figure 6-17).

Although the actual structural behaviour of the composite floor slab cannot be exactly replaced with an orthotropic plate, this method has been used in other engineering fields like marine and aerospace and past experimental results indicated good agreement between this idealisation and the real stiffened plate.

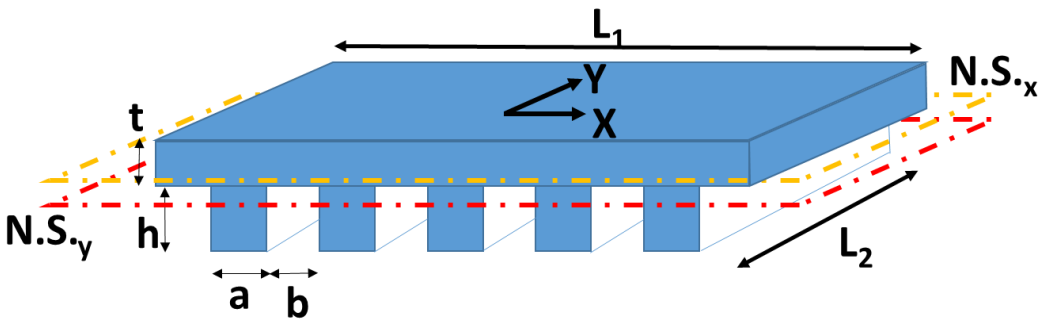

a) Composite slab schematic view

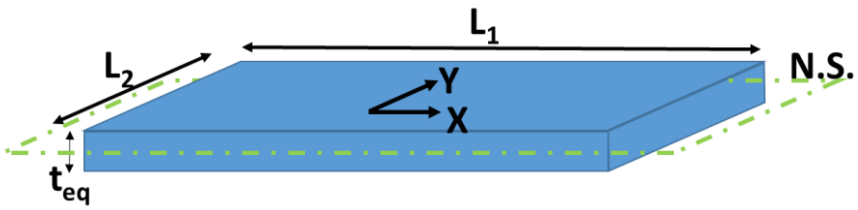

b) Equivalent orthotropic plate

Figure 6-17. Neutral surfaces in composite slab and equivalent orthotropic plate

To obtain an equivalent orthotropic plate for the composite slab, two conditions need to be satisfied

1) the stiffness of the composite slab and the equivalent orthotropic plate need to be equal and

2) the stresses in the equivalent orthotropic plate and the composite slab need to be equal.

The thickness of the equivalent orthotropic plate, and the elastic modulus and Poisson's ratio of both perpendicular directions ($E_x, E_y, \vartheta_x \; and \; \nu_y$) need to be obtained to satisfy these conditions.

The flexural stiffness of the composite floor (that is equal to the equivalent orthotropic plate) is required to calculate the critical buckling loads using orthotropic plate theory.

For an isotropic plate the flexural rigidity can be calculated using:

$$D = \frac{Et^3}{12(1-\nu^2)}$$

Where t is the plate thickness and E and ν are the elastic modulus and Poisson's ratio of the slab material respectively. Similar to the beam theory, the flexural moment (m_x) is equal to flexural stiffness (D) multiplied by the plate curvature ($\frac{\partial^2 w}{\partial x^2} + \nu \frac{\partial^2 w}{\partial y^2}$).

$$m_x = -D\left(\frac{\partial^2 w}{\partial x^2} + \nu \frac{\partial^2 w}{\partial y^2}\right) \qquad \text{Eq. (6-6)}$$

$$m_y = -D\left(\frac{\partial^2 w}{\partial y^2} + \nu \frac{\partial^2 w}{\partial x^2}\right) \qquad \text{Eq. (6-7)}$$

$$m_{xy} = -2B\left(\frac{\partial^2 w}{\partial x \partial y}\right) \qquad \text{Eq. (6-8)}$$

For simplicity in finding the flexural rigidities of the composite slab, a long simply supported slab is assumed. In this case the curvature in the direction perpendicular to the direction under study ($\nu \frac{\partial^2 w}{\partial y^2}$ or $\nu \frac{\partial^2 w}{\partial x^2}$) could be considered equal to zero. Therefore the Eqs. (6-6) and (6-7) change to Eqs. (6-9) and (6-10) respectively:

$$m_x = -D_x\left(\frac{d^2 w}{dx^2}\right) \qquad \text{Eq. (6-9)}$$

$$m_y = -D_y\left(\frac{d^2w}{dy^2}\right) \qquad \text{Eq. (6-10)}$$

Where D_x and D_y could be found using cross-section properties of the composite slab. The flexural stiffness of the composite slab in the Y direction (D_y), which includes the concrete topping and the ribs cross-section, could be found using the parallel axis theorem. The only difference is that the plate part (concrete topping) should be divided by $(1-\nu^2)$ for considering the plate action. Eq. (6-11) shows the flexural stiffness of the composite slab in the Y direction. The first bracket in this equation relates to zone 1 and the second bracket relates to zone 2, shown in Figure 6-18.

$$D_y = \left[\frac{Et^3}{12(1-\nu^2)} + \frac{Ete_y{}^2}{(1-\nu^2)}\right]_1 + \left[\frac{Eah^3}{12(a+b)} + \frac{Eha\left(\frac{h}{2}+\frac{t}{2}-e_y\right)^2}{(a+b)}\right]_2 \qquad \text{Eq. (6-11)}$$

Where E and ν are the elastic modulus and Poisson's ratio of the concrete material respectively. Other parameters are shown in Figure 6-18. It should be noted that e_y is the distance between the neutral axis and mid-height of the concrete topping.

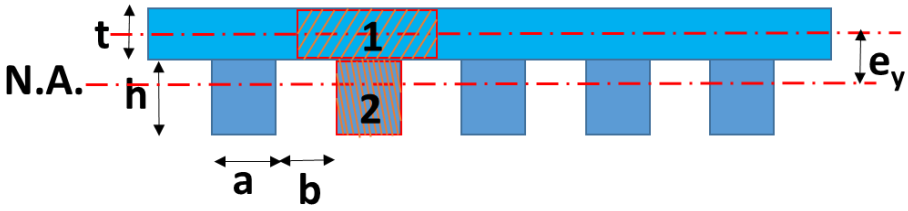

Figure 6-18. Composite slab cross-section

The flexural stiffness in the X direction, D_x, could not be found simply using cross-sectional properties because the thickness of the composite slab is not uniform in this direction and it changes between the ribs and concrete topping. Therefore the problem can be solved assuming series of flexural springs (ribs and concrete topping). Considering that the concrete topping and the ribs are acting as a flexural spring, the total stiffness of the composite slab can be found using Eq. (6-12). Where D_a and D_b are the flexural stiffness of one rib and one concrete topping respectively as shown in Figure 6-19.

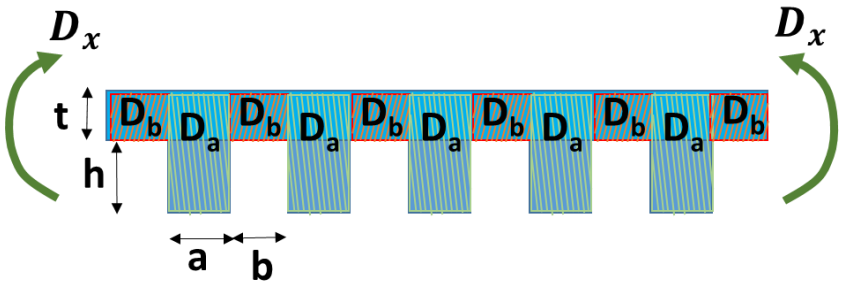

Figure 6-19. Flexural stiffness in the X direction, D_x, ribs and concrete topping are considered as series of springs

However, since the thickness changes suddenly from the concrete topping to the ribs, and also the ribs are not eccentric with concrete topping, a part of the ribs flexural stiffness contribute in the total slab stiffness as shown in Figure 6-20.

$$D_x = \frac{D_a D_b (a+b)}{(bD_a + aD_b)} \qquad \text{Eq. (6-12)}$$

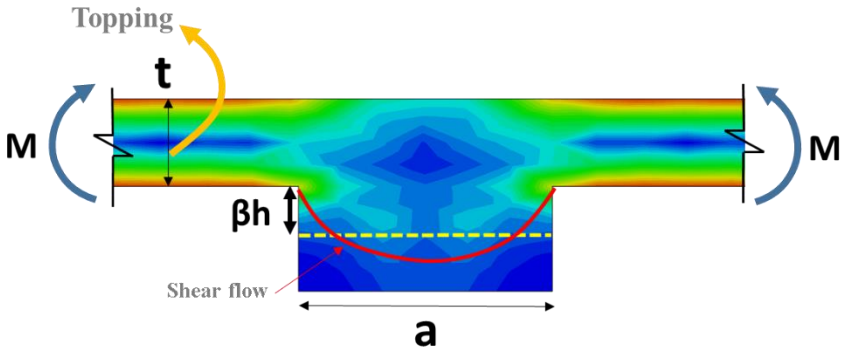

Figure 6-20. Effective height of the ribs contributing to the plate flexural stiffness

To address this issue, the parameter β (ribs height modification factor) is introduced for adjusting the ribs height to calculate the effective thickness of the ribs that contribute in the flexural stiffness of the slab (Eqs. (6-13) and (6-14)).

$$D_a = \frac{E(t+\beta h)^3}{12(1-\nu^2)} \qquad \text{Eq. (6-13)}$$

$$D_b = \frac{Et^3}{12(1-\nu^2)} \qquad \text{Eq. (6-14)}$$

In this study, β is found using a comprehensive FEM parametric study. A series of FEM models with different dimensions are created and the flexural stiffness of the models are

recorded. Then the parameter β is obtained by adjusting the FEM stiffness and the calculated stiffness using Eq. (6-12).

Models included a 20×3m panel which was loaded with uniform moment along the 20m long edge. The concrete topping thickness, ribs dimensions and the distance between ribs for different models are presented in Table 6-5.

Table 6-5. Concrete topping thickness, ribs dimensions and distance for the studied models

t (mm)	**a (mm)**	**b (mm)**	**h (mm)**	**b/a**	**h/a**	**Dx FEM (N.mm/mm)**	**β**
50	100	20	20	0.2	0.2	3.63E+09	0.5381
50	100	20	50	0.2	0.5	3.86E+09	0.2495
50	100	20	100	0.2	1	3.88E+09	0.1263
50	100	20	200	0.2	2	3.89E+09	0.0636
50	100	50	20	0.5	0.2	3.24E+09	0.5319
50	100	50	50	0.5	0.5	3.44E+09	0.2615
50	100	50	100	0.5	1	3.49E+09	0.1365
50	100	50	200	0.5	2	3.5E+09	0.0692
25	100	50	20	0.5	0.2	5.08E+08	0.5313
25	100	50	50	0.5	0.5	5.47E+08	0.2603
25	100	50	100	0.5	1	5.54E+08	0.1344
25	100	50	200	0.5	2	5.56E+08	0.0680
25	50	50	10	1	0.2	3.65E+08	0.5155
25	50	50	25	1	0.5	3.79E+08	0.2521
25	50	50	50	1	1	3.82E+08	0.1311
25	50	50	100	1	2	3.83E+08	0.0665
50	100	200	5	2	0.05	2.46E+09	0.7996
50	100	200	10	2	0.1	2.57E+09	0.6978
50	100	200	15	2	0.15	2.64E+09	0.6150
50	100	200	25	2	0.25	2.71E+09	0.4627
50	100	200	30	2	0.3	2.72E+09	0.3980
50	100	200	35	2	0.35	2.73E+09	0.3507
50	100	200	40	2	0.4	2.73E+09	0.3080
50	100	200	75	2	0.75	2.73E+09	0.1667
50	100	200	100	2	1	2.74E+09	0.1256
50	100	200	150	2	1.5	2.74E+09	0.0839
$E = 200\ GPa, \nu = 0.3$							

The results show that the parameter β is directly related to the ribs aspect ratio (h/a) and other parameters such as b/a did not have any significant effect. Figure 6-21 plots β against the rib aspect ratio (h/a). In order to find an equation that fits best to the plot, the curve is

divided in two parts for h/a values less than 0.4 and greater than 0.4. Eq. (6-15) shows the relationship between β and the rib aspect ratio.

$$\begin{cases} \beta = 0.9224e^{\left(\frac{-2.756h}{a}\right)} & for\ \frac{h}{a} \le 0.4 \quad (a) \\ \beta = \frac{a}{8h} & for\ \frac{h}{a} > 0.4 \quad (b) \end{cases} \qquad \text{Eq. (6-15)}$$

Alternatively, the following equation could be used for $\frac{h}{a} > 0.1$.

$$\beta = 0.136e^{\left(\frac{-0.745h}{a}\right)} \quad for\ \frac{h}{a} > 0.1 \qquad \text{Eq. (6-16)}$$

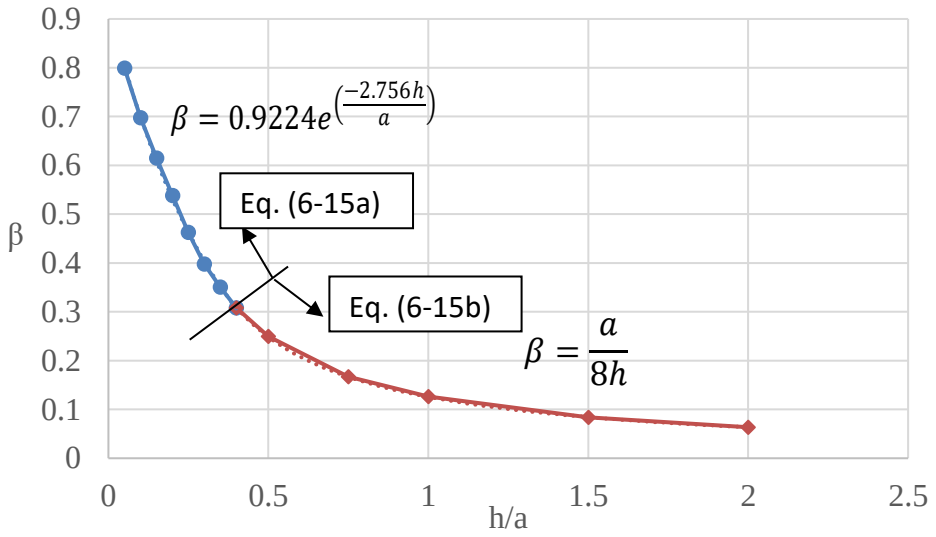

a) Eq. (6-15) plot

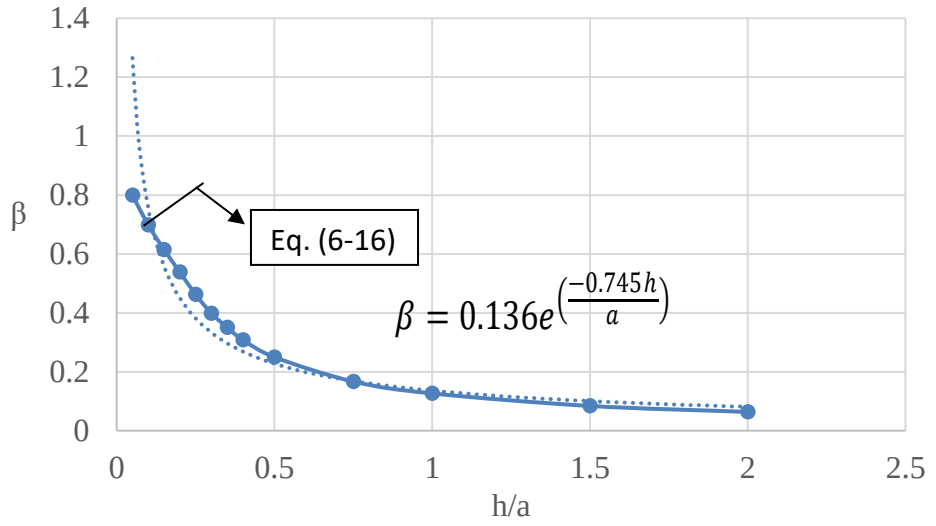

b) Eq. (6-16) plot

Figure 6-21. Parameter β against rib aspect ratio

- **Verification of plate stiffness equations with FEM models**

Two steel deck sections (ComFlor 60 and 80) are modelled to check the accuracy of the flexural rigidity equations presented in the previous section. The geometry of the ComFlor steel deck sections are shown in Figure 6-9. Table 6-6 presents the flexural rigidity of the FEM models and the calculated values using Eqs. (6-11) and (6-12).

Table 6-6. Flexural stiffness of steel deck sections

Flexural rigidities		**ComFlor 80** a=135mm, b=165mm, h=80mm, t=50mm,	Error (%)	**ComFlor 60** a=145mm, b=155mm, h=60mm, t=50mm,	Error (%)
$\boldsymbol{D_x}$ (N.mm)	FEM	375187359.2	2.04	389578768	1.61
	Eq. (6-12)	367533583.7		383277897.1	
$L_1 = 20m, L_2 = 4m, E = 25\ GPa, \nu = 0.2$					
$\boldsymbol{D_y}$ (N.mm)	FEM	2932455769	2.32	1861889197	1.94
	Eq. (6-11)	3000582869		1898051939	
$L_1 = 6m, L_2 = 4m, E = 25\ GPa, \nu = 0.2$					

The results show that the differences in the stiffness values were less than 2.5%. It should be noted that the FEM modelling parameters such as mesh size, element type and also numerical error could also have some share in this error.

- **Torsional stiffness of the orthotropic plate**

The torsional stiffness of the orthotropic plate is another parameter that is needed for calculating the critical elastic buckling load. Generally, the torsional rigidity is more difficult to obtain and usually it is calculated with a reasonable approximation. The torsional stiffness of two-way reinforced concrete slab of uniform thickness could be obtained using Eq. (6-17) (Szilard, 1974).

$$B = \sqrt{D_x D_y} \qquad \text{Eq. (6-17)}$$

To calculate the torsional stiffness of the composite slabs, the ribs and the slab are considered separately in Eq. (6-18) (Szilard, 1974).

$$B = \frac{Et^3}{12(1-\nu^2)} + \frac{G_{xy}}{2}\frac{ha^3\eta}{(a+b)}k_B \qquad \text{Eq. (6-18)}$$

Where G_{xy} is the concrete shear modulus and η is a numerical factor depending on the ribs aspect ratios which is presented in Table 6-7. The parameter k_B is a reduction factor accounting for the decrease in the torsional stiffness of the reinforced concrete beams due to concrete cracking. This parameter relates to ribs aspect ratio, reinforcement and also applied bending moment to the member (Szilard, 1974). In this study k_B is taken as zero conservatively.

Table 6-7. Parameter η (Szilard, 1974)

a/h	1	1.2	1.5	2	2.5	3	4	6	8	10	∞
η	0.140	0.166	0.196	0.229	0.249	0.263	0.281	0.299	0.307	0.313	0.333

- ***Buckling of an orthotropic plate***

The critical elastic buckling load of the composite slab (between secondary beams) is investigated using the plate flexural stiffness found in the previous section. Generally, investigating the buckling behaviour of an intra-panel section is more complicated than the inter-rib (local) buckling of the concrete topping. This complexity is due to the fact that

1) the intra-panel usually is subjected to a combination of different stresses,
2) boundary conditions might vary from simply supported to fully clamped and
3) the imposed forces to the panel usually are not uniform.

In this research, it is assumed that the governing in-plane imposed force to the diaphragm is in the form of shear stress coming from transfer forces. For simplicity, it is assumed that these shear forces are applied uniformly to the floor slab edges. And for obtaining more conservative results, all edges are considered simply supported.

Equation (6-19) presents the general governing differential equation of elastic stability for an orthogonal plate. This equation is similar to Eq. (6-1) for isotropic plates and only the flexural stiffness are different. With solving this differential equation for various boundary conditions and loading patterns, the critical buckling load $\bar{n}$, can be calculated. For solving the

differential equation Eq. (6-19) the in-plane stresses, $\bar{n}_{x0}$, $\bar{n}_{y0}$ and $\bar{n}_{xy0}$, are applied singly or in a certain combination.

$$D_x \frac{\partial^4 w}{\partial x^4} + 2\mathrm{B} \frac{\partial^4 w}{\partial x^2 \partial y^2} + D_y \frac{\partial^4 w}{\partial y^4} = \left(\bar{n}_{x0} \frac{\partial^2 w}{\partial x^2} + 2\bar{n}_{xy0} \frac{\partial^2 w}{\partial x\, \partial y} + \bar{n}_{y0} \frac{\partial^2 w}{\partial y^2} \right) \qquad \text{Eq. (6-19)}$$

Where $\bar{n}_{x0}$, $\bar{n}_{y0}$ and $\bar{n}_{xy0}$ are the axial and shear in-plane stresses applied at the boundaries of the middle surface of the orthotropic plate, and D_x, D_y and B are the orthotropic plate flexural stiffness in x and y directions and the torsional rigidity, respectively.

Considering the intra-panel member subjected to the pure shear ($\bar{n}_{x0} = \bar{n}_{y0} = 0$) stress, the solution of the differential equation (Ziemian, 2010) for the elastic critical shear stress (buckling stress) is expressed as Eq. (6-20):

$$N_{xy2} = K_s \frac{\pi^2}{t {L_2}^2} \sqrt[4]{D_x {D_y}^3} \qquad \text{Eq. (6-20)}$$

Where N_{xy2} is the elastic critical shear stress for the intra-panel zone, D_x and D_y are the orthotropic plate stiffness, and L_2 is the length perpendicular to X-axis as shown in Figure 6-17. The parameter K_s is the plate buckling coefficient determined by a theoretical critical-load analysis. This parameter is a function of plate geometry and boundary conditions. The parameter K_s is plotted for three edge support conditions in Figure 6-22 (Ziemian, 2010). In these plots D_1, D_2 and D_3 are D_x, D_y and B respectively.

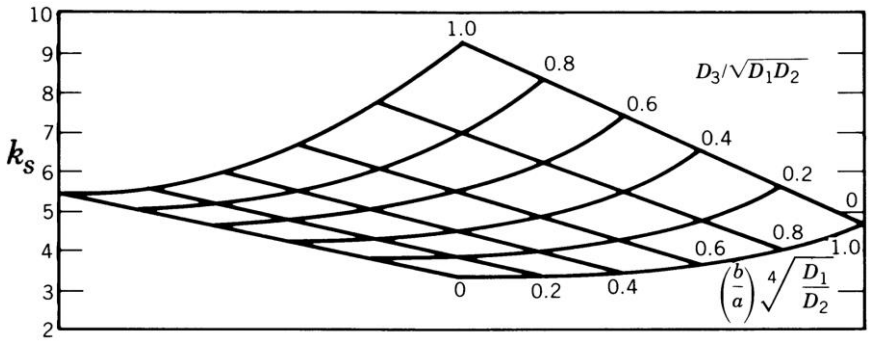

a) All edges simply supported

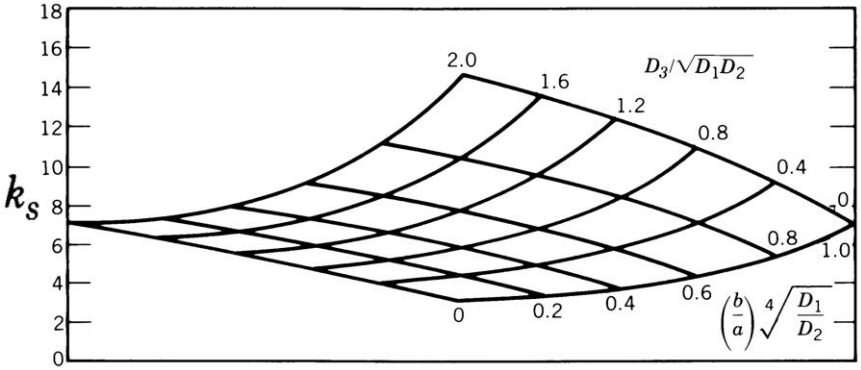

b) Edges perpendicular to y-axis clamped, other edges simply supported

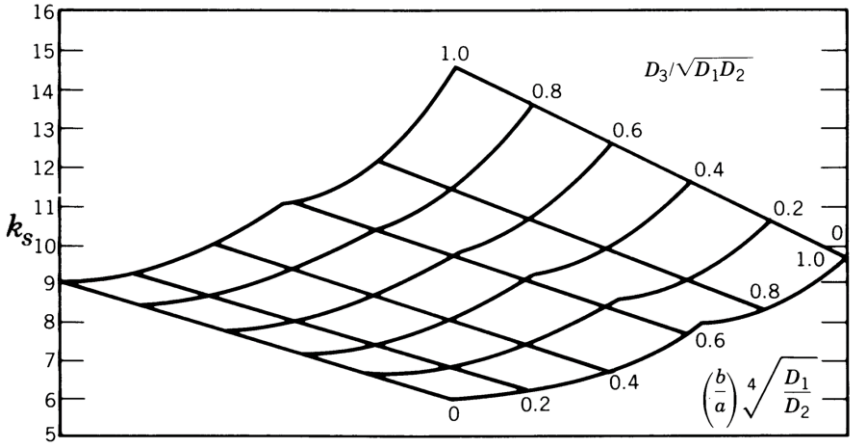

c) All edges clamped

Figure 6-22. Shear buckling coefficient for orthotropic plates (Ziemian, 2010), as adapted from Johns and Kirkpatrick (1971)

Based on the orthotropic plate stiffness, the parameter K_s can be extracted from the plots presented in Figure 6-22. It is noted that in this study all the boundary conditions are considered as simply supported, so Figure 6-22a is used, to obtain conservative results.

- **Case study**

The intra-panel elastic shear buckling for two ComFlor profiles (60 and 80), shown in Figure 6-9, is investigated both using Eq. (6-20) and the FEM model. Two floor slabs were designed using ComFlor Steel Composite Metal Deck Design software and they are used for the buckling study.

The gravity loads used for the design of ComFlor floor slabs include: 3 kPa imposed action (Q), 1 kPa for ceiling/services and finishes, 1 kPa for partitions, and self-weight of the floor

slab (G) was calculated by the software based on the slab thickness and the steel decking weight. It is assumed that the concrete compressive strength is 30 MPa with an elastic modulus of 25 GPa. It was tried to find the maximum possible span with 60 mm concrete topping for both ComFlor 60 and 80 steel decks. Figure 6-23 shows the assumptions and parameters used for design. The full design reports are presented in Appendix I.

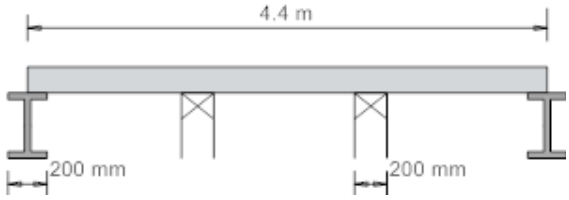

a) ComFlor 60, 4.4 m span, propped during construction

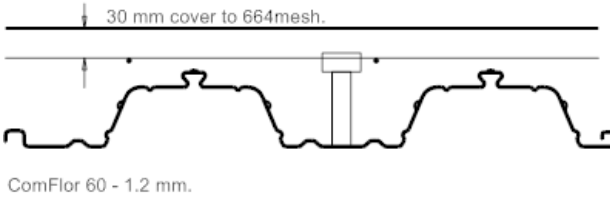

b) ComFlor 60, steel deck thickness 1.2 mm

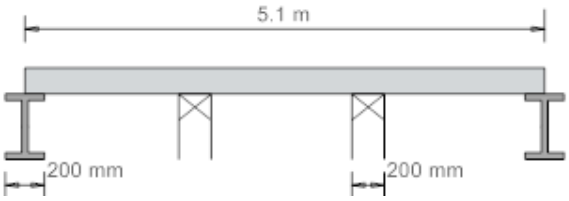

c) ComFlor 80, 5.1 m span, propped during construction

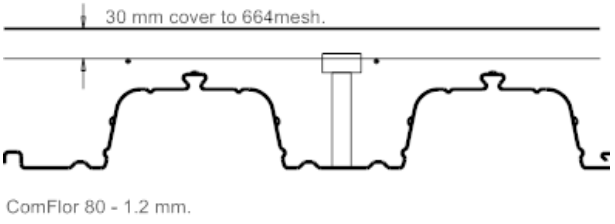

d) ComFlor 80, steel deck thickness 1.2 mm

Figure 6-23. ComFlor 60 and 80 with 60 mm concrete topping (ComFlor software)

The critical buckling loads of the floor slabs are studied with and without considering the stiffness reduction factor accounting for concrete cracking due to flexural moments. The stiffness reduction factor of 0.35 is selected based on Table C6.5 NZS3101 (2006) for members subjected to bending moments. Although the elastic shear buckling here is based on the assumption that the concrete is un-cracked, the cracking reduction factor is just considered for decreasing the bending rigidity which yields to lower buckling loads and gives more conservative result considering the tension behaviour of the concrete material.

Table 6-8 shows the results of critical shear stress using Eq. (6-20) for a 5 m long panel and also an infinite length panel, and widths, L_2, of 4.4m and 5m.

Table 6-8. Critical edge shear stress for ComFlor 60 and 80 with 60 mm topping ($f_c' = 30\ MPa$, $E_c = 25\ GPa$ and decking thickness 1.2mm)

		ComFlor 60	**ComFlor 80**
		$L_2 = 4.4\ m$	$L_2 = 5.1\ m$
		Total slab thickness =120 mm	Total slab thickness =140 mm
		N_{xy2} (MPa)	
Total Elastic	$L_1 = 5\ m$	101.7	93.5
	$L_1 \to \infty$	80.8	73.9
Considering stiffness reduction factors	$L_1 = 5\ m$	35.6	33.8
	$L_1 \to \infty$	28.3	26.9

To verify the results obtained using the analytical approach, the FEM modelling is used. Two ComFlor profiles (60 and 80) with 5m long are modelled in ABAQUS software. The material was considered to be elastic with 25 GPa elastic modulus and 0.2 Poisson's ratio. The intra-panel was subjected to pure shear loading and the shear forces and the corresponding shear displacement were recorded during the analysis.

As it was mentioned before, the plate buckling occurs by gradual distortion of the cross-section of the member. Therefore, for finding the buckling load, the models are analysed with and without geometric nonlinearity. The shear force-displacement of a model is shown in Figure 6-24 schematically. Where F_E is the analysis without the geometric nonlinearity and F_{NG} is the force-displacement plot considering the geometric nonlinearity. In this study, the buckling load is defined at the point where the difference between these two plots ($F_E - F_{NG}$) becomes more than 1% of the corresponding F_E value.

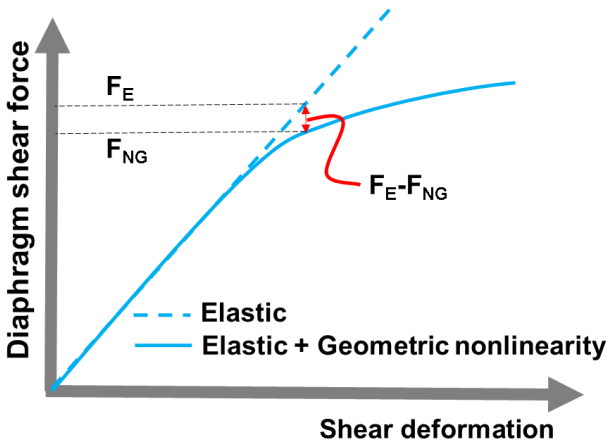

Figure 6-24. Shear force-displacement plot of a diaphragm with and without considering geometric nonlinearity

Figure 6-25 and Figure 6-26 show the FEM model and the floor slab deformed shape at the buckling step of the analysis and the recorded shear force-displacement.

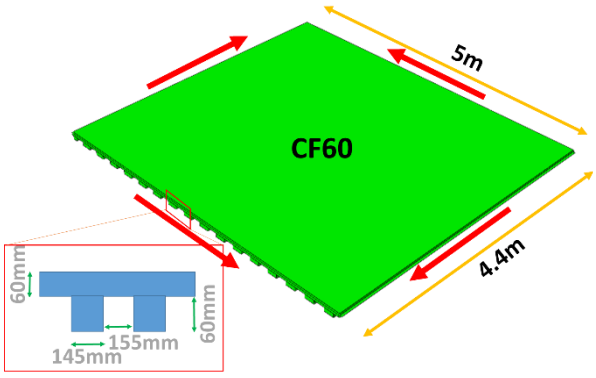

a) FEM model of ComFlor 60

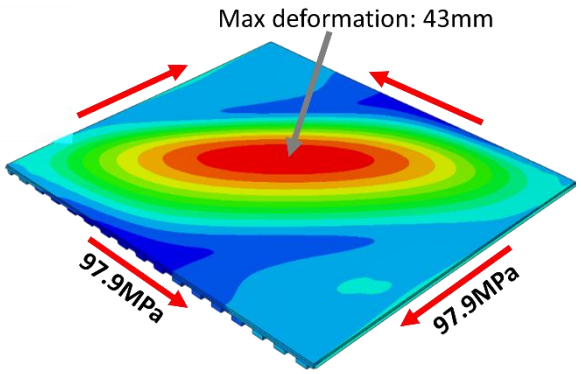

b) Out-of-plane displacement of the panel (displacement contour)

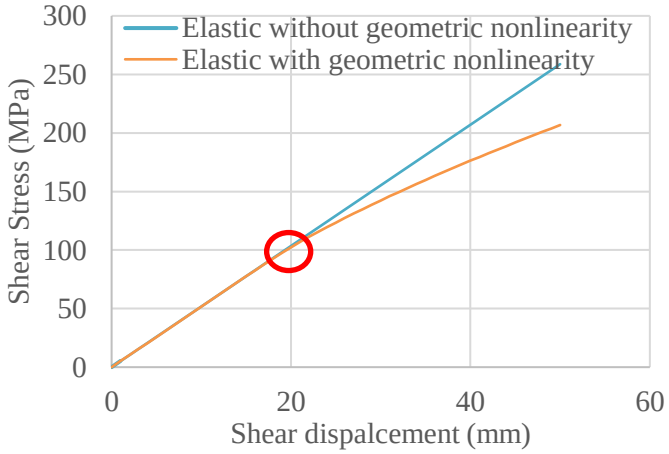

c) Shear force-displacement plot for ComFlor 60

Figure 6-25. FEM model of ComFlor 60 subjected to a pure shear condition

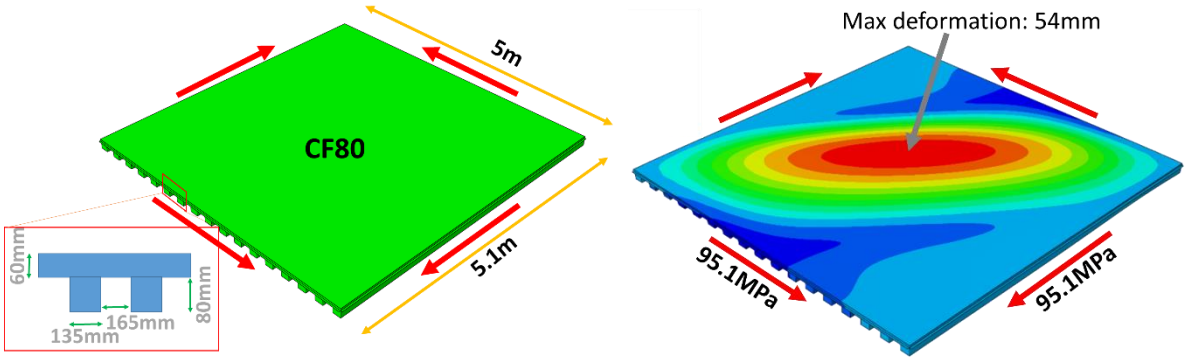

a) FEM model of ComFlor 80

b) Out-of-plane displacement of the panel (displacement contour)

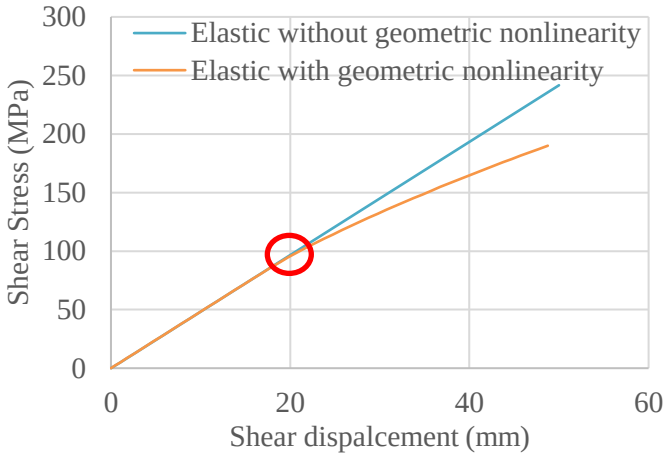

c) Shear force-displacement plot for ComFlor 80

Figure 6-26. FEM model of ComFlor 80 subjected to a pure shear condition

Each model was analysed two times with considering the geometric nonlinearity and without the geometric nonlinearity to find the critical buckling load. Based on these plots, the buckling stresses for ComFlor 60 and 80 are found 97.9 MPa and 95.1 MPa respectively. These are similar to the values from Eq. (6-20) given in Table 6-8 of 101.7 MPa and 93.5 MPa with errors being 3.7% and -1.8% respectively.

The results show that the analytical approach is able to estimate the critical buckling load reasonably compared to FEM models. In the next step, these critical buckling loads are compared with the ultimate shear strength of the panel to find out the possibility of the shear buckling for the studied intra-panels.

- **Slab shear strength**

The shear strength of the composite slabs can be calculated using the equation provided by NZS3404 (2007) Clause 13.4.10.2.

$$V_r = \min \begin{cases} \left(0.8\emptyset A_{rt} f_{yr} + 2.76\emptyset_c A_{cv}\right) \\ 0.5\emptyset_c f_c' A_{cv} \end{cases} \quad \text{Eq. (6-21)}$$

Where A_{rt} is the area of transverse reinforcements crossing shear planes, A_{cv} is the area of concrete in shear planes and f_{yr} is the yield stress of tension reinforcement. The reduction factors $\emptyset$ and $\emptyset_c$ are equal to 0.9 and 0.6 respectively. Here the upper bond value of this formula ($0.5\emptyset_c f_c' A_{cv}$) is considered as the shear strength of the composite slabs. The calculated shear strength values and the critical shear buckling loads for the infinitely long panel considering stiffness reduction factors are presented in Table 6-9.

Table 6-9. Calculated shear strength and the critical shear buckling loads for infinitely long ComFlor 60 and 80

	ComFlor 60	**ComFlor 80**
	Shear stress (MPa)	
	$L_2 = 4.4\ m$	$L_2 = 5.1\ m$
critical shear buckling stress (Eq. (6-20))	28.2	26.9
shear strength ($0.5\emptyset_c f_c'$)	9	9

The results show that the elastic shear buckling loads are about three times the upper bound shear strength of the composite slab. Therefore, it can be concluded that the elastic shear buckling does not govern in the studied cases. The critical shear buckling capacity of any other type of floor slab can be investigated using Eq. (6-20) and the orthotropic plate stiffness formulations (Eqs. (6-11) to (6-18)).

6.4.2.2 Intra-panel subjected to diagonal force (strut force), post-cracking stage

- **Theoretical development**

After crack formation in the concrete of the composite slab, the stress distribution changes and concrete compression struts form and the diaphragm imposed forces are transferred by a

strut-and-tie mechanism. The compression struts that are formed between secondary beams (i.e. within the panel) may experience instability under high axial loads. In this section, the critical compressive buckling load of a strut in the intra-panel zone is investigated.

The ribs in composite slab act as stiffeners for the concrete topping and also support the gravity forces. When the panel is subjected to in-plane shear forces, concrete strut forces are carried by the concrete topping because the ribs are not continuous. Here, the ribs provide out-of-plane restraint for the concrete struts as shown in Figure 6-27.

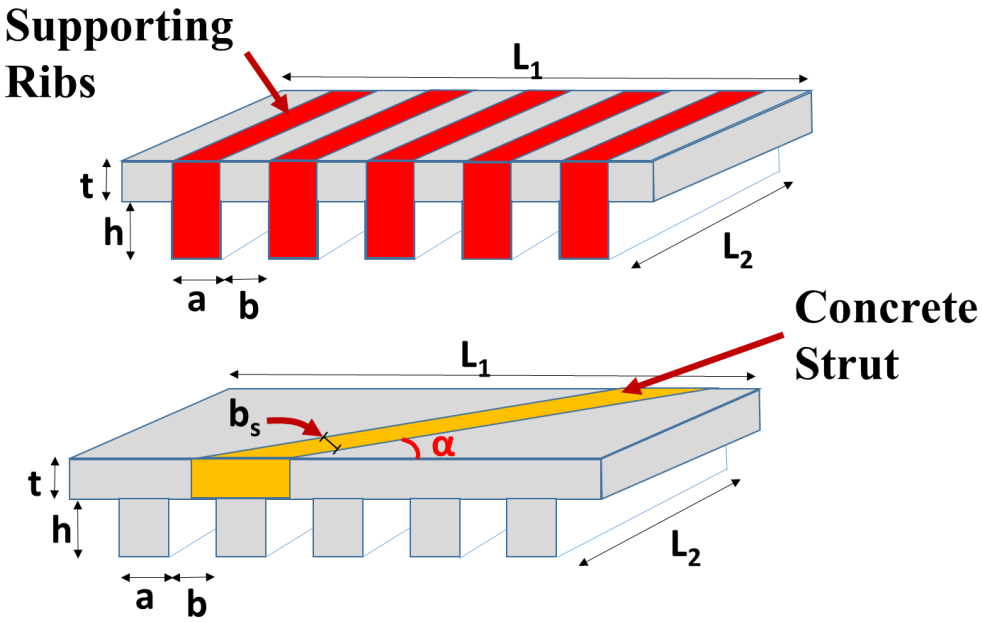

Figure 6-27. Concrete strut in the topping and the ribs acting as lateral supports

The angle of the concrete strut may be between 0º and 90º for satisfying the equilibrium conditions based on the imposed forces to the diaphragm, floor plan dimensions, and location of VLFR systems. In this study, it is assumed the struts are formed at a 45º angle for simplicity. Within a panel, a number of struts form diagonally in the concrete topping between cracks. The ribs, provided at a specific spacing provide lateral support for a number of compression struts as shown in Figure 6-28.

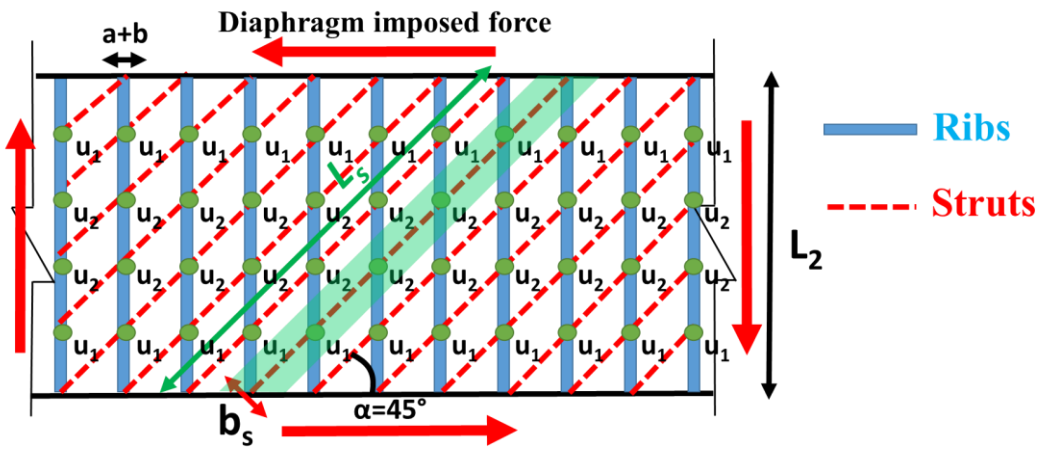

Figure 6-28. Schematic view of ribs and struts in an intra-panel

Considering this situation, the strut buckling model can be considered as a compression member that is supported by some rotational and translational springs at the intersection locations with ribs as shown in Figure 6-29. Which the stiffnesses and degrees of freedom of these springs are related to each other as it forms a mesh type system. Also, from Figure 6-28 it can be found that the degree of freedoms of each strut has a symmetry with respect to the strut mid-point due to the repetitive nature of the problem.

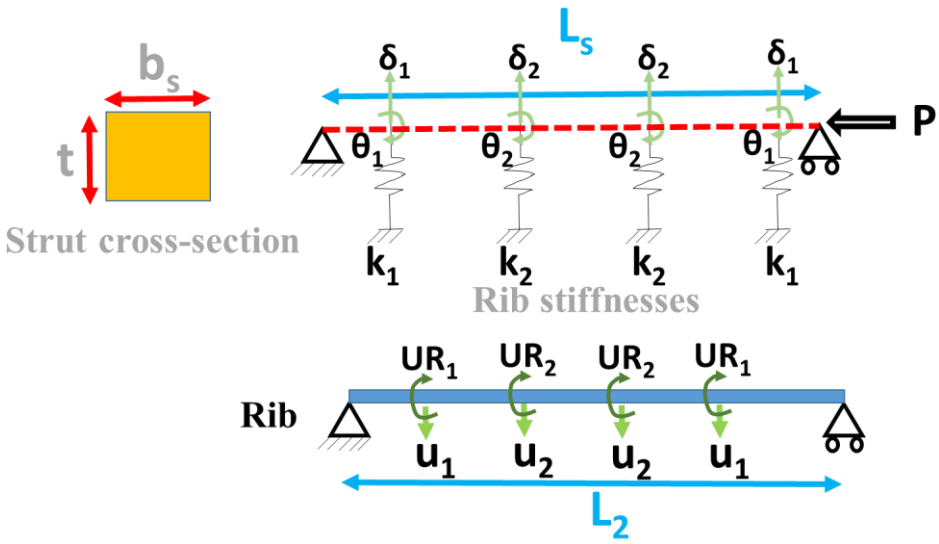

Figure 6-29. Compression strut supported with a number of rotational and translational springs

Part of the rotational stiffness provided for the struts is due to the torsional stiffness of the ribs (due to the angle between the struts and the ribs). The rotational DOFs are considered to be pinned for simplicity in the models described here thereby ignoring this effect.

By looking at only one strut and one rib, it can be found that the out-of-plane deformation of each strut corresponds to each rib as shown in Figure 6-30a. Therefore, the buckling problem here consists of the buckling of a compression member that has deformation compatibility with other flexural members with different stiffnesses (due to the location of rib intersection) at different locations along the strut length as shown in Figure 6-30b.

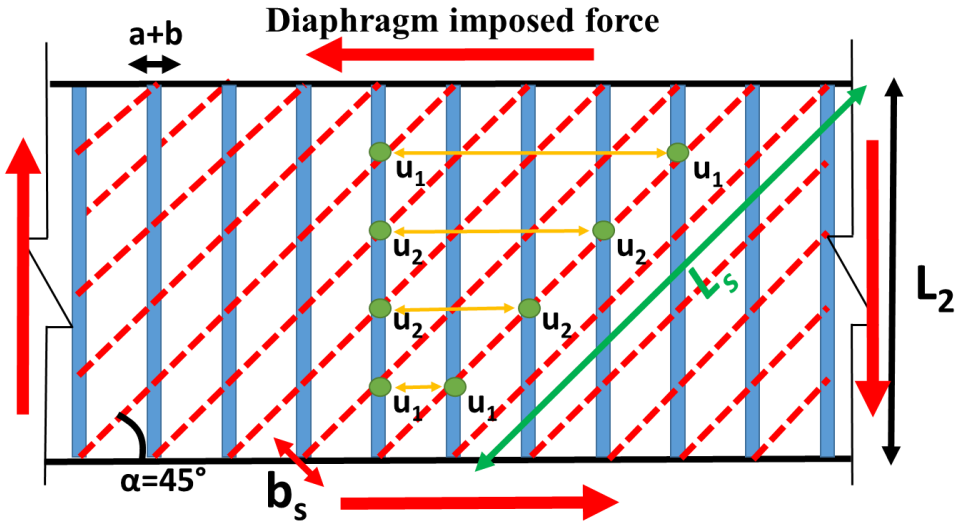

a) Out-of-plane deformation compatibility of struts and ribs

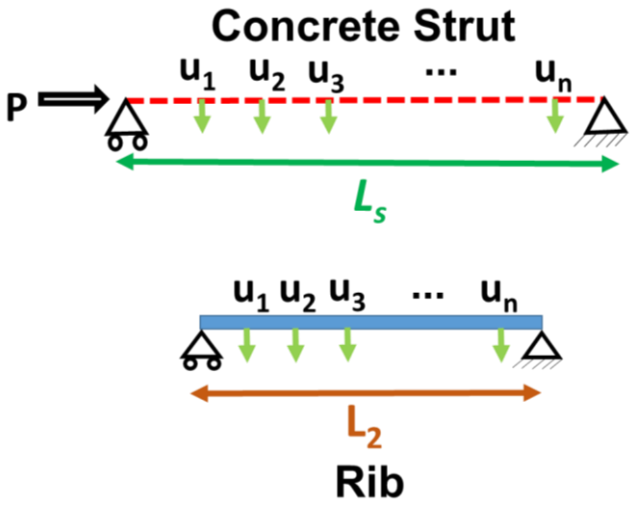

b) Buckling of the strut considering deformation compatibility with the rib

Figure 6-30. Deformation compatibility of struts and ribs

The limitations and assumptions of this buckling model include:

1. It is assumed the distance between the ribs and struts are equal and the rib and strut widths are infinitely small.
2. The effect of concrete topping reinforcement is not considered.
3. Each strut is considered separated from the neighbour strut because of the cracks.
4. The connections between the struts and the ribs are considered as pinned connections.
5. The panel length is considered infinite.
6. The depth of the rib is assumed to be the full slab depth including topping and the rib height. The breadth is the average through widths as shown in Figure 6-27.

To solve this problem the X-Y coordinate is selected for the strut and V-W coordinate is used for the rib to derive the mathematical equations. As shown in Figure 6-31, the compatibility force $f(x)$ is acting on the strut from the rib and $g(v)$ is the reaction of the $f(x)$ that is acting against the rib. Therefore, from equilibrium, the total applied force to the rib and the strut must be equal:

$$\int_0^{L_s} f(x)dx = \int_0^{L_2} g(v)dv \qquad \text{Eq. (6-22)}$$

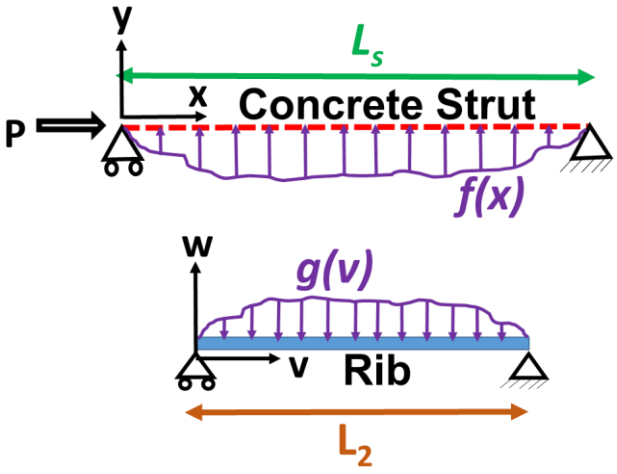

Figure 6-31. Compatibility forces between the strut and rib (f(x) and g(v))

Considering the geometry of the problem, the rib length is equal to $L_s \sin\alpha$, where α is the angle between the rib and the strut as shown in Figure 6-27 and Figure 6-28. Since the out-of-plane displacements of any point on a rib ($w(v)$) is equal to the corresponding point on the strut ($y(x)$):

$$y(x) = w(v) \qquad \text{Eq. (6-23)}$$

According to Figure 6-31:

$$\frac{x}{L_s} = \frac{v}{L_2} \qquad \text{Eq. (6-24)}$$

And taking the derivative of Eq. (6-24) gives

$$dv = \frac{L_2}{L_s}\, dx \qquad \text{Eq. (6-25)}$$

Substitution of Eqs. (6-24) and (6-25) into Eq. (6-22) leads to finding the relationship between $f(x)$ and $g(v)$

$$\int_0^{L_s} f(x)dx = \int_0^{L_s} g\left(\frac{xL_2}{L_s}\right)\frac{L_2}{L_s}\, dx$$

$$f(x) = g(v)\frac{L_2}{L_s} \qquad \text{Eq. (6-25a)}$$

Figure 6-32 shows the free body diagram of the rib and strut considering the imposed axial force to the strut. The equilibrium equations for each strut and rib are:

$$-EI_s\frac{d^2y}{dx^2} - Py + \int xf(x)dx + xV_s = 0 \qquad \text{Eq. (6-26)}$$

$$-EI_r\frac{d^2w}{dv^2} - \int vg(v)dv - vV_r = 0 \qquad \text{Eq. (6-27)}$$

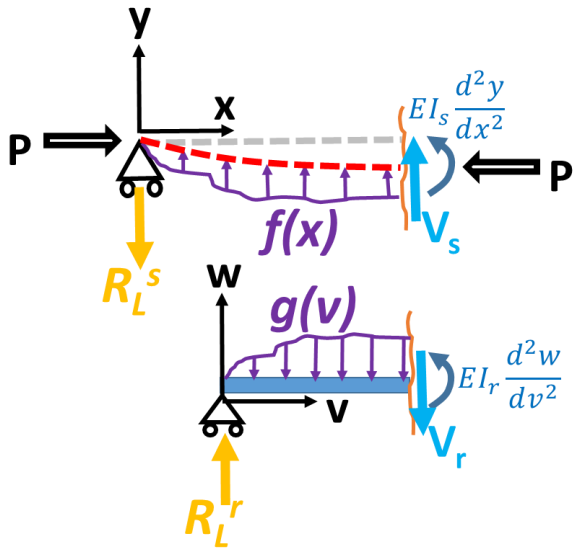

Figure 6-32. Free body diagram of strut and rib

For combining these two equilibrium equations, the relationships between $\int vg(v)dv$ and $\int xf(x)\,dx$, $\frac{d^2w}{dv^2}$ and $\frac{d^2y}{dx^2}$ need to be found. By substituting Eqs. (6-23) and (6-24) into $\int vg(v)dv$, leads to:

$$\int vg(v)dv = \int \left(\frac{xL_2}{L_s}\right)\left(\frac{L_s}{L_2}f(x)\right)\frac{L_2}{L_s}\,dx$$

$$\int vg(v)dv = \frac{L_2}{L_s}\int xf(x)\,dx \qquad \text{Eq. (6-28)}$$

Note $V_r = V_s$, because $f(x) = g(v)\frac{L_2}{L_s}$ and $x = \frac{L_s}{L_2}v$, therefore:

$$\int vg(v)dv + vV_r = \frac{L_2}{L_s}\left(\int xf(x)dx + xV_s\right) \qquad \text{Eq. (6-29)}$$

The relationships between $\frac{d^2w}{dv^2}$ and $\frac{d^2y}{dx^2}$ could be found by taking the second derivative of w with respect to v and using the chain rule as the following:

$$\frac{dw}{dv} = \frac{dw}{dx}\frac{dx}{dv} = \frac{dw}{dx}\frac{L_s}{L_2}$$

$$\frac{d}{dv}\left(\frac{dw}{dx}\frac{L_s}{L_2}\right) = \frac{d}{dx}\left(\frac{dw}{dx}\frac{L_s}{L_2}\right)\frac{dx}{dv} = \frac{d^2w}{dx^2}\left(\frac{L_s}{L_2}\right)^2$$

$$\frac{d^2w}{dv^2} = \frac{d^2w}{dx^2}\left(\frac{L_s}{L_2}\right)^2 = \frac{d^2y}{dx^2}\left(\frac{L_s}{L_2}\right)^2 \qquad \text{Eq. (6-30)}$$

Substitution of Eq. (6-29) and (6-30) into the equilibrium equation of the rib (Eq. (6-27)) leads to:

$$-\frac{L_s}{L_2} EI_r \frac{d^2y}{dx^2}\left(\frac{L_s}{L_2}\right)^2 = \int xf(x)\,dx + xV_s \qquad \text{Eq. (6-31)}$$

Using Eq. (6-31), the equilibrium equation of the strut changes to:

$$-EI_s \frac{d^2y}{dx^2} - Py - EI_r \frac{d^2y}{dx^2}\left(\frac{L_s}{L_2}\right)^3 = 0 \qquad \text{Eq. (6-32)}$$

Rearranging this equation yields to find the basic differential equation for the buckling of compression members which is:

$$-\frac{d^2y}{dx^2}\left(EI_s + EI_r\left(\frac{L_s}{L_2}\right)^3\right) - Py = 0 \qquad \text{Eq. (6-33)}$$

Considering:

$$k^2 = {P}\Big/{\left(EI_s + EI_r\left(\frac{L_s}{L_2}\right)^3\right)}$$

The differential equation becomes:

$$-\frac{d^2y}{dx^2} - k^2y = 0 \qquad \text{Eq. (6-34)}$$

The general solution of this differential equation can be written in the form of

$$y = A\sin kx + B\cos kx \qquad \text{Eq. (6-35)}$$

To evaluate the arbitrary constants A and B, the boundary conditions are used as the following:

$$y = 0 \;\; at\; x = 0$$

$$y = 0 \;\; at\; x = L_s$$

The first of these conditions when substituted into Eq. (6-35) leads to

$$B = 0$$

Consequently,

$$y = A \sin kx$$

And from the second condition, it is found that:

$$A \sin kx = 0$$

Where it leads to

$$k = \frac{n\pi}{L_s}$$

Therefore

$$P_{cr} = \frac{\pi^2\left(EI_s + EI_r\left(\frac{L_s}{L_2}\right)^3\right)}{{L_s}^2} \qquad \text{Eq. (6-36)}$$

Which can be rewritten as,

$$P_{cr} = \frac{\pi^2 EI_s \sin^3\alpha + \pi^2 EI_r}{{L_s}^2 \sin^3\alpha}$$

Eq. (6-36) is the critical buckling load of the strut that is supported by floor ribs. For simplicity in finding the slab strength, P_{cr} can be expressed in terms of critical buckling load per unit width of the intra-panel. For this, both I_s and I_r need to be divided by $(a + b)$. For considering the effect of stiffness reduction due to concrete cracking, the stiffness reduction factor of 0.35 is selected for the ribs which are subjected to bending moments and 0.8 for the struts which are in compression based on Table C6.5 NZS3101 (2006), therefore:

$$I_r = 0.35\frac{a(t+h)^3}{12(a+b)}$$

$$I_s = 0.8\frac{t^3 \sin\alpha}{12}$$

When the strut critical buckling capacity is found, it may be compared with the intra-panel imposed forces (demands). However, it should be noted that the demands always are not uniformly distributed. Figure 6-33 shows a situation where diagonal strut forces are applied to the intra-panel zone. These applied forces have different magnitudes. But the sum of the imposed strut forces can be used due to stiff boundary members providing redistribution. In

this study it is suggested that the sum of the imposed strut forces (demands) and the sum of intra-panel strut critical buckling strengths (capacity) be compared. This is because the struts are connected by the ribs, so diaphragm buckling only occurs when all struts reach their critical buckling force. This behaviour is consistent with the assumption used to develop the strut critical buckling load equation (Eq. (6-36)). It should be noted that the strut critical buckling load is calculated based on an infinite intra-panel length. Therefore, panels with finite length have more strut buckling resistance as it consists of a number of smaller struts (which also increase the ribs stiffness by providing out-of-plane support), near the end of the panel.

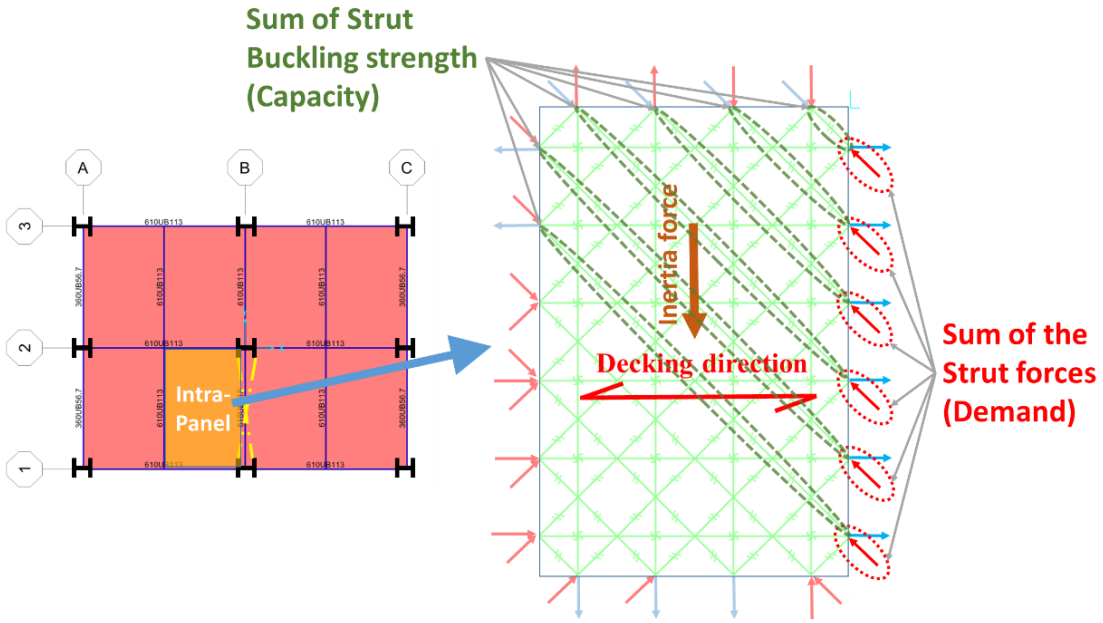

Figure 6-33. Intra-panel zone imposed forces (kN) derived from truss element modelling

- **Verification of the strut critical buckling load with FEM model**

FEM modelling is used to verify the results of the critical buckling load of a strut supported by ribs according to Eq. (6-36). The model consists of the concrete topping and the ribs. The concrete topping is subjected to the strut forces. The model is created based on the assumptions that were used to solve the strut buckling problem, therefore the struts are modelled separately and are connected to the ribs at the points of intersection using pinned connections. All the

material is elastic with an elastic modulus of 25 GPa and a Poisson's ratio of 0.2. Figure 6-34 shows the model and the critical buckling force of the strut.

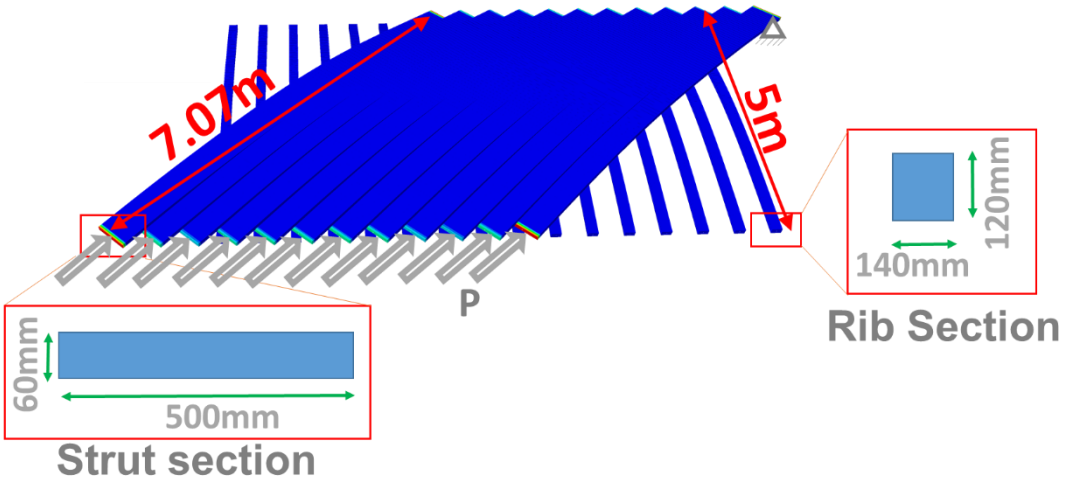

a) Overall view

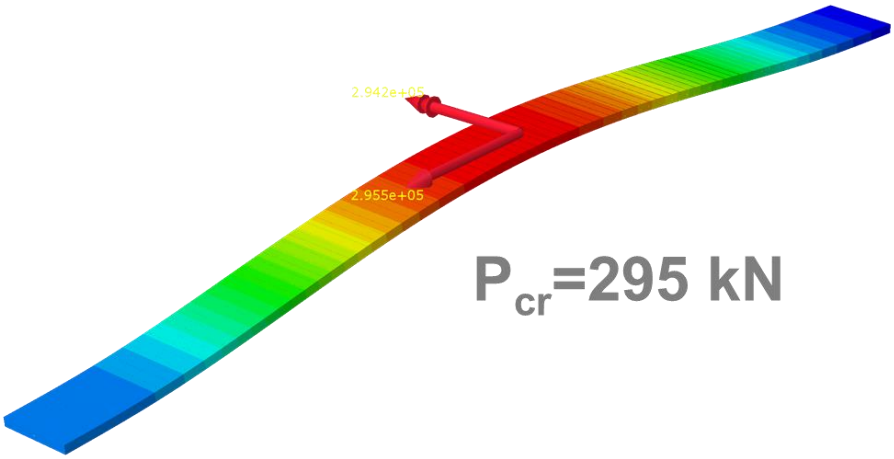

b) Strut view

Figure 6-34. FEM model and the critical buckling force of an arbitrary strut

The critical strut buckling force from FEM analysis is equal to 295 kN for the studied model. Putting the dimensions and the material properties of the FEM model in the Eq. (6-36) gives the critical buckling load equal to 325 kN with a 10% difference. Reasons for the difference may be the discrete modelling of ribs in the FE study and also using imperfection in the FEM model to initiate the buckling which decreases the ultimate buckling load.

Nevertheless, the answers are similar indicating consistency between the derivation and the FE study.

- **Discussion on the strut critical buckling strength (Eq. (6-36))**

One of the assumptions for finding the strut buckling formula that was mentioned in the previous section is that "it is assumed the distance between the ribs and struts are equal and the rib and strut widths are infinitely small". However, in a real floor slab, the ribs are located at a certain distance that means the struts are connected to the ribs at some points. This might cause an error in finding the strut critical buckling load. Here, the accuracy of the above assumption is examined by comparing the results of the Eq. (6-36) and the cases that the strut is supported with only one or two springs which they represent the rib stiffness. Figure 6-35 shows the cases considered and the corresponding model for each of them.

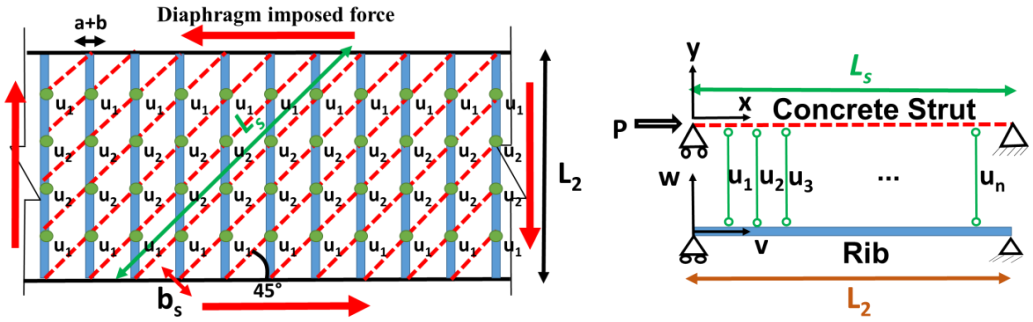

a) Many struts and ribs

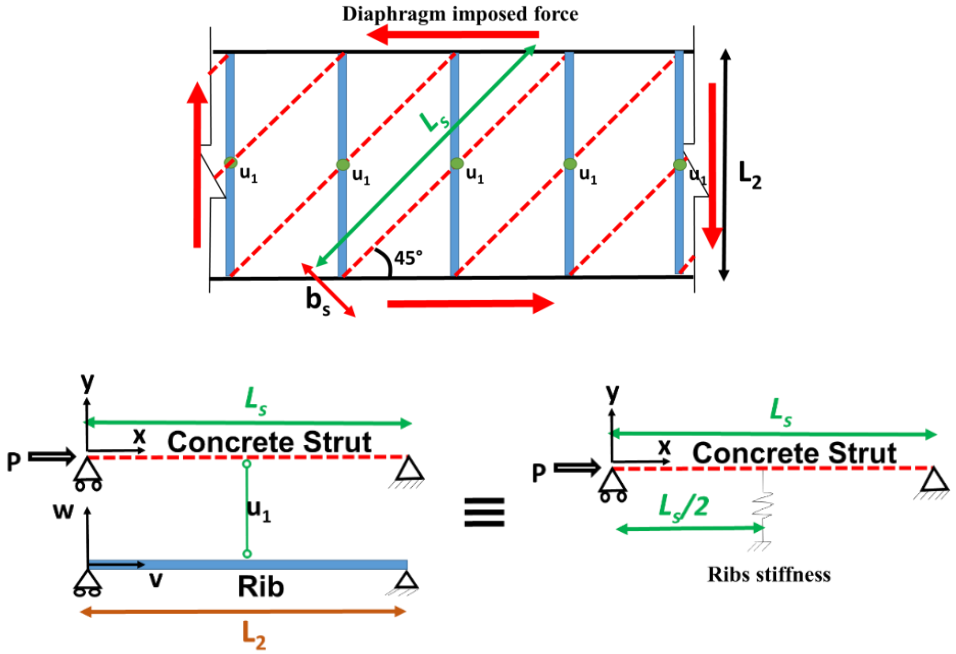

b) One rib per strut

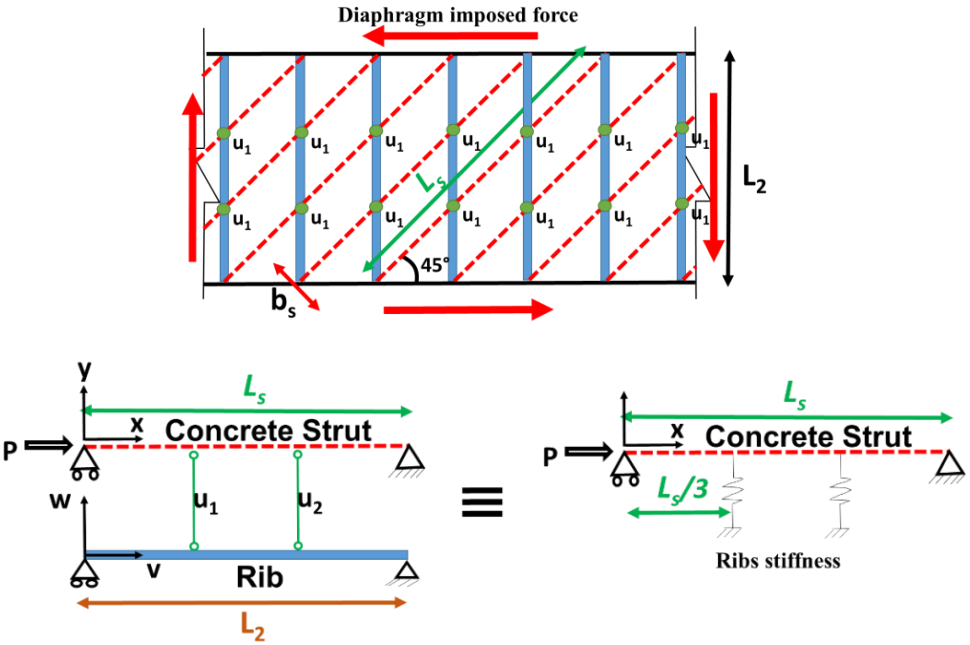

c) Two ribs per strut

Figure 6-35. Floor diaphragms and the strut models with different number of ribs

As it was discussed comprehensively in the previous section, the buckling load for the first model with many ribs per strut shown in Figure 6-35a can be calculated using Eq. (6-36).

When only one point of the rib (midpoint) is connected to the mid-point of the strut as per Figure 6-35b, the rib stiffness may be represented by a spring. In this case the spring stiffness

is $k_{r1} = \frac{48EI_r}{{L_2}^3}$. The same method may be used for a strut with two points of connection as shown in Figure 6-35c. Here the rib stiffness is replaced by two springs. In this case, the spring stiffness of each rib at each location along the rib is $k_{r2} = \frac{162EI_r}{5{L_2}^3}$. Note that if there are more ribs, all springs will not have the same stiffness.

The buckling load of this column could be found using various methods. These include stability functions, energy methods and solving the differential equation of the strut. The solutions to these problems are available in the literature. Here the solution presented is based on Shou-Ngo Tu (1944). The following equations give the strut elastic buckling load for one and two spring models.

For the one spring problem the following equations govern the critical buckling load:

$$min\begin{cases} \dfrac{4P\sqrt{\frac{P}{4EI}}}{\sqrt{\frac{PL^2}{4EI}}-\tan\left(\sqrt{\frac{PL^2}{4EI}}\right)} = k_{r1} \\ p = \frac{4\pi^2 EI}{L^2} \end{cases} \qquad \text{Eq. (6-37)}$$

Eq. (6-37) shows the buckling modes of the strut. When the spring is placed at the mid-point of the strut, with increasing the spring stiffness, buckling load increases until it reaches the point that the spring acts as lateral support. In this condition, the strut reaches the second Euler critical buckling load.

For the strut that is supported by two springs the following equations govern the critical buckling load:

$$min\begin{cases} \dfrac{3P\sqrt{\frac{P}{9EI}}}{\sqrt{\frac{PL^2}{9EI}}+\left[\sin\left(\sqrt{\frac{PL^2}{9EI}}\right)/\left(1-2\cos\left(\sqrt{\frac{PL^2}{9EI}}\right)\right)\right]} = k_{r2} \\ \dfrac{3P\sqrt{\frac{P}{9EI}}}{\left(\left(\sqrt{\frac{PL^2}{9EI}}\right)/3\right)-\left[\sin\left(\sqrt{\frac{PL^2}{9EI}}\right)/\left(1+2\cos\left(\sqrt{\frac{PL^2}{9EI}}\right)\right)\right]} = k_{r2} \\ p = \frac{9\pi^2 EI}{L^2} \end{cases} \qquad \text{Eq. (6-38)}$$

The possible buckling modes of each model are presented in Figure 6-36.

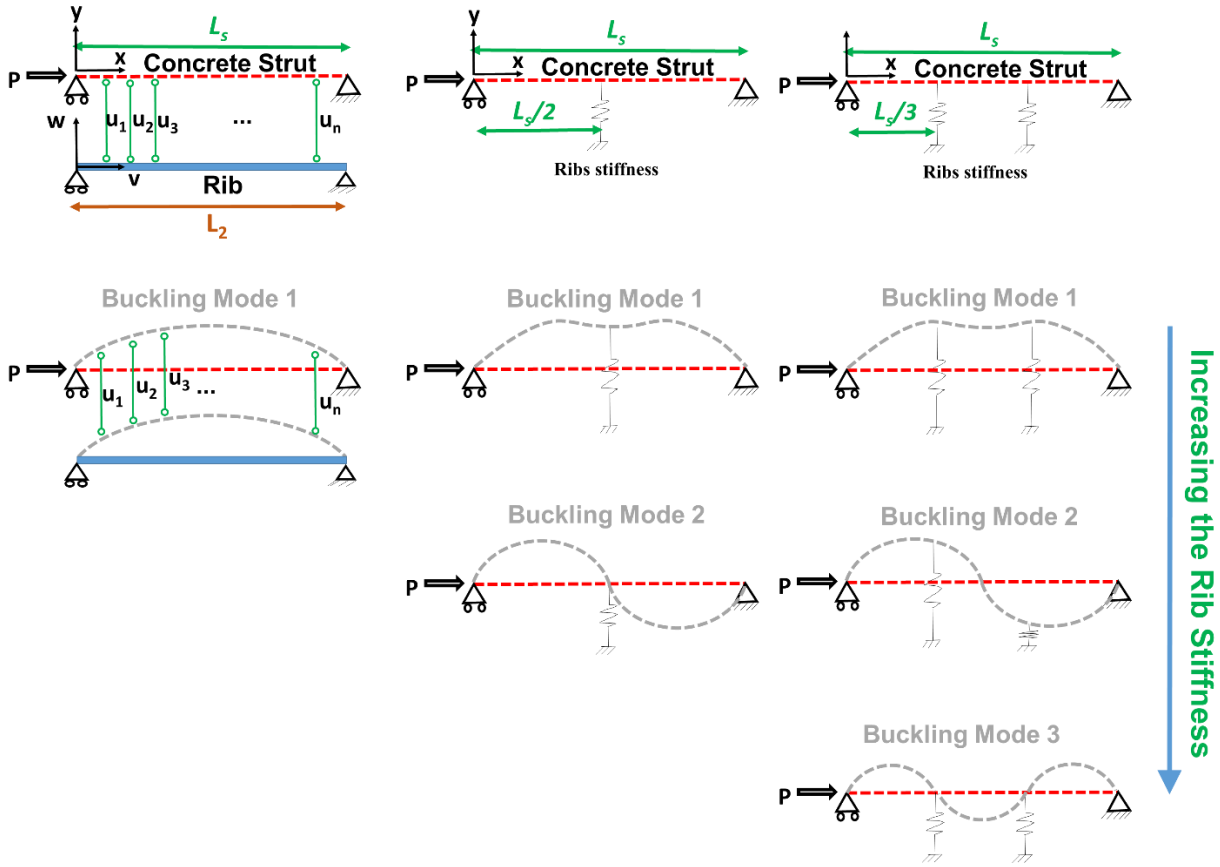

Figure 6-36. Strut buckling modes with one and two spring supports

In order to compare these three cases, the buckling load versus rib stiffness ratios are plotted in Figure 6-37. The strut buckling in the intra-panel zone is governed by the first mode (lowest force) for the continues model. In Figure 6-37 the first buckling mode of the continues model is compared with one and two spring models. The strut buckling loads are normalised by P_{Er}, which is the critical buckling load with no springs.

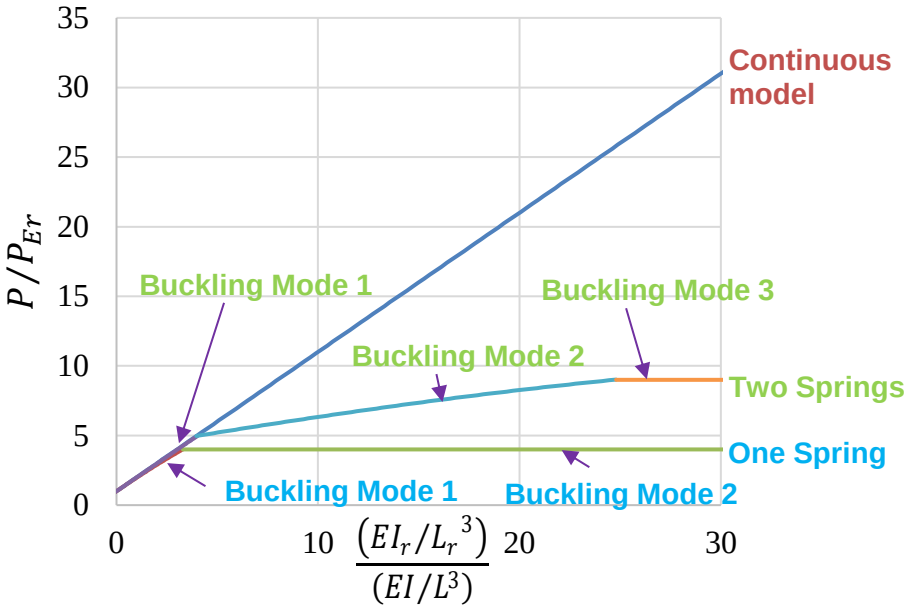

a) Strut buckling load ratio versus rib stiffness ratio

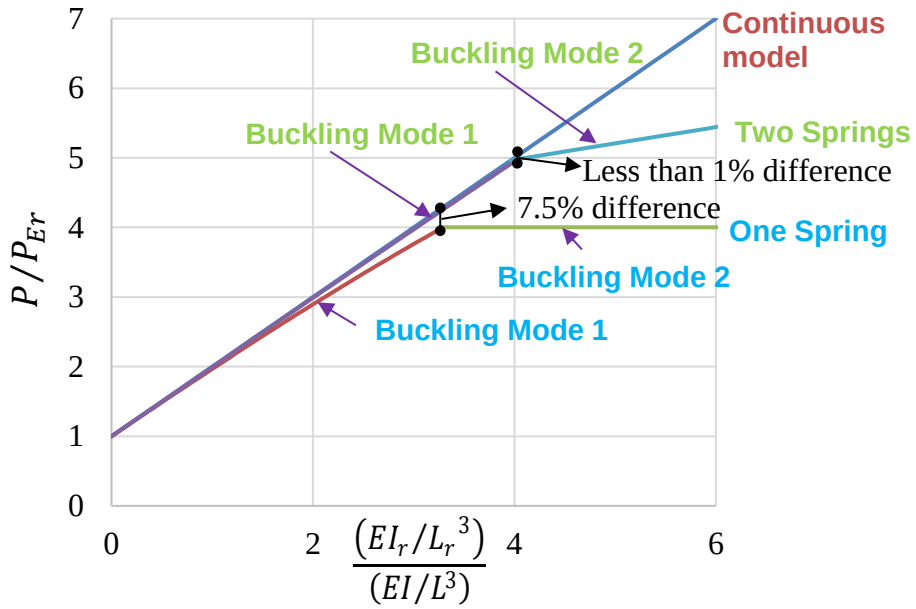

b) Enlarged view

Figure 6-37. Strut buckling load ratio versus rib stiffness ratio

Based on the plots in Figure 6-37, the difference between the critical buckling load at the ultimate strength of the first mode in the one spring model is less than 7.5% compared to the continuous model (rib connected continuously to the strut). This value is less than 1% for the two spring problem.

Therefore, considering that in a composite slab a strut is supported with a number of ribs (more than 2), the assumption of continuously connected ribs and struts provides a reasonable result.

6.4.3 Buckling mode 3, Global buckling (intra-bay buckling)

Another buckling mode that may occur in the composite floors is the "Global buckling" mode. In this buckling mode, the composite floor between the primary beams is considered to experience instability under the lateral imposed forces. The secondary beams act as the plate stiffeners for the composite slab.

Similarly to the intra-panel buckling modes investigated in the previous sections, buckling mode 3 also needs to be investigated in pre and post-cracking stages of the concrete. This is because, the concrete can crack at low tension stresses, therefore the state of the pure shear can change to diagonal compression due to concrete strut formation after the cracking. Figure 6-38 shows the composite floor between primary beams subjected to pure shear (pre-crack) and compression strut force (post-crack) conditions.

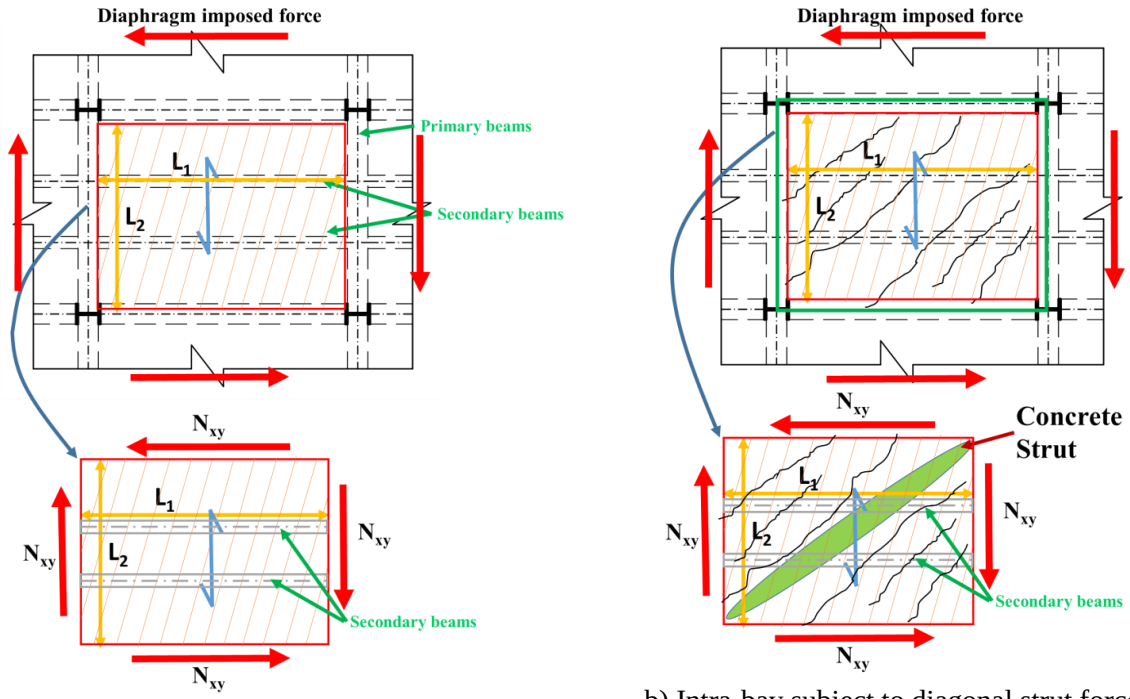

a) Intra-bay subject to pure shear, (pre-crack)

b) Intra-bay subject to diagonal strut forces, (post-crack)

Figure 6-38. Intra-bay loading conditions

Investigating the critical intra-bay buckling load subjected to non-uniform loads and different loading conditions is complicated. Also, the nature of imposed loads is not precisely known as they may vary during the earthquake. Therefore in this study the two scenarios investigated are:

1) When the bay carries force as uniform pure shear stress (pre-cracking) and

2) When the bay carries the applied forces using diagonal compression (struts) after concrete cracking.

In this section, the critical buckling loads are investigated analytically and the results are verified with the FEM models.

6.4.3.1 Intra-bay buckling, slab subjected to pure shear (pre-cracking)

Similarly to the intra-panel buckling discussion in Section 6.4.2, the method used for investigating the critical buckling load of the intra-bay is to study the buckling behaviour of the equivalent orthotropic plate member. In the next sections, the method for finding an equivalent orthotropic plate and the critical buckling load of the orthotropic plate is discussed.

- ***Equivalent orthotropic plate***

In the previous sections, the composite slab between secondary beams was considered, which was like a plate member that was stiffened by ribs in one direction. For the global buckling, the composite floor is supported by some secondary beams as well. These beams are placed perpendicular to the ribs direction. Thus the concrete topping is stiffened in two perpendicular directions (two-way stiffened plate).

Similarly to the intra-panel buckling mode, only finding the flexural stiffness of the composite floor (that is equal to the equivalent orthotropic plate) is required to find the critical buckling load using orthotropic plate theory.

The flexural stiffness of the composite floor in the Y direction (D_y) is the same as the intra-panel stiffness, this is because the secondary beams do not provide flexural stiffness in this

direction. So the flexural stiffness in the Y direction (D_y) could be found using the same rules as finding the moment of inertia of a simple beam section. The only difference is that the plate part (concrete topping) should be divided by $(1-\nu^2)$ for considering the plate action. Eq. (6-11) shows the flexural stiffness of the composite floor in the Y direction.

$$D_y = \frac{Et^3}{12(1-\nu^2)} + \frac{Ete_y{}^2}{(1-\nu^2)} + \frac{Eah^3}{12(a+b)} + \frac{Eha\left(\frac{h}{2}+\frac{t}{2}-e_y\right)^2}{(a+b)} \qquad \text{Eq. (6-11)}$$

Where E and ν are the elastic modulus and Poisson's ratio of the concrete material respectively. Other parameters are shown in Figure 6-39. It should be noted that e_y is the distance between the section neutral axis and the mid-height of the concrete topping.

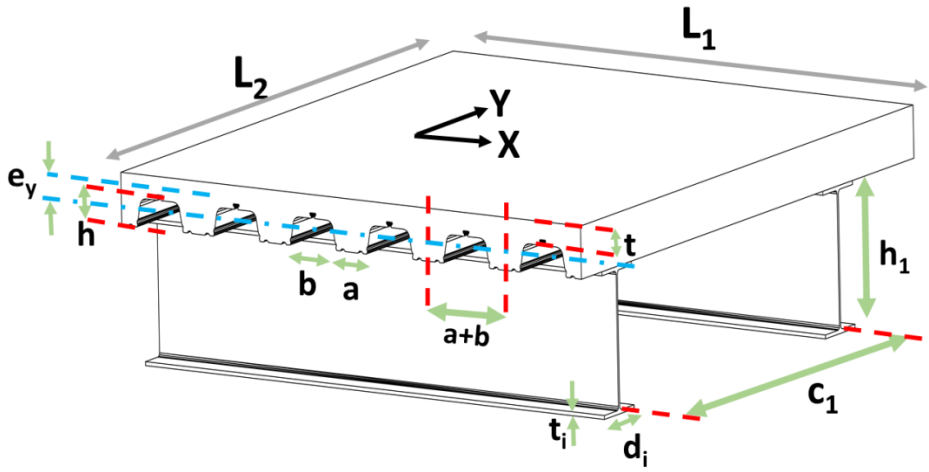

Figure 6-39. Composite slab with secondary beams

The flexural stiffness in the X direction, D_x, cannot be found simply using cross sectional properties because the thickness of the composite floor is not uniform and also the secondary beams increase the flexural stiffness in this direction. The method that is proposed here for finding the flexural stiffness of the composite slab stiffened with the secondary beams include finding the equivalent uniform plate thickness of the composite floor. Then, using the same rules as finding the moment of inertia of a composite beam section, the total slab stiffness including the secondary beams can be calculated.

Figure 6-40 shows the composite slab on the secondary beams and the equivalent uniform plate of the composite floor (t_{eq}).

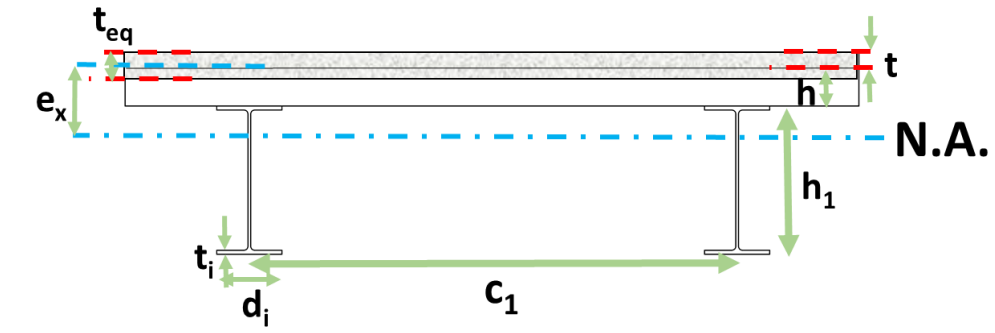

a) Composite slab on secondary beams

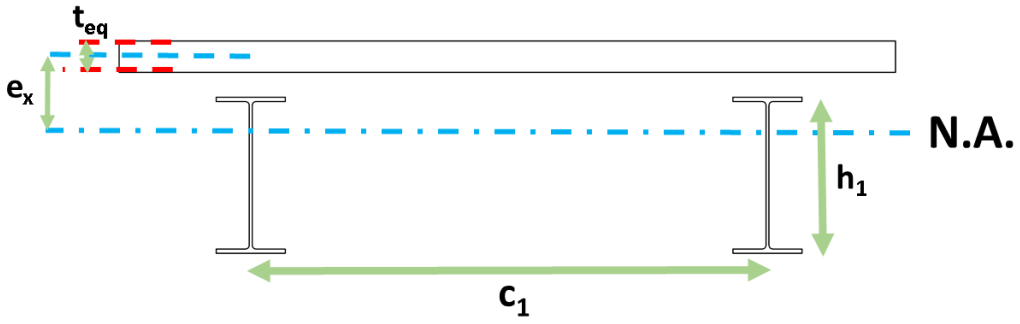

b) Equivalent uniform plate on secondary beams

Figure 6-40. Composite slab and the secondary beams cross-section

The equivalent uniform plate thickness can be calculated using the Eq. (6-39). The D_{xs} is the composite slab stiffness same as Eq. (6-12) that was used in intra-panel buckling consideration.

$$t_{eq} = \sqrt[3]{\frac{12(1-\nu^2)D_{xs}}{E}} \qquad \text{Eq. (6-39)}$$

Using the equivalent uniform plate thickness t_{eq} the intra-bay flexural stiffness D_x can be found using:

$$D_x = \frac{E{t_{eq}}^3}{12(1-\nu^2)} + \frac{Et_{eq}{e_x}^2}{(1-\nu^2)} + \frac{E_s I_y}{c_1} + \frac{E_s A_s\left(\frac{h_1}{2}+t+h-\frac{t_{eq}}{2}-e_x\right)^2}{c_1} \qquad \text{Eq. (6-40)}$$

Where E and ν are the elastic modulus and Poisson's ratio of the concrete material respectively, E_s and I_y are the elastic modulus and moment of inertia of the secondary beams respectively. Other parameters are shown in Figure 6-39 and Figure 6-40. It should be noted

that e_x is the distance between the section neutral axis and mid-height of the equivalent uniform plate thickness.

- **Verification of plate stiffness equations with FEM models**

Three composite floors (ComFlor 80) are modelled with different secondary beams to check the accuracy of the flexural stiffness equations presented in the previous section. Table 6-10 presents the flexural stiffness of the FEM models and the calculated values using Eqs. (6-11) and (6-40). Note that fine mesh size was used in FEM models.

Table 6-10. Flexural stiffness of the composite floors

		Steel beam properties		
		$I_y = 4.5e8\ mm^4$ $A_s = 6e4\ mm^2$ $c_1 = 2000$ mm $h_1 = 300$ mm	$I_y = 1.3e8\ mm^4$ $A_s = 4e4\ mm^2$ $c_1 = 2000$ mm $h_1 = 200$ mm	$I_y = 10.7e8\ mm^4$ $A_s = 8e4\ mm^2$ $c_1 = 2000$ mm $h_1 = 400$ mm
		Flexural stiffnesses		
$\boldsymbol{D_x}$ (N.mm)	FEM	38438212709	17851617357	69295053719
	Eq. (6-40)	38907462634	17924970510	70387129883
Error (%)		1.22	0.41	1.58
$E = 25\ GPa, \nu = 0.2$				
** ComFlor 80: a=135mm, b=165mm, h=80mm, t=50mm,				

The results show that the differences in the stiffness values are less than 2%. It should be noted that the FEM modelling parameters such as mesh size, element type and other numerical effects could also have some share in this error.

- **Torsional stiffness of the orthotropic plate**

For finding the torsional stiffness of the composite slab stiffened by secondary beams, the ribs, beams and the slab are considered separately in Eq. (6-41) (Szilard, 1974).

$$B = \frac{E{t_{eq}}^3}{12(1-\nu^2)} + \frac{G_{xy}}{2}\frac{ha^3\eta}{(a+b)}k_B + \frac{{G_{xy}}_s}{6}\left(\frac{\sum d_i t_i^3}{c_1}\right) \qquad \text{Eq. (6-41)}$$

Where G_{xy} and ${G_{xy}}_s$ are the concrete and steel shear modulus respectively. The parameter η is a numerical factor depending on the rib aspect ratios presented in Table 6-7. The parameter k_B is a reduction factor accounting for the decrease in the torsional stiffness of reinforced

concrete beams due to the concrete cracking. This parameter relates to ribs aspect ratio, reinforcement and also applied bending moment to the member (Szilard, 1974). In this study k_B is taken as zero conservatively. Also, d_i and t_i are the width and thickness of the secondary beam flanges and web.

- ***Buckling of an orthotropic plate***

The critical elastic buckling load of the composite floor is investigated using the plate flexural stiffness found in the previous section. The same method as was presented in the intra-panel buckling subjected to pure shear is used here considering the effect of secondary beams.

Using the intra-bay stiffness, the elastic critical shear stress (buckling stress) is expressed as Eq. (6-20):

$$N_{xy3} = K_s \frac{\pi^2}{t{L_2}^2} \sqrt[4]{D_x {D_y}^3} \qquad \text{Eq. (6-20)}$$

Where N_{xy3} is the elastic critical shear stress, D_x and D_y are the orthotropic plate stiffness, and L_2 is the length perpendicular to the x axis as shown in Figure 6-39. The parameter K_s is the plate buckling coefficient determined by a theoretical critical-load analysis. This parameter is a function of the plate geometry and the boundary conditions. The parameter K_s is plotted for three edge support conditions in Figure 6-22 (Ziemian, 2010). In these plots D_1, D_2 and D_3 are D_x, D_y and B respectively. Based on the orthotropic plate stiffness the parameter K_s can be extracted from the plots in Figure 6-22. In this study, all the boundary conditions are considered to be simply supported to obtain conservative results.

- **Case study**

The global elastic shear buckling strength of the intra-bay region for two ComFlor profiles (60 and 80), supported by one and two secondary beams are investigated using both Eq. (6-20) and FEM model. The studied models are shown in Figure 6-41.

The forces used for gravity design of the secondary beams include: 3 kPa imposed action (Q), and 5 kPa permanent action (G). It is assumed that the concrete compressive strength is 30 MPa with elastic modulus of 25 GPa.

The critical buckling load of the floor slabs is studied with and without considering the stiffness reduction factors accounting for concrete cracking due to flexural moments. The stiffness reduction factor of 0.35 is selected based on Table C6.5 NZS3101 (2006) for members subjected to bending moments. Although the elastic shear buckling here is based on the assumption that the concrete is un-cracked, the cracking reduction factor is considered for decreasing the bending rigidity which yields to lower buckling loads.

Table 6-11 presents the results of critical shear stress using Eq. (6-20) for floor slabs shown in Figure 6-41.

Table 6-11. Critical shear stresses for ComFlor 60 and 80 with secondary beams ($L_1 = L_2 = 6\ m$)

		N_{xy3} (MPa)	
		Secondary beams at 2 m (180UB18)	Secondary beams at 3 m (200UB22.3)
Total Elastic	**ComFlor 60**	112.3	99.9
Considering stiffness reduction factors		69.6	59.8
Total Elastic	**ComFlor 80**	142.6	125.7
Considering stiffness reduction factors		89.1	54

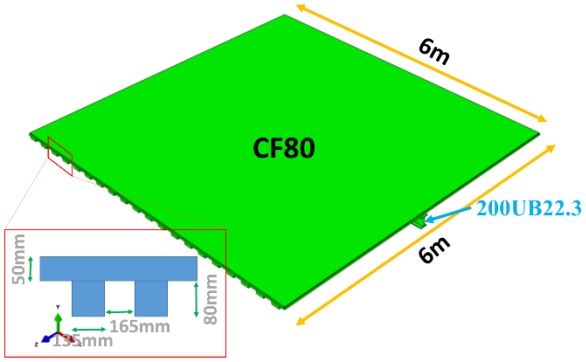

a) ComFlor 80 supported with one secondary beam

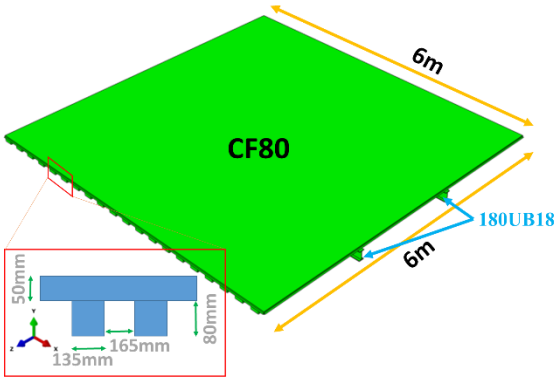

b) ComFlor 80 supported with two secondary beams

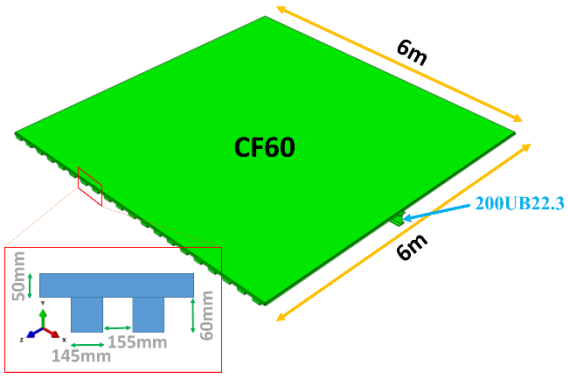

c) ComFlor 60 supported with one secondary beam

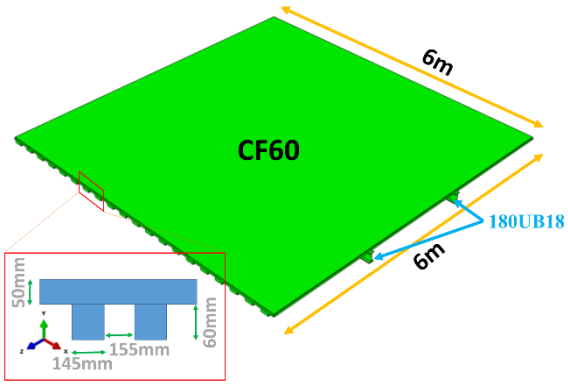

a) ComFlor 60 supported with two secondary beams

Figure 6-41. ComFlor 60 and 80 with secondary beams

To verify the results obtained using the analytical approach, the FEM modelling is used. Four models including two ComFlor profiles (60 and 80) with 2m and 3m spacing secondary beams were created in ABAQUS software. A 6×6m composite floor is selected for the modelling. The intra-bay region was subjected to pure shear loading and the shear force and corresponding shear displacement were recorded during analysis. Figure 6-42 shows the deformed shapes of the FEM models at the end of the analysis and the recorded shear force-displacement plots.

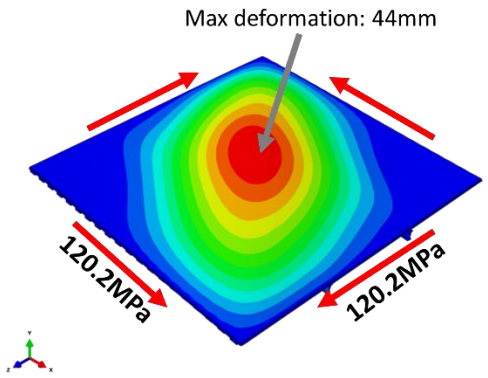

a) Deformed shape of the ComFlor 60 intra-bay (displacement contour at the buckling step), Secondary beams at 2m

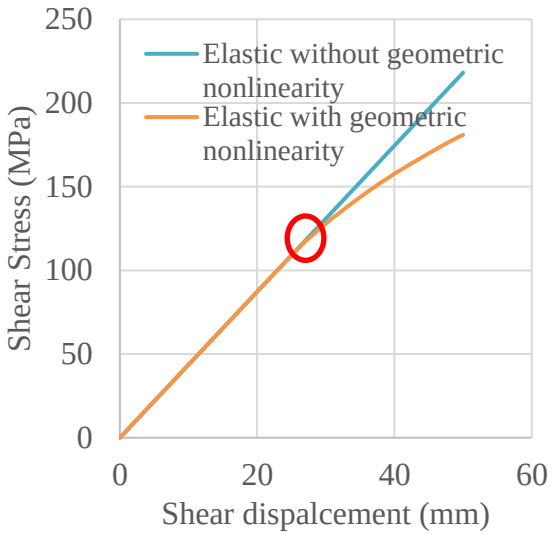

b) Shear force-displacement plot for ComFlor 60, secondary beams at 2m

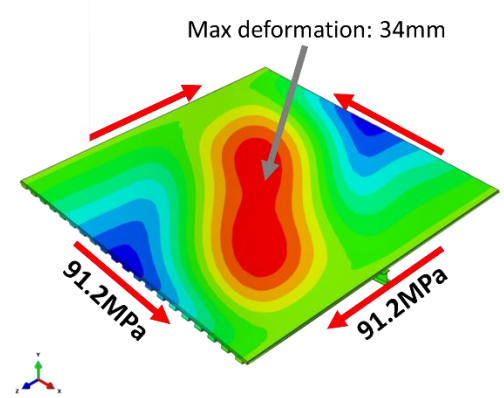

c) Deformed shape of the ComFlor 60 intra-bay (displacement contour at the buckling step), Secondary beams at 3m

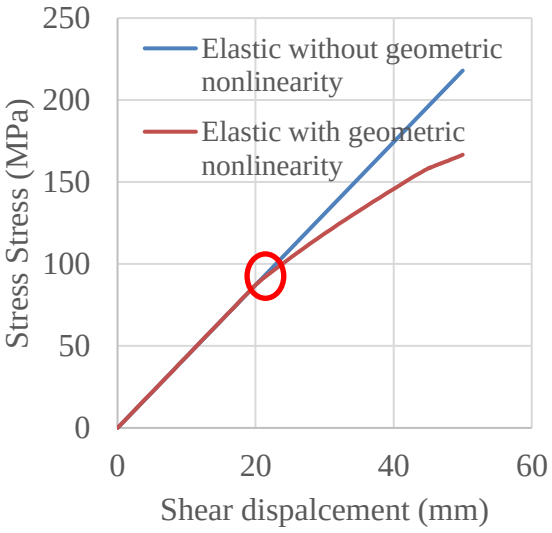

d) Shear force-displacement plot for ComFlor 60, secondary beams at 3m

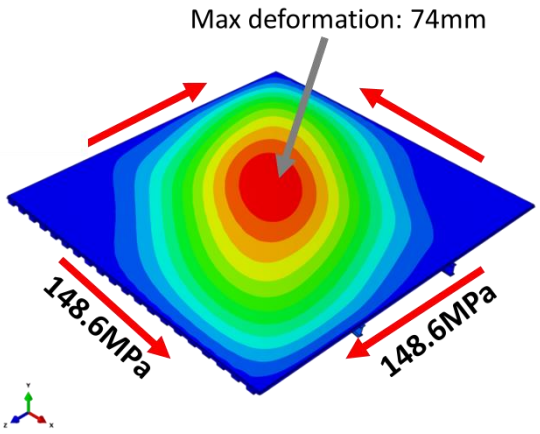

e) Deformed shape of the ComFlor 80 intra-bay (displacement contour at the buckling step), Secondary beams at 2m

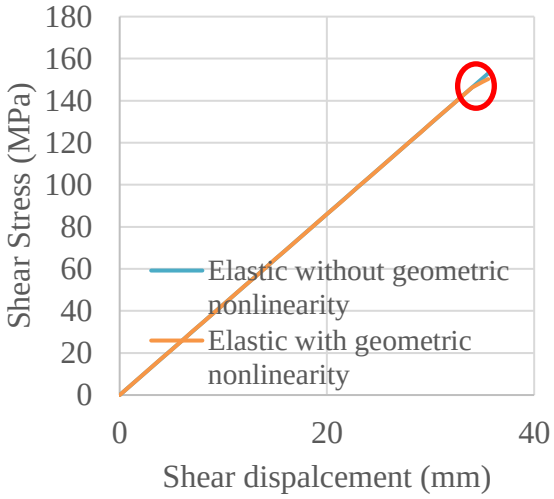

f) Shear force-displacement plot for ComFlor 80, secondary beams at 2m (note: the analysis failed to converge after 36mm)

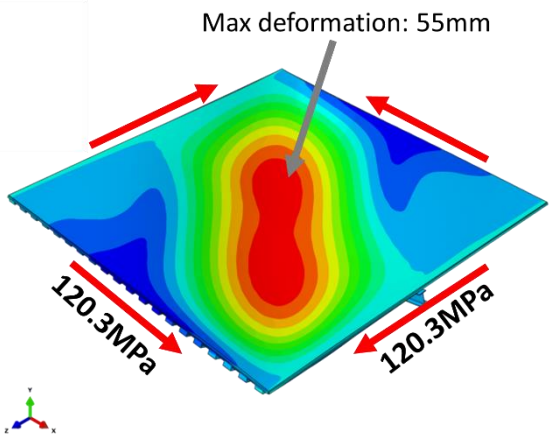

g) Deformed shape of the ComFlor 80 intra-bay (displacement contour at the buckling step), Secondary beams at 3m

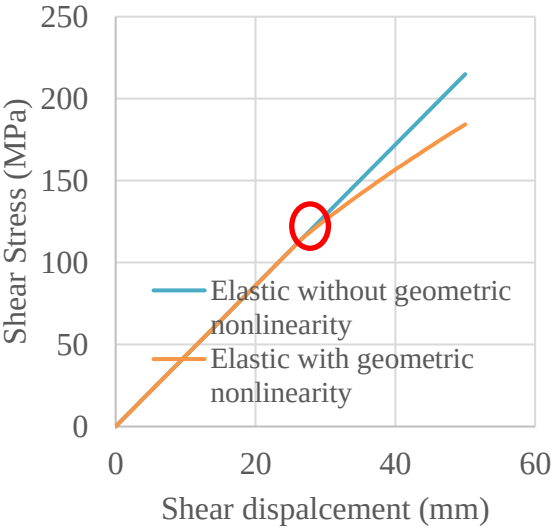

h) Shear force-displacement plot for ComFlor 80, secondary beams at 2m

Figure 6-42. FEM models of ComFlor 60 and 80 subjected to pure shear condition

The shear force-displacement of all models are plotted in Figure 6-42. Each model is analysed two times considering geometric nonlinearity and without geometric nonlinearity. Same as intra-panel buckling investigations, the buckling load is defined at the point where the difference between these two plots ($F_E - F_{NG}$) becomes more than 1% of the corresponding F_E value as shown in Figure 6-24 schematically. Where F_E is the analysis without the geometric nonlinearity and F_{NG} is the force-displacement plot considering the geometric nonlinearity.

Based on these plots, the critical buckling stress for ComFlor 60 and 80 with secondary beams at 2m spacing were 120.2MPa and 148.6MPa respectively. Similarly, the critical buckling stress for ComFlor 60 and 80 with secondary beams at 3m spacing were 91.2MPa and 120.3MPa respectively. These are similar to the values obtained from Eq. (6-20) given in Table 6-11 of 112.3MPa, 142.6MPa, 99.9MPa and 125.7MPa with errors being -6.5%, -4.1%, 9.5% and 4.4% respectively. The answers are similar indicating consistency between the values from Eq. (6-20) and the FE study.

These also show that the analytical approach is able to estimate the critical buckling load with less than 10% error compared to the FEM models. In the next step, these critical buckling loads are compared with the ultimate intra-bay shear strength to determine the likelihood of the shear buckling.

- **Slab shear strength**

As mentioned in Section 6.4.2, the intra-panel buckling, the shear strength of the composite slabs can be calculated using the equation provided by NZS3404 (2007) Clause 13.4.10.2.

$$V_r = \min \begin{cases} \left(0.8\emptyset A_{rt} f_{yr} + 2.76\emptyset_c A_{cv}\right) \\ 0.5\emptyset_c f_c' A_{cv} \end{cases} \quad \text{Eq. (6-21)}$$

Where A_{rt} is the area of transverse reinforcements crossing shear planes, A_{cv} is the area of concrete in shear planes and f_{yr} is the yield stress of tension reinforcement. The reduction factors $\emptyset$ and $\emptyset_c$ are equal to 0.9 and 0.6 respectively. Here the upper bond value of this formula ($0.5\emptyset_c f_c' A_{cv}$) is considered as the shear strength of the composite slab. The calculated shear strength values and the critical shear buckling loads for the studied intra-bays with 3m spacing between secondary beams are presented in Table 6-12. It should be noted that critical shear buckling loads are calculated using stiffness reduction factors.

Table 6-12. The calculated shear strength values and the critical shear buckling stresses for ComFlor 60 and 80 intra-bays with secondary beams at 3m spacing (concrete stiffness reduction factor=0.35)

	ComFlor 60	**ComFlor 80**
	Shear stress (MPa)	
Critical shear buckling stress (Eq. (6-20)), considering stiffness reduction factor	59.7	73.9
Slab shear strength ($0.5\emptyset_c f'_c$)	9	9

The results show that the elastic shear buckling loads are more than six times the upper bound shear strength of the composite slab. Therefore, it can be concluded that the elastic shear buckling does not govern in the studied cases. The critical shear buckling of any other type of floor slab could be investigated using Eq. (6-20) and the orthotropic plate stiffness formulations given in Eqs. (6-39) to (6-41).

6.4.3.2 Global buckling, subjected to diagonal force (strut force), post-cracking

The same method as the one was used for finding the strut buckling load of the intra-panel (Section 6.4.2) is used here. The only difference is that the strut is supported by the ribs and the secondary beams simultaneously. Therefore, adding the stiffness of the secondary beams changes Eq. (6-36) into:

$$P_{cr} = \frac{\pi^2 EI_s}{{L_s}^2} + \frac{\pi^2 EI_r}{{L_2}^2 \sin\alpha} + \psi \frac{\pi^2 E_s I_{sb}}{{L_1}^2 \cos\alpha} \qquad \text{Eq.(6-42)}$$

Where E_s and I_{sb} are the elastic modulus and moment of inertia of secondary beams per unit length of the slab, respectively. The length of the secondary beams is denoted by L_1. The parameter ψ is the buckling correction factor. This parameter is found based on the solution of the strut buckling loads supported with one and two springs along the length as discussed in Section 6.4.2.2. It was shown that when the strut is supported by only one spring at the mid-point, the maximum difference in the critical buckling load compare to the continuous model is less than 7.5% (see Figure 6-37). For the strut supported with two springs this value is less

than 1%. Therefore, $\psi = 0.9$ is suggested when the intra-bay is supported with one secondary beam and $\psi = 1.0$ for more than one secondary beams.

When the stiffnesses of the secondary beams increase, they laterally restrain the compression strut as shown in Figure 6-43. This leads the strut to buckle at higher loads corresponding to higher buckling modes. Therefore, the critical buckling load of the strut should be found using Eq. (6-43) which considers the strut higher buckling modes. In this equation, n is the number of secondary beams within each bay.

$$P_{cr} = min\begin{Bmatrix} \frac{\pi^2 EI_s}{{L_s}^2} + \frac{\pi^2 EI_r}{{L_2}^2 \sin\alpha} + \psi \frac{\pi^2 E_s I_{sb}}{{L_1}^2 \cos\alpha} \\ (n+1)^2 \left(\frac{\pi^2 EI_s}{{L_s}^2} + \frac{\pi^2 EI_r}{{L_2}^2 \sin\alpha} \right) \end{Bmatrix} \quad \text{Eq. (6-43)}$$

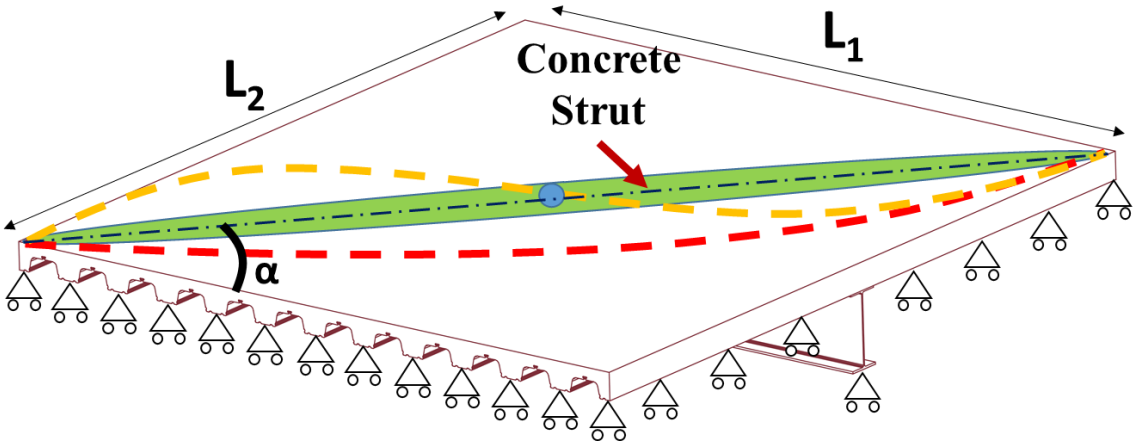

Figure 6-43. Possible mode shapes of strut buckling in an intra-bay

Similarly to the intra-panel strut buckling, when the strut critical buckling capacity is found, it may be compared with the intra-bay imposed forces (demands). It is suggested that the sum of the imposed strut forces (demands) and sum of intra-panel strut critical buckling strengths (capacity) be compared. The sum of the imposed strut forces can be used due to stiff boundary members providing force redistribution.

6.5 Effect of gravity forces on the ultimate diaphragm buckling loads

Floor slabs in the structures are primarily designed to carry gravity forces and transfer them to other structural elements. The gravity forces acting on the diaphragms cause some out-of-plane deformation. Maximum allowable values of this deformation are generally given in the literature.

These out-of-plane deformations can affect the in-plane buckling behaviour of the floor slab. Note that the out-of-plane deformations cannot change the elastic buckling load of a member, however, these can considerably increase the out-of-plane deformations. These large lateral deformations may cause yielding in the material. When material yields, the elastic buckling load calculated is no longer valid as the material properties have changed. Therefore, in this study only the initiation of the buckling is investigated providing that the material is still elastic. In the following, the effect of gravity forces on the buckling behaviour of the diaphragms is investigated.

- **Effect of gravity forces on the ultimate shear buckling load (pre-crack)**

Figure 6-44 shows the diaphragm out-of-plane deformation and the imposed shear loads schematically. To obtain the effect of out-of-plane deformations on the shear buckling capacity of the diaphragms, a number of FEM models are created considering maximum out-of-plane deformations ranging from L/800 to L/200. In these models both the intra-panel (between secondary beams) and the intra-bay (between primary beams and considering the secondary beams) modes are investigated.

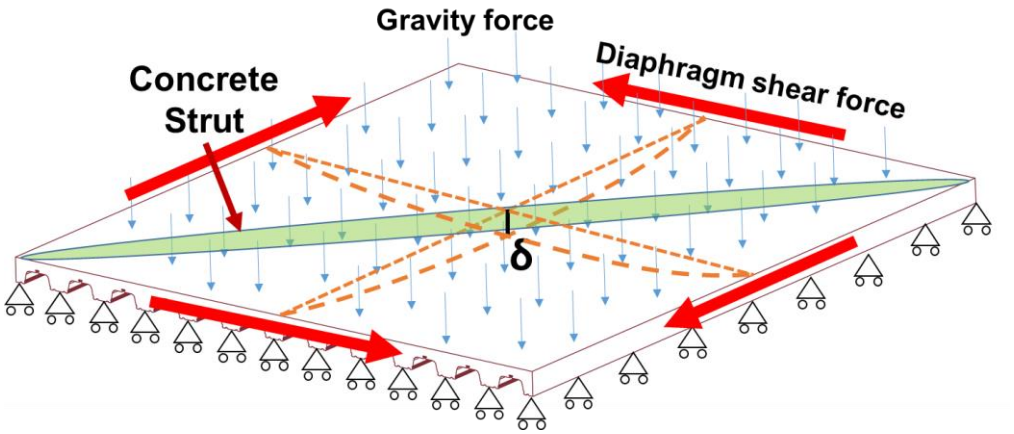

Figure 6-44. Diaphragm out-of-plane deformation and imposed shear loads

For the FEM models, a 6m×6 m composite slab with ComFlor 80 is selected both with and without secondary beams. Two 180UB18 steel beams are used as secondary beams and different level of out-of-plane deformations are applied to the floor slabs prior to imposing the lateral forces. Figure 6-45 shows the intra-panel buckling loads corresponding to each level of out-of-plane deformation. It can be seen that with increasing the initial out-of-plane deformations, the critical buckling load decreased.

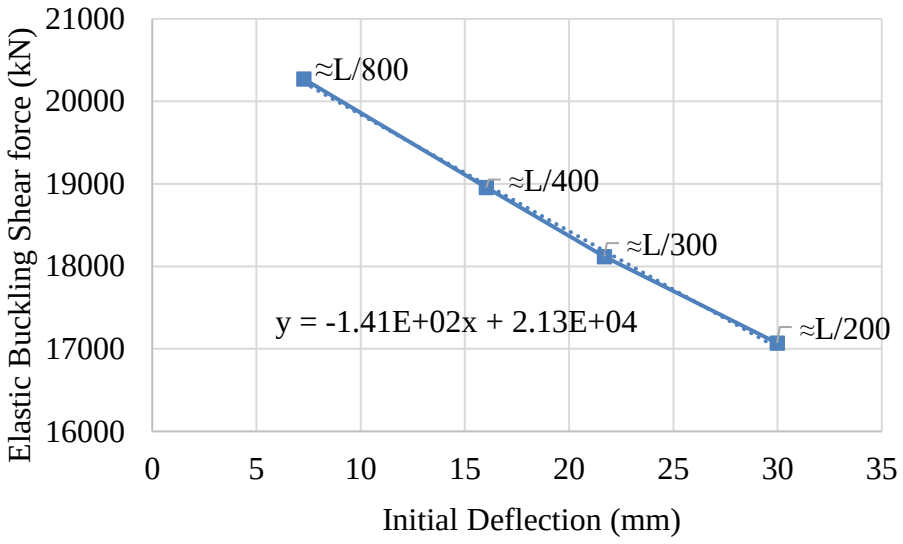

Figure 6-45. Effect of out-of-plane deformation on intra-panel slab

According to the linear regression shown in Figure 6-45, the buckling force at zero initial deflection may be about 21,300 kN, therefore the ratio of buckling force at L/300 (assuming the allowable initial deflection is L/300) to zero initial deflection is about 0.85 for the studied

intra-panel model. The same method is used for the intra-bay as shown in Figure 6-46. Note that a certain amount of initial deflection is required to obtain a buckling load. Therefore, buckling load corresponding to zero initial deflection could not be computed using the created FEM model.

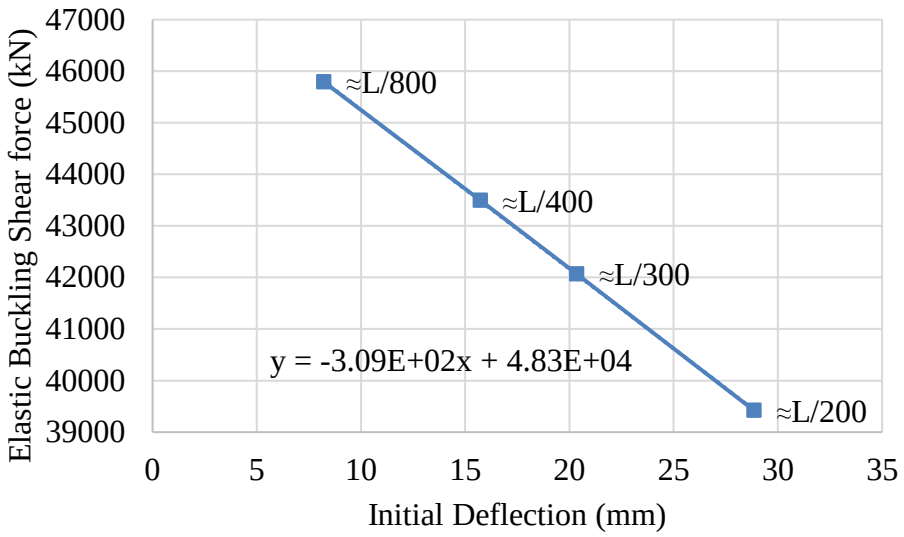

Figure 6-46. Effect of out-of-plane deformation on intra-bay slab

Similar to the intra-panel model, if the initial deflection considered to be L/300, based on the linear regression shown in Figure 6-46, the buckling force at zero initial deflection could be about 48,300 kN, therefore the ratio of the buckling force at L/300 to zero initial deflection is about 0.875 for the studied intra-bay.

- **Effect of gravity forces on the ultimate strut buckling strength (post-crack)**

Figure 6-47 shows the strut formed in the diaphragm with some initial out-of-plane deformation (δ). In this section, the initial deflection is explicitly considered in solving the differential equation of the strut buckling. It is assumed that the out-of-plane deflection is due to a uniformly distributed gravity force acting on the diaphragm.

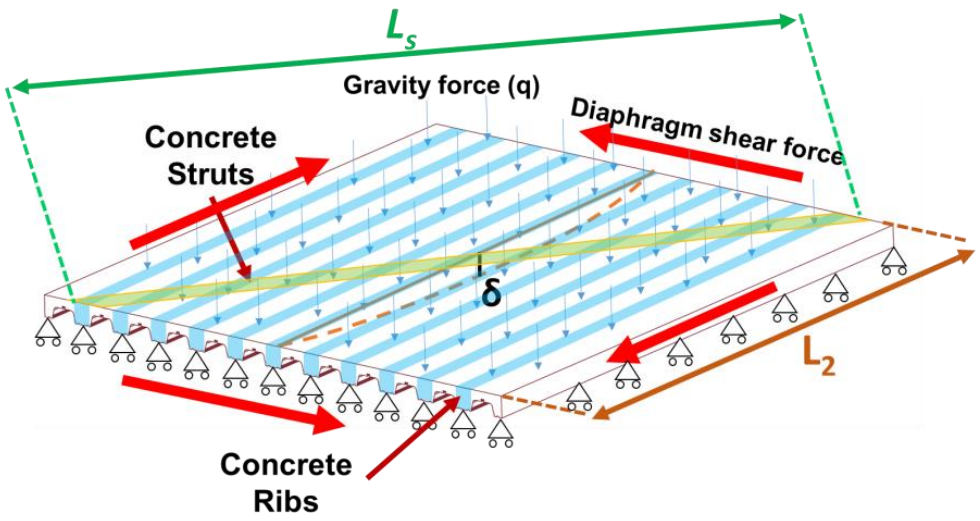

Figure 6-47. Strut formed in diaphragm with initial out-of-plane deformation

The gravity force reactions are distributed between the struts and the ribs based on their flexural stiffnesses as shown in Figure 6-48. Also, based on deformation compatibility the maximum deflection of both the strut and the rib, which occurs at the middle of the panel should be the same.

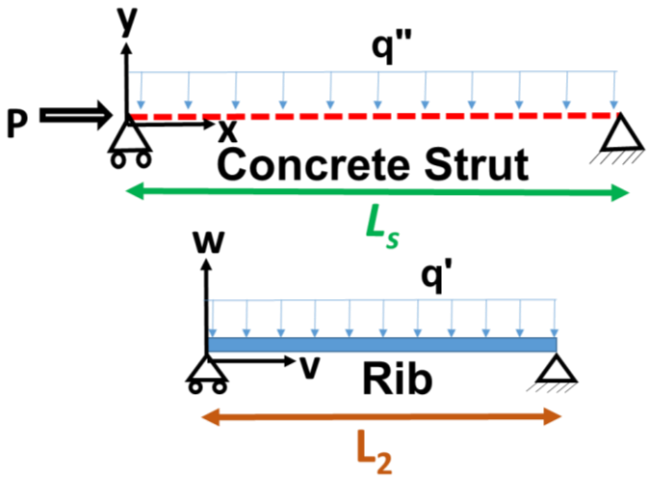

Figure 6-48. The gravity force distributed between the struts and the ribs

Using deformation compatibility, the relation between the components of the gravity force carried by the strut and the rib in the panel can be found. The mid-point deflections of the rib and strut are equal to:

$$\delta_{Rib} = \frac{5q'L_2^4}{384EI_r}$$

$$\delta_{Strut} = \frac{5q''L_s^4}{384EI_s}$$

Where q' and q'' are the gravity forces per unit length carried by the rib and the strut respectively. Deformation compatibility leads to:

$$\delta_{Strut} = \delta_{Rib}$$ Eq. (6-44)

$$\frac{q'}{q''} = \frac{L_s^4 I_r}{L_2^4 I_s}$$ Eq. (6-45)

The free body diagram of the strut and the rib is shown in Figure 6-49. Based on these diagrams the differential equations can be written as:

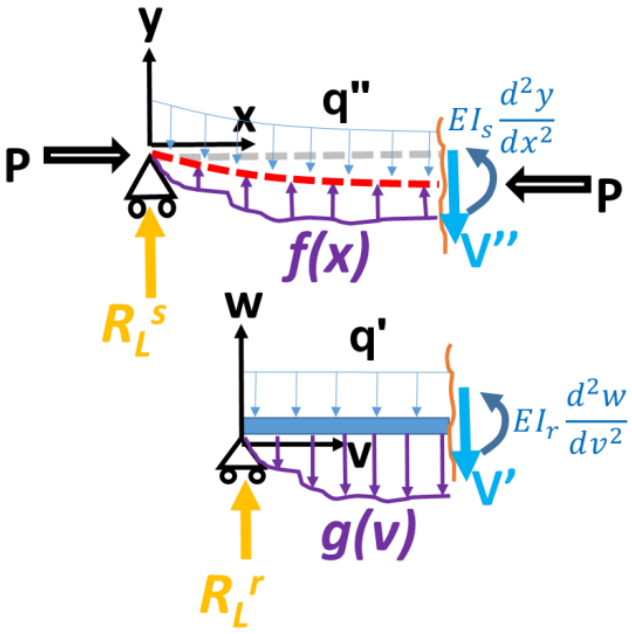

Figure 6-49. Free body diagram of the strut and the rib

$$\sum {}_A M_{Strut} = 0$$

$$-EI_s \frac{d^2y}{dx^2} - Py + \int_0^x xf(x)dx - xV'' - \int_0^x xq''dx = 0$$ Eq. (4-46)

$$\sum {}_B M_{Rib} = 0$$

$$-EI_r \frac{d^2w}{dv^2} - \int_0^v vg(v)dv - vV' - \int_0^v vq'dv = 0$$ Eq. (4-47)

Where V'' and V' are the strut and the rib shear forces respectively, and can be written as:

$$V'' = R_L^s + \int_0^x f(x)\,dx - \int_0^x q''\,dx$$ Eq. (6-48)

$$V' = R_L^r - \int_0^v g(v)dv - \int_0^v q'\,dv$$ Eq. (6-49)

Substituting Eq. (6-22) in Eqs. (6-48) and (6-49) leads to:

$$V'' + V' = R_L^s - xq'' + R_L^r - vq'$$ Eq. (6-50)

Also, substituting Eq. (6-28) into the differential equation of the rib Eq. (6-47) gives:

$$\int xf(x)\,dx = \frac{L_s}{L_2}\left[-vV' - \frac{v^2}{2}q' - EI_r\frac{d^2y}{dx^2}\left(\frac{L_s}{L_2}\right)^2\right]$$ Eq. (6-51)

Using Eq. (6-51) the equilibrium differential equation of the strut can be rewritten as:

$$-EI_s\frac{d^2y}{dx^2} - Py + \frac{L_s}{L_2}\left[-vV' - \frac{v^2}{2}q' - EI_r\frac{d^2y}{dx^2}\left(\frac{L_s}{L_2}\right)^2\right] - xV'' - \int_0^x xq''\,dx = 0$$

Eq. (6-52)

Substituting Eq. (6-50) into Eq. (6-52) gives the differential equation of the system considering the initial deflection due to the gravity forces, which is:

$$-EI_s\frac{d^2y}{dx^2} - Py - EI_r\frac{d^2y}{dx^2}\left(\frac{L_s}{L_2}\right)^3 + \frac{L_2}{L_s}q'\frac{x^2}{2} - \frac{L_2}{2}q'x - \frac{L_s}{2}q''x + q''\frac{x^2}{2} = 0$$ Eq. (6-53)

By defining the α, β and γ parameters as the following

$$\alpha = EI_s + \left(\frac{L_s}{L_2}\right)^3 EI_r$$

$$\beta = q''\frac{L_s}{2} + q'\frac{L_2}{2}$$

$$\gamma = \frac{q''}{2} + \frac{L_2}{L_s}\frac{q'}{2}$$

The differential Eq. (6-53) becomes:

$$-\alpha\frac{d^2y}{dx^2} - Py = \beta x - \gamma x^2$$ Eq. (6-54)

Considering:

$$k^2 = {}^{P}/_{\alpha}$$

The solution to Eq. (6-54) consists of a complementary and a particular part. The solution for the homogeneous linear differential equation is the same as Eq. (6-36) and the particular solution is any solution to the entire equation such as $y = -\frac{\beta}{P}x + \frac{\gamma}{P}x^2 - \frac{2\gamma\alpha}{P^2}$. Therefore the entire solution can be written as:

$$y = A\sin kx + B\cos kx - \frac{\beta}{P}x + \frac{\gamma}{P}x^2 - \frac{2\gamma\alpha}{P^2} \quad \text{Eq. (6-55)}$$

To evaluate the arbitrary constants A and B, the boundary conditions are used as the following:

$$(y)_{x=0,L_S} = 0$$

$$\left(\frac{dy}{dx}\right)_{x=\frac{L_S}{2}} = 0$$

The first of these conditions when substituted into Eq. (6-55) leads to

$$B = \frac{2\gamma\alpha}{P^2} \quad \text{Eq. (6-56)}$$

And from the second condition, it is found that:

$$A = \frac{2\gamma\alpha k\sin\left(k\frac{L_S}{2}\right) + P\beta - P\gamma L_S}{P^2 k\cos\left(k\frac{L_S}{2}\right)} \quad \text{Eq. (6-57)}$$

By substituting A and B into Eq. (6-55) and putting $x = \frac{L_S}{2}$, the maximum out-of-plane deformation of the strut considering the compression axial force can be calculated as:

$$\delta_{Max} = y_{x=\frac{L_S}{2}} = \frac{(\beta-\gamma L_S)}{Pk}\tan\left(k\frac{L_S}{2}\right) + \frac{2\gamma\alpha}{P^2}\sec\left(k\frac{L_S}{2}\right) - \frac{2\beta L_S P + \gamma {L_S}^2 P - 2\gamma\alpha}{4P^2} \quad \text{Eq. (6-58)}$$

Figure 6-50 plots $\frac{\delta_{Max}}{\delta_{Rib}}$ for different $\frac{P}{P_{cr}}$ where the P_{cr} is found using Eq. (6-36). Now, if the limiting value for $\frac{\delta_{Max}}{\delta_{Rib}}$ be estimated, the critical strut buckling load considering the gravity forces (out-of-plane deflection) can simply be found using this plot.

δ_{Rib} is given in Eq. (6-43b) as a function of the gravity force per unit length carried by the rib, q'. This q' does not need to be computed as it cancels out in $\frac{\delta_{Max}}{\delta_{Rib}}$ ratio.

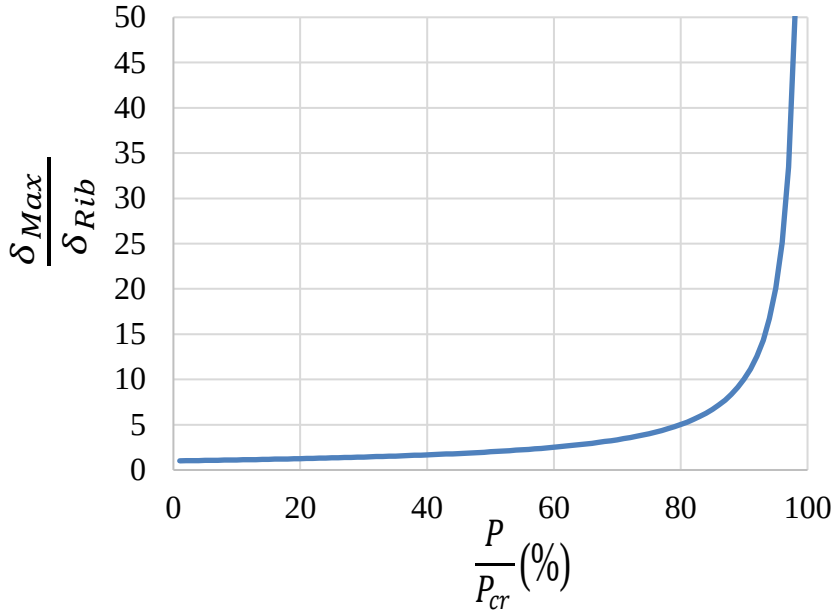

Figure 6-50. Plot of the displacement ratio $\frac{\delta_{Max}}{\delta_{Rib}}$ against different $\frac{P}{P_{cr}}$

To obtain $\frac{\delta_{Max}}{\delta_{Rib}}$, the maximum value for δ_{Rib} under serviceability limit state is considered to be $L/300$ (NZS1170.0 2002, Table C1). Also, it is assumed that δ_{Max} corresponds to the rib deflection when the first yield occurs in the rib section (M_y). Considering $q_{rib,U}$ is the ultimate gravity load per unit length causing M_y in the rib, $\frac{\delta_{Max}}{\delta_{Rib}}$ can be found as:

$$M_y = \frac{q_{rib,U}{L_2}^2}{8}$$

$$\delta_{Max} = \frac{5q_{rib,U}{L_2}^4}{384EI_r} = \frac{5{L_2}^2 M_y}{48EI_r}$$

$$\frac{\delta_{Max}}{\delta_{Rib}} = \left(\frac{5{L_2}^2 M_y}{48EI_r}\right) \Big/ \left(\frac{L_2}{300}\right)$$

$$\frac{\delta_{Max}}{\delta_{Rib}} = \frac{31.25L_2 M_y}{EI_r} \qquad \text{Eq. (6-59)}$$

Where M_y is the yield moment of the rib section, L_2 and I_r are the rib length and moment of inertia respectively. And E is the elastic modulus of the concrete which is calculated based on NZS3101 (2006) Clause 5.2.3 using Eq. (6-60).

$$E(MPa) = 3320\sqrt{f_c'(MPa)} + 6900 \quad \text{Eq. (6-60)}$$

Therefore for finding the ratio $\frac{\delta_{Max}}{\delta_{Rib}}$, the yield moment ($M_y$) and the rib length ($L_2$) are required. For this, the steel deck profiles, ComFlor 60 and 80, are selected and designed for gravity loads using ComFlor Steel Composite Metal Deck Design software.

The gravity forces used for the design of ComFlor floor slabs include: 3 kPa imposed action (Q), 1 kPa for ceiling/services and finishes, 1 kPa for partitions, and self-weight of the floor slab (G) was calculated by the software based on the slab thickness and section details. It is assumed that the concrete compressive strength is 30 MPa with an elastic modulus of 25 GPa. Four steel plate thicknesses (0.75, 0.9, 1 and 1.2 mm) and three topping thickness (60, 70 and 90 mm) are considered for design. To achieve larger spans that decrease the buckling strength, it is assumed that the floors are propped during construction.

For finding the yield moment (M_y) of the rib of each designed floor slab, section analysis is used to calculate the yield moment corresponding to the first yield in the steel decking or concrete compressive strain equal to 0.003. Table 6-13 and Table 6-14 are presenting the analysis result in terms of the yield moment (M_y), section reinforcement ratio (ρ) and the maximum possible span (L_2) with that particular floor slab and gravity forces. The value of M_y obtained using this method was the same as that from the ComFlor Steel Composite Metal Deck Design software. The value of ρ was computed considering the tension area of the steel decking. The L_2 was taken from ComFlor Steel Composite Metal Deck Design software. The limit states considered by ComFlor software include strength, deflection and vibration. These

are described in detail in the ComFlor manual. The design summary of two sample slabs are presented in Appendix I.

Table 6-13. Analysis results for ComFlor 80

Concrete topping		**Steel deck plate thickness**			
		0.75	0.9	1	1.2
60 mm	M_y (kN.m)	10.5	12.1	13.3	15.6
	ρ (%)	1.17	1.4	1.56	1.87
	L_2 (m)	4.7	4.8	4.9	5
70 mm	M_y (kN.m)	11.5	13.5	14.8	17.3
	ρ (%)	1.09	1.31	1.46	1.75
	L_2 (m)	4.9	5	5.1	5.3
90 mm	M_y (kN.m)	13.4	16	17.5	20.5
	ρ (%)	0.96	1.16	1.29	1.54
	L_2 (m)	5.1	5.3	5.4	5.6

Table 6-14. Analysis results for ComFlor 60

Concrete topping		**Steel deck plate thickness**			
		0.75	0.9	1	1.2
60 mm	M_y (kN.m)	8.8	10.4	11.4	13.2
	ρ (%)	1.14	1.37	1.52	1.83
	L_2 (m)	4.1	4.2	4.3	4.4
70 mm	M_y (kN.m)	10.6	11.5	12.6	14.7
	ρ (%)	1.05	1.27	1.41	1.69
	L_2 (m)	4.4	4.5	4.5	4.6
90 mm	M_y (kN.m)	11.6	13.9	15.2	17.9
	ρ (%)	0.91	1.1	1.22	1.46
	L_2 (m)	4.7	4.9	5	5.2

From Table 6-13 and Table 6-14 it can be seen that the reinforcement ratio of all 24 slabs is between 0.9% and 1.9%. Using the reinforcement ratios and based on Figure 6-51 from NZS3101 (2006) Clause C6.9.1 which represents effective stiffness of rectangular beams with grade 500 reinforcement against reinforcement ratio, shows the stiffness reduction factor due to flexural cracking is between 0.38 and 0.58 for 30 MPa concrete. In this study, the reduction factor was selected to be 0.40 as a lower bound value when 30MPa concrete is used.

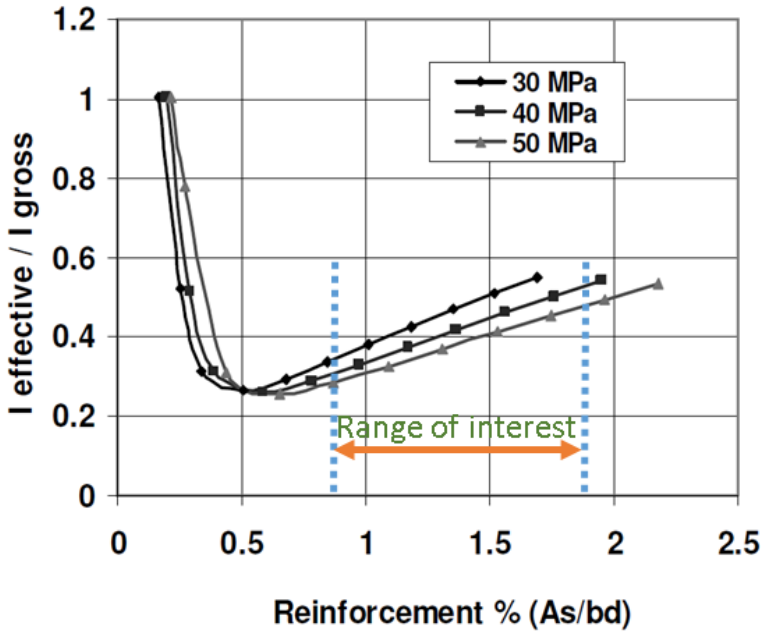

Figure 6-51. Effective stiffness of rectangular beam with grade 500 reinforcement, NZS3101 (2006) Clause C6.9.1

The value of $\frac{\delta_{Max}}{\delta_{Rib}}$ is obtained using Eq. (6-59). The rib stiffness, I_r, is computed using I_{gross} and the stiffness reduction factor of 0.40. The yield moment is from Table 6-13 and Table 6-14. The maximum possible length, L_2, is from Table 6-13 and Table 6-14 to obtain the maximum $\frac{\delta_{Max}}{\delta_{Rib}}$. The results are presented in Table 6-15.

Table 6-15. Ratio of ultimate deflection to the allowable deflection for all investigated 24 slabs

		$\frac{\delta_{Max}}{\delta_{Rib}}$			
		Steel deck plate thickness			
ComFlor type	Concrete topping	0.75	0.9	1	1.2
ComFlor 80	60 mm	4.96	5.9	6.59	7.85
	70 mm	4.63	5.54	6.18	7.51
	90 mm	3.86	4.78	5.33	6.5
ComFlor 60	60 mm	5.39	6.52	7.31	8.71
	70 mm	5.47	6.08	6.66	7.95
	90 mm	4.18	5.2	5.83	7.12

This Table shows that the ratio of maximum deflection to the allowable serviceability limit state deflection $\frac{\delta_{Max}}{\delta_{Rib}}$ varies between 3.8 and 8.7 for different rib sections. As can be seen in Figure 6-50 that as $\frac{\delta_{Max}}{\delta_{Rib}}$ increases the buckling strength of the strut increases toward P_{cr} for very large deflection ratios. Therefore, conservatively the value of $\frac{\delta_{Max}}{\delta_{Rib}}$ is selected be equal to 4 which approximately is the lowest ratio based on the Table 6-15 to achieve more conservative results.

Figure 6-52 shows an enlarged view of Figure 6-50. For this range of displacement ratio, the lower bound axial force capacity is about $0.75P_{cr}$ since $\frac{P}{P_{cr}} = 0.75$ for $\frac{\delta_{Max}}{\delta_{Rib}} = 4.0$ as shown in Figure 6-52.

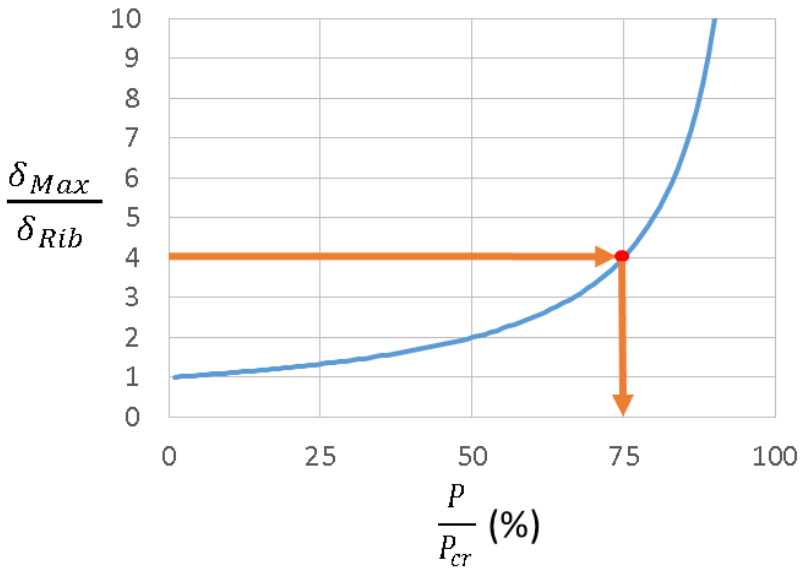

Figure 6-52. An enlarged view of Figure 6-50, showing the strut buckling capacity is about $0.75P_{cr}$ with the out of plane deflections

6.6 Discussion and conclusion

In this chapter the diaphragm buckling issue was discussed extensively. The buckling modes considered in this study include:

i. Local buckling of the concrete topping between the floor ribs (inter-rib buckling),

ii. Buckling of the diaphragm between secondary beams (intra-panel buckling), and

iii. Global buckling of the diaphragm between primary beams (intra-bay buckling).

All of the buckling modes are studied for both pre-crack and post-crack conditions of the concrete slab. The critical buckling of each mode is calculated using analytical methods, and in some cases, the results are verified with FEM modelling using ABAQUS software. It was found that:

i. Local buckling will not occur for conventional floor slabs. This is because the minimum thickness required results in high buckling forces and concrete shear or crushing are likely to occur much earlier than buckling as described in Section 6.4.1.

ii. For the intra-panel and intra-bay buckling modes the critical slab in-plane shear forces which cause buckling need to be checked both before and after cracking. A simple formula is provided to do this. It considered pinned end condition, out-of-plane deformations and the corrugated nature of the composite slab. It was shown that in the studied examples the shear buckling does not govern. The strut buckling is more probable to occur due to the high axial strength of concrete material.

The reduction in the horizontal critical buckling loads due to vertical gravity forces that cause initial vertical deflection in the floor slabs is also investigated. It was found that:

i. The intra-panel critical elastic buckling capacity decreased by up to 15% considering the initial deflection equal to L/300.

ii. The Global buckling mode (intra-bay) critical elastic buckling capacity decreased by up to 12.5% considering the initial deflection equal to L/300.

iii. For the strut buckling of intra-panel and intra-bay modes, it was found that for the ComFlor 60 and 80 profiles with 60 mm to 90 mm concrete topping thicknesses,

the strut buckling capacity decreased to about 0.75 times the critical buckling capacity corresponding to the zero initial deflection.

Based on the results of studying the effect of initial deflection, the elastic buckling strength reduction factor accounting for the presence of gravity forces on the floor slab can conservatively be considered equal to 0.75. This value may be used in design.

6.7 Summary of the method for calculating the diaphragm critical buckling loads

Notations used in the following formulations are presented in Table 6-16.

Table 6-16. Notations used in the formulation of diaphragm buckling considerations

N_{xy1}	Elastic critical shear stress (MPa)
b	Plate width (distance between ribs) (mm)
t	Concrete topping thickness (mm)
E	Concrete elastic modulus (MPa)
ν	Concrete Poisson's ratio
k_s	Plate shear buckling coefficient
N_{cr}	Elastic critical axial stress (MPa)
k	Plate axial buckling coefficient
τ_c and ∂_c	Imposed shear and axial stresses to the concrete topping (MPa)
e_y	Distance between concrete topping centre line to the section neutral axis (mm)
h	Steel deck height (mm)
a	Steel deck rib width (mm)
β	Ribs height modification factor
G_{xy}	Elastic shear modulus of concrete (MPa)
η	Numerical factor depending on the ribs aspect ratios
k_B	Reduction factor accounting for the decrease in the torsional stiffness of reinforced concrete beams due to concrete cracking
N_{xy2}	Elastic critical shear stress of intra-panel orthogonal plate (MPa)
D_x	Flexural stiffness of the composite slab in the direction perpendicular to ribs (N.mm)
D_y	Flexural stiffness of the composite slab in the ribs direction (N.mm)
L_2	Slab length parallel to the ribs (mm)
f_c'	Concrete compressive strength (MPa)
I_s	Moment of inertia of the concrete strut per unit width (mm^4)
I_r	Moment of inertia of the rib per unit width(mm^4)
L_s	Strut length (mm)
α	The angle between the concrete strut and the ribs
L_1	Slab length perpendicular to the ribs (mm)

L_2	Slab length parallel to the ribs (mm)
V_{SB2}	Slab shear buckling strength per unit length due to intra-panel buckling (N/mm)
V_{strut2}	Slab shear from strut buckling capacity per unit length (intra-panel buckling) (N/mm)
t_{eq}	Equivalent plate thickness to the composite slab in the X direction (mm)
e_x	Distance between equivalent slab centre line to the section neutral axis (mm)
E_s	Steel elastic modulus (MPa)
I_y	Moment of inertia of secondary beams (mm^4)
A_s	Cross-section area of secondary beams (mm^2)
h_1	Steel beam height (secondary beam) (mm)
c_1	Distance between secondary beams (mm)
d_i	Width of steel beam flanges and web (mm)
t_i	Thickness of steel beam flanges and web (mm)
G_{xys}	Elastic shear modulus of steel (MPa)
N_{xy3}	Elastic critical shear stress of intra-bay orthogonal plate (MPa)
V_{SB3}	Slab shear buckling strength per unit length due to intra-bay buckling (N/mm)
I_{sb}	Is the secondary beam moment of inertia per unit width of the slab (I_y/c_1) (mm^3)
ψ	Buckling correction factor, 0.9 for a composite floor with one secondary beam, 1 for more than one
n	Number of secondary beams per bay
V_{strut3}	Slab shear from strut buckling capacity per unit length (intra-bay buckling) (N/mm)
P_{cr3}	Strut buckling capacity per unit length (intra-bay) (N/mm)
P_{cr2}	Strut buckling capacity per unit length (intra-panel buckling) (N/mm)
$N_{existing}$	Maximum imposed shear stress to intra-panel (MPa)

➢ Buckling mode 1, inter-rib (local) buckling

1. ***Calculate critical shear buckling of the inter-rib subjected to pure shear, (pre-crack condition)***

$$N_{xy1} = k_s \frac{E\pi^2}{12(1-\nu^2)(b/t)^2}$$

The k_s can conservatively considered equal to 5.4.

2. ***Calculate critical buckling load of the inter-rib subjected to strut forces, (post-crack condition)***

$$N_{cr} = k \frac{E\pi^2}{12(1-\nu^2)(b/t)^2}$$

The k can considered equal to 4 conservatively.

The imposed shear and axial stresses on the inter-rib zone can be obtained from truss element modelling results considering the rib and the strut relative directions. In the following the angle between the strut and ribs is considered 45° and P is the maximum recorded strut force.

$$\tau_c = \partial_c = \frac{0.5P}{A_{truss}}$$

Find the demand to capacity ratio (DCR) using the following equation:

$$\left(\frac{\partial_c}{N_{xy1}}\right) + \left(\frac{\tau_c}{N_{cr}}\right)^2 \leq 1$$

➢ Buckling mode 2, Intra-panel buckling

1. ***Calculate critical shear buckling of the intra-panel subjected to pure shear, (pre-crack condition)***
2. Preliminary check:

If the equation below is satisfied, there is no need to check the critical shear buckling of the intra-panel subjected to pure shear:

$$N_{existing} \leq 0.75 \times 3.5 \frac{\pi^2}{t{L_2}^2} \sqrt[4]{D_x {D_y}^3}$$

Where $\sqrt[4]{D_x {D_y}^3}$ for different topping thickness can be found using the plots shown in Figure 6-53 for ComFlor 60 and 80 (these values are calculated using flexural stiffness reduction factor 0.35 based on Table C6.5 NZS3101, 2006). And $N_{existing}$ is the maximum imposed shear stress to the intra-panel.

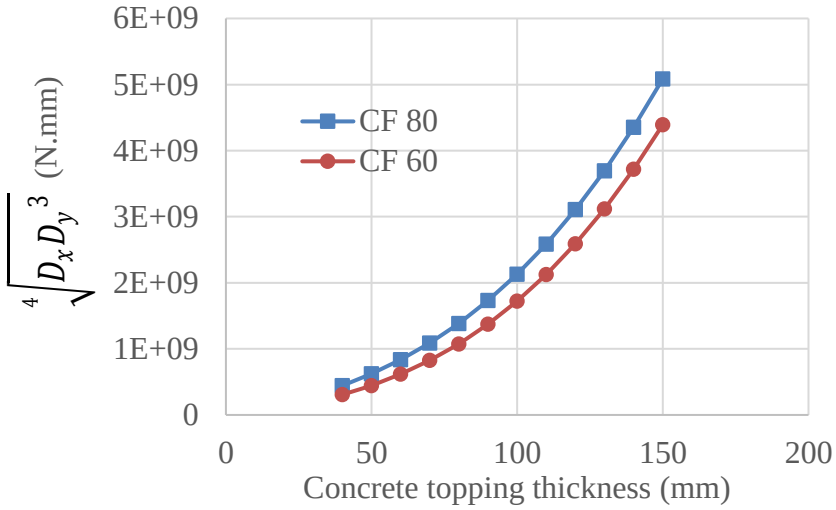

Figure 6-53. Calculated values of $\sqrt[4]{D_x {D_y}^3}$ for ComFlor 60 and 80 against different concrete topping thickness

First, the properties of the equivalent orthotropic plate need to be found:

Find the flexural stiffness of the composite slab in the ribs direction (D_y):

$$D_y = 0.35\left(\frac{Et^3}{12(1-\nu^2)} + \frac{Ete_y{}^2}{(1-\nu^2)} + \frac{Eah^3}{12(a+b)} + \frac{Eha\left(\frac{h}{2}+\frac{t}{2}-e_y\right)^2}{(a+b)}\right)$$

Find the flexural stiffness of the composite slab in the direction perpendicular to ribs (D_x):

$$D_x = 0.35\left(\frac{D_a D_b (a+b)}{(bD_a + aD_b)}\right)$$

$$D_a = \frac{E(t+\beta h)^3}{12(1-\nu^2)}$$

$$D_b = \frac{Et^3}{12(1-\nu^2)}$$

$$\begin{cases} \beta = 0.9224e^{\left(\frac{-2.756h}{a}\right)} & for\ \frac{h}{a} \le 0.4 \\ \beta = \frac{a}{8h} & for\ \frac{h}{a} > 0.4 \end{cases}$$

Alternatively, the following equation could be used for $\frac{h}{a} > 0.1$.

$$\beta = 0.136e^{\left(\frac{-0.745h}{a}\right)} \quad for\ \frac{h}{a} > 0.1$$

Find the torsional stiffness of the composite slab (B):

$$B = \frac{Et^3}{12(1-\nu^2)} + \frac{G_{xy}}{2}\frac{ha^3\eta}{(a+b)}k_B$$

Where k_B can be considered zero conservatively.

Table 6-7. Parameter η (Szilard, 1974)

a/h	1	1.2	1.5	2	2.5	3	4	6	8	10	∞
η	0.140	0.166	0.196	0.229	0.249	0.263	0.281	0.299	0.307	0.313	0.333

To calculate the critical buckling shear loads the flexural stiffness D_x and D_y could be multiplied by flexural stiffness reduction factor (0.35) to account for concrete flexural cracking.

$$N_{xy2} = K_s \frac{\pi^2}{t{L_2}^2}\sqrt[4]{D_x {D_y}^3}$$

$$V_{SB2} = 0.75 \times tN_{xy2}$$

The calculated buckling load is multiplied by 0.75 to account for the out-of-straightness effect due to existing gravity forces.

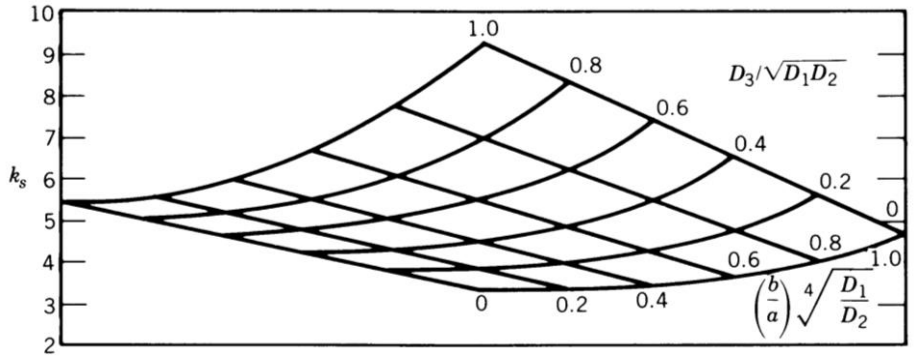

Figure 6-22. Shear buckling coefficient for orthotropic plates (Ziemian, 2010), as adapted from Johns and Kirkpatrick (1971)

3. Intra-panel subjected to diagonal force (strut force), post-crack condition

The strut critical buckling load per unit width of the strut is calculated using:

$$P_{cr2} = 0.75 \times \frac{\pi^2\left(EI_s + EI_r\left(\frac{L_s}{L_2}\right)^3\right)}{{L_s}^2} = \frac{\pi^2 EI_s \sin^3\alpha + \pi^2 EI_r}{{L_s}^2 \sin^3\alpha}$$

$$I_r = 0.35\frac{a(t+h)^3}{12(a+b)}$$

$$I_s = 0.8\frac{t^3 \sin\alpha}{12}$$

$$L_s = \frac{L_2}{\sin\alpha}$$

In this study, it is suggested that the sum of the imposed strut forces (demands) and the sum of intra-panel strut critical buckling strengths (capacity) be compared.

➢ Buckling mode 3, Global buckling

1. Calculate critical shear buckling of the intra-bay subjected to pure shear, (pre-crack condition)

❖ Preliminary check:

If the equation below is satisfied, there is no need to check the critical shear buckling of the intra-bay subjected to pure shear:

$$N_{existing} \leq 0.75 \times 3.5 \frac{\pi^2}{t{L_2}^2} \sqrt[4]{D_x {D_y}^3}$$

Where $\sqrt[4]{D_x {D_y}^3}$ for different topping thickness can be found using the plots shown in Figure 6-53 for ComFlor 60 and 80 ignoring the secondary beams (these values are calculated using flexural stiffness reduction factor 0.35 based on Table C6.5 NZS3101, 2006). And $N_{existing}$ is the maximum imposed shear stress to the intra-bay.

First, the properties of the equivalent orthotropic plate need to be found:

Find the flexural stiffness of the composite floor in the ribs direction (D_y) same as the intra-panel:

$$D_y = 0.35\left(\frac{Et^3}{12(1-\nu^2)} + \frac{Ete_y{}^2}{(1-\nu^2)} + \frac{Eah^3}{12(a+b)} + \frac{Eha\left(\frac{h}{2}+\frac{t}{2}-e_y\right)^2}{(a+b)}\right)$$

Find the flexural stiffness of the composite floor in the direction perpendicular to ribs (D_x):

The equivalent plate thickness to the composite slab should be calculated: (D_{xs} is the composite slab stiffness equal to D_x for the intra-panel without considering stiffness reduction factor)

$$D_{xs} = \frac{D_a D_b (a+b)}{(bD_a + aD_b)}$$

$$t_{eq} = \sqrt[3]{\frac{12(1-\nu^2)D_{xs}}{E}}$$

$$D_x = \frac{Et_{eq}{}^3}{12(1-\nu^2)} + \frac{Et_{eq}e_x{}^2}{(1-\nu^2)} + \frac{E_s I_y}{c_1} + \frac{E_s A_s\left(\frac{h_1}{2}+t+h-\frac{t_{eq}}{2}-e_x\right)^2}{c_1}$$

The torsional stiffness of the composite slab is calculated using:

$$B = \frac{Et_{eq}{}^3}{12(1-\nu^2)} + \frac{G_{xy}}{2}\frac{ha^3\eta}{(a+b)}k_B + \frac{G_{xy_s}}{6}\left(\frac{\sum d_i t_i{}^3}{c_1}\right)$$

Where k_B can be considered zero conservatively.

Elastic critical shear stress (buckling stress) is expressed as:

$$N_{xy3} = K_s \frac{\pi^2}{tL_2{}^2}\sqrt[4]{D_x D_y{}^3}$$

$$V_{SB3} = 0.75 \times tN_{xy3}$$

Parameter K_s should be found using Figure 6-22.

2. Intra-bay subjected to diagonal force (strut force), post-crack

The strut critical buckling load per unit width of the strut is calculated using:

$$P_{cr3} = 0.75 \times min\begin{cases}\frac{\pi^2 EI_s}{L_s{}^2} + \frac{\pi^2 EI_r}{L_2{}^2 \sin\alpha} + \psi\frac{\pi^2 E_s I_{sb}}{L_1{}^2\cos\alpha} \\ (n+1)^2\left(\frac{\pi^2 EI_s}{L_s{}^2} + \frac{\pi^2 EI_r}{L_2{}^2\sin\alpha}\right)\end{cases}$$

Same as the intra-panel buckling mode, it is suggested that the sum of the imposed strut forces (demands) and the sum of intra-bay strut critical buckling strengths (capacity) be compared.

References

[1] AS/NZS 1170.0 (2002), Structural design actions-Part 0: General principles.

[2] Bolluyt, J. E. (1980). Behavior of composite steel deck diaphragms.

[3] Bresler, B., & Pister, K. S. (1958, September). Strength of concrete under combined stresses. In Journal Proceedings (Vol. 55, No. 9, pp. 321-345).

[4] Bruneau, M., MacRae, G. (2017). "Reconstructing Christchurch: A Seismic Shift in Building Structural Systems", Quake Centre, University of Canterbury.

[5] ANSI/SDI (2011). American National Standards Institute/Steel Deck Institute, C-2011 Standard for Composite Steel Floor Deck-Slabs.

[6] ComFlor Steel Composite Metal Deck Design software, Ver 9.0.33.0

[7] CSA, C. (2014). S16-14. Design of Steel Structures, Canadian Standards Association, Toronto, ON.

[8] Henry, R. S., Dizhur, D., Elwood, K. J., Hare, J., & Brunsdon, D. (2017). Damage to concrete buildings with precast floors during the 2016 Kaikoura earthquake. Bulletin of the New Zealand Society for Earthquake Engineering, 50(2), 174-186.

[9] https://www.comflor.nz/technical-resources/#AP

[10] Iguchi, S. (1938). Die knickung der rechteckigen platte durch Schubkräfte. Ingenieur-Archiv, 9(1), 1-12.

[11] Johns, D. J., & Kirkpatrick, D. L. I. (1971). Shear buckling of isotropic and orthotropic plates: a review. HM Stationery Office.

[12] NZS 3101 (2006). Concrete structures standard. Standards New Zealand, Wellington, NZ.

[13] NZS 3404 (2007). Steel Structures Standard. Standards New Zealand, Wellington, New Zealand. Including Amendments 1 and 2, 2001/2007.

[14] Product guide, ComFlor 210 composite floor decking, S&T Stainless Ltd.

[15] Product guide, ComFlor 60 composite floor decking, S&T Stainless Ltd.

[16] Product guide, ComFlor 80 composite floor decking, S&T Stainless Ltd.

[17] Seide, P., & Stein, M. (1949). Compressive buckling of simply supported plates with longitudinal stiffeners.

[18] Seide, P. (1953). The effect of longitudinal stiffeners located on one side of a plate on the compressive buckling stress of the plate-stiffener combination.

[19] Shou-Ngo Tu. (1944). Column with Equal-Spaced Elastic Supports. Journal of the Aeronautical Sciences, 11(1), 67-72.

[20] Szilard, R. (1974). Theory and analysis of plates: classical and numerical methods. 1974. Prentice-Hall, Englewood, 10, 35-48.

[21] Wittrick, W. H. (1954). Correlation between some stability problems for orthotropic and isotropic plates under bi-axial and uni-axial direct stress. The Aeronautical Quarterly, 4(1), 83-92.

[22] Yu, C., & Schafer, B. W. (2006). Effect of longitudinal stress gradient on the ultimate strength of thin plates. Thin-walled structures, 44(7), 787-799.

[23] Ziemian, R. D. (Ed.). (2010). Guide to stability design criteria for metal structures. John Wiley & Sons.

7 Diaphragm Lateral Force Method

7.1 Introduction

The issue of finding a simplified lateral force method/pattern that can predict likely earthquake force and deformation demands has been studied for decades by many researchers (e.g. Veletsos and Newmark, 1960). Structural engineers have been using simplified lateral force methods considering some assumptions for designing structural elements. This is because a simplified method (e.g. Equivalent Static Analysis) may obtain relatively reasonable results in comparison with complex and more realistic methods (e.g. Linear Time History analysis but reduced for ductility) in most cases. These simplified methods may be found in most loading standards.

The simplified lateral force methods are well developed for designing structural elements such as beams and columns. However, different methods are required for obtaining diaphragm in-plane demands. There are some simplified methods proposed by different researchers for obtaining diaphragm global in-plane demands. However, none of them is widely accepted and each has some advantages and disadvantages.

Methods for estimating floor diaphragm global demands need to have the following features to be used in design offices widely:

1) Simplicity
2) Compatibility with commonly used analysis software packages
3) Accuracy: indicate likely in-plane demands from the different causes

In this study a diaphragm lateral force method is proposed based on an elastic structure deformation hypothesis to satisfy (1) and (2) above. This is conducted by seeking answers to the following questions:

1. What causes the diaphragm in-plane demands?

2. What are the available lateral force methods have been proposed to estimate diaphragm in-plane demands for design/assessment?
3. Can an improved method obtain diaphragm in-plane forces be proposed?
4. Which lateral force methods are best to meet the requirements of simplicity, compatibility with existing design tools and accuracy?

7.2 Slab in-plane demands

Diaphragm in-plane demands originate from different sources such as i) inertia forces, ii) transfer forces, iii) slab bearing forces, iv) compatibility forces and v) interaction with other elements as described in Chapter 2. These in-plane forces could be categorised into global and local demand groups based on their effect on the diaphragm. Global diaphragm demands may be obtained from structural analysis using proper lateral loading method or NLTH analysis. However, local demands need to be considered for designing different components of the diaphragm locally. In the following both global and local demands are described in detail.

7.2.1 Diaphragm global in-plane demands

Diaphragm global demands may be defined as diaphragm imposed forces that act on most areas of the diaphragm. Failure to resist these forces may lead to damage to the structure, a significant change in force distribution between vertical lateral force resisting (VLFR) systems of the structure, and possibility to collapse.

- **Inertia forces**

Considering the above definition, inertia forces (referred as i above) which are a product of diaphragm mass times the diaphragm accelerations during ground shaking can be categorised as global demand. Although these inertia forces usually are not significant to cause damage to diaphragms, in some situations such as long narrow diaphragms with few

lines of VLFR system along the length, inertia forces may cause large lateral displacements and damage to the diaphragm and the gravity load carrying system of the structure.

- **Transfer forces**

Another global diaphragm demand is diaphragm transfer force (which is ii above). Transfer forces may occur as a result of deformation incompatibility of different VLFR elements of a structure such as moment frames and RC walls wanting to move different amounts at different levels under the applied loading. Also, structure irregularities in height or discontinuities in plan location of the VLFR elements, may generate transfer forces between the two displaced VLFR systems above and below the level. A common discontinuity of vertical elements in the plan is at a podium level.

7.2.2 Diaphragm local in-plane demands

In contrary to the global demands, diaphragm local demands can be defined as the forces that effect on some areas of the diaphragm and may cause local damage to the diaphragm.

- **Slab bearing forces**

One example of diaphragm local demand is the slab bearing forces (which is iii above). These occur when a construction gap is not provided between the slab and column. As the column sways, it bears against the concrete slab that imposes an extra bearing force on the slab. This force must be transferred through the slab to the shear studs and the beam, and back to the column. The magnitude of slab bearing forces is a function of concrete compressive strength, number and strength of shear studs, and force transferring mechanisms into the column. Slab bearing forces may cause local damage to the concrete near the column. This has been discussed by Chaudhari et al. (2015) and MacRae and Bull (2015) in detail as well as Section 2.6 of Chapter 2.

- **Compatibility forces**

Another source of diaphragm local demands is the compatibility force (which is iv above). When neutral axes of composite beams on either side of the column are at different heights due to the composite action, the distance between the beam-ends tends to increase, causing slab tension forces and beam compression forces (MacRae and Clifton, 2015). This elongation in steel beams is expected to be much less than that of a concrete beam where cracks/gaps open at both ends of the beam (MacRae et al. 2013). However, it should be considered in the analysis because it can impose extra forces on the columns as well as on the beam plastic hinge region and the beam-column connections. Beam elongation measurements by MacRae et al. (2013) on some steel beam-column-slab subassemblies showed that the beams tend to shorten as a result of buckling of the beam and spalling of the concrete at the slab/column interface. The residual shortening, measured as the shortening at zero column drift, was less than 2mm during cycles up to about 3.5% drift. This may not be significant for a typical steel beam, but subassemblies showing gap opening characteristics such as those with reinforced concrete beams may place much higher demands on the diaphragm (SESOC 2011). This diaphragm local demand is out of the scope of this research.

- **Interaction with other elements**

Interaction with other elements (which is v above) may also impose in-plane forces on the diaphragms. This can be categorised as another source of diaphragm local demands. Inclined columns, ramps and stairs can develop diaphragm in-plane tension and compression forces due to gravity and lateral forces and they should be considered in diaphragm design. Interaction of the diaphragm with other structural elements should be considered in every design project specifically and a general method could not be developed for obtaining this diaphragm local demand.

7.3 Available diaphragm force methods, limitations and possible solutions

7.3.1 Available method

A number of lateral force methods have been proposed for obtaining diaphragm global in-plane demands. These methods range from a simple static method (e.g. ESA) to a more complex and realistic methods, like NLTH analysis. Amongst the simple methods that are used with elastic frame analysis there is no widely accepted method to obtain diaphragm in-plane demands. Every simplifying assumption results in losing a level of accuracy. Some lateral force methods include:

1) ESA considering structure ductility (CESA)

The ESA method is based on the assumption that the first mode behaviour dominates the building deformation and all the structure mass participates in this mode. The lateral forces in this method are reduced based on structural ductility considering yielding in VLFR system. Although this method can be used for obtaining frame and wall design forces in some cases, it underestimates diaphragm inertial demands especially in lower stories (Bull, 1997, Nakaki, 2000, and Fleischman et al. 2002).

2) Overstrength ESA (OESA)

The OESA method is the CESA scaled by the building's overstrength factor. It better estimates floor diaphragm forces, but the diaphragm inertial demands near the base of the structure may be underestimated.

3) Elastic ESA, (EESA)

The elastic ESA, EESA, is similar to the ESA method without considering structure ductility. This method may provide a better estimation of diaphragm inertial forces as well as lateral deformation of the structure. The lateral deformation estimation can help to obtain

likely diaphragm transfer forces. This method also underestimates diaphragm inertial demands in lower stories.

4) Parts and Components method (P&C)

The "Parts and Components" method is a force-based design approach, which is used for the design of "parts" or "components" of a structure. These forces are designed to be applied at every level independently and not together with those at other levels. This method is applicable to floors in structures where the seismic resisting systems for a given direction of loading are the same type, and of similar stiffness, so that transfer forces are not significant.

5) pseudo-Equivalent Static Analysis (pESA)

The pseudo-Equivalent Static Analysis (pESA) method (Bull, 1997 and Gardiner, 2011) modifies the ESA method to account for increased forces in the lower levels of structure, and overstrength actions, which develop in the lateral force resisting systems. Both inertia and transfer force effects result from the analysis with one lateral force distribution.

6) Sabelli et al. (2011) method

Sabelli et al. (2011) suggest conducting a number of frame analyses to capture the likely combination of transfer and inertial effects. *N* different analyses are needed in each direction for a frame with *N* levels. In the equivalent static analysis method, floor forces reduced for ductility are applied at each level, but greater forces, corresponding to the acceleration expected of the diaphragm, are applied at the level of diaphragm considered.

An alternative method (Tiong and Lyes, 2014) applies the overstrength force distribution to the frame, but make sure that the forces at the level considered are no less than those resulting from the anticipated in the Parts and Components method. This method has similarities to that of Sabelli et al. (2011) but it is more conservative. This approach is more suitable for diaphragms that do not act as transfer diaphragm which means the inertia forces govern the design criteria.

7) Pushover analysis

Pushover is a static-nonlinear analysis method where a structure is subjected to gravity loading and a monotonic displacement-controlled lateral load pattern. The lateral forces are increased until either the total capacity of the structure is exceeded, or a predetermined displacement of the structure is reached. A variation of the pushover method is adaptive pushover method that was developed to mitigate the uncertainties related to the lateral force pattern. In this method the lateral loading pattern is updated at each loading step according to the structure lateral deformation and structure stiffness matrix. This model explicitly considers the structure overstrength.

8) Modal response spectrum method (RSA)

Modal response spectrum method (RSA) is a linear-dynamic statistical analysis method which measures the contribution from each mode of vibration to indicate the likely maximum seismic response of an elastic structure. The modal response spectrum analysis is generally used when the higher mode effects are considered to be significant. In this method one analysis is performed to obtain diaphragm in-plane demands.

9) NLTH

This method evaluates the nonlinear response of a structure, including the diaphragm, to given ground motion, or suite of records. To do this, it requires the diaphragm to be modelled as an assemblage of elements and members with appropriate boundary conditions and member properties, not just modelled using a rigid diaphragm option.

7.3.2 Available method limitations

Here, some of the disadvantages of these lateral force models are presented as follows.

- **ESA considering structure ductility (CESA)**
  - For a multi-story building, peak floor accelerations may be greater than those implied from methods used to obtain peak storey shears at each level. This is

because the peak floor accelerations may be due to the higher mode accelerations. Therefore, the CESA method forces do not strictly estimate likely peak elastic floor accelerations at a particular level.

- The CESA forces are calibrated to estimate storey shears rather than level forces and forces are assumed to be applied at all stories simultaneously. They are reduced from the elastic level due to ductility.
- CESA method may underestimate the diaphragm inertia forces in lower floors (Gardiner 2011).

- **Overstrength ESA (OESA)**
  - This method needs to obtain building overstrength. The lateral forces are also reduced from the elastic level due to ductility.
  - The OESA also may underestimate the diaphragm inertia forces in lower floors because it is based on CESA method.
- **Elastic ESA (EESA)**
  - For a regular structure with similar VLFR systems (such that transfer forces are unlikely to occur), inertia forces govern the floor diaphragm design. In this case, using the EESA method may underestimate the diaphragm inertia forces in lower floors (Gardiner 2011).
  - Does not consider yielding in VLFR system of structure and may overestimate diaphragm transfer forces.
- **Parts and Components method (P&C)**
  - Demands in P&C method based solely on the peak floor accelerations at one level by itself. These forces are not generally appropriate for use in diaphragm design because they are applied on one storey at a time so transfer force effects are not included. There is no clear rationale for applying floor forces all at once.

- The duration of the peak force/acceleration demand may significantly affect the structural response. For example, if a high force/acceleration demand occurs only briefly, causing a very small inelastic displacement, then its effect may be small. Designing for the peak values may, therefore, result in conservative forces (MacRae and Bull, 2015, Bruere and Colley 2015).
- Many studies have been conducted to estimate the peak floor accelerations at different floor levels. These differ markedly between researchers because the results depend on the structural framing type, selected acceleration records, and the analysis assumptions. (e.g. Dantanarayana et al. 2012).
- This method does not consider yielding in VLFR system of the structure.

- **pseudo-Equivalent Static Analysis (pESA)**
  - pESA method accounts for the structure overstrength and higher mode effects. However it has some limitations such as i) it is limited for up to nine storey structures, ii) it is calibrated with moment resisting frame and dual system structures, and iii) for structures with longer periods the bottom portion of the lateral loading pattern may govern over the height of the structure which may provide over-conservative results (Gardiner 2011).
- **Sabelli et al. (2011) method**
  - Sabelli et al. (2011) method require N different analyses in each direction for an N storey structure. Also it does not consider structure over-strength.
  - Determination of diaphragm specific forces requires judgement from the user to extract meaningful information from the response spectrum analysis. This is because the design actions lose their sign through modal combination process and are not in equilibrium.

- This method considers reduced design level forces depending on the assumed ductility of the structure.

- **Pushover analysis**
  - First mode static pushover analysis does not provide information about higher mode effects but it does include frame overstrength effects. Material/member overstrength may also be included in the analysis.
  - The maximum diaphragm force may not occur at the maximum lateral displacement of the structure as shown in Appendix A.
  - The results of this method may be sensitive to the selected loading pattern and target displacement. Pushover analysis may underestimate storey drifts at lower levels (Fenwick and Davidson 1991, 1997).

- **Modal response spectrum method (RSA)**
  - Modal response spectrum analysis accounts for higher mode effects. However, its results cannot directly be used for diaphragm analysis and need engineering judgment. The design actions lose their sign through the modal combination process and are not in equilibrium.
  - Does not directly consider yielding explicitly.
  - In a structure that is designed to sustain some level of inelastic deformation, the higher modes effects may be underestimated in the response of the structure.

- **NLTH**
  - Nonlinear time history analysis (NLTH) may be used to find likely diaphragm forces for a set of earthquake records. This method presents more realistic results compare to other methods accounting for structure nonlinear behaviour, higher mode effects, strength degradation, hysteresis effects and structure overstrength. The NLTH analysis should be performed by an experienced engineer and the

results may be affected by the analysis assumptions and the ground motion selection.

- The NLTH analyses are time-consuming in terms of modelling, analysis and post-processing the analysis results.

Considering the above discussions about different lateral force methods, in this study it is clear that all methods have applications/conceptual limitations. Below a simple method is proposed to overcome some of the above issues. This method will be included in the accuracy evaluation with some of the methods above.

7.4 Proposed diaphragm force method, Diaphragm ESA (DESA)

The proposed DESA method may be applied to both structures within and beyond CESA method limitations. These situations are described as follows.

7.4.1 Structures within CESA method limitations

Building loading standards (e.g. NZS1170.5, 2004 and ASCE 7-16) usually use the equivalent static analysis method, CESA, to estimate likely demands in VLFR systems of the structure. The CESA method has some limitations because of the simplifying assumptions used in this method. A number of these limitations include:

I. It is suitable for regular structures, the definition of regular structure is usually provided in the relevant lateral loading standard (e.g. NZS1170.5, 2004).

II. It is limited to a certain building height or structural period.

III. It is developed to obtain earthquake-induced storey shear forces in VLFR systems of the structure, considering a reduction for ductility.

If the CESA method is used to obtain the diaphragm in-plane global demands, it may underestimate diaphragm in-plane forces because it does not account for diaphragm likely accelerations (inertial forces) and the structure likely lateral deformation (transfer effects).

However, EESA may provide reasonable diaphragm forces for upper-level floors, however for lower-levels, it may underestimate the diaphragm demands (Gardiner, 2011 and NZS1170.5 2004 Appendix A to C5.7). This underestimation is mainly because the floor accelerations are usually larger than the EESA method estimations at lower levels.

Based on these, some modifications to the CESA method may make it applicable for calculating diaphragm in-plane demands. The modifications include:

1. The intensity of the CESA method forces should be scaled to present likely diaphragm in-plane demands.

   As it was mentioned in Section 7.2.1, diaphragm transfer forces are mainly due to deformation incompatibility of different VLFR systems of the structure. In this study, the hypothesis is that if a lateral force method can represent likely deformed shape of a structure, it can obtain likely diaphragm transfer forces.

   Figure 7-1 shows the base shear versus the overall drift behaviour of a structure schematically. As can be seen from this Figure, based on the general concept of designing a structure for lateral actions, the lateral deformation of a structure at the design level may be obtained using the EESA ($\mu = 1$) method. The EESA method is the simplest tool that can be used for finding likely deformed shape of a structure.

   To determine the structure horizontal deformations according to NZS 1170.5 (2004), the horizontal deformations obtained from CESA method (μ design) should be multiplied by a scale factor equal to the structure ductility factor, μ design. This gives a similar result as EESA analysis for long period structures (e.g. $T_1 > 0.7s$). However, for shorter period structures

the EESA lateral deformations should be multiplied by μ/k_μ to obtain likely lateral deformation based on equal displacement assumption.

In the proposed method, DESA, the EESA lateral forces are considered to be used for all structural periods ignoring the magnification factor μ/k_μ for short period structures.

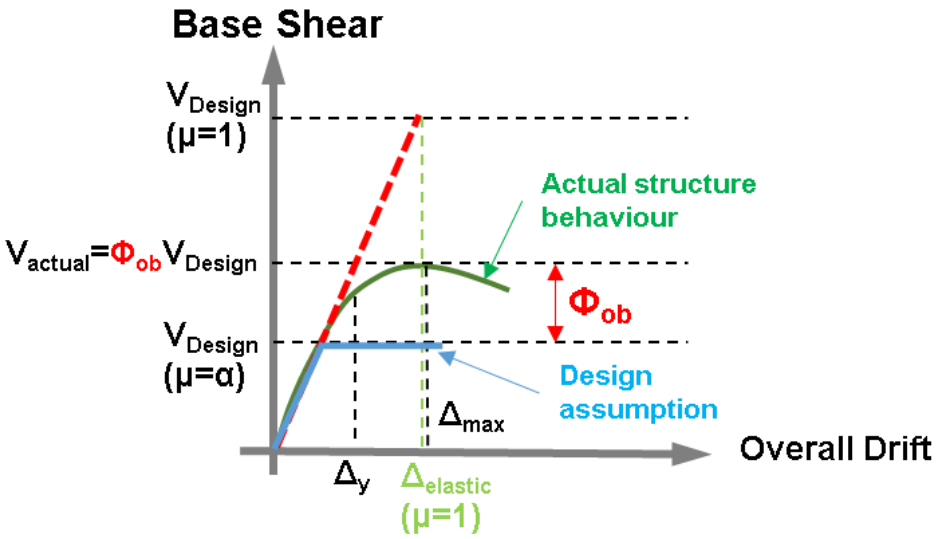

Figure 7-1. Schematic representation of base shear-overall drift response of a structure with ductility μ=α

2. The EESA method can estimate likely diaphragm accelerations at upper floors, but for estimating likely accelerations at lower floors the calculated forces from the EESA method need to be increased.

   Gardiner (2011) proposed an increase to the OESA method, pESA, at lower levels. It was conducted by developing spectral shape curves based on NLTH analyses results. A horizontal design coefficient factor was obtained using the proposed spectral shape curves and multiplied by floor weights directly to increase the lateral forces at lower levels. It was shown that this method predicted diaphragm global in-plane demands with more accuracy compared to other simplified elastic methods. However, this method has

some limitations as described in Section 7.3.1 and cannot be used as for all cases that the CESA method is applicable.

By investigating the spectral shape curves developed by Gardiner (2011) it can be found that the modified spectral shape values for different soil categories and structural systems are nearly equal or below the NZS1170.5 (2004) spectral shape values and only for soil type C these are above NZS1170.5 (2004) spectral shape values.

In this study it is suggested to use NZS1170.5 (2004) spectral shapes in the lack of accurate spectral shape values to obtain diaphragm in-plane demands.

Based on the above discussions, some modifications to the CESA method are proposed to estimate diaphragm in-plane demands. The proposed lateral force at any level, F_{di}, is the maximum of the EESA horizontal forces at each level, $F_i^{\mu=1}$, and the elastic horizontal design action coefficient times the storey weight, $C_d^{\mu=1}(T_1)W_i$, according to Eq. (7-1). The proposed method, DESA, is shown in Figure 7-2 schematically. The forces are applied at the same time.

$$F_{di} = Max\left\{C_d^{\mu=1}(T_1)W_i, F_i^{\mu=1}\right\} \qquad \text{Eq. (7-1)}$$

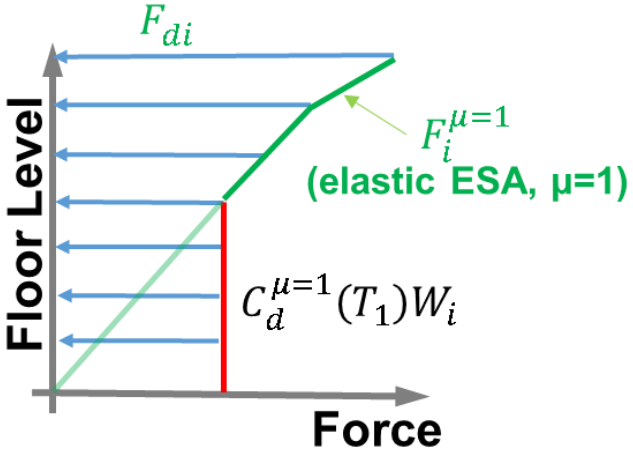

Figure 7-2. Schematic loading pattern of the proposed method (DESA)

These modifications to the CESA method may improve the underestimation of diaphragm in-plane demand at lower levels. Also may provide more reasonable results in term of transfer forces by estimating likey deformed shape of the structure (EESA).

7.4.2 Structures beyond CESA method limitations

In high-rise buildings that are beyond the CESA method height limitations and/or irregular structures that the CESA method is not suggested to be used by different loading standards (e.g. NZS1170.5, 2004), response spectrum or time history analysis should be used to design VLFR elements.

In this study it is suggested to use the first mode lateral forces scaled to the EESA base shear force. Similar to the EESA method, this may estimate likely diaphragm accelerations at upper floors, but it does not consider higher mode effects. Therefore, the lateral forces at lower floors need to be increased. Here, it is suggested to use the maximum of 1) the first mode lateral forces scaled to the EESA base shear at each level, $F(mode\ 1)_i^{\mu=1}$, and 2) the elastic horizontal design action coefficient times the storey weight, $C_d^{\mu=1}(T_1)W_i$, according to Eq. (7-2). The proposed method, DESA, is shown in Figure 7-3 schematically. The forces are applied at the same time.

$$F_{di} = Max\left\{C_d^{\mu=1}(T_1)W_i, F(mode\ 1)_i^{\mu=1}\right\} \qquad \text{Eq. (7-2)}$$

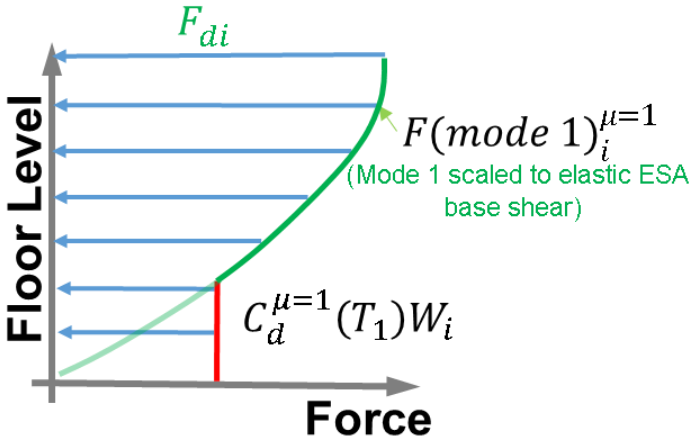

Figure 7-3. The DESA method for structures beyond CESA limitations

To investigate the proposed method and compare its results with other lateral force methods, a number of NLTH analysis are conducted considering different parameters which are described in the next section.

7.5 Comparing lateral force methods

7.5.1 NLTH analyses

In this section the proposed lateral force method, DESA, is compared with a number of available loading methods. Twenty-three models are studied in which the details are described in the following sections. The investigated methods include:

i. CESA
ii. EESA
iii. pESA
iv. OESA
v. DESA
vi. P&C
vii. Pushover analysis
viii. NLTH analysis

7.5.1.1 Model selection

Different parameters such as VLFR system type, stiffness distribution along the structure height, number of storey and structure ductility are investigated. Table 7-1 presents a summary of the FE models.

Table 7-1. Models investigated to compare different lateral loading methods

	Model	*Stiffness type*	*No. storeys*	*T (s)*	*W/F stiffness*	*Ductility*	*Structure type*	*Soil type*
Moment frame	**Model 1**	CS	5	0.6	-	1	Shear type	D
	Model 2	CS	5	0.6	-	2	Shear type	D
	Model 3	CD	5	0.6	-	1	Shear type	D
	Model 4	CS	5	0.6	-	4	Shear type	D
	Model 5	CS	2	0.3	-	1	Shear type	D
	Model 6	CS	9	1	-	1	Shear type	D
	Model 7	CS	9	1	-	1	Shear type	C
	Model 8	CS	9	1	-	4	Shear type	D
	Model 9	CS	9	1	-	4	Shear type	C
	Model 10	CS	15	1.8	-	1	Shear type	D
Dual	**Model 11**	CS	5	0.6	1	1	Dual system	D
	Model 12	CS	5	0.6	1	2	Dual system	D
	Model 13	CS	5	0.6	1	4	Dual system	D
	Model 14	CS	5	0.6	5	1	Dual system	D
	Model 15	CS	5	0.6	10	1	Dual system	D
	Model 16	CS	2	0.3	1	1	Dual system	D
	Model 17	CS	9	1	1	1	Dual system	D
	Model 18	CS	9	1	1	1	Dual system	C
	Model 19	CS	9	1	1	4	Dual system	D
	Model 20	CS	9	1	1	4	Dual system	C
	Model 21	CS	15	1.8	1	1	Dual system	D

Two 20-storey structures with moment frame and dual VLFR systems are also investigated using the DESA method. Both models are designed for $\mu = 1$ and subsoil type D. Table 7-2 presents details of the FE models. Note that the structural periods are obtained from Modal analyses.

Table 7-2. Models investigated to compare the DESA method with NLTH analysis

Model	*Stiffness type*	*No. storeys*	*T (s)*	*W/F stiffness*	*Ductility*	*Structure type*	*Soil type*
Model 22	CS	20	2.5	-	1	Moment frame	D
Model 23	CS	20	2.5	1	1	Dual	D

The selected structures are categorised as “moment frame” and “dual” based on the VLFR systems. Moment frame structures refer to the structures with one type of VLFR system such as moment resisting frame. For dual models, a combination of moment resisting frame and shear wall is considered to achieve large transfer forces. The reason for selecting

the combination of shear wall and moment frame is to obtain the largest transfer forces considering the lateral deformation incompatibility of these systems. Braced frames may perform between moment frames (shear behaviour) and shear walls (flexural behaviour) depending on the design assumptions and lateral imposed forces. Therefore, the combination of moment frames and braced frames may not provide the largest transfer forces. Figure 7-4 shows the floor plan of "moment frame" and "dual" structures schematically. Torsion is restrained in all models.

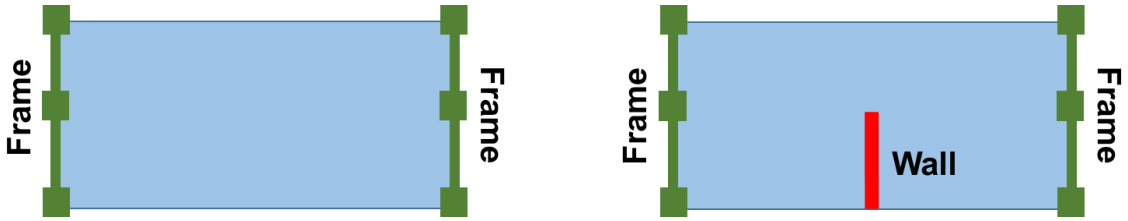

a) Moment frame structure b) Dual structure

Figure 7-4. Floor plan of investigated structures

One of the parameters that may affect the results is the storey stiffness distribution in height. It is expected that the stiffness of a realistic frame falls between two extreme design models of "constant stiffness, CS" and "constant drift, CD" (Sadashiva, 2010). The constant stiffness, CS, models are designed such that all the storeys have similar stiffness. The constant drift, CD, models are designed such that all the storeys have a constant inter-storey drift under a specific lateral force. These two model types and their deflection profiles are shown in Figure 7-5. In this study, the storey stiffness distribution is only investigated in the moment frame models, while the dual type models are only considered as constant stiffness, CS.

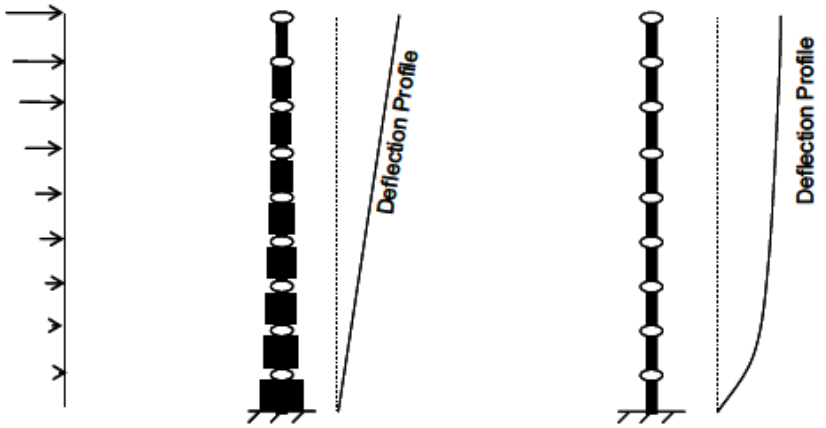

a) Lateral force b) Constant drift model, CD c) Constant stiffness model, CS

Figure 7-5. Deformed shape pattern of CD and CS structures, (Sadashiva, 2010)

To investigate the effect of structure height, the models are selected to represent a range of structures with 2, 5, 9 and 15 storey structures. According to NZS1170.5 (2004), the CESA method may be used for structures with a largest translational period, calculated according to Eq. (7-3), less than 2.0 seconds. Where k_t depends on the structural system and, h_n is the height in meters, as follows:

$$T_1 = 1.25 k_t h_n{}^{0.75} \qquad \text{Eq. (7-3)}$$

For structural steel moment-resisting frame $k_t = 0.085$, also considering $T_1 = 2.0s$, the structure height limit results in 50m which is about 15 storeys considering the storey height of 3.4m.

Ductility of the structure is another parameter that may affect the diaphragm in-plane forces. This parameter is investigated here considering $\mu = 1$ for elastic structures, $\mu = 2$ and $\mu = 4$ to consider yielding in VLFR elements.

7.5.1.2 Design parameters and analysis assumptions

- **Design parameters**

All the structures are designed using the ESA method lateral forces according to NZS 1170.5 (2004). NLTH analyses conducted using SAP2000 software. The assumptions used for lateral loading of the models include:

1) The structure location is assumed in Wellington, New Zealand with subsoil types C and D.
2) The shortest distance from the site to the nearest fault, $D = 0$;
3) Return period factor, $R_u = 1$;
4) Zone hazard factor, $Z = 0.4$ (Wellington),
5) Structural ductility factors, $\mu = 1, 2, 4$;

- **Analysis and modelling assumptions**

Four ground motion records were chosen to represent likely earthquakes in Wellington, New Zealand, considering motion characteristics based on Gardiner (2011) study. The selected ground motions are listed in Table 7-3. All the time history records were scaled according to NZS 1170.5 (2004) loading standard. The scaling procedure minimises the difference between the design response spectra and spectral acceleration of the time history records over the range of 0.4 to 1.3 times the fundamental period of the structure.

Table 7-3. Selected earthquake records for NLTH analysis

Location	Station	Date	Magnitude
Landers, California	Lucerne	28 June 1992	7.3
USA, El Centro, Imperial Valley	El Centro	19 May 1940	7.0
Iran, Tabas	Tabas	16 September 1978	7.2
Kocaeli, Turkey	Izmit	17 August 1999	7.4

The NZS 1170.5 (2004) requires that for time history analysis the time step shall not be greater than the step at which the records are digitised. Also it is required that the time step shall be less than or equal to the minimum of i) $T_1/100$, ii) T_n and iii) 0.01 second. Where T_1 is the largest translational period of the first mode in the direction of interest and T_n is the period of the highest mode in the same direction required to achieve 90% mass participation. The time step used for all analyses in this study was considered 0.003s based on the fundamental period of the 2-storey structure, 0.3s.

The damping model that is used in this research is the Proportional Rayleigh Damping model. For all models, 5% damping ratio was considered in the first and third modes. The damping ratio of the mode n, which represent the highest mode that achieves 90% mass participation, was checked to be less than 40% based on Clause 6.4.6 of NZS1170.5 (2004).

Note that the damping ratio of the steel structures is usually between 2-3%, however in this study 5% damping ratio is selected foe NLTH analyses. This is because the ESA method lateral forces are obtained from 1170.5 (2004) based on considering 5% damping ratio and since the aim of this study is to compare the results of different methods with NLTH analysis, assumptions should be consistent. Furthermore, if different damping ratio is used in NLTH analysis, the lateral forces obtained using ESA method should also be changed using equations provided in the literature to account for that damping ratio.

The weights used in the analysis are based on the values in Table 7-4. The reduced gravity load combination considered as $G + \psi_E Q$, where $\psi_E = 0.3$ for most of the structures other than storage or structures with installed heavy machinery. Therefore, considering a tributary area of 162 m^2 for each frame, the lumped mass on each frame for every storey is equal to 97.5ton.

Table 7-4. Storey structural mass used for FE modelling

Dead Load, G	5 kPa
Live Load, Q	3 kPa
Tributary areas for each frame	162 m^2
Lumped mass on each frame	97.5ton

Note that The NLTH analysis results reported in this study are the average of results obtained from four NLTH analyses using the selected ground motions.

In pushover analysis, first mode lateral loads are selected as the lateral load pattern. Also, diaphragm in-plane forces were obtained at the loading step that the lateral displacement of the top of the structure reached to the lateral displacement corresponding to EESA method.

The general modelling assumptions include:

1. Diaphragm stiffness is much larger than frame and wall stiffness
2. Flexural deformation of moment frames due to columns axial deformations and shear deformation of the wall elements are ignored
3. It is assumed both moment frame and shear wall systems have the same tributary area for lateral loading
4. Elastic-perfectly plastic moment-curvature is assumed for both frame and wall elements
5. Masses are lumped at the nodes in the analytical models
6. Soil-structure interaction is ignored
7. Rayleigh damping is used in all models
8. Storey height is considered 3.4m

7.5.1.3 Modelling method and verification

Since the aim of this study is to investigate the diaphragm in-plane forces, the models are simplified. The simplified models include a cantilever column representing the wall system, and a column with rotational restraints at each storey to represent the behaviour of the moment frame structure as shown in Figure 7-6c-d. The rotational restraint at the beam-column nodes on the moment frame column causes the point of contraflexure to be at the mid-height of each storey under the lateral loading.

Columns representing VLFR system, are connected at every storey with a horizontal member representing the diaphragm as shown in Figure 7-6b-d. Verification of the simplified 2D model with the corresponding 3D model is presented in Appendix J.

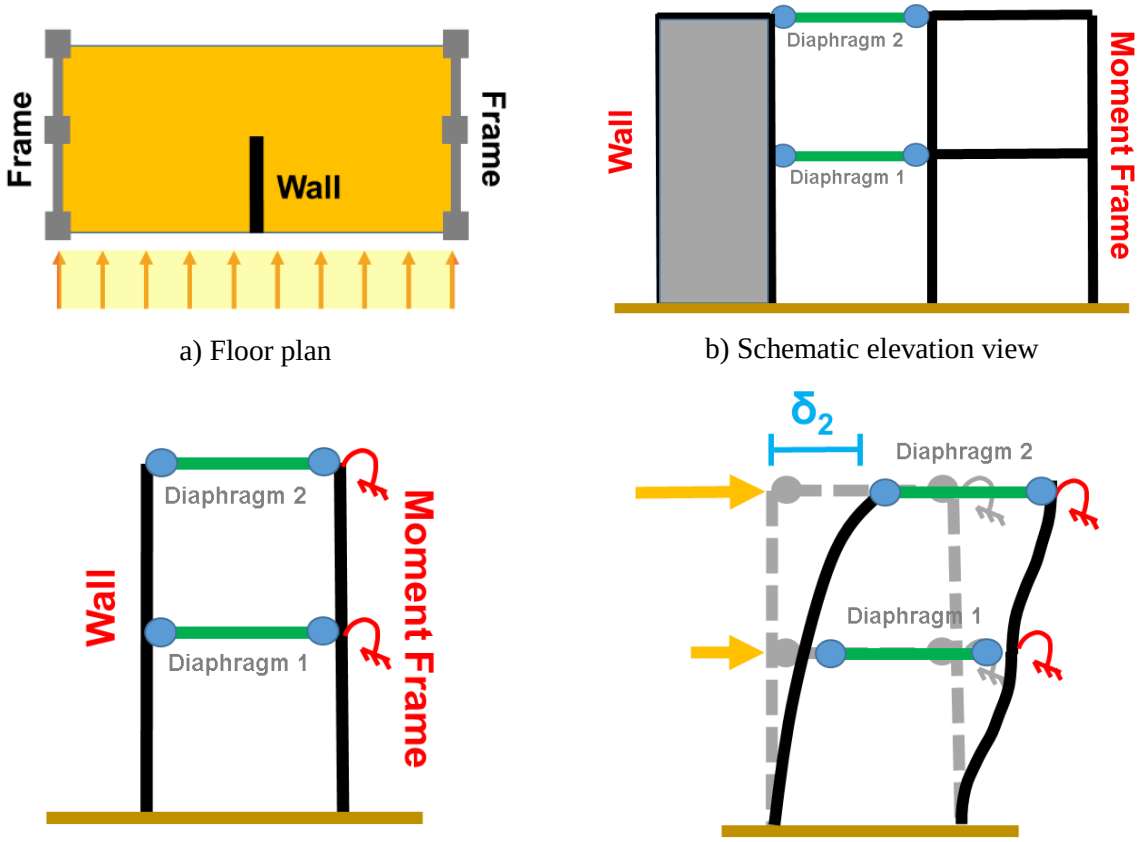

a) Floor plan

b) Schematic elevation view

c) Simplified model

d) Deformed shape of the simplified model subjected to lateral forces

Figure 7-6. Two storey structure and the simplified model

To obtain inertia and transfer forces two models are created for each structure. In one model inertia forces and transfer forces are obtained separately and in the other model the combination of these forces is obtained. This is because the maximum diaphragm force does not necessarily equal to the sum of maximum inertia and transfer forces because these may not occur at the same time. Figure 7-7 shows the modelling methods for obtaining inertia and transfer forces combined and separately.

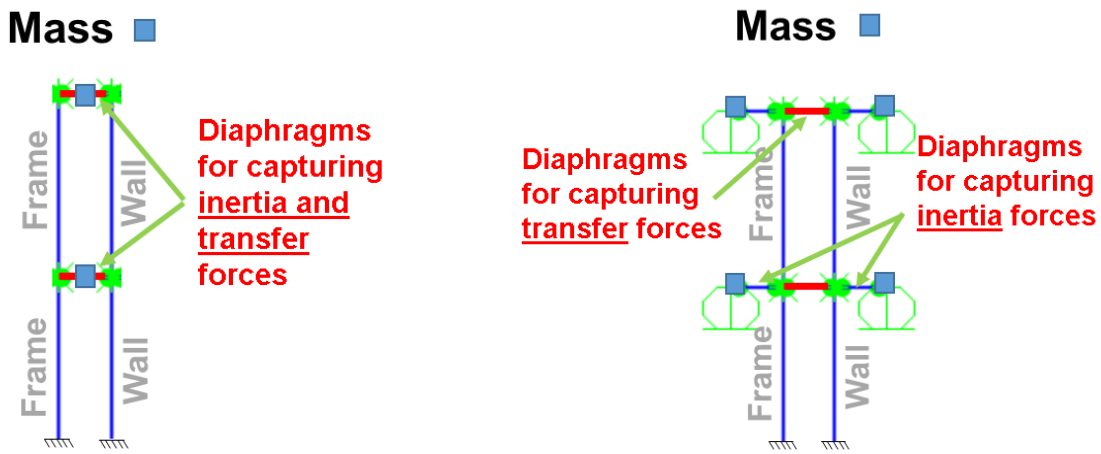

a) Simplified model for obtaining inertia and transfer forces together

b) Simplified model for obtaining inertia and transfer forces separately

Figure 7-7. Modelling methods for obtaining inertia and transfer forces

In the simplified 2D model shown in Figure 7-7a, the storey mass is located at the mid-point of the diaphragm element. In this model, maxima of the diaphragm element force represents the maxima of the combination of inertia and transfer forces. However, in the model shown in Figure 7-7b, the storey masses are attached to the VLFR systems with rigid links. This modelling method allows obtaining the inertia and transfer forces separately.

7.5.2 Results and discussion

7.5.2.1 Moment frame structures

In moment frame structures described in Table 7-1, there is no diaphragm transfer forces and the only source of diaphragm global in-plane demand is the inertia force. In this section the effect of different parameters on the diaphragm inertia forces is investigated.

- **Effect of ductility**

Figure 7-8 presents the magnitude of inertia forces obtained from the diaphragms of five storey structures with different design ductility according to NZS1170.5 (2004). As can be seen in this Figure, the EESA method predicted likely diaphragm demands in upper floors. However, the inertia forces on the lower floors were underestimated. The proposed method

shows better agreement with NLTH results in comparison with the EESA method because of the increase in diaphragm forces at the lower levels.

It also indicates that the proposed method, DESA, underestimated the diaphragm forces of the structure with ductility $\mu = 1$ by up to 20% in lower levels. The proposed method estimations for the structure with ductility $\mu = 2$ were less than 10% compared to NLTH analyses. For $\mu = 4$ the DESA overestimated the NLTH response by about 30%. These results were expected as the DESA method does not consider structure ductility and uses elastic forces to obtain diaphragm in-plane demands.

P&C diaphragm forces are much larger than other methods. This was consistent in all graphs. Therefore, the P&C analysis result is only shown in Figure 7-8a and in the following plots these have been removed to allow easier interpretation of graphs.

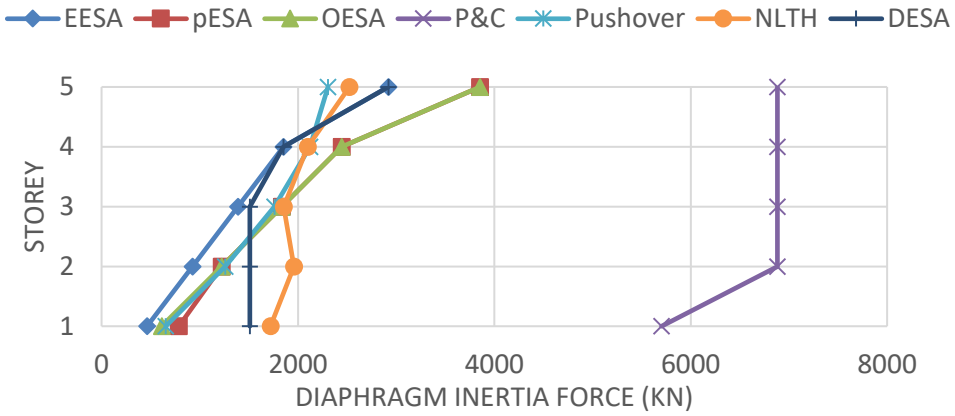

a) Model 1, five-storey structure with ductility $\mu = 1$

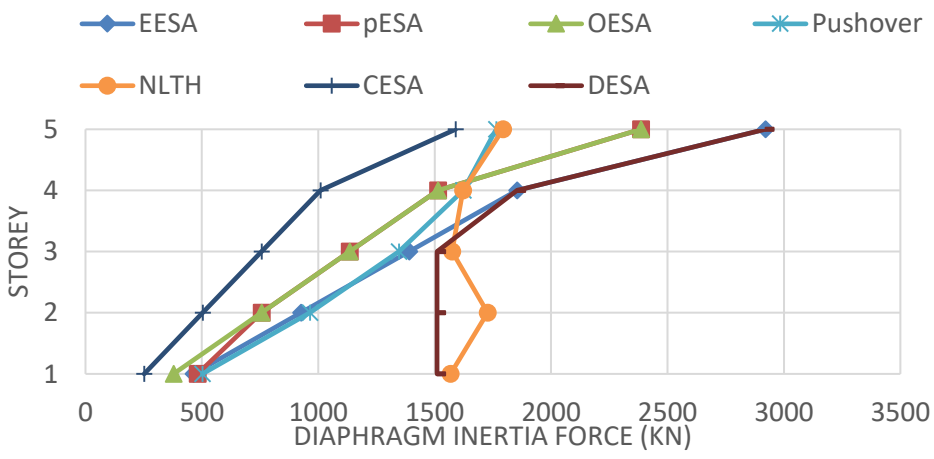

b) Model 2, five-storey structure with ductility $\mu = 2$

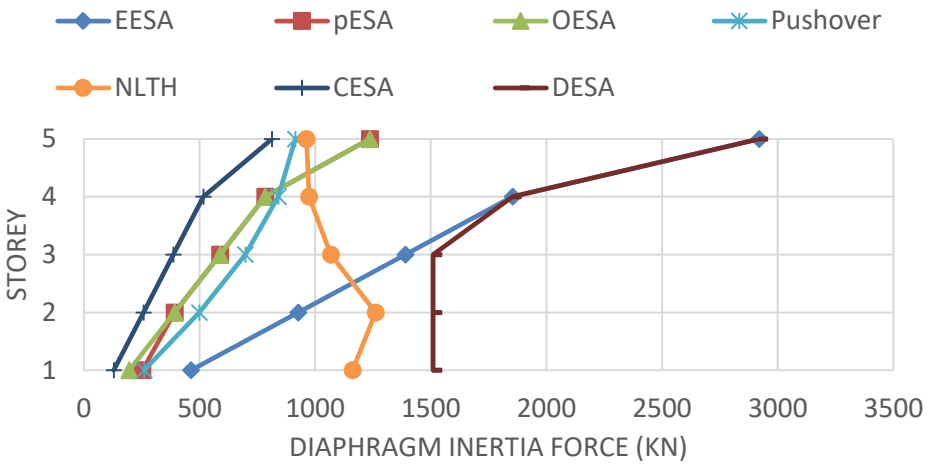

c) Model 4, five-storey structure with ductility $\mu = 4$

Figure 7-8. In-plane diaphragm inertia forces for five-storey moment frame structures with different ductility (T=0.6s)

The same behaviour was observed for the nine-storey structure with ductility $\mu = 1$ and 4 as shown in Figure 7-9a and b. The diaphragm forces obtained using the proposed DESA method, underestimated the diaphragm inertia forces by about 30% on average compared to NLTH analysis for the nine-storey elastic structure, Figure 7-9a. However, the DESA overestimated the NLTH response by about 100% for the structure with $\mu = 4$, Figure 7-9b.

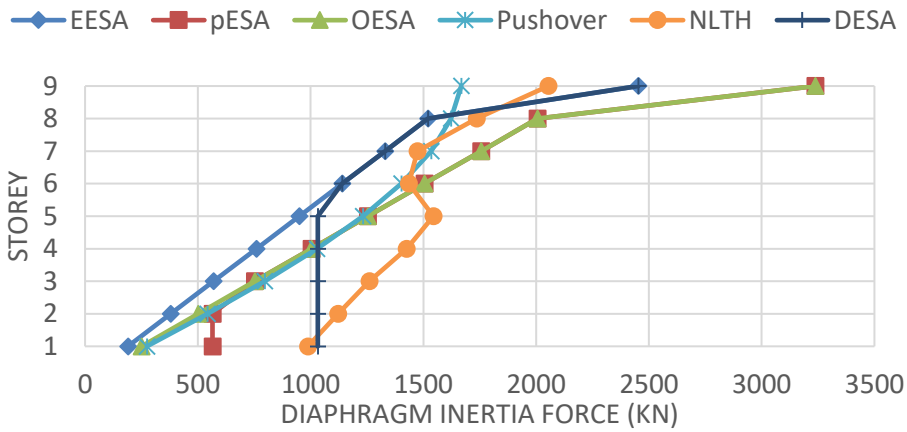

a) Model 6, nine-storey structure with ductility $\mu = 1$

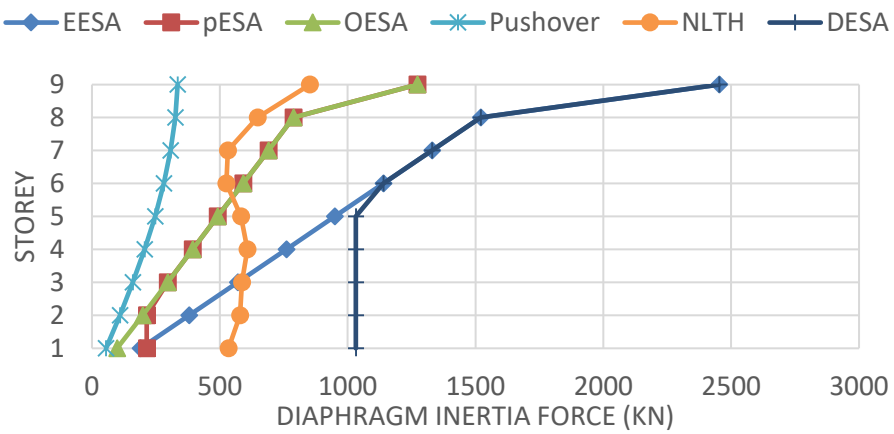

b) Model 8, nine-storey structure with ductility $\mu = 4$

Figure 7-9. In-plane diaphragm inertia forces for nine-storey moment frame structures with different ductility (T=1.0 s)

- **Effect of structure height**

The analyses results of Models 5, 1, 6 and, 10, indicate the effect of structural height, are plotted in Figure 7-10. As can be seen, the proposed method improved the ESA method results for lower floor levels. However, similar to Figure 7-8a, the proposed method underestimated the diaphragm in-plane demands on the lower floors for structures with ductility $\mu = 1$.

The average underestimation of diaphragm in-plan forces using the proposed method, DESA, for the bottom half portion of the models studied in comparison with the NLTH analyses results is 22%, 17%, 12% and 40% respectively for two, five, nine and fifteen storey structures with $\mu = 1$.

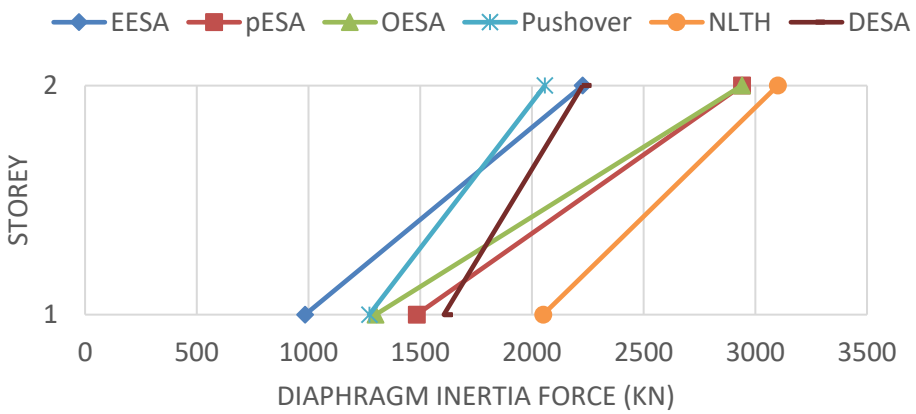

a) Model 5, two-storey structure with ductility $\mu = 1$

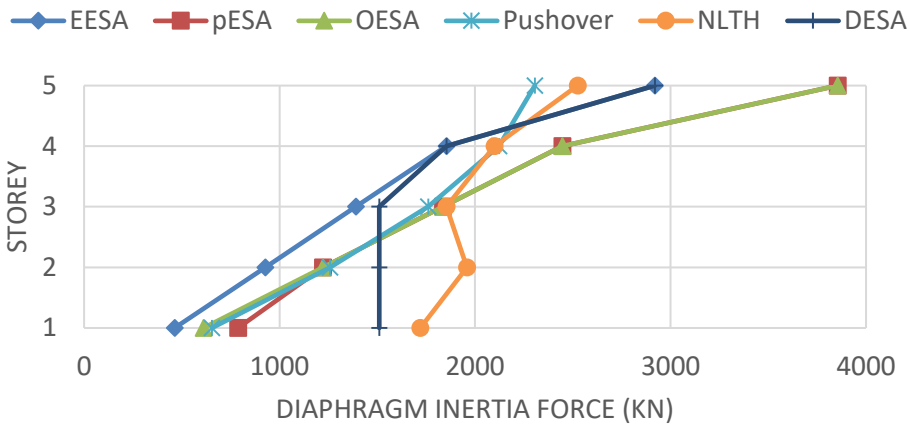

b) Model 1, five-storey structure with ductility $\mu = 1$

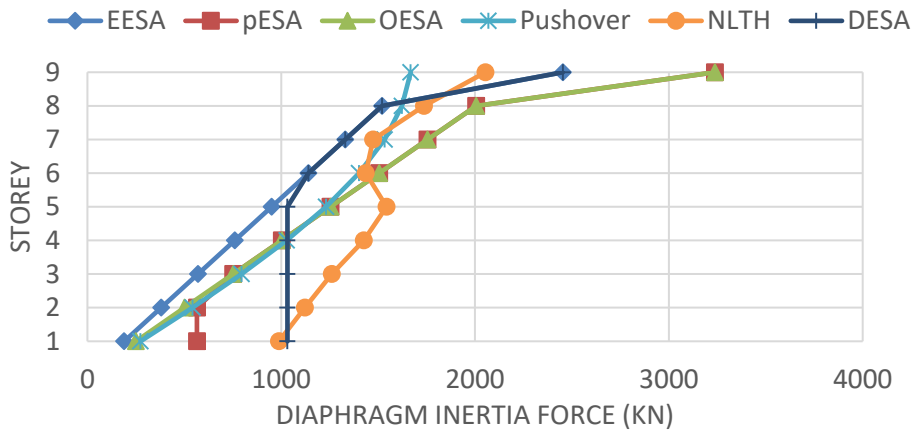

c) Model 6, nine-storey structure with ductility $\mu = 1$

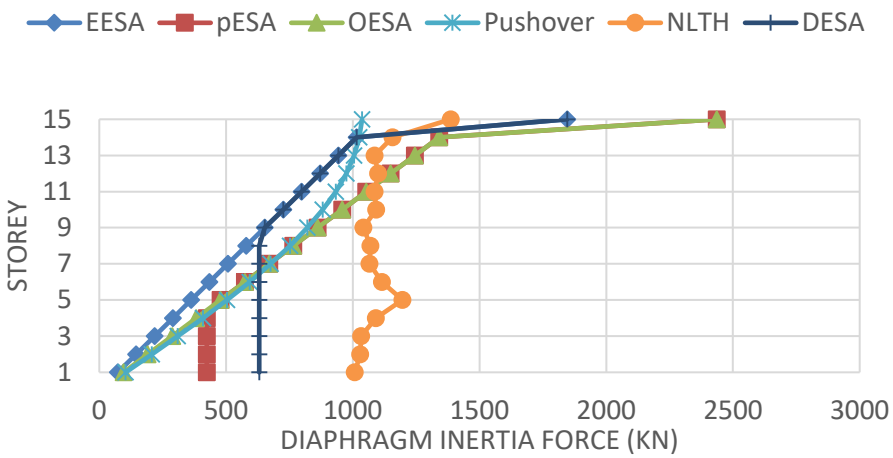

d) Model 10, fifteen-storey structure with ductility $\mu = 1$

Figure 7-10. In-plane diaphragm inertia forces for moment frame structures with different number of storeys

Despite the underestimation mentioned in the previous paragraph, the proposed method presented more reasonable results than other studied methods in terms of lower story in-plane demands. This conclusion is based on the models studied here and other methods may be developed to increase the accuracy.

- **Storey stiffness distribution**

Figure 7-11 presents the magnitude of inertia forces obtained from the diaphragms of elastic five-storey moment frame structures with constant drift and constant stiffness VLFR systems. As can be seen in this Figure, the proposed method provided more reasonable results in comparison with other static methods. The peak diaphragm in-plane forces obtained from the NLTH analyses showed that different storey stiffness distributions, CS and CD, may change the distribution of peak diaphragm in-plane forces. However, the average was similar in the studied case.

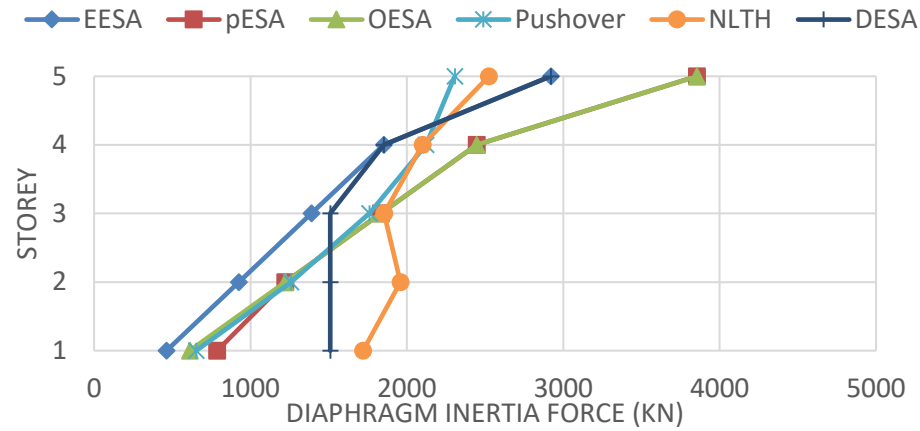

a) Model 1, constant stiffness VLFR system

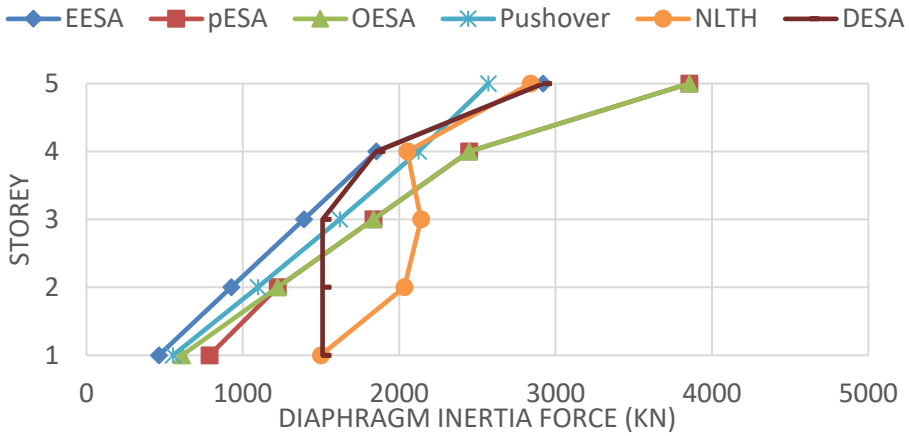

b) Model 3, constant drift VLFR system

Figure 7-11. In-plane diaphragm inertia forces for elastic five-storey structures with different storey stiffness distribution and ductility μ=1

- **Subsoil type effect**

Figure 7-12 presents the behaviour of Models 6 to 9 considering ductility $\mu = 1$ and 4 and subsoil types C and D. From Figure 7-12a and b it can be seen that pESA method underestimated diaphragm in-plane forces at lower levels for structure on subsoil D, however, they are overestimated for the same structure on subsoil type C. This is because of the modified spectral shape values obtained by Gardiner (2011) which result in larger lateral forces for subsoil C. The same situation occurred for the structure with $\mu = 4$ as shown in Figure 7-12c and d, where the proposed method overestimated the diaphragm in-plane forces

by about 100%. While, the pESA method provided results that are more reasonable compared to NLTH analysis specially for subsoil type C.

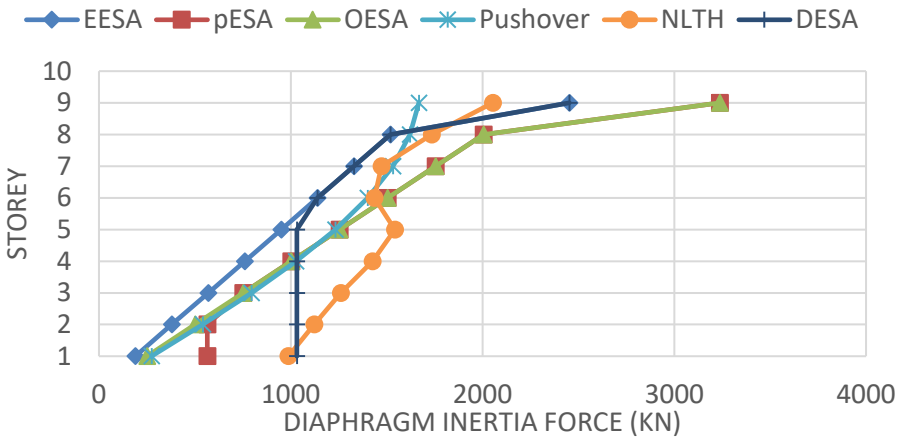

a) Model 6, nine-storey structure with ductility $\mu = 1$ and subsoil D

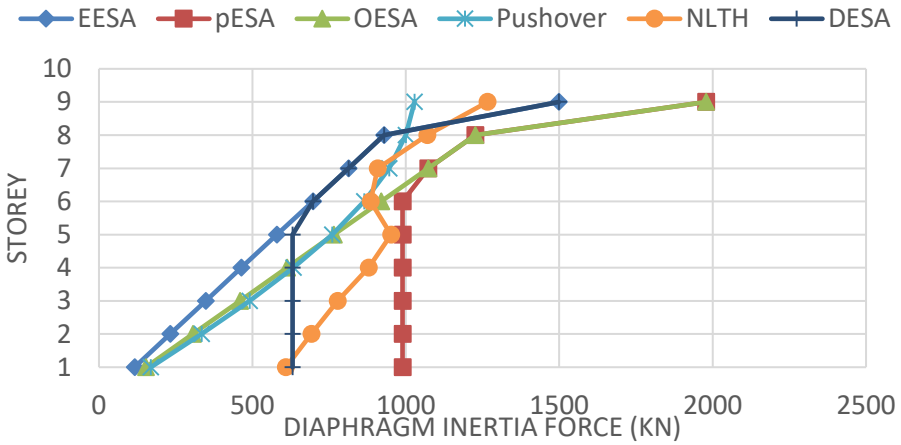

b) Model 7, nine-storey structure with ductility $\mu = 1$ and subsoil C

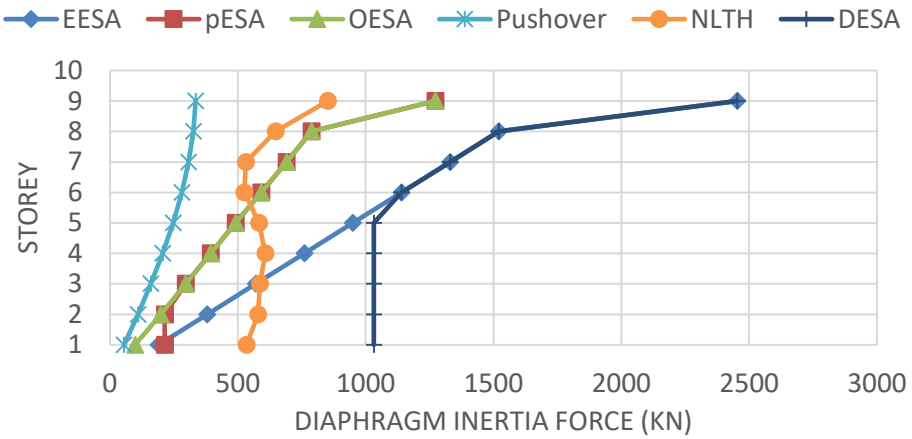

c) Model 8, nine-storey structure with ductility $\mu = 4$ and subsoil D

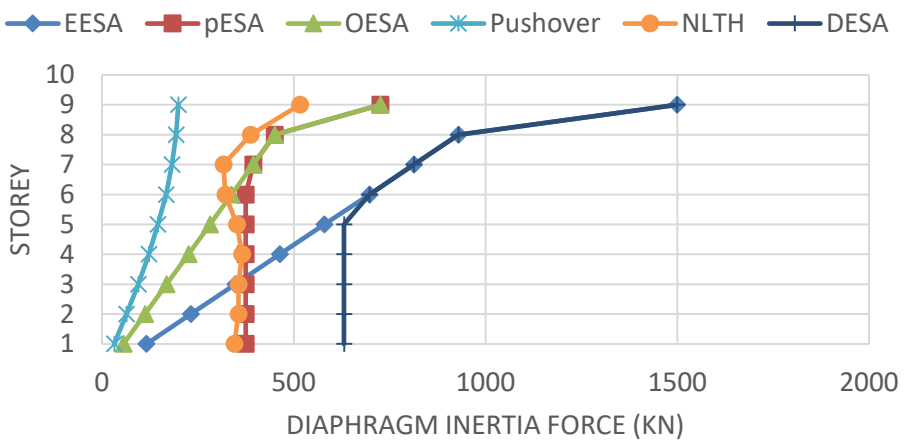

d) Model 9, nine-storey structure with ductility $\mu = 4$ and subsoil C

Figure 7-12. In-plane diaphragm inertia forces for nine-storey structures with different ductility and subsoil types

7.5.2.2 Dual VLFR system structures

Structures consist of two VLFR systems, a shear wall and a moment resisting frame, are considered as Dual type structures. In these structures, the diaphragm in-plane force is a combination of inertia and transfer forces. The imposed transfer forces are due to deformation incompatibility of different VLFR systems. Figure 7-13 shows the analysis results of Model 11 which is a five storey elastic structure with shear wall to moment resisting frame stiffness ratio of one. The analysis results are obtained in terms of peak inertia and transfer forces and also peak total in-plane forces. The peak total in-plane diaphragm force in NLTH analysis is not necessarily equal to the sum of the peak inertia and transfer forces because they may occur at different time steps.

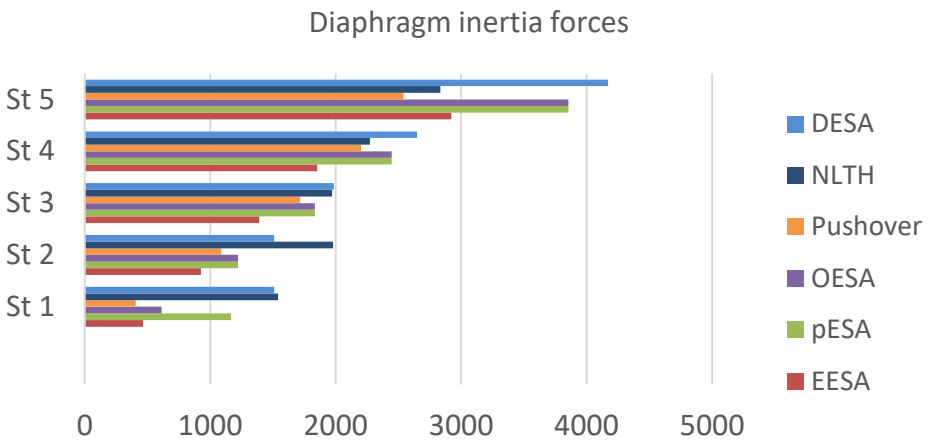

a) Diaphragm inertia forces

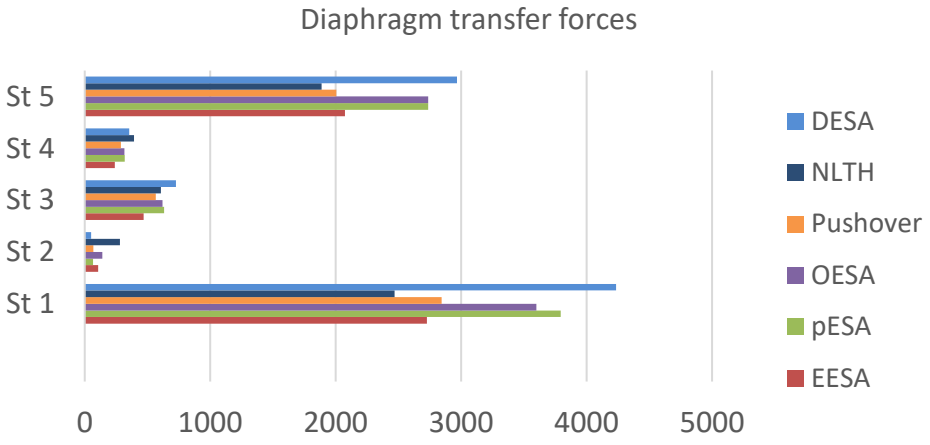

b) Diaphragm transfer forces

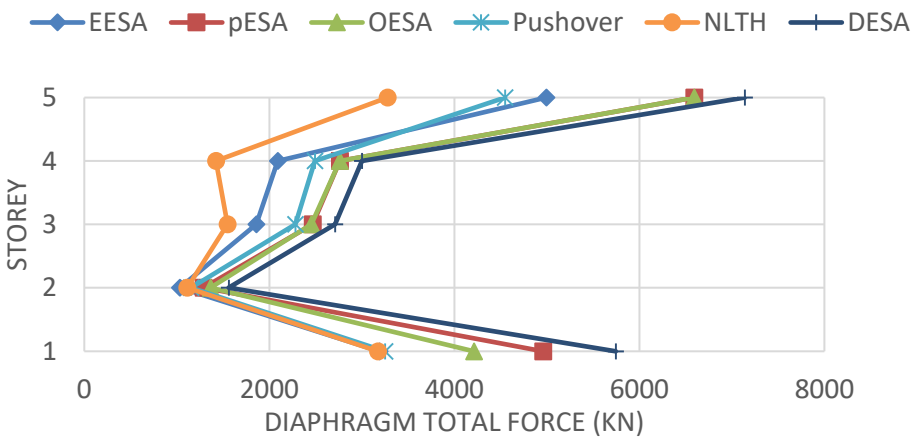

c) Total diaphragm forces

Figure 7-13. Diaphragm forces for Model 11

In the following only the total diaphragm in-plane forces are presented. The peak inertia and transfer forces of all dual-type models are presented in Appendix K.

- **Effect of ductility**

Figure 7-14 shows the total diaphragm in-plane forces for five and nine storey structures with different ductilities. In these models, the diaphragm transfer forces govern the total diaphragm in-plane demand. Therefore, the effect of inertia forces decreased. In these models the shear wall to moment resisting frame stiffness ratio equal to one was selected in order to maximize transfer forces according to Gardiner's (2011) study.

Figure 7-14a shows that the ESA method presents similar results to NLTH analysis for both the bottom and the top portion of the structure. This is because the effect of inertia forces are less than transfer forces in these models and the effect of underestimation of diaphragm accelerations on the lower levels decreased. It is noted that with changing the wall to frame stiffness ratio these results may change and inertia forces may increase in comparison with transfer forces and govern the diaphragm in-plane demands.

The proposed method overestimated the diaphragm total in-plane demands of the studied models. For example, the total in-plane demands of the third floor of five-storey structures as shown in Figure 7-14a,b and c were overestimated by about 75%, 24% and 37% for structures with $\mu = 1, 2 \text{ and } 4$ respectively.

The same behaviour was observed for the nine-storey structure with ductility $\mu = 1$ and 4 as shown in Figure 7-14d and e. The diaphragm forces obtained using the proposed method, and the pESA overestimated the diaphragm inertia forces of Model 17 up to about 45% and 60% on average compared to NLTH analysis. However, for the nine-storey structure with $\mu = 4$, Figure 7-14e they were overestimated with about 200% and 40% using the proposed, DESA, and the pESA methods.

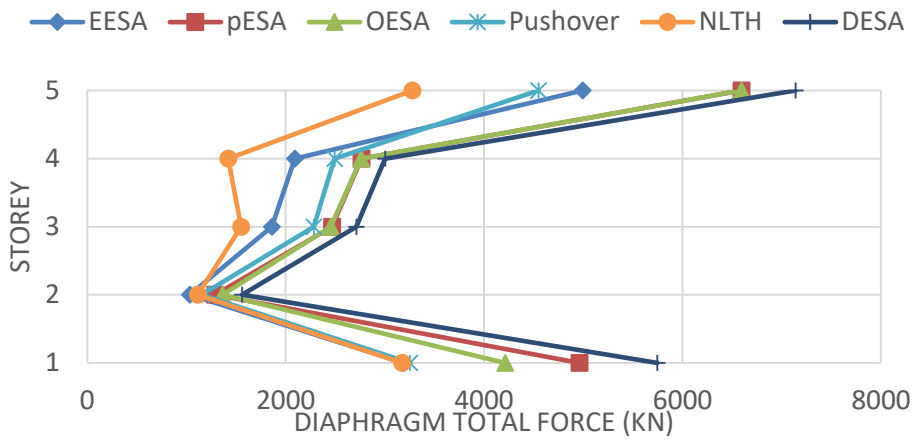

a) Model 11, five-storey structure with ductility $\mu = 1$

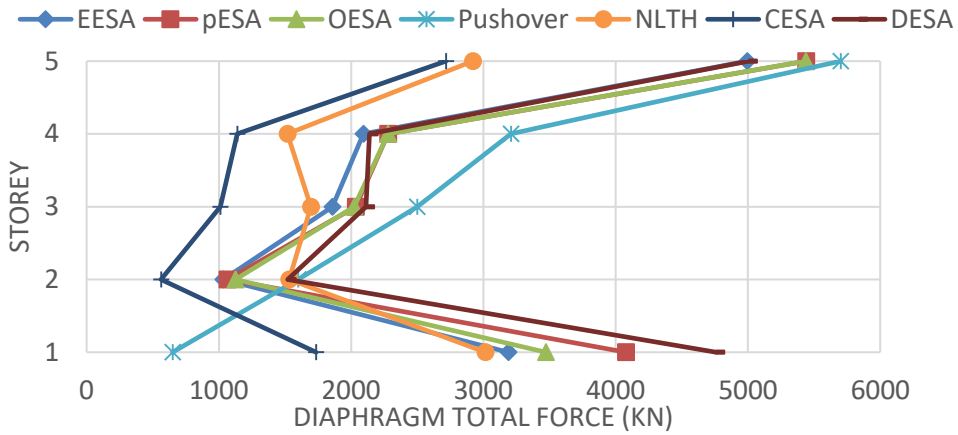

b) Model 12, five-storey structure with ductility $\mu = 2$

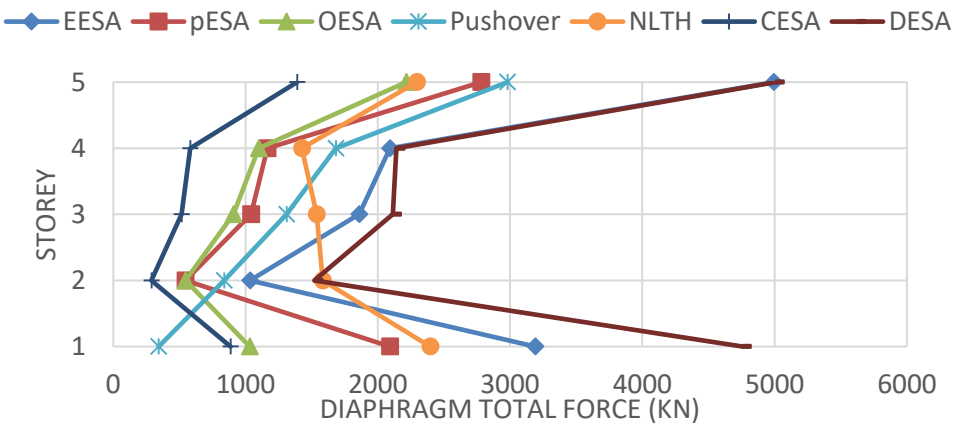

c) Model 13, five-storey structure with ductility $\mu = 4$

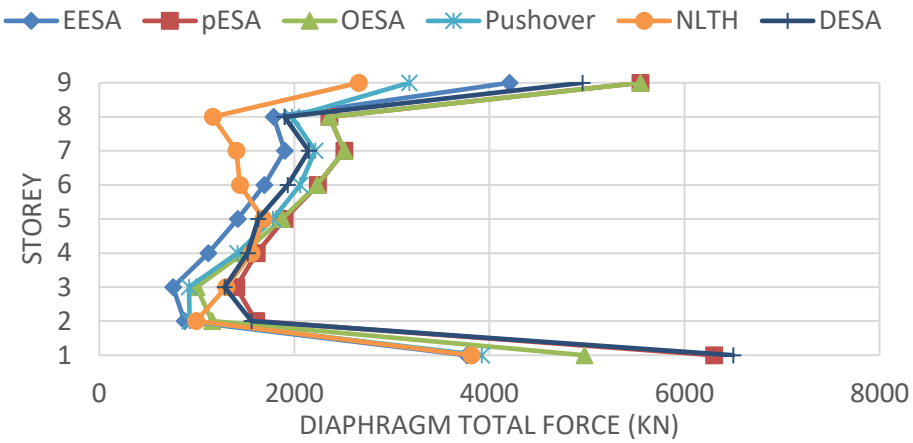

d) Model 17, nine-storey structure with ductility $\mu = 1$

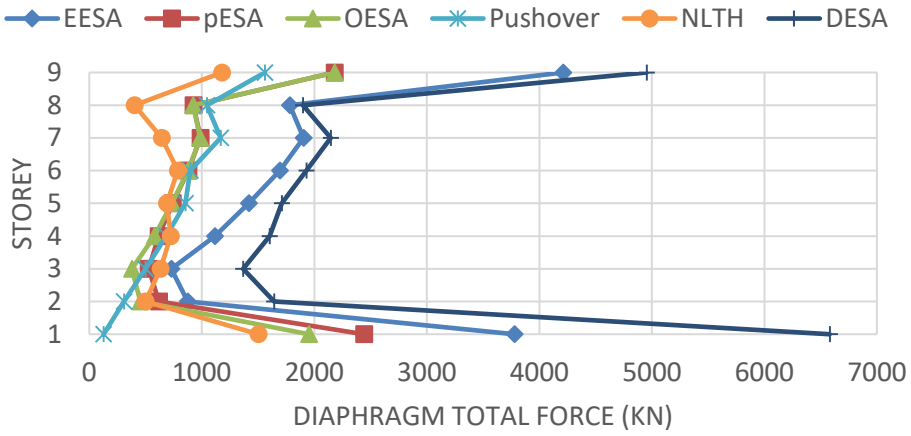

e) Model 19, nine-storey structure with ductility $\mu = 4$

Figure 7-14. In-plane diaphragm total forces of structures with different ductility

- **Effect of structure height**

The results of Models 16, 11, 17 and 21 with two, five, nine and fifteen stories respectively designed to $\mu = 1$ are plotted in Figure 7-15. The results of five, nine and fifteen storey structures show similar results, such that the total diaphragm in-plane demands increased in the top and bottom storeys. This is because of deformation incompatibility between the shear wall and moment resisting frame structural systems.

Similar to the results shown in Figure 7-14, the ESA method shows reasonable results for the models shown in Figure 7-15, which is because of the dominance of transfer forces in

these models. These results support the hypothesis that the ESA method may estimate likely transfer forces because it can obtain the likely lateral deformed shape of the structure.

The analyses results presented in Figure 7-15 indicate that the proposed method overestimated diaphragm in-plane demands of two, five and nine storey structures in comparison with NLTH analysis. However, in Model 21, fifteen-storey structure, the pESA method overestimated the total diaphragm in-plane forces by about 130% on average compared to NLTH analysis and the proposed, DESA, method overestimated the total diaphragm in-plane forces by about 60% on average compared to NLTH analysis.

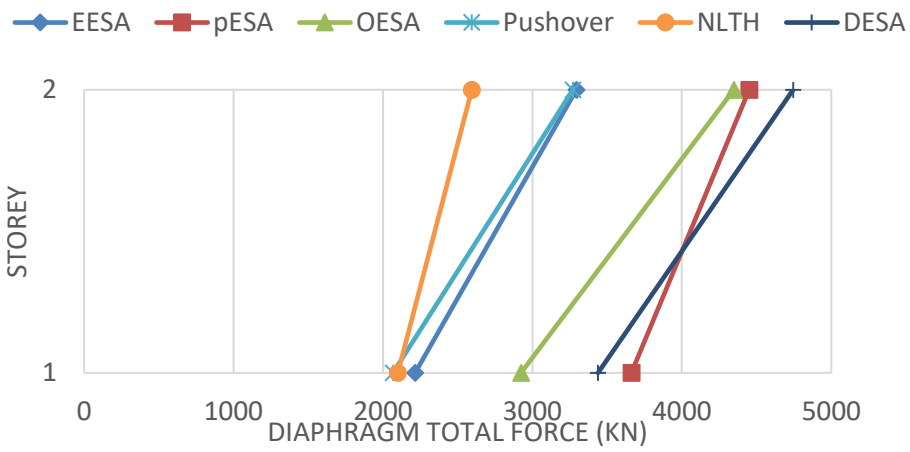

a) Model 16, two-storey structure with ductility $\mu = 1$

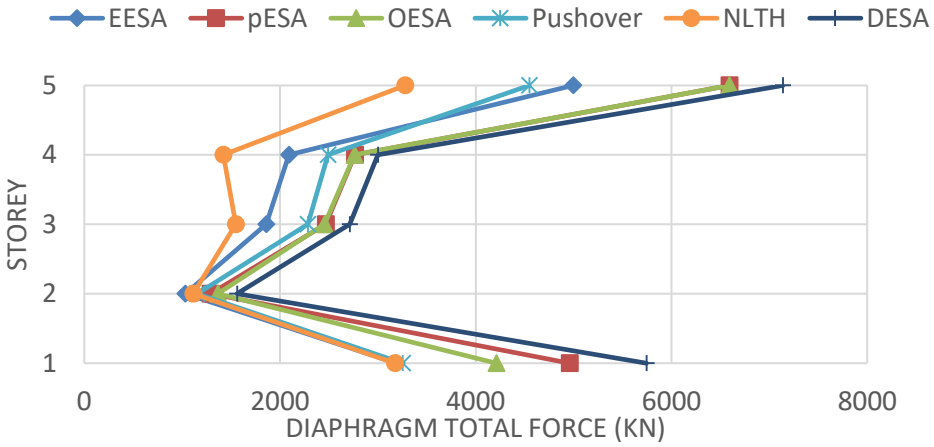

b) Model 11, five-storey structure with ductility $\mu = 1$

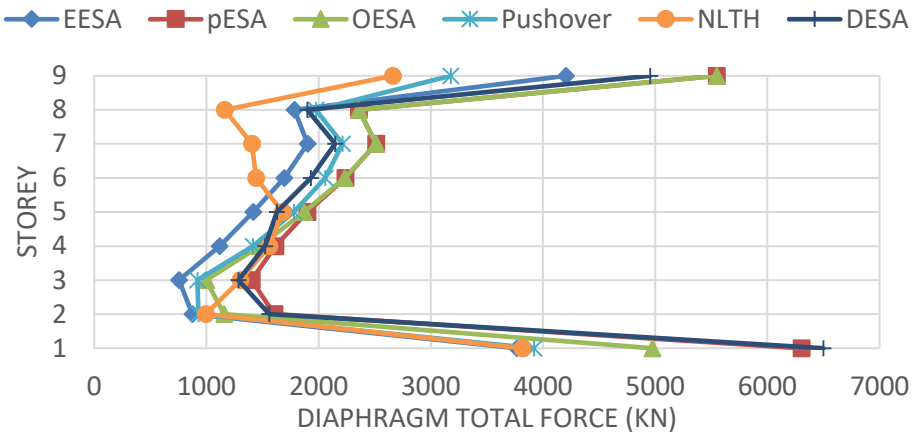

c) Model 17, nine-storey structure with ductility $\mu = 1$

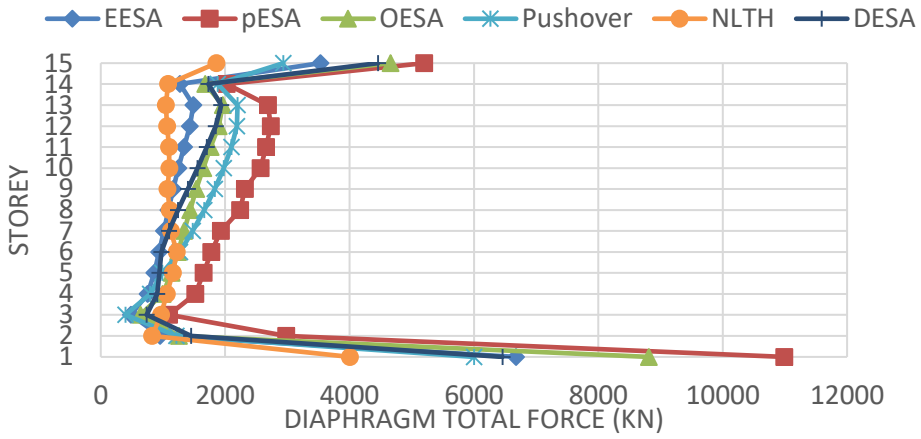

d) Model 21, fifteen-storey structure with ductility $\mu = 1$

Figure 7-15. In-plane diaphragm total forces of structures with different number of stories

Similar results may be obtained for structures designed for $\mu = 4$, Models 13 and 19, as shown in Figure 7-14c and e. These indicated that the proposed method overestimated diaphragm in-plane demands of five and nine storey structures designed with $\mu = 4$ in comparison with NLTH analysis by about 68% and 230% on average. However, the pESA method underestimated the total diaphragm in-plane forces of the five-storey structure by about 20% and overstimated the total diaphragm in-plane forces of the nine-storey structure by about 40% on average compared to NLTH analysis.

It is noted that these results may change with changing the structure configuration, design ductility, period and VLFR system relative stiffnesses.

- **Effect of different wall to frame stiffness ratios**

Figure 7-16 shows the analysis results of five storey structures with wall to frame stiffness ratios, WTFSR, of 1, 5 and 10. These stiffness ratios were calculated as the relative base shears of the elastically responding frame and the wall elements when subjected to the CESA load distribution. In all of these three cases, the stiffnesses were modified to obtain the same fundamental period of 0.6s.

When $WTFSR = 0$, this implies frame action. when $WTFSR \rightarrow \infty$, this is all wall action. In both of these cases, there are no transfer forces, so inertial forces control the response. Transfer forces are more significant in the intermediate WTFSR ratios. Gardiner (2011) showed that the "fighting effect" between the wall and the frame systems is maximum when the wall to frame stiffness ratio is one.

Figure 7-16 shows that with increasing the wall to frame stiffness ratio, the effect of diaphragm transfer force decreased. These results are consistent with findings of Gardiner (2011).

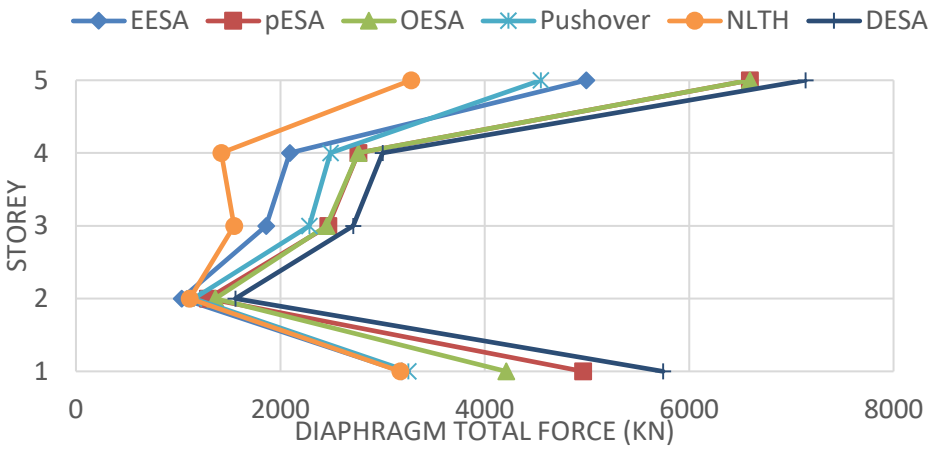

a) Model 11, WTFSR=1

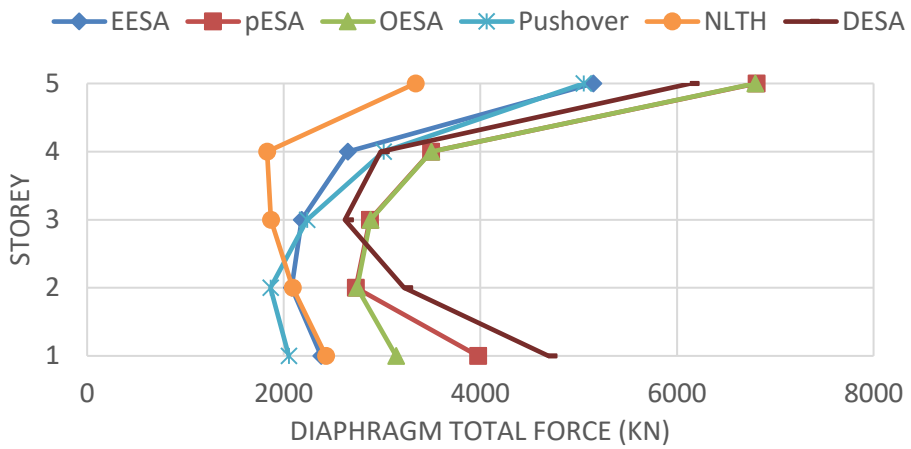

b) Model 14, WTFSR=5

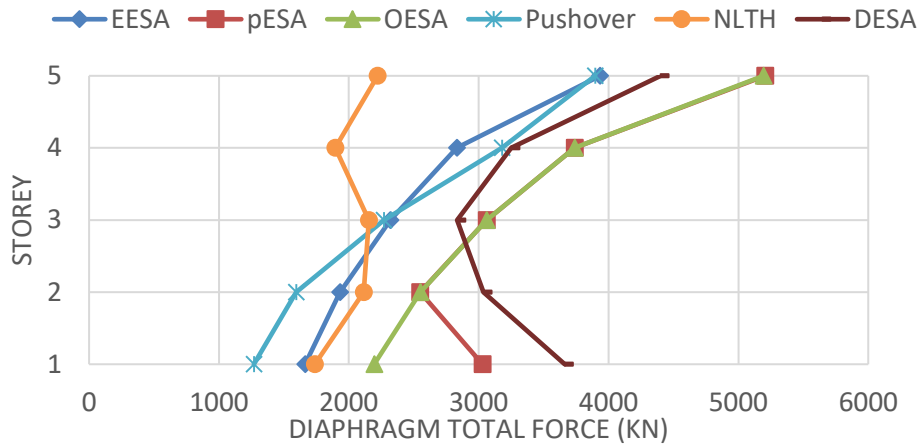

c) Model 15, WTFSR=10

Figure 7-16. In-plane diaphragm total forces of five-storey structures with different wall to frame stiffness ratios

As can be seen from the analyses results shown in Figure 7-16, the EESA method provides similar results as NLTH analysis for the structure with wall to frame stiffness ratio of one. With increasing the wall to frame stiffness ratio, the effect of transfer forces decreases, therefore the diaphragm in-plane demands of lower levels were underestimated. The proposed method overestimated the diaphragm in-plane demands for all three models shown in Figure 7-16 by up to 60% on average.

- **Subsoil type effect**

Figure 7-17 presents the behaviour of Models 17 to 20 considering ductility $\mu = 1$ and 4 and subsoil types C and D. Figure 7-17a and b show that the pESA and DESA methods

overestimated diaphragm in-plane forces for elastic structure ($\mu = 1$) on subsoil D by about 60% and 45% on average compared to NLTH analysis respectively. However, the diaphragm in-plane forces for the same structure on subsoil C were overestimated by about 200% and 85% using the pESA and DESA methods respectively. This is because of the modified spectral shape values obtained by Gardiner (2011). For the structure with $\mu = 4$ as shown in Figure 7-17c and d, the proposed method overestimated the diaphragm in-plane forces by about 200% for both subsoils D and C. While, the pESA method provided more reasonable diaphragm total in-plane forces compared to NLTH analysis with up to 40% and 80% overestimation on average for subsoils D and C respectively.

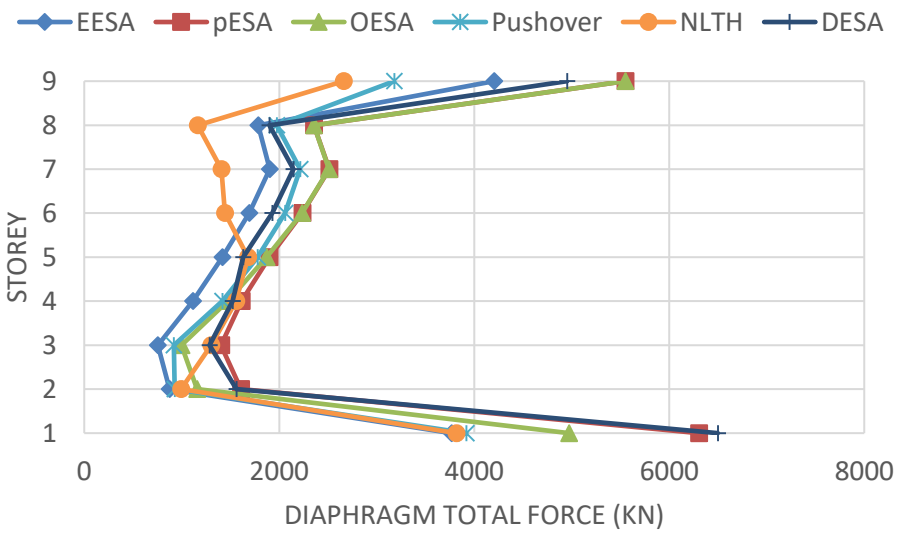

a) Model 17, nine-storey structure with ductility $\mu = 1$ and subsoil D

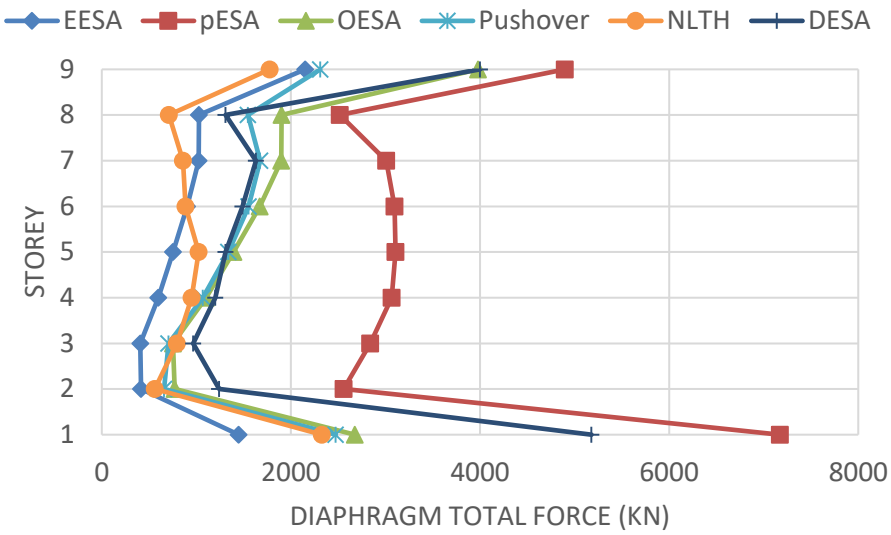

b) Model 18, nine-storey structure with ductility $\mu = 1$ and subsoil C

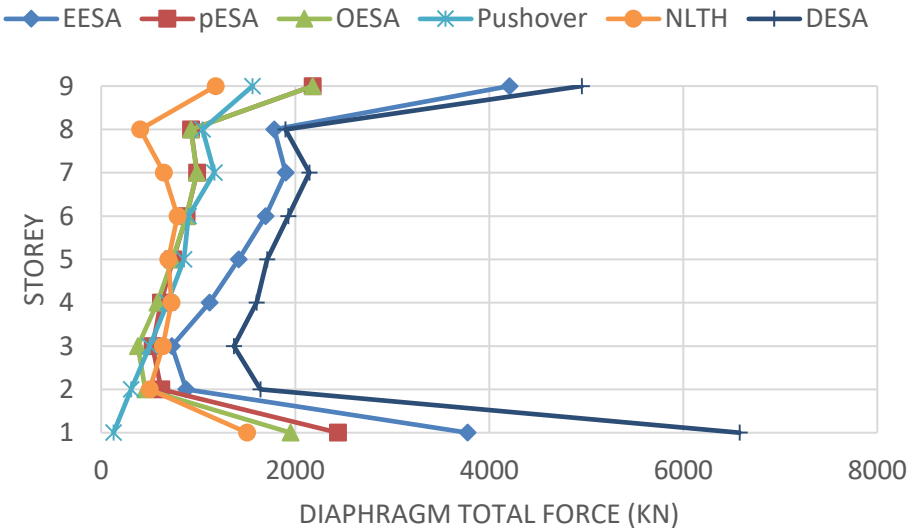

c) Model 19, nine-storey structure with ductility $\mu = 4$ and subsoil D

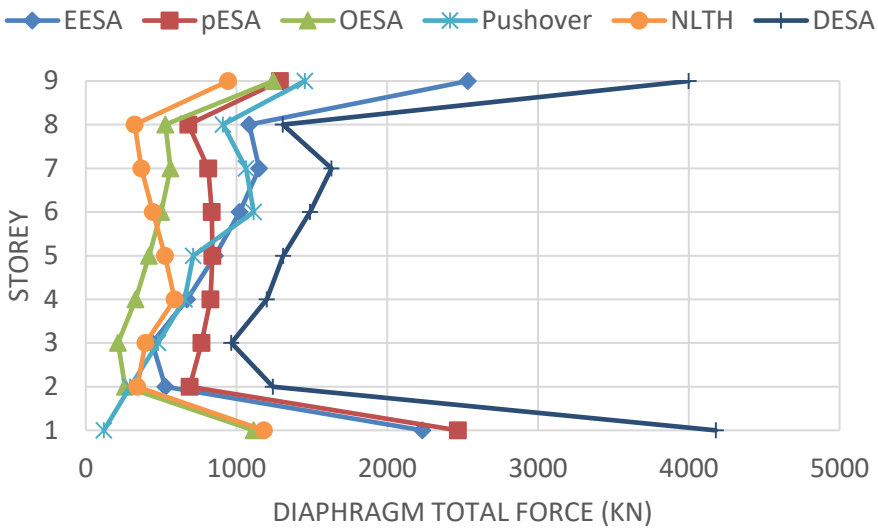

d) Model 20, nine-storey structure with ductility $\mu = 4$ and subsoil C

Figure 7-17. In-plane diaphragm total forces of nine-storey structures with different ductility and subsoil types

- **Structures beyond CESA method limitations**

Figure 7-18 shows the lateral force pattern obtained using the proposed method for both Models 22 and 23.

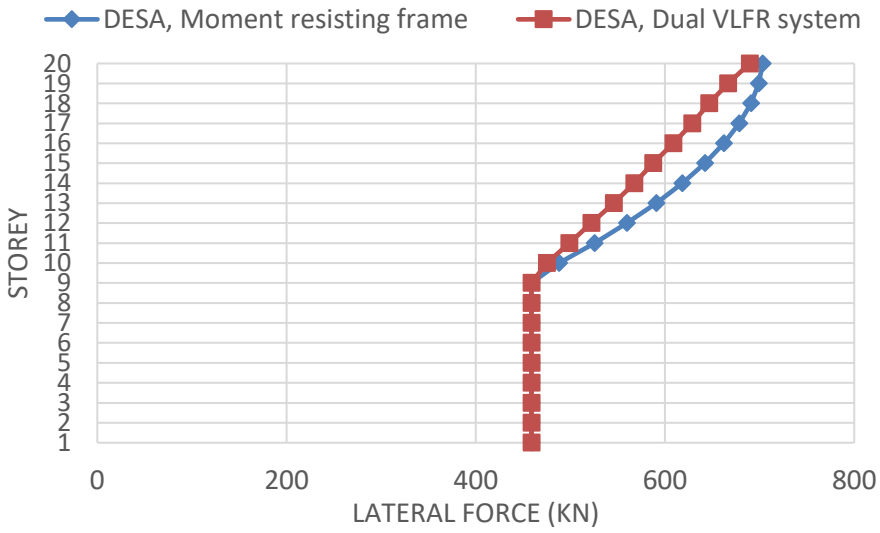

Figure 7-18. Lateral force pattern obtained using the proposed method

Figure 7-19 presents the analysis results of twenty-storey structures. As can be seen, the proposed method underestimated diaphragm in-plane forces for both moment frame and dual

type structure with about 75% and 55% on average compared to NLTH analysis for the FE models studied.

In the moment frame structure, Model 22, there is no transfer forces and the governing diaphragm in-plane demand is the inertia forces. Therefore a method that is able to estimate likely diaphragm accelerations may provide more accurate results than the DESA method. The proposed method is based on estimating likely structure lateral deformation to obtain diaphragm transfer forces. Note in cases that inertial forces control the response, perhaps it is not necessary to consider peak diaphragm accelerations, because the duration of the peak force/acceleration demand may significantly affect the structural response. For example, if high force/acceleration demands occur only briefly, causing a small inelastic displacement, then its effect may be minor on the global diaphragm performance. Therefore designing for the peak values may be conservative (MacRae and Bull, 2015, Bruere and Colley 2015). Also, the analysis and modelling assumptions such as damping and nonlinear behaviour of the structural elements may affect the peak accelerations recorded.

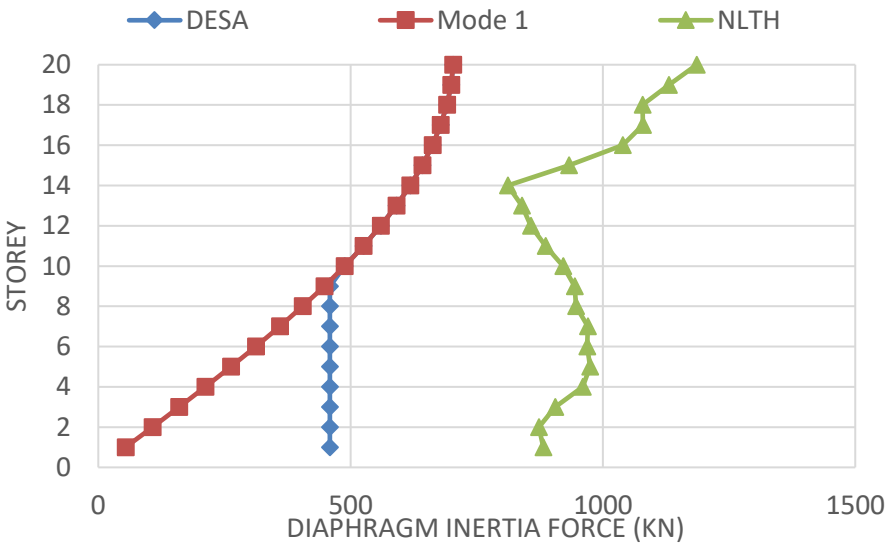

a) Model 22, twenty-storey structure with ductility $\mu = 1$ and moment frame system

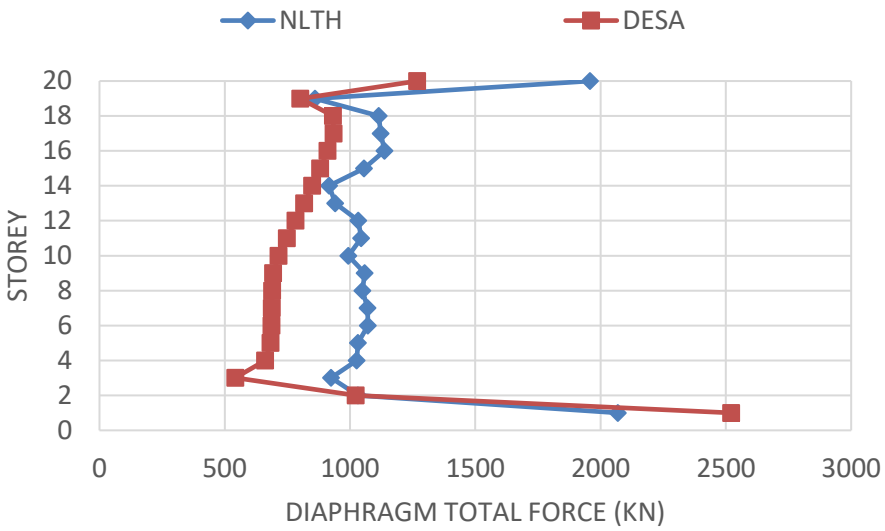

b) Model 23, twenty-storey structure with ductility $\mu = 1$ and dual VLFR system

Figure 7-19. Total in-plane diaphragm forces of twenty-storey structures

Here, both Models 22 and 23 shown in Figure 7-19 are designed for $\mu = 1$. It is expected that the diaphragm in-plane demands decrease with increasing ductility due to yielding in VLFR system members. Therefore, here elastic structures are considered to be compared with the proposed method that is based on EESA method.

7.5.3 Discussion on the proposed method

As mentioned in Section 7.4, a hypothesis used in the proposed method is that diaphragm transfer forces may be obtained using elastic ESA ($\mu = 1$) lateral forces because they provide the likely deformed shape of a long period structure according to the equal displacement assumption. However, they ignore important response features, such as structure ductility, redistribution of internal forces due to yielding of structural elements, hysteretic effects and, degradation due to stiffness and strength. Despite all these limitations, the ESA method is a widely accepted method in many loading standards (e.g. NZS1170.5 2004 and ASCE/SEI 7–16).

The results of the FE models studied in Section 7.5.2 showed that the proposed method may be used as a more general method because it is based on EESA method. In addition, it

may remove some limitations of the CESA and pESA methods such as height limitation and overstrength calculation. However, it may result in some overestimation and underestimation of response in different cases. In the following the limitations of the proposed method are discussed.

Based on the analyses conducted it was found that:

1. The proposed method underestimated diaphragm in-plane demands for structures with low ductility (e.g. $\mu < 2$) these include any structure where the actual overall lateral strength ($\phi_{ob}V_{design}$ shown in Figure 7-1) is greater than that required from the EESA forces. For steel structures it is common that members are sized to meet deflection limits causing higher force strength.
2. The proposed method overestimated diaphragm in-plane forces for the ductile structures (e.g. $\mu \geq 3$) analysed. This is because the proposed method use the EESA lateral forces, while increasing the structure ductility may reduce the diaphragm in-plane force due to yielding in some structural elements.
3. In the process of assessment or retrofit of an existing building, this method may result in large diaphragm in-plane demands which cause the retrofit process impossible or result in a large demand to capacity ratios.
4. The proposed method considers peak demands. It is possible that some inelasticity (e.g. shear stud inelastic deformation) may result in very small inelastic demands and provide satisfactory behaviour. This is described further in Chapter 8.

7.6 Conclusion

Based on the analyses conducted in this study, it was found that:

1) Diaphragm in-plane force demands include i) inertia forces, ii) transfer forces, iii) slab bearing forces, iv) compatibility forces, and v) forces from interaction with other elements. These in-plane forces may be categorised into global demand (i and ii) and local demand (iii, iv and v) groups based on their effect on the diaphragm. The global diaphragm demands may be obtained using lateral force methods or NLTH analysis. However, the local demands need to be considered for designing different components of the diaphragm locally.
2) The available lateral force methods to obtain diaphragm in-plane demands range from a simple static method, (e.g. CESA), to complex and more realistic methods, (e.g. NLTH). A number of lateral force methods that have been used for obtaining diaphragm global in-plane demands include: 1) ESA considering structure ductility (CESA), 2) Overstrength ESA (OESA), 3) Elastic ESA, (EESA), 4) Parts and Components method (P&C), 5) pseudo-Equivalent Static Analysis (pESA), 6) Sabelli et al. (2011) method, 7) Pushover analysis, 8) Modal response spectrum method (RSA), and 9) NLTH. These were evaluated for their suitability for use in design.
3) A new method, Diaphragm ESA (DESA), was proposed based on the hypothesis that if a lateral loading method can represent likely deformed shape of a structure, it can obtain likely diaphragm transfer forces. This is because diaphragm transfer forces are mainly due to deformation incompatibility of different VLFR systems. This method assumes the lateral deformation of a long period structure at the design level may be estimated using the EESA ($\mu = 1$) method according to the equal displacement assumption. Also, the bottom portion of the EESA lateral forces are increased in the proposed method to approximate the higher mode effects.

For high-rise buildings beyond the CESA method limitations, it is suggested to use the first mode lateral forces scaled to the EESA base shear and increase the lateral forces at lower floors. In the studied models, this method underestimated likely diaphragm acceleration by up to 55% on average; however, it estimated the likely diaphragm transfer forces with 75% underestimation on average compared to NLTH analysis. Note that high force/acceleration demands obtained from analyses may occur only briefly, causing a small inelastic displacement, then its effect may be minor. Designing for the peak values may therefore be conservative.

4) The analyses results showed that the proposed method may remove some limitations of the CESA and pESA methods such as height limit and overstrength calculation process. However, it may result in some overestimation and underestimation of response in different cases and ignore some important response features, such as structure ductility, redistribution of internal forces, hysteretic effects, stiffness and strength degradation. The advantages and disadvantages of different lateral force methods were discussed so that one can decide which method can provide more reasonable results based on the accuracy and time required for the analysis.

Note that the proposed method needs more research and study to show its limitations and the level of conservatism it may provide. The primary aims of proposing this method were a) to introduce the concept that transfer forces may be obtained using elastic ESA method that can predict likely lateral deformations of the structure, b) to provide a method which usually obtains conservative results in absence of any other widely accepted method, c) to be applicable to structures with wide range of hights and d) to be simple enough for use in a design office and do not require to calculate the structure over-strength to obtain lateral forces.

References

[1] American Society of Civil Engineers, Structural Engineering Institute (2016), Minimum Design Loads for Buildings and Other Structures. American Society of Civil Engineers, Structural Engineering Institute, Reston, Virginia. ASCE/SEI 7–16

[2] Bruere R. J. and Davies-Colley M. (2015). "Effect of Reducing Maximum Response on Concrete Floor Diaphragms", Final Year Projects, Dept. of Civil and Natural Resources Engineering, University of Canterbury. Project supervisors: MacRae GA and Bull DK.

[3] Chaudhari T. D., MacRae G. A., Bull D., Chase G., Hicks S., Clifton G. C. and Hobbs M. (2015). "Composite Slab Effects on Beam-Column Subassembly Seismic Performance", 8th International Conference on Behavior of Steel Structures in Seismic Areas, Shanghai, China.

[4] Dantanarayana H. N., MacRae G. A., Dhakal R. P., Yeow T. Z. & Uma S. R. (2012) "Quantifying Building Engineering Demand Parameters in Seismic Events", 14 World Conference on Earthquake Engineering, Lisbon, Portugal, August 2012. Paper number 3424.

[5] Fenwick, R. C. and Davidson, B. J. (1991). The Seismic Response of Multi-storey Buildings, Department of Civil Engineering, University of Auckland. Report number 495.

[6] Fenwick, R. C. and Davidson, B. J. (1997). "P-delta Actions and the Loadings Code." SESOC 10(1): 58-62.

[7] Gardiner D. R. (2011). "Design Recommendations and Methods for Reinforced Concrete Floor Diaphragms Subjected to Seismic Forces", PhD Thesis, University of Canterbury.

[8] MacRae G. A. and Bull D. (2015). "Diaphragm Design, ENEQ650: Seismic Design of Steel and Composite Structures", Postgraduate Class notes, University of Canterbury, 2015.

[9] MacRae G. A. and Clifton G. C. (2015). "Research on Seismic Performance of Steel Structures", Steel Innovations Conference, Auckland, New Zealand.

[10] MacRae G. A., Hobbs M., Bull D., Chaudhari T., Leon R., Clifton G. C. and Chase C. (2013). "Slab Effects on Beam-Column Subassemblies – Beam Strength and Elongation Issues", Composite Construction VII Conf., Palm Cove, Queensland, Australia.

[11] NZS 1170.5 (2004). Structural Design Actions-Part, 5. Standards New Zealand, Wellington, New Zealand. Including Amendment 1, 2016.

[12] Sabelli R., Sabol T. A. and Easterling W. S. (2011). "Seismic Design of Composite Steel Deck and Concrete-filled Diaphragms A Guide for Practicing Engineers", NEHRP Seismic Design Technical Brief No. 5.

[13] Sadashiva, V. K. (2010). Quantifying structural irregularity effects for simple seismic design.

[14] SESOC (2011). Design of Conventional Structural Systems Following the Canterbury Earthquakes: Structural Engineering Society of New Zealand, ENG.SESOC.0016.1, Version No. 4:21.

[15] Veletsos, A. S., & Newmark, N. M. (1960, July). Effect of inelastic behaviour on the response of simple systems to earthquake motions. Department of Civil Engineering, University of Illinois.

8 Diaphragm Stiffness and Strength Considerations

8.1 Introduction

In practice, the elastic analysis is commonly used by engineers to perform structural analysis and design. The elastic analysis only considers one stiffness of each element (which may be the initial stiffness, or the cracked stiffness of an RC member) and does not provide information about the nonlinear behaviour of different structural elements or the force redistribution due to change of stiffness or yielding of structural members. Also in the elastic analysis the main structural members are usually modelled and the effect of other elements (e.g. beam-column connections, shear studs and slab bearing elements) are often ignored. Ignoring these factors may cause:

1) different lateral forces between vertical lateral force resisting (VLFR) systems,
2) an over or underestimate of a) diaphragm transfer forces, b) beam-column connection axial forces, and c) shear stud demands

To obtain a more realistic result, the effects of different structural components need to be incorporated into the model, and nonlinear analysis should be performed. However, this may not be easily achieved due to limitations in most of commonly used engineering software packages and lack of knowledge about the nonlinear behaviour of some structural elements. Therefore, the force redistribution, and possible effects of nonlinear behaviour of different structural elements, needs to be considered using rational assumptions.

In this chapter, a number of FE models are used to investigate:

1. How can standard diaphragm design/assessment processes be modified to consider diaphragm stiffness (considering cracking) and strength, shear stud behaviour, and beam system axial strength?

2. How do beam-end connection and shear stud demands obtained from the proposed diaphragm design process compare with those from NLTH analysis?
3. What is the effect of providing intentional gaps between the slab and columns particularly on the beam-end connections and shear studs?
4. What is the amount of composite beam mid-point vertical deflection due to gravity and earthquake lateral loading?

8.2 Diaphragm design/assessment process

8.2.1 General concept

In practice, diaphragms may not be designed explicitly as it is usually assumed these structural elements are very stiff and strong in-plane. However, in cases that diaphragms are explicitly designed, the assumed diaphragm in-plane stiffness and the adequacy of the provided in-plane strength may be questionable because there is no commonly accepted diaphragm analysis method and design procedure.

Diaphragm in-plane design and diaphragm components design have been discussed by many researchers such as Bull (2004), Naeim and Boppana (2001), Sabelli et al. (2011), Scarry (2014), Cowie et al. (2014), and Moehle (2015). Section C5 of The Seismic Assessment of Existing Buildings (2017), hereafter referred to as the Assessment Guideline is the only one of the above that provides step-by-step diaphragm design/assessment procedures.

The design/assessment flowchart of the Assessment Guideline (2017) for designing diaphragms is shown in Figure 8-1 in the boxes 1 to 6. Diaphragm in-plane design process shown in Figure 8-1 includes two major parts:

1) Obtaining diaphragm in-plane demands using appropriate lateral force method and reasonable diaphragm in-plane stiffness assumption (Steps 1-3 shown in Figure 8-1).

To obtain diaphragm in-plane forces/demands, the entire structure is first modelled. This is because diaphragm transfer forces, and interaction with other elements, are usually the result of deformation incompatibility of different structural elements and/or discontinuities in plan location of the VLFR elements. Therefore, modelling only one storey of the structure and imposing inertia forces to the diaphragm may not provide likely diaphragm in-plane demands.

The term “out-of-plane forces”, F_{vi}, refers to the reaction of VLFR elements to the diaphragm. This can be changed to "vertical element lateral reactions", however to keep consistency with Assessment Guideline (2017) it is written “out-of-plane forces” in the following flowcharts.

2) Modelling and obtaining diaphragm internal forces to check diaphragm strength (Steps 4-6 shown in Figure 8-1).

Section C5.5.4.2 of the Assessment Guideline (2017) state that for buildings with significant asymmetry in the location of lateral force-resisting elements, such as the distribution across the building plan, termination up the height of the building, varying stiffness and/or strength between vertical elements, may require a more advanced analysis than simple hand-drawn strut and tie solutions (described in Section 3.2.1). For these types of structures, the truss element method (described in Section 3.3) was suggested to be used to obtain diaphragm design actions.

Modifications/amplifications of concepts in this flowchart include:

1. Beam axial capacity check, shown in Box 7 in Figure 8-1 and the method of Cowie et al. (2014) may be followed.
2. Proposing diamond truss model to improve beam axial force and shear stud demand estimations and obtain more accurate result using less truss mesh units (Chapter 3). This modifies Box 4.

3. Web-Side-Plate connection axial strength check (Chapter 4). This modifies Box 8.
4. Shear stud lateral strength check (Chapter 5). This modifies Box 9.
5. Diaphragm buckling strength check (Chapter 6). This modifies Box 10.
6. Proposing DESA method to obtain diaphragm lateral forces (Chapter 7). This affects Box 2.
7. Diaphragm in-plane stiffness consideration (Chapter 8 Section 8.2.2). This modifies Box 1.

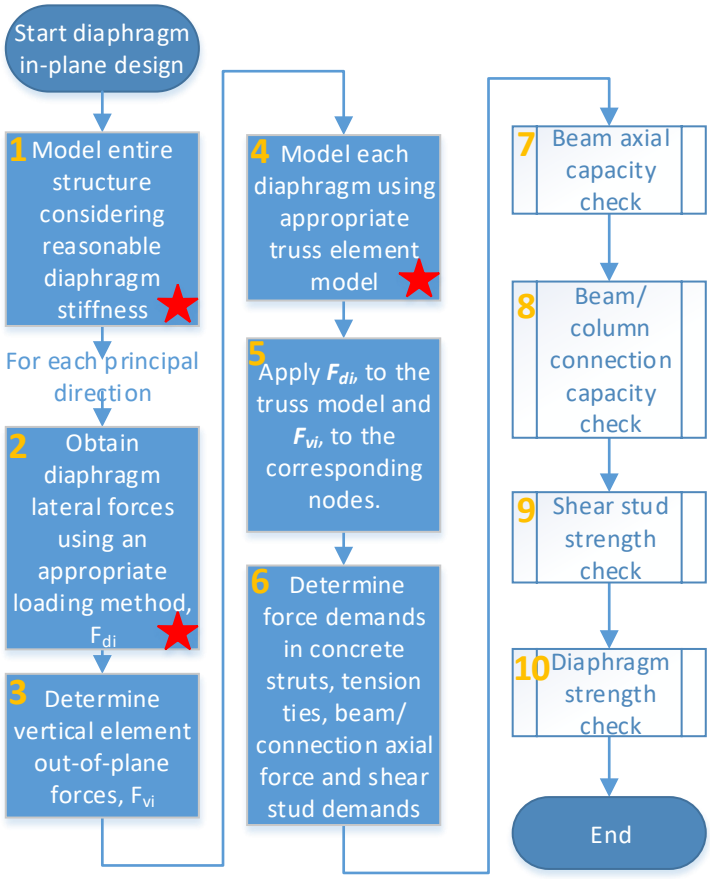

Figure 8-1. Diaphragm design flowchart

8.2.2 Diaphragm in-plane stiffness considerations

The reaction forces of VLFR elements obtained from the structural model (Box 3 in the above flowchart) may depend on the relative diaphragm in-plane stiffness to the VLFR system stiffness. Standards do consider diaphragm in-plane stiffness, and categorize diaphragms as

either ‘rigid’ or ‘flexible’ for analysis. Different building standards require different limitations for considering the flexibility of diaphragm in the analysis. Clause 6.1.4 of NZS 1170.5 (2004) state that diaphragms may be considered as infinitely rigid in-plane where the maximum lateral deformation of the diaphragm itself is less than or equal to twice the average of floor lateral deflections. Based on these categories, the majority of diaphragms in multi-storey buildings with concrete floors may be characterized as rigid (NZS 1170.5, 2004).

Diaphragms are usually considered to remain elastic during the expected design earthquake level allowing minor local inelastic deformations. However, concrete cracking may occur under large diaphragm forces. In some concrete buildings, the diaphragm consists of a thick concrete slab and the cracking effects may not significantly decrease diaphragm in-plane stiffness. However, in steel frame structures diaphragms usually consist of a thin concrete topping above the steel decking that may crack under a lower level of in-plane forces and decrease the in-plane stiffness.

According to the commentary of Section 6 of NZS 1170.5, 2004 (C6.1.4) one approach for diaphragm modelling is to undertake nonlinear modelling of all the structural elements including the diaphragms. In this case, all the inertia and transfer forces may be obtained considering more realistic stiffness and strength and also stiffness reduction due to cracking of the VLFR systems and the diaphragm. However, the accuracy of such an analysis depends on the modelling assumptions and requires considerable experience and technical knowledge to obtain reasonable results.

In Appendix L, a simple one-storey structure is investigated to demonstrate the effect of diaphragm stiffness assumption on distributing lateral forces between VLFR systems. The analysis conducted showed that the lateral force distribution between VLFR systems may change by up to 60% by increasing the frame to diaphragm stiffness ratio from 1 to 10 where the relative stiffness of VLFR systems is 0.1. Also, the diaphragm in-plane force ratio and

therefore the force itself may increase by about 185% by decreasing the frame to diaphragm stiffness ratio from 10 to 1 where the relative stiffness of VLFR systems is 3. These values indicate the importance of using a reasonable diaphragm in-plane stiffness in the analysis to obtain likely lateral force distribution between VLFR systems and diaphragm in-plane demands.

Here, two approaches are recommended to address the issue of diaphragm cracking effects on distributing lateral forces between VLFR systems and obtaining diaphragm in-plane demands. In approach one, the diaphragm is assumed to remain elastic and is modelled using elastic in-plane properties. Then using the obtained internal forces, the assumption of the elastic diaphragm will be checked. If the assumption is correct, design/assessment may be continued using the obtained results. Otherwise, the diaphragm in-plane stiffness should be reduced to account for concrete cracking. In approach two, it is suggested to perform two analyses using both elastic and cracked diaphragm in-plane stiffnesses and use the envelope values for design/assessment. These approaches are presented here as step-by-step procedures.

- **Approach one**

Step 1. Obtain “diaphragm lateral forces” (e.g. DESA method in Chapter 7).

Step 2. Impose the “diaphragm lateral forces” on the whole structure model. Note that elastic diaphragm stiffness should be considered in the analysis.

Step 3. Obtain VLFR element reaction forces by calculating the difference in shear forces above and below the diaphragm.

Step 4. Model each storey separately using Truss Model 2 (Chapter 3) with diagonal compression-only and orthogonal compression/tension elements (representing un-cracked diaphragm properties)

Step 5. Compute the tensile forces in the orthogonal truss members.

Step 6. Check the maximum orthogonal member tension force, F_{Ti}, and compare with the concrete tension capacity according to NZS3101 (2006), $F_{cr} = 0.6at\sqrt{f_c'(MPa)}$, where F_{cr}, a and t are the tensile strength of orthogonal member considering concrete tensile capacity (MPa), truss mesh unit width (mm) and concrete topping thickness (mm) respectively. Note: considering the topping thickness is reasonable for the decking transverse direction, but conservative for the longitudinal direction.

Step 7. If the orthogonal member tension forces are less than the concrete tension capacity, $F_{Ti} < F_{cr}$, then the assumption of using elastic diaphragm (un-cracked) stiffness may be valid and design with this assumption may be continued.

Step 8. Otherwise, if $F_{Ti} > F_{cr}$, then the assumption of elastic diaphragm stiffness is not correct and analysis should be performed from Step 2 using the cracked diaphragm in-plane stiffness. Note: standard methods to obtain diaphragm cracked stiffness are not available. In the absence of these, in this study the cracked stiffness is considered as 10% of the elastic in-plane stiffness.

Step 9. Obtain the load path through the diaphragm and check different components such as the in-plane strength of the diaphragm, beam, and shear studs.

A flowchart of the above steps is presented in Figure 8-2.

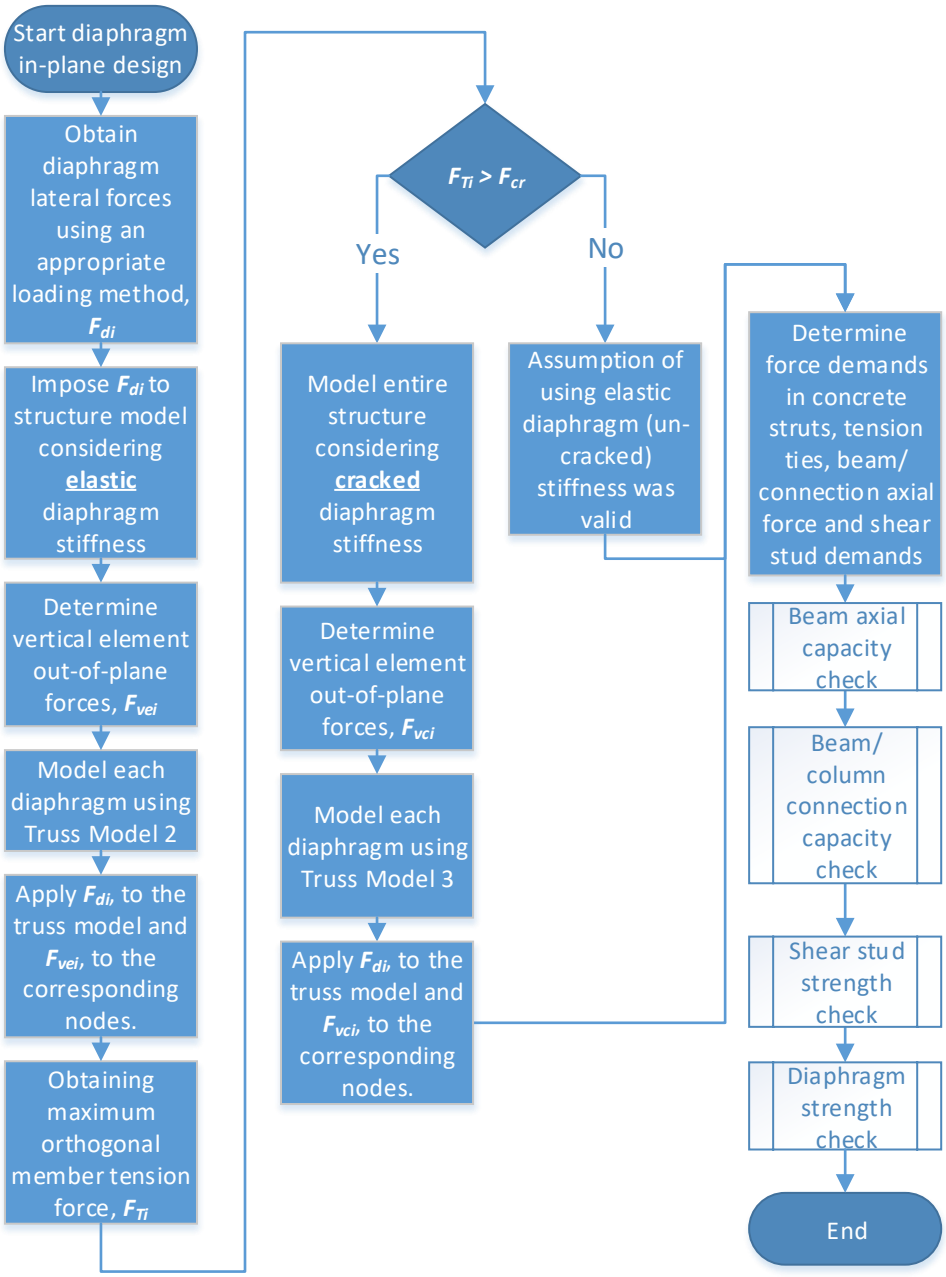

Figure 8-2. Flowchart of Approach One

- **Approach two**

Step 1. Obtain "diaphragm lateral forces" (e.g. DESA method in Chapter 7).

Step 2. Impose the "diaphragm lateral forces" on the whole structure model. Note that elastic diaphragm stiffness should be considered in the analysis.

Step 3. Obtain VLFR element reaction forces by calculating the difference in shear forces above and below the diaphragm.

Step 4. Model each storey separately using Truss Model 2 (Chapter 3) with diagonal compression-only and orthogonal compression/tension elements (representing un-cracked diaphragm properties)

Step 5. Compute diaphragm internal forces, beam axial forces, beam-column connection forces and shear stud demands for design. These forces are denoted by ME.

Step 6. Impose the "diaphragm lateral forces" (from Step 1) to the whole structure model. Note that cracked diaphragm stiffness should be considered in the analysis. Standard methods to obtain diaphragm cracked stiffness are not available. In the absence of these, in this study the cracked stiffness is considered as 10% of the elastic in-plane stiffness.

Step 7. Obtain VLFR element reaction forces by calculating the difference in shear forces above and below the diaphragm.

Step 8. Model each storey separately using Truss Model 3 (Chapter 3) with diagonal compression-only and orthogonal reinforcement tension/concrete compression members (representing cracked diaphragm properties).

Step 9. Compute diaphragm internal forces, beam axial forces, beam-column connection forces and shear stud demands for design. These forces are denoted by MC.

Step 10. Check different components such as the in-plane strength of the diaphragm, beam, and shear studs using envelope values (i.e. the maximum) of ME (Step 5 above) and MC (Step 8 above) forces.

A flowchart of the above steps is presented in Figure 8-3.

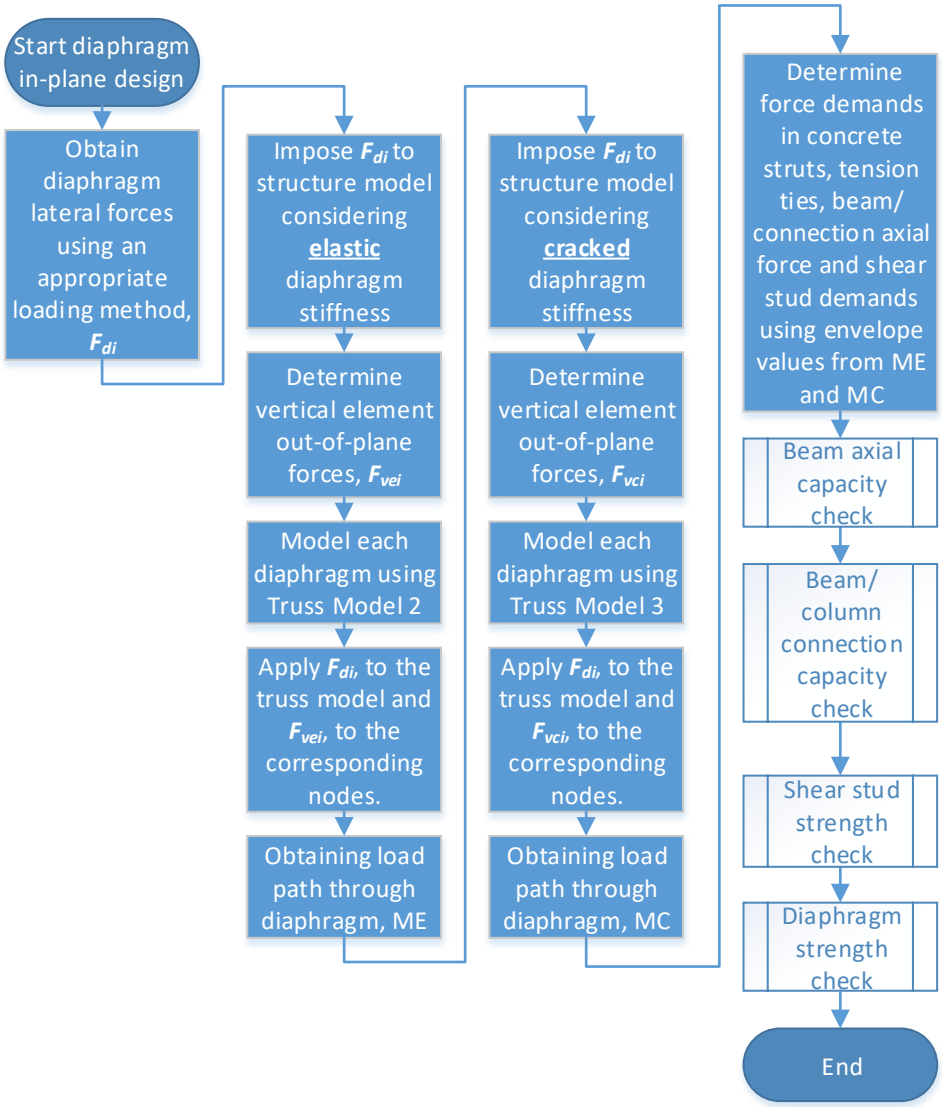

Figure 8-3. Flowchart of Approach Two

The concrete material in diaphragms may crack before lateral forces are imposed to the diaphragm due to different causes such as shrinkage, creep, gravity loads and diaphragm in-plane forces from interaction with other elements. Also, the expected lateral forces may be larger than the calculated in-plane demands and cause diaphragm cracking. Considering these effects, it is recommended to use the second approach in design. Also, it is recommended to use the same approach to design VLFR systems of the structure; this allows consideration of force redistribution due to diaphragm cracking and reduction in diaphragm in-plane stiffness.

8.3 FE modelling

To verify the proposed diaphragm design flowchart, a simple steel structure is assumed and designed using NZS3404 (2007). Also, the floor diaphragm of the selected model is designed using elastic analysis according to the flowchart shown in Figure 8-3. Design assumptions and loadings are presented in Appendix M in detail. Here also, the designed structure is analysed using NLTH analysis to compare the results with the design values.

8.3.1 Model geometry and design assumptions

Figure 8-4 shows the selected one-storey model. The storey height is considered 3.5m. The structure has two bays in both X and Y directions with 8m and 6m long spans respectively. The lateral force resisting system of the structure in the X-direction is moment resisting frame, MRF, and in the Y-direction is a combination of moment resisting frame (exterior frames) and braced frame (interior frame). The composite slab ribs are assumed to be placed parallel to the X-direction. One secondary beam is used in each bay, parallel to the Y-direction to support the composite slab in the 8m long span as shown in Figure 8-4.

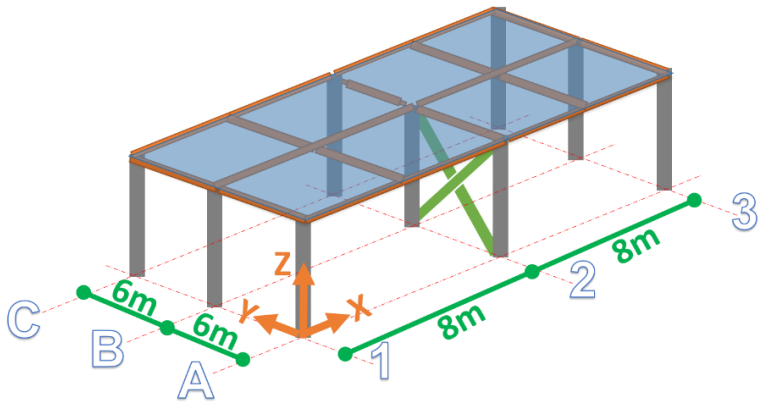

a) Schematic 3D model view

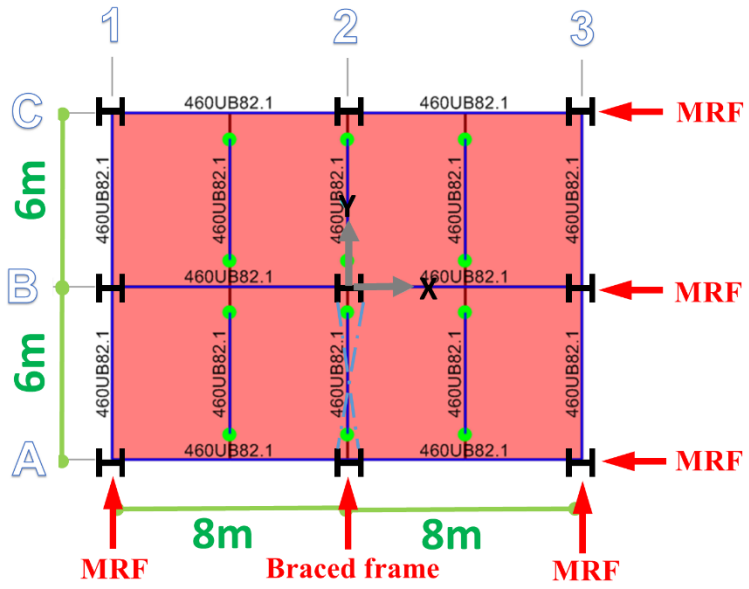

b) Plan view

Figure 8-4. Structure dimensions and lateral force resisting systems

8.3.2 Structural elements design

Structural elements include beams, columns, and braces were designed according to NZS3404 (2007) assuming design ductility $\mu = 1$. This design ductility, $\mu = 1$, is selected to avoid inelasticity in the VLFR systems under expected lateral forces and simplify FE modelling. All the steel beams are considered to have the same size. This simplifies the modelling process and helps to use the same offset value for all the beams in models that the composite beam effects are investigated. The floor diaphragm of the selected model is also designed using elastic analysis according to the flowchart shown in Figure 8-3. Design assumptions and loadings are presented in Appendix M in detail.

8.3.3 Analysis assumptions

Three ground motion records were chosen to represent the likely earthquakes in Wellington, New Zealand, considering motion characteristics (Gardiner 2011, NZS1170.5 2004). The selected ground motions are listed in Table 8-1. All the time history records were scaled according to the NZS 1170.5 (2004) loading standard. This scaling procedure minimises

the difference between the design response spectra and spectral acceleration of the time history records over the range of 0.4 to 1.3 times the fundamental period of the structure.

Table 8-1. Selected earthquake records for NLTH analysis

Location	Station	Date	Magnitude
Landers, California	Lucerne	28 June 1992	7.3
El Centro, Imperial Valley	El Centro	19 May 1940	7.0
Kocaeli, Turkey	Izmit	17 August 1999	7.4

The NZS 1170.5 (2004) requires that for time history analysis the analysis time-step shall not be greater than the step at which the records are digitised. Also it is required that the time step shall be less than or equal to the minimum of i) $T_1/100$, ii) T_n and iii) 0.01 second. Where T_1 is the largest translational period of the first mode in the direction of interest and T_n is the period of the highest mode in the same direction required to achieve the 90% mass. The time step used for all analyses in this study was 0.0015s since the fundamental period was 0.15s for the base model. Note that different floor models were used in the global analysis, Section 8.4.

The damping model that is used in this research is the Initial stiffness Proportional Rayleigh Damping model. For all models, 5% damping ratio was considered in the first and third modes. The damping ratio of mode n, which represent the highest mode that achieves 90% mass participation, was checked to be less than 40% based on Clause 6.4.6 of NZS1170.5 (2004).

The structural weights used in the analysis are based on the values used for design in Appendix M. The gravity load combination is considered as $G + \psi_E Q$, where $G = 5kPa$, $Q = 3kPa$ and $\psi_E = 0.3$.

8.3.4 WSP connection nonlinear behaviour

The axial behaviour of WSP connections was investigated in Chapter 4 in detail. For the FE models studied, it was found that the axial compression behaviour of the WSP connections considered was elastic up to $\delta_{yc} = 0.4 - 0.5\text{mm}$ axial deformation. After this point the cleat

plate started to yield and buckled due to lateral deformations and the P-Δ effect. Also, it was shown that the post-peak behaviour of WSP connections depended on the connection geometry and boundary conditions such that for a laterally unrestraint double coped connection, the post-peak strength (at about 4mm axial deformation) was as low as 50% of the peak strength for the connection considered as shown in Figure 4-47. However, for an uncoped laterally restrained connection, the post-peak strength (at about 4mm axial deformation) decreased from the peak strength by about 10% as shown in Figure 4-48.

In this chapter the axial behaviour of the WSP connections is assumed to be elastic-perfectly plastic for structural analysis. The yield axial compression deformation, δ_{yc}, is assumed to be 0.5mm. From the FE analyses conducted in Chapter 4, the ratio of the peak axial compression strength, P_{c-FEM}, to the peak axial tension strength, P_{t-FEM}, for the range of WSP connections was between 0.3 and 0.5. However, the design axial tension strength calculated by the hand methods of Section 4.9 and including a strength reduction factors considering material and section property uncertainty as well as construction imperfections, $\emptyset P_{t-Calc}$, of the WSP connections was lower than that from the FE analyses results. This is because of modelling inaccuracy as well as the strength reduction factor effect. Also the elastic stiffnesses in compression and tension were found to be similar for a WSP connection.

In WSP analyses to be used in design, the connection tension strength is obtained using the design strength, $\emptyset P_{t-Calc}$, to be consistent with the diaphragm design assumptions and calculations. The yield axial tension deformation can be obtained assuming the same elastic stiffness for both tension and compression behaviours. Figure 8-5 shows the axial behavior of a WSP connection considered for structural analysis in this Chapter. This force-displacement behaviour was assigned to the beam-ends using nonlinear link elements in SAP2000 (2015). Note that the hole oversize effect was not considered here.

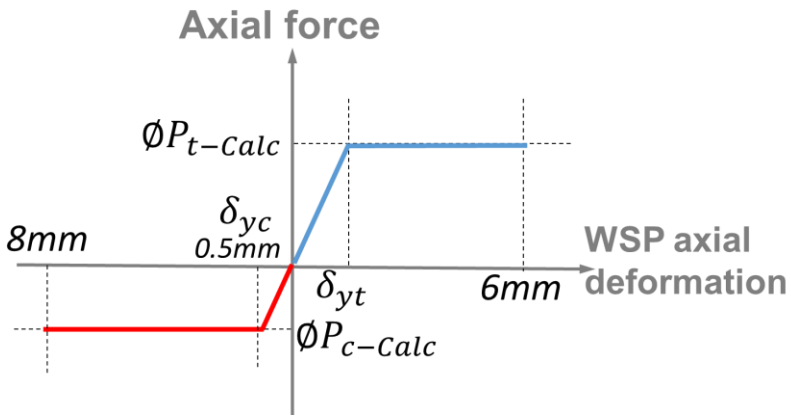

Figure 8-5. WSP connection axial force-deformation behaviour

Since the connection force-displacement behaviour needs to be used in NLTH analysis, the hysteresis behaviour of the connection is an important parameter that may affect the results. All WSP connections in Chapter 4 were studied under monotonic axial force alone. The WSP connection that was investigated in Section 4.6.1 is analysed under reversed cyclic loading to obtain the cyclic hysteretic characteristics for frame modelling. Figure 8-6 presents the connection details, loading and boundary conditions of the model studied. In this model the top flange is restrained against lateral movements at the locations of shear studs. The connection between the beam web and cleat plate explicitly considered the bolt action with the nonlinear bolt behaviour described in Section 4.4.2.

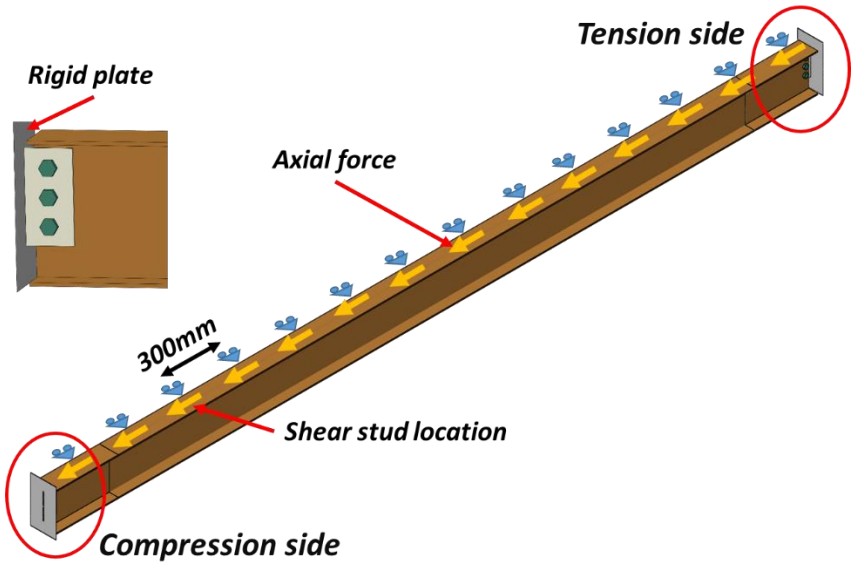

a) Boundary conditions for WSP connection model

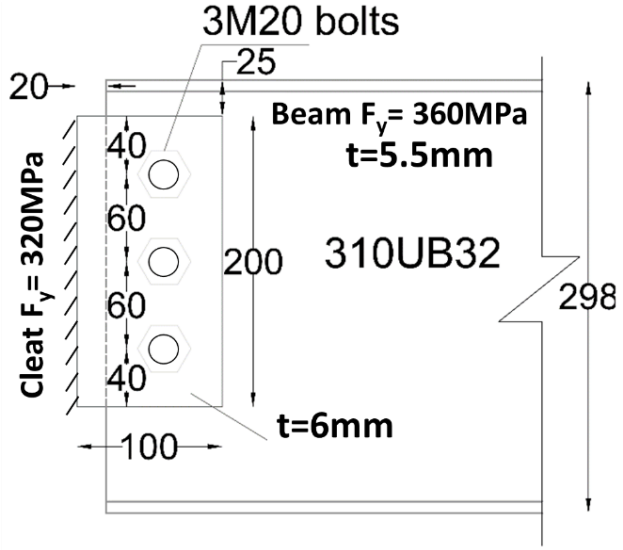

b) WSP connection details (all dimensions in mm)

Figure 8-6. WSP connection details, loading and boundary conditions

Figure 8-7 shows the hysteresis behaviour of the connection. As can be seen, the hysteresis plot shows a pinched behaviour. This is because the cleat plate lateral deformation is opposite under tension and compression forces. Therefore, changing from compression to tension or vice versa requires large lateral deformations and creates pinching behaviour. The inelastic mechanism is primarily due to cleat yielding in compression, and cleat or web yielding in tension.

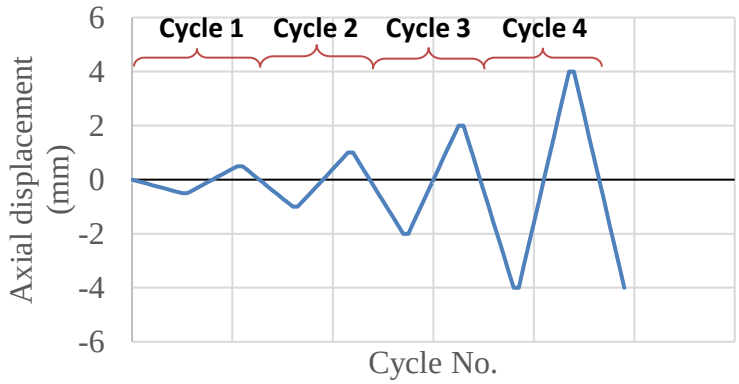

a) Loading pattern

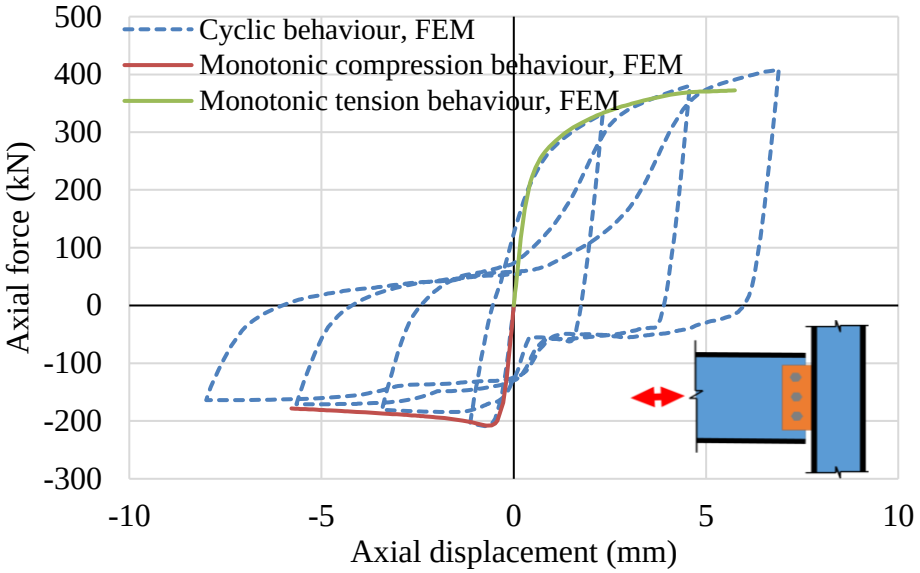

b) Axial force-displacement

Figure 8-7. Cyclic plot of the WSP connection, FE model (ABAQUS)

There are few hysteresis models available in SAP2000 (2015) software that can be used for nonlinear link elements. In this study the "Pivot hysteresis model" from the SAP2000 (2015) library is used to simulate the axial force behaviour of WSP connections. This model was developed by Dowell et al. (1998). It is particularly well suited for reinforced concrete members, and is based on the observation that unloading and reverse loading tend to be directed toward specific points, called pivots points, in the action-deformation plane. The following parameters are required for the Pivot model (http://docs.csiamerica.com):

- α_1, which locates the pivot point, P_1, for unloading to zero force from the positive force. Unloading occurs toward, P_1, a point on the extension of the positive elastic line, but at a negative force value of α_1;times the positive yield force.
- α_2, which locates the pivot point, P_2, for unloading to zero from the negative force. Unloading occurs towards a point on the extension of the negative elastic line, but at a positive force value of α_2 times the negative yield force.
- β_1, which locates the pivot point for loading from zero in the direction of positive force. Loading occurs toward a point on the positive elastic line at a force value

of β_1 times the positive yield force, where $0.0 < \beta_1 < 1.0$. Beyond that point, loading occurs along a secant line to the point of maximum previous positive deformation on the backbone curve.

- β_2 , which locates the pivot point for reverse loading from zero toward negative force. Reloading occurs toward a point on the positive elastic line at a force value of β_2 times the positive yield force, where $0.0 < \beta_2 < 1.0$. Beyond that point, loading occurs along a secant line to the point of maximum previous negative deformation on the backbone curve.
- η, which determines the amount of degradation of the elastic slopes after plastic deformation, where $0.0 < \eta < 1.0$. Here $\eta = 0.0$ indicates no degradation, and $\eta = 1.0$ indicates unloading occurs along a secant curves to the origin.

These parameters and the hysteresis behaviour are shown in Figure 8-8.

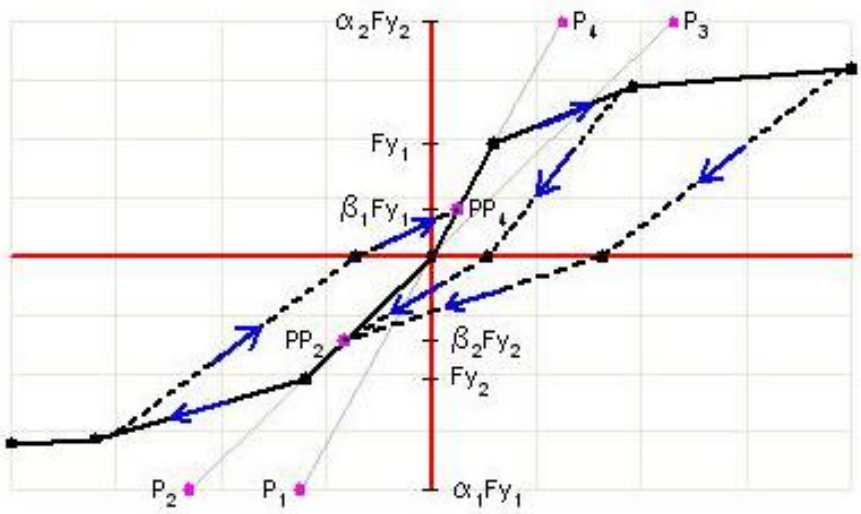

Figure 8-8. Pivot hysteresis behaviour, SAP2000 (2015)

Pivot hysteresis parameters for the hysteresis behaviour of the WSP connection are presented in Table 8-2. Using these parameters the hysteresis force-displacement behaviour of the nonlinear link element representing the WSP connection in SAP2000 (2015) is shown in Figure 8-9. As can be seen, the Pivot hysteresis model can represent likely hysteresis behaviour of WSP connection reasonably.

Table 8-2. Pivot hysteresis parameters for WSP connection

Parameter	Value
α_1	100
α_2	4
β_1	0.3
β_2	0.6
η	0

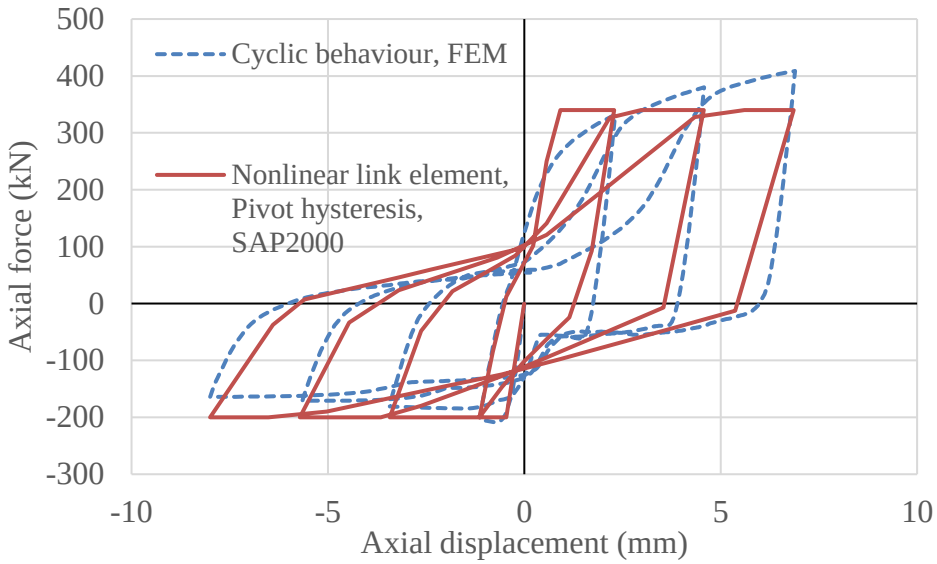

Figure 8-9. Detailed FEM and pivot Hysteresis behaviours of the WSP connection

8.3.5 Shear stud force-slip behaviour

The shear strength of an individual shear stud depends on the shear stud diameter, the materials properties, the concrete slab properties, the orientation of the steel decking, the position of the stud within the ribs, and the number of studs. A number of force-slip relationships for shear studs are available in the literature. The force-slip curves are usually obtained using push-out tests on shear studs.

Johnson and Molenstra (1991) proposed an empirical equation to represent the monotonic force-slip, $q - S$, relationship of shear studs, Eq. (8-1), using the shear stud ultimate strength, q_r.

$$q = q_r\left(1 - e^{-\beta S}\right)^{\alpha} \qquad \text{Eq. (8-1)}$$

In this equation, α and β are empirical values that in this study are considered equal to 0.989 and 1.535 respectively. These values are based on Johnson and Molenstra (1991) results for 19mm shear studs. Shear stud strength, q_r, can be calculated using equations provided in different building standards e.g. NZS3404 (2007), Eurocode 4 (2004), AS/NZS 2327 (2017) and AISC/ANSI 360-16 (2016).

In this study, the shear force-slip behaviour of shear studs is idealised as shown in Figure 8-10. The idealisation is performed to obtain the same energy using elastic-perfectly plastic behaviour. Considering S_{max} and S_e are the ultimate slip and yield slip of a shear stud respectively, the yield slip can be obtained in Eqs (8-2) and (8-3) equal to $S_e = 1.3mm$. where, $\beta = 1.535$ and $S_{max} = 7.2mm$ in this study.

$$\frac{S_e q_r}{2} + q_r(S_{max} - S_e) = \int_0^{S_{max}} q_r\left(1 - e^{-\beta S}\right) dS \qquad \text{Eq. (8-2)}$$

$$S_e = \frac{2}{\beta}\left(1 - e^{-\beta S_{max}}\right) \qquad \text{Eq. (8-3)}$$

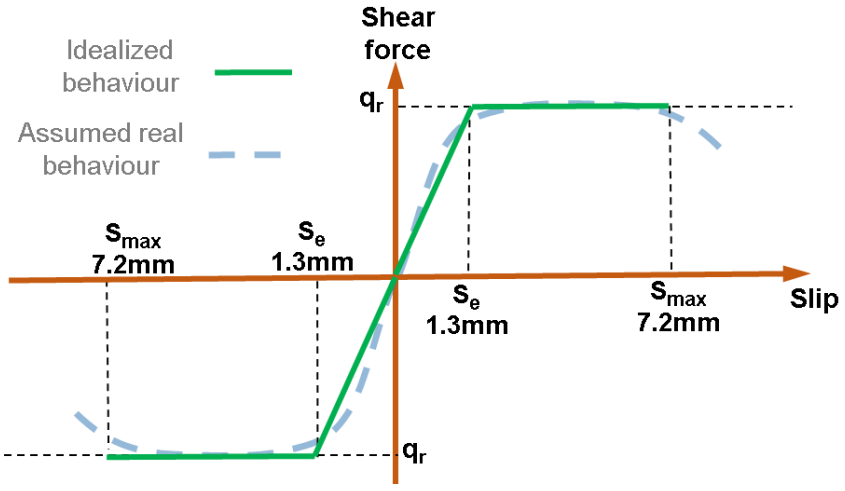

Figure 8-10. Shear stud behaviour considered

As it was explained in Chapter 5 in detail, the hysteresis behaviour of shear studs plays a key role in identifying the behaviour of composite beams under lateral forces. Most of the research studies in the literature have focused on the monotonic behaviour of shear studs. This is because the gravity load capacity and stiffness of composite beams were mostly of interest

to the researchers. The behaviour of shear studs subjected to fully reversed cyclic loading was investigated by Oehlers and Coughlan (1986), Nakajima et al. (2003) and Civjan and Singh (2003). Figure 8-11 shows an example of force-slip hysteresis curve for shear studs.

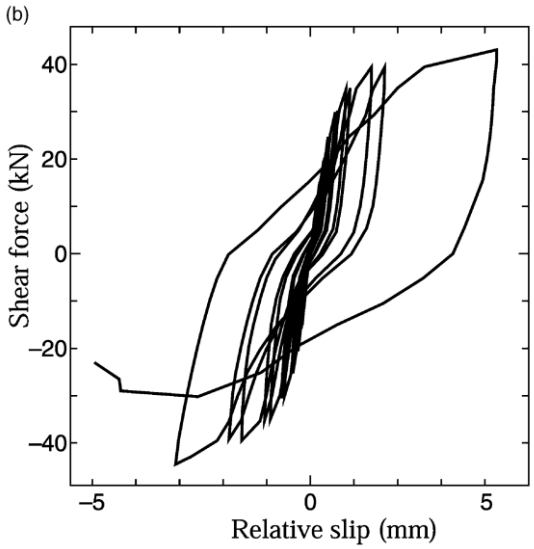

Figure 8-11. Shear stud behaviour subjected to fully reversed cyclic loading, 13mm diameter shear stud, Nakajima et al. (2003)

Here, the hysteresis behaviour of the shear studs is simulated using Pivot hysteresis model that was described in Section 8.3.4. Pivot hysteresis parameters calibrated to the hysteresis behaviour of the shear stud shown in Figure 8-11 are presented in Table 8-3.

Table 8-3. Pivot hysteresis parameters for shear stud modelling

Parameter	**Value**
α_1	20
α_2	20
β_1	0.3
β_2	0.3
η	0

Using these parameters, the hysteresis force-slip behaviour of shear stud shown in Figure 8-11 is presented in Figure 8-12. As can be seen, Pivot hysteresis model shows a good agreement with the experimental results in terms of representing overall behaviour.

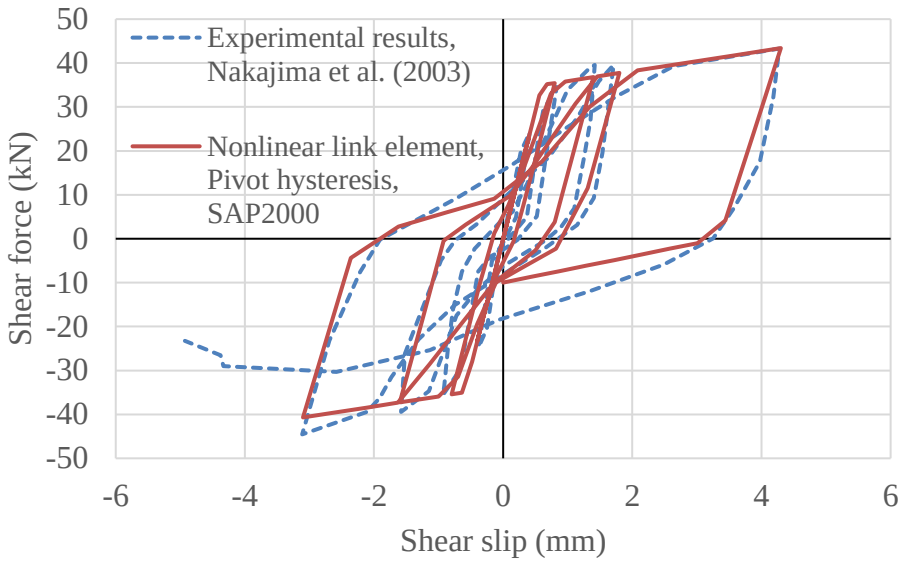

Figure 8-12. Force-slip behaviour of shear stud, experimental (Nakajima et al., 2003) and Pivot Hysteresis model

8.3.6 Slab bearing force-displacement behaviour

Slab-column interaction may affect the frame seismic behaviour. It may increase or decrease the beam and beam-column connection axial force and there is a possibility of slab damage due to high bearing forces. Figure 8-13 shows the method used in this study to consider the slab bearing effects (no gap condition) in the FE models.

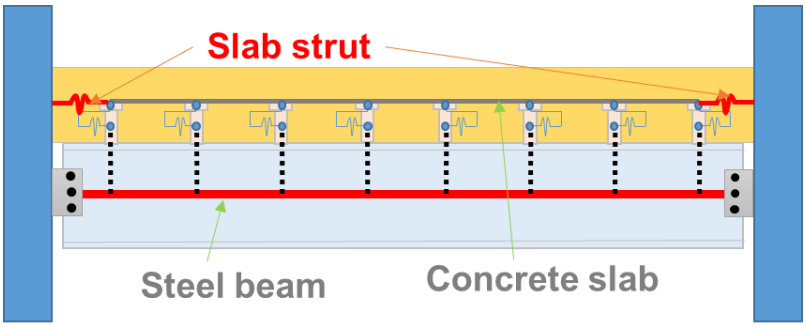

Figure 8-13. Slab element at beam-column connection

The slab bearing force can be calculated using Clause 12.10.2.4 of NZS3404 (2007) as shown in Eq. (8-4). Where t_{ef} and b_{sef} are the thickness and width of the concrete in direct contact with the column. The long term increase in concrete stress, f'_{cos}, is taken as 10 MPa. This equation shows that the slab bearing force may be limited by the total strength of the steel

beams connected to the column in the loading direction, $\sum(A_g F_y)_i$. Note that, this equation is suitable for beams in moment resisting frames, and for simply supported beams the connection axial strengths should be used instead of $\sum(A_g F_y)_i$. In Eq. (8-4) only Mechanism 1, direct compression on the column flange, is considered and Mechanism 2 which is due to concrete struts inclined at 45° to the column sides (Braconi et al. 2010), is ignored in this equation.

$$N_{slab} = min\left\{1.3 t_{ef} b_{sef} (f_c' + f_{cos}'); \sum(A_g F_y)_i\right\} \quad \text{Eq. (8-4)}$$

In this study the slab bearing force-displacement behaviour is defined using the unconfined concrete stress-strain curve provided by Park and Paulay (1975). The maximum compressive concrete stress, $1.3(f_c' + f_{cos}') = 52MPa$, is multiplied by the contact area with the outer column flange, $t_{ef} b_{sef}$, to obtain the slab bearing force, N_{slab}. To calculate the strut axial deformation, it is arbitrarily considered that the distance between the column face to the first effective shear stud is 500mm and the strains are multiplied by this length to obtain axial deformations. To consider the hysteresis behaviour of the slab strut, Takeda hysteresis behaviour (Takeda et al. 1970), available in the SAP2000 (2015) library is used. Note that the tension behaviour of the concrete contact element is ignored. Figure 8-14 presents the hysteresis behaviour of the slab strut, between the column face and the first shear stud, $N_{slab} = 675$kN in this case.

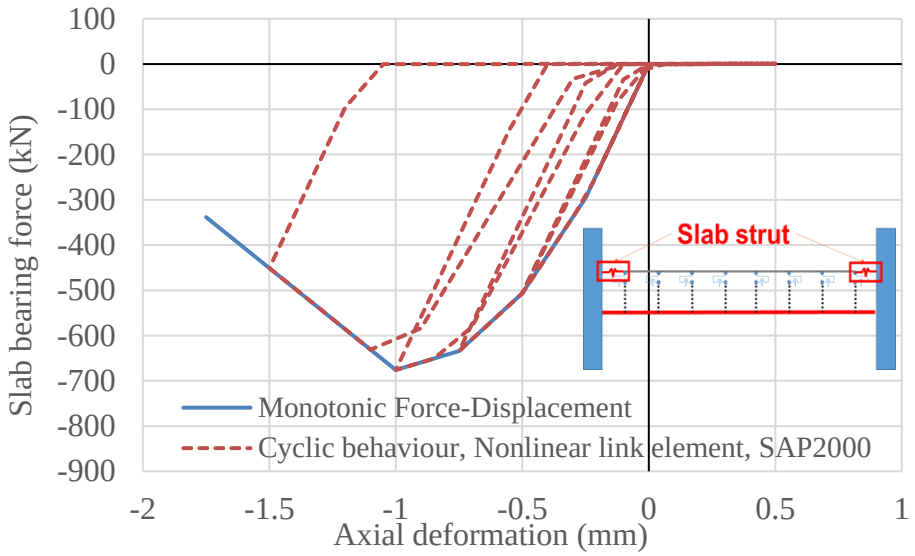

Figure 8-14. Slab-column bearing strut behaviour ($N_{slab} = 675$kN in this case)

Although the concrete strut considers the slab bearing effects, it has the following limitations:

1. Bending strength and stiffness of the slab are ignored
2. Force transfer along the column sides and within the shear key between column flanges are ignored
3. Effects of concrete reinforcement are ignored
4. The slab strut is located at the mid-height of the concrete topping thickness in this case, considering transverse decking direction

8.4 Nonlinear-static and NLTH analyses

8.4.1 Lateral force distribution between VLRF systems, NL-static analyses

Models 1-5, shown in Table 8-4, are considered to investigate the effect of diaphragm cracking and nonlinear behaviour of WSP connections and shear studs on the lateral force distribution between VLFR systems. Model 1 is the same as the selected model that was shown in Figure 8-4. The diaphragm in Model 1 is simulated using elastic shell elements considering

no reduction in stiffness due to concrete cracking. In Model 2 the diaphragm is modelled using elastic compression only diagonal truss element modelling method (Truss Model 2) that was described in Table 3.2. The effect of concrete cracking is also considered in Model 3 using the cracked compression only diagonal truss element modelling (Truss Model 3). The effects of considering WSP axial stiffness and shear stud stiffness are also considered in Models 4 and 5. In all models, it was assumed that a gap is provided around columns, and the composite beam effect was not considered. Note that the fundamental period of structures changed by less than 1% for Models 1-5 even though WSP axial and shear stud stiffnesses considered.

Table 8-4. Model details

	WSP axial stiffness	**Shear stud stiffness**	**Diaphragm modelling**
Model 1	Full*	Full*	Elastic shell
Model 2	Full*	Full*	C-only diagonal member, Diamond truss method (elastic)
Model 3	Full*	Full*	C-only diagonal member, Diamond truss method (cracked)
Model 4	Computed according to Section 8.3.4	Full*	C-only diagonal member, Diamond truss method (elastic)
Model 5	Computed according to Section 8.3.4	Computed according to Section 8.3.5	C-only diagonal member, Diamond truss method (elastic)
* The WSP axial stiffness and shear stud stiffness was considered infinitely stiff. Note: gap was provided around the columns and the slab was modelled at the beam centreline level without considering vertical offset.			

Figure 8-15 shows the base reaction forces of each frame of the models studied. These reaction forces are presented in Table 8-5 for Models 1-5. It can be seen that,

i) by decreasing diaphragm stiffness from elastic stiffness, Model 1, to cracked in-plane stiffness, Model 3, the reaction force on the braced frame decreased and transferred to moment resisting frames. Such that the moment frame base shear increased by 50% in Model 3 compared to Model 1.

ii) adding the beam-column connection axial behaviour based on Section 8.3.2, Model 4, the lateral stiffness of the braced frame decreased and lateral forces more transferred to the moment frames compared to Model 2.

iii) similar to Model 4, adding shear stud stiffness in Model 5, decreased diaphragm in-plane stiffness and caused more force to be transferred to moment frames compared to Model 2 and 4. This is because decreasing diaphragm stiffness caused lateral forces to be distributed more based on tributary area rather than the relative stiffness of VLFR systems as described in Appendix L.

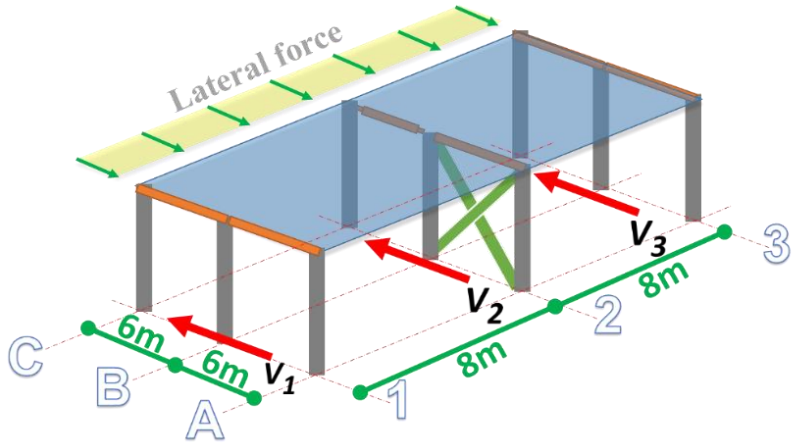

Figure 8-15. Reaction forces of each VLFR system

Table 8-5. Frame base shear of Models 1-5

	Frame base shears (kN)	
	V_2	V_1+V_3
Model 1, shell elastic	887.4	63
Model 2, truss elastic	882.9	67.5
Model 3, truss cracked	853	97.4
Model 4, truss elastic+WSP	881.4	69
Model 5, truss elastic+WSP+shear stud	868.4	82

8.4.2 WSP axial force and shear stud demands, NLTH analyses

The beam-column connection axial forces were obtained in the diaphragm design process of Model 1 presented in Appendix M. These beam-column connection axial forces are shown in Table 8-6 for the middle frame (braced frame), Frame 2. These values were obtained from diaphragm truss model without considering beam-column connection and shear stud stiffnesses. Here, Models 1, 4 and 5 above are investigated using NLTH analysis to compare

the WSP connection and shear stud demands obtained from more realistic Models 4 and 5 in comparison with the demands used in design, Appendix M.

Table 8-6. Maximum beam axial forces at the beam-column connections considering gap around the column, Frame 2, Model 1 static analysis

	Braced bay (kN)		**Pinned beam (kN)**	
Axis	A	B	B	C
Elastic diaphragm model	+408	+218	*+294*	+14
	-404	-138	*-214*	-14

In Model 4 only WSP connection behaviour is considered and in Model 5 both WSP connection and shear studs stiffnesses are modelled. In these models, it is assumed that the beam between axes B and C in the middle frame, Frame 2, is connected to the columns using WSP connections as shown in Figure 8-16.

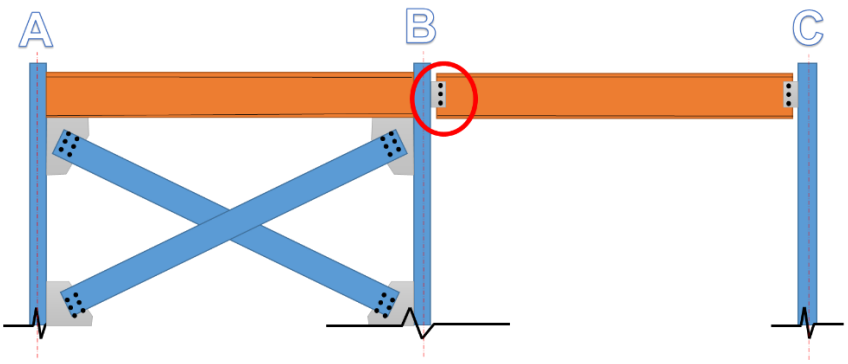

Figure 8-16. Frame 2 elevation, BC beam connected to the column using WSP connections

- **Model 1**

Figure 8-17a plots the beam-end axial force of Model 1 shown in Figure 8-16 by a red circle. The axial force demands obtained from NLTH analysis were larger than the static elastic analysis results by up to 35%. This is consistent with the results obtained in Chapter 7 for structures with low ductility. Figure 8-17b plots the shear stud demands on the beam B-C from NLTH analysis. In Appendix M it was shown that the maximum shear stud demand on this beam from the static elastic analysis was 308kN. Shear stud forces obtained from NLTH analysis were larger than the static elastic analysis results by up to 12%.

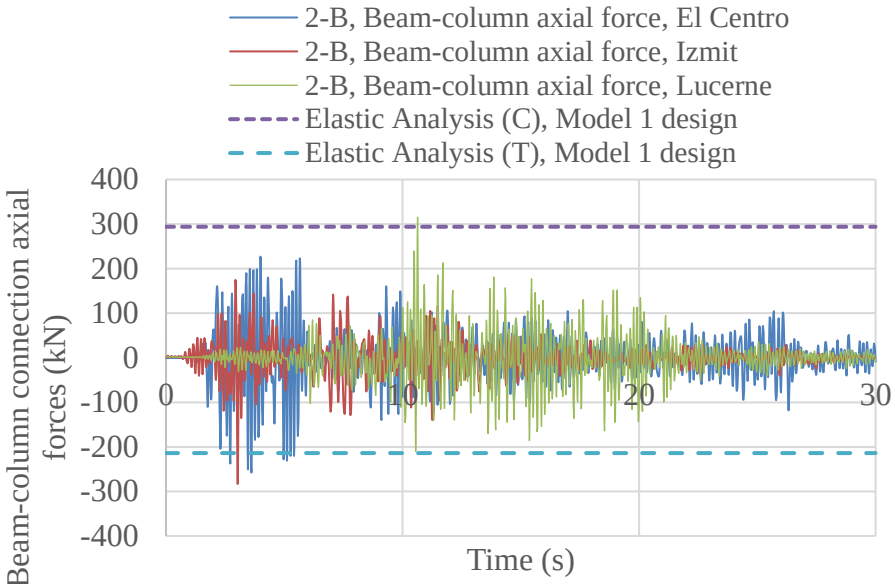

a) WSP axial force, connection B-C

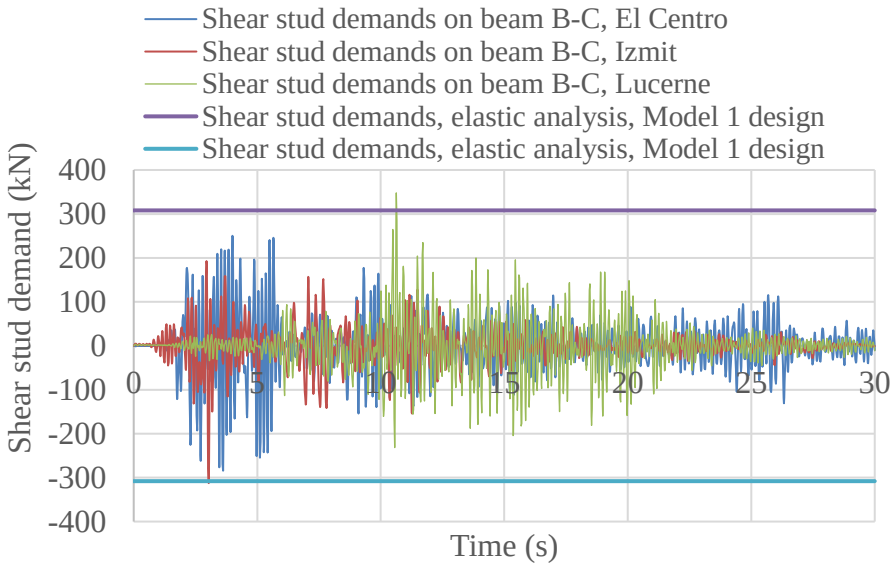

b) Shear stud demand of Model 1, beam B-C

Figure 8-17. Model 1 WSP and shear stud demands to 3 records

- **Model 4**

Figure 8-18 plots the beam-column connection axial forces and axial deformations for WSP connection of Model 4 shown in Figure 8-16 by a red circle. The axial force demands obtained from NLTH analysis shown in Figure 8-18 were about 20% lower than the elastic analysis results without considering beam-column connection axial stiffness. According to the

WSP axial forces and deformations obtained from NLTH analysis shown in Figure 8-18, no yielding was observed in the WSP connection.

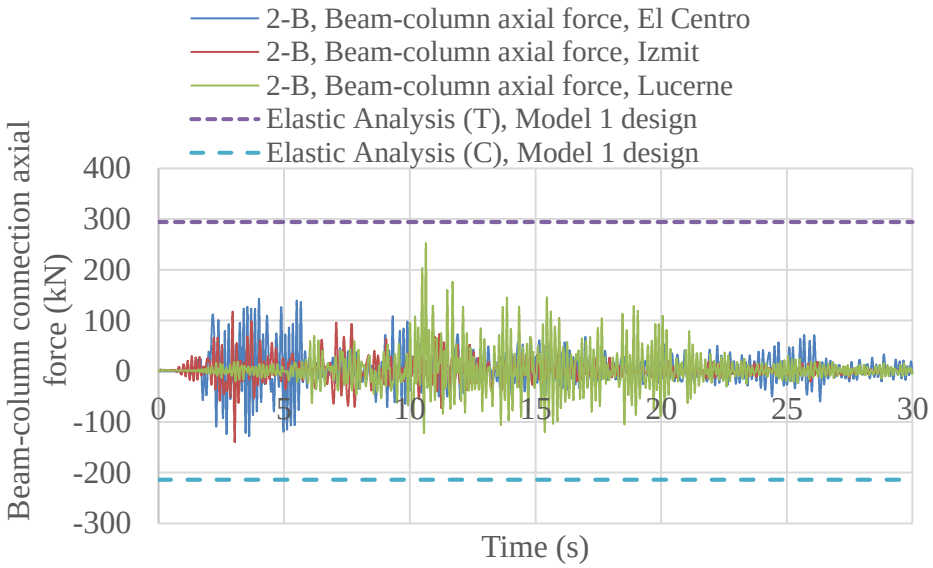

a) WSP axial force, connection B-C

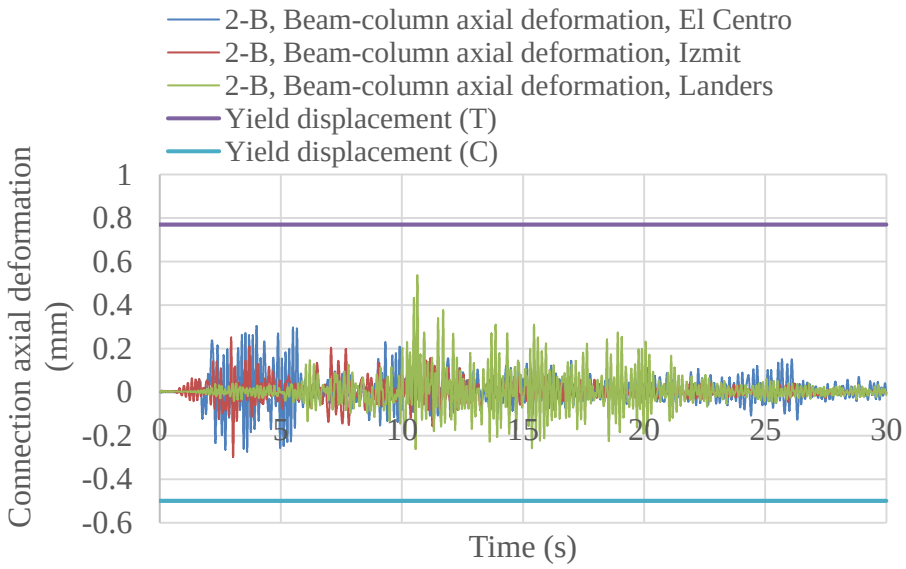

b) WSP axial deformation, connection B-C

Figure 8-18. Model 4 WSP demands to 3 records

Figure 8-19 plots the shear stud demands on the beam B-C from NLTH analysis. In Appendix M it was shown that the maximum shear stud demand on this beam from the elastic analysis was 308kN. NLTH analysis results reached about 97% of the calculated elastic value for the ground motions considered here. Note that shear studs were assumed infinitely stiff and strong in Model 4, and the effect of shear stud stiffness is considered in Model 5.

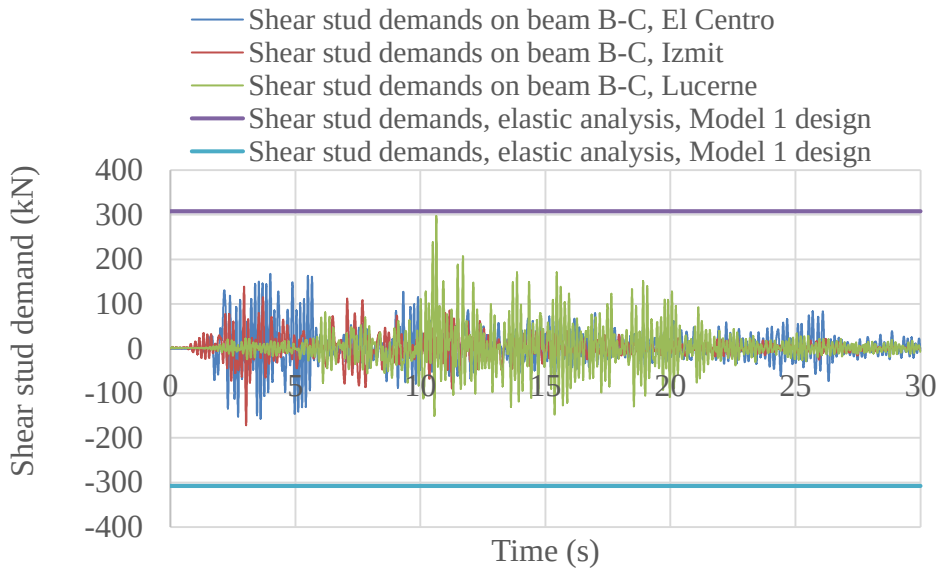

Figure 8-19. Shear stud demand of Model 4 obtained from NLTH and elastic analysis

- **Model 5**

Figure 8-20 plots the beam-column connection axial forces and axial deformations for WSP connection of Model 5 shown in Figure 8-16 by a red circle. The axial force demands obtained from NLTH analysis shown in Figure 8-20 were about 10% higher than the elastic analysis results without considering beam-column connection and shear stud stiffnesses. According to WSP axial forces and deformations obtained from NLTH analysis, no yielding was observed in the WSP connection. However, the axial force reached to about 96% of the connection yield strength.

The beam-column connection axial compression forces obtained from Model 5 showed an increase by up to 50% compared to Model 4. This is because of considering shear stud stiffness in this model. Modelling the shear studs decreased the total beam axial stiffness of both beams A-B and B-C because the shear studs and the beam axial behaviour are series springs. The stiffness and strength of shear studs placed on all beams were the same in Model 5. Therefore, the stiffness of beam A-B decreased more than beam B-C and more force transferred to the beam B-C.

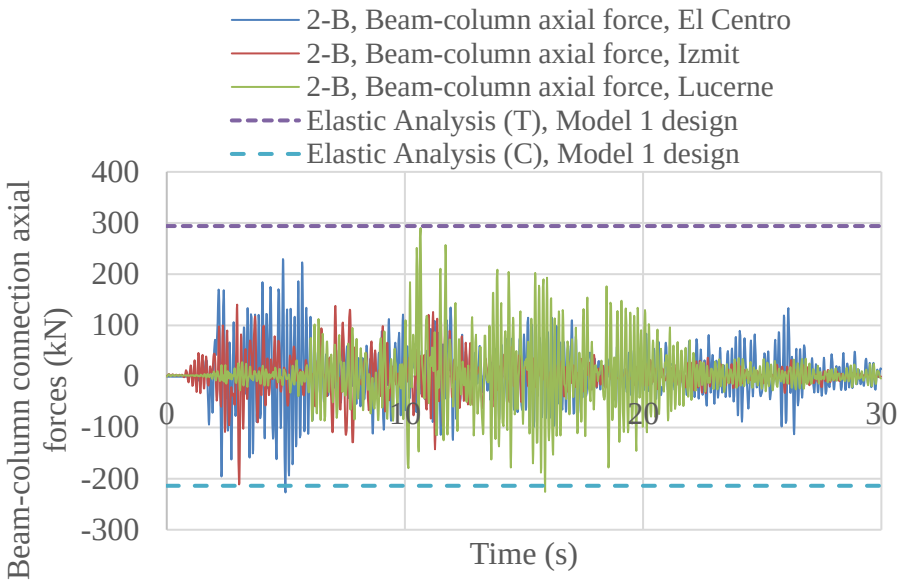

a) WSP axial force, connection B-C

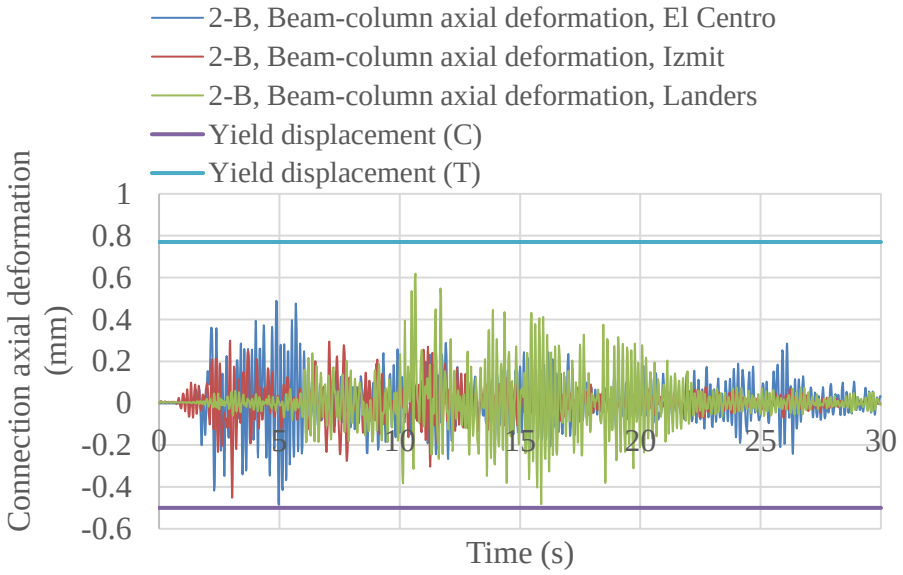

b) WSP axial deformation, connection B-C

Figure 8-20. Model 5 WSP demands to 3 records

Figure 8-21 plots the shear stud demands on the beam B-C of Model 5 from NLTH analysis. The maximum shear stud demand from the elastic analysis was 308kN for beam B-C and 622 for beam A-B in Appendix M. NLTH analysis results reached to about 6% higher demands than that obtained from the elastic analysis for the beam B-C. The maximum shear stud demand on Beam A-B obtained from NLTH analysis was 1008kN in Model 4 and decrease to 703kN in Model 5 (30% decrease).

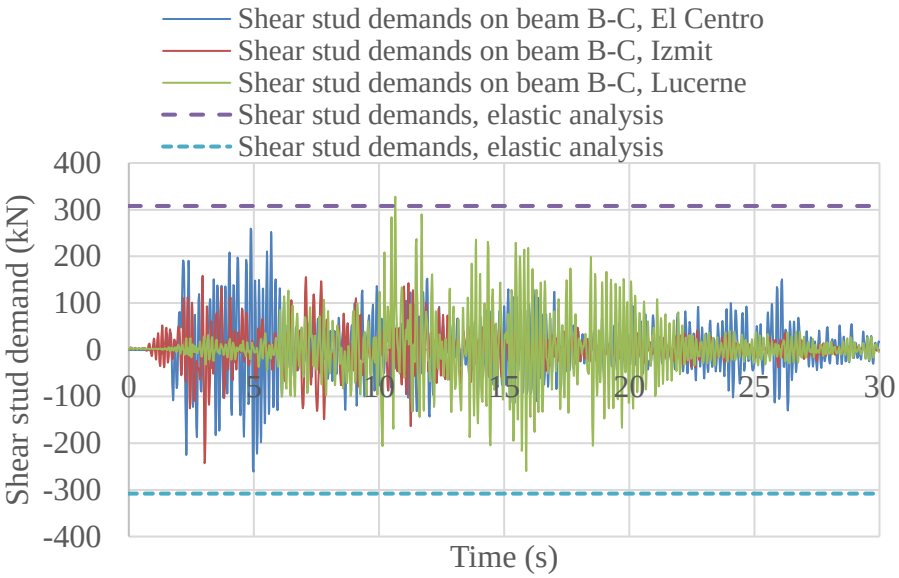

Figure 8-21. Shear stud demand of Model 5 obtained from NLTH and elastic analysis

Table 8-7 presents the peak connection axial and shear stud forces from NLTH. From this Table, it can be seen that considering the effect of beam-column connection axial stiffness in the analysis decreased the beam-column connection axial demand compared to the elastic model analysis without beam-column connection axial stiffness. This is because considering connection stiffness reduced the beam axial stiffness and lateral forces distributed to other stiffer elements/frames.

Also, it was found that when the beam-column connection and/or shear stud stiffnesses are not considered in the model, the beam axial forces and frame lateral forces may be overestimated or underestimated depending on their relative stiffness. Meanwhile, in some cases this may result in yielding some structural elements and cause force redistribution.

Table 8-7. Summary of peak connection axial and shear stud forces from NLTH and elastic static analyses

		Connection tension force (kN)	***Connection compression force (kN)***	***Shear stud demands (kN)***
	Design forces	294	-214	308
TH record 1, El Centro	Model 1	227	-258	284
	Model 4	142	-128	167
	Model 5	229	-227	261
TH record 2, Izmit	Model 1	175	-283	312
	Model 4	118	-139	171
	Model 5	140	-211	242
TH record 3, Lucerne	Model 1	315	-210	348
	Model 4	252	-122	297
	Model 5	290	-225	327

8.5 Load transfer from diaphragm to VLFR system

Lateral force transfer issue from diaphragm to the VLFR systems of structure was discussed in Chapter 2. Usually, buildings have a limited number of lateral force resisting frames, which are designed to carry horizontal forces from the diaphragms to the foundation. These horizontal forces could either

i. be transferred only through the seismic frame beams or

ii. be transferred through beams in gravity frames (collectors) as well as the seismic frames.

In the first case, forces on the diaphragm, including inertial and transfer forces, are transferred to the seismic beam via shear studs on the beam. For this mechanism, with force only considered to be transferred into the seismic frame(s), sufficient shear studs should only be placed on the seismic beam and ensuring that the beam, and its connections, can transfer the axial forces induced into the columns. Also, the ability of gravity beams lateral force transfer should be limited. This may be achieved by ensuring that there are no shear studs on the gravity beams and reducing the friction between the top of these gravity beams and the diaphragm.

In the second case, when the composite action of the gravity beams is desired and shear studs are placed on these beams, these beams and their connections need to be designed for the expected axial forces from diaphragm. In this case, strut-and-tie mechanism with reinforcing steel perpendicular to all beams is required.

When design is conducted assuming the seismic beams carry all horizontal forces from the diaphragm (including those from inertial and transfer effects), yet shear connectors are placed on the gravity beams, axial force demands in the gravity beam connections may be greater than their axial strength, and this may result in beam/connection yielding and in some cases failure/collapse.

8.5.1 Case study

In this section, Model 5 that was introduced in Section 8.4 is considered to investigate a case when beams in the gravity frames are not designed to carry lateral forces while having shear studs to take the advantages of the composite action to carry gravity loads. Different number of gravity bays connected to the seismic frame is considered, as shown in Figure 8-22, to increase the diaphragm in-plane forces that need to be transferred to the braced frame.

The axial behaviour of the WSP connections is defined according to Section 8.3.4 using the axial strengths obtained in Appendix M (234kN compression and 361kN tension). In all models, enough shear studs to carry total diaphragm lateral force are provided on the braced bay beam, 2-AB in Figure 8-5. Note that in these models yielding of slab reinforcements is considered in defining the orthogonal truss members' behaviour.

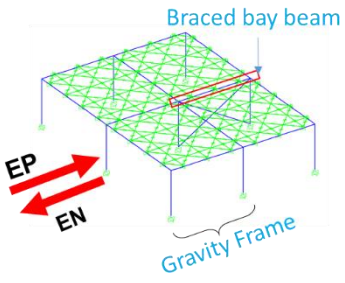

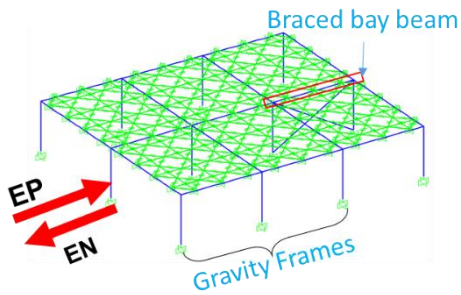

a) Model 5 with one gravity bay

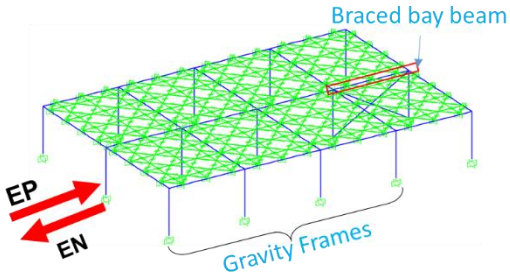

b) Model 5 with two gravity bays

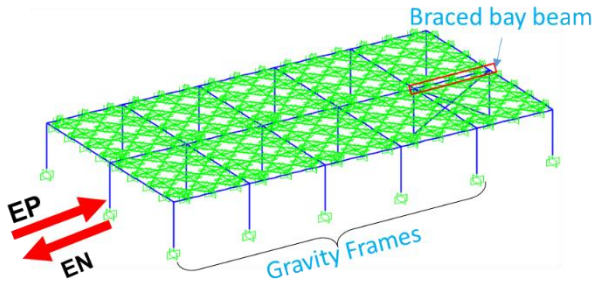

c) Model 5 with three gravity bays

d) Model 5 with four gravity bays

Figure 8-22. Models with different number of gravity bays

These models are investigated under nonlinear static analysis. The maximum tension and compression forces and deformations of the WSP connection located on the 2-B axis of each model, shown in Figure 8-16, are obtained. Table 8-8 presents the analyses results for these models. As can be seen, the axial force and deformation demands on WSP connections increased with increasing the number of gravity bays. In models with three and four gravity bays, the axial tensile deformation of the WSP connections under negative earthquake force, EN, exceeded its maximum tensile deformation capacity, 6mm in this case. This means these connections fractured in tension. For the positive earthquake force, EP, the WSP connections yielded in models with three and four gravity bays, however, their maximum deformation did not reach to the axial fracture deformation.

Table 8-8. WSP axial force and deformations obtained from analyses

	EP		***EN***	
	Axial compression deformation (kN)	Axial compression force (mm)	Axial tension deformation (mm)	Axial tension force (kN)
Model 5 with one gravity bay	-0.22	104	0.45	215
Model 5 with two gravity bays	-0.37	175	4.66	361
Model 5 with three gravity bays	-0.83	234	**16.22**	361
Model 5 with four gravity bays	-0.84	234	**19.32**	361

The difference observed between the axial deformation demands of WSP connections shown in Table 8-8 is because of the in-plane behaviour and load transfer mechanism of the slab. For the positive earthquake direction, EP, The deformation of these WSP connections are subject to and is limited by the deformations of the diaphragm and shear studs on the seismic frame beams. Therefore, the diaphragm forces were transferred to the braced frame through compression struts in the slab and axial forces in the WSP connections as shown in Figure 8-23a. As the compression concrete struts were stiffer than the WSP connection axial stiffness, most of the in-plane force was transferred through these struts and the axial deformation of the WSP connection was limited to the axial deformation of the concrete struts. In the negative earthquake direction, EN, the diaphragm in-plane forces transferred to the braced bay using tension ties (slab reinforcements) and collector beams (WSP connections). Therefore, increasing the number of bays increased the reinforcement axial demands and caused yielding in reinforcements causing high axial tension demands in the WSP connections as shown in Figure 8-23b.

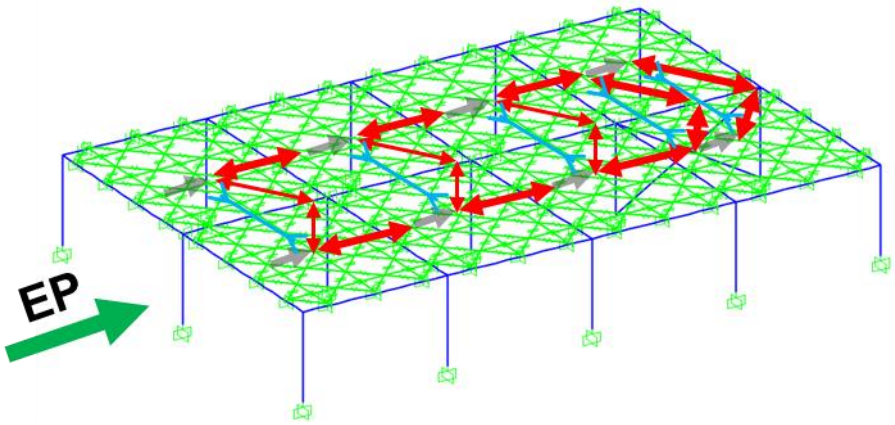

a) Positive earthquake direction

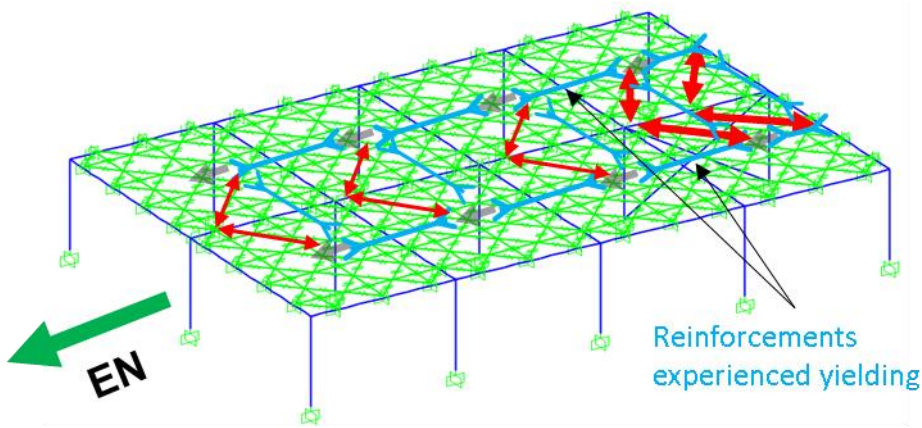

b) Negative earthquake direction

Figure 8-23. Likely strut and tie formed in diaphragm with three gravity bays

This issue may be mitigated by putting more reinforcements in the slab. However the reinforcement ratio cannot be increased more than a certain value as it may cause other problems for the slab such as concrete delamination. In this study, it is suggested to design WSP connections for likely axial forces obtained from elastic analysis to avoid yielding or failure of these connections under the expected level of earthquake. In Section 8.4.2 it was shown that the axial forces obtained from elastic design analysis were higher than those from the more detailed nonlinear analysis because of considering the axial flexibility of the WSP connection. Therefore designing the WSP connection axial behaviour for forces obtained from the elastic analysis may provide conservative results and prevent undesirable failure in these connections under the expected level of earthquake.

8.6 Gapping effect

The concrete slabs in steel frame structures are often cast without providing any gap around the columns. Based on the current NZ design approach in NZS 3404 (2007), structural steel beams are designed for earthquake-induced forces without considering the slab effects. This is because the top of the slab is unconfined and the beam composite strength degrades to the bare beam strength due to concrete failure/crushing (Chaudhari et al. 2015). However, the NZ design approach (NZS 3404, 2007) states that columns and connections are required to be

designed to resist beam over-strength actions considering slab effects. The NZ standard therefore considers the most conservative scenario by (a) ignoring the strength increase from the slab in design of the beam to resist the seismic loads in a force-based design, and (b) considering its effect when determining the over-strength actions at the column and beam-column connection from the inelastically responding composite beams.

Another approach is not to consider the slab effects either for the beam design or for columns and connections design. This may be conducted by isolating the column, and the elements connected to it, from the slab (MacRae and Clifton, 2015a). The slab can be separated from the column using a fire-proof material or a diamond gap cut all around the column as shown in Figure 8-24.

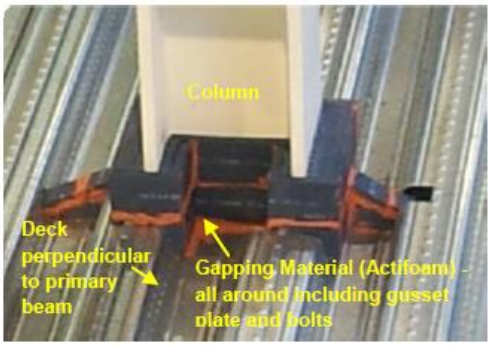

a) Gap around the column (Chaudhari et al. 2015)

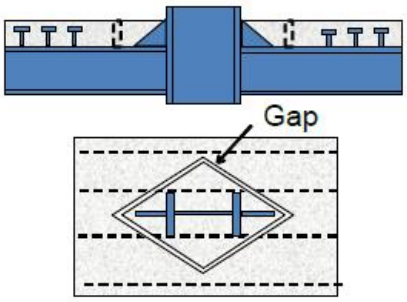

b) Gap within the slab (MacRae and Clifton, 2015b)

Figure 8-24. Gapping around column

Chaudhari et al. (2015) indicate that gapping around column

1) eliminates the slab effect on beam over-strength, resulting in smaller columns,
2) reduces slab damage and strength degradation
3) has the possibility of reducing ratcheting where the structure tends to yield predominantly in one direction because the same strength is in each direction of loading (MacRae and Clifton, 2015b), and
4) decreases beam/connection axial forces.

The disadvantages of gapping may be

1) Increasing the chance of column instability by twisting due to having no slab to restrain it, such instability has been seen in columns with beams tested with reduced beam sections by Chi and Uang (2002).
2) The initial stiffness and strength of the structure decrease (in the first cycle) so the period increases and the structure is likely to have greater displacements (MacRae and Clifton, 2015b).
3) Gap installation costs may be significant (MacRae and Bull, 2015).

8.6.1 Gapping/no gapping forces

Whether gaps are provided between the slab and column or not, diaphragm forces are more likely to be transferred to the column through the beam axial forces at least on the hogging side of the beam. This is because it is assumed that as the frame sways, a gap opens between the concrete slab and the column and diaphragm forces need to be transferred through the shear stud to the beam and from the beam to the column. Also, on the far side of the beam, the column bears against the slab and impose additional force to the slab that needs to be transferred back to the column through the beam.

These bearing forces were observed in Chaudhari (2017) experimental tests that the column bears against the slab and impose additional forces to the beam. A similar observation was made by Astaneh et al. (2002) which investigated the seismic behaviour of WSP connections supporting floor slabs. Figure 8-25 shows one of the specimens investigated by Astaneh et al. (2002) and the cleat plate fracture due to the column rotation and axial tension forces at the end of the test.

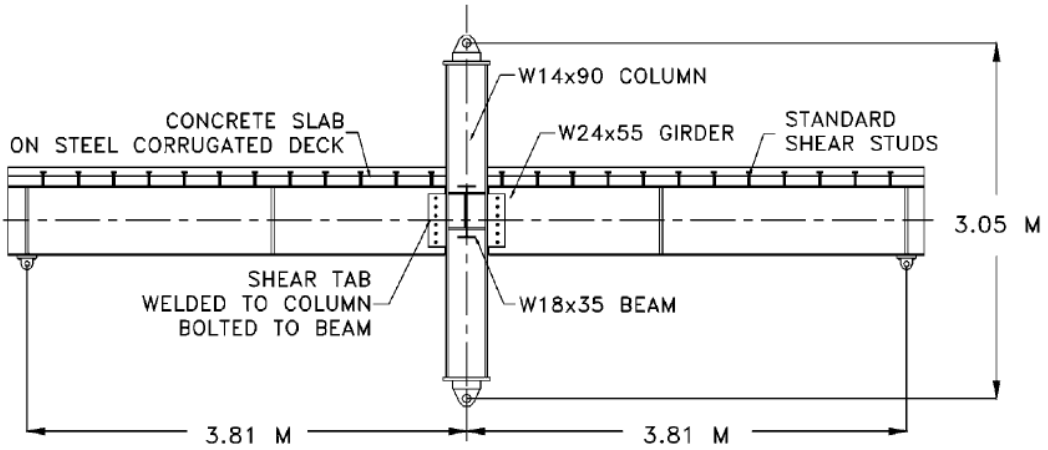

a) Elevation of a specimen with slab, (Astaneh et al. 2002)

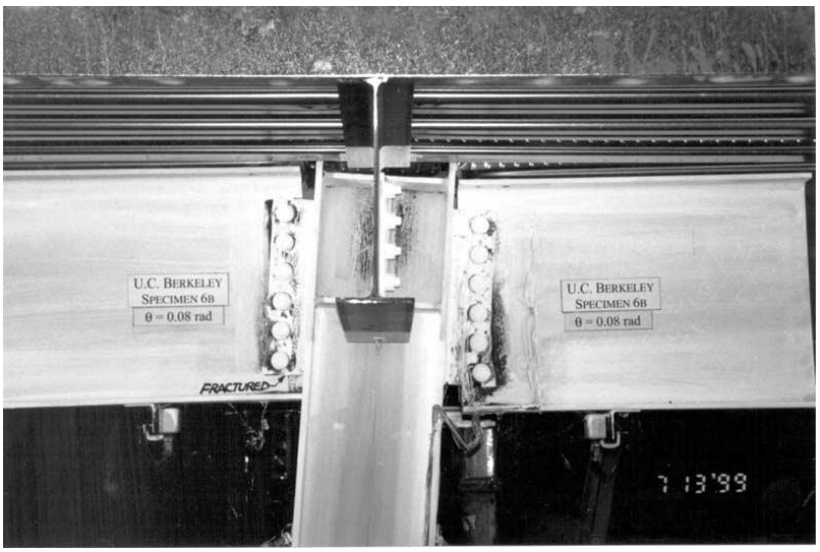

b) Fracture of cleat plate for 6-bolt specimen, (Astaneh et al. 2002)

Figure 8-25. Specimen tested by Astaneh et al. (2002)

Note that the slab bearing forces in Chaudhari (2017) and Astaneh et al. (2002) experiments were obtained using reversed cyclic loading tests that the lateral forces were applied at the column/beam ends. However, in an earthquake event, lateral forces are mainly caused by diaphragm accelerations and are applied to the diaphragms not to column/beam ends. Therefore, shear stud flexibility and possible lateral movements of the diaphragm are not considered in the tests. The diaphragm in-plane movements may increase or decrease the slab bearing effects. According to the above discussion, the gap opening issue and slab bearing forces can be investigated in two scenarios depending on the relative lateral deformation of the frame and diaphragm force direction.

1. Inertia forces govern diaphragm in-plane demands
2. Transfer forces govern diaphragm in-plane demands

8.6.1.1 Inertia forces govern diaphragm in-plane demands

Figure 8-26 shows the condition that inertia forces govern diaphragm in-plane demands schematically. The slab bearing force (on the left-hand side) and gap opening (on the right-hand side of the beam) depend on the relative stiffness of shear studs and storey stiffness. Such that when the shear stud deformation, δ_s, is larger than the column lateral deformation due to storey drift, δ_c, the slab bears against the column on the left hand side, as shown in Figure 8-26b, and a part of diaphragm in-plane forces may be transferred to the column through slab bearing. This means that slab-column bearing forces on the right hand side of the beam decrease, and some slab force is transferred directly to the column on the beam left hand side. Note that if the shear stud slip δ_s is greater than the lateral shear stud slip capacity calculated in Chapter 5 considering gravity load effects, the shear stud fracture may occur.

When the column lateral displacement, δ_c, on the beam hogging side is greater than the slab lateral movement, δ_s, in the same direction, then the slab bears against the column face on the right hand side shown in Figure 8-26b. Therefore, additional diaphragm in-plane force may be imposed on the diaphragm from the right hand column thereby increasing both shear stud and right hand side beam-column connection demands.

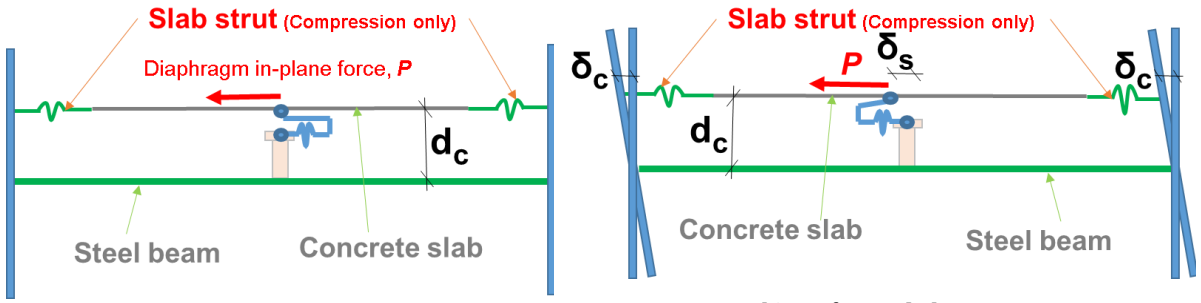

a) Un-deformed shape b) Deformed shape

Figure 8-26. Lateral deformation of slab and columns subject to lateral forces

8.6.1.2 Transfer forces govern diaphragm in-plane demands

In the second scenario where transfer forces govern diaphragm in-plane demands, lateral forces are mostly applied to the diaphragm from deformation incompatibility of different VLFR systems (transfer forces). Figure 8-27 shows a dual VLFR system structure with shear wall and moment resisting frame under lateral forces. The in-plane forces imposed on the diaphragms at the first and top floors are presented schematically. It is shown that at the lower storeys, the diaphragm in-plane force transferred to the frames is opposite to the frame lateral deformation. While at the upper floors the diaphragm in-plane force transferred to the frames is in the same direction as frame lateral deformation. These are shown in Figure 8-27c and d.

As can be seen in Figure 8-27c, in the lower floors a gap opens on the right-hand side of the beam, and slab bears against the column on the left. Since the slab in-plane forces are in the opposite direction, they may help to reduce beam-column connection tension forces. For the upper floors, the slab in-plane forces are in the same direction as the frame deformation and it is similar to the condition that only inertia forces govern the diaphragm in-plane demands.

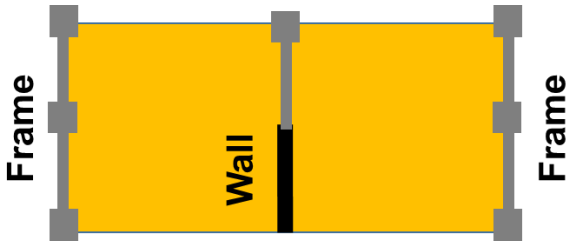

a) Floor plan

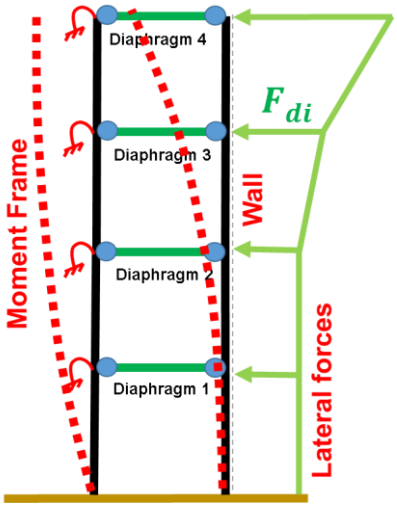

b) Lateral forces and shear wall/moment frame deformed shapes

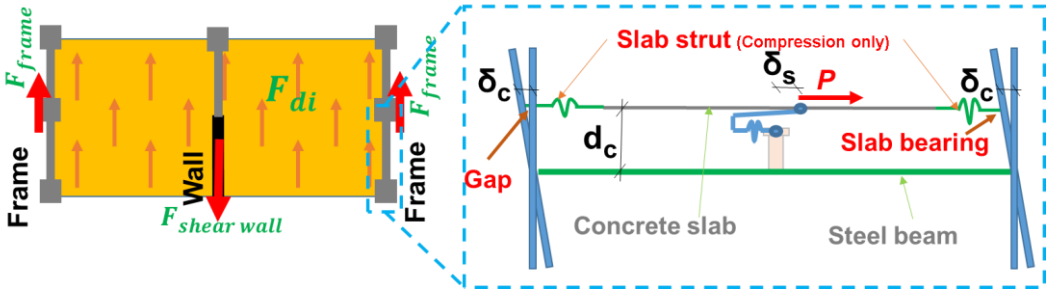

c) First floor, Diaphragm 1, lateral forces and deformations

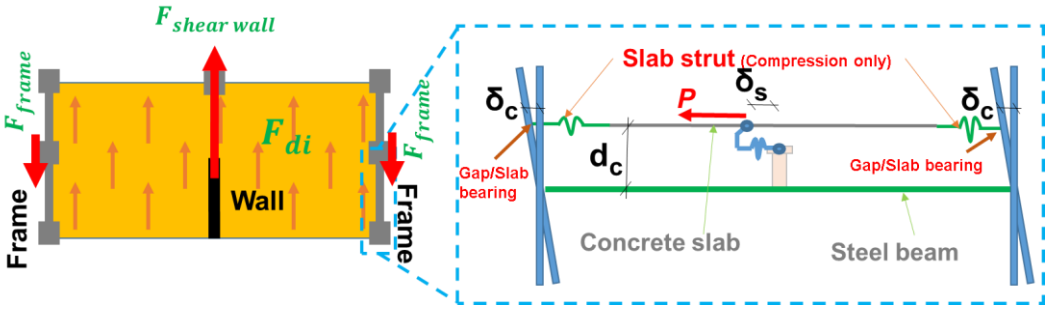

d) Fourth floor, Diaphragm 4, lateral forces and deformations

Figure 8-27. Gap opening properties in dual type structure system

8.6.2 FE modelling of gapping effect

Two FE truss models are created to investigate the gapping effect on beam-column connection axial force and shear stud demands. Diaphragms in these models are simulated using one truss mesh unit per bay for simplicity. In Model 6, a gap is provided around the columns. In the diagonal truss modelling method a gap is considered around the columns due to the configuration of truss elements by default as was discussed in Chapter 3. An additional compression-only truss element can be used to consider slab-column interaction in such a slab-offset model as described in Section 8.3.6. This is conducted in Model 7 where the concrete slab is placed on top of the steel beams with an offset equal to $d_c = \frac{d_{beam}+t_{slab}}{2}$ as shown in Figure 8-13.

Figure 8-28 shows the beam axial forces and slab-column bearing forces on frame 2 (Figure 8-4) for Models 6 and 7. In Model 6 shown in Figure 8-28a all diaphragm in-plane forces transferred through beam axial force, however, in Model 7, some diaphragm in-plane force transferred through the bearing of the slab against the column. This decreased the shear

stud and beam axial force demands. In this case the shear stud deformation, δ_s, is larger than the column lateral deformation due to storey drift, δ_c, and the slab bears against the column on the left hand side shown in Figure 8-28b.

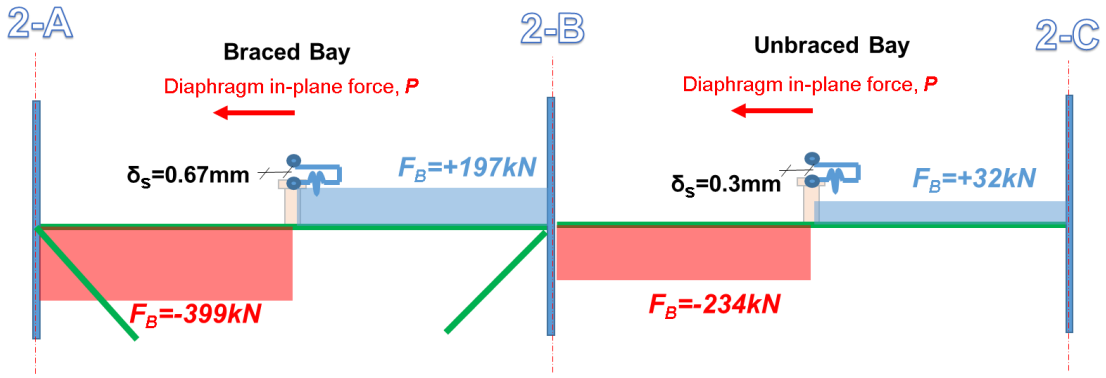

a) Model 6, (gap provided)

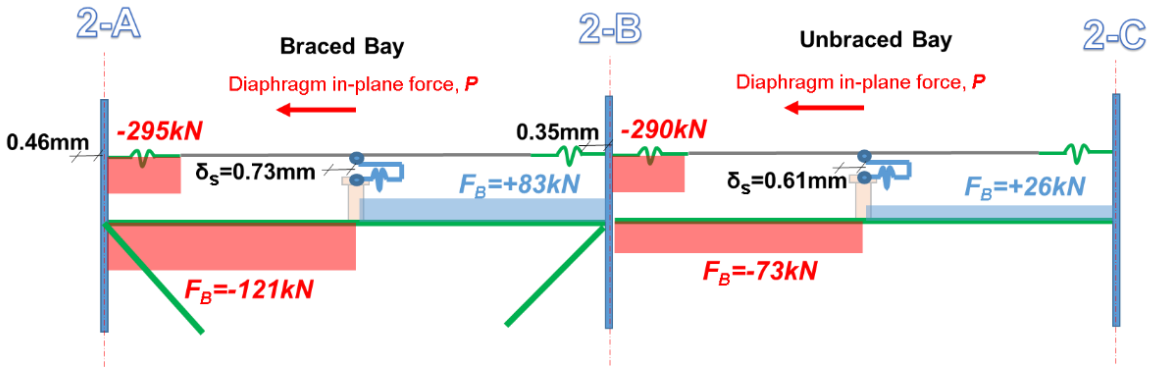

b) Model 7, (without gap)

Figure 8-28. Beam axial force, F_B, and shear stud displacements, δ_s, with and without slab-column gap

Another case was also considered where the brace area was reduced to zero. This decreased the storey stiffness, and all three frames in the structure (Frames 1, 2 and 3 in Figure 8-4) had the same member sizes. It is noted that some transfer forces still exist as the tributary area to stiffness ratio for frames 1 and 3 is lower than it is for frame 2. Figure 8-29 shows the axial force diagram for no gapping. This is referred to as Model 7-1. It can be seen that slab bearing forces were on the beam right-hand side, while they were on the left-hand side in Figure 8-28b. Also, the tension on the right-hand side of beams in both bays increased significantly causing

a significant increase in beam connection demands. The beam-column connections on the beam 2-BC, are yielded under axial forces and limited the slab bearing force on this beam.

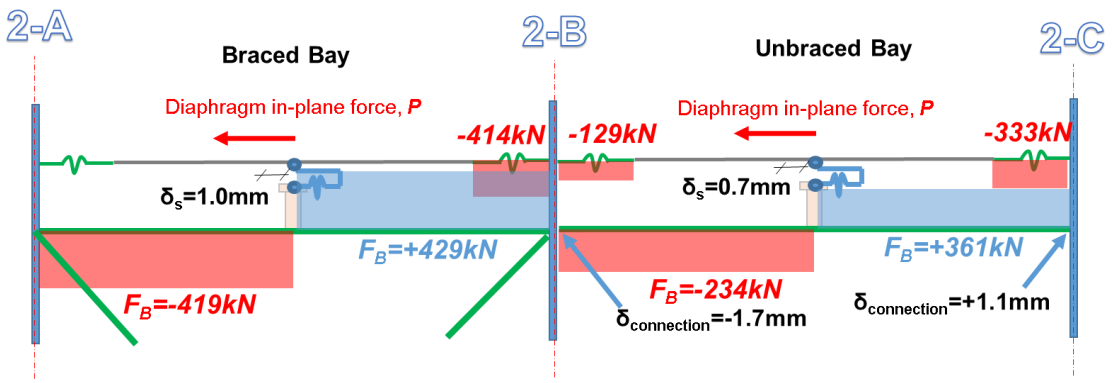

Figure 8-29. Beam axial force, F_B, and shear stud displacements, δ_s, without slab-column gap

From the above discussion and modelling, it is recommended that a gap be provided around the columns to prevent large axial forces due to slab bearing on the beam-column connection. It is noted that diaphragm in-plane forces should be transferred to the VLFR system through beam axial forces. Therefore, most diaphragm in-plane forces need to be transferred to the VLFR systems using shear studs. The full load path should be considered as well as the possibility of shear stud yielding which decreases composite action. In this case, loss of composite action should be considered in design using recommendations provided in Chapter 5 and the beam should be designed to carry gravity loads without composite action. Design steps, given in Figure 8-1, are applied to an example given in Appendix M.

When the gap is not provided around the column the slab bearing force in Clause 12.10.2.4 of NZS3404 (2007) is calculated based on the minimum of the concrete bearing capacity and the steel beam axial strength. However, for gravity beams, the sum of the beam-column connection tension and compression strengths should be used as a limiting case in this equation.

8.7 Composite beam vertical deflection

In Chapter 5 it was shown that diaphragm in-plane forces may cause yielding in shear studs on the steel beams. Shear stud yielding eliminates shear flow between the concrete slab

and the steel beam, causing loss of composite action. Here, Model 8, is created considering composite beam effects (offsetting the concrete slab from the steel beam) to study composite beam vertical deflection under earthquake loading using NLTH analysis. Also, different parameters such as composite action level and lateral force magnitude on the composite beam behaviour are studied. These are achieved by changing the shear stud strength representing different composite action levels and increasing the number of bays to increase diaphragm in-plane demands.

8.7.1 Modelling

The vertical deflection of the beam mid-point at the braced bay (beam 2-AB) and shear stud forces obtained from NLTH analysis are shown in Figure 8-30. This beam was designed considering 25% composite action. The total lateral strength of shear stud on the beam was calculated using the proposed method in Chapter 5 equal to the sum of all shear stud strengths in this case. The total lateral force strength of shear studs on the braced bay (25% composite action) was assumed to be 1100kN.

As can be seen from Figure 8-30a, vertical deflection of the beam mid-point increased from 9.8mm to about 10.9mm at the end of the analysis. This is about an 11% increase in the initial vertical deflection under gravity loads. The maximum shear stud demands from NLTH analysis was about 600kN as shown in Figure 8-30b. This is about 54% of the total shear stud lateral strength. This is consistent with the design recommendation provided in Chapter 5 to design beams in low-damage structures; which was recommended that if the lateral shear force demand on shear studs of a composite beam is limited to 50% of the shear studs lateral strength, the beam mid-point vertical deflection may not increase by more than 10% under lateral loading. It is also noted that for larger earthquakes, further beam deflection could occur.

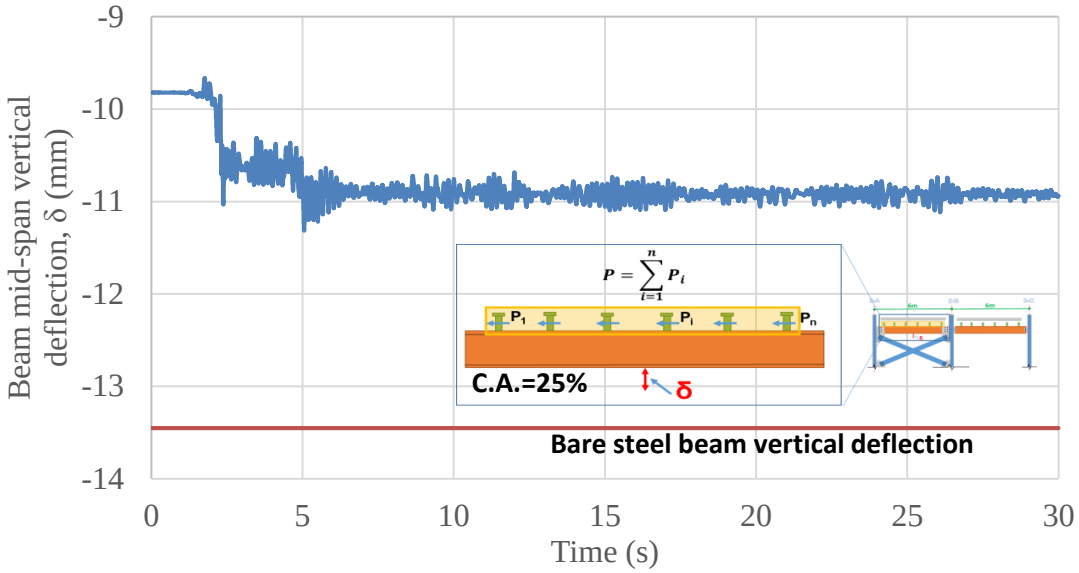

a) Beam mid-point vertical deflection

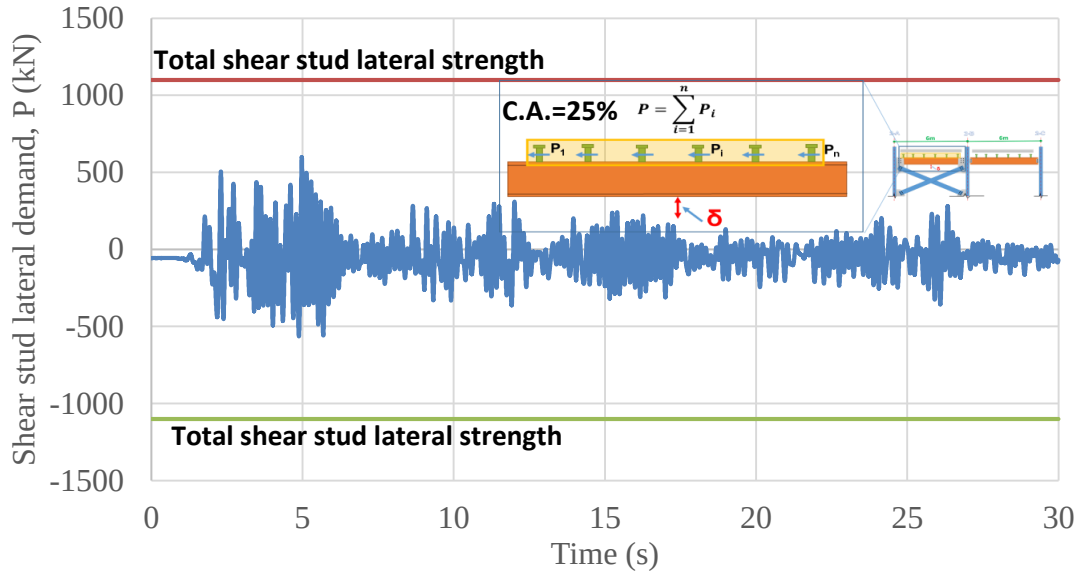

b) Shear stud demands

Figure 8-30. Beam mid-point vertical deflection and shear stud demand, Model 8 with 25% composite action (record: El Centro 1940)

In order to investigate the effect of composite action level, Model 8 was analysed considering 100% composite action. Figure 8-31 shows the beam mid-point vertical deflection and shear stud lateral force demand. As can be seen in Figure 8-31b, maximum shear stud demand is limited to 15% of the total shear studs strength, and no residual deformation was obtained at the beam mid-span. This is because the lateral forces did not cause yielding in any shear stud.

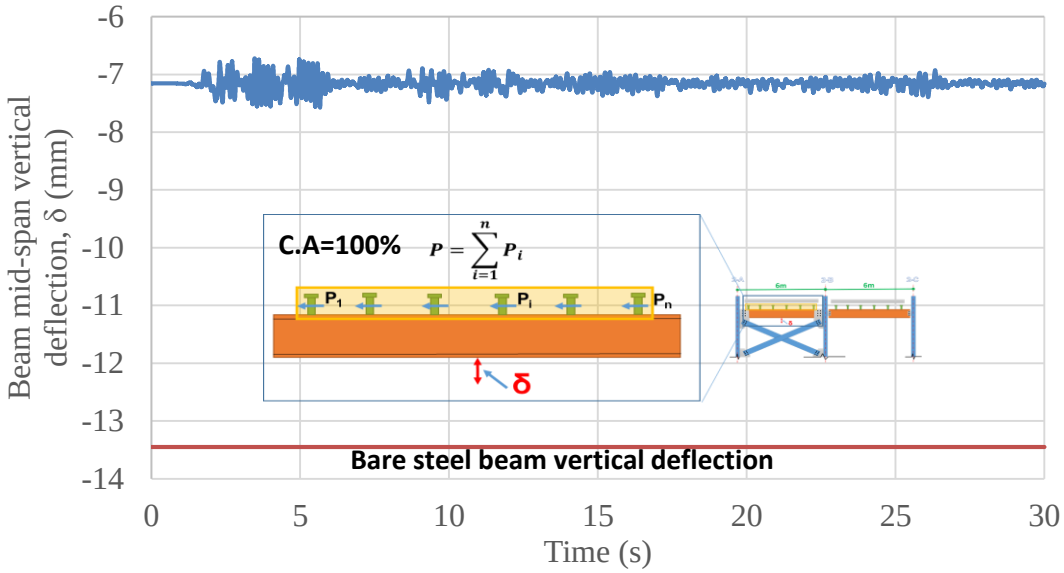

a) Beam mid-point vertical deflection

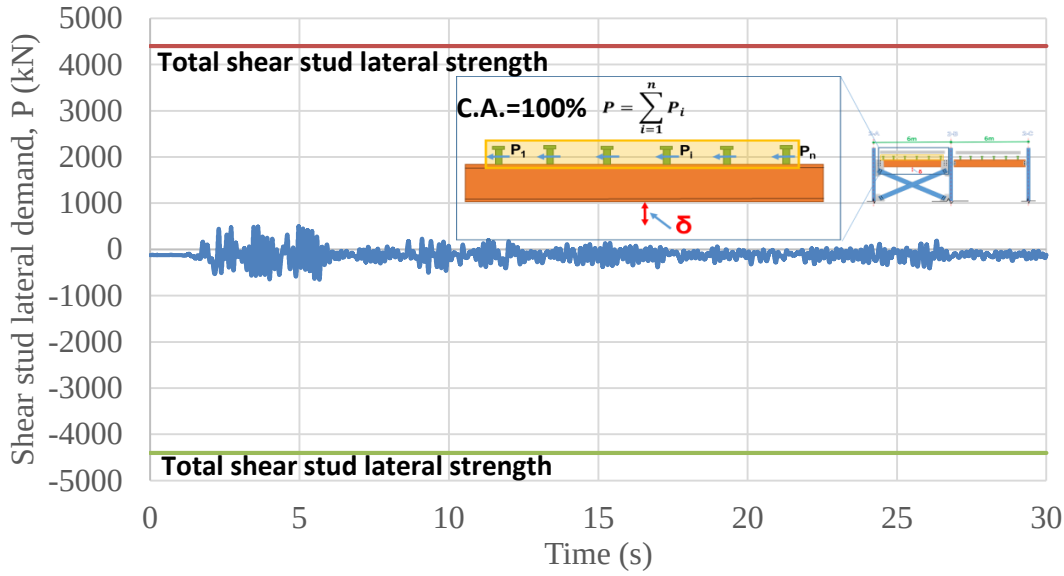

b) Shear stud demands

Figure 8-31. Beam mid-point vertical deflection and shear stud demand, Model 8 with 100% composite action (record: El Centro 1940)

In another model, the number of bays was increased and the shear studs on the beams of gravity frames were removed to transfer all the lateral forces to the shear studs on the beam in the braced bay, 2-AB, as shown in Figure 8-32. This beam was designed considering 50% composite action.

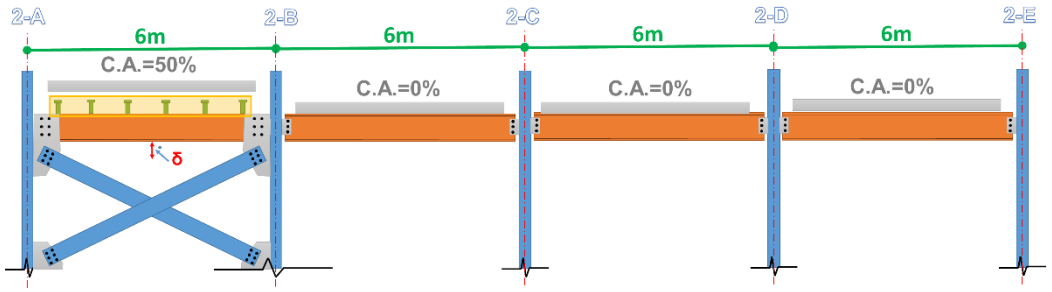

Figure 8-32. Model 8 with multiple bays, 50% composite action for beam between axis 2-AB

In this case, shear studs yielded under lateral loading as shown in Figure 8-33. At about a time of 2.5s into the record, shear studs reached the total lateral force resistance and at the same time, the beam mid-point vertical deflection reached to the bare steel beam deflection. After this point, some of the beam vertical deflection was recovered. The vertical deflection of the beam mid-point increased from 8.5mm to about 10.9mm at the end of the analysis, which is about 28% increase in the initial vertical deflection under gravity loads.

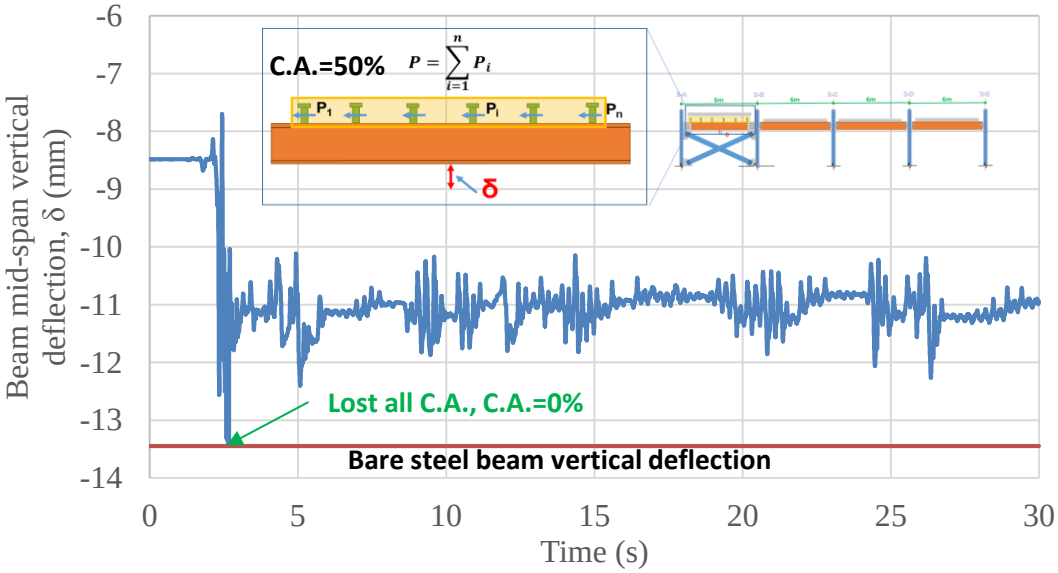

a) Beam mid-point vertical deflection

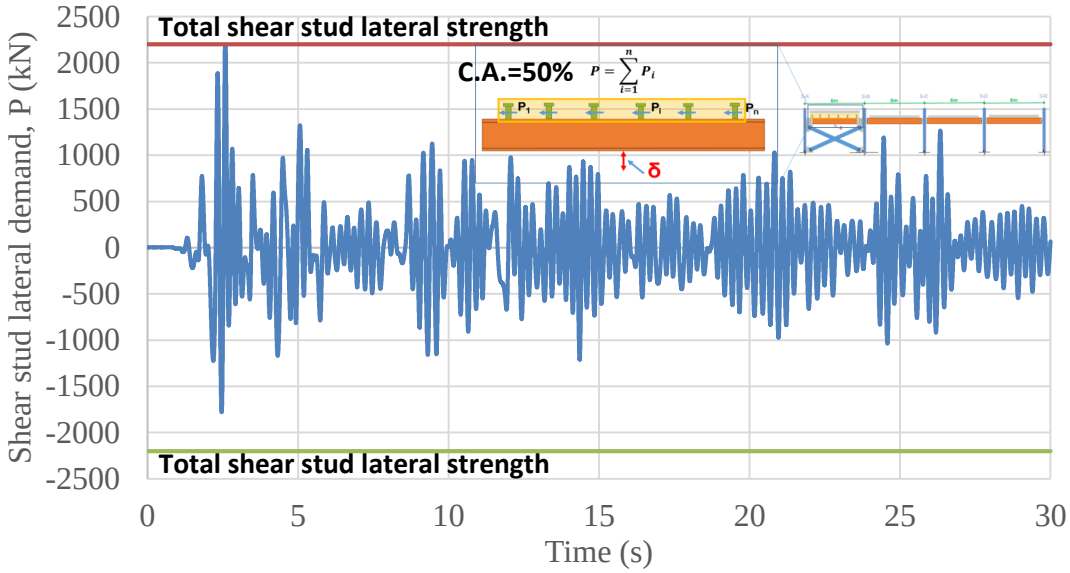

b) Shear stud demands

Figure 8-33. Beam mid-point vertical deflection and shear stud demand, Model 8 with 50% composite action and multiple bays (record: El Centro 1940)

The reason for recovering a part of the beam vertical deflection as was shown in Figure 8-33a, may be due to the level of lateral slip that each shear stud experiences on different locations of the beam. Figure 8-34a shows a schematic composite beam subjected to gravity and lateral forces and the location of shear studs ($3L - 3R$). The lateral force is assumed to be initially to the left, causing all studs to yield (Figure 8-34c). The positions of shear studs on the shear force-slip plot are shown with $3L - 3R$ points. When the direction of imposed in-plane force changes, unloading occurs, and with a force to the right, each shear stud follows the unloading path corresponding to the level of slip experienced. Therefore, the shear stud with the lowest slip, $3R$, will reach to higher shear force level, as shown in Figure 8-34d. The shear stud, $3L$, with the highest slip in Figure 8-34c will have the lowest force level as shown in Figure 8-34d. Figure 8-34e shows the shear forces imposed to the beam top flange from shear studs, and the beam moment diagram corresponding to that. This shows that the resulting imposed moment from shear studs to the beam is opposite to the moment due to gravity loads and may decrease the beam vertical deflection and recover some of the vertical deflection caused by loss of composite action.

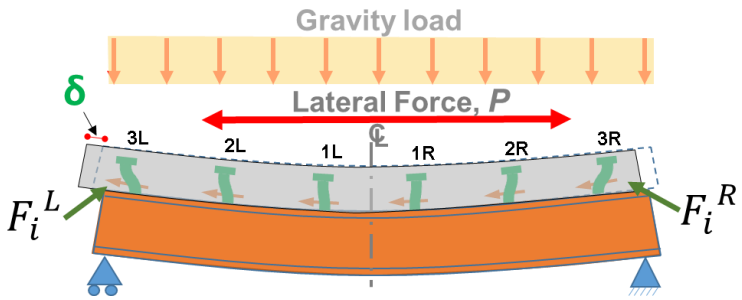

a) Shear stud, labelling, deformations under gravity and lateral forces

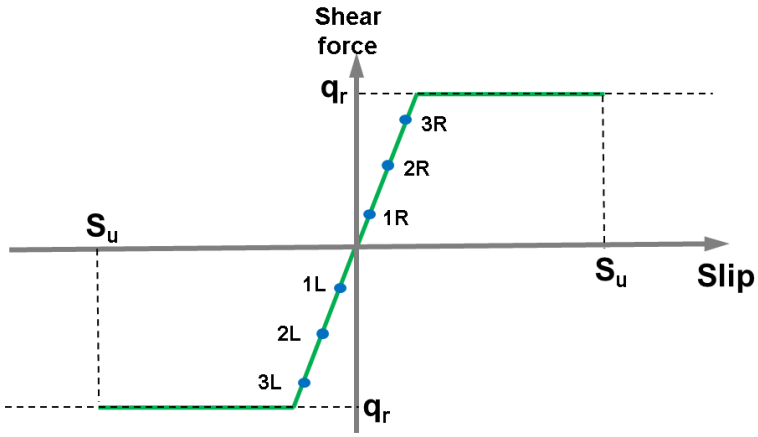

b) Shear stud forces under gravity loads

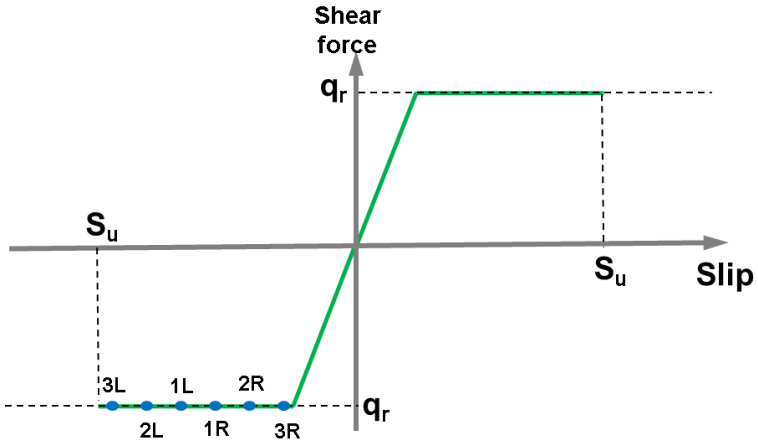

c) Shear stud forces under gravity and lateral force to the left

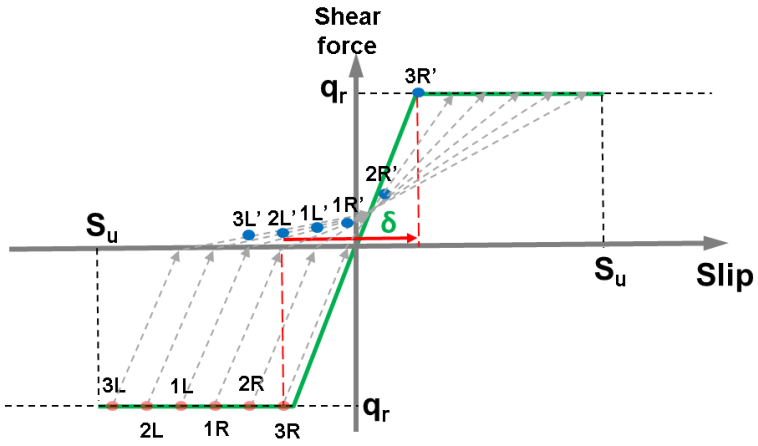

d) Shear stud forces after unloading and a small loading to the right

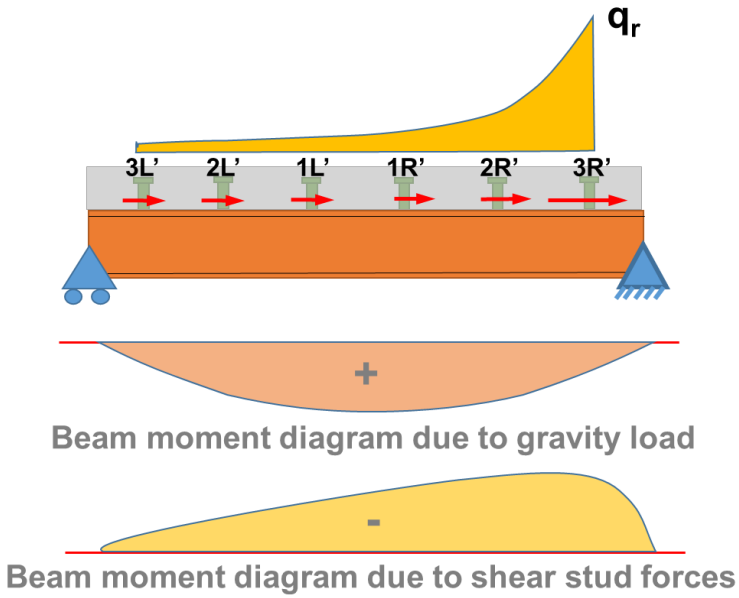

e) Shear stud forces on beam top flange from Figure 8-34d and the corresponding moment diagram

Figure 8-34. Schematic view of composite beam under gravity and cyclic lateral forces

8.8 Conclusions

This chapter described considerations directly related to the design of composite floors in steel buildings subjected to lateral forces. It is shown that:

1) The Assessment Guideline (2017) procedure may be modified to consider i) beam axial capacity, ii) beam-column connection capacity, iii) shear stud strength, and iv) diaphragm buckling strength. In addition, modifications were suggested to model the structure, and to

obtain appropriate forces for design. Two approaches are recommended considering diaphragm cracking effects to obtain diaphragm in-plane demands.

Approach One. In this approach, the diaphragm is assumed to remain elastic and is modelled using elastic in-plane properties. Then using the obtained internal forces the assumption of the elastic diaphragm should be checked. If the assumption is correct, design/assessment may be continued using the obtained results. Otherwise, the diaphragm in-plane stiffness should be reduced to account for concrete cracking.

Approach Two. In this approach, it is suggested to perform two analyses using both elastic and cracked diaphragm in-plane stiffnesses and use the envelope values for design/assessment of the diaphragm.

The diaphragm design approach seeks to:

i. Keep the diaphragm elastic without buckling.
ii. Have WSP demands lower that the WSP axial capacity.
iii. Prevent shear studs from fracture under the combination of earthquake lateral forces and gravity load effects.
iv. Ensure that fixed-end beam capacities are not reduced due to axial force effects.

2) The beam-end connection and shear stud demands depend on the records considered and on the modelling assumptions. For the structure selected and designed according to the proposed DESA method, individual frame demands increased by up to 50% as a result of diaphragm cracking. Considering the beam-column connection axial stiffness in the analysis decreased the beam-column connection axial demands compared to the model without beam-column connection axial stiffness. This is because it reduced the beam axial stiffness and lateral forces distributed to other stiffer elements/frames through the floor diaphragm. Also, it was shown that if the axial stiffness of the beam-column connection and/or shear stud stiffness are not considered in modelling, the beam axial forces and frame lateral forces

may be overestimated or underestimated depending on their relative stiffness. It is suggested to design WSP connections for likely axial forces obtained from elastic analysis even if they are not considered as part of diaphragm in-plane load transfer to the VLFR system but are connected to the slab through mechanical attachments (e.g. shear studs).

4) The load path through collector beams should be considered in design even if it is assumed that all diaphragm in-plane forces are directly transferred to the lateral force resisting frames. This should be conducted to obtain robust load path and avoid beam-column connection failure and possible collapse.

3) The slab-bearing forces can be obtained by modelling the frame with appropriate beam-connection axial stiffnesses, slab offset and imposed displacements. They depend on the relative stiffness of the frame, which affects the column deformations, and the shear stud group stiffness affecting the slab slip. For design without considering such an analysis it is recommended that i) a gap be provided around the columns to prevent large axial forces due to slab bearing on the beam-column connection. ii) When the gap is not provided around the column the slab bearing force should be considered when designing beam end connections, beams and shear studs. Note that in both cases above, general load path and column stability considerations should be considered.

4) It was shown, by means of time history analyses, that the static beam vertical deflection increased after the shear studs yielded in cyclic action by up to 28% in the cases considered. This was consistent with the findings of Chapter 5. It emphasises the need to design beams to carry the seismic gravity loads without composite action.

References

[1] ANSI, A. 360-16. (2016). Specification for structural steel buildings

[2] AS/NZS 2327 (2017). Composite structures, Composite steel-concrete construction in buildings.

[3] Astaneh-Asl, A., Liu, J., & McMullin, K. M. (2002). Behavior and design of single plate shear connections. Journal of Constructional Steel Research, 58(5-8), 1121-1141.

[4] Braconi, A., Elamary, A., and Salvatore, W. 2010. Seismic behaviour of beam-to-column partial-strength joints for steel-concrete composite frames, Journal of Constructional Steel Research, (66), 1431-1444.

[5] Bull, D. K. (2004). "Understanding the Complexities of Designing diaphragms in Buildings for Earthquakes", Bulletin of the New Zealand Society for Earthquake Engineering, 37 (2): 70-88.

[6] Chaudhari, T. D. (2017). "Seismic performance evaluation of steel frame building with different composite slab configurations", PhD Thesis, University of Canterbury.

[7] Chaudhari, T. D., MacRae, G. A., Bull, D., Chase, G., Hicks, S., Clifton, G. C. and Hobbs, M. (2015). "Composite Slab Effects on Beam–Column Subassembly Seismic Performance", 8th International Conference on Behavior of Steel Structures in Seismic Areas, Shanghai, China.

[8] Chi, B. and Uang, C. M. (2002). "Cyclic Response and Design Recommendations of Reduced Beam Section Moment Connections with Deep Columns", J. Struct. Engrg., ASCE, 128(4): 464-473

[9] Civjan, S. A., & Singh, P. (2003). Behavior of shear studs subjected to fully reversed cyclic loading. Journal of Structural Engineering, 129(11), 1466-1474.

[10] Cowie, K. A., Fussell, A. J., Clifton, G. C., MacRae, G. A. and Hicks, S. J. (2014). "Seismic Design of Composite Metal Deck and Concrete-Filled Diaphragms–A Discussion Paper", NZSEE Conference.

[11] Dowell, O. K., Seible, F., & Wilson, E. L. (1998). Pivot hysteresis model for reinforced concrete members. ACI Structural Journal, 95, 607-617.

[12] EN, C. 1994. 1-1, (2004) Eurocode 4: Design of composite steel and concrete structures.

[13] Gardiner, D. R. (2011). "Design Recommendations and Methods for Reinforced Concrete Floor Diaphragms Subjected to Seismic Forces", PhD Thesis, University of Canterbury.

[14] Holmes Consulting Group, Practice Note No. 8.1, Version No. 1, (2014). Modelling Diaphragm Force Distributions - Simple Grillage Method. by Bull D. K. and Galloway B.

[15] http://docs.csiamerica.com

[16] Johnson, R. P., Molenstra, N., & EPPIB. (1991). Partial shear connection in composite beams for buildings. Proceedings of the Institution of Civil Engineers, 91(4), 679-704.

[17] MacRae, G. A. and Bull, D. (2015). "Diaphragm Design, ENEQ650: Seismic Design of Steel and Composite Structures", Postgraduate Class notes, University of Canterbury, 2015.

[18] MacRae, G. A. and Clifton, G. C. (2015a). "Research on Seismic Performance of Steel Structures", Steel Innovations Conference, Auckland, New Zealand.

[19] MacRae, G. A. and Clifton, G. C. (2015b). "Research on Seismic Performance of Steel Structures", Steel Innovations Conference, Auckland, New Zealand.

[20] Moehle, J. P. (2015). Seismic design of reinforced concrete buildings (pp. 230-235). New York: McGraw-Hill Education.

[21] Naeim, F., & Boppana, R. R. (2001). Seismic Design of Floor Diaphragms. In The Seismic Design Handbook (pp. 373-407). Springer, Boston, MA.

[22] Nakajima, A., Saiki, I., Kokai, M., Doi, K., Takabayashi, Y., & Ooe, H. (2003). Cyclic shear force–slip behavior of studs under alternating and pulsating load condition. Engineering Structures, 25(5), 537-545.

[23] NZS 1170.5 (2004). Structural Design Actions-Part, 5. Standards New Zealand, Wellington, New Zealand. Including Amendment 1, 2016.

[24] NZS 3101 (2006). Concrete structures standard. Standards New Zealand, Wellington, NZ.

[25] NZS 3404 (2007). Steel Structures Standard. Standards New Zealand, Wellington, New Zealand. Including Amendments 1 and 2, 2001/2007.

[26] Oehlers, D. J., & Coughlan, C. G. (1986). The shear stiffness of stud shear connections in composite beams. Journal of Constructional Steel Research, 6(4), 273-284.

[27] Park, R. L., Park, R., & Paulay, T. (1975). Reinforced concrete structures. John Wiley & Sons.

[28] Sabelli, R., Sabol, T. A. and Easterling, W. S. (2011). "Seismic Design of Composite Steel Deck and Concrete-filled Diaphragms A Guide for Practicing Engineers", NEHRP Seismic Design Technical Brief No. 5.

[29] SAP2000, C. S. I. (2015). Computer & Structures Inc. Linear and nonlinear static and dynamic analysis of three-dimensional structures. Berkeley (CA): Computer & Structures.

[30] Scarry, J. M. (2014). "Floor diaphragms – Seismic bulwark or Achilles' heel", NZSEE Conference Paper Number O19.

[31] Takeda, T., Sozen, M. A., & Nielsen, N. N. (1970). Reinforced concrete response to simulated earthquakes. Journal of the Structural Division, 96(12), 2557-2573.

[32] The Seismic Assessment of Existing Buildings, Technical Guidelines for Engineering Assessments, (2017).

9 Conclusions and Future Research Works

9.1 Summary

Diaphragm design issues were investigated in this research include: i) diaphragm in-plane modelling method using truss elements, ii) diaphragm in-plane load path through shear studs to the beam and from the beam to the column through the WSP connection, iii) diaphragm buckling strength, iv) global diaphragm in-plane demands, and v) diaphragm design steps.

In summary, the unique contributions this research make to the field of diaphragm design include:

1) A new diamond shape truss framework was proposed.
2) The stiffness/strength performance of truss models considering compression-only diagonal members, which is appropriate for design, was quantified.
3) A method to assess the axial compressive strength of steel beam web side plate (WSP) connections, considering the gravity loads effect, was proposed.
4) A method was proposed to estimate the lateral shear strength of a group of shear studs on a steel beam in the presence of gravity loads and considering shear stud fracture.
5) A method was developed to estimate diaphragm buckling strength considering gravity loads and possible out-of-straightness.
6) A lateral force method, removing some limitations of existing methods, to estimate diaphragm likely in-plane demands was proposed.
7) A step-by-step diaphragm design approach, with a corresponding example, was provided.

9.2 Key findings

From the analytical investigations and analyses conducted in this research, the main findings obtained include:

9.2.1 Truss element modelling

A new Diamond ⌖ truss framework model was proposed and compared with the diagonal ☒ truss model. Also, different possible truss element modelling methods considering the combination of compression/tension, compression only and tension only truss elements were studied. It was found that:

1) For elastic truss models where all elements were tension/compression, the error in estimating diaphragm deformations was reduced to less than 10% for the diaphragm alone when a sufficient number of elements were used. However, the diamond ⌖ configuration was more accurate requiring fewer elements to obtain the same accuracy. In addition, using the diamond ⌖ model gives more realistic results in terms of the beam axial forces.
2) Different possible diamond truss models, placed in a framework to represent a diaphragm, were compared with a nonlinear solid element FEM model in terms of their in-plane stiffness and internal forces. Based on the analyses conducted, Truss Model 2, with diagonal compression-only and orthogonal compression/tension elements (representing un-cracked diaphragm properties), and Truss Model 3, with diagonal compression-only and orthogonal reinforcement tension/concrete compression members (representing cracked diaphragm properties) satisfied the criteria of providing simple outputs usable for design and reasonable accuracy.
3) For analyses conducted of a one-storey and a three storey structure, a 10% increase in diaphragm flexibility caused 7% and 2% increase in total structural displacement at the diaphragm levels respectively.

9.2.2 Web-Side-Plate connection axial strength

The axial behaviour of WSP connections was investigated considering different geometry, boundary condition and initial conditions. A method to assess the axial compressive strength of WSP connections considering gravity loads was proposed. In this study it was found that:

1) The axial compression capacity of a WSP connection is lower than the axial tensile capacity because of axial force eccentricity, cleat plate slenderness, and the P-Δ effect. For the connection subjected to the axial tension force, axial force increases to reach the first controlling failure limit state.
2) The axial compression strengths obtained using the proposed method were compared with thirty-four FE models considering different parameters. The average calculated compression strength according to the proposed method was 80% with a standard deviation of 14% that obtained from FEM analysis. For tension side, the average of calculated tension strength from the proposed method was about 89% with a standard deviation of 3% that obtained from FEM analysis. Note that the following parameters considered in the proposed strength approach were not considered in the FEM models. These included: residual stress effect and out-of-straightness effect. To consider these and also possible packing effect in design, a strength multiplier of 0.75 was suggested.

9.2.3 Shear studs design to transfer lateral forces

A method was proposed to calculate the lateral strength of shear studs on composite and non-composite beams in the presence of gravity loads. It was found that:

1) The maximum total lateral force resistance of shear studs depends on the level of shear stud slip under gravity load. In the absence of gravity load, the total lateral force resistance of shear studs is equal to the sum of all shear stud strengths.

2) Yielding of the shear studs under a combination of gravity and lateral loads reduced or eliminated the shear flow at the steel beam-concrete slab interface and decreased composite action. This caused loss of composite action and increased the beam vertical deflection.
3) A design method was developed to estimate the lateral force resistance of a beam shear stud group considering gravity loads and shear stud fracture. Numerical FEM studies indicated strengths in the range of 1.0-1.25 times that from the design method. Also the steel beam alone should be designed to carry un-factored gravity loads, $D + L$ to prevent collapse under gravity loads. This is because the composite action of the beams subjected to lateral forces may be eliminated or decreased.
4) For composite beams in low damage structures, or structures where it is desired that the building be permitted to continue operation after at least one major earthquake, a maximum acceptable increase in vertical deflection of gravity beams was arbitrary chosen to be 10%. To meet this limit, the ratio of slab lateral force demand applied to the shear studs in a bay should be less than 50% of the peak total resistance of these shear studs. This value is appropriate for the likely range of gravity loading, beam depth and level of composite action. Also the steel beam alone should be designed to carry un-factored gravity loads, $D + L$.

9.2.4 Floor diaphragm buckling

The floor diaphragm buckling modes under in-plane forces that were considered in this research include:

i. Local buckling of the concrete topping between the slab ribs (inter-rib buckling),
ii. Buckling of the diaphragm between secondary beams (intra-panel buckling), and
iii. Global buckling of the diaphragm between primary beams (intra-bay buckling).

All of the buckling modes were studied for both pre-crack and post-crack conditions of the concrete slab. The critical buckling of each mode was calculated using analytical methods, and in cases, the results were verified with FEM modelling using ABAQUS software. It was found that:

1) For the local buckling, the minimum topping thickness results in high buckling forces, therefore concrete shear or crushing are likely to occur much earlier than buckling. Local buckling is therefore not likely to occur in conventional floor slabs.
2) for the intra-panel and intra-bay buckling modes the critical slab in-plane shear forces which cause buckling need to be checked both before and after cracking. A simple formula was provided to do this. It considered pinned end condition, out-of-plane deformations and the corrugated nature of the composite slab. It was shown that in the studied examples the shear buckling did not govern.
3) initial deflection effects on the elastic buckling strength due to gravity loads on the floor slab could be conservatively considered by a strength multiplier of 0.75 in design.

9.2.5 Diaphragm lateral force method

Global diaphragm in-plane force demands resulting from inertia forces and transfer forces may be obtained using lateral force methods or NLTH analysis. A lateral force method was proposed, called Diaphragm ESA (DESA). It removes some of the limitations of the available lateral force methods. The proposed method was compared with a number of available lateral force methods that have been used for obtaining diaphragm global in-plane demands including: 1) ESA considering structure ductility (CESA), 2) Overstrength ESA (OESA), 3) Elastic ESA, (EESA), 4) Parts and Components method (P&C), 5) pseudo-Equivalent Static Analysis (pESA), 7) Pushover analysis, and 9) NLTH. It was found that:

1) The DESA method was proposed based on the hypothesis that if a lateral loading method can represent likely deformed shape of a structure, it can obtain likely diaphragm transfer forces. This is because diaphragm transfer forces are mainly due to the deformation incompatibility of different VLFR systems. This method assumes the lateral deformation of a long period structure at the design level may be estimated using the EESA ($\mu = 1$) method according to the equal displacement assumption. Also, the bottom portion of the EESA lateral forces are increased in the proposed method to approximate the higher mode effects.
2) For high-rise buildings beyond the CESA method limitations, it is suggested to use the first mode lateral forces scaled to the EESA base shear and increase the lateral forces at lower floors.
3) The analyses results showed that the proposed method may remove some limitations of the CESA and pESA methods such as height limit and overstrength calculation process. However, it may result in some overestimation and underestimation of response in different cases and ignore some important response features, such as structure ductility, redistribution of internal forces, hysteretic effects, stiffness and strength degradation. The advantages and disadvantages of different lateral force methods were discussed so that one can decide which method can provide more reasonable results based on the accuracy and time required for the analysis.

9.2.6 Diaphragm stiffness and strength considerations

Design considerations directly related to the composite floors in steel buildings subjected to lateral forces described. A number of FE analyses performed to investigate the effects of reduction in diaphragm in-plane stiffness, shear stud stiffness and WSP connection axial

stiffness in the analyses. Some diaphragm design issues such as slab-column gapping effect and the vertical deflection of composite beams were also investigated. It was found that:

1) The Assessment Guideline (2017) procedure may be modified to consider i) beam axial capacity, ii) beam-column connection capacity, iii) shear stud strength, and iv) diaphragm buckling strength. In addition, modifications were suggested to model the structure, and to obtain appropriate forces for design. Two approaches were recommended to obtain diaphragm in-plane demands considering diaphragm cracking effects. The proposed diaphragm design approaches seek to:
    a) Keep the diaphragm elastic without buckling.
    b) Have WSP demands lower that the WSP axial capacity.
    c) Prevent shear studs from fracture under the combination of earthquake lateral forces and gravity loads effects.
    d) Ensure that beam fixed-end capacity is not reduced due to axial force effects.
2) For the structure selected and designed according to the DESA method, individual frame demands increased by up to 50% as a result of diaphragm cracking. Also, considering the beam-column connection axial stiffness in the analysis decreased the beam-column connection axial demands compared to the model without beam-column connection axial stiffness. This is because it reduced the beam axial stiffness and lateral forces distributed to other stiffer elements/frames through the floor diaphragm.
3) The load path through collector beams should be considered in design even if it is assumed that all diaphragm in-plane forces are directly transferred to the lateral force resisting frames. This should be conducted to obtain robust load path and avoid beam-column connection failure and possible collapse.

4) It was shown, by means of time history analyses, that the static beam vertical deflection increased after the shear studs yielded in cyclic action by up to 28% in the cases considered. This was consistent with the findings of Chapter 5. It emphasises the need to design beams to carry the seismic gravity loads without composite action.

9.3 Suggested future research

Research topics, following on from the studies conducted here, that have the potential to make a significant impact include the following.

9.3.1 Investigating axial behaviour of different simple beam-column connections

The axial behaviour of WSP connections, as the most common simple beam-column connection used in the steel frame structures, was investigated in this research. However, there are other types of pinned connections as shown in Figure 9-1.

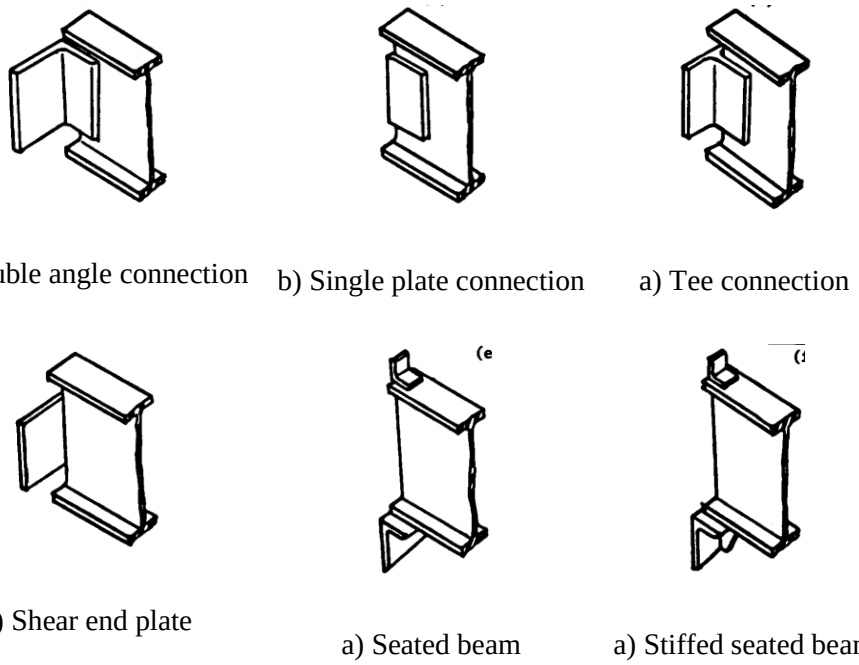

Figure 9-1. Simple beam-column connection types, (Astaneh, 1989b)

Here it is suggested to investigate the axial force carrying behaviour of other commonly used simple beam-column connections and provide design methods for them.

9.3.2 Investigating the behaviour of the top-plate connection

The top-plate connection detail is shown in Figure 9-2. This connection may be used where the WSP connection axial strength (or any other simple beam-column connection) is less than the demand from the beam axial forces.

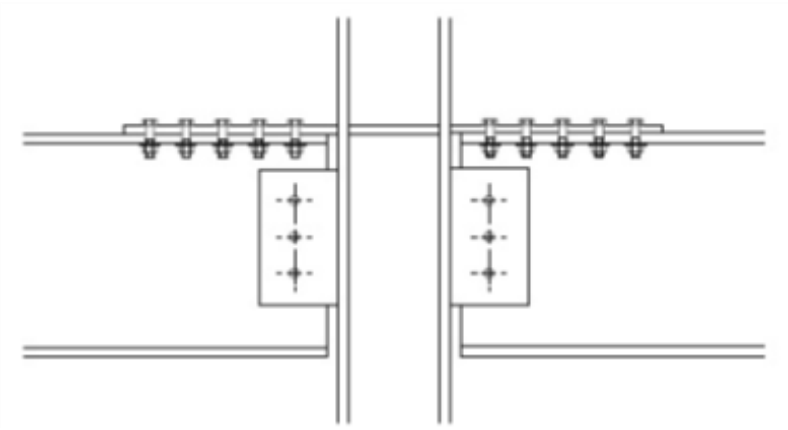

Figure 9-2. Top plate connection to transfer collector beam axial forces (Cowie et al., 2014)

9.3.3 Performing experimental tests on axial behaviour of the WSP connections

The axial force behaviour of the WSP connections was studied using analytical and numerical methods in this research. It may be beneficial to perform an experimental investigation of the axial behaviour of WSP connections and compare the results (stiffness, strength and deformation capacity) obtained from the experiments with the proposed method.

9.3.4 Performing experimental tests on lateral force resistance of shear studs on composite beam and its effect on the vertical beam deflection

The lateral force resistance of shear studs under monotonic and cyclic loads has been investigated by many researchers (e.g. Johnson and Molenstra 1991). However, the lateral

force carrying of shear studs placed on a composite beam in combination of gravity loads is not investigated. Here, it is suggested to perform a lateral pushover tests on composite beams in the presence of gravity loads to investigate the effects of gravity loads on the lateral force resistance of shear studs. This may also provide some information about the loss of composite action under lateral forces.

9.3.5 Further research on the diaphragm lateral force method

Lateral force method to obtain diaphragm in-plane demands was investigated in Chapter 7 of this research. It is suggested to perform more NLTH analysis on different structural systems to further improve methods of diaphragm force prediction.

9.3.6 Obtaining reasonable reduction factor for in-plane stiffness of diaphragms considering concrete cracking

In Chapter 8, it was shown that the reduction in the diaphragm in-plane stiffness due to the concrete cracking may change the lateral force distribution between the different VLFR systems and also the diaphragm itself. It was recommended to consider the possibility of cracked diaphragm stiffness in the analysis and design. However, there is a need to obtain a diaphragm stiffness reduction factor to use in the elastic analyses with more realistic tension stiffening effects.

9.3.7 Experimental investigation on the slab forces

There is not much published experimental test information about the behaviour of slabs subject to in-plane forces. In-plane slab forces in experimental investigations are most easily applied to the slab boundary elements. However inertia forces are generated within the slab itself and should also be considered in testing with realistic gravity forces, shear studs, connections and boundary conditions. Such testing can be used to evaluate the methods proposed in this thesis, and to improve them.

References

[1] Astaneh, A. (1989b). Demand and supply of ductility in steel shear connections. Journal of Constructional Steel Research, 14(1), 1-19.

[2] Cowie, K. A., Fussell, A. J., Clifton, G. C., MacRae, G. A., & Hicks, S. J. (2014, March). Seismic design of composite metal deck and concrete-filled diaphragms–A discussion paper. In NZSEE Conference.

[3] Johnson, R. P., Molenstra, N., & EPPIB. (1991). Partial shear connection in composite beams for buildings. Proceedings of the Institution of Civil Engineers, 91(4), 679-704.

[4] NZS 3404 Parts 1 and 2:1997, Steel Structures Standard.

[5] The Seismic Assessment of Existing Buildings, Technical Guidelines for Engineering Assessments, (2017).

Appendix A: Transfer Forces

Different parameters may affect the magnitude of diaphragm transfer forces such as stiffness, strength and location of vertical lateral force resisting (VLFR) elements in plan. In this Appendix, the possibilities for transfer forces considering the following are described (MacRae and Bull, 2015):

1. VFLR element differential stiffness/strength on single storey structures
2. Multi-storey effects.

A.1 VFLR element differential stiffness/strength

In this case, a simple floor plan is considered for evaluating transfer forces in a one-storey building, as shown in Figure A-1a. Different possibilities in terms of VFLR element strength and stiffness are considered for evaluating transfer forces in the diaphragm. To avoid torsional effects, the floor plan is considered symmetric. Figure A-1b presents the simplified elevation of this floor plan.

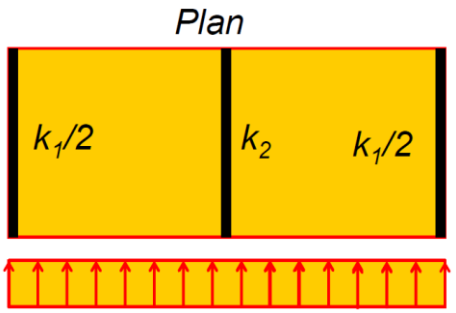

a) Floor plan

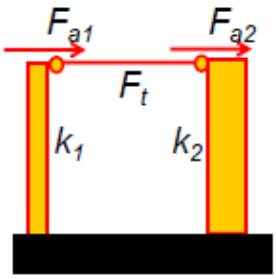

b) Simplified elevation

Figure A-1. Simple floor plan of one storey building (MacRae and Bull, 2015)

Two stages considered here for evaluating the transfer forces are:

1. The elastic stage in which all lateral force resistance elements are elastic (at the point the first yield occur in one of the elements)

2. The post-yield stage, where one lateral force resisting element (in Figure A-1b) has yielded, and the second is about to yield

The maximum transfer force can occur either before or after yield so both stages need to be considered to find the maximum diaphragm transfer force, F_t:

- Elastic stage:

The total lateral force imposed on the floor is denoted by F_a, and F_{a1}, F_{a2} are forces in each lateral load-resisting element.

$$F_a = F_{a1} + F_{a2}$$

Here, $F_{a1} = F_{a2}$ due to the equal tributary area.

If $k_1 = 0$, $|F_t| = F_{a1} = F_a/2$

If $k_2 = 0$, $|F_t| = F_{a2} = F_a/2$

If $k_1 = k_2$, $F_t = 0$

In general, before yield

$$F_1 = F_a[k_1/(k_1 + k_2)]$$

$$F_2 = F_a[k_2/(k_1 + k_2)]$$

$$F_t = F_a[0.5 - k_1/(k_1 + k_2)]$$

- Post-yield stage:

$$F_t = \frac{F_{y1} + F_{y2}}{2} - F_{y1}$$

$$F_t = \frac{F_{y1} - F_{y2}}{2} - F_{y1}$$

Where F_{y1} and F_{y2} are the yield strength of VFLR elements 1 and 2 respectively. Based on these equations and considering different stiffness and strength for lateral load resisting elements, different possibilities for transfer forces can be obtained as shown in Figure A-2 (MacRae and Bull, 2015).

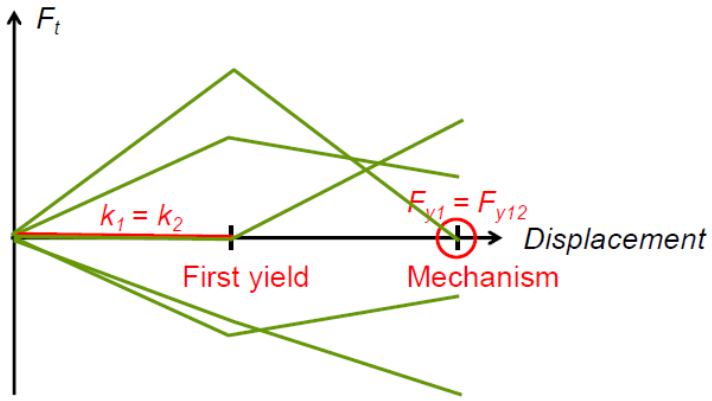

Figure A-2. Possibilities for diaphragm transfer forces in a single storey structure (MacRae and Bull, 2015)

A.2 Multi-storey effects

In this case, a shear-type frame and a wall are connected with diaphragms, in a two-storey building. The simplified elevation of the studied structure is shown in Figure A-3a.

In this case, it is assumed that the frame has uniform strength and stiffness over the height, and the wall yields in flexure only at the base.

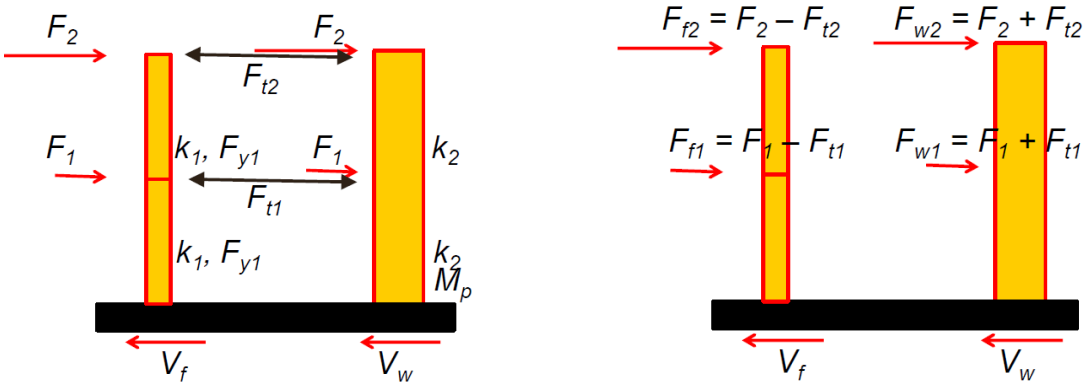

a) Simplified elevation b) Free body diagram

Figure A-3. Simplified elevation and free body diagram of two storey structure (MacRae and Bull, 2015)

Here F_{t1} and F_{t2} are diaphragm transfer forces at the first and second floor respectively, F_f and F_w represents the frame and wall forces, and V_f and V_w represent the frame and wall shear reaction forces respectively. The transfer forces are only obtained at the formation of a full mechanism in this example.

1) Considering a mechanism with $V_{fy1} = V_{fy2} = V_b$ and $V_w = V_f = V_b$

Figure A-4 shows the frame and wall forces for this case. The diaphragm transfer forces are evaluated as $F_{t2} = \frac{2V_b}{3} - \frac{V_b}{3} = \frac{V_b}{3}$ (tension) for the second floor and $F_{t1} = \frac{V_b}{3}$ (compression) for the first floor.

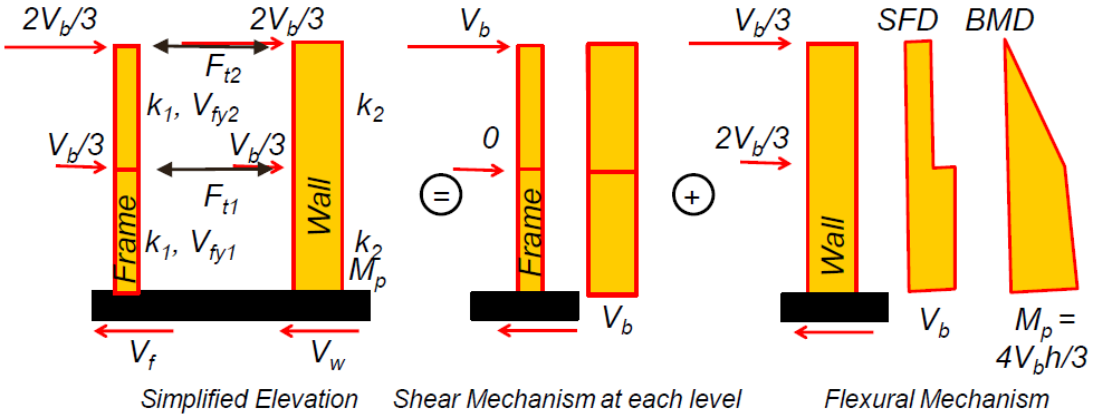

Figure A-4. Frame and wall forces when $V_{fy1} = V_{fy2} = V_b$ and $V_w = V_f = V_b$ (MacRae and Bull, 2015)

2) Considering a mechanism with frame $V_{fy1} = 1.5V_{fy2} = V_b$ and $V_w = V_{fy1} = V_b$

Figure A-5 shows the frame and wall forces for this case. The diaphragm transfer forces are evaluated as $F_{t2} = F_{t1} = 0$. The different distribution of shear strength causes different transfer forces.

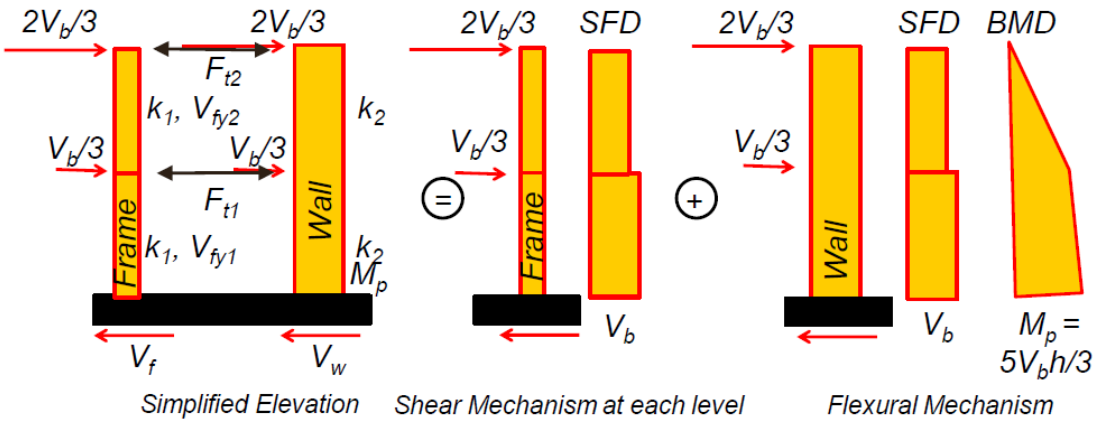

Figure A-5. Frame and wall forces when $V_{fy1} = 1.5V_{fy2} = V_b$ and $V_w = V_{fy1} = V_b$ (MacRae and Bull, 2015)

It may be seen that transfer forces are affected by

1) The displacement at which it is considered (sometimes it increases or decreases)
2) The strengths/stiffness magnitudes and distributions of VLFR elements
3) The lateral force distribution

Simple elastic design methods, such as ESA and pESA, do not explicitly consider all these effects, but if strength is somewhat proportional to stiffness, the peak transfer force is likely to occur at the peak displacement.

References

[1] MacRae GA and Bull D (2015). "Diaphragm Design, ENEQ650: Seismic Design of Steel and Composite Structures", Postgraduate Class notes, University of Canterbury, 2015.

Appendix B: Diamond ⌖ Model Cross-Section Areas

Similar to the diagonal model (Hrennikoff, 1941), the cross-section area of truss members can be derived by equating the framework deformations with elastic strains of the corresponding plate member. Figure B-1 shows three general loading conditions that are used to determine the framework properties. The plate is assumed to continue in both directions, and only two truss mesh units in each direction are shown in this Figure. In the first loading condition, Figure B-1a, the plate is loaded uniformly with normal load per unit length P in the X-direction and υP (υ is Poisson's ratio of the plate material) in the Y-direction. The second loading condition, Figure B-1b, is achieved by changing the X and Y-directions. The third loading condition, Figure B-1c, includes uniform tangential loading per unit length P, applied to the plate edges in the X and Y-directions. The right hand side of each Figure shows the square truss mesh unit of the diamond model.

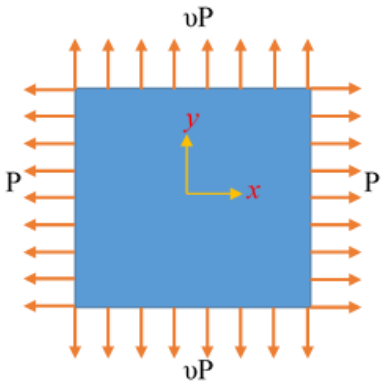

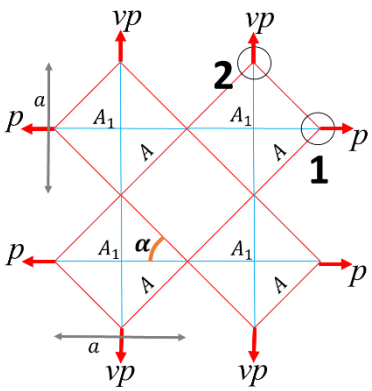

a) Plate and truss framework subjected to normal force per unit length, P, in the X-direction and νP in the Y-direction

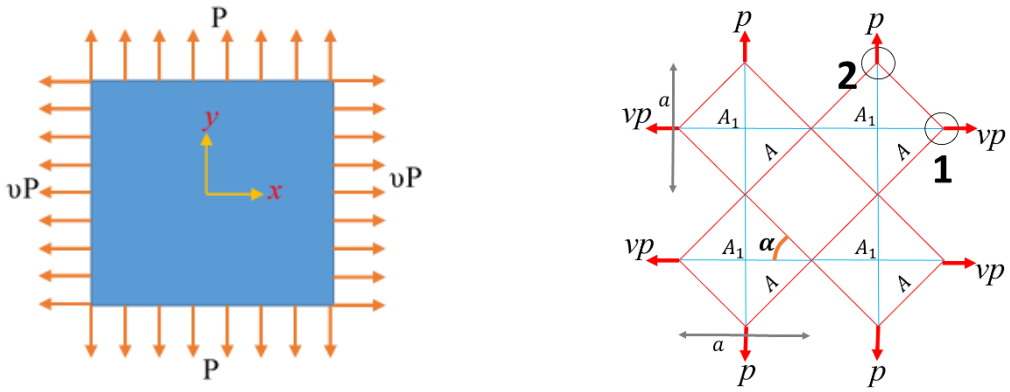

b) Plate and truss framework subjected to normal force per unit length, P, in the Y-direction and νP in the X-direction

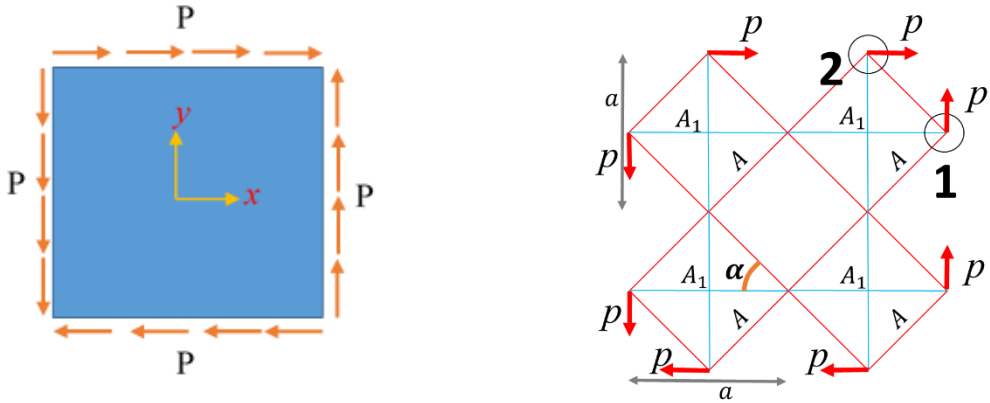

c) Plate and truss framework subjected to pure shear force per unit length, P

Figure B-1. General loading conditions for determining truss framework properties, p is the normal edge force to each element where $p = Pa$, truss framework continues in both directions

Based on solid mechanics (e.g. Timoshenko and Goodier, 1970), the axial strains in the X and Y-directions, ε_x and ε_y for the first case of loading (Figure B-1a), can be obtained as follows for a plate member.

$$\varepsilon_x = \frac{p(1-\nu^2)}{Eta} \qquad \text{Eq. (B-1)}$$

$$\varepsilon_y = 0 \qquad \text{Eq. (B-2)}$$

Here, p is the normal edge force to each element ($p = Pa$) and E and ν are the elastic modulus and Poisson's ratio of plate material respectively. The horizontal and vertical dimensions of each square truss mesh unit and the plate thickness are denoted as a and t

respectively. The same equations are applicable to the second case by changing the X and Y-directions.

Shear deformation of the plate subjected to tangential force can be obtained using Eq. (B-3) (e.g. Timoshenko and Goodier, 1970).

$$\gamma_{xy} = \frac{2(1+\nu)p}{Eta} \qquad \text{Eq. (B-3)}$$

By equating the strains of the truss framework and the plate, Eqs. (B-1) to (B-3), the truss element characteristics can be obtained. Figure B-2 presents an enlarged view of Figure B-1a with more details. The equations used for finding the truss element cross-sections are presented in the following.

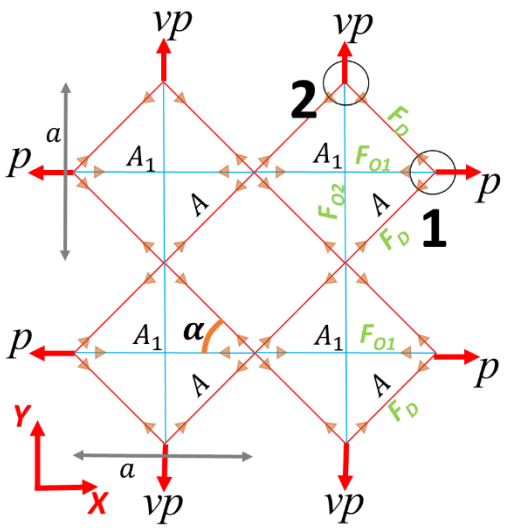

Figure B-2. Diamond truss framework subjected to normal force p in the X-direction and νp in the Y-direction

Force equilibrium in the X-direction at Point 1 shown in Figure B-2, gives:

$$F_{O1} + 2F_D \cos\alpha - p = 0 \qquad \text{Eq. (B-3a)}$$

Where F_{O1} is the internal force of the orthogonal member in the X-direction and F_D is the diagonal member internal force. Writing the force equilibrium in the Y-direction at Point 2 also gives:

$$F_{O2} + 2F_D \cos\alpha - \nu p = 0 \qquad \text{Eq. (B-3b)}$$

It is known that the lateral deformation (deformation in the Y-direction, Eq. (B-2)) is zero due to applied νp in this direction. Therefore $F_{O2} = 0$ and by substituting this in the Y-direction force equilibrium, Eq. (B-3b), the diagonal member force can be found:

$$F_D = \frac{\nu p}{2\cos\alpha} \qquad \text{Eq. (B-3c)}$$

Considering the truss framework units are square ($\alpha = 45°$), by substituting F_D into the force equilibrium in the X-direction, Eq. (B-3a), the orthogonal member force (F_{O1}) can be obtained as:

$$F_{O1} = p(1 - \nu)$$

The axial strain of the orthogonal truss member in the X-direction, which needs to be equal to the axial strain of the corresponding plate member, can be calculated using:

$$\varepsilon_x = \frac{p(1-\nu)}{EA_1}$$

By equating the axial strain of the plate given in Eq. (B-1) and the truss element axial strain above, the cross-section area of the orthogonal truss element member can be found:

$$A_1 = {at}/{(1 + \nu)} \qquad \text{Eq. (B-4)}$$

By changing the loading condition to normal force p in Y-direction and νp in X-direction, the same result can be found for the orthogonal member cross-section area in the Y-direction.

In case of tangential (shear) forces applied to the truss framework as shown in Figure B-1c, all orthogonal members are unstressed due to the symmetry in the truss pattern. However, all the diagonal members are stressed with equal tension and compression values. Force equilibrium in the Y-direction at Point 1 gives:

$$2F_D \sin\alpha - p = 0$$

Considering square truss mesh units ($\alpha = 45°$), the diagonal member internal force subjected to shear stresses is:

$$|F_D| = \frac{p}{\sqrt{2}} \qquad \text{Eq. (B-4a)}$$

Similarly, the force equilibrium in the X-direction at Point 1 in Figure B-1c shows that the orthogonal member internal force is zero.

$$F_D \cos\alpha - F_D \cos\alpha + F_{O1} = 0$$

$$F_{O1} = 0$$

The axial deformation (change in length) of the diagonal truss members is equal to:

$$\delta = \frac{pa\sqrt{2}}{\sqrt{2}EA}$$

$$\delta = \frac{pa}{EA} \qquad \text{Eq. (B-4b)}$$

Which transforms the square pattern into a parallelogram as shown in Figure B-3.

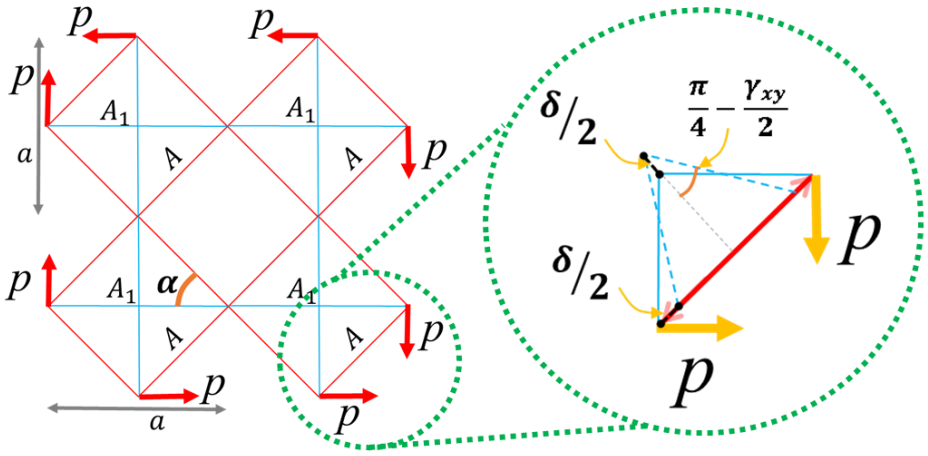

Figure B-3. Diamond model deformed shape subjected to shear force

As shown in Figure B-3, the shear strain in the framework, γ_{xy}, can be found from:

$$\tan\left(\frac{\pi}{4} + \frac{\gamma_{xy}}{2}\right) = \frac{\frac{a}{\sqrt{2}} - \frac{\delta}{2}}{\frac{a}{\sqrt{2}} + \frac{\delta}{2}}$$

$$= \frac{1 - \frac{\delta}{a\sqrt{2}}}{1 + \frac{\delta}{a\sqrt{2}}} \qquad \text{Eq. (B-4c)}$$

From the mathematical rule of trigonometric addition formulas (e.g. Abramowitz and Stegun, 1965) and assuming small deformations which, $\tan(\gamma) \cong \gamma$,

$$\tan\left(\frac{\pi}{4}+\frac{\gamma_{xy}}{2}\right)=\frac{\tan\frac{\pi}{4}-\tan\frac{\gamma_{xy}}{2}}{1+\tan\frac{\pi}{4}\tan\frac{\gamma_{xy}}{2}}$$

$$=\frac{1-\frac{\gamma_{xy}}{2}}{1+\frac{\gamma_{xy}}{2}}$$

By equating the above equation with Eq. (B-4c) and substituting Eq. (B-4b), the shear strain, γ_{xy}, can be obtained as:

$$\gamma_{xy}=\frac{p\sqrt{2}}{EA} \qquad \text{Eq. (B-4d)}$$

By equating the plate and truss framework shear strains, using Eq. (B-3) and Eq. (B-4d), the diagonal truss element cross-section area can be found:

$$A=\frac{at}{\sqrt{2}(1+\nu)} \qquad \text{Eq. (B-5)}$$

Poisson's ratio, ν, should be calculated to satisfy the deformation compatibility equation. Figure B-4 shows the framework deformation in the X-direction subjected to normal force, p, in the X-direction and νp in the Y-direction.

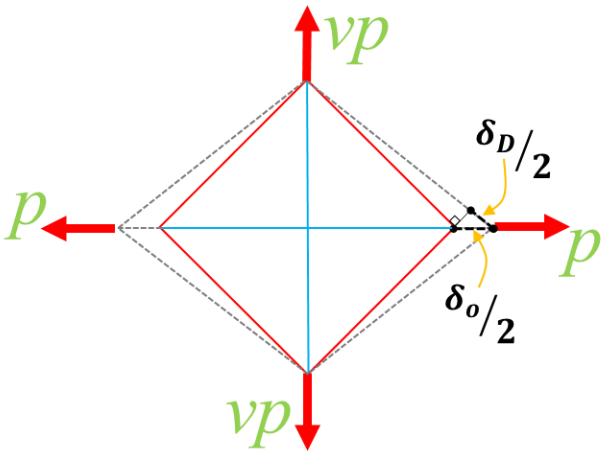

Figure B-4. Diamond framework deformation in the X-direction subjected to normal force p in the X-direction and νp in the Y-direction

The deformation compatibility can be achieved by writing the relationship between the orthogonal and diagonal member deformations as:

$$\frac{\delta_D}{2} = \frac{\delta_O}{2}\cos 45 \qquad \text{Eq. (B-5a)}$$

The truss element axial deformations are denoted by δ_D and δ_O for diagonal and orthogonal members respectively.

Considering the truss element axial forces obtained using equilibrium in the X-direction, Eq. (B-3a), and truss member cross-section areas given in Eqs. (B-4) and (B-5), δ_D and δ_O are calculated as:

$$\delta_D = \frac{\nu p\sqrt{2}(1+\nu)}{Et}$$

$$\delta_O = \frac{p(1-\nu^2)}{Et}$$

Substituting these axial deformations into Eq. (B-5a), gives:

$$\frac{\nu p\sqrt{2}(1+\nu)}{Et} = \frac{p(1-\nu^2)}{\sqrt{2}Et}$$

From which $\nu = \frac{1}{3}$ results.

Considering the Poisson's ratio $\nu = \frac{1}{3}$, the cross-section area of the orthogonal and the diagonal members are obtained using Eqs. (B-4) and (B-5) respectively as:

$A_1 = 0.75at$ (Orthogonal member)

$A = 0.53at$ (Diagonal member)

Where a is the dimension of the framework pattern and t is the plate thickness.

References

[1] Abramowitz, M., & Stegun, I. A. (1965). Handbook of mathematical functions: with formulas, graphs, and mathematical Tables (Vol. 55). Courier Corporation.

[2] Hrennikoff, A. (1941). Solution of problems of elasticity by the framework method. Journal of applied mechanics, 8 (4):169-75.

[3] Timoshenko, S. P., & Goodier, J. N. (1970). Theory of Elasticity, (216).

Appendix C: Non-Square Elastic Framework Properties

The cross-section area of the truss members of a non-square elastic framework can be obtained using a similar method to the diagonal (Hrennikoff, 1941) and the diamond truss frameworks. The cross-section area of truss members can be derived by equating the framework deformations with elastic strains of the corresponding plate member. Figure C-1 shows three general loading conditions that are used to determine the framework properties. The plate is assumed to continue in both directions, and only two truss mesh units in each direction are shown in this Figure. In the first loading case, Figure C-1a, the plate is loaded uniformly with normal load per unit length P in the X-direction and νP (υ is Poisson's ratio of the plate material) in the Y-direction. The second loading condition, Figure C-1b, is achieved by changing the X and Y-directions. The third loading condition, Figure C-1c, includes uniform tangential loading per unit length P, applied to the plate edges in the X and Y-directions. The right hand side of each Figure shows the square truss mesh unit of the diamond model.

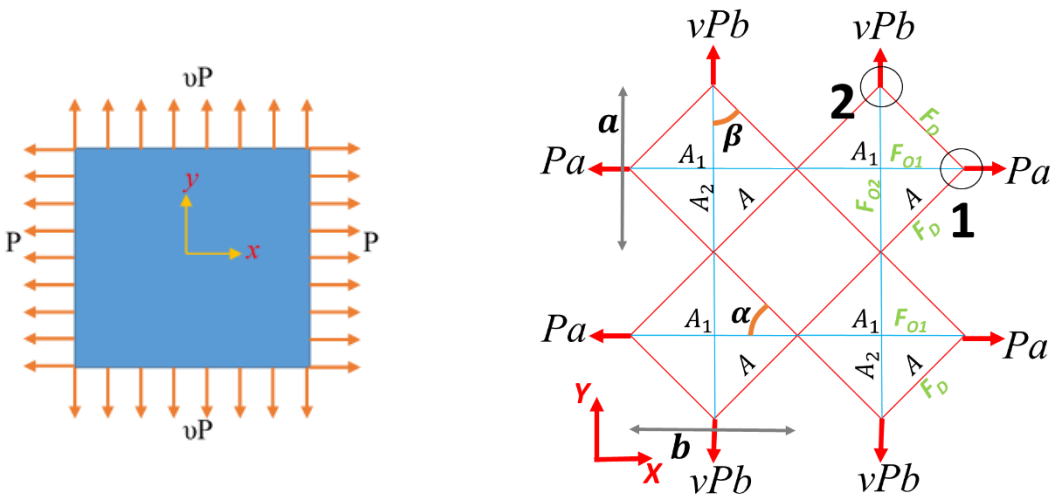

a) Plate and truss framework subjected to normal force per unit length, P, in the X-direction and νP

in the Y-direction

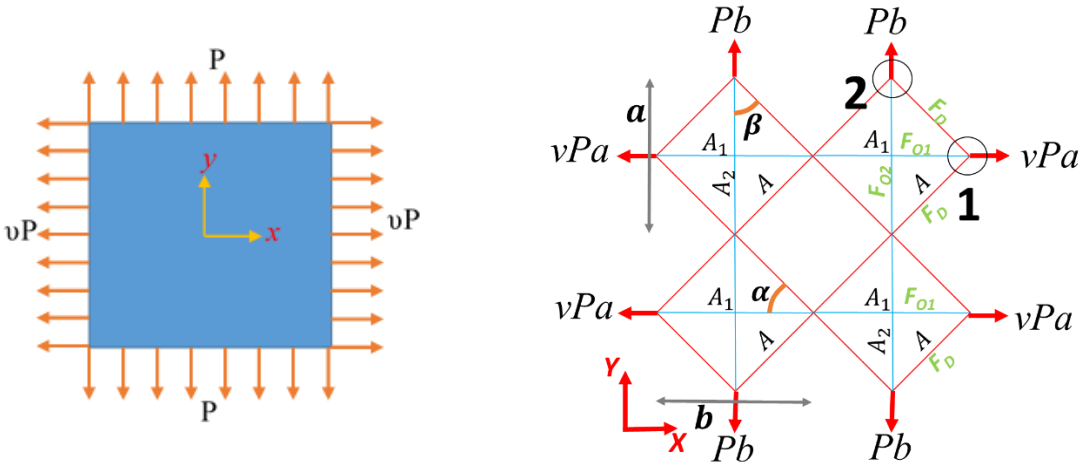

b) Plate and truss framework subjected to normal force per unit length, P, in the Y-direction and νP in the X-direction

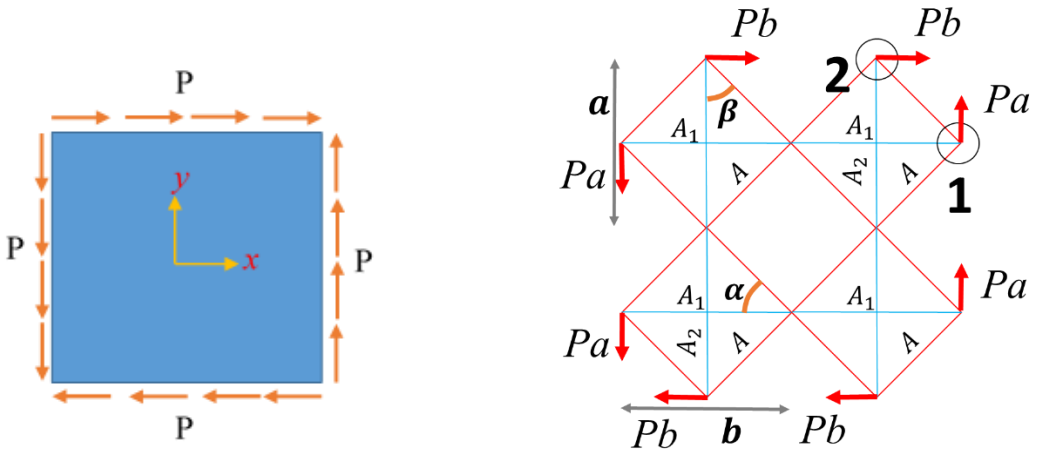

c) Plate and truss framework subjected to pure shear force per unit length, P

Figure C-1. General loading conditions for determining truss framework properties, truss framework continues in both directions

Strains in the truss framework for each case in Figure C-1 can be calculated based on the applied normal/tangential force per unit length, P, truss element cross-sections, A_i, and the configuration represented by the angles α and β. Then the framework strains are equated to the corresponding strains in the plate member ε_x, ε_y and γ_{xy} loaded the same way.

Based on solid mechanics (e.g. Timoshenko and Goodier, 1970), the axial strains in the X and Y-directions, ε_x and ε_y for the first case of loading (Figure C-1a), can be obtained as follows for a plate member.

$$\varepsilon_x = \frac{Pa(1-\nu^2)}{Eta} \qquad \text{Eq. (C-1)}$$

$$\varepsilon_y = 0 \qquad \text{Eq. (C-2)}$$

Here Pa is the normal edge force to each element in the X-direction and E and ν are the elastic modulus and Poisson's ratio of plate material respectively. The horizontal and vertical dimensions of each square truss mesh unit and the plate thickness are denoted as b, a and t respectively. The plate strains for the second loading case, shown in Figure C-1b, can be obtained by replacing a by b in Eq. () as:

$$\varepsilon_y = \frac{Pb(1-\nu^2)}{Etb} \qquad \text{Eq. (C-3)}$$

$$\varepsilon_x = 0 \qquad \text{Eq. (C-4)}$$

Shear deformation of the plate subjected to tangential force can be obtained using Eq. (C-5) (e.g. Timoshenko and Goodier, 1970).

$$\gamma_{xy} = \frac{2(1+\nu)Pa}{Eta} \qquad \text{Eq. (C-5)}$$

By equating the strains of the truss framework and the plate, Eqs. (C-1) to (C-5), the truss element characteristics can be obtained. Figure C-2 presents an enlarged view of Figure C-1a with more details. The equations used for finding the truss element cross-sections are presented in the following.

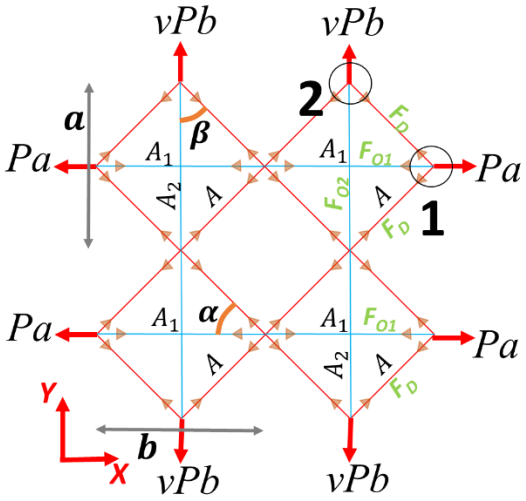

Figure C-2. Truss framework subjected to normal force Pa per truss mesh unit in the X-direction and νPb in the Y-direction

Force equilibrium in the X-direction at Point 1 shown in Figure C-2, gives:

$$F_{O1} + 2F_D \cos\alpha - Pa = 0 \qquad \text{Eq. (C-6)}$$

Where F_{O1} is the internal force of the orthogonal member in the X-direction and F_D is the diagonal member internal force. Writing the force equilibrium in the Y-direction at Point 2 also gives:

$$F_{O2} + 2F_D \sin\alpha - \nu Pb = 0 \qquad \text{Eq. (C-7)}$$

It is known that the lateral deformation (deformation in the Y-direction, Eq. (C-2)) is zero due to applied νPb in this direction. Therefore $F_{O2} = 0$ and by substituting this in the Y-direction force equilibrium, Eq. (C-7), the diagonal member force can be found:

$$F_D = \frac{\nu Pb}{2\sin\alpha} \qquad \text{Eq. (C-8)}$$

By substituting F_D into the force equilibrium in the X-direction, Eq. (C-6), the orthogonal member force (F_{O1}) can be obtained as:

$$F_{O1} = P(a - \nu b \cot\alpha) \qquad \text{Eq. (C-9)}$$

Using $\cot\alpha = {}^{b}/_{a}$,

$$F_{O1} = P(a - \frac{\nu b^2}{a}) \quad \text{Eq. (C-10)}$$

The axial strain of the orthogonal truss member in the X-direction, which should to be equal to the axial strain of the corresponding plate member, can be calculated using:

$$\varepsilon_x = \frac{P(a - \frac{\nu b^2}{a})}{EA_1} \quad \text{Eq. (C-11)}$$

By equating the axial strain of the plate given in Eq. (C-1) and the truss element axial strain, Eq. (C-11) , the cross-section area of the orthogonal truss element member in the X-direction can be found:

$$A_1 = at\frac{\left(1 - \nu b^2/a^2\right)}{1 - \nu^2} \quad \text{Eq. (C-12)}$$

By changing the loading condition to normal force Pb in the Y-direction and νPa in the X-direction, Figure C-1b, the same result can be found for the orthogonal member cross-section area in the Y-direction.

$$A_2 = bt\frac{\left(1 - \nu a^2/b^2\right)}{1 - \nu^2} \quad \text{Eq. (C-13)}$$

In case of tangential (shear) forces applied to the truss framework as shown in Figure C-1c, all orthogonal members are unstressed due to the symmetry in the truss framework pattern. However, all the diagonal members are stressed with equal tension and compression values. Force equilibrium in the Y-direction at Point 1, shown in Figure C-1c, gives:

$$2F_D \sin\alpha - Pa = 0 \quad \text{Eq. (C-14)}$$

Using $sin\,\alpha = a/\sqrt{a^2 + b^2}$, the diagonal member force subjected to shear stresses is:

$$|F_D| = \frac{P\sqrt{a^2 + b^2}}{2} \quad \text{Eq. (C-15)}$$

Similarly, the force equilibrium in the X-direction at Point 1 in Figure C-1c shows that the orthogonal member internal force is zero.

$$F_D \cos\alpha - F_D \cos\alpha + F_{O1} = 0$$

$$F_{O1} = 0 \qquad \text{Eq. (C-16)}$$

The axial deformation (change in length) of the diagonal truss members is equal to:

$$\delta_D = \frac{P(a^2+b^2)}{4EA} \qquad \text{Eq. (C-17)}$$

Which transforms the rectangular mesh unit into a parallelogram as shown in Figure C-3.

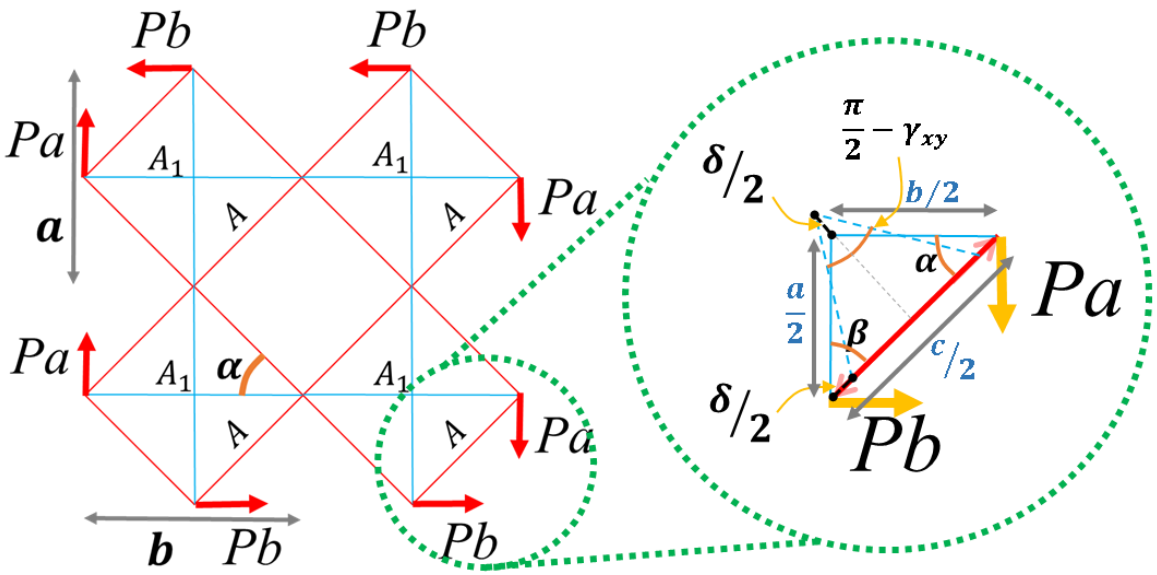

Figure C-3. Truss framework deformed shape subjected to shear forces

By writing the law of cosines for the deformed triangle shown in Figure C-3, the shear strain in the framework, γ_{xy}, is found:

$$\frac{c^2}{4} = \frac{a^2}{4} + \frac{b^2}{4} - \frac{2ab\cos\left(\frac{\pi}{2}-\gamma_{xy}\right)}{4} \qquad \text{Eq. (C-18)}$$

Using $cos\left(\frac{\pi}{2}-\gamma_{xy}\right) = sin(\gamma_{xy})$ and considering small deformations assumption, $sin(\gamma_{xy}) \cong \gamma_{xy}$,

$$c^2 = a^2 + b^2 - 2ab\gamma_{xy} \qquad \text{Eq. (C-19)}$$

Considering $\frac{c}{2} = \left(\frac{\sqrt{a^2+b^2}}{2} - \delta_D\right)$ and expanding Eq. (C-19) gives:

$$4\left(\frac{a^2+b^2}{4} - \frac{P(a^2+b^2)\sqrt{a^2+b^2}}{4EA_D}\right) = a^2 + b^2 - 2ab\gamma_{xy} \qquad \text{Eq. (C-20)}$$

In Eq. (C-20), ${\delta_D}^2$ is taken zero because of small deformation assumption. By substituting γ_{xy} from Eq.(C-5) into Eq. (C-20), A_D is obtained as:

$$A = \frac{\sqrt{a^2+b^2}(a^2+b^2)}{4ab(1+\nu)}t \qquad \text{Eq. (C-21)}$$

Poisson's ratio, ν, should be calculated to satisfy the deformation compatibility equation. Figure C-4 shows the framework deformation in the X-direction subjected to normal force, Pa, in the X-direction and νPb in the Y-direction.

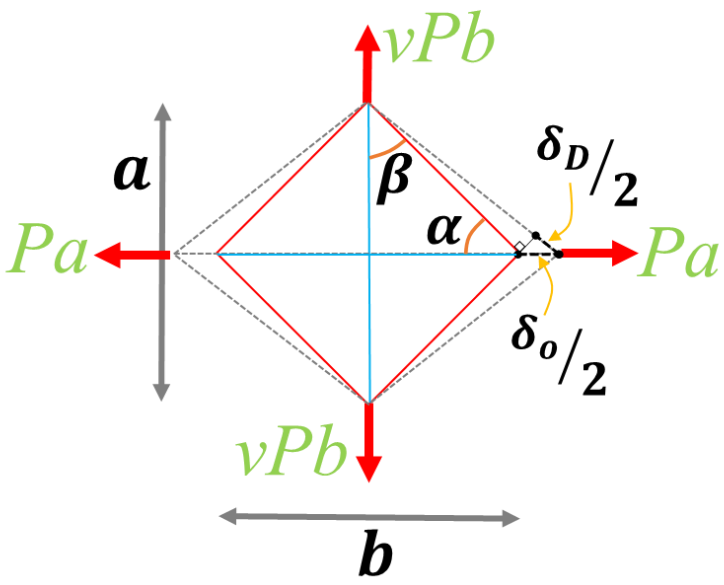

Figure C-4. Truss framework deformation in the X-direction subjected to normal force Pa in the X-direction and νPb in the Y-direction

The deformation compatibility can be achieved by writing the relationship between the orthogonal and diagonal member deformations as:

$$\frac{\delta_D}{2} = \frac{\delta_O}{2}\cos\alpha \qquad \text{Eq. (C-22)}$$

The truss element axial deformations are denoted by δ_D and δ_O for diagonal and orthogonal members respectively.

Considering the truss element axial forces obtained using equilibrium in the X-direction, Eq. (C-10), and truss member cross-sections given in Eqs. (C-12) and (C-21), δ_D and δ_O are calculated as:

$$\delta_D = \frac{\nu P b^2 2(1+\nu)}{\mathrm{E}\sqrt{a^2+b^2}t} \qquad \text{Eq. (C-23)}$$

$$\delta_O = \frac{Pb(1-\nu^2)}{Et} \qquad \text{Eq. (C-24)}$$

Substituting these axial deformations, Eq. (C-23) and (C-24), into Eq. (C-22), gives:

$$\frac{\nu P b^2 2(1+\nu)}{\mathrm{E}\sqrt{a^2+b^2}t} = \frac{Pb(1-\nu^2)}{Et}\frac{b}{\sqrt{a^2+b^2}} \qquad \text{Eq. (C-25)}$$

From which $\nu = \frac{1}{3}$ results.

Considering a square mesh unite, $a = b$, and Poisson's ratio $\nu = \frac{1}{3}$, the cross-section area of the orthogonal and the diagonal members are obtained using Eqs. (C-12), (C-13) and (C-21) respectively as $A_1 = 0.75at$, $A_2 = 0.75at$ and $A = 0.53at$.

References

[1] Hrennikoff, A. (1941). Solution of problems of elasticity by the framework method. Journal of applied mechanics, 8 (4):169-75.

[2] Timoshenko, S. P., & Goodier, J. N. (1970). Theory of Elasticity, (216).

Appendix D: FEM Modelling Parameters

D.1 Element selection

ABAQUS is a powerful software in offering a wide range of element types for the FE modelling. These include one-dimensional beam elements, two-dimensional shell, three-dimensional solid elements, connector elements and membrane elements.

In this research, three dimensional 8-node reduced integration solid elements, which are called C3D8R in ABAQUS element library, are used to model the cleat plates, bolts and parts of the beam. Also, two dimensional 4-node reduced integration shell elements, which are called S4R in ABAQUS element library, are used to model the middle part of the steel beam. These elements are used to reduce the computational costs and analysis time. Figure D-1 shows 3D8R and S4R elements used in this study.

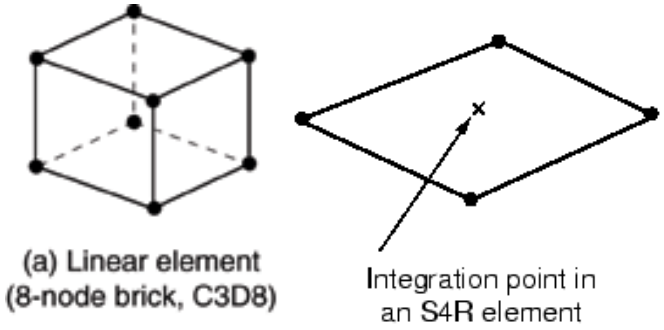

Figure D-1. C3D8R and S4R elements (Hibbitt, 2010)

D.2 Material properties

Nonlinear behaviour of the steel beam, cleat plate and bolts are simulated using an isotropic hardening material model based on the von-Mises yield criterion. This material model is called “Plastic” in ABAQUS material library.

An elastic-perfectly plastic stress-strain relationship is used to model the high-strength bolts material, and a bilinear stress-strain relationship with 1% hardening is used for the steel

beam and cleat plate. These stress-strain relationships were used by Mahamid et al. (2007) for FEM modelling of WSP connections. All the engineering stress-strain data converted into true stress-strain as required for ABAQUS material input (Hibbitt, 2010). The Elastic modulus and Poisson's ratio of the steel material are considered 200GPa and 0.3 respectively.

Figure D-2 shows the engineering stress-strain relationships of the beam and cleat plate and bolt materials schematically. The values of yield and ultimate stresses are selected based on the experimental studies that were used for the FEM model verification described in Appendices E and F.

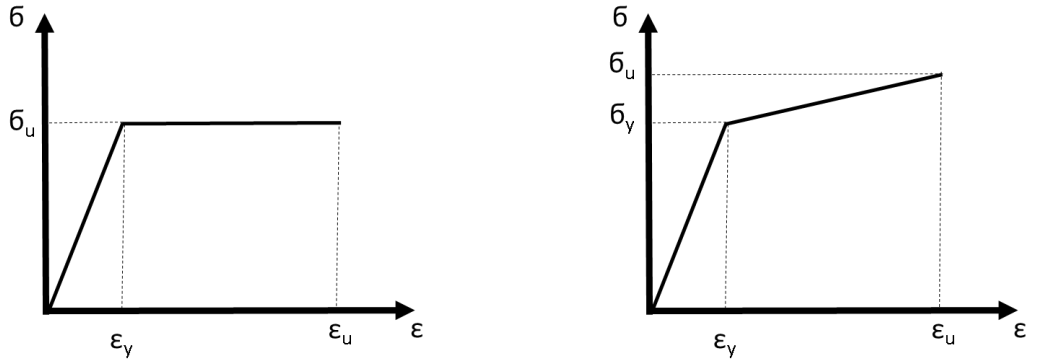

a) Bolt material b) Steel beam and cleat plate material

Figure D-2. Stress-strain relationships for FE simulations

D.3 Mesh sensitivity study

In FEM analysis, results may be sensitive to the number and size of elements used in the model. Generally, in highly stressed zones such as the cleat plate, bolts and the beam web fine mesh is required to achieve more accurate results. However, at regions far from the connection that may have less effect on the connection axial behaviour, coarse mesh can be used to decrease computational costs and analysis time.

Here, a short parametric study is conducted to obtain adequate mesh size in high stresses regions. A cleat plate with one bolt subjected to shear force applied to the bolt-ends is considered. The results are compared in terms of the vertical displacement versus the shear force reactions of the cleat plate.

As mentioned in Section D.1, C3D8R solid elements are used to model the cleat plate, beam and bolts. Therefore around curved surfaces such as bolt holes, more elements are required to be able to simulate a smooth curved surface. In this study, 2mm mesh size is used for bolts and bolt-holes in the cleat plate and the beam web. Figure D-3 shows the models with different mesh sizes.

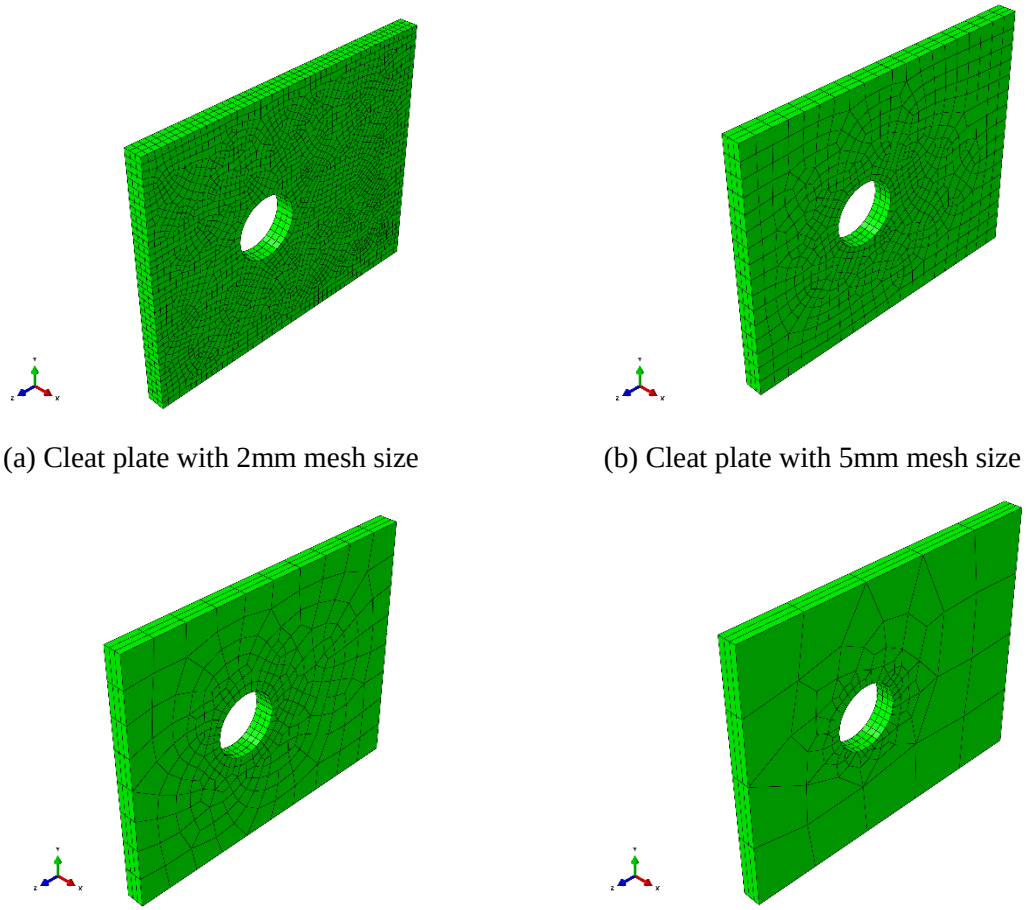

(a) Cleat plate with 2mm mesh size

(b) Cleat plate with 5mm mesh size

(c) Cleat plate with 10mm mesh size

(d) Cleat plate with 20mm mesh size

Figure D-3. Cleat plate with different mesh size

Vertical displacement of the cleat plate versus shear force reaction plots of each model are presented in Figure D-4. It shows that models with mesh size 2 and 5mm were reasonably similar. However, Model with 10mm mesh size showed 5% higher reaction force compared to the 2mm mesh size model. Also, the 20mm mesh size model indicated nearly 8% higher reaction force than the 2mm mesh size model. Table D-1 indicates total number of elements

and analysis time for these models. In this study, 5mm mesh size is selected as a reasonable mesh size based on the analysis time and the results obtained.

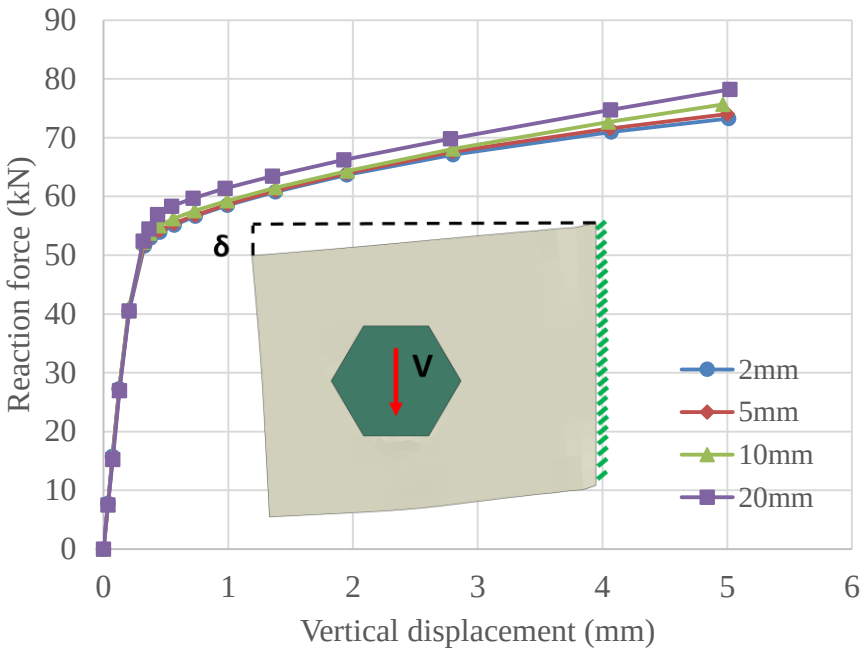

Figure D-4. Vertical displacement of the cleat plate versus shear force reaction curves of models with 2,5,10 and 20mm mesh size

Table D-1. Information of models for mesh sensitivity analysis

Model	*Cleat mesh size (mm)*	*Number of total elements*	*Analysis time (s)*
1	2	11354	186
2	5	6218	93
3	10	5162	70
4	20	4619	61

D.4 Geometric nonlinearity

ABAQUS software is able to consider geometric nonlinearities when the "NLGEOM" option is activated in the analysis steps. Nonlinear geometry was activated for all models analysed in Chapter 4 to capture local or global buckling modes and/or instability of models.

References

[1] Hibbitt, K., Karlsson, B., & Sorensen, P. (2010). ABAQUS/Standard User's Manual. Version 6.11. Providence, RI: Dassault Systèmes Simulia Corp.

[2] Mahamid, M., Rahman, A. D. E. E. B., & Ghorbanpoor, A. (2007). The Analyses of Extended Shear Tab Steel Connections Part II: Stiffened Connections. ENGINEERING JOURNAL-AMERICAN INSTITUTE OF STEEL CONSTRUCTION, 44(2), 133.

Appendix E: FEM Model Verification with Astaneh et al. (1988) Experimental Results

Experimental investigation on shear force carrying behaviour of WSP connections that conducted by Astaneh et al. (1988) is used to verify the FEM models of this study. In the following sections a brief description of the test details, results, and FEM model verification are presented.

E.1 Description of experimental study

Astaneh et al. (1988) investigated the shear resistance and rotational ductility of WSP connections by testing three full-scale specimens. All specimens were considered to have a single vertical row of bolts. Specimen 1, 2 and 3 had three, five and seven bolts respectively. In this study, specimen 2 is selected for FEM model verification.

E.1.1 Specimen 2 details

The specimen 2 consisted of W10×77 wide flange section for the column and W18×55 wide flange section for the beam and 15×3/8×4-1/4 in. (381×9.5×108 mm) cleat plate. The cleat plate was connected to the column using ¼ in. (6.35mm) fillet weld.

Bolts used for connecting the beam web to the cleat plate were ¾ in. (19mm) Grade A325-N. All bolts were tightened up to 70% of the proof load by using turn of the nut method. The bolt-holes were standard round hole with a nominal diameter of 13/16 in. (20.6mm). The bolt spacing was 3 in. (76mm) centre by centre, and the edge distances was 1.5 in. (38mm) from top and bottom of the cleat plate. Figure E-1 shows the 5-bolt specimen schematically.

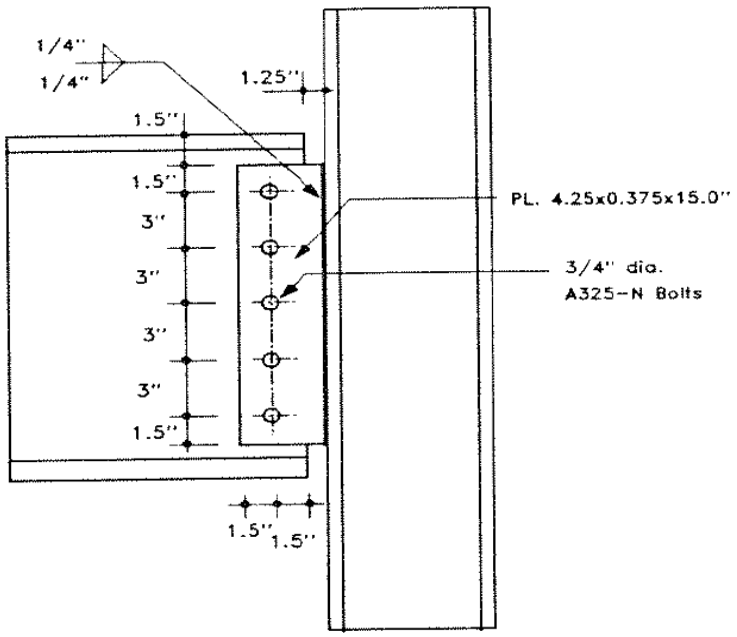

Figure E-1. Specimen 2 details (Astaneh et al., 1988)

E.1.2 Test setup

Figure E-2 shows the test setup of the experiments. In this test setup, two actuators were used to control the amount of imposed shear force and the rotation to the connection. Actuator S shown in Figure E-2 was force-control to apply shear force to the connection and actuator R was displacement-control to impose rotation to the connection.

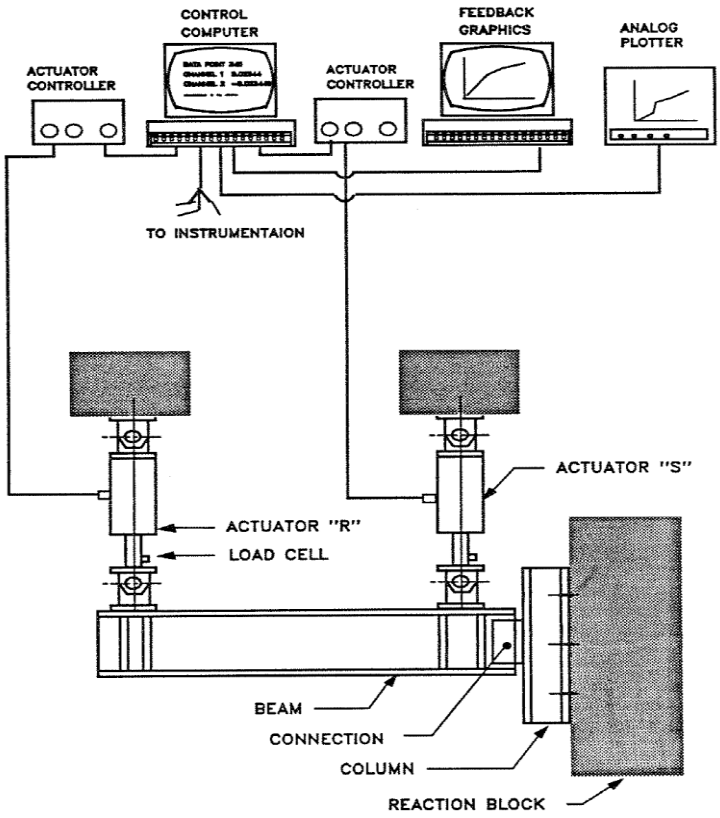

Figure E-2. Test setup (Astaneh et al., 1988)

The shear force-rotation relationship used for loading the specimens is shown in Figure E-3. Astaneh (1989) studied the shear-rotation relationship for the end supports of simply supported beams using a computer program considering different beam cross-sections and span lengths. These shear force-rotations covered the elastic loading part up to the beam failure. Figure E-3 shows three shear force-rotation curves. Two dashed curves shown in this Figure represent the shear force-rotation values for a shallow beam with large span and a deep beam with a small span as an upper and lower bonds. The solid line which is between these two upper and lower bonds was used to apply loads and deformations to the specimen.

Segment AB on the loading curve shown in Figure E-3 corresponds to the elastic behaviour of the beam. At the point B the beam mid-span starts to yield. In segment BC the beam at the mid-span experiences yielding. Therefore the connection rotation demand increases without much increase in the connection shear force demand. At the point C the

plastic hinge reached to the fully plastic moment strength of the beam, M_p, at the beam mid-span. Segment CD is related to strain hardening behaviour in the beam until the rotation reaches to 0.1 rad (Astaneh et al., 1989).

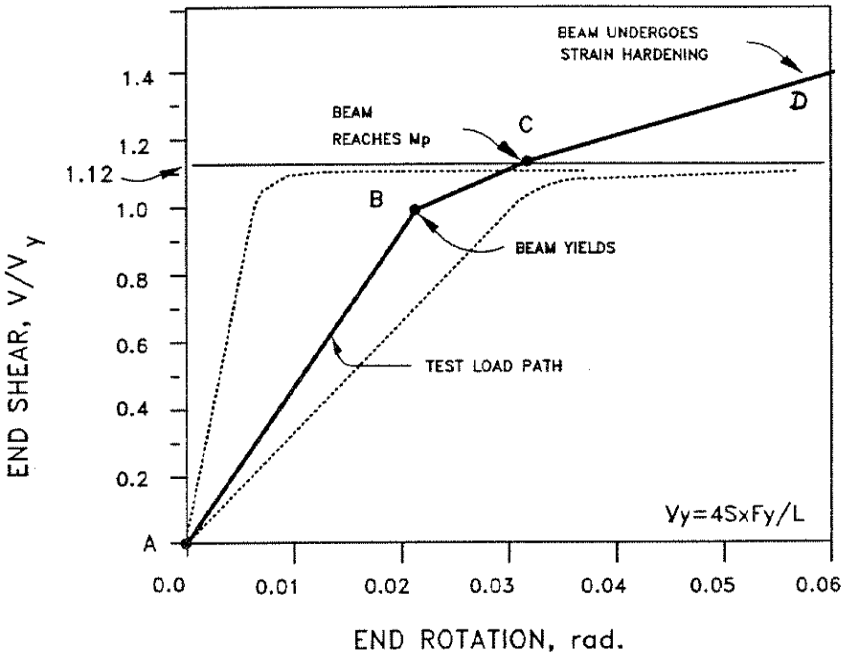

Figure E-3. Shear-rotation curve used for loading specimens (Astaneh 1989)

E.2 FEM modelling

E.2.1 Model geometry

The specimen details, interactions, boundary conditions and materials are considered in the FE modelling. To decrease the computational costs, part of the beam beyond the actuator S, shown in Figure E-2, is not modelled. In the following sections, model details, loading method and boundary conditions are explained in detail. Figure E-4 shows all parts of the FEM model include bolts, cleat plate and beam.

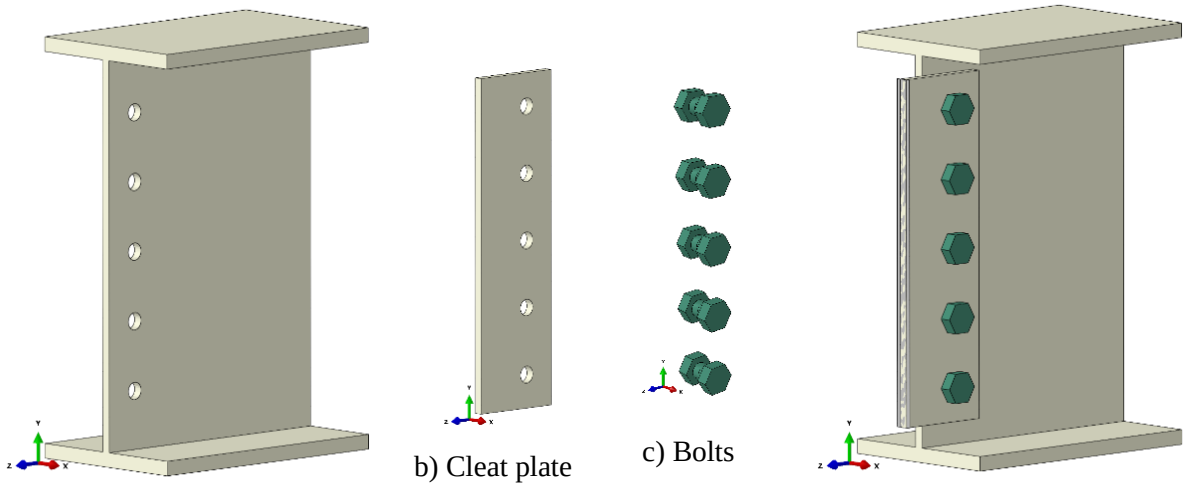

a) Beam b) Cleat plate c) Bolts d) Model assembly

Figure E-4. FEM model parts

E.2.2 Material properties

The steel materials yield strengths used in this model are based on the reported values by Astaneh et al. (1988). It was reported that the structural steel Grade A36 with the yield strength of 35.5 ksi (244.7 MPa) and the ultimate strength of 60 ksi (413.6 MPa) was used for the beam and the cleat plate. Also, A325 bolts were used for connecting the cleat plate to the beam web. In the FEM model, the bolt material is simulated using the elastic-perfectly plastic behaviour considering the bolt ultimate strength. The cleat and the steel beam material are simulated using the bilinear stress-strain behaviour considering 1% strain hardening as described in Appendix D.

E.2.3 Interactions

The behaviour of this type of connection is highly associated with the forces that transfer from one part to another. Therefore, interaction between the parts of the FEM model is a key parameter in this simulation. Here, the “Surface-to-Surface” interaction existing in ABAQUS interaction options is used between the in contact surfaces of cleat plate, beam web, and the bolts.

In the "Surface-to-Surface" interaction, two main interaction behaviours include "normal" and "tangential" should be defined. For the "normal" behaviour, "hard" contact is used. Separation of parts is allowed during the analyses. For the "tangential behaviour", "Penalty" friction formulation with a friction coefficient of 0.3 is defined. The contact surfaces used in the model are shown in Figure E-5.

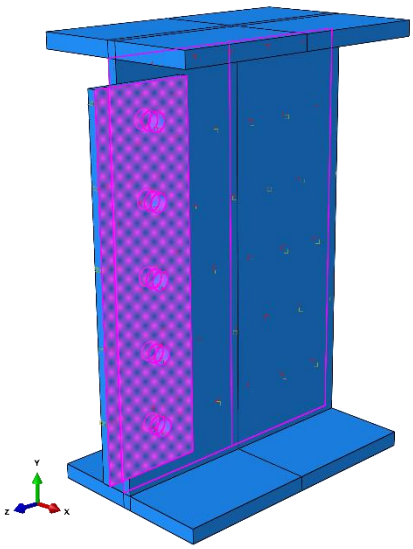

a) Cleat plate and beam web surfaces in contact with bolts

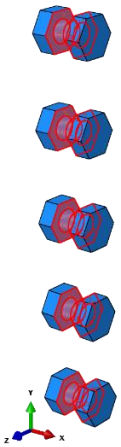

b) Bolts surfaces in contact with cleat plate and beam web

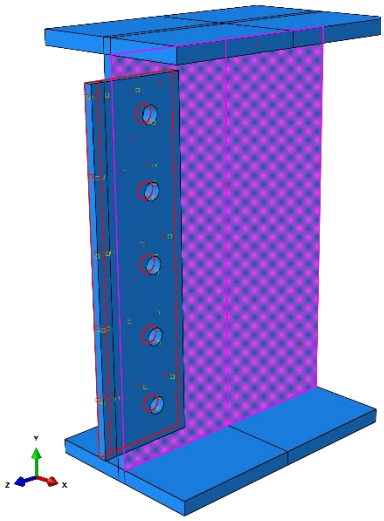

c) Contact surface between beam web and cleat plate

Figure E-5. Interaction surfaces between bolts, cleat plate and beam

E.2.4 Bolt pre-tensioning

Bolt pre-tensioning is considered in the FE model as the bolts in the tests were tightened up to 70% of proof-load. ABAQUS software provides a method to apply bolt pre-tension force by using "bolt-load" option in the "load" module. Using this feature, a certain amount of pre-tension force can be applied to the bolts. The amount of bolt pre-tension load or the bolt length can be chosen to remain the same in all the following analysis steps. When the bolt length is chosen to remain constant, the bolt behaves with its mechanical properties plus the existing pre-tension force; this option is used in the FE simulations of this study. Figure E-6 shows the bolt cross-section with the bolt pre-tension forces.

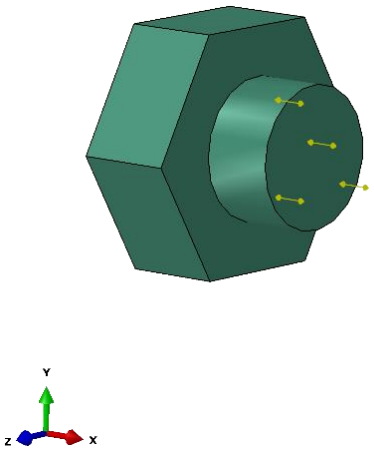

Figure E-6. Bolt pre-tension force (ABAQUS)

E.2.5 Boundary conditions and loading method

As it was mentioned in Section E.1.2, the loading method used by Astaneh et al. (1988) consisted of imposing shear force and rotation to the connection at the same time according to the shear-rotation curve shown in Figure E-3. Thus, they used two actuators, one for applying shear force (force-control) and one for applying rotation (displacement-control) to the connection. In ABAQUS software it is possible to impose shear force at the location of the load-control actuator and apply displacement at the location of the displacement-control actuator. However, when a displacement is applied at the end of the beam, it can change the

amount of imposed shear force to the connection. Therefore, in the FE model, the loading pattern is applied to the end of the cleat plate instead of the beam, which provides similar results.

As shown in Figure E-7, part of the beam with is located between the force-control actuator and the connection is modelled. One end of the beam is fully restraint and the other end is connected to the cleat plate. Both shear force and rotation are applied to the cleat plate support.

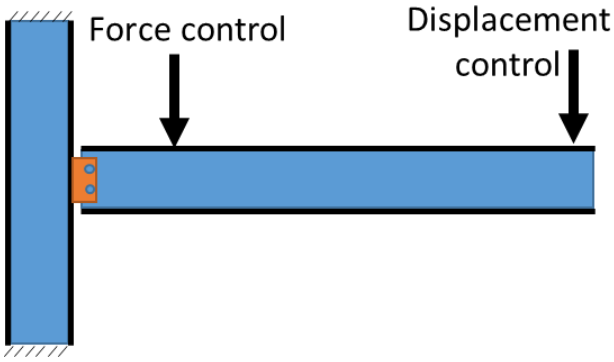

a) Loading method used in the experiments (Astaneh et al. 1988)

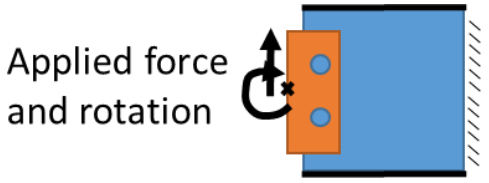

b) Loading method used in the FEM model

Figure E-7. Loading method

E.2.6 Mesh

Based on the mesh sensitivity study described in Appendix D, 5mm mesh size is used to model the cleat plate and the beam web near connection area and 2mm mesh size is used to model the curved surfaces such as bolts and bolt-holes. Four elements were used along the thickness of the beam web and the cleat plate to capture the contact forces along the thickness of the plates. Figure E-8 shows the meshing on different parts of the model. The total number of elements is 30,585 in this model.

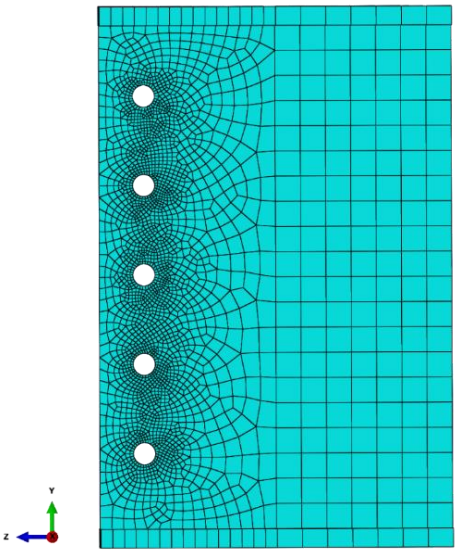

a) Beam web

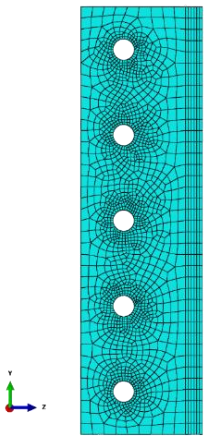

b) Cleat plate

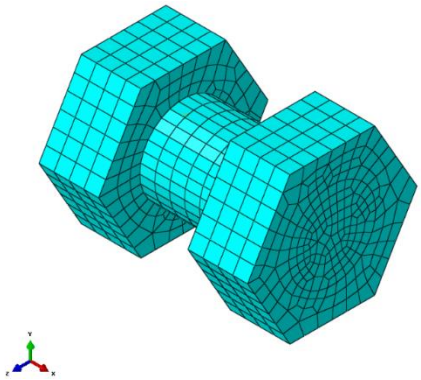

c) Bolts

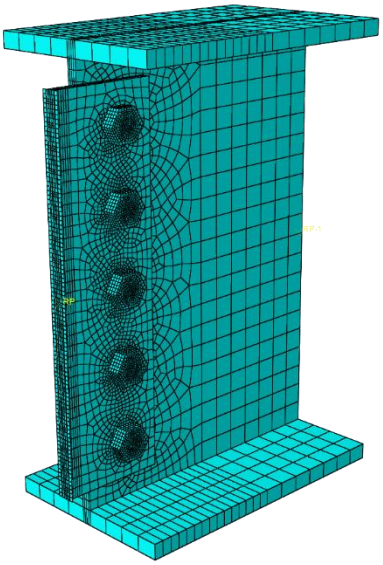

d) Full model

Figure E-8. Mesh on different parts of the model

E.3 FEM results

Astaneh et al. (1988) reported that the slip between the cleat plate and the beam web of the specimen 2 (which is modelled in this study) occurred when the connection shear force reached to 54 kips (231 kN). Local yielding of the beam web due to bolt bearing was also observed at 83 kips (369 kN) and at 130 kips (578 kN) buckling occurred at the bottom of the

beam web. It caused 3.1mm gap between the beam web and the cleat plate. Connection failure occurred at 137k kips (610 kN) with 0.054 rad rotation.

The FEM modelling results are compared with the experimental results in terms of:

i) Shear force-vertical deformation of the connection and shear force-vertical deformation of the cleat plate

ii) Beam web local buckling

iii) Failure modes

iv) Connection free body force diagram

E.3.1 Shear force-vertical deformation behaviour

Figure E-9 shows the vertical deformation versus connection shear force of the beam and the cleat plate for both the experimental test of Astaneh et al. (1988) and the FEM model. The computed total connection deformation, plotted in Figure E-9a, and the cleat plate deformation, plotted in Figure E-9b, showed good agreement with the experimental results with less than 3% difference at the maximum shear force recorded.

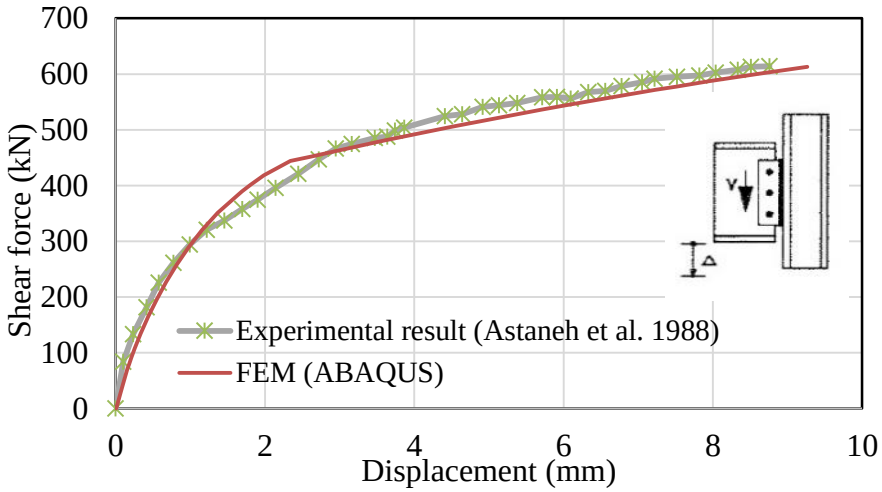

a) Shear force-total connection deformation

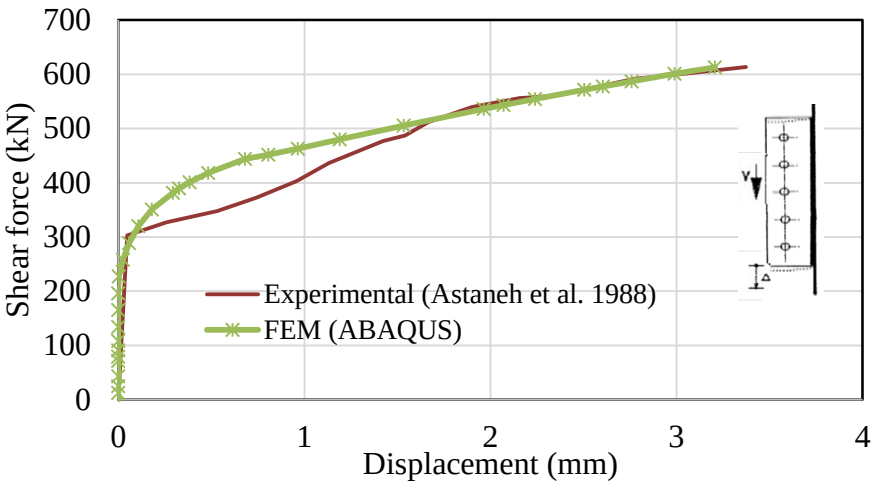

b) Shear force-cleat plate deformation

Figure E-9. Vertical deformation of beam and cleat plate versus connection shear force

E.3.2 Beam web local buckling

The value of reported out-of-plane deformation due to the web local buckling was 3.1 mm in the experimental study for the specimen 2. Figure E-10 shows the beam web local buckling obtained from the FEM simulation. The maximum out-of-plane displacements of the beam web recorded near the uppermost bolt and the bottom bolt are about 3.7mm and 3mm respectively. These values are respectively 19% higher and 3% lower than the reported value from the experimental study by Astaneh et al. (1988).

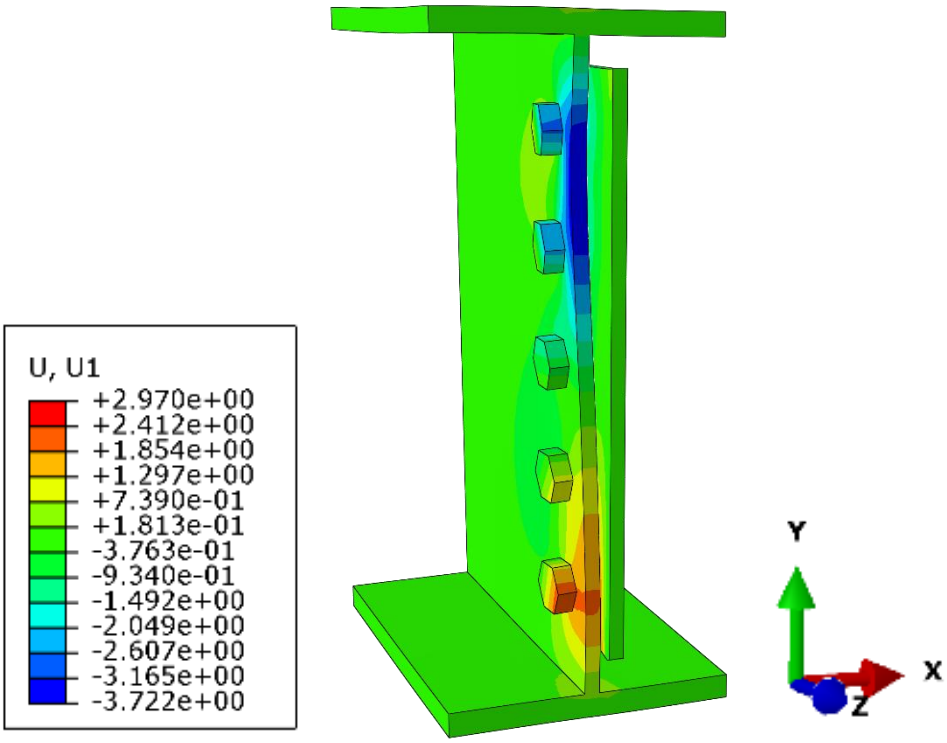

Figure E-10. Beam web local buckling from FEM simulation, (U1 presents out-of-plane deformation, X-direction, in mm)

E.3.3 Failure mode

The main failure mode that was reported by Astaneh et al. (1988) for specimen 2 was bolt shear failure. Since the failure of the materials is not considered in the simulations, the failure state is predicted by using "equivalent plastic strain" which can be obtained from ABAQUS software results. This parameter shows the level of plastic deformation of each element in terms of equivalent uniaxial strain. Therefore, the "equivalent plastic strain" may be compared with the material ultimate strain to identify the failure point.

Based on the stress-strain relationship of A325 bolts that was investigated by Kulak et al. (2001), shown in Figure E-11, the ultimate strain of A325 bolts may be considered equal to 0.20. Figure E-12a,b show the bolt group in the FEM model. Places at the bolts cross-section that experienced "equivalent plastic strain" larger than 0.20 are shown in Figure E-12b as failure zones.

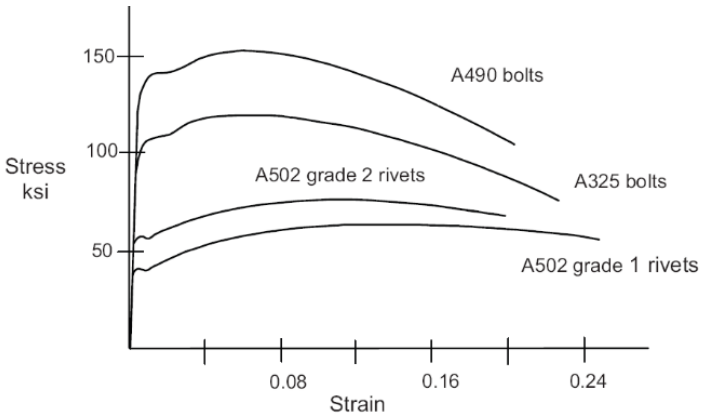

Figure E-11. Stress-strain relationship for different bolt grades (Kulak et al., 2001)

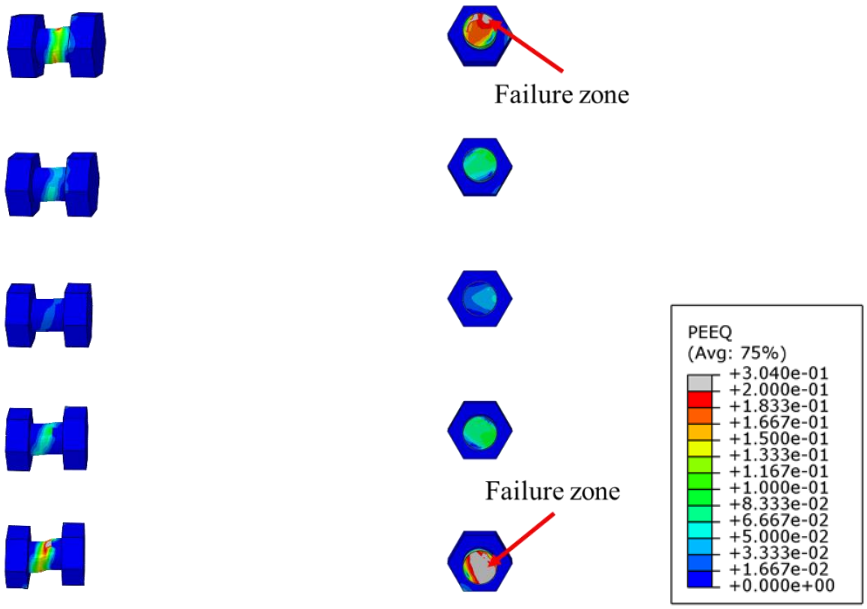

a) Bolt ultimate deformation

b) Bolt failure zones

c) Deformation and fracture of bolt in the experimental study (Astaneh et al., 1988)

Figure E-12. Bolt shear failure at the end of analysis

E.3.4 Connection free body diagram

The free body diagram of the cleat plate, the bolts and the beam web were sketched by Astaneh et al. (1988) based on the experimental observations and bolt bearing deformations as shown in Figure E-13a. The free body diagram of the FEM model is also presented in

Figure E-13b,c and d. It can be seen in this Figure that the direction of forces in both experimental and FEM model match.

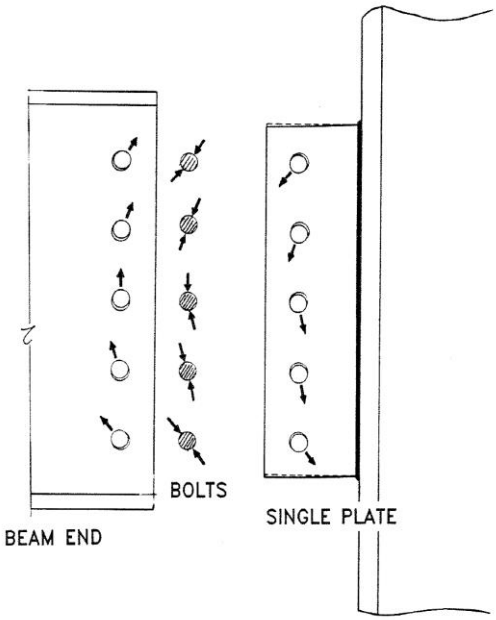

a) Free body diagram of experimental tests (Astaneh et al., 1988)

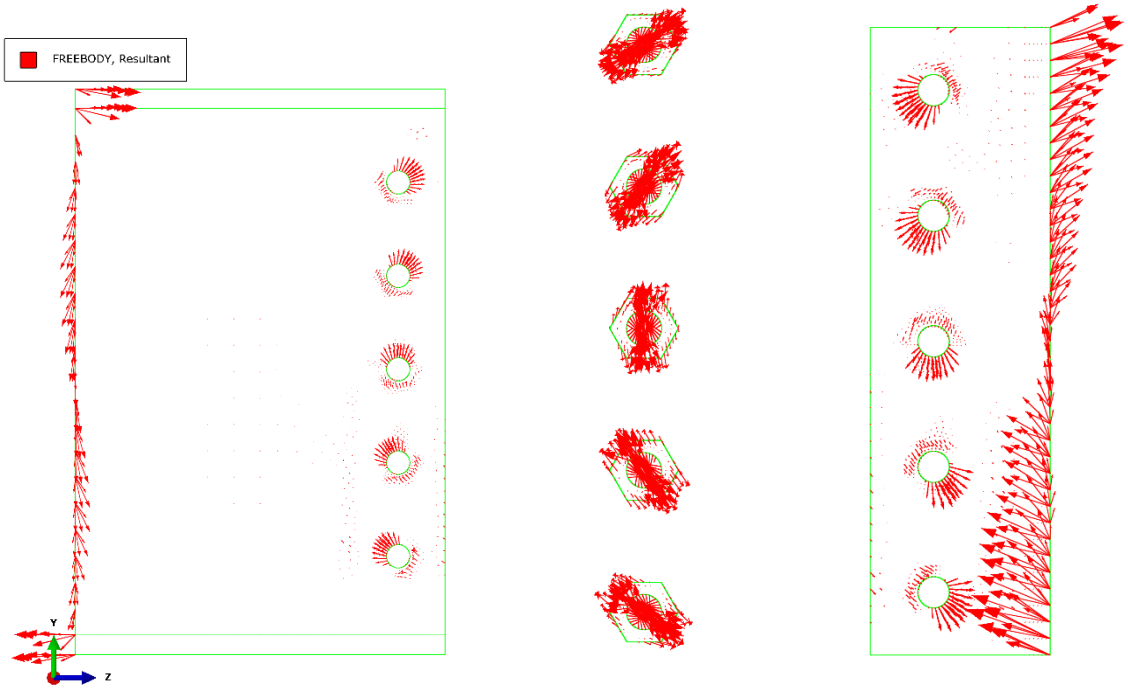

b) Forces on the beam web (FEM)

c) Forces on the bolt (FEM)

d) Forces on the cleat plate (FEM)

Figure E-13. Connection free body diagram

References

[1] Astaneh, A., McMULLIN, K. M. & Call, S. M. (1988). Design of single plate framing connections," Report No. UCB/SEMM-88/12 to the American Institute of Steel Construction. University of California at Berkeley.

[2] Astaneh, A. (1989b). Demand and supply of ductility in steel shear connections. Journal of Constructional Steel Research, 14(1), 1-19.

[3] Kulak, G. L., Fisher, J. W., & Struik, J. H. (2001). Guide to Design Criteria for Bolted and Riveted Joints Second Edition.

Appendix F: FEM Model Verification with Sherman and Ghorbanpoor (2002) Experimental Results

Experimental investigation on shear force carrying behaviour of extended WSP connections conducted by Sherman and Ghorbanpoor (2002) is used to verify the FEM models of this study. In the following sections, a brief description of the test details, results and FEM modelling verification are presented.

F.1 Description of experimental study

Sherman and Ghorbanpoor (2002) investigated thirty-one extended WSP connections experimentally. The purpose of their research was to develop a design procedure for extended WSP connections under shear forces. Based on the AISC steel construction Manual (2011), when the distance between the bolt-line and the weld-line is greater than 89mm, the connection is considered as extended WSP connection.

Here, specimen 3U of Sherman and Ghorbanpoor (2002) study is selected for FEM model verification.

F.1.1 Specimen 3U details

The specimen 3U consisted of W8×31 wide flange section for the column, W12×87 wide flange section for the beam and 9×3/8×9 in. (228×9.4×228 mm) cleat plate. The beams and columns material were ASTM A-572 Grade-50 and the cleat plate material was ASTM A36 Grade 36. Cleat plate was connected to the column with 5/16-in. (8mm) fillet weld on both sides of the plate.

The bolts used for connecting the beam web to the cleat plate were ¾ in. (19mm) Grade A325-X. The bolt-holes were standard round hole with a nominal diameter of 13/16 in. (20.6mm). The bolt spacing was 3 in. (76mm) centre by centre, and the edge distances was

1.5 in. (38mm) from top and bottom of the cleat plate. Figure F-1 shows the specimen 3U schematically.

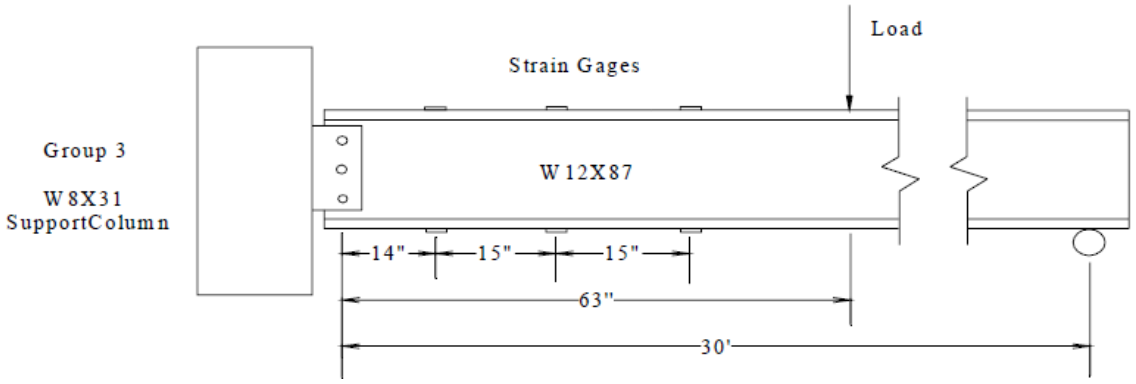

Figure F-1. Specimen 3U of Sherman and Ghorbanpoor (2002) experimental study

F.1.2 Test setup

Figure F-2 shows the test setup that was used by Sherman and Ghorbanpoor (2002). In this test setup, the far end of the beam was supported by a roller connection as shown in Figure F-2a. The support column was connected to the reaction wall using cross beams and steel rods as shown in Figure F-2b and c.

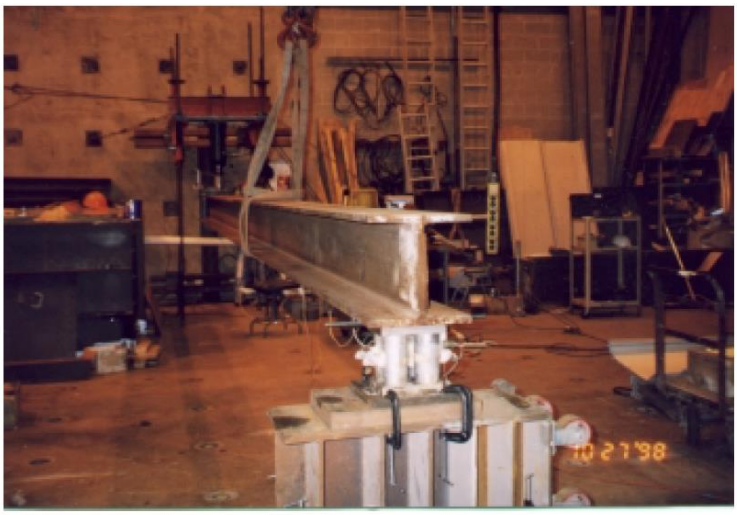

a) Beam far end support

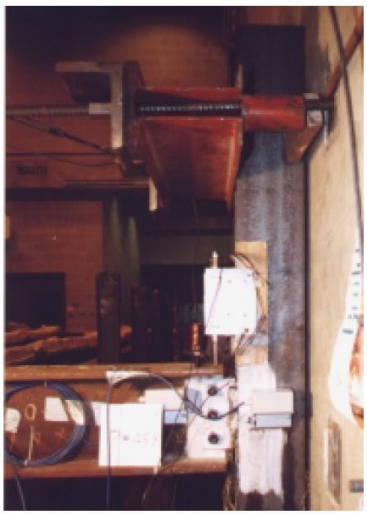

b) Support column connection to reaction wall

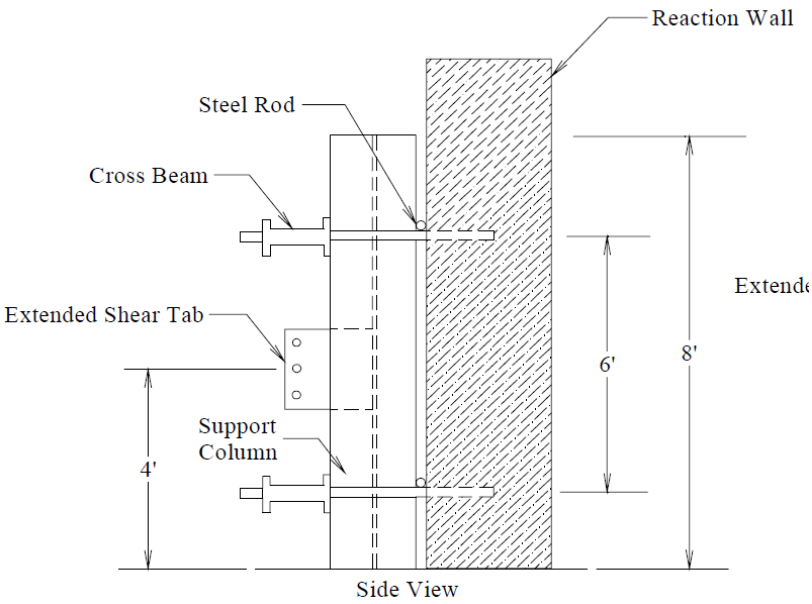

c) Details of support column connection to reaction wall

Figure F-2. Test setup (Sherman and Ghorbanpoor, 2002)

The location of the point load shown in Figure F-1 and the beam length were selected such that the beam end rotation and the shear reaction be similar to a corresponding uniformly loaded simply supported beam. The shear force was applied by a hydraulic jack at 1600mm distance from the WSP connection.

F.2 FEM modelling

F.2.1 Model geometry

The specimen details, interactions, boundary conditions and materials are considered in the FE modelling. To decrease the computational costs, part of the beam, which may not experience high-stress levels, is modelled using the shell elements instead of the solid elements, as shown in Figure F-3a. In the following sections, specimen details, loading method and boundary conditions are explained in detail. Figure F-3 shows all parts of the FEM model include bolts, cleat plate and beam.

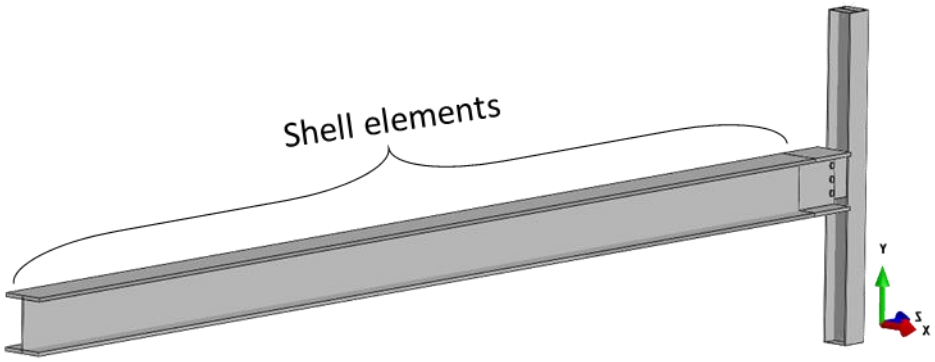

a) Model assembly

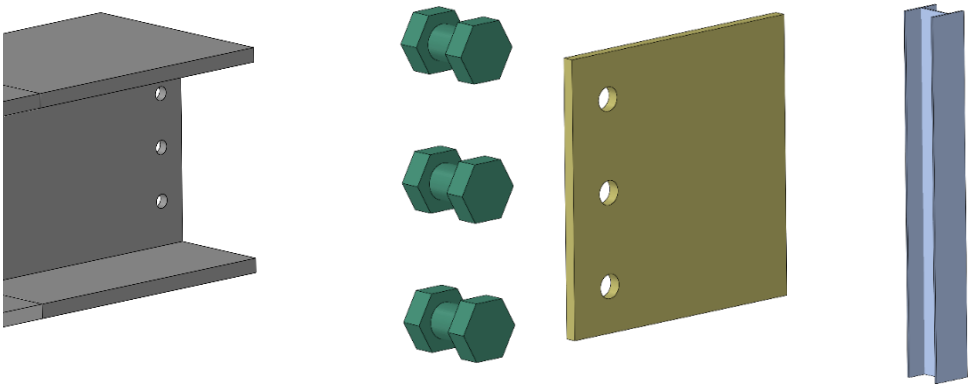

b) Beam end c) Bolts d) Cleat plate e) Support column

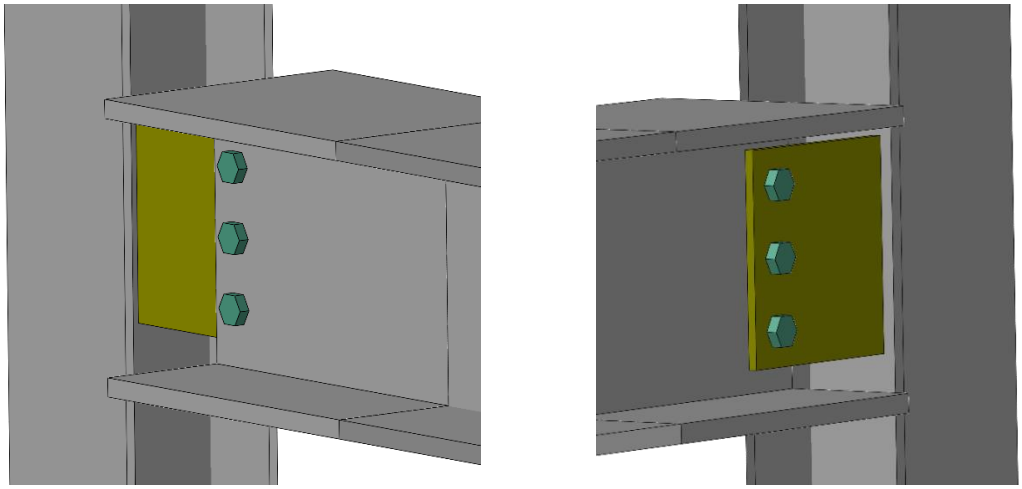

f) Back view g) Front view

Figure F-3. FEM model parts

F.2.2 Material properties

Material properties used in this model are based on the reported values by Sherman and Ghorbanpoor (2002). It was reported that the beams and columns material was ASTM A-572 Grade-50 steel and the cleat plate material was ASTM A36 Grade 36 steel. Also, A325 bolts

were used for connecting the cleat plate to the beam web. In the FEM model, the bolt material is simulated using the elastic-perfectly plastic behaviour considering the bolt ultimate strength. The cleat and the steel beam material are simulated using the bilinear stress-strain behaviour considering 1% strain hardening as described in Appendix D. Table F-1 presents the material strengths for the cleat plate, the beam and the column parts.

Table F-1. Material tensile strengths (Sherman and Ghorbanpoor, 2002)

Member	**Yield strength (MPa)**	**Ultimate strength (MPa)**	**Elongation (%)**
Cleat plate	293	458.5	34
Column (W8×31) web	380.6	519.2	31
Beam (W12×87) web	391	494.3	37

F.2.3 Interactions

The behaviour of this type of connection is highly associated with the forces that transfer from one part to another. Therefore, interaction between the parts of the FEM model is a key parameter in this simulation. Here, the “Surface-to-Surface” interaction existing in ABAQUS interaction options is used between the cleat plate, the beam web, and the bolts.

In the “Surface-to-Surface” interaction, two main interaction behaviours which include “normal” and “tangential” should be defined. For the “normal” behaviour, “hard” contact with allowing separation after contact is used. For the “tangential behaviour”, “Penalty” friction formulation with a friction coefficient of 0.3 is defined. The contact surfaces defined in the model are shown in Figure F-4.

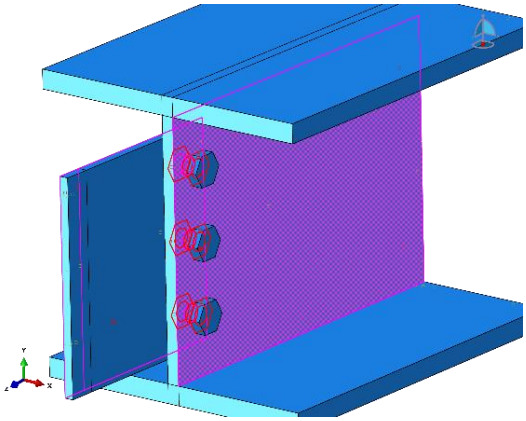

a) Cleat plate and beam web surfaces in contact with bolts

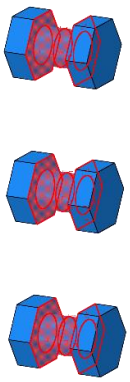

b) Bolts surfaces in contact with cleat plate and beam web

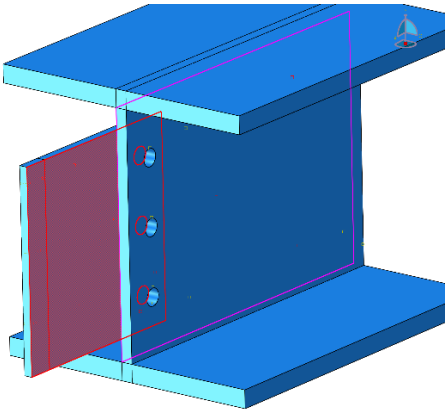

c) Contact surface between beam web and cleat plate

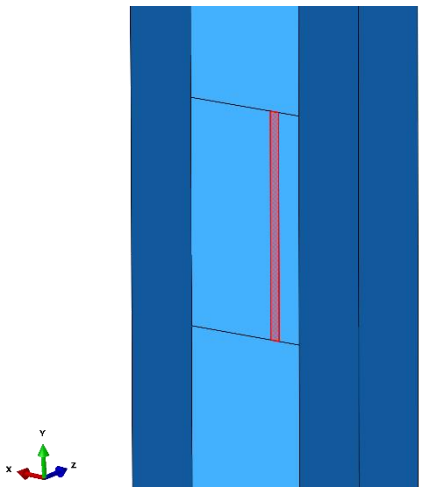

d) Tied surface of support column to cleat plate

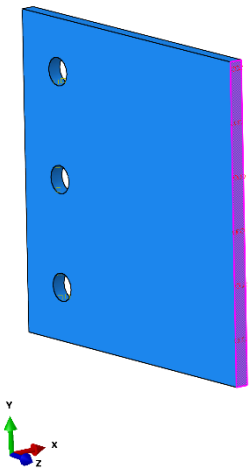

e) Tied surface of cleat plate to support column

Figure F-4. Interaction surfaces between bolts, cleat plate, beam and support column

According to the experimental results, the welded connection between the cleat plate and the support column web did not experience any damage or fracture. Therefore, in this study it is considered the cleat plate is fully connected to the support column web using “Tie” interaction available in ABAQUS interaction options.

F.2.4 Boundary conditions and loading method

The loading configuration and boundary conditions are modelled similarly to the experimental specimen of Sherman and Ghorbanpoor (2002). The point load is applied at 1600mm distance from the connection. The far end of the beam is supported using roller support. For preventing stress concentration and localised deformations, the point load is applied to 100mm length of the beam. The top end of the column is restraint with roller support and a pinned connection is used at the bottom end of the column. The shear force reaction of the connection is obtained through the column vertical reaction force. Figure F-5 shows the loading configuration in the FE model.

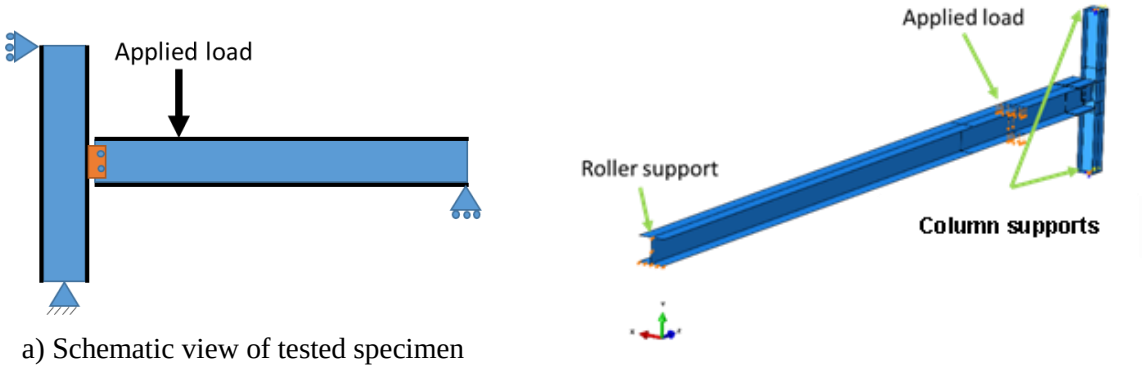

a) Schematic view of tested specimen

b) FEM model

Figure F-5. Boundary condition and loading of FEM model

F.2.5 Mesh

Based on the mesh sensitivity study described in Appendix D, 5mm mesh size is used to model the cleat plate, the column web near the connection and the beam web. Also, 2mm mesh size is used to model curved surfaces such as bolts and bolt-holes. Four elements were used along the thickness of the beam web and the cleat plate to capture the contact forces along the thickness of the plates. Figure F-6 shows the meshing on different parts of the model. The total number of nodes and elements in this model are 74903 and 62015 respectively.

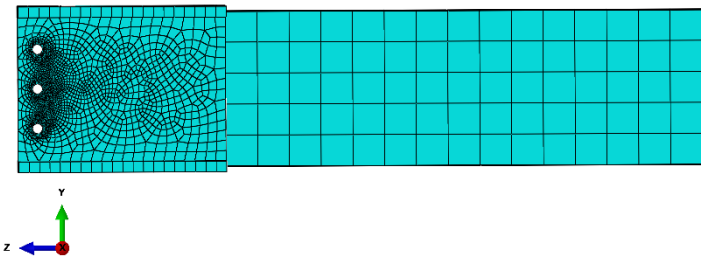

a) Beam web

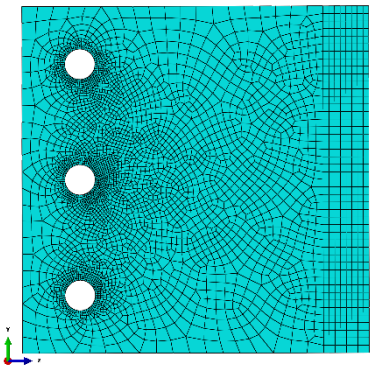

b) Cleat plate

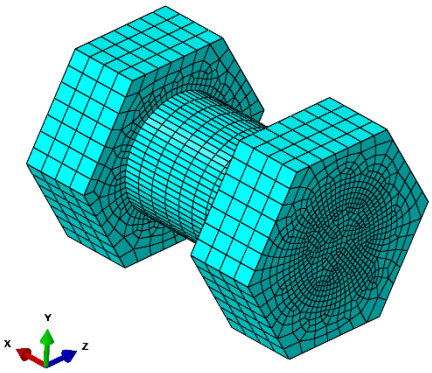

c) Bolt

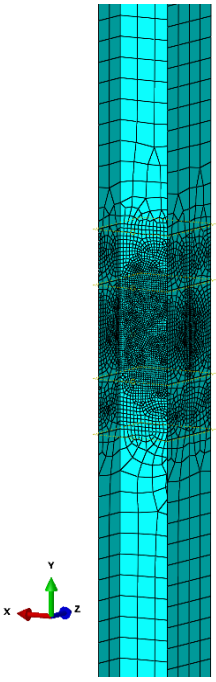

d) Support column

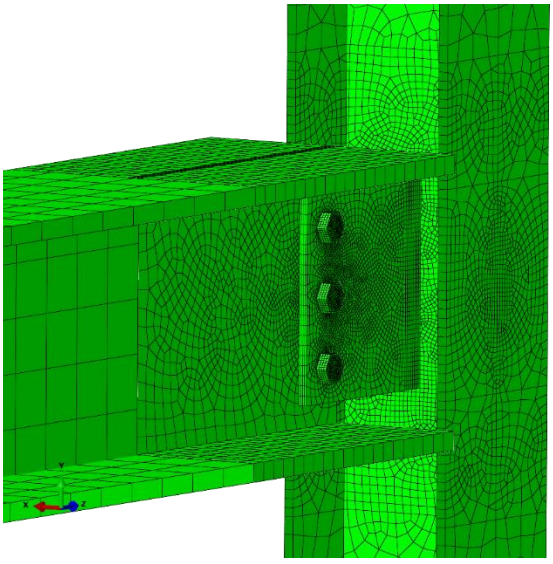

e) Connection assembly

Figure F-6. Mesh on different parts of the model

F.3 FEM results

The FEM modelling results are compared with the experimental results of Sherman and Ghorbanpoor (2002) in terms of:

i) Shear force-vertical deformation of the connection

ii) Shear force-beam rotation and shear force-column rotation

iii) Specimen failure modes

F.3.1 Shear force-vertical deformation behaviour

Figure F-7 shows the beam vertical deformation versus the connection shear force for the experimental test of Sherman and Ghorbanpoor (2002) and the FEM model. This Figure shows good agreement between the experimental and the FEM simulation results with less than 10% error in estimating connection ultimate strength at 9mm vertical deflection.

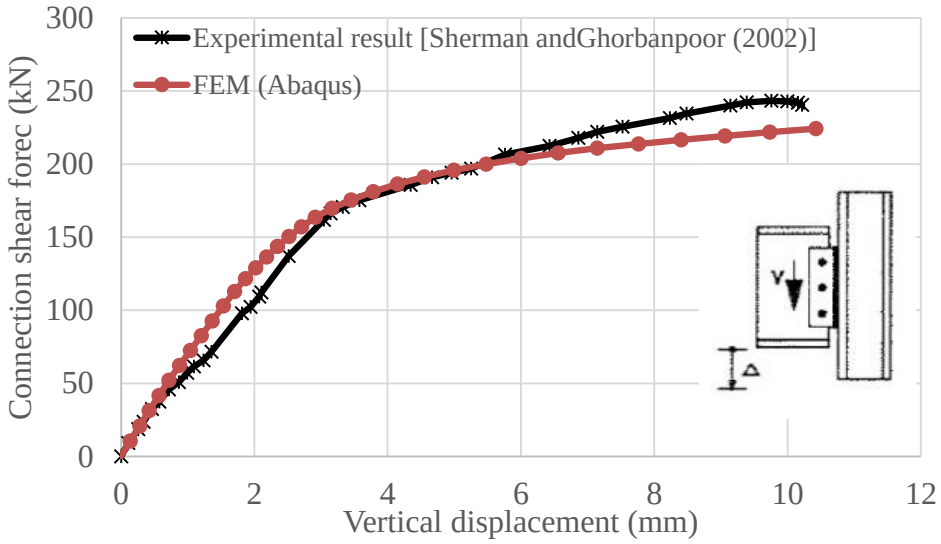

Figure F-7. Shear force-vertical deformation of the connection for both FEM model and tested specimen

F.3.2 Beam and column rotation

In the experimental tests of Sherman and Ghorbanpoor (2002), two tilt-meters were used to measure the rotation of the column web (support member) and the beam rotation near the connection. One tilt-meter was attached to the centreline of the column flange in the same

vertical location as the other tilt-meter was attached to the beam web. Figure F-8 shows the location of tilt-meters on the tested specimen. The rotations of the same points in the FEM models are obtained. Figure F-9 presents the experimental results as well as the FE model results.

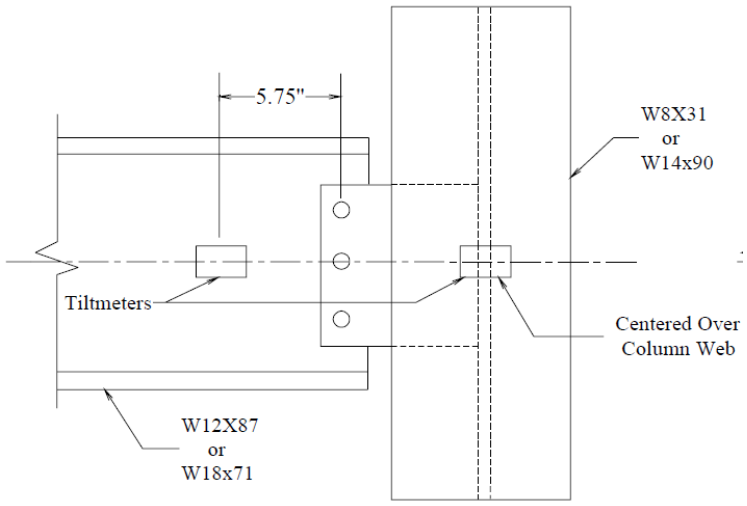

Figure F-8. Location of tilt-meters on column flange and beam web (Sherman and Ghorbanpoor, 2002)

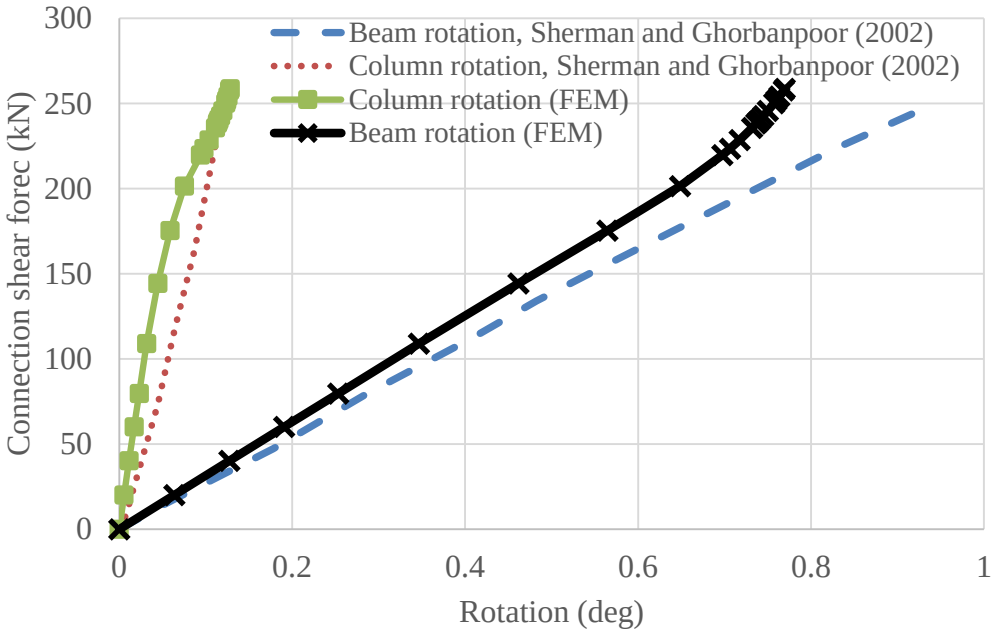

Figure F-9. Beam web and column flange rotations, experimental and FEM modelling results

As can be seen in Figure F-9, the beam and column rotations of the FEM model are lower than the experimental results. This may be because of perfect boundary conditions and the connection assumptions that are used in the FEM model.

F.3.3 Failure mode

The failure modes of the tested specimens were identified with visual inspection and monitoring parameters such as:

i) Shear force-twist angle of the cleat plate

ii) Shear force-vertical displacement of the connection

iii) Shear force-rotation of the support column web

When any of the above parameters first started to decrease stiffness, that parameter was identified as the primary failure mode. The failure modes that were reported for the specimen 3U by Sherman and Ghorbanpoor 2002 include column web mechanism followed by bolt shear failure.

Figure F-10 shows the shear force-twist angle of the cleat plate and the column web rotation versus the connection shear force. These plots indicate that web mechanism failure occurred at about 170 kN and after that the stiffness decreased. Similar to the experimental results, the column web mechanism is identified as the first failure mode in the FEM model, as shown in Figure F-10b and c

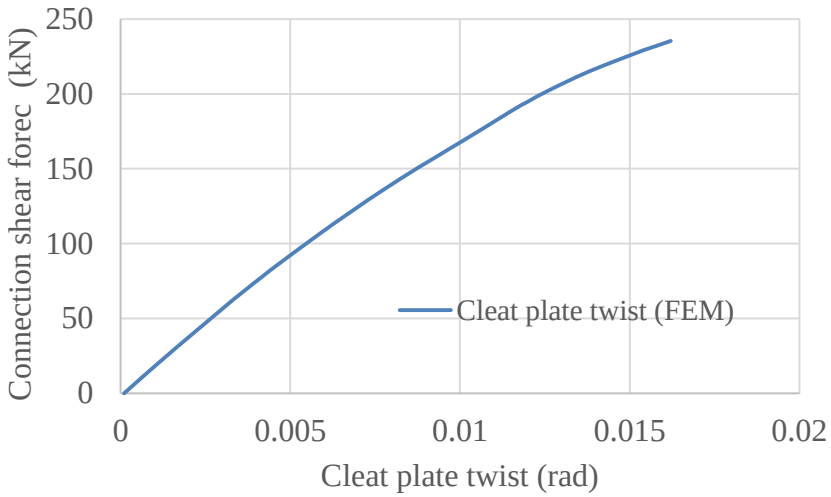

a) Cleat plate twist-connection shear force plot

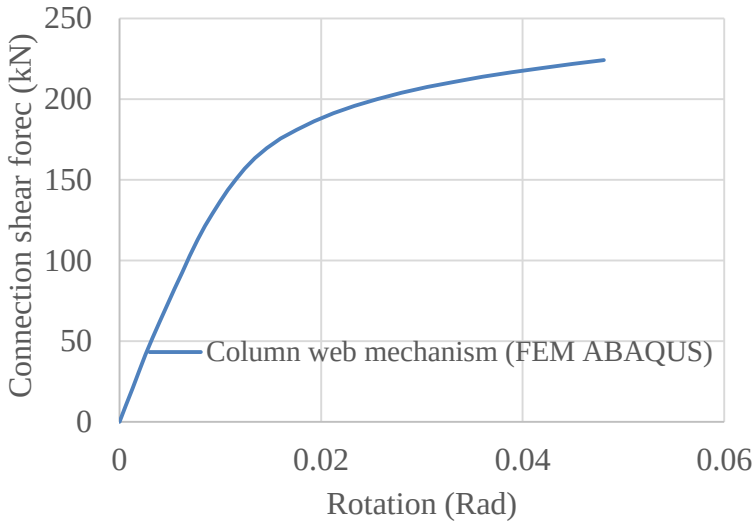

b) Column web rotation-connection shear force plot

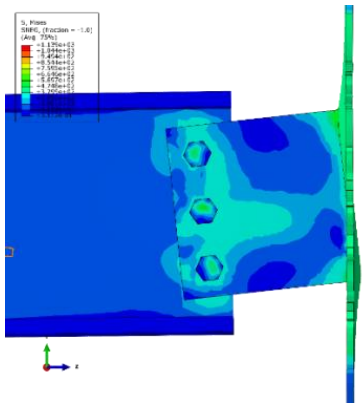

c) Column web deformation at 10mm vertical deflection

Figure F-10. Cleat plate twist and column web mechanism plots

Another failure mode that was mentioned in the experimental report, was bolt shear failure. Since the failure of the materials is not considered in the simulations, the failure state is predicted by using "equivalent plastic strain" which can be obtained from ABAQUS software results. This parameter shows the level of plastic deformation of each element in terms of equivalent uniaxial strain. Therefore, the "equivalent plastic strain" may be compared to the material ultimate strain to identify the failure point. Based on the stress-strain relationship of A325 bolts that was investigated by Kulak et al. (2001), shown in Figure F-11, the ultimate strain of A325 bolts may be considered equal to 0.20.

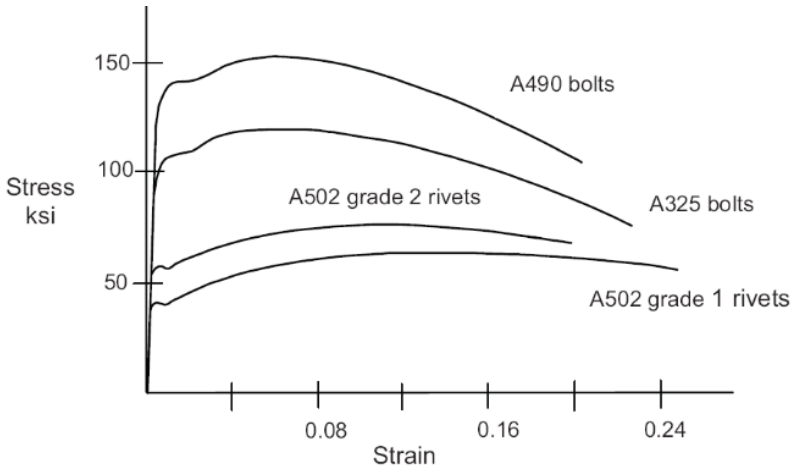

Figure F-11. Stress-strain relationship for different bolt grades (Kulak et al., 2001)

Figure F-12a,b show the bolt group in the FEM model. Places at the bolts cross-section that experienced "equivalent plastic strain" larger than 0.20 are shown in Figure F-12b as material failure zones.

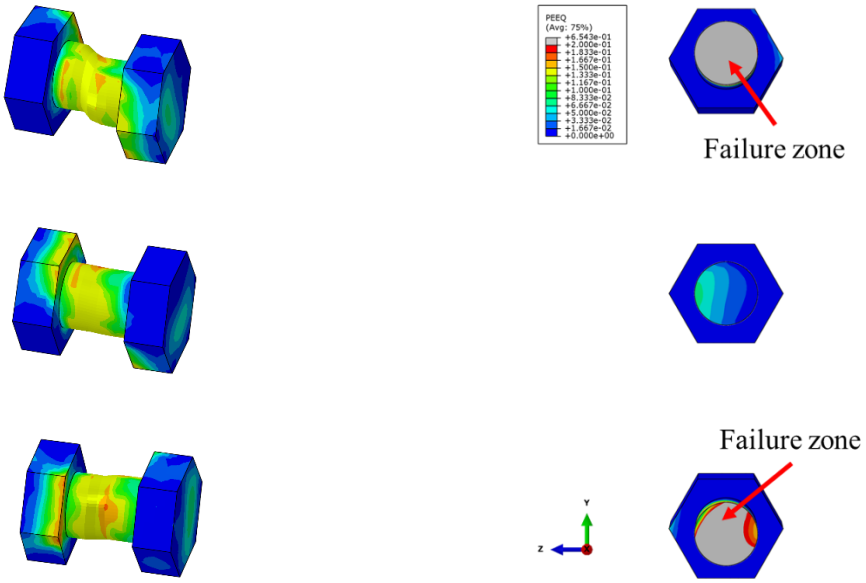

a) Bolts ultimate deformation

b) Bolts failure zones

c) Deformation and fracture of bolt in the experimental study (Sherman and Ghorbanpoor, 2002)

Figure F-12. Bolt shear failure at the end of analysis

References

[1] Sherman, D. R., & Ghorbanpoor, A. (2002). Design of Extended Shear Tabs," Final report for the American Institute of Steel Construction. October, University of Wisconsin, Milwaukee, Wisconsin.

[2] Kulak, G. L., Fisher, J. W., & Struik, J. H. (2001). Guide to Design Criteria for Bolted and Riveted Joints Second Edition.

Appendix G: Cleat Plate Effective Length Factor and Verification

The effect of different support conditions and cleat plate to beam web connections on the cleat plate effective length factor are investigated. Comparisons are made between the cleat effective length factor derived from solving stability functions and FEM models.

G.1 Configuration 1

In this case, the cleat plate and the beam web are connected with a pinned connection. The far end of the beam web is restrained from lateral translation but it is free to rotate as shown in Figure G-1.

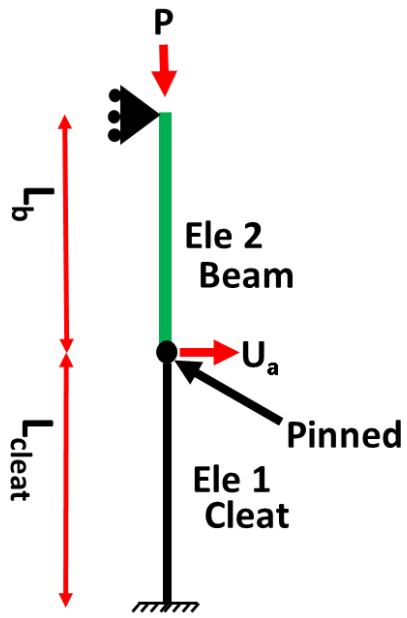

Figure G-1. Cleat plate and beam web pinned together

Figure G-2 plots the cleat plate effective length factor in terms of the cleat plate length to the beam web length ratio. This plot is derived from solving the stability function of the structure shown in Figure G-1.

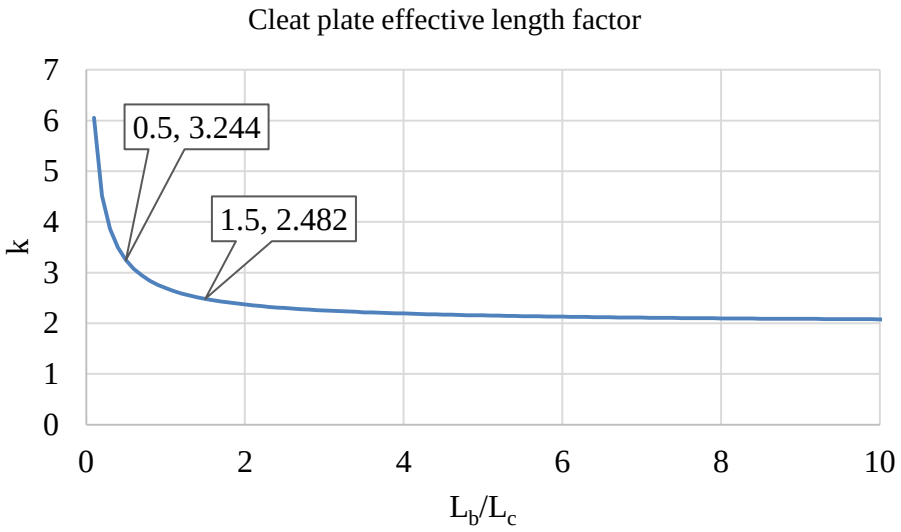

Figure G-2. Cleat plate effective length factor obtained from stability function

Two cases with the beam web to the cleat plate length ratios of 1.5 and 0.5 are investigated using FE models.

G.1.1 Model 1

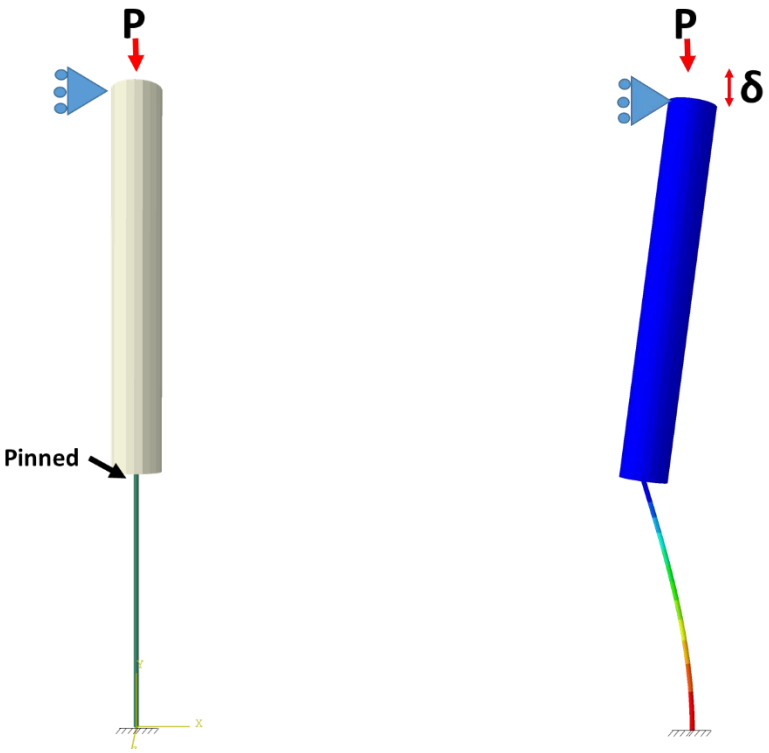

a) FEM model b) Deformed shape

Figure G-3. FEM model with beam web length to cleat plate length ratio of 1.5

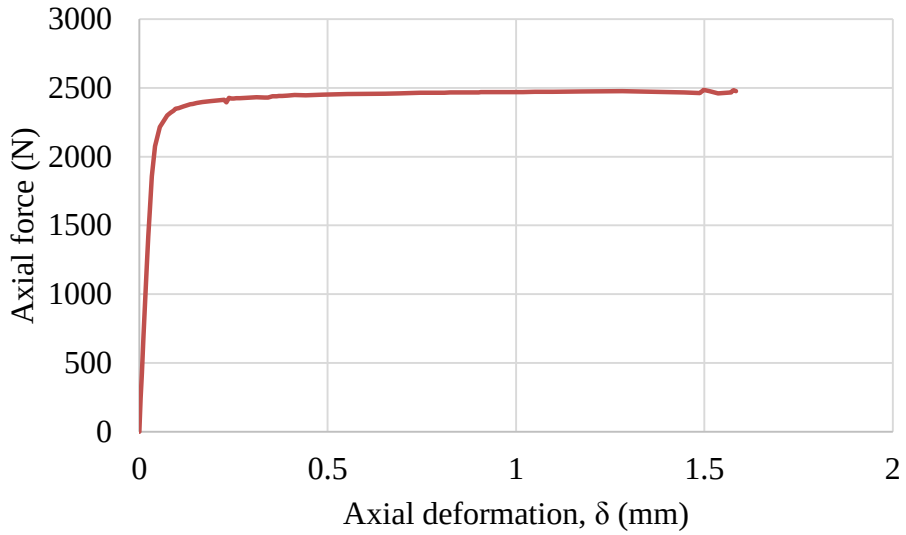

Figure G-4. Axial force-deformation of FE model, $P_{cr} = 2448\ N$

Cleat effective length calculation based on the FE model result:

$$P_{cr} = \frac{\pi^2 E I_{cleat}}{(kL_{cleat})^2}$$

$P_{cr} = 2448\ N$

$E = 200\ GPa$

$I = 7854\ mm^4$

$L = 1000\ mm$

➔ $k = 2.49$ (FEM)

$k = 2.482$ (Stability Function)

G.1.2 Model 2

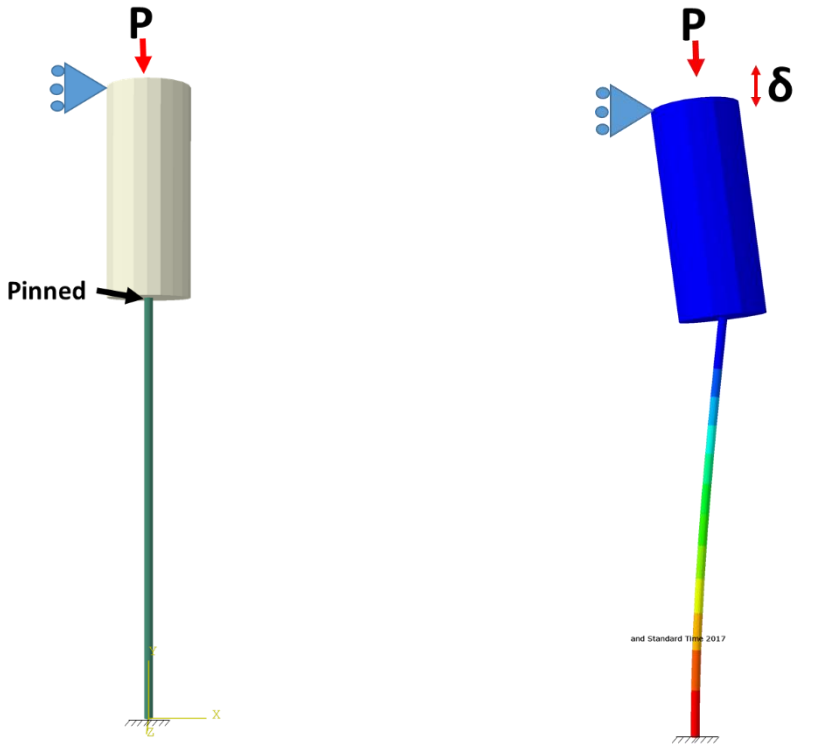

a) FEM model b) Deformed shape

Figure G-5. FEM model with beam web length to cleat plate length ratio of 0.5

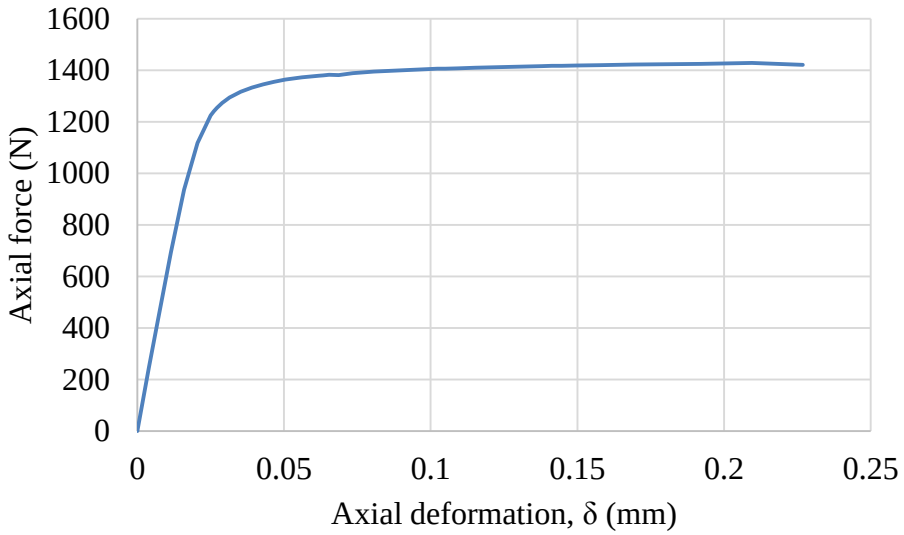

Figure G-6. Axial force-deformation of FE model, $P_{cr} = 1428\ N$

Cleat effective length calculation based on the FE model result:

$$P_{cr} = \frac{\pi^2 E I_{cleat}}{(kL_{cleat})^2} \qquad \rightarrow k = 3.295 \text{ (FEM)}$$

$P_{cr} = 1428\ N$ $k = 3.244$ (Stability Function)

$E = 200\ GPa$

$I = 7854\ mm^4$

$L = 1000\ mm$

G.2 Configuration 2

In this case, the cleat plate and the beam web are rigidly connected. The far end of the beam web is restrained from lateral translation and rotation as shown in Figure G-7.

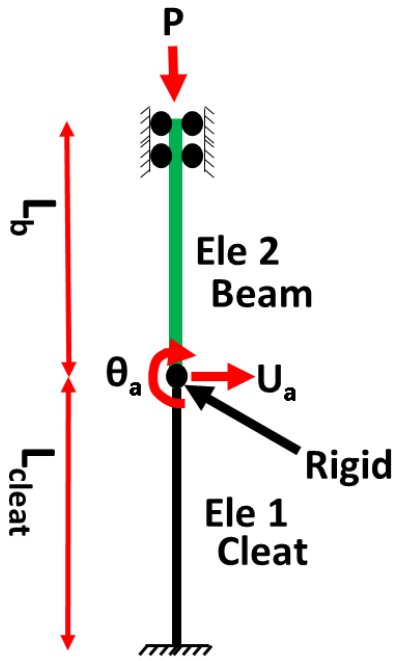

Figure G-7. Cleat plate and beam web rigidly connected

The cleat plate effective length factor is calculated using the stability function. The stability function of the cleat plate shown in Figure G-7 can be obtained as:

Cleat plate stiffness matrix: $K_1 = \frac{EI_1}{L_1}\begin{bmatrix} f_1/L_1^2 & g_1/L_1 \\ g_1/L_1 & s_1 \end{bmatrix}$

Beam web stiffness matrix: $K_2 = \frac{EI_2}{L_2}\begin{bmatrix} f_2/L_2^2 & g_2/L_2 \\ g_2/L_2 & s_2 \end{bmatrix}$

Where,

$s_i = \frac{\emptyset_i(\sin\emptyset_i - \emptyset_i\cos\emptyset_i)}{2(1-\cos\emptyset_i)-\emptyset_i\sin\emptyset_i}$

$r_i = \frac{{\emptyset_i}^2 - \emptyset_i\sin\emptyset_i}{2(1-\cos\emptyset_i)-\emptyset_i\sin\emptyset_i}$

$f_i = 2(s+r) - {\emptyset_i}^2$

$g_i = s_i + r_i$

$\emptyset_i = \sqrt{\frac{PL_i^2}{EI_i}}$

$k_i = \frac{\pi}{\emptyset_i}$

Assembling stiffness matrices:

$$K_{total} = \begin{bmatrix} \frac{EI_1}{L_1} \times f_1/L_1^2 + \frac{EI_2}{L_2} \times f_2/L_2^2 & \frac{EI_1}{L_1} \times g_1/L_1 + \frac{EI_2}{L_2} \times g_2/L_2 \\ \frac{EI_1}{L_1} \times g_1/L_1 + \frac{EI_2}{L_2} \times g_2/L_2 & \frac{EI_1}{L_1} \times s_1 + \frac{EI_2}{L_2} \times s_2 \end{bmatrix}$$

By solving the determinant equation $det[K_{total}] = 0$, $\emptyset_i$ and the cleat effective length factor can be obtained.

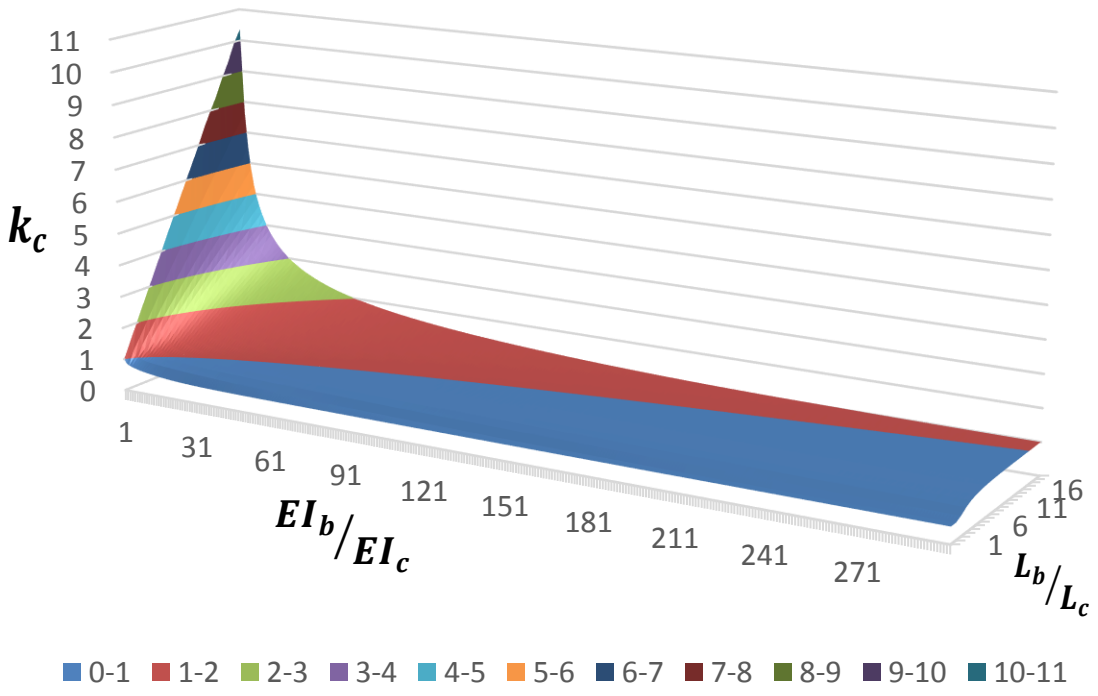

Figure G-8. 3D plot indicating k_c for cleat member with different length and stiffness ratios

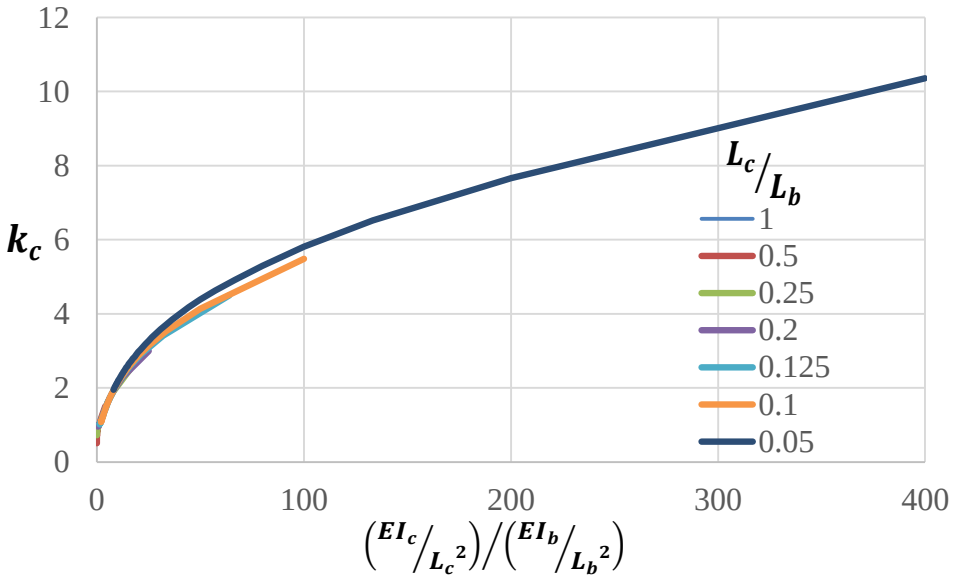

Figure G-9. Effective length factor, k_c, for cleat member with different length and stiffness ratios

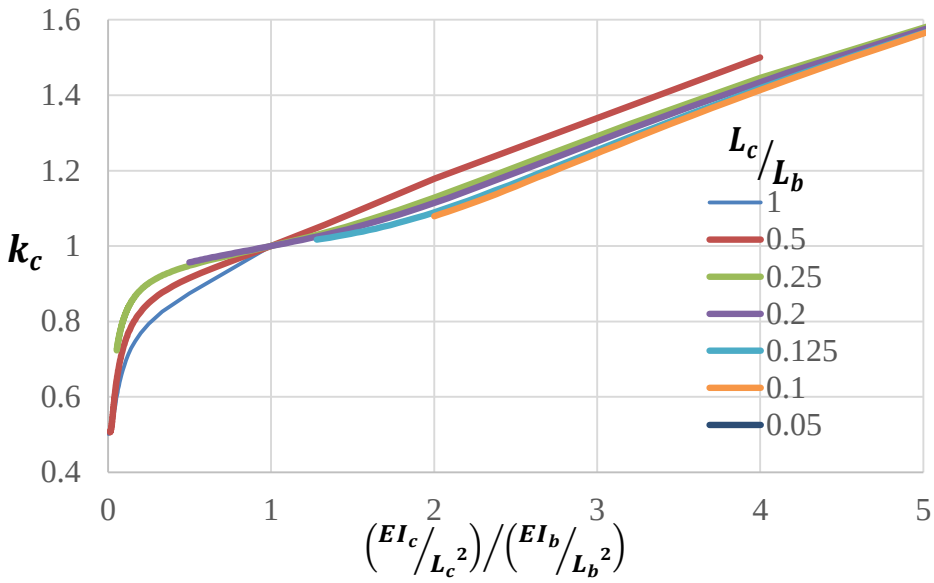

Figure G-10. An enlarged view of Figure G-9

G.2.1 Model 1

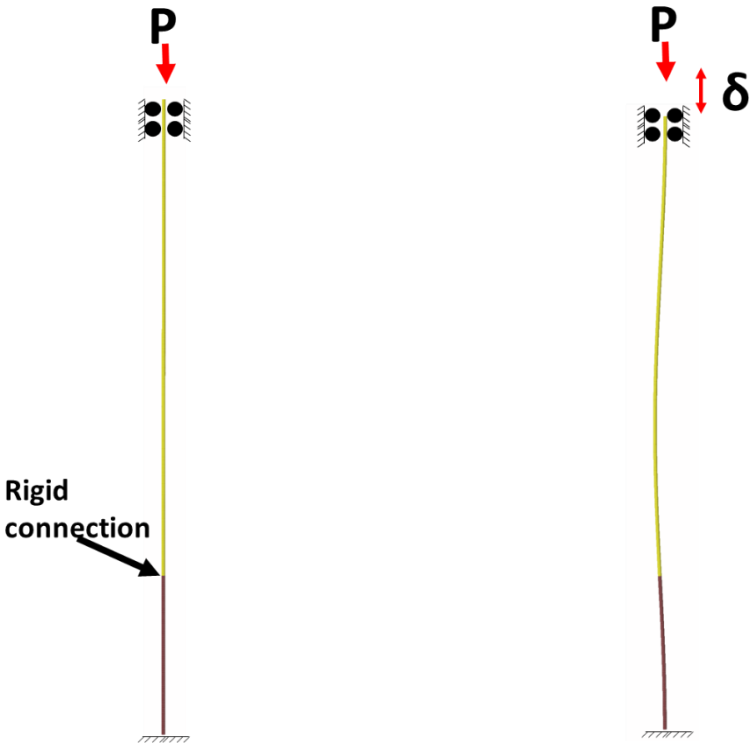

a) FEM model b) Deformed shape

Figure G-11. FEM model with beam web length to cleat plate length ratio of 3 and $EI_b/EI_c = 1$, $\left(EI_c/L_c^2\right)/\left(EI_b/L_b^2\right) = 9$

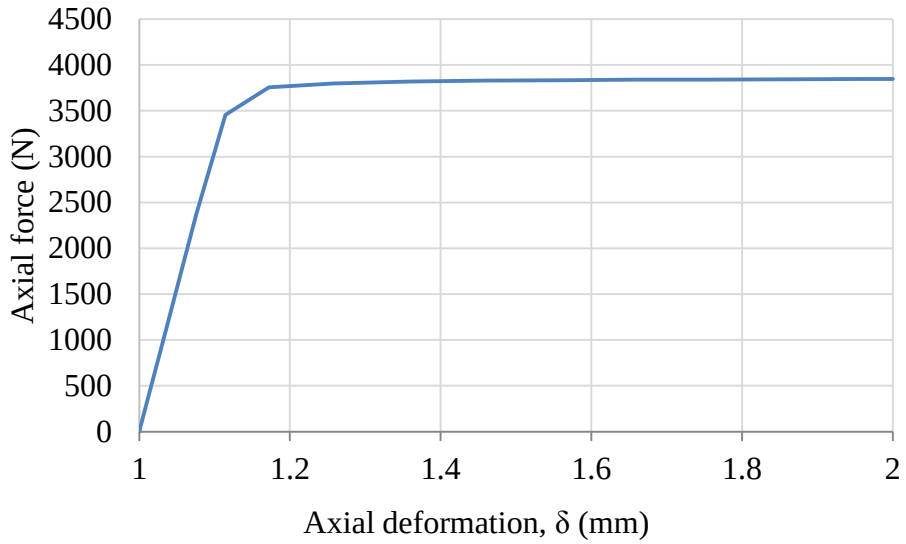

Figure G-12. Axial force-deformation of FE model, $P_{cr} = 3847\ N$

Cleat effective length calculation based on the FE model result:

$$P_{cr} = \frac{\pi^2 E I_{cleat}}{(kL_{cleat})^2}$$

$P_{cr} = 3847\ N$

$E = 200\ GPa$

$I = 7854\ mm^4$

$L = 1000\ mm$

➔ $k = 2.007$ (FEM)

$k = 1.994$ (Stability function)

G.2.2 Model 2

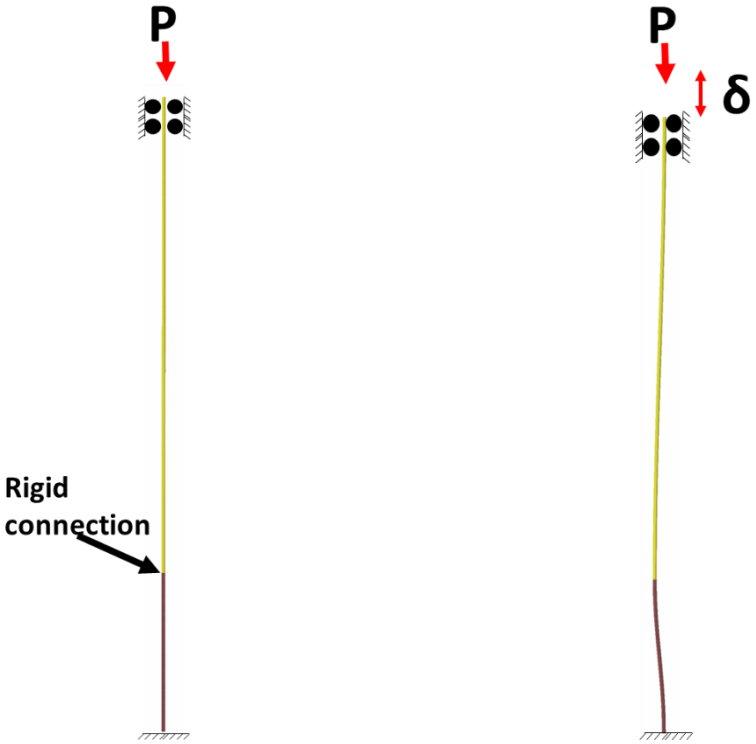

a) FEM model b) Deformed shape

Figure G-13. FEM model with beam web length to cleat plate length ratio of 3 and $EI_b/EI_c = 9$

$$\left({EI_c}/{L_c{}^2}\right)/\left({EI_b}/{L_b{}^2}\right) = 1$$

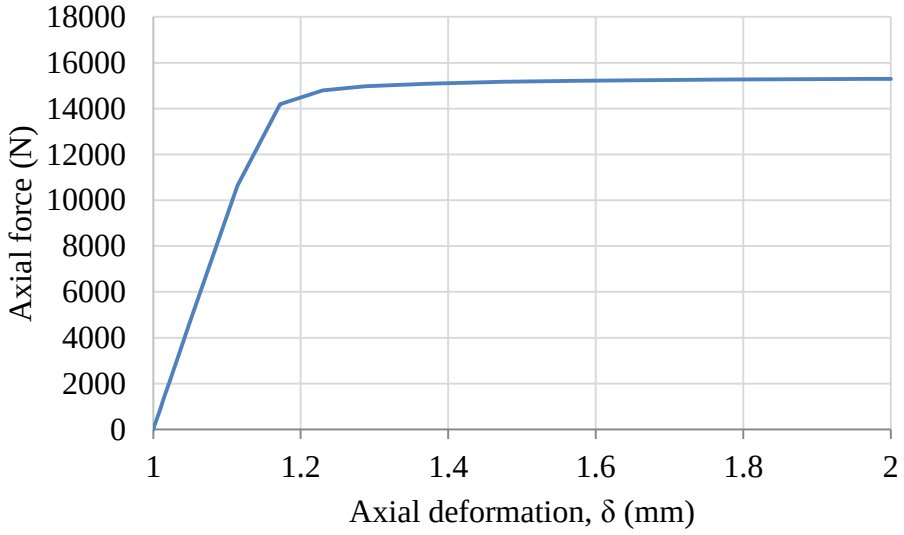

Figure G-14. Axial force-deformation of FE model, $P_{cr} = 15300\ N$

Cleat effective length calculation based on the FE model result:

$$P_{cr} = \frac{\pi^2 E I_{cleat}}{(kL_{cleat})^2}$$

$P_{cr} = 15300\ N$

$E = 200\ GPa$

$I = 7854\ mm^4$

$L = 1000\ mm$

➔ $k = 1.006$ (FEM)

$k = 0.9995$ (Stability function)

G.2.3 Model 1

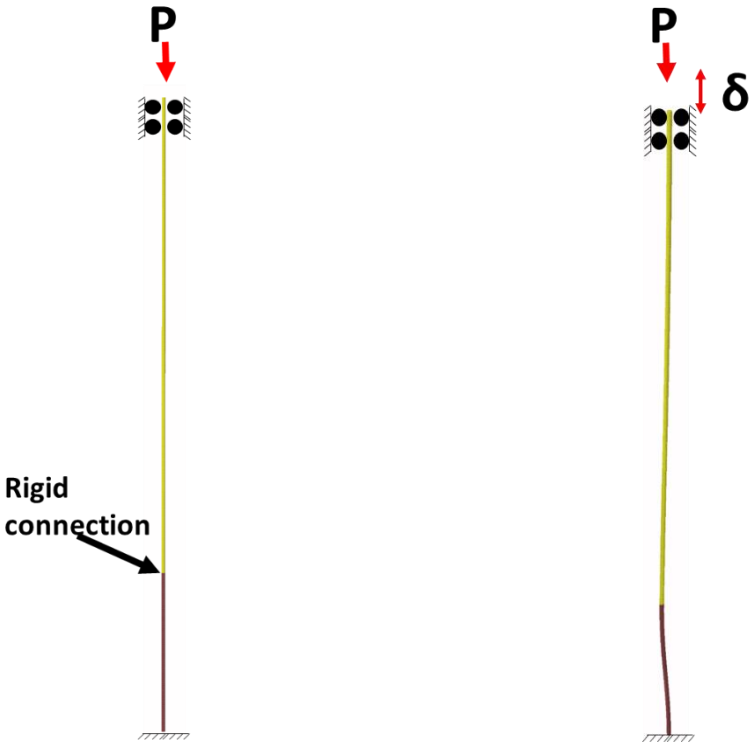

a) FEM model

b) Deformed shape

Figure G-15. FEM model with beam web length to cleat plate length ratio of 3 and $EI_b/EI_c = 25$

$$\left({EI_c}/{L_c^2}\right)/\left({EI_b}/{L_b^2}\right) = 0.45$$

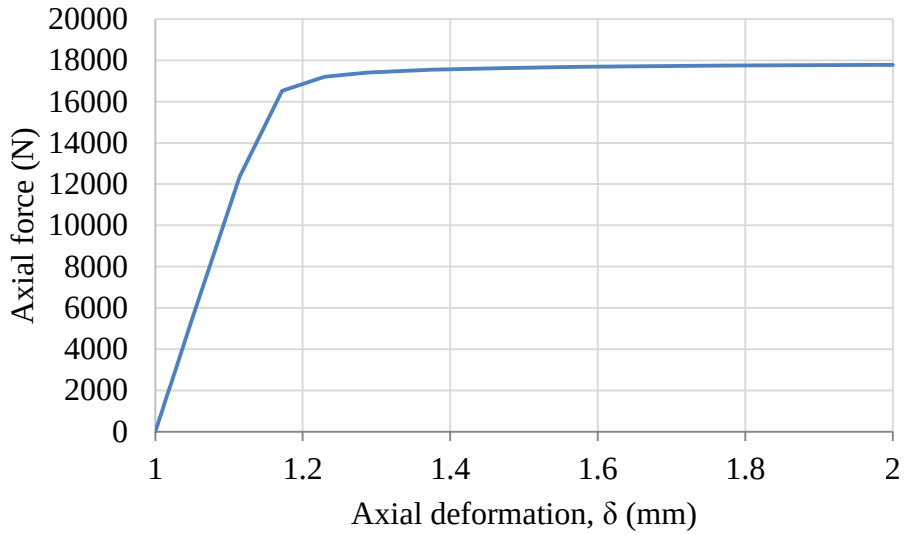

Figure G-16. Axial force-deformation of FE model, $P_{cr} = 17788\ N$

Cleat effective length calculation based on the FE model result:

$$P_{cr} = \frac{\pi^2 E I_{cleat}}{(k L_{cleat})^2}$$

$P_{cr} = 17788\ N$

$E = 200\ GPa$

$I = 7854\ mm^4$

$L = 1000\ mm$

➔ $k = 0.9335$ (FEM)

$k = 0.9272$ (Stability function)

G.3 Configuration 3

In this case, the cleat plate and the beam web are rigidly connected. The far end of the beam web is restrained from lateral translation but it is free to rotate as shown in Figure G-17.

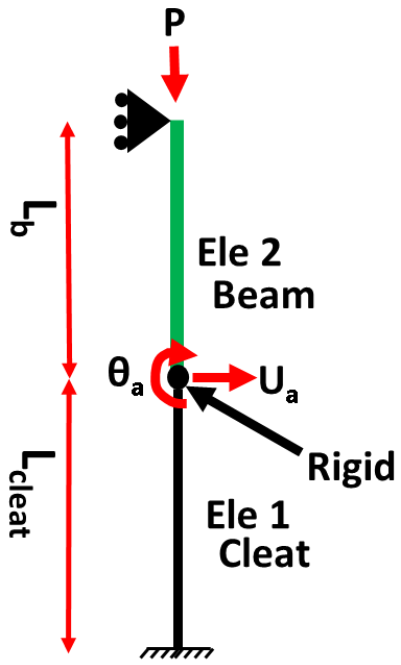

Figure G-17. Cleat plate and beam web rigidly connected

The cleat plate effective length factor is calculated using stability function. The stability function of the cleat plate shown in Figure G-17 can be obtained as

Cleat plate stiffness matrix: $K_1 = \frac{EI_1}{L_1}\begin{bmatrix} f_1/L_1^2 & g_1/L_1 \\ g_1/L_1 & s_1 \end{bmatrix}$

Beam web stiffness matrix: $K_2 = \frac{EI_2}{L_2}\begin{bmatrix} f_2/L_2^2 - g_2^2/s_2L_2^2 & g_2/L_2 - g_2r_2/s_2L_2 \\ g_2/L_2 - g_2r_2/s_2L_2 & s_2 - r_2^2/s_2 \end{bmatrix}$

Where,

$s_i = \frac{\emptyset_i(\sin\emptyset_i - \emptyset_i\cos\emptyset_i)}{2(1-\cos\emptyset_i) - \emptyset_i\sin\emptyset_i}$

$r_i = \frac{\emptyset_i{}^2 - \emptyset_i\sin\emptyset_i}{2(1-\cos\emptyset_i) - \emptyset_i\sin\emptyset_i}$

$f_i = 2(s+r) - \emptyset_i{}^2$

$g_i = s_i + r_i$

$$\emptyset_i = \sqrt{\frac{PL_i^2}{EI_i}}$$

$$k_i = \frac{\pi}{\emptyset_i}$$

Assembling stiffness matrices:

$$K_{total} =$$

$$\begin{bmatrix} \frac{EI_1}{L_1} \times {f_1}/{L_1^2} + \frac{EI_2}{L_2} \times ({f_2}/{L_2^2} - {g_2^2}/{s_2 L_2^2}) & \frac{EI_1}{L_1} \times {g_1}/{L_1} - \frac{EI_2}{L_2} \times ({g_2}/{L_2} - {g_2 r_2}/{s_2 L_2}) \\ \frac{EI_1}{L_1} \times {g_1}/{L_1} - \frac{EI_2}{L_2} \times ({g_2}/{L_2} - {g_2 r_2}/{s_2 L_2}) & \frac{EI_1}{L_1} \times s_1 + \frac{EI_2}{L_2} \times (s_2 - {r_2^2}/{s_2}) \end{bmatrix}$$

By solving the determinant equation $det[K_{total}] = 0$, $\emptyset_i$ and the cleat effective length factor can be obtained.

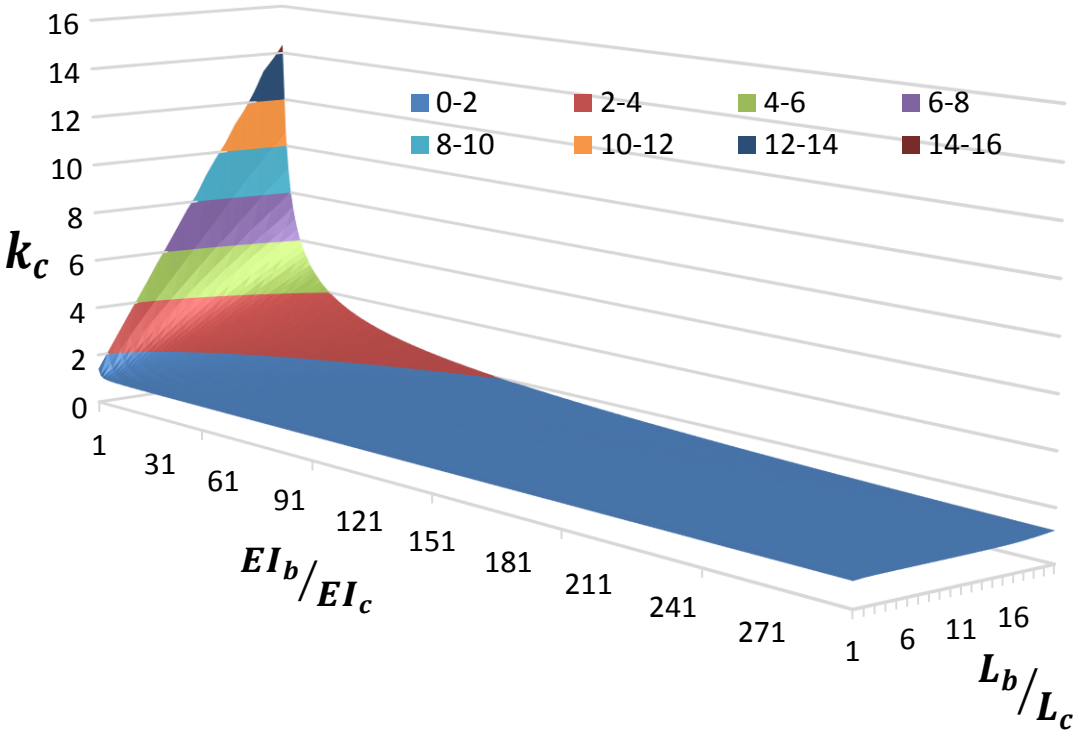

Figure G-18. 3D plot indicating k_c for cleat member with different length and stiffness ratios

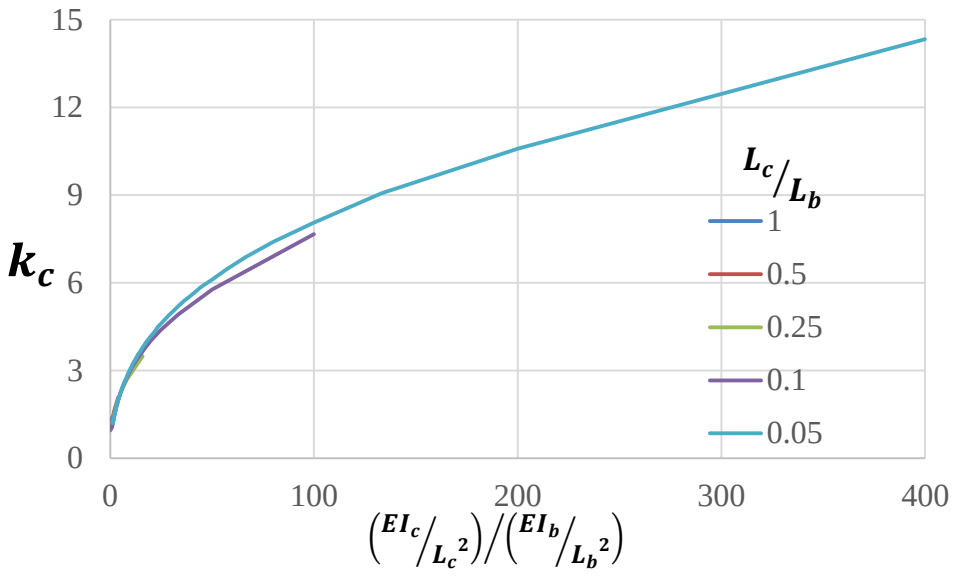

Figure G-19. Effective length factor, k_c, for cleat member with different length and stiffness ratios

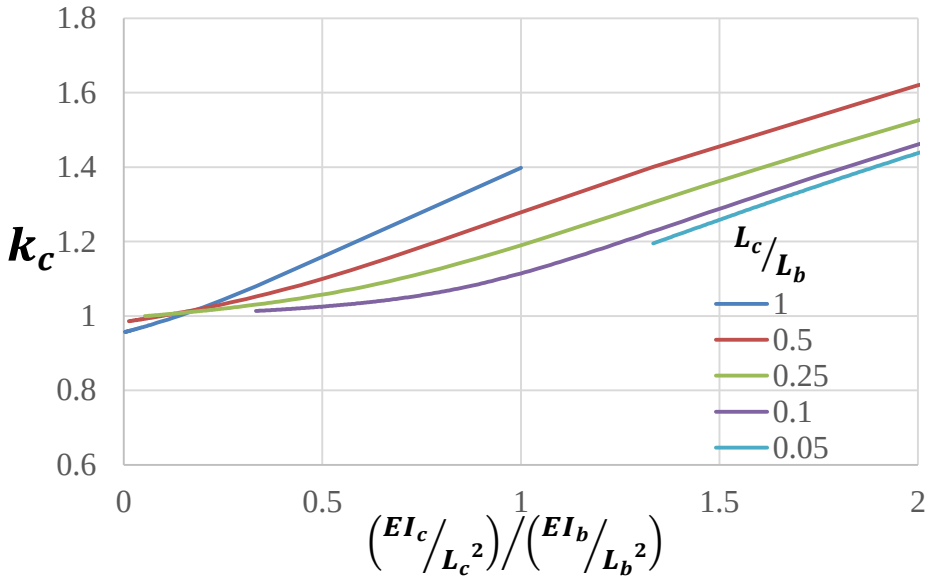

Figure G-20. An enlarged view of Figure G-19

G.3.1 Model 1

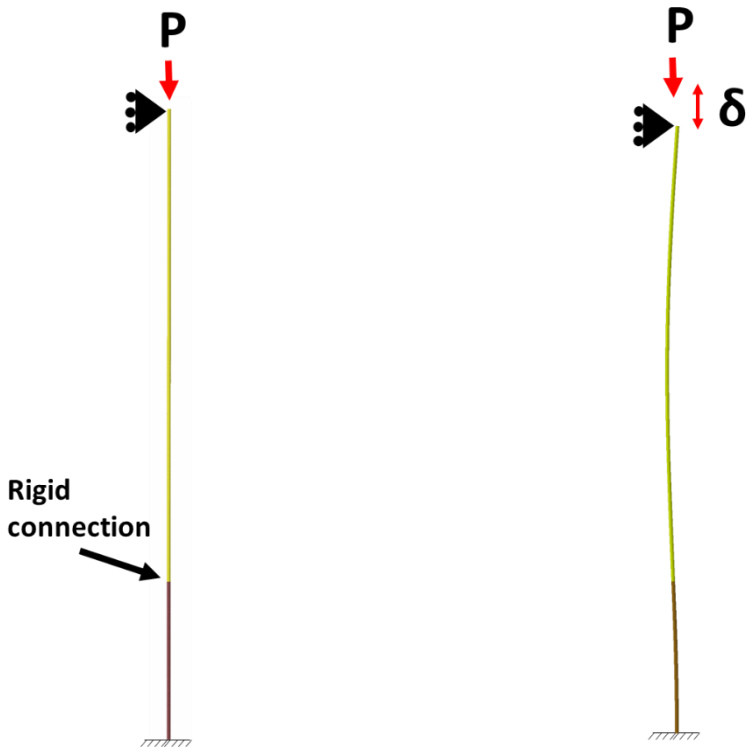

a) FEM model b) Deformed shape

Figure G-21. FEM model with beam web length to cleat plate length ratio of 3 and $EI_b/EI_c = 1$

$$\left({EI_c}/{L_c{}^2}\right)/\left({EI_b}/{L_b{}^2}\right) = 9$$

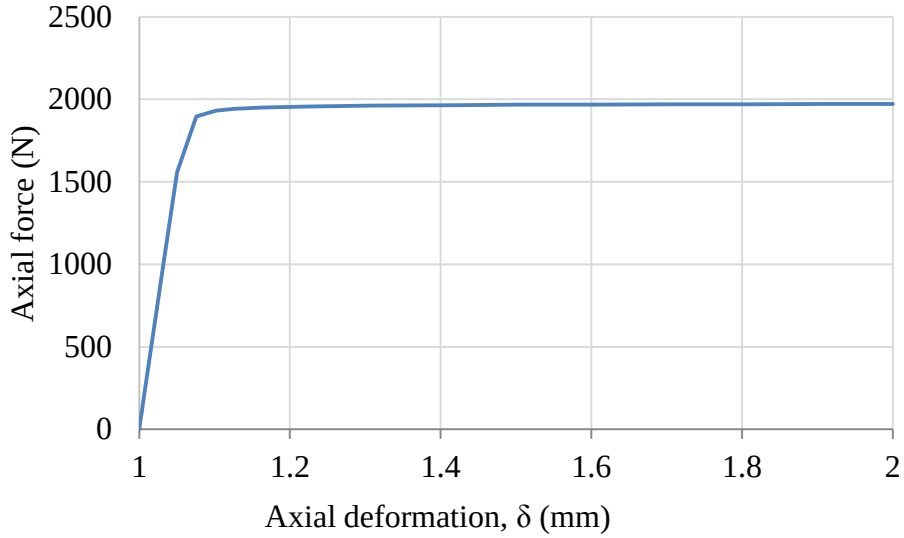

Figure G-22. Axial force-deformation of FE model, $P_{cr} = 1971\ N$

Cleat effective length calculation based on the FE model result:

$$P_{cr} = \frac{\pi^2 E I_{cleat}}{(kL_{cleat})^2}$$

$P_{cr} = 1971\ N$

$E = 200\ GPa$

$I = 7854\ mm^4$

$L = 1000\ mm$

➔ $k = 2.804$ (FEM)

$k = 2.794$ (Stability function)

G.3.2 Model 2

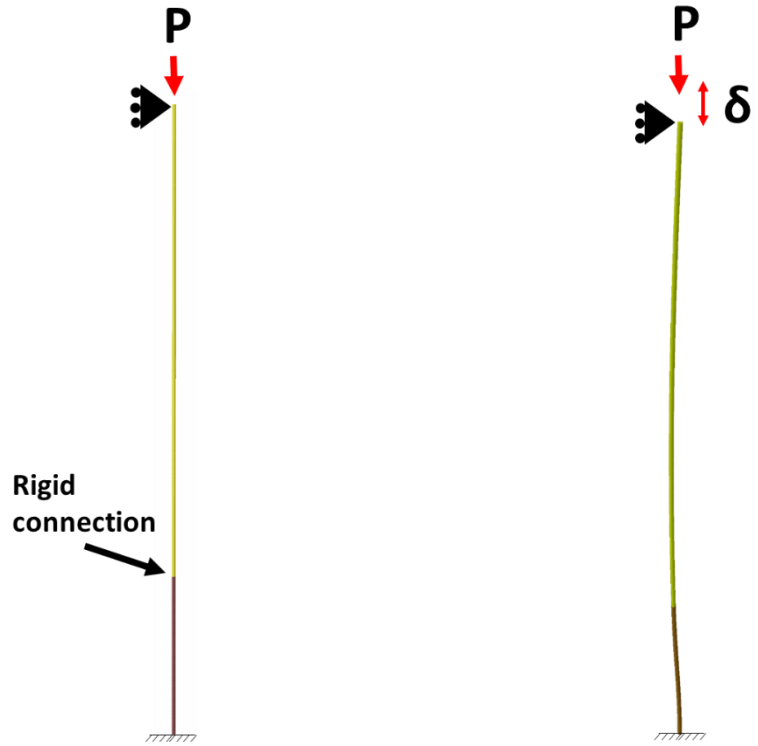

a) FEM model b) Deformed shape

Figure G-23. FEM model with beam web length to cleat plate length ratio of 3 and $EI_b/EI_c = 9$

$$\left({EI_c}/{L_c{}^2}\right)/\left({EI_b}/{L_b{}^2}\right) = 1$$

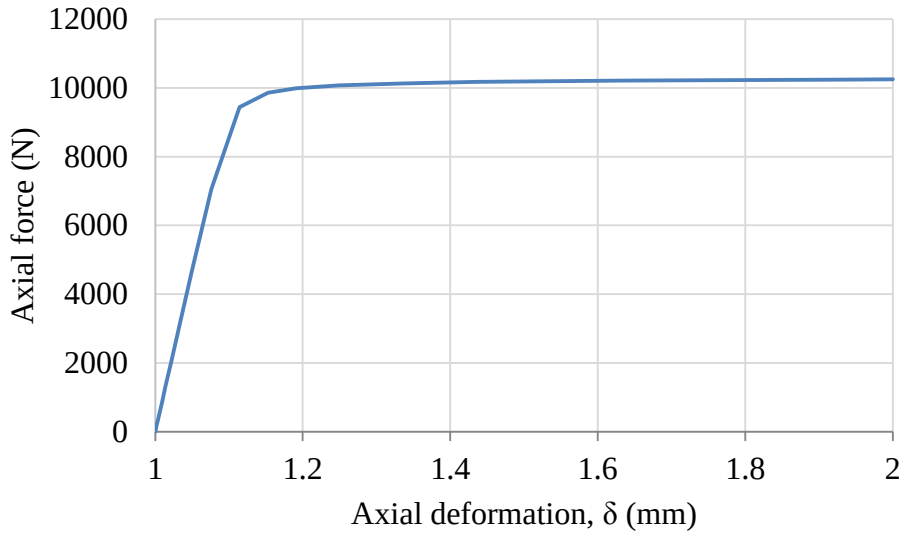

Figure G-24. Axial force-deformation of FE model, $P_{cr} = 10247\ N$

Cleat effective length calculation based on the FE model result:

$$P_{cr} = \frac{\pi^2 E I_{cleat}}{(kL_{cleat})^2}$$

$P_{cr} = 10247\ N$

$E = 200\ GPa$

$I = 7854\ mm^4$

$L = 1000\ mm$

➔ $k = 1.229$ (FEM)

$k = 1.223$ (Stability function)

G.3.3 Model 3

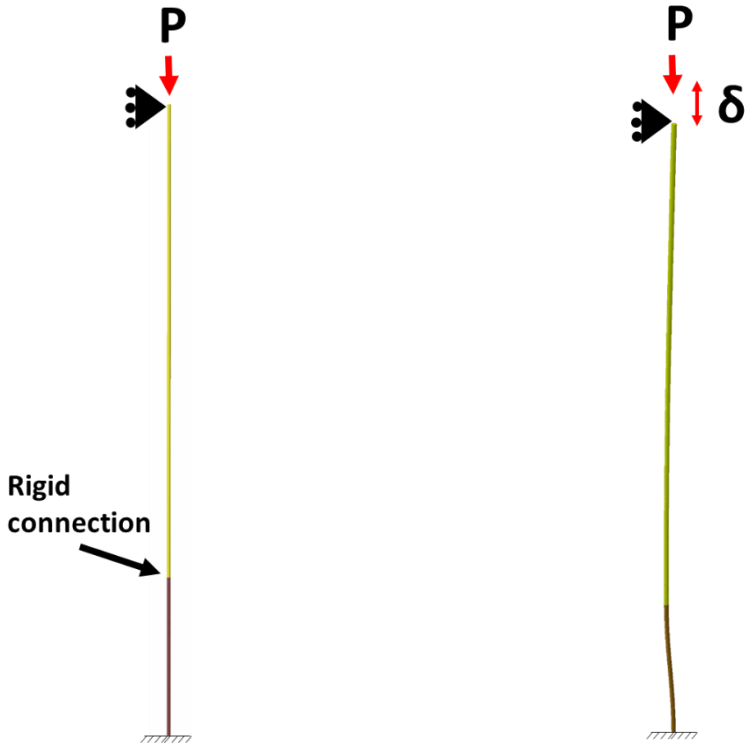

a) FEM model b) Deformed shape

Figure G-25. FEM model with beam web length to cleat plate length ratio of 3 and $EI_b/EI_c = 20$

$$\left({EI_c}/{L_c{}^2}\right)/\left({EI_b}/{L_b{}^2}\right) = 0.45$$

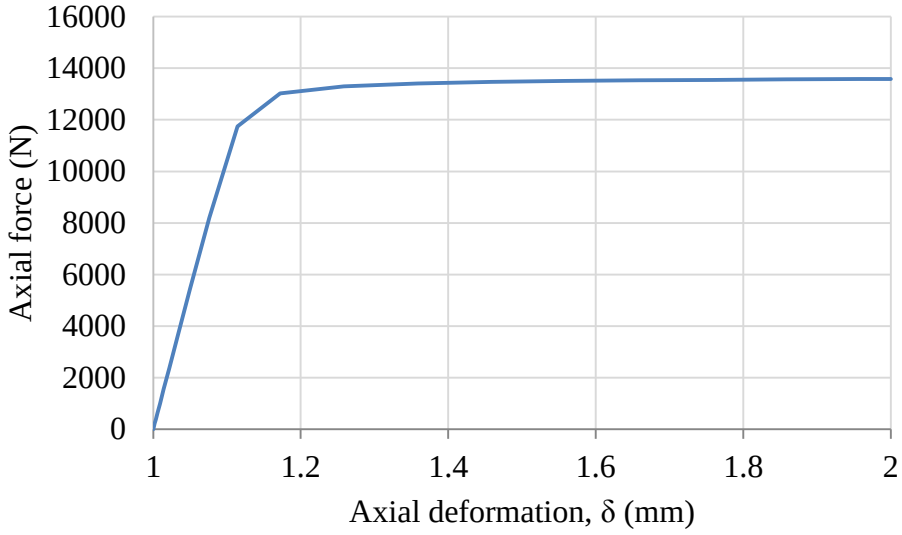

Figure G-26. Axial force-deformation of FE model, $P_{cr} = 13583\ N$

Cleat effective length calculation based on the FE model result:

$$P_{cr} = \frac{\pi^2 E I_{cleat}}{(kL_{cleat})^2}$$

$P_{cr} = 13583\ N$

$E = 200\ GPa$

$I = 7854\ mm^4$

$L = 1000\ mm$

➔ $k = 1.068$ (FEM)

$k = 1.061$ (Stability function)

G.4 Configuration 4

In this case, the cleat plate and the beam web are rigidly connected. The far end of the beam web is free to move laterally but it cannot rotate as shown in Figure G-27.

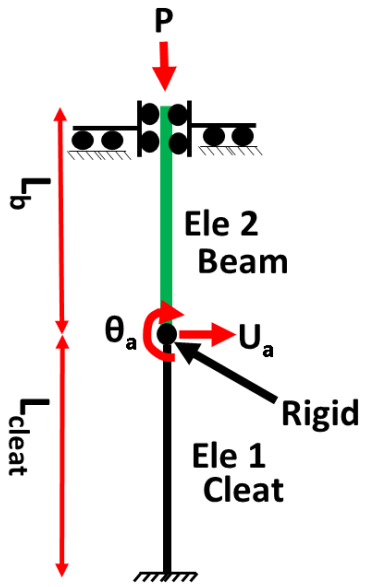

Figure G-27. Cleat plate and beam web rigidly connected

The cleat plate effective length factor is calculated using stability function. The stability function of the cleat plate shown in Figure G-27 can be obtained as

Cleat plate stiffness matrix: $K_1 = \frac{EI_1}{L_1}\begin{bmatrix} f_1/L_1^2 & g_1/L_1 \\ g_1/L_1 & s_1 \end{bmatrix}$

Beam web stiffness matrix: $K_2 = \frac{EI_2}{L_2}\begin{bmatrix} 0 & 0 \\ 0 & s_2 - g_2^2/f_2 \end{bmatrix}$

Where,

$s_i = \frac{\emptyset_i(\sin\emptyset_i - \emptyset_i\cos\emptyset_i)}{2(1-\cos\emptyset_i)-\emptyset_i\sin\emptyset_i}$

$r_i = \frac{{\emptyset_i}^2 - \emptyset_i\sin\emptyset_i}{2(1-\cos\emptyset_i)-\emptyset_i\sin\emptyset_i}$

$f_i = 2(s+r) - {\emptyset_i}^2$

$g_i = s_i + r_i$

$\emptyset_i = \sqrt{\frac{PL_i^2}{EI_i}}$

$k_i = \frac{\pi}{\emptyset_i}$

Assembling stiffness matrices:

$$K_{total} = \begin{bmatrix} \frac{EI_1}{L_1} \times f_1/L_1^2 & \frac{EI_1}{L_1} \times g_1/L_1 \\ \frac{EI_1}{L_1} \times g_1/L_1 & \frac{EI_1}{L_1} \times s_1 + \frac{EI_2}{L_2} \times (s_2 - g_2^2/f_2) \end{bmatrix}$$

By solving the determinant equation $det[K_{total}] = 0$, $\emptyset_i$ and the cleat effective length factor can be obtained.

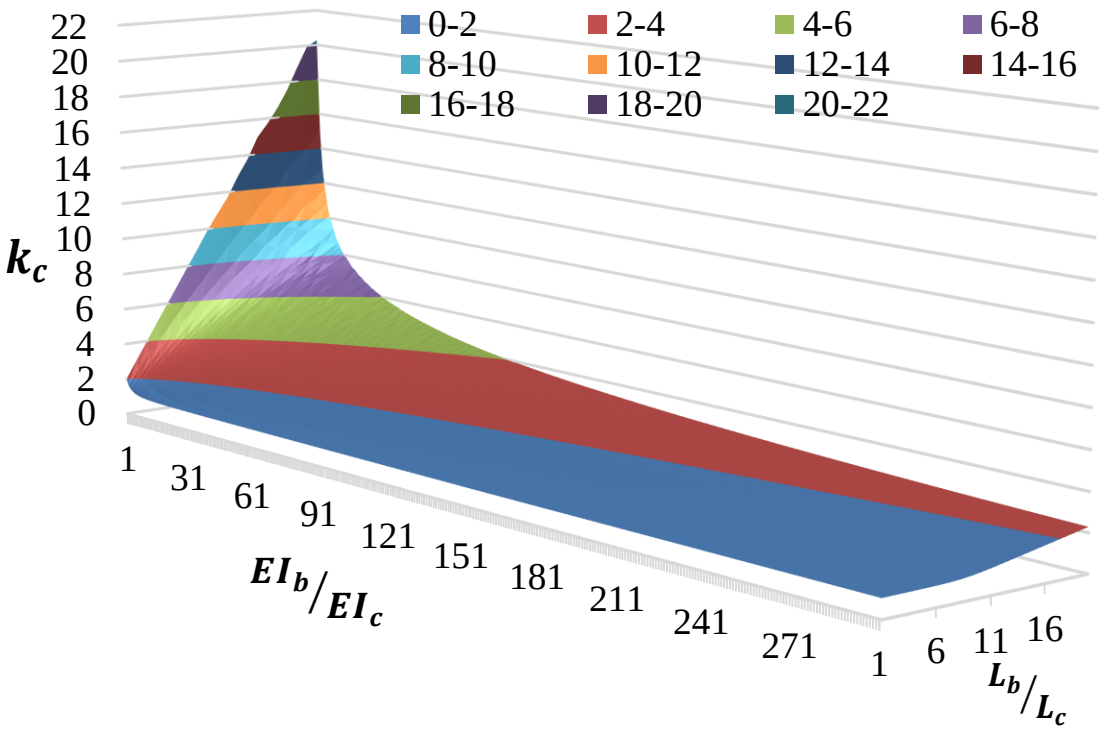

Figure G-28. 3D plot indicating k_c for cleat member with different length and stiffness ratios

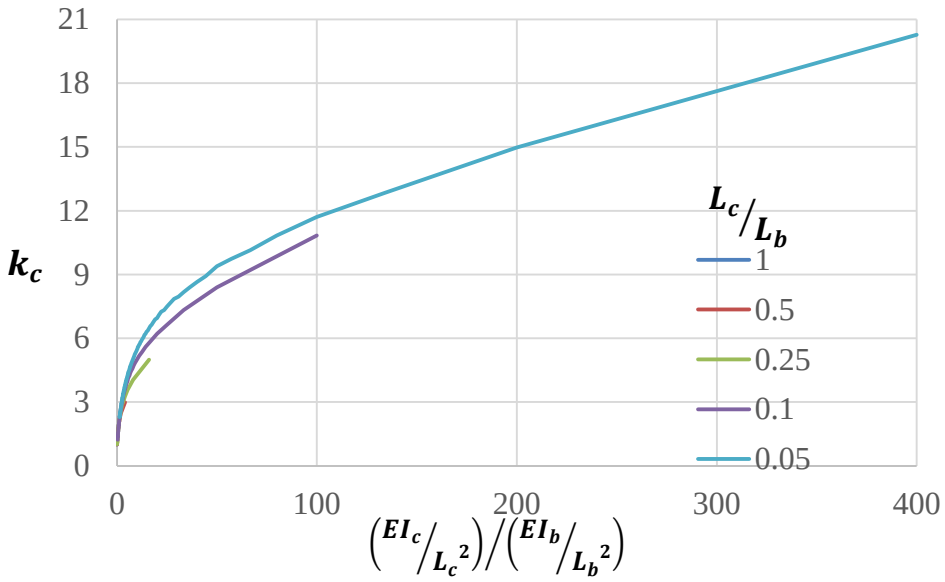

Figure G-29. Effective length factor, k_c, for cleat member with different length and stiffness ratios

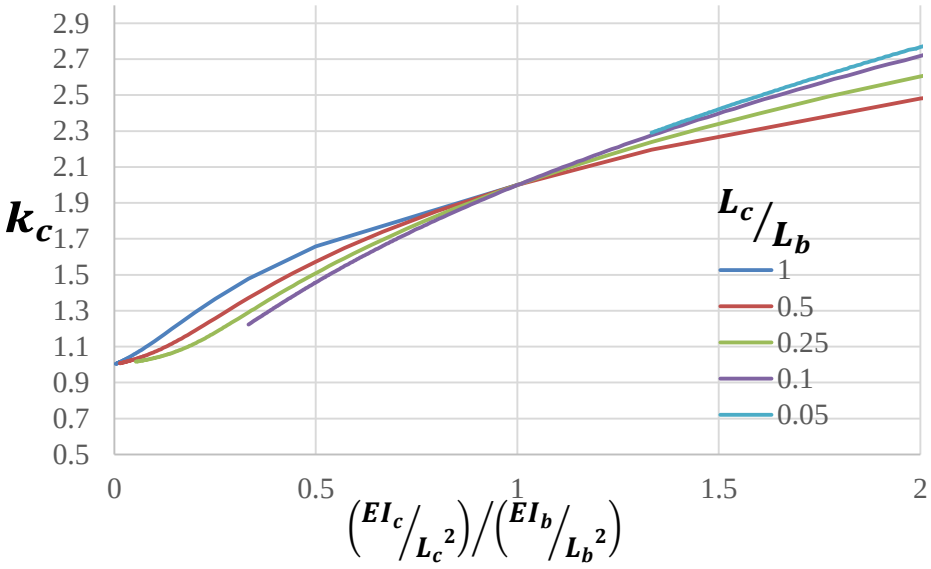

Figure G-30. An enlarged view of Figure G-29

G.4.1 Model 1

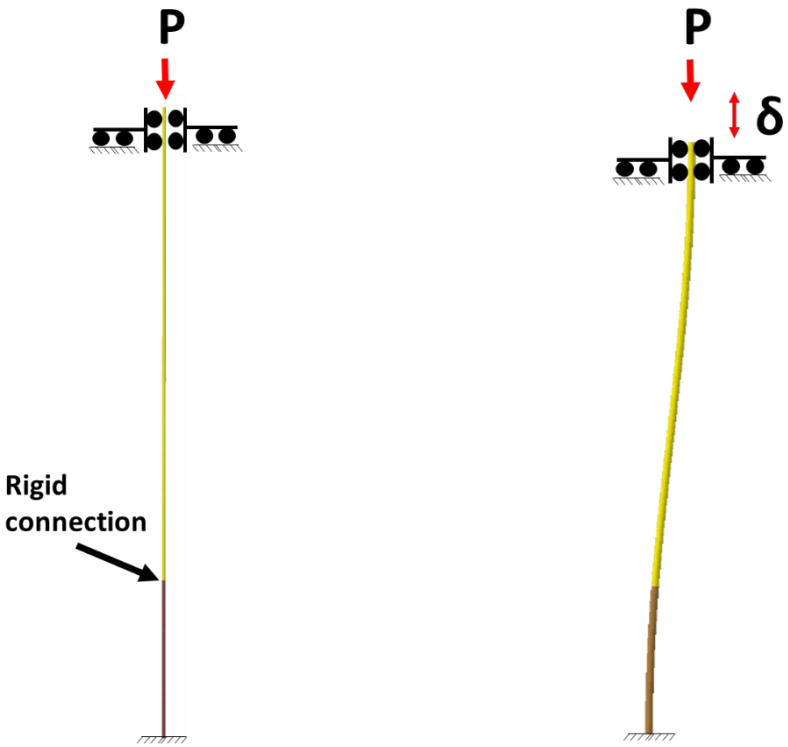

a) FEM model b) Deformed shape

Figure G-31. FEM model with beam web length to cleat plate length ratio of 3 and $EI_b/EI_c = 1$

$$\left(EI_c/L_c^2\right)/\left(EI_b/L_b^2\right) = 9$$

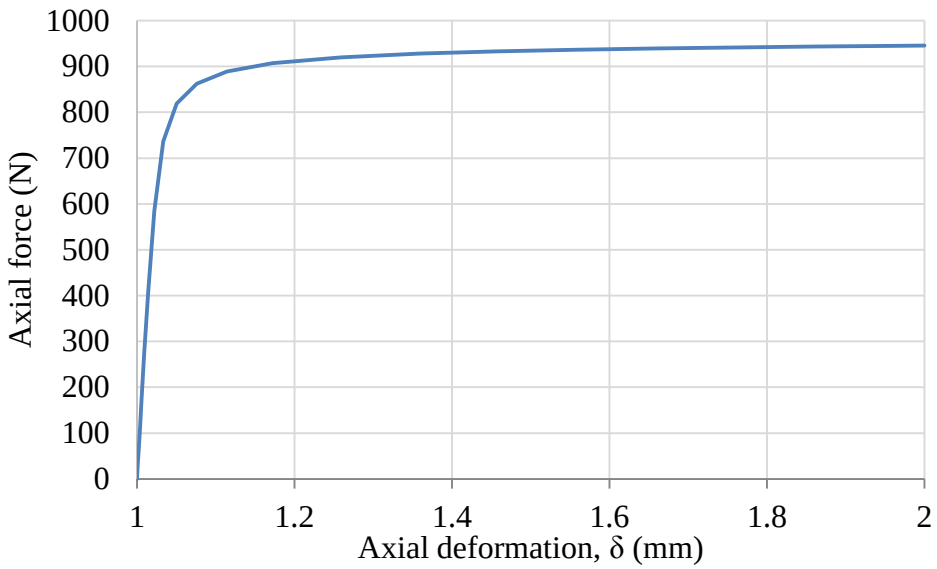

Figure G-32. Axial force-deformation of FE model, $P_{cr} = 945\ N$

Cleat effective length calculation based on the FE model result:

$$P_{cr} = \frac{\pi^2 E I_{cleat}}{(kL_{cleat})^2}$$

$P_{cr} = 945\ N$

$E = 200\ GPa$

$I = 7854\ mm^4$

$L = 1000\ mm$

➔ $k = 4.050$ (FEM)

$k = 3.989$ (Stability function)

G.4.2 Model 2

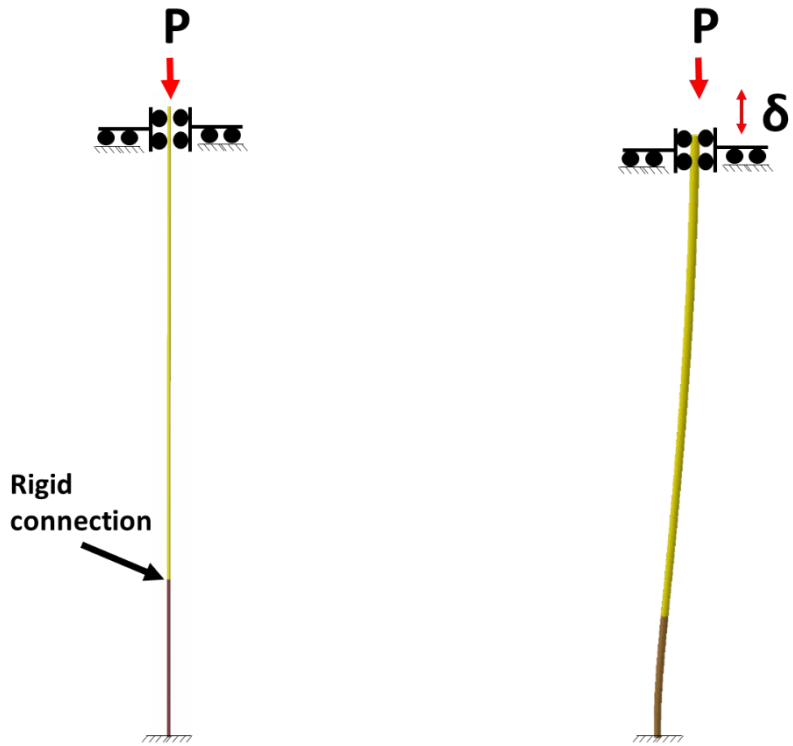

a) FEM model b) Deformed shape

Figure G-33. FEM model with beam web length to cleat plate length ratio of 3 and $EI_b/EI_c = 9$

$$\left({EI_c}/{L_c{}^2}\right)/\left({EI_b}/{L_b{}^2}\right) = 1$$

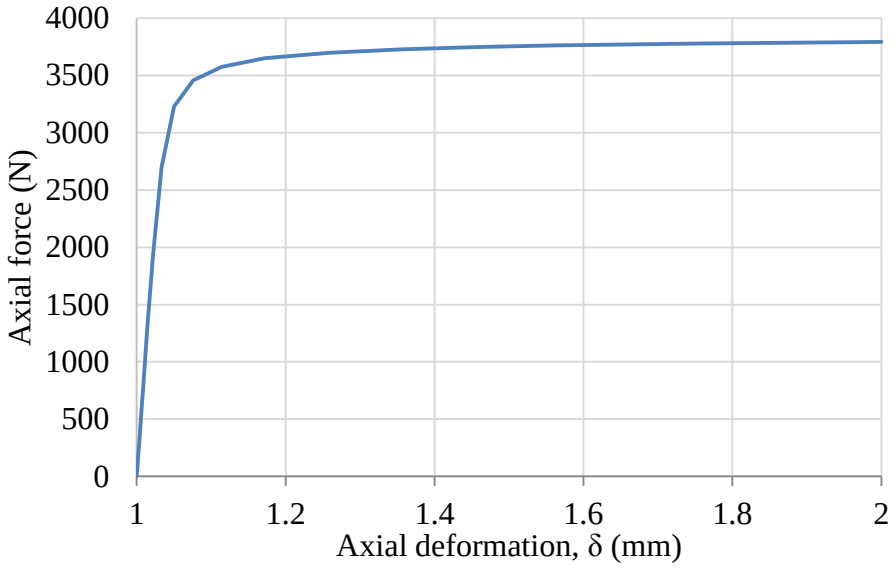

Figure G-34. Axial force-deformation of FE model, $P_{cr} = 3792\ N$

Cleat effective length calculation based on the FE model result:

$$P_{cr} = \frac{\pi^2 EI_{cleat}}{(kL_{cleat})^2}$$

$P_{cr} = 3792\ N$

$E = 200\ GPa$

$I = 7854\ mm^4$

$L = 1000\ mm$

➔ $k = 2.021$ (FEM)

$k = 1.999$ (Stability function)

G.4.3 Model 2

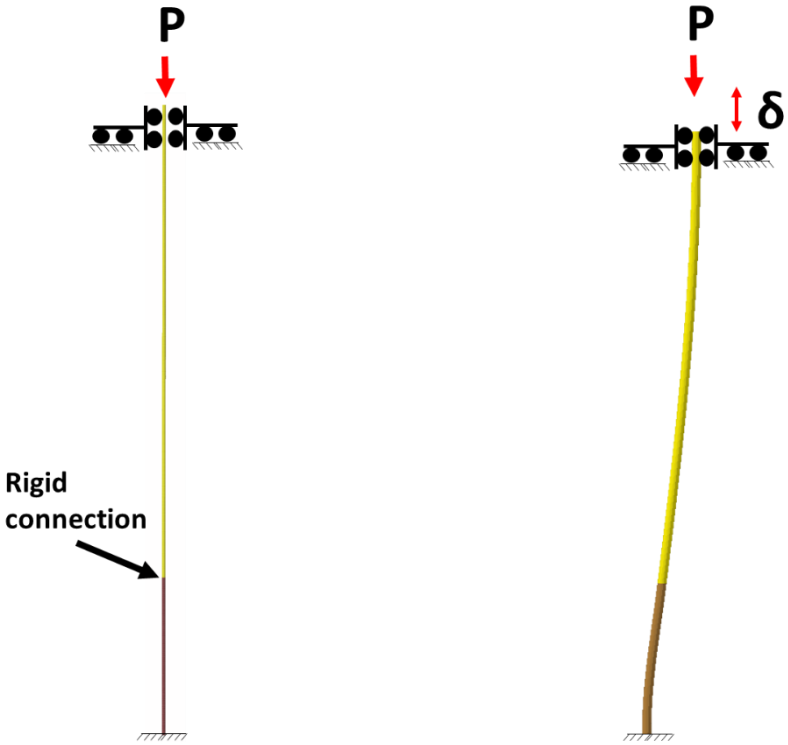

a) FEM model

b) Deformed shape

Figure G-35. FEM model with beam web length to cleat plate length ratio of 3 and $EI_b/EI_c = 20$

$$\left({EI_c}/{L_c^{\,2}}\right)/\left({EI_b}/{L_b^{\,2}}\right) = 0.45$$

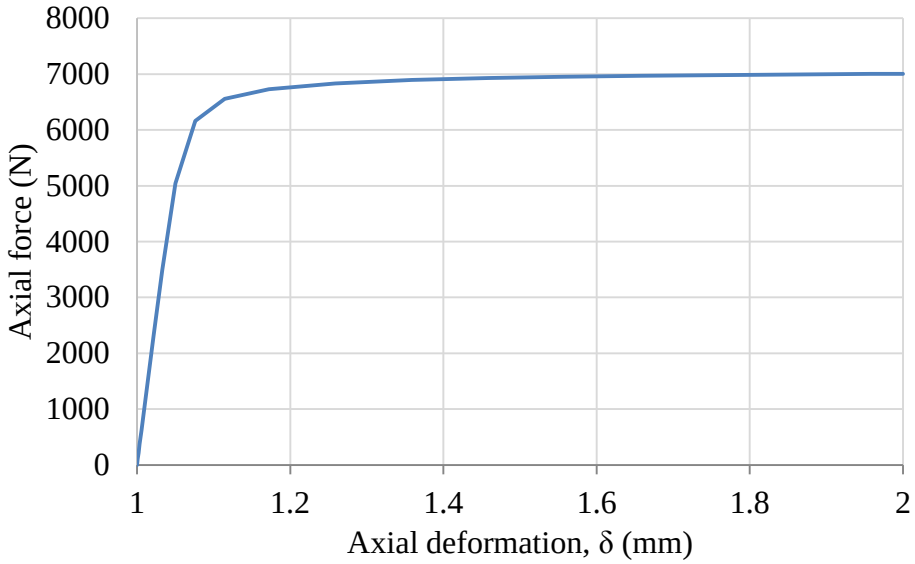

Figure G-36. Axial force-deformation of FE model, $P_{cr} = 7005N$

Cleat effective length calculation based on the FE model result:

$$P_{cr} = \frac{\pi^2 E I_{cleat}}{(kL_{cleat})^2}$$

$P_{cr} = 7005\ N$

$E = 200\ GPa$

$I = 7854\ mm^4$

$L = 1000\ mm$

➔ $k = 1.487$ (FEM)

$k = 1.472$ (Stability function)

Appendix H: Closed-Form Assessment of Shear Stud Slip in Composite Beams

Composite beam design is usually based on the assumption that shear connectors are sufficiently stiff and longitudinal shear forces are transferred with nearly zero slip. This may be correct in the case of full composite action, however for partially composite beams, larger slips may occur to transfer longitudinal shear between the concrete slab and the steel beam. In this study, the shear stud slip demands under gravity loads are investigated using a closed form solution. The closed-form solution results are verified with a number of FE models.

In this study the main assumptions to obtain the shear stud slips include:

1. Concrete does not carry bending moment and shear due to cracking.
2. Creep and shrinkage effects of the concrete material are ignored.
3. The shear force-slip behaviour of shear studs is considered either elastic or elastic perfectly-plastic.

H.1 Elastic shear stud behaviour

The solution to this problem was provided by Johnson (2008). Here the method is described and a similar procedure is derived for the elastic-perfectly plastic shear stud behaviour. Figure H-1 shows an elevation of a composite beam of length dx.

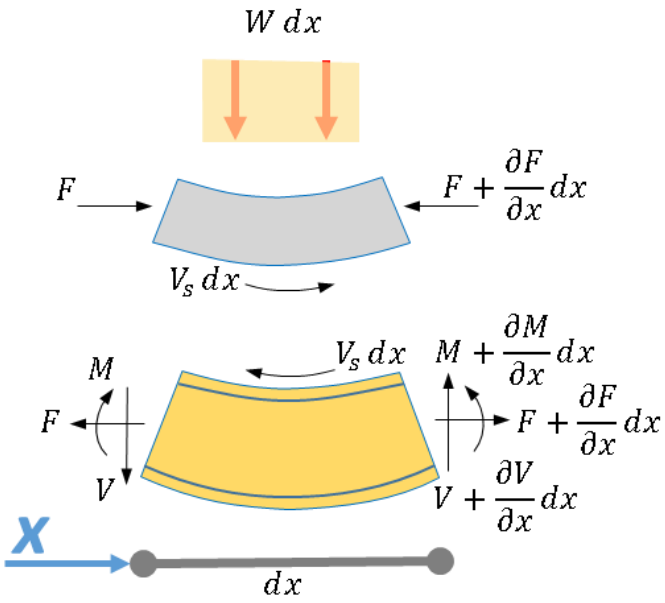

Figure H-1. Elevation of element of composite beam

To calculate the slip at the steel beam and concrete slab interface, equilibrium, elasticity and compatibility conditions should be satisfied. The problem could be solved with different methods such as energy method, differential equations and numerical solutions. In this study, differential equations are used to obtain the shear stud slips at any point along the beam length.

The shear stud forces at the concrete-steel interface are considered as longitudinal shear per unit length, V_s, for simplicity. If the distance between the shear studs denoted by D, then the shear force-slip relationship for each elastic shear stud can be obtained as:

$$DV_S = kS \qquad \text{Eq. (H-1)}$$

Where k is the shear stud linear stiffness and S is the shear stud slip. This equation can be rewritten with nonlinear behaviour of shear studs using the shear force-slip relationship provided by Johnson and Molenstra (1991) as:

$$DV_S = q_r\left(1 - e^{-\beta S}\right)^{\alpha} \qquad \text{Eq. (H-2)}$$

In this equation, α and β are empirical values that in this study are considered equal to 1 and 1.535 respectively. These values are based on Johnson and Molenstra (1991) results for

19mm shear studs. Shear stud strength, q_r, can simply be calculated using equations provided in different building standards (e.g. NZS3404 (2007), Eurocode 4 (2004) and AISC/ANSI 360-16).

From the equilibrium of the composite beam element shown in Figure H-1:

$$\sum F_x = 0 \rightarrow \quad \frac{dF}{dx} = -V_S \qquad \text{Eq. (H-3)}$$

$$\sum F_y = 0 \rightarrow \quad V = Wx \qquad \text{Eq. (H-4)}$$

$$\sum M_o = 0 \rightarrow \quad \frac{dM}{dx} + V = V_S \frac{d}{2} \qquad \text{Eq. (H-5)}$$

Using elasticity equations the composite beam curvature is equal to:

$$\kappa = \frac{M}{EI} \qquad \text{Eq. (H-6)}$$

Since it is assumed the concrete slab does not carry bending moment, its curvature is assumed to be equal to the steel beam curvature. Maximum compression and tension strains of the steel beam and the concrete slab can be obtained from:

$$\varepsilon_{Steel} = -\frac{1}{2}\kappa h_s + \frac{F}{EA} \qquad \text{Eq. (H-7)}$$

$$\varepsilon_{Concrete} = \frac{1}{2}\kappa h_c - \frac{F}{E_c A_c} \qquad \text{Eq. (H-8)}$$

Where h_s and h_c are the steel beam and the concrete slab heights respectively. The elastic modulus and cross-section area of the steel beam and the concrete slab are respectively denoted by EA and $E_c A_c$. The difference between ε_{Steel} and $\varepsilon_{Concrete}$ gives the slip strain, $\frac{dS}{dx}$.

$$\frac{dS}{dx} = \varepsilon_{Concrete} - \varepsilon_{Steel} \qquad \text{Eq. (H-9)}$$

$$\frac{dS}{dx} = \kappa \frac{d}{2} - F\left(\frac{1}{EA} + \frac{1}{E_c A_c}\right) \qquad \text{Eq. (H-10)}$$

By taking derivative of Eq. (H-10) with respect to x gives:

$$\frac{d^2 S}{dx^2} = \frac{d\kappa}{dx}\frac{d}{2} - \frac{dF}{dx}\left(\frac{1}{EA} + \frac{1}{E_c A_c}\right) \qquad \text{Eq. (H-11)}$$

Based on the equilibrium condition in the x direction, $\frac{dF}{dx}$ is equal to $-V_S$ which is related to the shear stud slip, S. However, $\frac{d\kappa}{dx}$ should be eliminated from this equation to achieve a differential equation for S. For this, the derivative of Eq. (H-6) is taken with respect to x:

$$\frac{d\kappa}{dx} = \frac{d}{dx}\frac{M}{EI} \quad \text{Eq. (H-12)}$$

$$\frac{d\kappa}{dx} = \frac{1}{EI}\left(V_S\frac{d}{2} - Wx\right) \quad \text{Eq. (H-13)}$$

By substituting Eq. (H-13) into Eq. (H-11), the differential equation for S is obtained:

$$\frac{d^2S}{dx^2} = \frac{d}{2EI}\left(V_S\frac{d}{2} - Wx\right) - \frac{dF}{dx}\left(\frac{1}{EA} + \frac{1}{E_cA_c}\right) \quad \text{Eq. (H-14)}$$

Considering,

$$\gamma = \left(\frac{1}{EA} + \frac{1}{E_cA_c}\right) \quad \text{Eq. (H-15)}$$

$$\alpha = \frac{dW}{2EI} \quad \text{Eq. (H-16)}$$

$$\eta = \frac{d^2}{4EI} \quad \text{Eq. (H-17)}$$

$$\lambda = \frac{k}{D}(\gamma + \eta) \quad \text{Eq. (H-18)}$$

The differential equation (H-14) can be rewritten using Eqs. (H-15) to (H-18) as:

$$\frac{d^2S}{dx^2} - \lambda S = -x\alpha \quad \text{Eq. (H-19)}$$

Solving Eq. (H-19) for S gives:

$$S = C_1e^{\sqrt{\lambda}x} + C_2e^{-\sqrt{\lambda}x} + \frac{\alpha}{\lambda}x \quad \text{Eq. (H-20)}$$

Boundary and initial conditions are required to obtain C_1 and C_2 coefficients. From the symmetry of the beam, it is known that the slip is zero at the beam mid-span:

$$S = 0 \quad at\ x = 0 \quad \text{Eq. (H-21)}$$

At the supports ε_{Steel} and $\varepsilon_{Concrete}$ are equal to zero which results in zero slip strain:

$$\frac{dS}{dx} = 0 \;\; at \; x = \pm\frac{L}{2} \qquad \text{Eq. (H-22)}$$

Using the above boundary conditions, C_1 and C_2 can simply be obtained. However, slips that are calculated using Eq. (H-20) are only valid for elastic shear studs. Figure H-2 plots the shear stud force-slip behaviour provided by Johnson and Molenstra (1991) and the corresponding linear behavior.

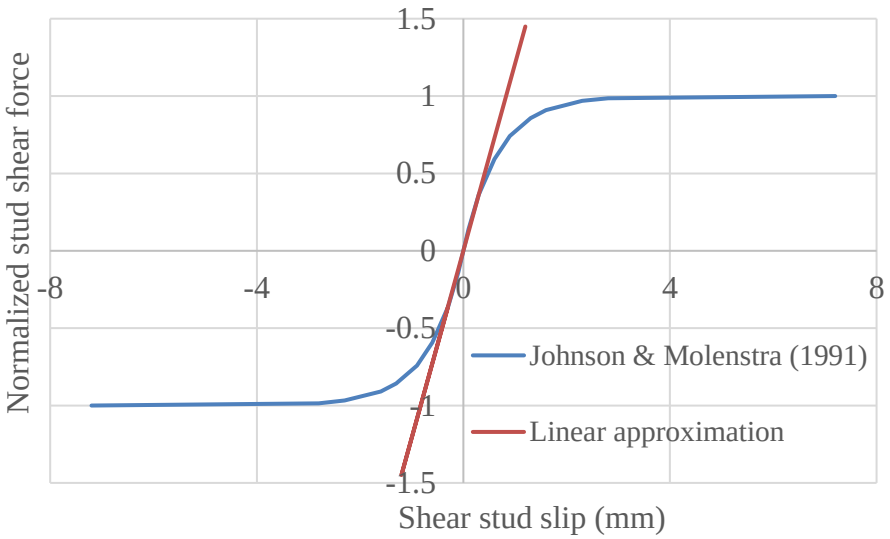

Figure H-2. Shear stud nonlinear behaviour and linear approximation

This plot shows that the shear stud behaviour may be assumed elastic up to nearly 0.6mm slip in this case. Therefore the results obtained from Eq. (H-20) are valid for shear slips less than 0.6mm. This slip value may be changed considering different shear stud sizes and the parameters affecting shear stud stiffness and ductility.

H.2 Nonlinear shear stud behaviour

In Section H.1 the shear slip calculation assuming elastic shear stud behaviour was investigated. Here, nonlinear behaviour of shear studs is considered to obtain the shear stud slips under gravity loads up to the shear stud failure. If instead of using the shear stud elastic behaviour, Eq. (H-1), the nonlinear shear force-slip behaviour, Eq. (H-2), be substituted in

Eq. (H-14), the differential equation (H-19) will be changed to a nonlinear differential equation as:

$$\frac{d^2S}{dx^2} - \psi\left(1 - e^{-\beta S}\right)^{\alpha} = -x\alpha \qquad \text{Eq. (H-23)}$$

Where,

$$\psi = \frac{q_r}{D}(\gamma + \eta) \qquad \text{Eq. (H-24)}$$

By the author's knowledge, there is no explicit solution for this differential equation while it can be solved using numerical techniques. The numerical solution needs to be performed for each case separately and cannot be generalised for all cases. To overcome this problem and obtain a closed form solution for calculating the slip which considers the nonlinear behaviour of the shear studs, the shear stud behaviour is approximated by an elastic-perfectly plastic curve as shown in Figure H-3. The yield point of the elastic-perfectly plastic curve is obtained using the equal energy approach. Equating the area under each curve by taking integration from Eq. (H-2) gives the yield slip as:

$$S_e = \frac{2}{\beta}\left(1 - e^{-\beta S_{max}}\right) \qquad \text{Eq. (H-25)}$$

Where β is an empirical parameter. In this study $\beta = 1.535$ is considered according to Johnson and Molenstra (1991) research for 19mm shear studs. Also, For a 19mm diameter shear stud, S_{max} can be considered equal to 7.2mm based on Johnson and Molenstra (1991) study. Therefore the yield slip, S_e, is calculated equal to 1.3mm in this case.

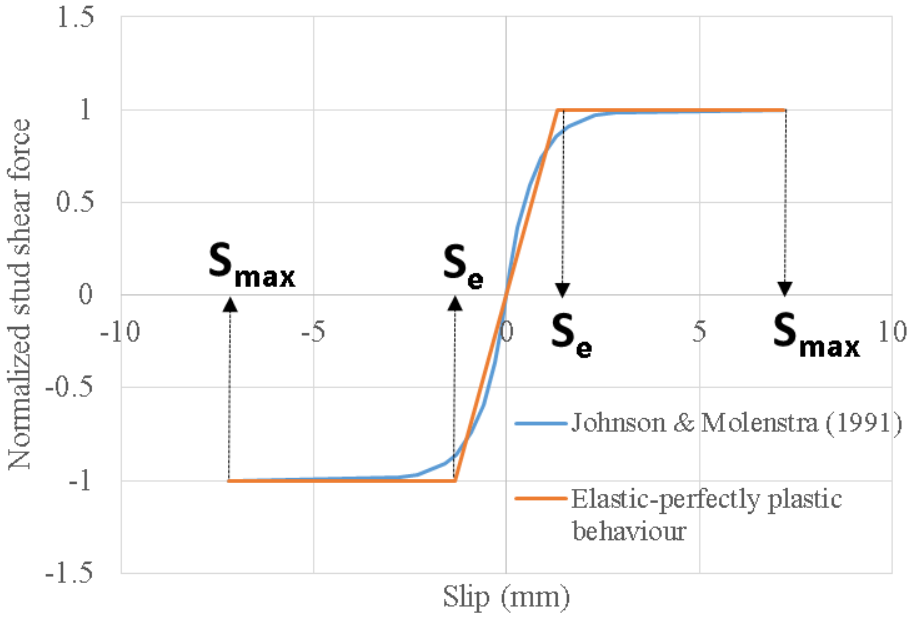

Figure H-3. Elastic-perfectly plastic behaviour of shear studs considered in this study

The elastic perfectly-plastic longitudinal shear behaviour at the concrete-steel interface, V_s, can be written as:

$$DV_S = \begin{cases} \frac{q_r}{S_e} S & for \quad S \le S_e \\ q_r & for \quad S_e < S \le S_{max} \end{cases} \qquad \text{Eq. (H-26)}$$

Using the above shear-slip behaviour a closed form solution for the slip problem can be derived by solving a system of differential equations using two longitudinal shear equations, V_s. For $S \le S_e$ the differential equation is similar to the first case, described in Section H.1, that the shear stud behaviour was considered elastic. The elastic solution is valid for shear studs between the beam centre line and point x_1 or $-x_1$ on the beam. Where, at point x_1 and $-x_1$, the shear slip reaches to the elastic slip value, S_e.

$$\frac{d^2 S_1}{dx^2} - \lambda_1 S_1 = -x\alpha \qquad for \; -x_1 \le x \le x_1 \qquad \text{Eq. (H-27)}$$

Where,

$$\lambda_1 = \frac{q_r}{S_e D}(\gamma + \eta) \qquad \text{Eq. (H-28)}$$

Solving Eq. (H-27) for S_1 gives:

$$S_1 = C_1 e^{\sqrt{\lambda_1}x} + C_2 e^{-\sqrt{\lambda_1}x} + \frac{\alpha}{\lambda_1}x \qquad for\ -x_1 \le x \le x_1 \qquad \text{Eq. (H-29)}$$

For the second part of the shear stud behaviour, the plastic zone, the slip differential equation changes to:

$$\frac{d^2 S_2}{dx^2} - \lambda_2 S_2 = -x\alpha \qquad for\ x_1 \le x \le \frac{L}{2}\ \ and\ -\frac{L}{2} \le x \le -x_1 \qquad \text{Eq. (H-30)}$$

Where,

$$\lambda_2 = \frac{q_r}{D}(\gamma + \eta) \qquad \text{Eq. (H-31)}$$

Solving Eq. (H-30) for S_2 gives:

$$S_2 = -\frac{\alpha}{6}x^3 + \frac{\lambda_2}{2}x^2 + C_3 x + C_4 \qquad for\ x_1 \le x \le \frac{L}{2}\ \ and\ -\frac{L}{2} \le x \le -x_1 \text{Eq. (H-32)}$$

Boundary and initial conditions are required to obtain C_1, C_2, C_3 and C_4 coefficients in both equations simultaneously. From the symmetry of the beam, it is known that the slip is zero at the beam mid-span:

$$S_1 = 0 \quad at\ x = 0 \qquad \text{Eq. (H-33)}$$

Also at the supports ε_{Steel} and $\varepsilon_{Concrete}$ are equal to zero which gives zero slip strain:

$$\frac{dS_2}{dx} = 0 \ \ at\ x = \pm\frac{L}{2} \qquad \text{Eq. (H-34)}$$

At point $x = x_1$ the slip and the slip strain of both equations are equal to satisfy the compatibility condition.

$$S_1 = S_2 \quad at\ x = x_1 \qquad \text{Eq. (H-35)}$$

$$\frac{dS_1}{dx} = \frac{dS_2}{dx} \ \ at\ x = x_1 \qquad \text{Eq. (H-36)}$$

Using the above boundary conditions C_1, C_2, C_3 and C_4 coefficients are obtained as:

$$C_1 = \frac{-\frac{\alpha}{2}{x_1}^2 + \lambda_2 x_1 - \frac{\alpha}{\lambda_2} + \frac{\alpha}{8}L^2 - \frac{\lambda_2}{2}L}{\sqrt{\lambda_1}\left(e^{\sqrt{\lambda_1}x_1} + e^{-\sqrt{\lambda_1}x_1}\right)} \qquad \text{Eq. (H-37)}$$

$$C_2 = -\frac{-\frac{\alpha}{2}x_1{}^2+\lambda_2 x_1-\frac{\alpha}{\lambda_2}+\frac{\alpha}{8}L^2-\frac{\lambda_2}{2}L}{\sqrt{\lambda_1}\left(e^{\sqrt{\lambda_1}x_1}+e^{-\sqrt{\lambda_1}x_1}\right)} \quad \text{Eq. (H-38)}$$

$$C_3 = \frac{\alpha}{8}L^2 - \frac{\lambda_2}{2}L \quad \text{Eq. (H-39)}$$

$$C_4 = C_1\left(e^{\sqrt{\lambda_1}x_1} - e^{-\sqrt{\lambda_1}x_1}\right) + \frac{\alpha}{\lambda_1}x_1 + \frac{\alpha}{6}x_1{}^3 - \frac{\lambda_2}{2}x_1{}^2 - \frac{\alpha L^2}{8}x_1 + \frac{\lambda_2 L}{2}x_1 \quad \text{Eq. (H-40)}$$

As can be seen from the above equations, all the parameters are known except x_1 which is required to be obtained by a try and error procedure. For example, x_1 should be assumed and the corresponding S_1 be calculated, if $S_1 = S_e$, then the selected x_1 is correct. If $S_1 > S_e$ then smaller x_1 should be selected and vice versa. If $S_1 < S_e$ at $x = \pm\frac{L}{2}$ shows that the shear studs are elastic and S_2 equation is not required. In this study a spreadsheet was developed to calculate the shear stud slip by conducting the try and error procedure automatically.

H.3 Verification of the closed-form assessment

H.3.1 FEM models

Three FE models consist of a 6m long beam are considered to verify the closed-form solution developed in Section H.2. In the studied models 360UB50.7 steel section is used considering 50% composite action. The cross-section dimension of the concrete slab on top of the steel beam is 1500×150mm. The yield stress and the elastic modulus of the steel material are considered $340MPa$ and $200GPa$ respectively. The compressive strength and the elastic modulus of the concrete are considered $30MPa$ and $25GPa$ respectively. In the models both the concrete and the steel materials are considered elastic while yielding was allowed in the shear studs. The idealized shear stud behaviour is considered as shown in Figure H-4.

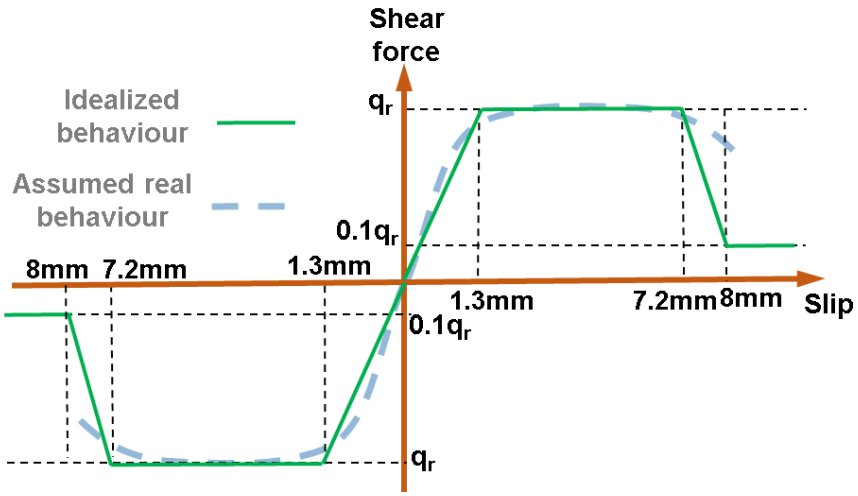

Figure H-4. Shear stud behaviour

The beam-end supports are considered as simply supported. The imposed uniform gravity load on models 1-3 are 60N/mm, 90N/mm and 110N/mm respectively.

H.3.2 Modelling method

To model the composite beams, SAP2000 software is used. Figure H-5 shows the modelling method that was used in this study. The steel beam and the concrete slab elements are placed at the centre line of the steel beam and the concrete slab respectively. Nonlinear link elements are used for modelling shear studs. The shear stud nonlinear links are connected to the concrete slab and the steel beam elements using rigid links as shown in Figure H-5. In this model the flexural stiffness of the concrete slab is ignored due to the concrete cracking.

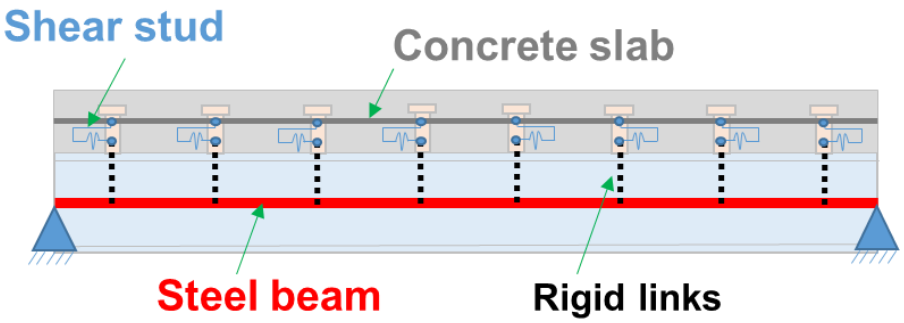

Figure H-5. Method used for modelling composite beam

H.3.3 Results

The maximum slip of each model at the beam ends are obtained. The obtained slips are compared with the calculated slip using the closed-form solution developed in Section H.2. Table H-1 summarizes the results.

Table H-1. FEM and closed-form solution results

	Shear stud slip (mm)		
	Model-1 W=60N/mm	Model-2 W=90N/mm	Model-3 W=110N/mm
FEM model	1.15	2.47	4.06
Closed-form solution	1.22	2.7	4.38
Error (%)	6%	9%	8%
360UB50.7 steel section, 50% composite action			

The results indicate that the closed form solution estimated the shear stud slip with less than 10% error for the studied models. The difference between the FEM model results and the closed form solution may be due to using a number of discrete shear studs in the model instead of a distributed shear force per unit length at the steel-concrete interface.

References

[1] ANSI, A. 360–16.(2016). Specification for structural steel buildings

[2] EN, C. 1994. 1-1, (2004) Eurocode 4: Design of composite steel and concrete structures.

[3] Johnson, R. P. (2008). Composite structures of steel and concrete: beams, slabs, columns, and frames for buildings. John Wiley & Sons.

[4] Johnson, R. P., Molenstra, N., & EPPIB. (1991). Partial shear connection in composite beams for buildings. Proceedings of the Institution of Civil Engineers, 91(4), 679-704.

[5] NZS 3404 (2007). Steel Structures Standard. Standards New Zealand, Wellington, New Zealand. Including Amendments 1 and 2, 2001/2007.

Appendix I: ComFlor 60 and 80 Gravity Design Reports

I.1 ComFlor 60

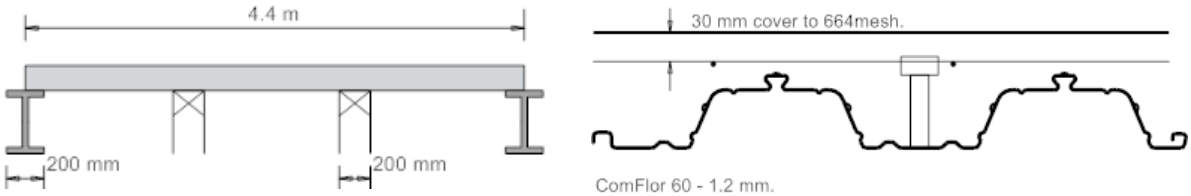

a) ComFlor 60, 4.4 m span, propped

b) ComFlor 60, steel deck thickness 1.2 mm

Figure I-1. ComFlor 60 with 60 mm concrete topping (ComFlor software)

FULL OUTPUT

NOTE: SECTION DESIGNED TO BRITISH STANDARDS

Construction Stage:	**PASS**	**Max Unity Factor = 0.14**
Normal Stage:	**PASS**	**Max Unity Factor = 0.81**
Fire Condition:	**PASS**	**Max Unity Factor = 0.00**
Serviceability:	**SATISFACTORY**	**Max Unity Factor = 0.94**

***** SECTION ADEQUATE *****

FLOOR PLAN DATA : (propped composite construction with ComFlor 60/1.2/G500 decking)

Beam centres	4.40 m	Span type	SINGLE
Beam or wall width	200 mm	Propping	DOUBLE (at 1/3 span)
Prop width	200 mm		

PROFILE DATA : (ComFlor 60/1.2/G500 decking)

Depth	60 mm	Pitch of deck ribs	300 mm
Trough width	120 mm	Crest width	130.7 mm
Nominal sheet thickness	1.20 mm	Design sheet thickness	1.16 mm
Deck weight	0.14 kN/m²	Yield strength	500 N/mm²

CONCRETE SLAB : [Normal Weight Concrete ; Mesh : 664/188]

Overall slab depth	120 mm		
Concrete characteristic strength	30 N/mm²	Concrete wet density	2400 kg/m³
Modular ratio	10	Concrete dry density	2350 kg/m³
Bar reinforcement	NONE		
Mesh reinforcement :			
Mesh	664/188	Yield strength	460 N/mm²
Cover to Mesh	30 mm	Mesh Layers	Single
Account for End Anchorage	NO	Shear connectors per rib	N/A
Diameter of Shear Connectors	N/A		
Screeds	N/A		

SECTION PROPERTIES :

***NOTE - 1: All values of inertia are expressed in steel units
***NOTE - 2: Average inertia is used for deflection calculations for the composite stage
***NOTE - 3: Cracked dynamic inertia is used for natural frequency calculations

DECK PROFILE:

Sagging Inertia, Ixx	132.910 cm4/m	Area of profile (Net), Ap	1721 mm²/m
Hogging Inertia, Iyy	121.600 cm4/m		

COMPOSITE:

Inertia, Ixx - Uncracked	1262 cm4/m	Cracked	713 cm4/m
Average inertia	987 cm4/m	Cracked inertia (dynamic)	819 cm4/m
Shear bond coefficients - Mr	208.86	Kr	0.014700
Concrete volume	0.088 m³/m/m		

LOADS ACTING ON SLAB :

*** NOTE: Slab subjected to uniformly distributed loads (UDL) ONLY

Imposed (occupancy)	3.00 kN/m²	Partitions	1.00 kN/m²
Ceilings and services	0.50 kN/m²	Finishes	0.50 kN/m²
Self weight of concrete slab (wet)	2.08 kN/m²	Self weight of decking	0.14 kN/m²
Self weight of concrete slab (dry)	2.04 kN/m²	Screeds	NONE
Construction load	1.5 kN/m²		

LINE LOADS PERPENDICULAR TO DECK SPAN :

None

LINE LOADS PARALLEL TO DECK SPAN :

None

FIRE DATA :

Design method	SIMPLE	Fire resistance perioc	30 mins
Non-permanent imposed loads	0.0 kN/m²		

PARTIAL SAFETY FACTORS :

Dead (self weight)	1.40	Imposed	1.60
Super imposed dead	1.40	Fire (occupancy loads)	0.80

CONSTRUCTION STAGE

LOADINGS	**Unfactored(kN/m²)**	**Factored(kN/m²)**
Self weight of decking	0.14	0.19
Self weight of concrete slab (wet)	2.08	2.91
Construction load (one span)	1.50	2.40
Construction load (adjacent span(s))	0.50	0.80
Total factored load (maximum)	= 0.19 + 2.91 + 0.00 + 2.40	
	= 5.50 kN/m²	

NOTE: Critical span is longer span

EFFECTIVE SPAN OF DECK :

Effective span Le, is the smaller of

1) c/c of supports = 4.40 m
2) clear span + deck depth = 1.27 + 60.0 / 1000
= 1.33 m

Therefore Le = 1.33 m

SHEAR RESISTANCE CHECK :

*** Check at first interior prop position

Applied shear = [1.100 * 0.19 + 1.200 * 2.91 + 1.200 * 0.05 + 2.500 * 2.40/3] * 1.33 / 2
= 3.82 kN/m

Shear strength of decking, pv = 253.5 N/mm²

Shear resistance, Pv = 117.6 kN/m

UNITY FACTOR = 0.03 PASS

WEB CRUSHING RESISTANCE CHECK :

*** Check at first interior prop position

Applied reaction 7.64 kN/m

Web crushing resistance, Pw 76.06 kN/m

UNITY FACTOR = 0.10 PASS

BENDING RESISTANCE CHECK :

SAGGING:

Max applied moment = [0.080 * 0.19 + 0.094 * 2.91 + 0.094 * 0.05 + 0.094 * 2.40] * 1.33^2
= 0.91 kNm/m

Moment resistance, Mc = 15.21 kNm/m

UNITY FACTOR = 0.06 PASS

HOGGING:

Max. applied moment = 0.99 kNm/m

Moment resistance, Mc = 13.07 kNm/m

UNITY FACTOR = 0.08 PASS

INTERACTION OF BENDING MOMENT AND SHEAR :

*** Check at first interior prop position

Applied shear = 3.82 kN/m

Shear resistance, Pv = 117.61 kN/m

Applied moment = 0.99 kNm/m

Moment resistance, Mc = 13.07 kNm/m

UNITY FACTOR = [3.82/117.61]^2 + [0.99/13.07]^2
= 0.01 PASS

INTERACTION OF BENDING MOMENT AND WEB CRUSHING :

*** Check at first interior prop position

Applied reaction = 7.64 kN/m

Web crushing resistance, Pw = 117.61 kN/m

Applied moment = 0.99 kNm/m

Moment resistance, Mc = 13.07 kNm/m

UNITY FACTOR = [7.64/76.06 + 0.99/13.07]
= 0.18 < 1.25 PASS

DEFLECTION CHECK :

Allowable deflection δmax, is the lesser of

1) Effective span/180 (= 7.4 mm), and
2) 20 mm (absolute maximum value), and
3) Slab depth/10 = (12.0 mm)

Max. self weight deflection = 0.18 mm
(< 7.37 mm) SATISFACTORY

***NOTE: Deflection within code limits; ponding is not considered

NORMAL STAGE

LOADINGS : (see construction load calculations for details):

	Unfactored (kN/m²)	Factored (kN/m²)
Dead	0.14 + 2.04	
	= 2.17	3.04
Imposed	3.00 + 1.00	
	= 4.00	6.40
Superimposed dead	0.50 + 0.50 + 0.00	
	= 1.00	1.40
Total	= 7.17 kN/m²	10.84 kN/m²

EFFECTIVE SPAN :

Effective span Le, is the smaller of

1) c/c of supports

2) clear span + slab overall depth - depth to centroid = 4.2 + 120 / 1000 - 33.85 / 1000

= 4.29 m

Therefore Le = 4.29 m

SHEAR RESISTANCE CHECK :

Maximum applied shear = 0.5 * 10.84 * 4.29

= 23.23 kN/m

Shear stress in concrete, v = 0.56 N/mm²

Shear strength of concrete, vc = 1.24 N/mm²

Shear resistance = 144.65 * 86.15 * 1.24 / 300.00

= 51.57 kN/m

UNITY FACTOR = 0.45 PASS

PUNCHING SHEAR CHECK :

Not Applicable

SHEAR BOND RESISTANCE CHECK :

Shear span = 4.29 / 4

= 1.07 m

Applied shear = 23.33 kN/m

Shear bond resistance = 28.67 kN/m

Anchorage resistance = 0 kN/m

Total shear resistance = (28668.13/1000) + [(0/1000)]/2 = 28.67 kN/m

UNITY FACTOR = 0.81 PASS

BENDING RESISTANCE CHECK :

Applied bending moment = 0.125 * 10.84 * 4.29^2

= 25.00 kNm/m

Depth of concrete stress block = 38.77 mm

NOTE: depth of concrete in compression may be limited to 0.45 ds

Tension in decking = 523.36 kN/m

Tension in bar reinforcement = 0.00 kN/m

Depth to position of resultant tension = (0.0 * 90.0 + 523.4 * 86.1) / (0.0 + 523.4)

= 86.15 mm

Lever arm = 66.77 mm

NOTE: lever arm may be limited to 0.95 ds

Compression in concrete

= 523.36 kN/m

Moment resistance = 523.36 * 66.77/1000

= 34.94 kNm/m

UNITY FACTOR = 0.72 PASS

DEFLECTION CHECK :

Allowable deflection δ_{max-i} under imposed loads, is the lesser of

1) Effective span/350 (= 12.2 mm), and	
2) Absolute maximum value (mm) = 20	
Imposed load deflection	= 0.013 * 4.50 * (4.29* 1000)^4 / (205*9871674)/1000
	= 8.7 mm (< 12.2 mm) SATISFACTORY
Allowable total deflection δmax-t, is the lesser of	
1) Effective span/250 or 17.1 mm, and	
2) 30 mm (SCI recommended absolute maximum value)	
Deflection due to prop removal	= 5.7 mm (based on long-term value of inertia)
Deflection due to imposed loads	= 8.7 mm (based on average inertia)
Additional deflection due to superimposed dead loads	= 2.2 mm (based on average inertia)
Total deflection	= 5.7 + 8.7 + 2.2
	= 16.6 mm (< 17.1 mm) SATISFACTORY

DYNAMIC SENSITIVITY :

***** NOTE: loads are dead + super-imposed dead + 10% imposed**

Dynamic inertia (cracked section)	= 819 cm4
Maximum deflection	= 0.013 * 3.57 * (4.29* 1000)^4 / (205*8187081)/1000
	= 9.44 mm
Frequency	= 18 / √ 9.44)
	= 5.86 Hz (> 5.00 Hz) SATISFACTORY

I.2 ComFlor 80

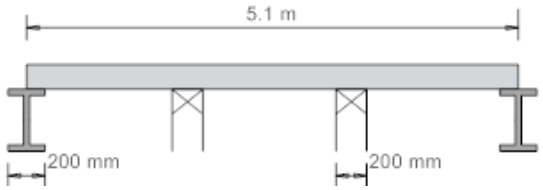

c) ComFlor 80, 5.1 m span, propped

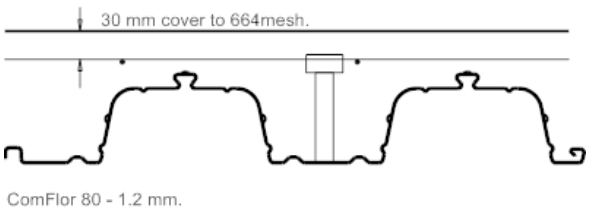

d) ComFlor 80, steel deck thickness 1.2 mm

Figure I-2. ComFlor 80 with 60 mm concrete topping (ComFlor software)

FULL OUTPUT

NOTE: SECTION DESIGNED TO BRITISH STANDARDS

Construction Stage:	**PASS**	**Max Unity Factor = 0.17**
Normal Stage:	**PASS**	**Max Unity Factor = 0.84**
Fire Condition:	**PASS**	**Max Unity Factor = 0.00**
Serviceability:	**SATISFACTORY**	**Max Unity Factor = 0.97**

***** SECTION ADEQUATE *****

FLOOR PLAN DATA : (propped composite construction with ComFlor 80/1.2/G500 decking)

Beam centres	5.10 m	Span type	SINGLE
Beam or wall width	200 mm	Propping	DOUBLE (at 1/3 span)
Prop width	200 mm		

PROFILE DATA : (ComFlor 80/1.2/G500 decking)

Depth	80 mm	Pitch of deck ribs	300 mm
Trough width	120 mm	Crest width	150.0 mm
Nominal sheet thickness	1.20 mm	Design sheet thickness	1.15 mm
Deck weight	0.15 kN/m²	Yield strength	500 N/mm²

CONCRETE SLAB : [Normal Weight Concrete ; Mesh : 664/188]

Overall slab depth	140 mm		
Concrete characteristic strength	30 N/mm²	Concrete wet density	2400 kg/m³
Modular ratio	10	Concrete dry density	2350 kg/m³
Bar reinforcement	NONE		
Mesh reinforcement :			
Mesh	664/188	Yield strength	460 N/mm²
Cover to Mesh	30 mm	Mesh Layers	Single
Account for End Anchorage	NO	Shear connectors per rib	N/A
Diameter of Shear Connectors	N/A		
Screeds	N/A		

SECTION PROPERTIES :

***NOTE - 1: All values of inertia are expressed in steel units
***NOTE - 2: Average inertia is used for deflection calculations for the composite stage
***NOTE - 3: Cracked dynamic inertia is used for natural frequency calculations

DECK PROFILE:

Sagging Inertia, Ixx	216.420 cm4/m	Area of profile (Net), Ap	1914 mm²/m
Hogging Inertia, Iyy	180.650 cm4/m		

COMPOSITE:

Inertia, Ixx - Uncracked	2007 cm4/m	Cracked	1170 cm4/m
Average inertia	1589 cm4/m	Cracked inertia (dynamic)	1339 cm4/m
Shear bond coefficients - Mr	138.43	Kr	0.034400
Concrete volume	0.095 $m^3/m/m$		

LOADS ACTING ON SLAB :

*** NOTE: Slab subjected to uniformly distributed loads (UDL) ONLY

Imposed (occupancy)	3.00 kN/m^2	Partitions	1.00 kN/m^2
Ceilings and services	0.50 kN/m^2	Finishes	0.50 kN/m^2
Self weight of concrete slab (wet)	2.24 kN/m^2	Self weight of decking	0.15 kN/m^2
Self weight of concrete slab (dry)	2.19 kN/m^2	Screeds	NONE
Construction load	1.5 kN/m^2		

LINE LOADS PERPENDICULAR TO DECK SPAN :

None

LINE LOADS PARALLEL TO DECK SPAN :

None

FIRE DATA :

Design method	SIMPLE	Fire resistance period	30 mins
Non-permanent imposed loads	0.0 kN/m^2		

PARTIAL SAFETY FACTORS :

Dead (self weight)	1.40	Imposed	1.60
Super imposed dead	1.40	Fire (occupancy loads)	0.80

CONSTRUCTION STAGE

LOADINGS	Unfactored(kN/m²)	Factored(kN/m²)
Self weight of decking	0.15	0.21
Self weight of concrete slab (wet)	2.24	3.14
Construction load (one span)	1.50	2.40
Construction load (adjacent span(s))	0.50	0.80
Total factored load (maximum)	= 0.21 + 3.14 + 0.00 + 2.40	
	= 5.74 kN/m²	

NOTE: Critical span is longer span

EFFECTIVE SPAN OF DECK :

Effective span Le, is the smaller of

1) c/c of supports	= 5.10 m
2) clear span + deck depth	= 1.50 + 80.0 / 1000
	= 1.58 m
Therefore Le	= 1.58 m

SHEAR RESISTANCE CHECK :

*** Check at first interior prop position

Applied shear	= [1.100 * 0.21 + 1.200 * 3.14 + 1.200 * 0.05 + 2.500 * 2.40/3] * 1.58 / 2	
	= 4.78 kN/m	
Shear strength of decking, pv	= 200.3 N/mm²	
Shear resistance, Pv	= 122.8 kN/m	
UNITY FACTOR	= 0.04	PASS

WEB CRUSHING RESISTANCE CHECK :

*** Check at first interior prop position

Applied reaction	9.55 kN/m	
Web crushing resistance, Pw	84.72 kN/m	
UNITY FACTOR	= 0.11	PASS

BENDING RESISTANCE CHECK :

SAGGING:

Max applied moment	= [0.080 * 0.21 + 0.094 * 3.14 + 0.094 * 0.05 + 0.094 * 2.40] * 1.58^2	
	= 1.35 kNm/m	
Moment resistance, Mc	= 20.74 kNm/m	
UNITY FACTOR	= 0.07	PASS

HOGGING:

Max. applied moment	= 1.48 kNm/m	
Moment resistance, Mc	= 14.78 kNm/m	
UNITY FACTOR	= 0.10	PASS

INTERACTION OF BENDING MOMENT AND SHEAR :

*** Check at first interior prop position

Applied shear	= 4.78 kN/m	
Shear resistance, Pv	= 122.83 kN/m	
Applied moment	= 1.48 kNm/m	
Moment resistance, Mc	= 14.78 kNm/m	
UNITY FACTOR	= [4.78/122.83]^2 + [1.48/14.78]^2	
	= 0.01	PASS

INTERACTION OF BENDING MOMENT AND WEB CRUSHING :

*** Check at first interior prop position

Applied reaction	= 9.55 kN/m	
Web crushing resistance, Pw	= 122.83 kN/m	
Applied moment	= 1.48 kNm/m	
Moment resistance, Mc	= 14.78 kNm/m	
UNITY FACTOR	= [9.55/84.72 + 1.48/14.78]	
	= 0.21 < 1.25	PASS

DEFLECTION CHECK :

Allowable deflection ðmax, is the lesser of

1) Effective span/180 (= 8.8 mm), and
2) 20 mm (absolute maximum value), and
3) Slab depth/10 = (14.0 mm)

Max. self weight deflection	= 0.23 mm	
	(< 8.78 mm)	SATISFACTORY

***NOTE: Deflection within code limits; ponding is not considered

NORMAL STAGE

LOADINGS : (see construction load calculations for details):

	Unfactored (kN/m²)	Factored (kN/m²)
Dead	0.15 + 2.19	
	= 2.34	3.28
Imposed	3.00 + 1.00	
	= 4.00	5.40
Superimposed dead	0.50 + 0.50 + 0.00	
	= 1.00	1.40
Total	= 7.34 kN/m²	11.08 kN/m²

EFFECTIVE SPAN :

Effective span Le, is the smaller of

1) c/c of supports

2) clear span + slab overall depth - depth to centroid = 4.9 + 140 / 1000 - 36.64 / 1000
= 5 m

Therefore Le = 5 m

SHEAR RESISTANCE CHECK :

Maximum applied shear = 0.5 * 11.08 * 5.00
= 27.71 kN/m

Shear stress in concrete, v = 0.60 N/mm²

Shear strength of concrete, vc = 1.16 N/mm²

Shear resistance = 135.00 * 103.36 * 1.16 / 300.00
= 53.80 kN/m

UNITY FACTOR = 0.52 PASS

PUNCHING SHEAR CHECK :

Not Applicable

SHEAR BOND RESISTANCE CHECK :

Shear span = 5.00 / 4
= 1.25 m

Applied shear = 27.83 kN/m

Shear bond resistance = 33.10 kN/m

Anchorage resistance = 0 kN/m

Total shear resistance = (33097.72/1000) + [(0/1000)]/2 = 33.1 kN/m

UNITY FACTOR = 0.84 PASS

BENDING RESISTANCE CHECK :

Applied bending moment = 0.125 * 11.08 * 5.00^2
= 34.81 kNm/m

Depth of concrete stress block = 46.51 mm

NOTE: depth of concrete in compression may be limited to 0.45 ds

Tension in decking = 627.91 kN/m

Tension in bar reinforcement = 0.00 kN/m

Depth to position of resultant tension = (0.0 * 110.0 + 627.9 * 103.4) / (0.0 + 627.9)
= 103.36 mm

Lever arm = 80.10 mm

NOTE: lever arm may be limited to 0.95 ds

Compression in concrete
= 627.91 kN/m

Moment resistance = 627.91 * 80.10/1000
= 50.30 kNm/m

UNITY FACTOR = 0.69 PASS

DEFLECTION CHECK :

Allowable deflection $\delta max\text{-}i$ under imposed loads, is the lesser of

1) Effective span/350 (= 14.3 mm), and	
2) Absolute maximum value (mm) = 20	
Imposed load deflection	= 0.013 * 4.50 * (5.00* 1000)^4 / (205*15885100)/1000
	= 10.0 mm (< 14.3 mm) SATISFACTORY
Allowable total deflection δmax-t, is the lesser of	
1) Effective span/250 or 20.0 mm, and	
2) 30 mm (SCI recommended absolute maximum value)	
Deflection due to prop removal	= 7.2 mm (based on long-term value of inertia)
Deflection due to imposed loads	= 10.0 mm (based on average inertia)
Additional deflection due to superimposed dead loads	= 2.5 mm (based on average inertia)
Total deflection	= 7.2 + 10.0 + 2.5
	= 19.7 mm (< 20.0 mm) SATISFACTORY

DYNAMIC SENSITIVITY :

***** NOTE: loads are dead + super-imposed dead + 10% imposed**

Dynamic inertia (cracked section)	= 1339 cm4
Maximum deflection	= 0.013 * 3.74 * (5.00* 1000)^4 / (205*13387440)/1000
	= 11.22 mm
Frequency	= 18 / √ 11.22)
	= 5.37 Hz (> 5.00 Hz) SATISFACTORY

References

[1] ComFlor Steel Composite Metal Deck Design software, Ver 9.0.33.0

Appendix J: Simplified 2D Structural Modelling Verification

J.1 Simplified 2D modelling method

Simplified 2D modelling method is verified with the corresponding 3D model for using in NLTH analyses. The simplified model includes a cantilever column representing the wall system and a column with rotational restraints at each storey to represent the moment frame structure. For the moment frame structure, it is assumed that the point of contraflexure is at the mid-height of each storey under lateral loading. These columns, representing VLFR systems, are connected at every storey with a horizontal member representing the diaphragm as shown in Figure J-1.

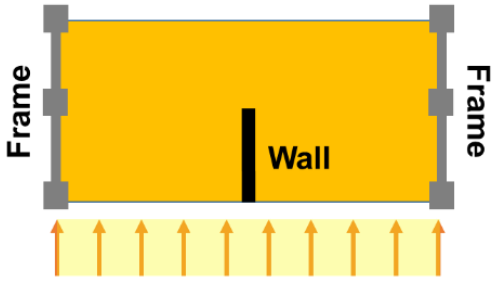

a) Floor plan

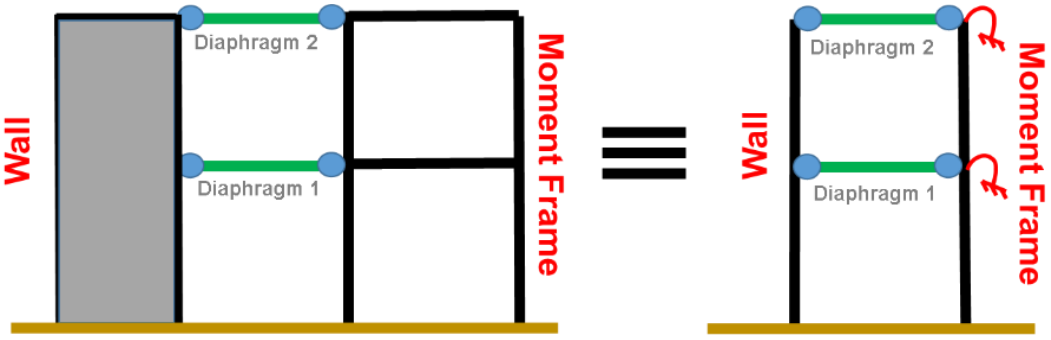

b) Simplified model

Figure J-1. Two storey structure and the simplified model

A five storey structure shown in Figure J-2 is selected to verify the simplified modelling method. Similar lateral forces are applied to both 3D and 2D models. The lateral forces are

applied at the lumped mass locations in the 2D model, while they are applied to the 3D model as a uniformly distributed force on each floor.

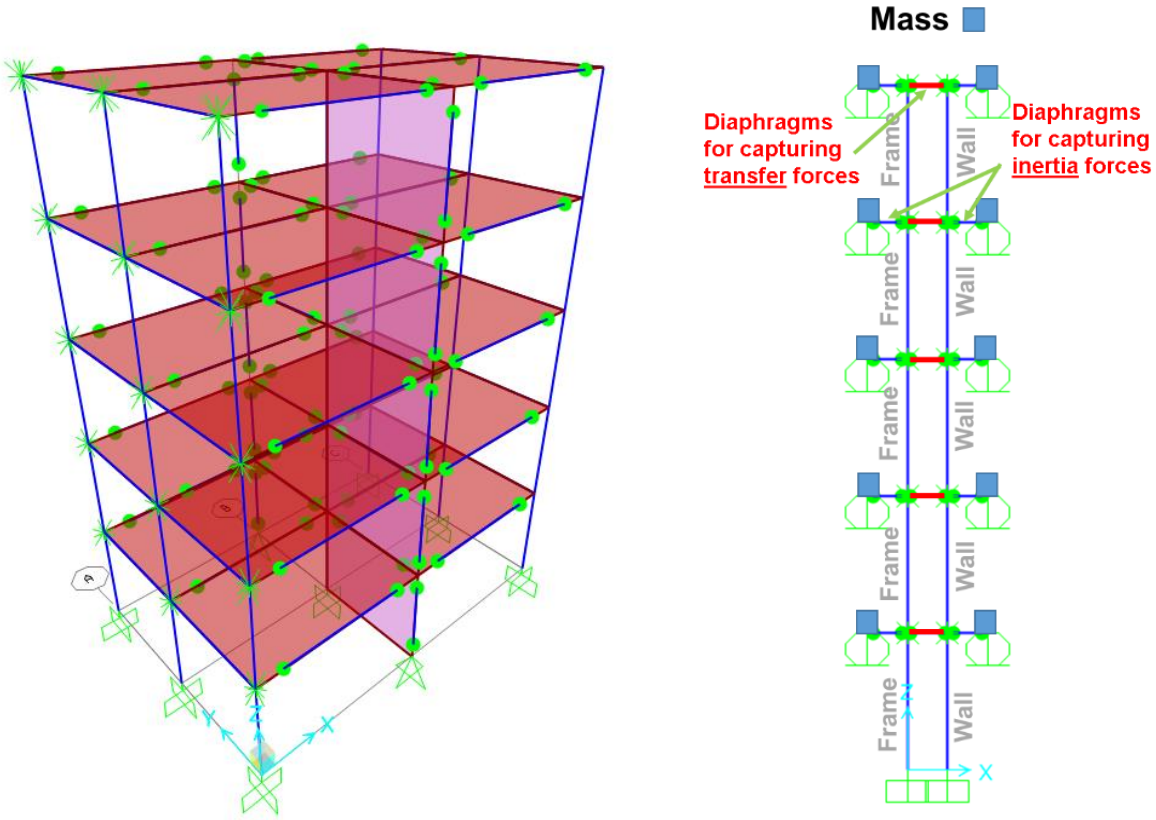

a) 3D model

b) Simplified 2D model

Figure J-2. Five storey structure and its simplified model

J.2 Analysis results

The analysis results of the 3D and the simplified 2D models are investigated in terms of building modal periods and diaphragm in-plane forces.

J.2.1 Modal periods of 2D and 3D models

Table J-1 presents the periods of first three modes of the 3D and 2D models. These indicate that the simplified model has similar dynamic properties to the 3D model. Since the lumped mass placed on the 2D model is similar to the mass of the 3D model, the modal periods indicate that the stiffness matrix of the 2D and 3D models are similar.

Table J-1. Modal periods of the 3D and 2D models

	3D model (s)	**2D model (s)**
Mode 1	0.605	0.602
Mode 2	0.191	0.191
Mode 3	0.101	0.101

J.2.2 Diaphragm in-plane forces

The simplified model can only provide one value as diaphragm in-plane inertia and/or transfer force in each level. Therefore, the in-plane diaphragm shear force distribution cannot be obtained using the simplified model. Here the correlation between the values obtained using the simplified model with the diaphragm in-plane forces in the 3D model is investigated. The diaphragm forces of the fifth floor of the selected model shown in Figure J-2 is used to investigate both inertia and transfer forces in both models. The results are presented in Figure J-3.

The maximum diaphragm transfer force in the 3D model that was obtained was equal to1028kN. However, the transfer force of the fifth floor of the simplified 2D model is about 2074kN. This shows that the maximum diaphragm transfer force obtained from the simplified model is twice the diaphragm in-plane shear force for the floor plan configuration shown in Figure J-1a. Similarly, the maximum diaphragm inertia force in the 3D model is 730kN, while the diaphragm inertia force in the 2D model is 2920kN. This shows that the maximum diaphragm inertia force obtained from the simplified model is four times the diaphragm in-plane shear force in this floor plan configuration.

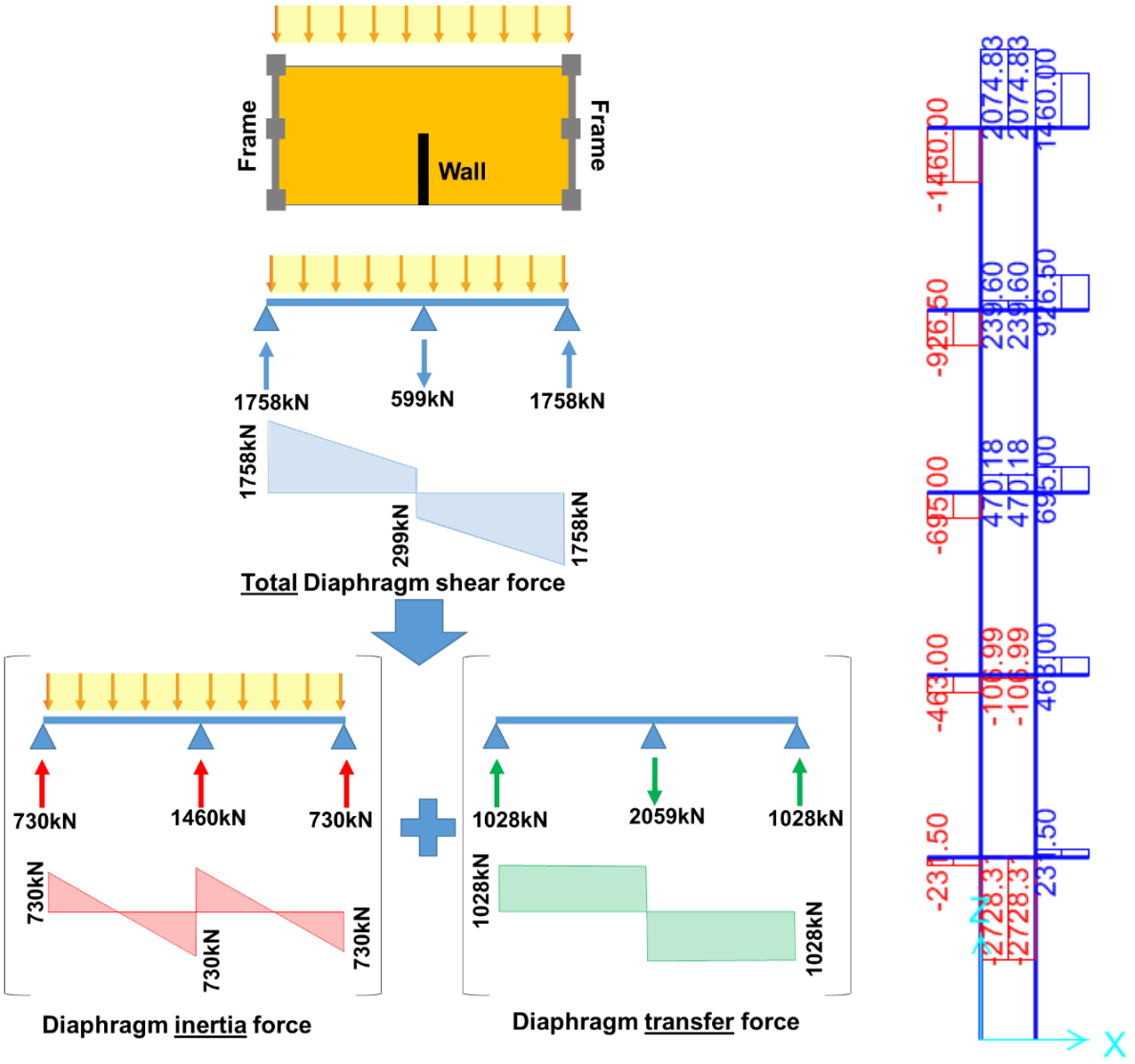

a) Diaphragm in-plane forces of the fifth floor, 3D model

b) 2D model results

Figure J-3. Diaphragm in-plane forces of the 3D and 2D models

Note that if instead of the floor plan shown in Figure J-1a, the floor plan shown in Figure J-4 be considered, then the total inertia forces obtained from the 2D model should be multiplied by 0.125 to provide similar values as the diaphragm in-plane shear force in the 3D model. Similarly, the transfer forces obtained from the 2D model should be multiplied by 0.25 to provide similar values as the diaphragm in-plane shear force in the 3D model.

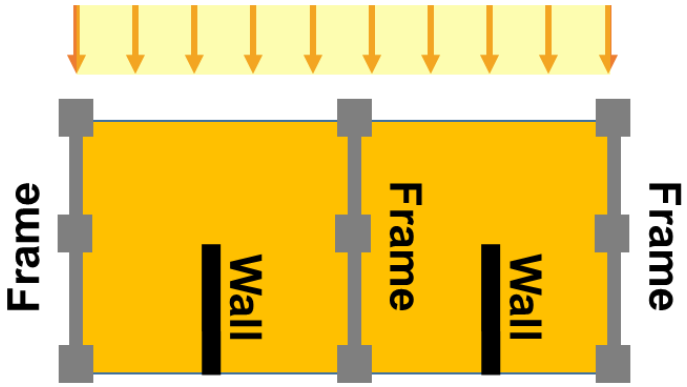

Figure J-4. Floor plan consisting of two shear walls and three moment frames

Appendix K: Diaphragm Inertia and Transfer Forces of the Studied Dual Structures

- **Model 11**

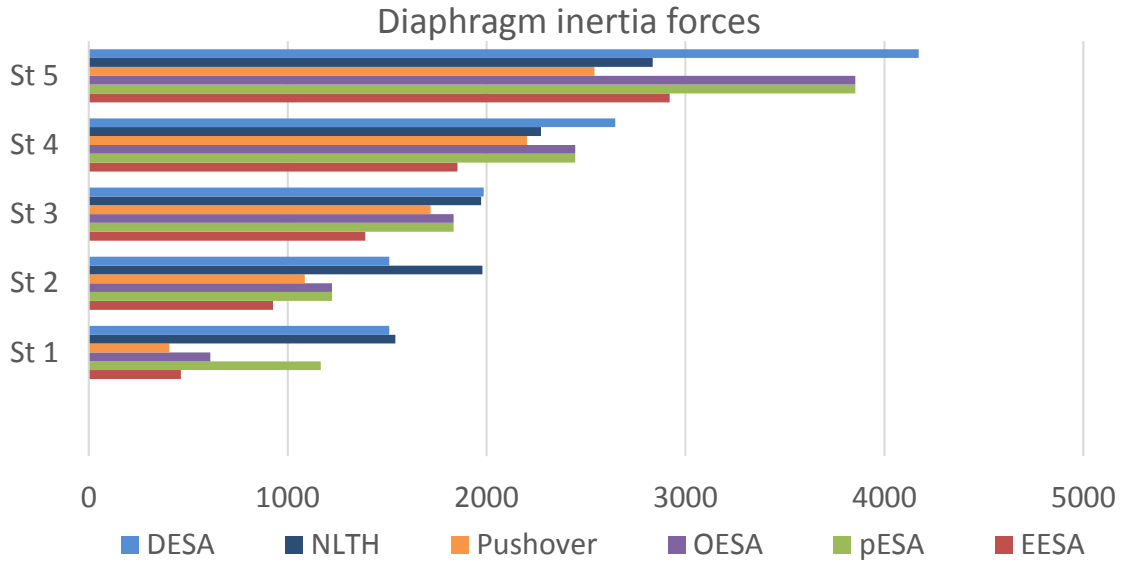

a) Diaphragm inertia forces

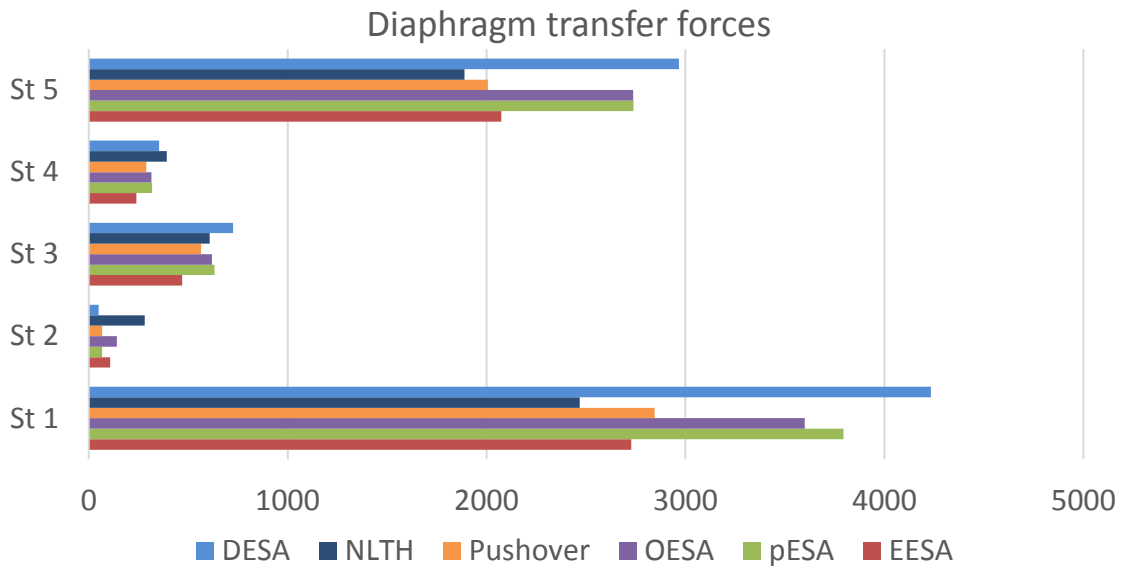

b) Diaphragm transfer forces

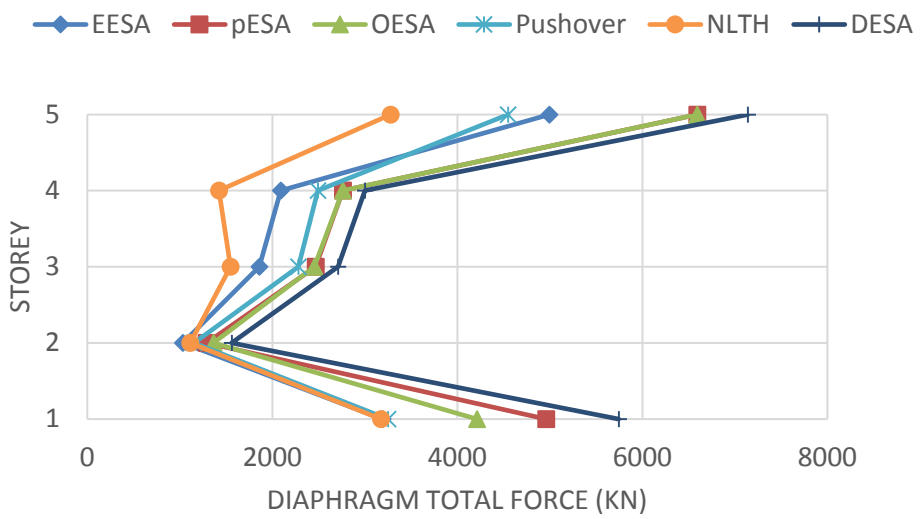

c) Total diaphragm forces

Figure K-1. Diaphragm in-plane forces of model 11

- **Model 12**

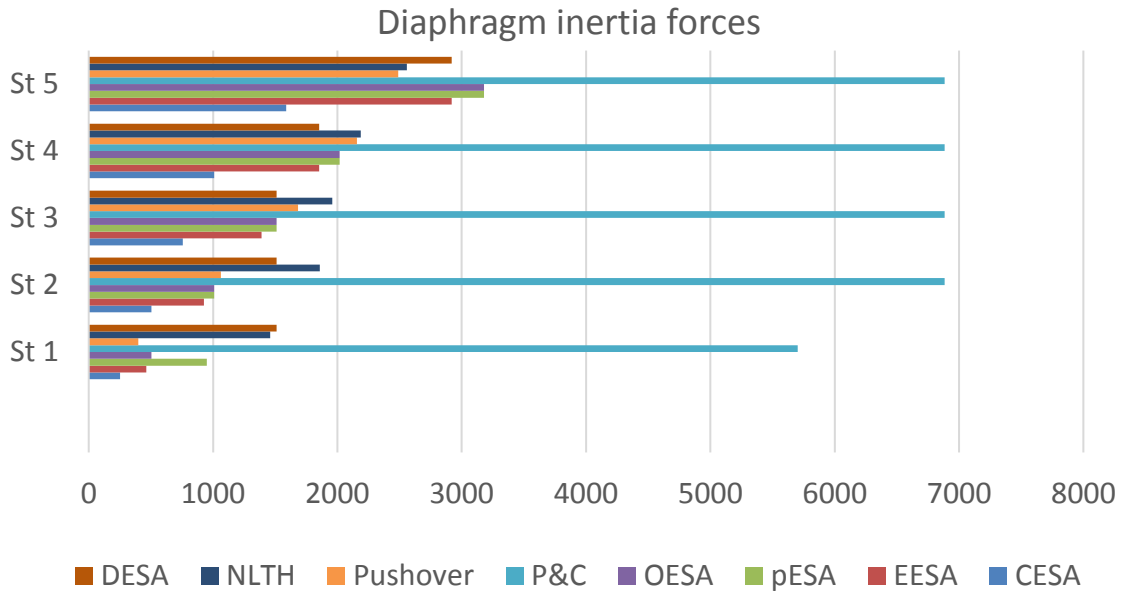

a) Diaphragm inertia forces

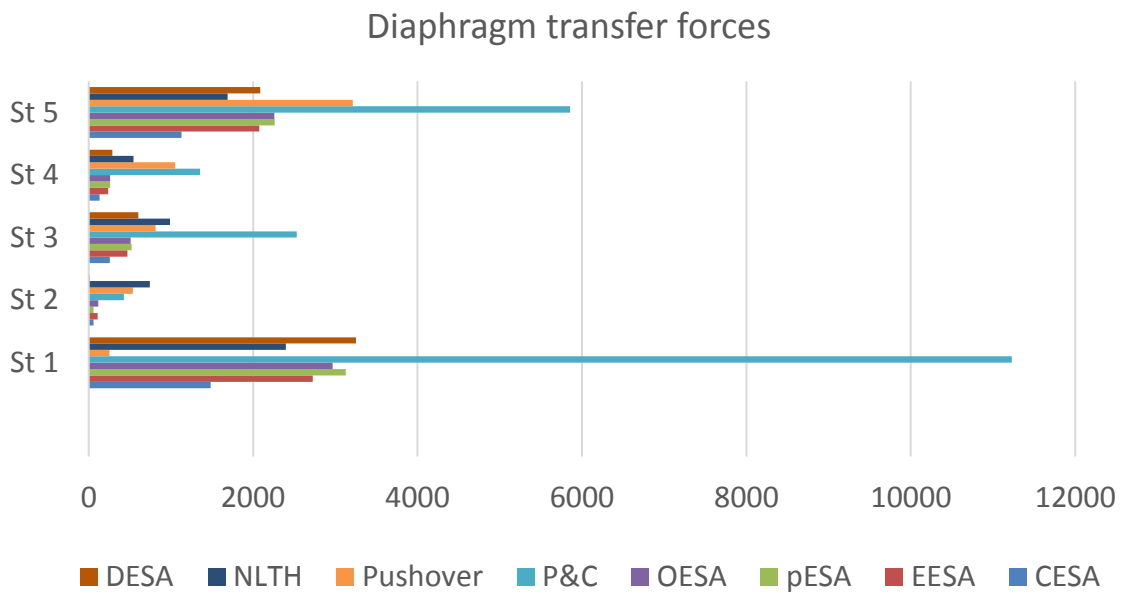

b) Diaphragm transfer forces

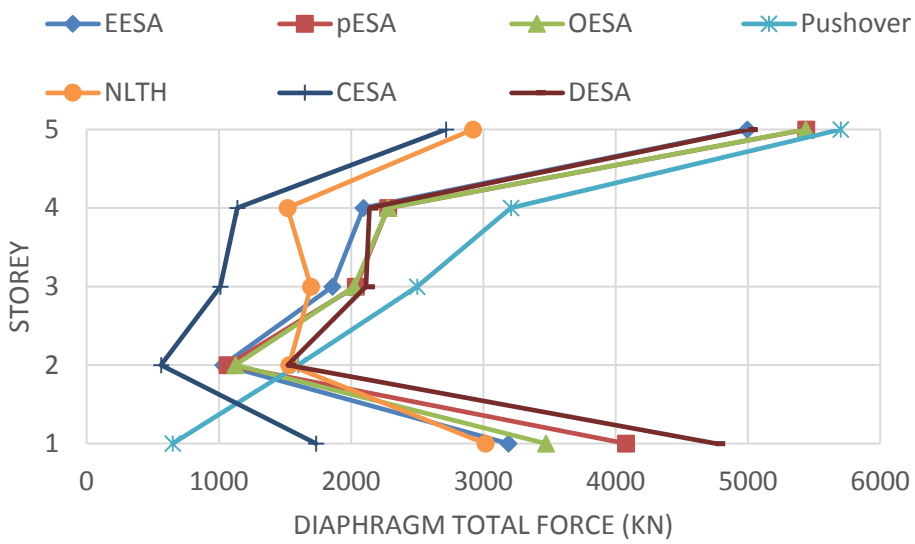

c) Total diaphragm forces

Figure K-2. Diaphragm in-plane forces of model 12

- **Model 13**

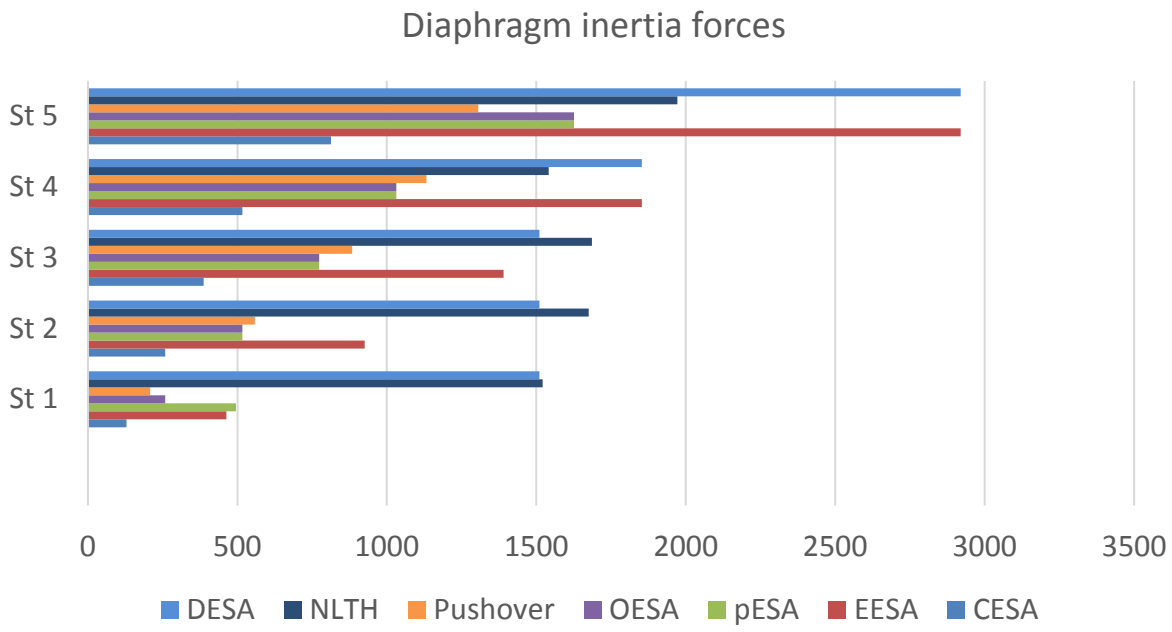

a) Diaphragm inertia forces

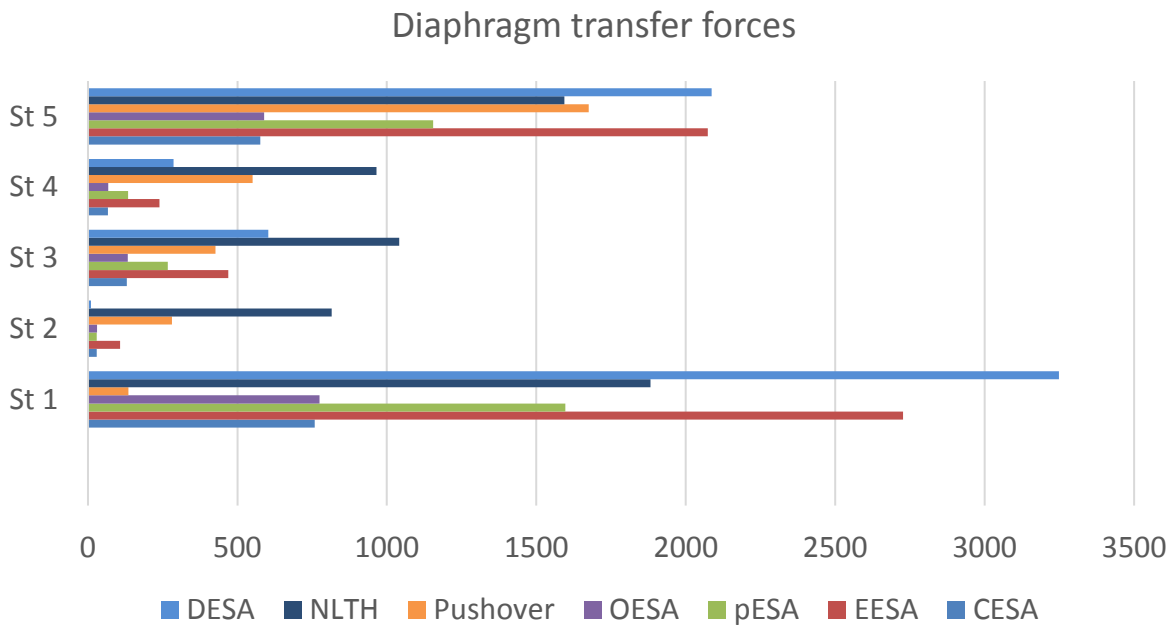

b) Diaphragm transfer forces

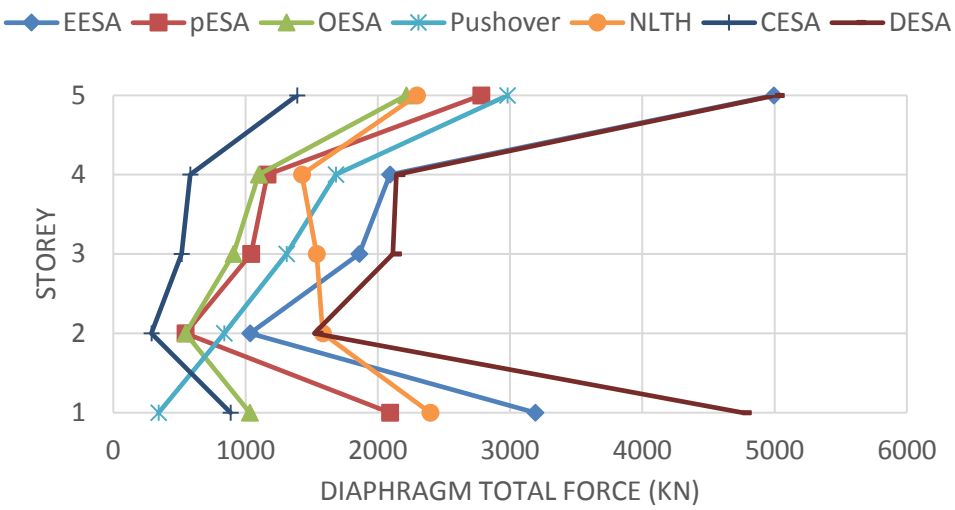

c) Total diaphragm forces

Figure K-3. Diaphragm in-plane forces of model 13

- **Model 14**

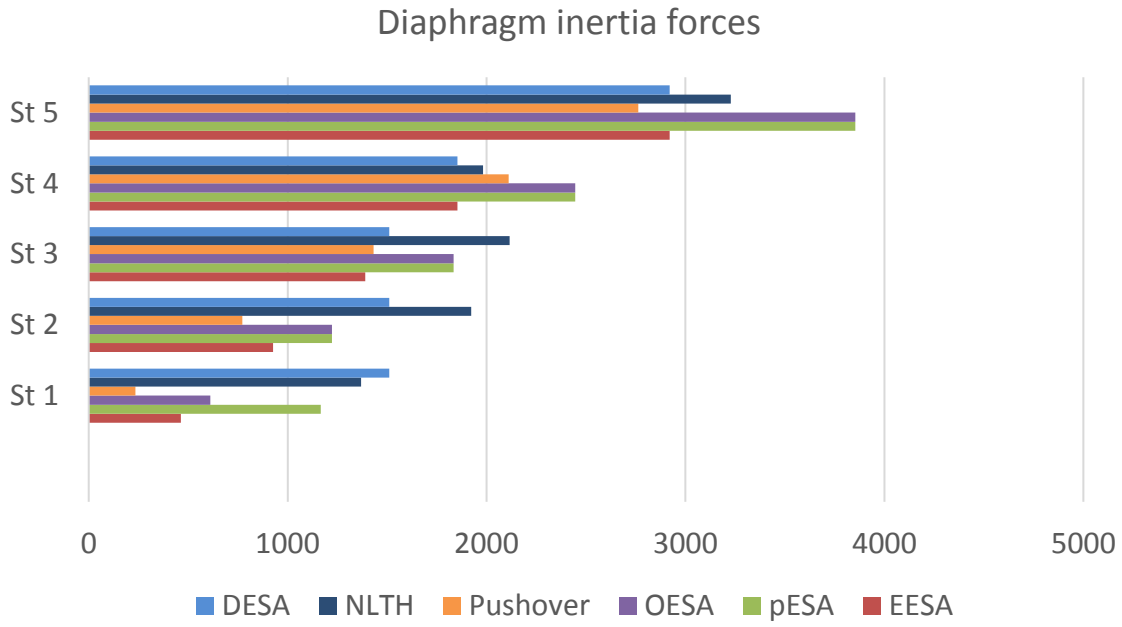

a) Diaphragm inertia forces

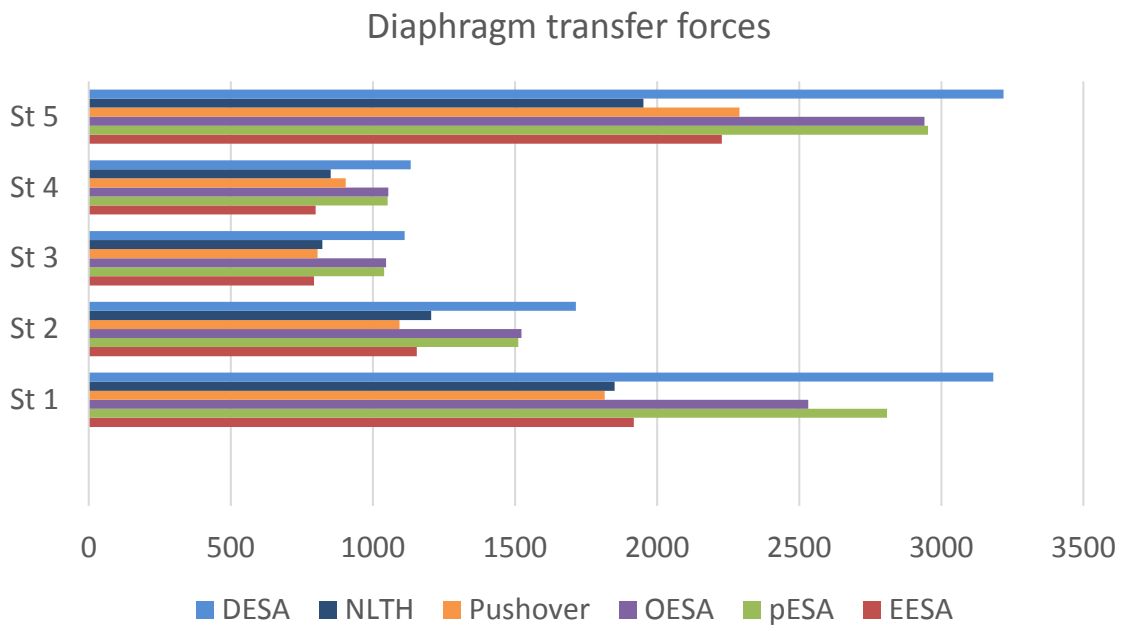

b) Diaphragm transfer forces

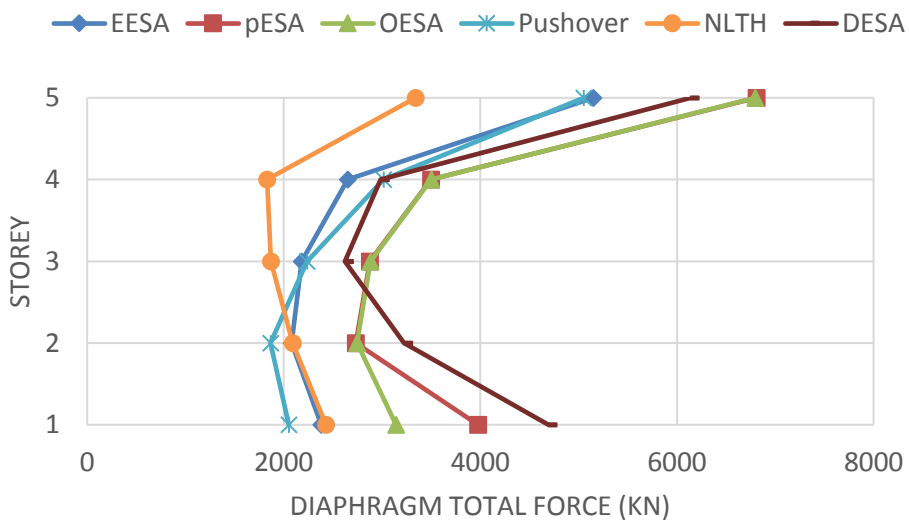

c) Total diaphragm forces

Figure K-4. Diaphragm in-plane forces of model 14

- **Model 15**

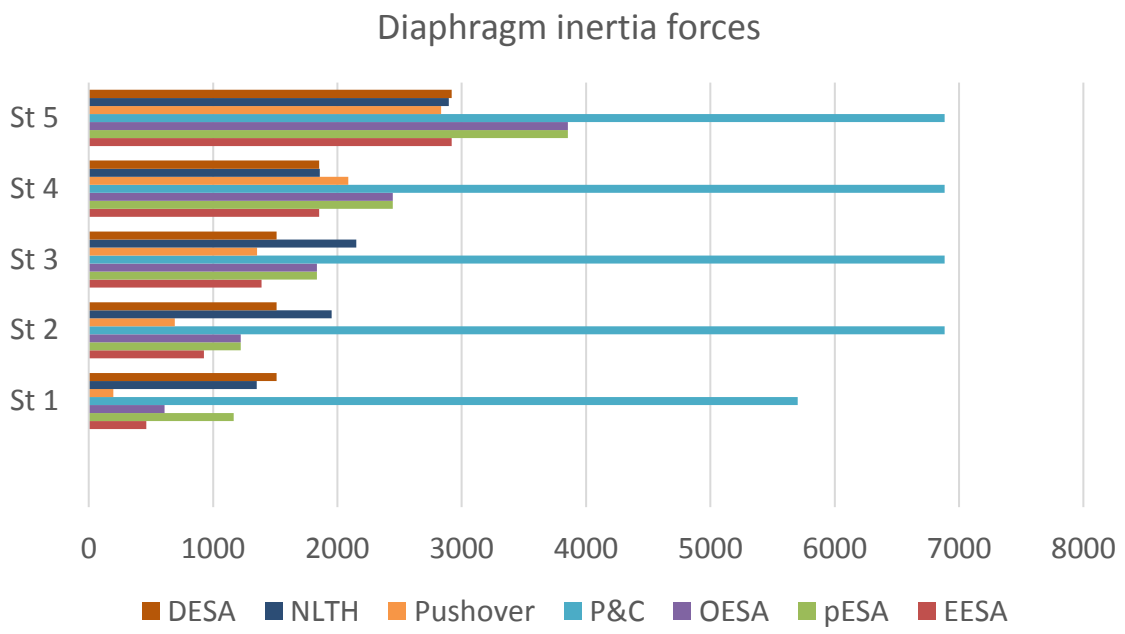

a) Diaphragm inertia forces

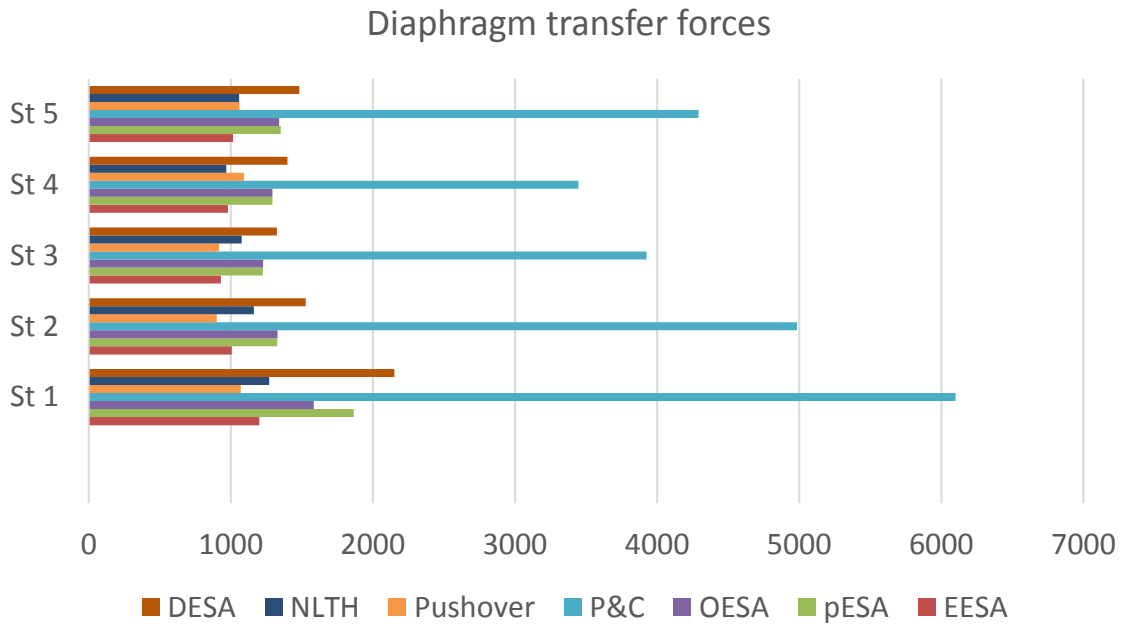

b) Diaphragm transfer forces

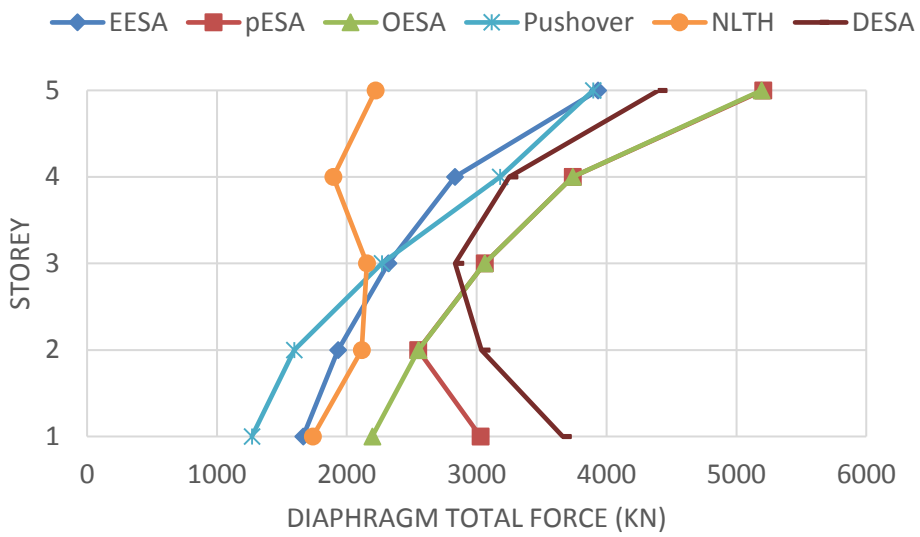

c) Total diaphragm forces

Figure K-5. Diaphragm in-plane forces of model 15

- **Model 16**

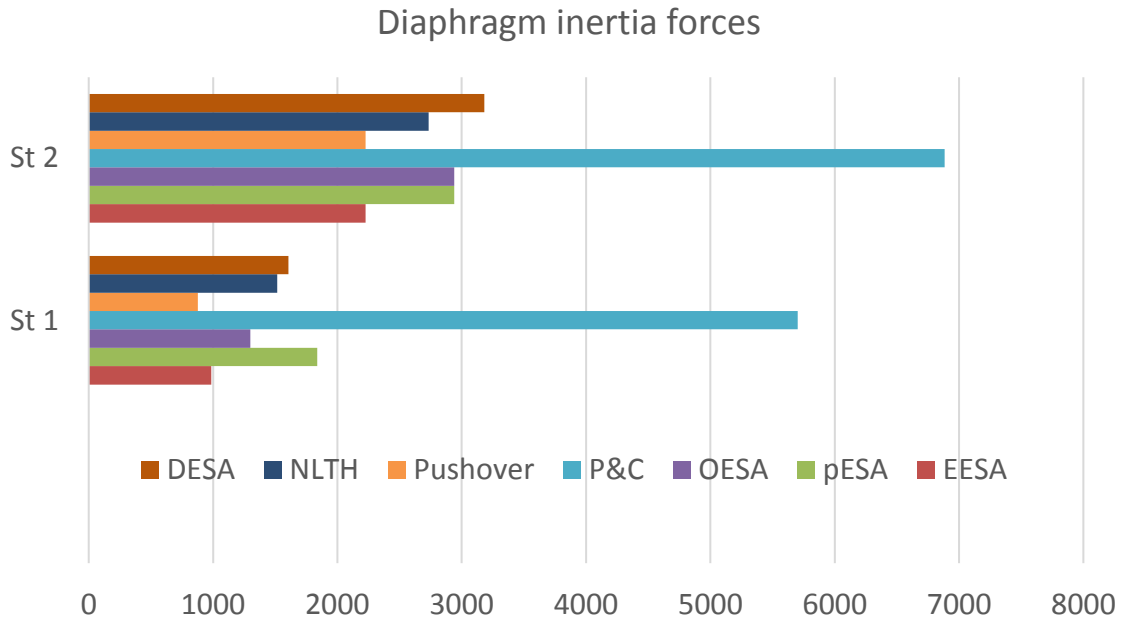

a) Diaphragm inertia forces

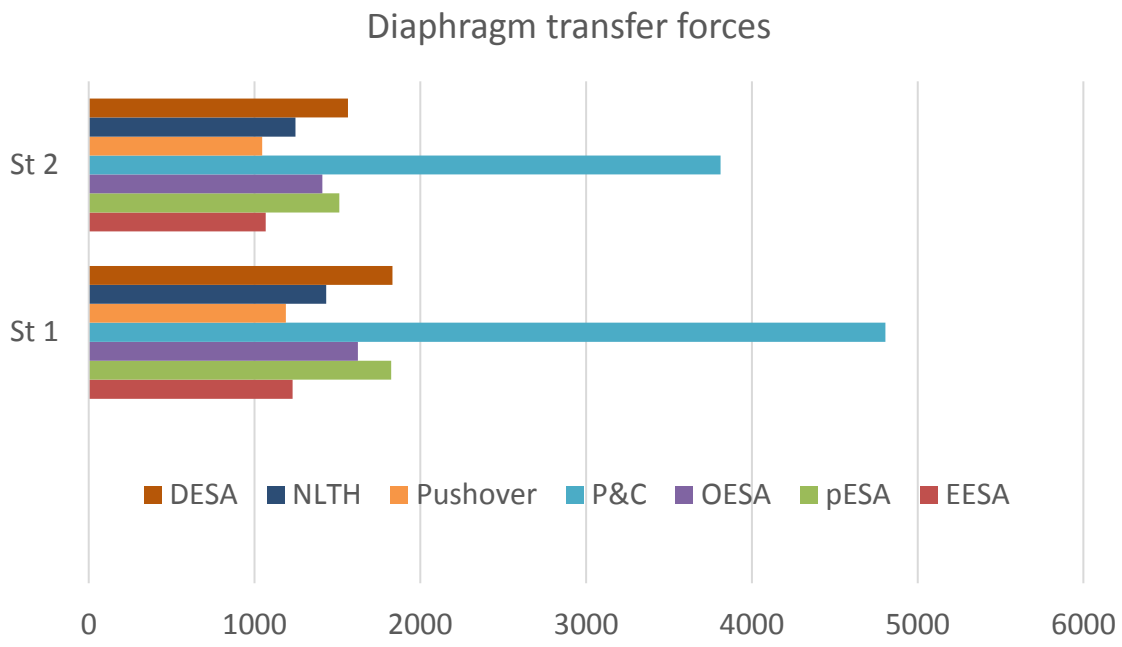

b) Diaphragm transfer forces

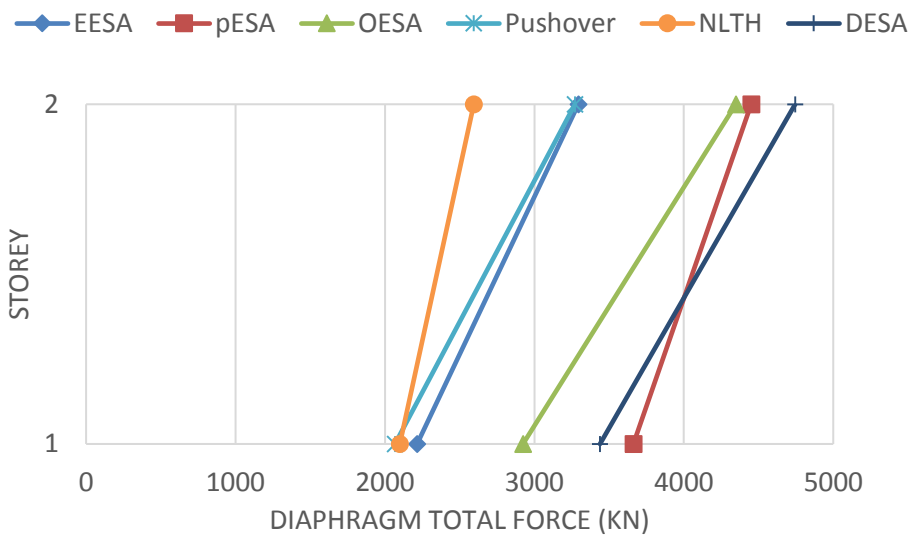

c) Total diaphragm forces

Figure K-6. Diaphragm in-plane forces of model 16

- **Model 17**

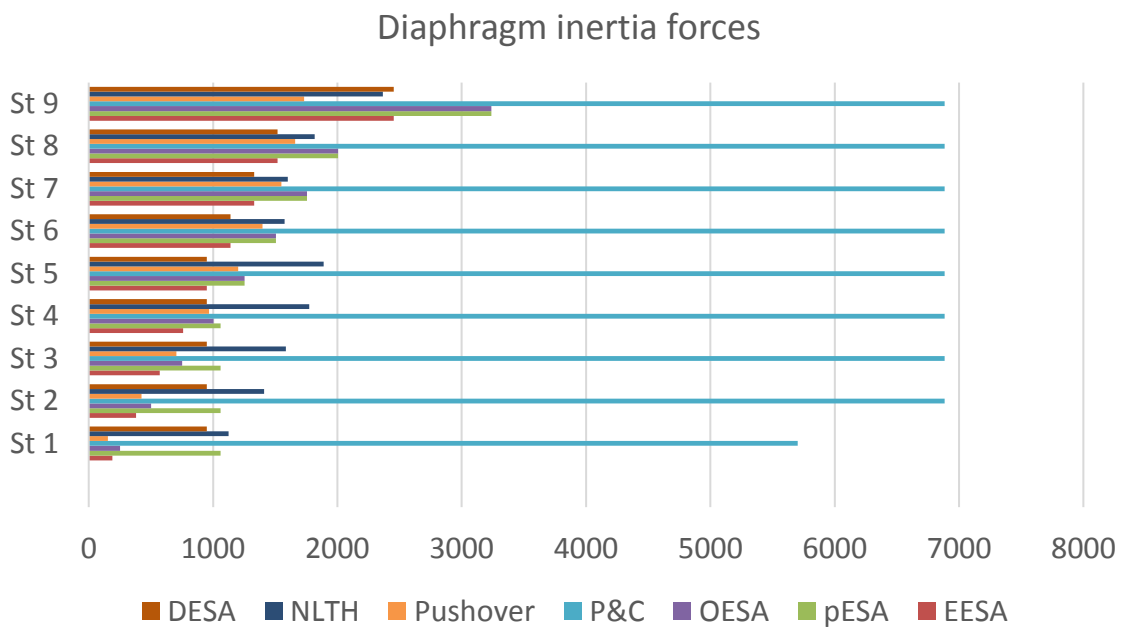

a) Diaphragm inertia forces

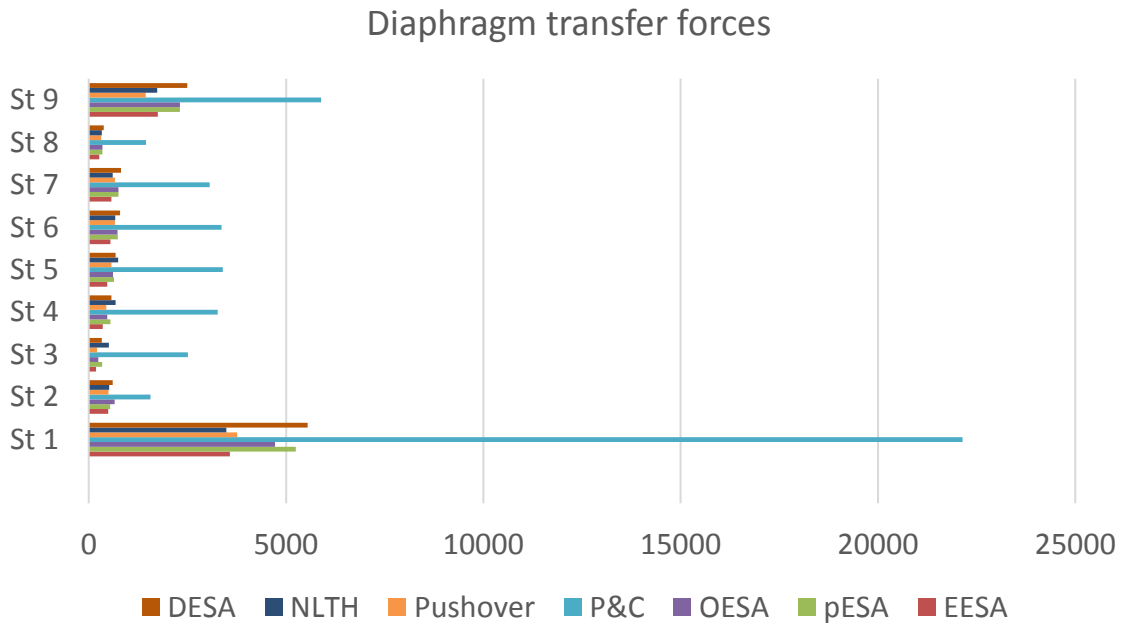

b) Diaphragm transfer forces

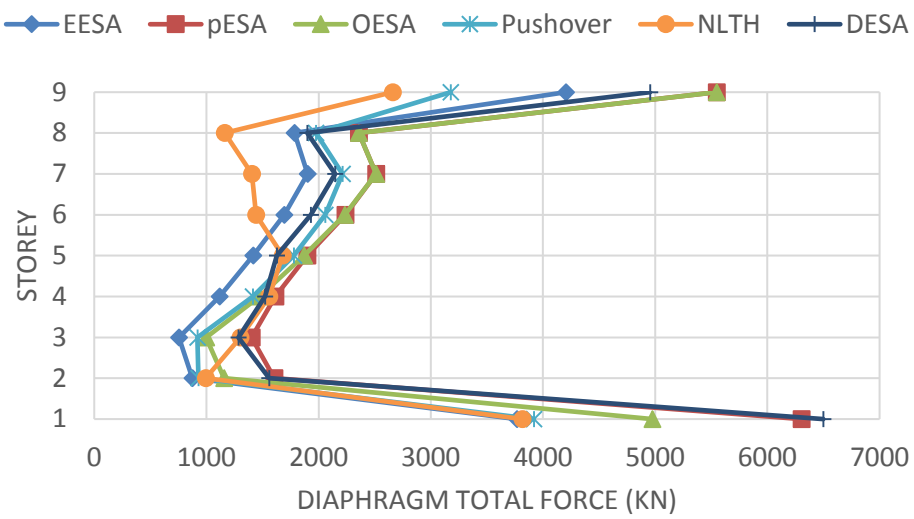

c) Total diaphragm forces

Figure K-7. Diaphragm in-plane forces of model 17

- **Model 18**

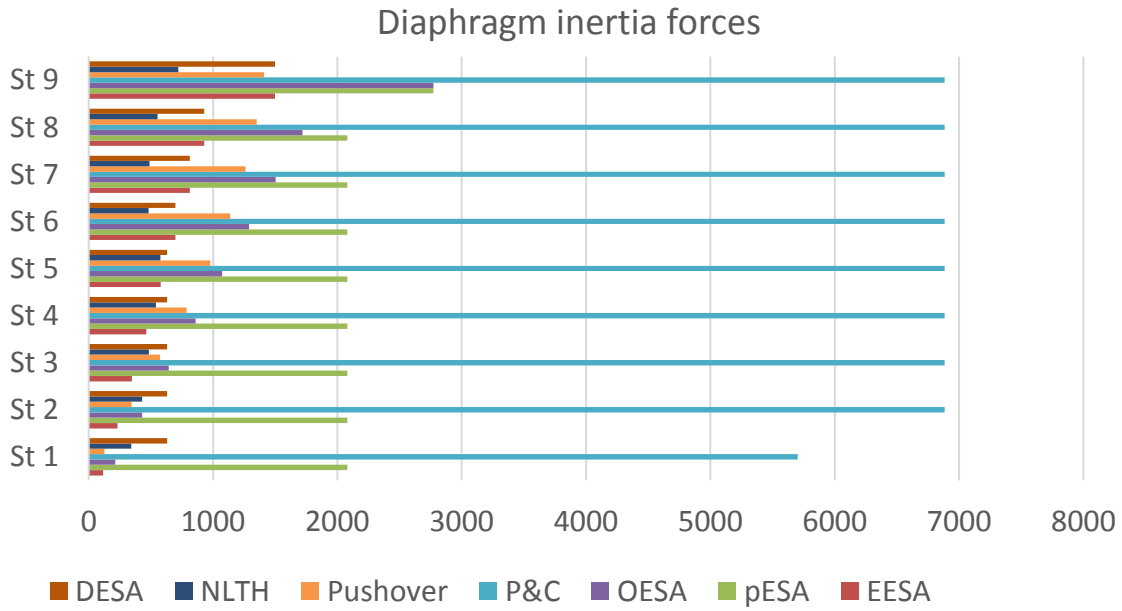

a) Diaphragm inertia forces

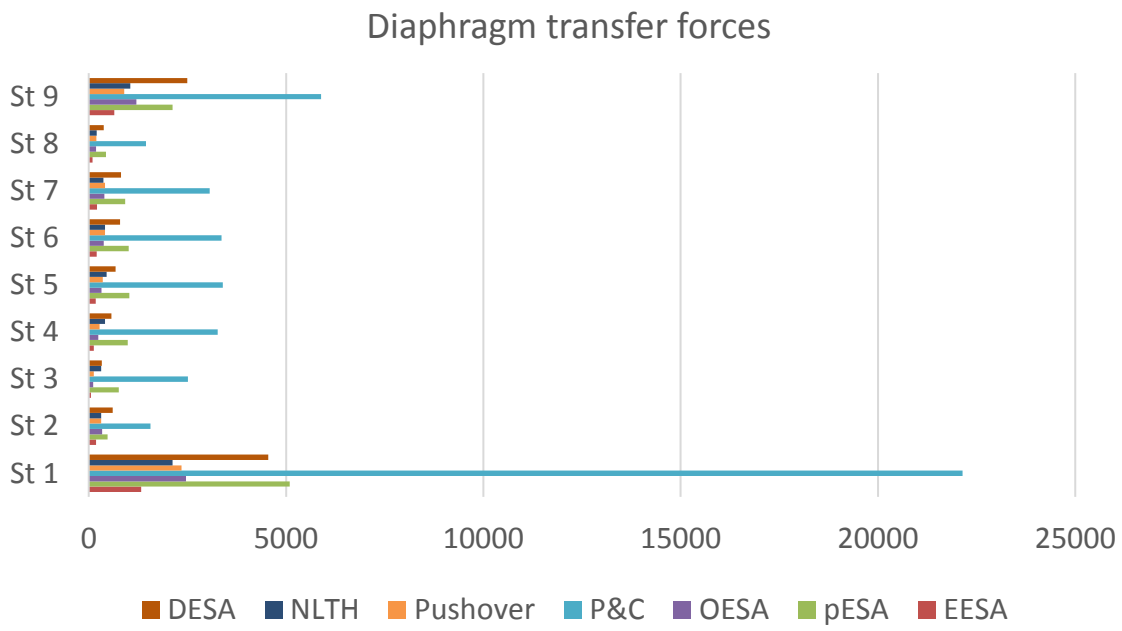

b) Diaphragm transfer forces

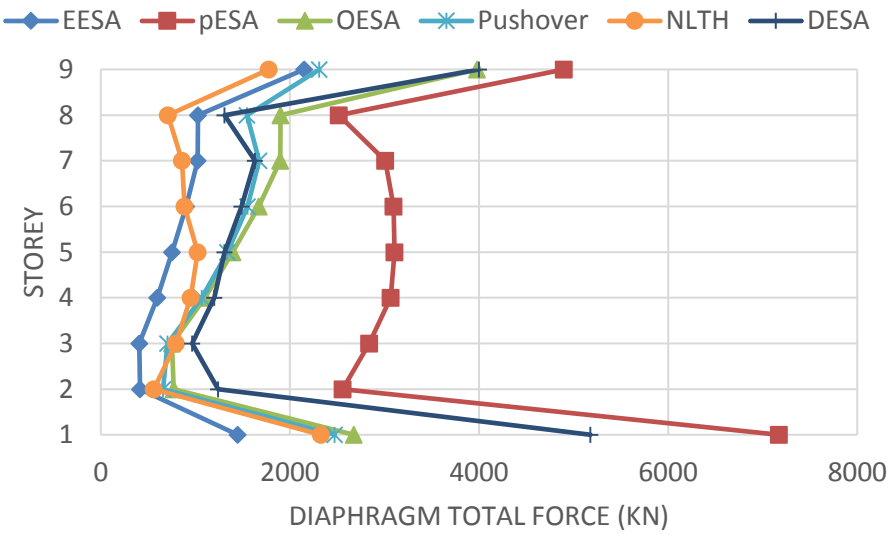

c) Total diaphragm forces

Figure K-8. Diaphragm in-plane forces of model 18

- **Model 19**

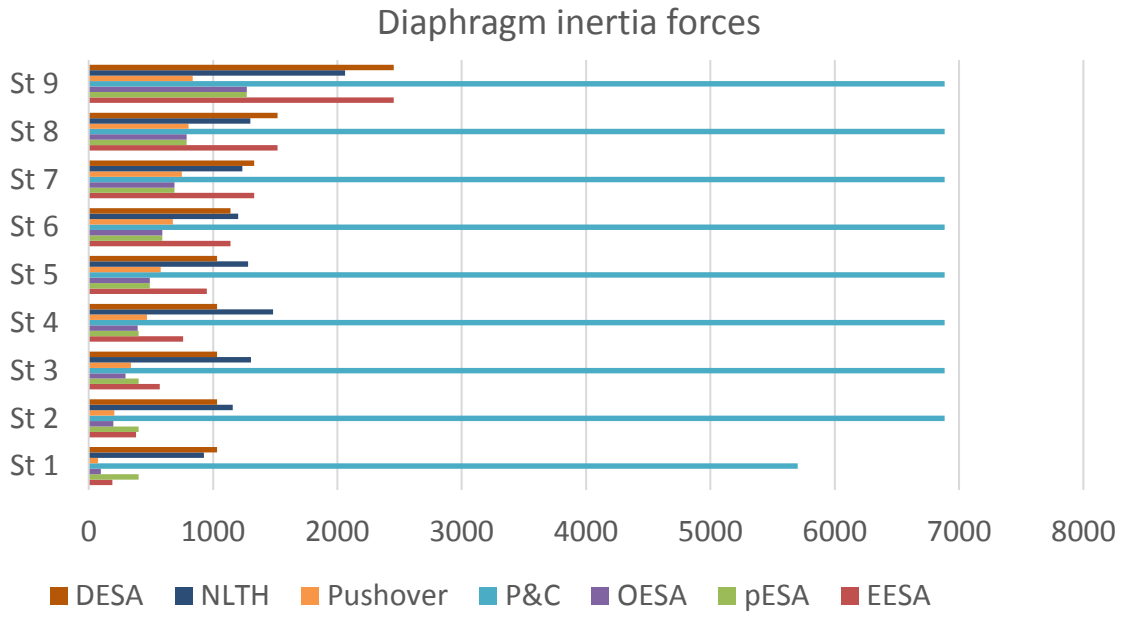

a) Diaphragm inertia forces

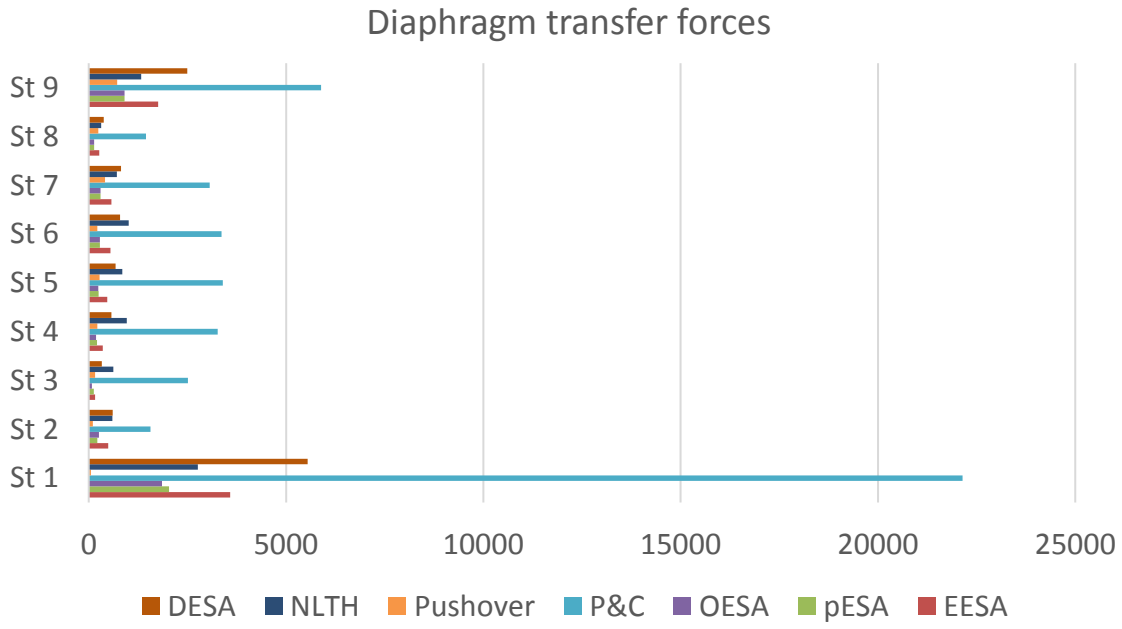

b) Diaphragm transfer forces

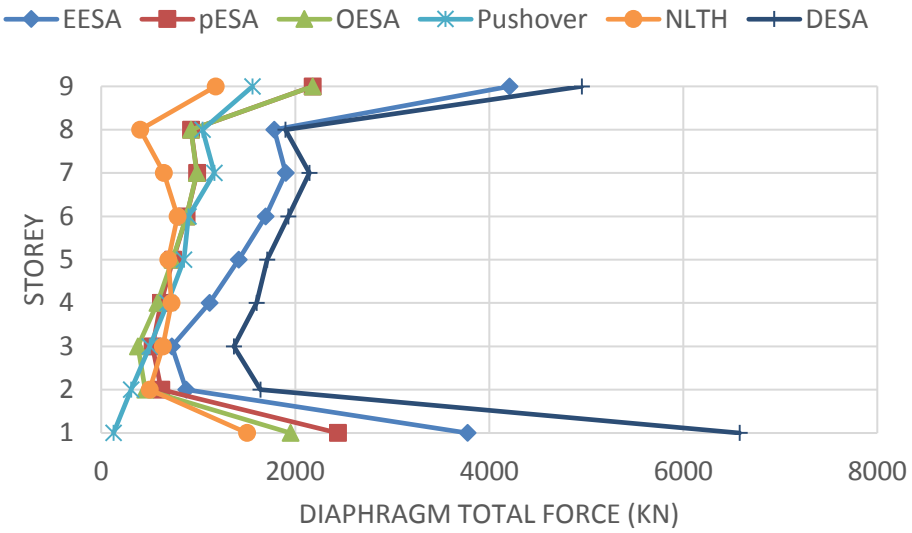

c) Total diaphragm forces

Figure K-9. Diaphragm in-plane forces of model 19

- **Model 20**

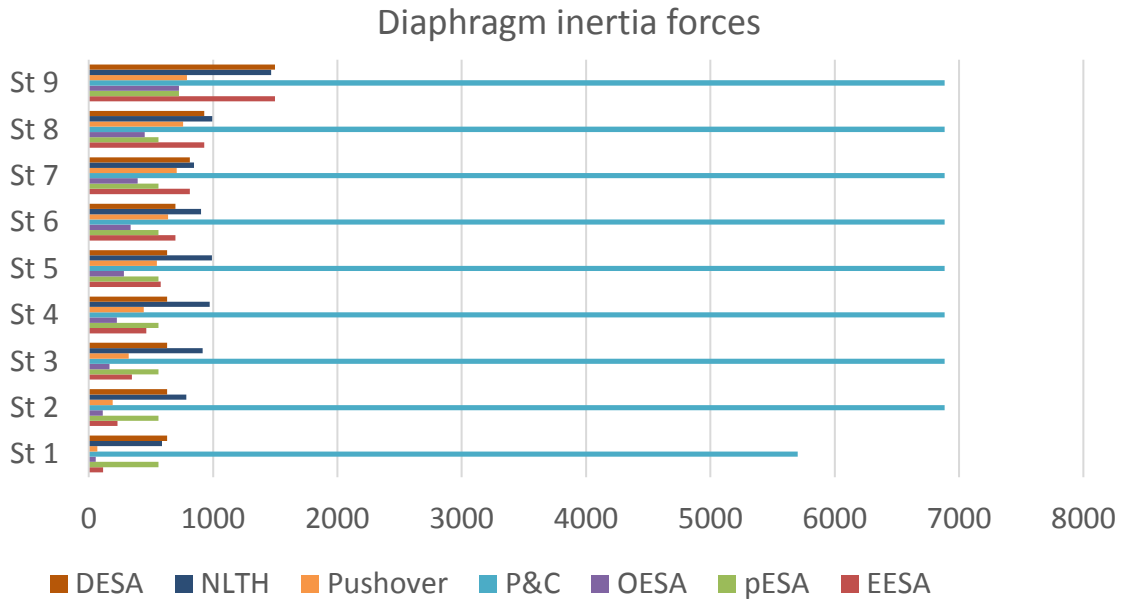

a) Diaphragm inertia forces

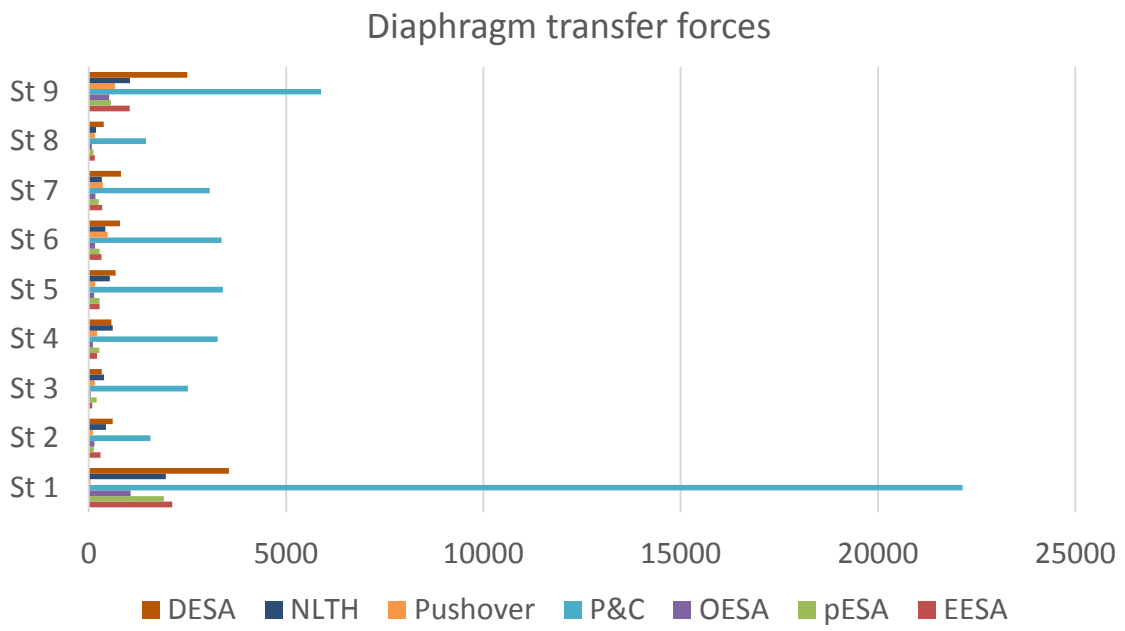

b) Diaphragm transfer forces

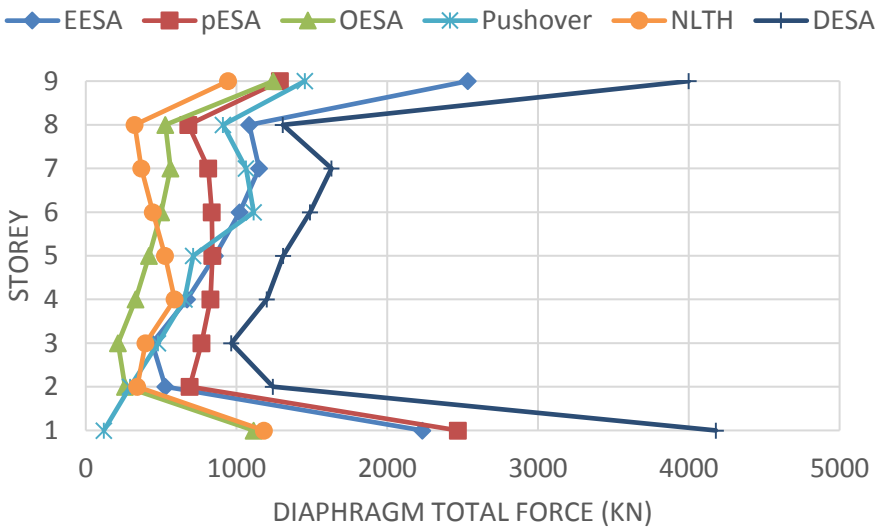

c) Total diaphragm forces

Figure K-10. Diaphragm in-plane forces of model 20

- **Model 21**

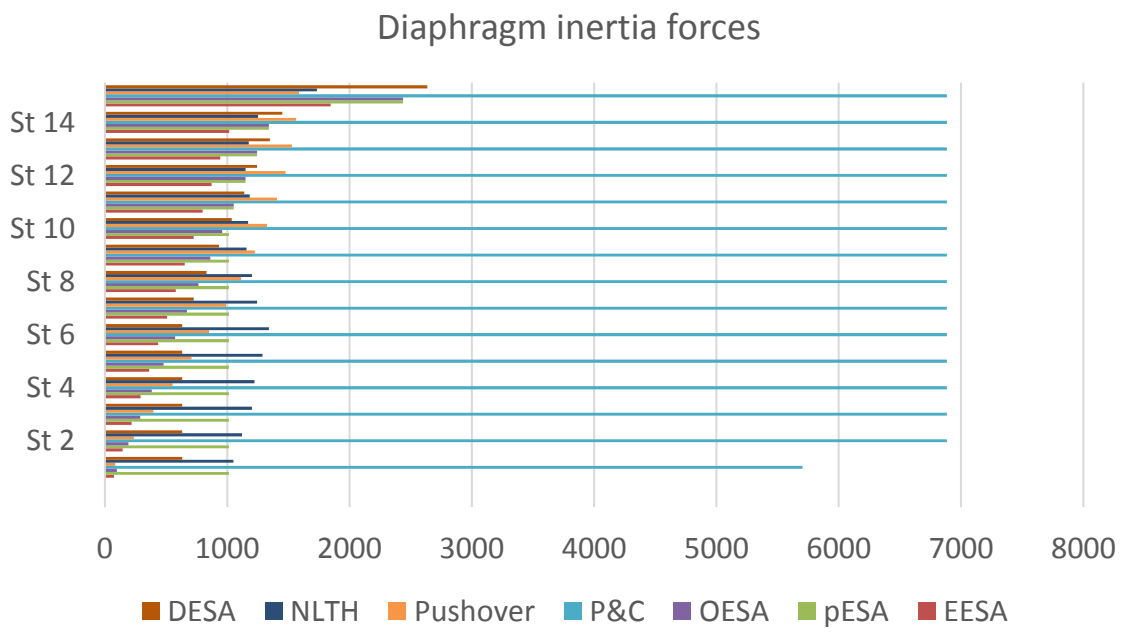

a) Diaphragm inertia forces

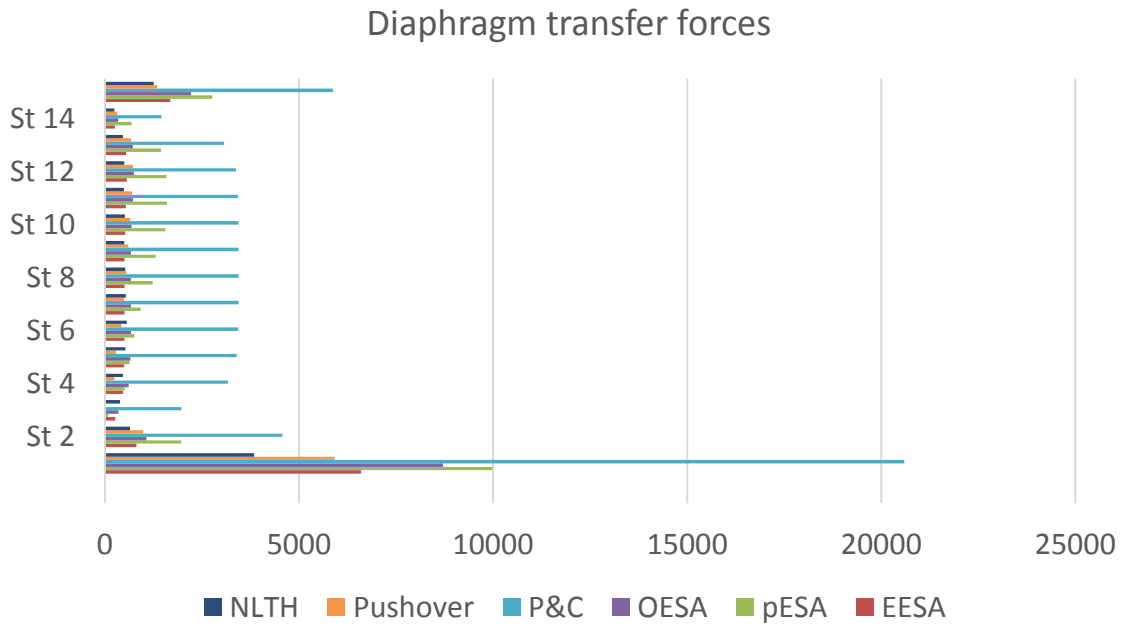

b) Diaphragm transfer forces

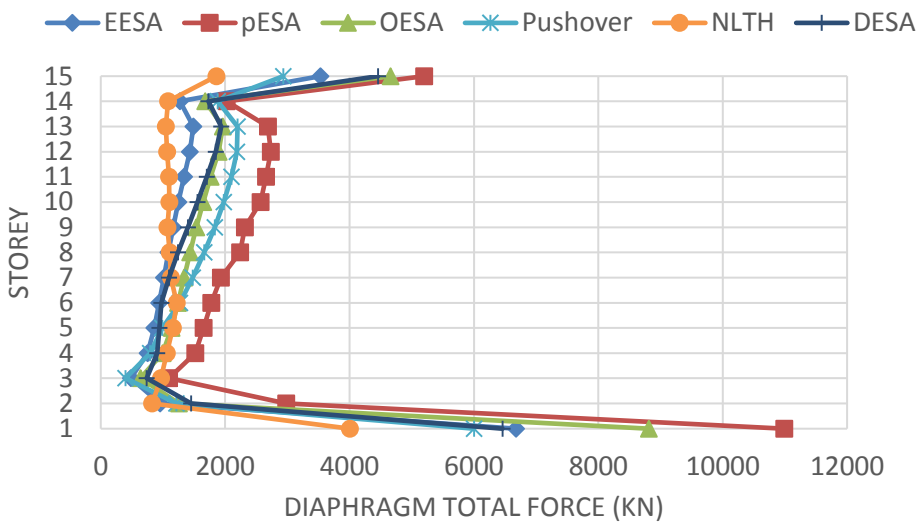

c) Total diaphragm forces

Figure K-11. Diaphragm in-plane forces of model 21

Appendix L: Lateral Force Distribution Between VLFR Systems Considering Diaphragm Flexibility

A simple one-storey structure shown in Figure L-1, is selected to demonstrate the effect of diaphragm in-plane stiffness assumption on distributing lateral forces between VLFR systems. The floor plan and the equivalent simplified model that are used to calculate the force distribution and diaphragm in-plane forces are shown in Figure L-1b and c. In this model the total inertia force, F_a, is imposed uniformly to the floor slab. The lateral forces imposed to the frames 1 and 2, F_{a1} and F_{a2}, are assumed equal, $F_{a1} = F_{a2}$, due to the same tributary area of each VLFR frame.

$$F_a = F_{a1} + F_{a2} \qquad \text{Eq. (L-1)}$$

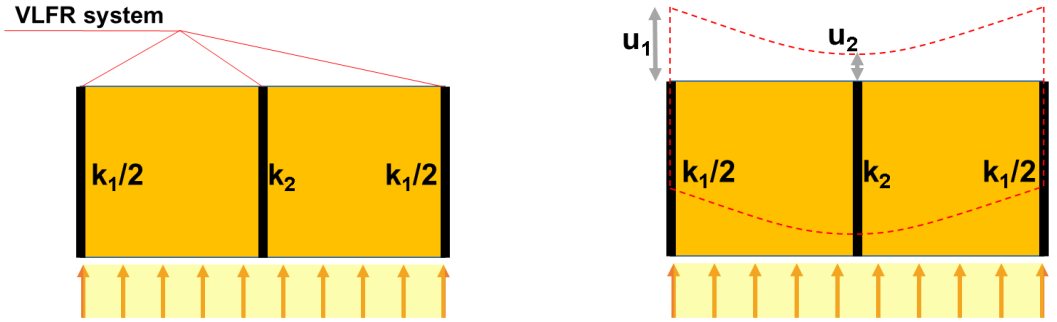

a) Floor plan b) Schematic lateral deformation

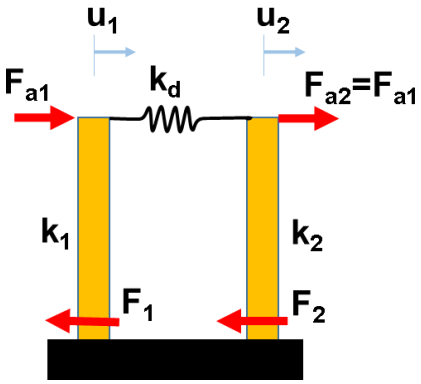

c) Simplified model

Figure L-1. Model considered to demonstrate the effect of diaphragm flexibility on lateral force distribution between VLFR frames

The stiffness matrix of the structure shown in Figure L-1c considering two degrees of freedom, u_1 and u_2, can be written as Eq. (L-2). Where k_1 and k_2 are the frames 1 and 2 stiffnesses respectively and k_d is the diaphragm in-plane stiffness.

$$[K] = \begin{bmatrix} k_1 + k_d & -k_d \\ -k_d & k_2 + k_d \end{bmatrix} \quad \text{Eq. (L-2)}$$

By solving the force equation, $[F] = [K][u]$, lateral displacements of frames 1 and 2, u_1 and u_2, can be obtained considering the effect of diaphragm stiffness, k_d, as:

$$u_1 = \frac{(0.5k_2+k_d)F_a}{k_1k_d+k_1k_2+k_2k_d} \quad \text{Eq. (L-3)}$$

$$u_2 = \frac{(0.5k_1+k_d)F_a}{k_1k_d+k_1k_2+k_2k_d} \quad \text{Eq. (L-4)}$$

Knowing the lateral displacement of each frame, u_{i}, and its stiffness, k_{i}, the base shears F_1 and F_2 of each frame can be obtained as:

$$F_1 = \frac{(0.5k_1k_2+k_1k_d)F_a}{k_1k_d+k_1k_2+k_2k_d} \quad \text{Eq. (L-5)}$$

$$F_2 = \frac{(0.5k_1k_2+k_2k_d)F_a}{k_1k_d+k_1k_2+k_2k_d} \quad \text{Eq. (L-6)}$$

The diaphragm in-plane force can also be calculated by multiplying the diaphragm in-plane stiffness, k_d, by the difference between the lateral deformations of frames 1 and 2 as:

$$F_d = k_d(u_1 - u_2) \quad \text{Eq. (L-7)}$$

$$F_d = k_d\left(\frac{0.5(k_1-k_2)F_a}{k_1k_d+k_1k_2+k_2k_d}\right) \quad \text{Eq. (L-8)}$$

Figure L-2 plots the ratio of frame 1 base shear to the total lateral force, $\frac{F_1}{F_a}$, against the stiffness ratio of frame 1 to frame 2, $\frac{k_1}{k_2}$, for different frame 1 to diaphragm stiffness ratios, $\frac{k_1}{k_d}$. This plot shows where the VLFR system stiffness is much larger than the diaphragm in-plane stiffness, $\frac{k_1}{k_d} = \infty$, lateral force is distributed based on the tributary area of each frame.

However, for rigid diaphragms, $\frac{k_1}{k_d} = 0$, the lateral force is distributed based on the relative stiffness of frames. It can be seen from this Figure that the base shear of frame 1 increases by up to 60% by changing $\frac{k_1}{k_d}$ from 1 to 10 where $\frac{k_1}{k_2}$ is 0.1.

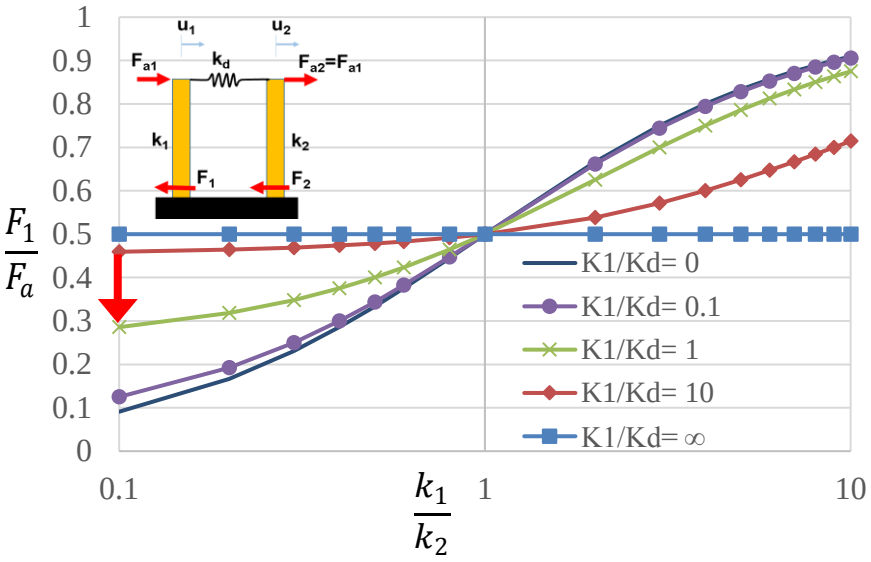

Figure L-2. Frame 1 base shear

Figure L-3 plots the ratio of diaphragm in-plane force to the total lateral force, $\frac{F_d}{F_a}$, against frame 1 to frame 2 stiffness ratio, $\frac{k_1}{k_2}$, for different frame 1 to diaphragm stiffness ratios, $\frac{k_1}{k_d}$. This Figure shows the diaphragm in-plane force is maximum where the diaphragm in-plane stiffness is much larger than VLFR systems, $\frac{k_1}{k_d} = 0$. The diaphragm in-plane force decreases with decreasing the diaphragm in-plane stiffness. For example, diaphragm in-plane force increases up to 185% by increasing the diaphragm stiffness ratio, $\frac{k_1}{k_d}$, from 10 to 1 where $\frac{k_1}{k_2}$ is 3.

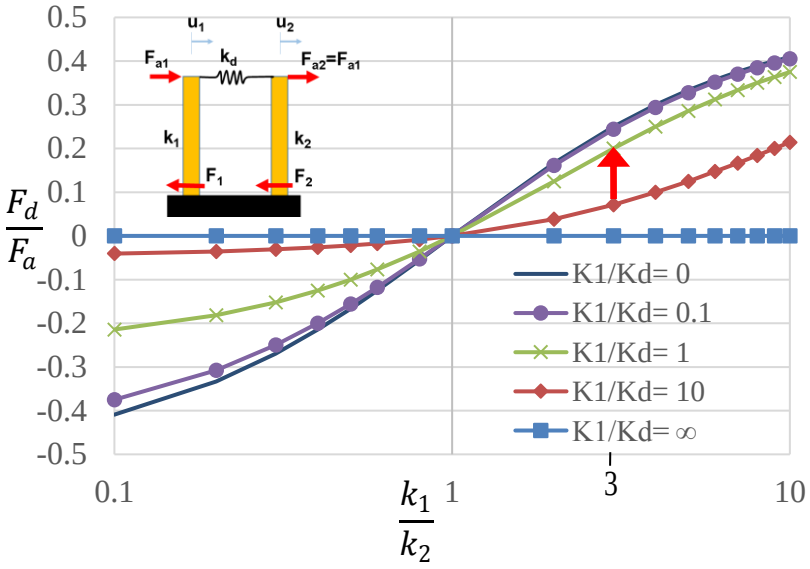

Figure L-3. Diaphragm in-plane force

Figure L-2 and Figure L-3 indicate the importance of using reasonable diaphragm in-plane stiffness in the analysis to obtain likely lateral force distribution between VLFR systems and diaphragm in-plane demands.

Appendix M: Base Model Diaphragm Design

M.1 Structure details

M.1.1 Geometry and VLFR system

Figure M-1 shows the base model floor plan. Storey height is considered 3.5m. The structure has two bays in both X and Y directions with 8m and 6m long spans respectively. The lateral force resisting system of the structure in the X-direction is assumed moment resisting frame, MRF. In the Y-direction, the lateral force resisting system is assumed a combination of moment resisting frames (exterior frames) and braced frame (interior frame). Torsion is restrained in this model.

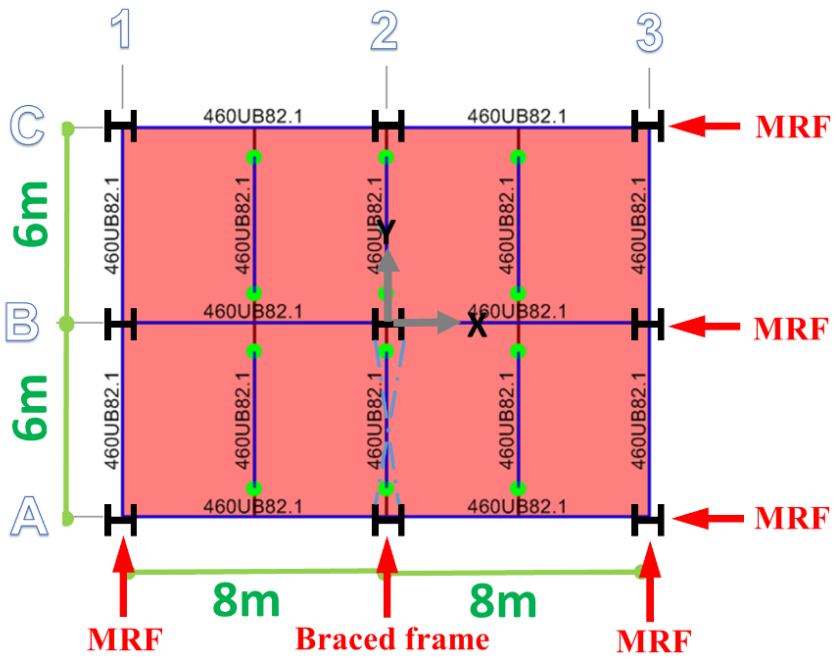

Figure M-1.Base model floor plan and lateral force resisting systems

M.1.2 Material properties

The concrete compressive strength is considered 30MPa with an elastic modulus of 25GPa in design. The steel material strength for structural members such as beams and columns is considered 340MPa. The slab reinforcement strength is considered 460MPa.

M.1.3 Loading

- **Gravity loading**

Gravity loads used in the structural analyses are based on the values given in Table M-1. The reduced gravity load combination of $G + 0.3Q$ is considered to calculate the structure weight for lateral loading calculations. This load combination was also used to assign the storey mass to the models in NLTH analysis.

Table M-1. Gravity loads assumed for analysis

Live load (Q)	3 kPa	Imposed action
Dead load (G)	1 kPa	Ceiling/Services and finishes
	1 kPa	Partitions
	3 kPa	Structural elements and floor slab self-weight

- **Lateral loading**

The earthquake lateral loads are obtained using NZS1170.5 (2004) loading standard considering ductility $\mu = 1$. This ductility is assumed because the focus of this study is to investigate the diaphragm performance considering the WSP beam-column connection and shear stud flexibilities. Also it helps to reduce the numerical modelling complexity.

The lateral loading parameters assumed in this study are summarised below:

- Subsoil type → D
- Near Fault Factor → N(T,D) = 1
- Building Importance Level → IL2
- Hazard Factor (Wellington, New Zealand) → Z =0.4
- Performance Factor → $Sp_{(ULS)}$=0.7
- Risk Factor ULS (1/500 years) → $Ru_{(ULS)}$=1.0
- Fundamental period of structure → T(1)=0.15s

Based on the above assumptions the horizontal design action coefficient in the Y-direction, $C_{dy}(T_1)$, is calculated $C_{dy}(T_1) = 0.84$. The effective structure mass considering

the reduced gravity load combination, $G + 0.3Q$, is equal to $M_1 = 115ton$. Therefore the total base shear is 951kN for the base model.

M.2 Structure design steps

M.2.1 Structural elements design

Structural elements include beams, columns, and braces are designed according to NZS3404 (2007) standard. In this study, all the steel beams are considered to have the same size. This can simplify the numerical models and also in the models that the composite beams are modelled by offsetting the slab from the steel beam, it helps to use the same offset value for all the beams in each floor. Note that the structural members were designed for the envelope of forces obtained from structural analysis using elastic and cracked diaphragm stiffness as described in Section 8.2.

M.2.2 Floor-slab design for gravity loads

The floor slabs are designed using ComFlor Steel Composite Metal Deck Design software under gravity loading. The direction of composite slab ribs is assumed to be parallel to the X-direction. Considering the secondary beams at the mid-span of 8-meter bays, the maximum unsupported span is 4m.

The gravity loads used for the design are in accordance with Table M-1. Note that the self-weight of the floor slab (G) was calculated by the software using the slab thickness and steel decking details. Figure M-2 and Table M-2 show the assumptions and parameters used in design.

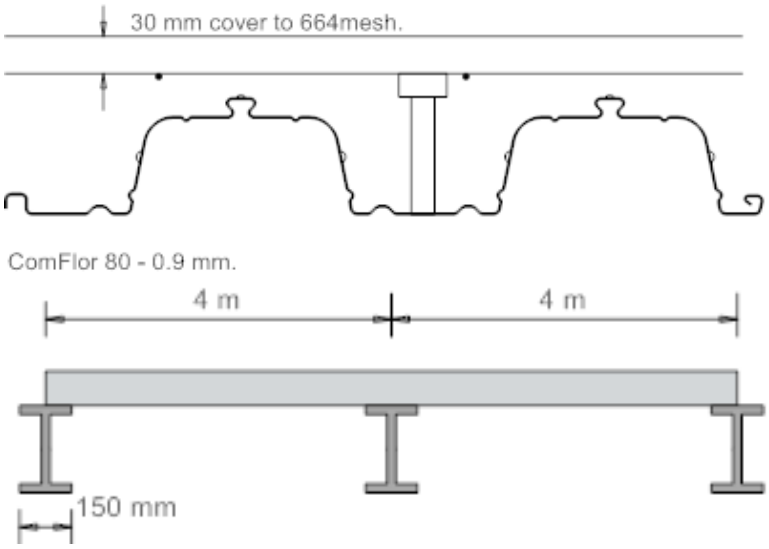

Figure M-2. Composite slab details

Table M-2. Composite slab design assumptions

FLOOR PLAN DATA : (unpropped composite construction with ComFlor 80/0.9/G550 decking)	Beam centres - equal 4.00 m Span type DOUBLE Beam or wall width 150 mm Propping NONE
PROFILE DATA : (ComFlor 80/0.9/G550 decking)	Depth 80 mm Pitch of deck ribs 300 mm Trough width 120 mm Crest width 150.0 mm Nominal sheet thickness 0.90 mm Design sheet thickness 0.86 mm Deck weight 0.11 kN/m^2 Yield strength 550 N/mm^2
CONCRETE SLAB : [Normal Weight Concrete ; Mesh : 664/188]	Overall slab depth 145 mm Concrete characteristic strength 30 N/mm^2 Concrete wet density 2400 kg/m^3
Bar reinforcement	NONE
Mesh reinforcement	Mesh 664/188 Yield strength 460 N/mm^2 Cover to Mesh 30 mm Mesh Layers Single Account for End Anchorage Diameter of Shear Connectors 19 mm

M.3 Diaphragm in-plane design

Figure M-3 shows the diaphragm design flowchart that is used here to design the diaphragm of the base model. Each design step is described in the following in detail.

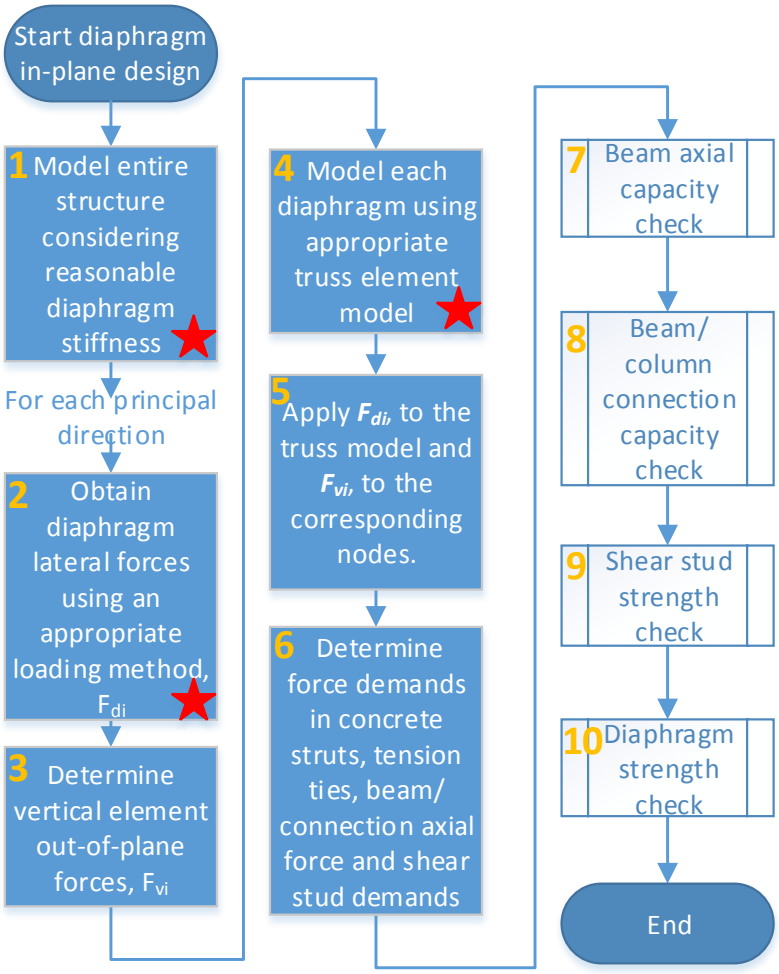

Figure M-3. Diaphragm in-plane design flowchart

M.3.1 Step 1, Structure 3D modelling

The structure model in this step is the same as the model used for structural elements design. In this model appropriate diaphragm stiffness should be considered. According to the diaphragm design approaches described in Section 8.2, structural analyses are performed two times considering elastic and cracked diaphragm in-plane stiffness. The diaphragm in-plane stiffness reduction factor is considered 0.1 in this study.

M.3.2 Step 2, Diaphragm lateral forces

Here, diaphragm lateral forces are obtained using the DESA method described in Chapter 7. According to the DESA method:

- $C_{dy}(T_1) = 0.84$ considering ductility factor $\mu = 1$
- Lateral force per unit area of the floor slab is $4.95kPa$

M.3.3 Step 3, Diaphragm in-plane forces from VLFR elements

Diaphragm in-plane forces from VLFR elements can be obtained by calculating the difference between the shear forces of the structural elements above and below the diaphragm. These forces should be in equilibrium with the imposed lateral forces, DESA, in each level. Figure M-4 shows the diaphragm imposed forces from VLFR elements for elastic and cracked diaphragms.

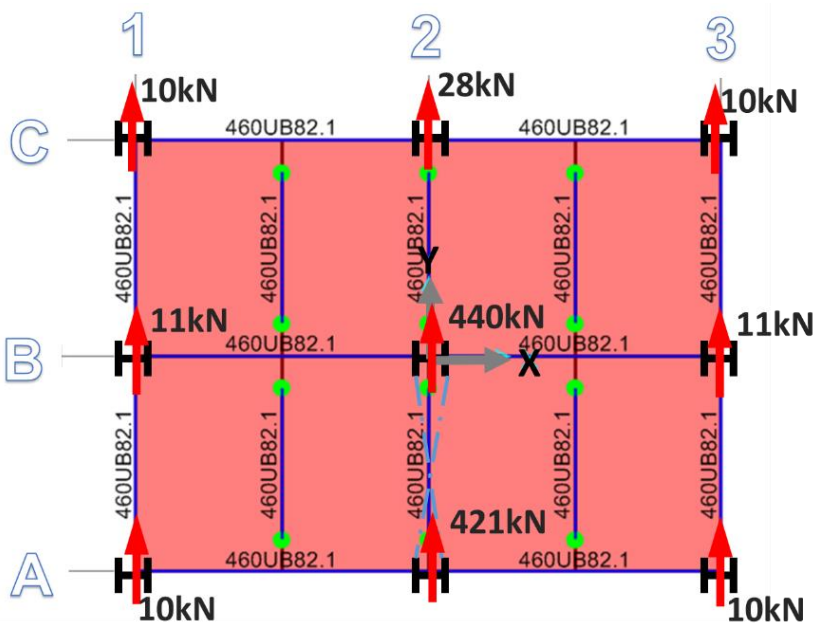

a) Elastic diaphragm

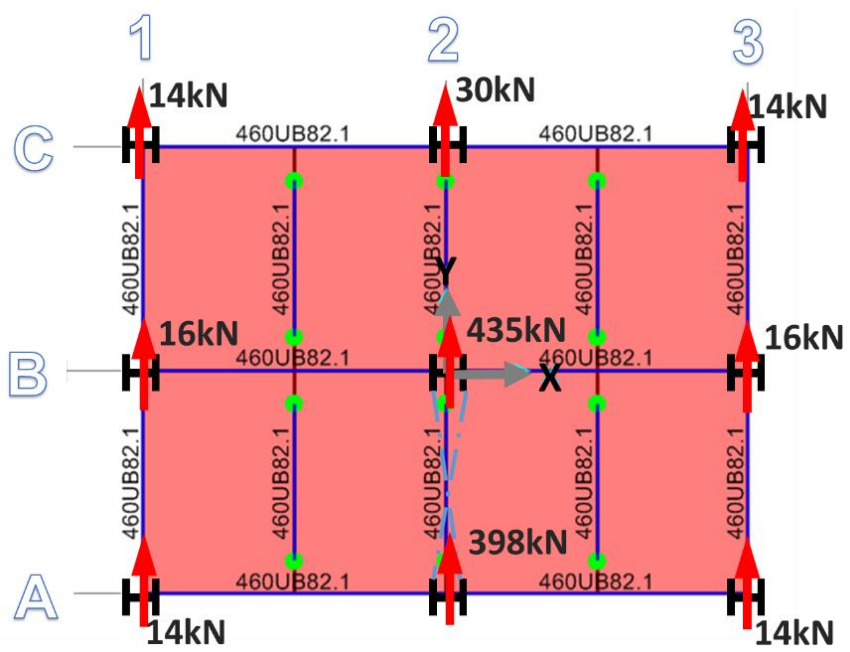

a) Cracked diaphragm

Figure M-4. Diaphragm imposed forces from VLFR elements

M.3.4 Step 4, Diaphragm truss modelling

According to the findings of Chapter 3, Truss Model 2 and Truss Model 3 are used to model and analyse the diaphragm of the base model considering elastic and cracked in-plane behaviour respectively. Table M-3 shows the cross-section properties of the truss members. To model the diaphragm using truss elements, 2×2m mesh size is considered in this study.

Table M-3. Cross-section properties of Truss models 2 and 3

	Diagonal member		Orthogonal member	
Model description	Compression	Tension	Compression	Tension
Truss Model 2 (elastic)	at	0	$0.585at$	at
	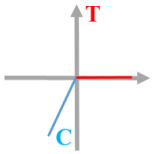		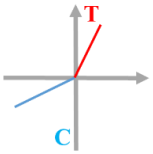	
Truss Model 3 (cracked)	$0.725at$	0	$0.97at$	A_s
	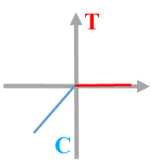		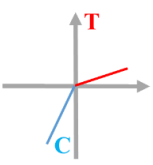	

As can be seen from Figure M-5, the concrete thickness above the highest point of the steel decking is equal to 50mm. However, the effective concrete thickness that may be used for calculating the cross-section properties of truss element is equal to 65mm in this case. This is because small portions on top of the flat surface of the steel decking may not affect the diaphragm in-plane stiffness significantly. Meanwhile, to calculate the diaphragm strength (diagonal strut strength and buckling) 50mm concrete topping is considered.

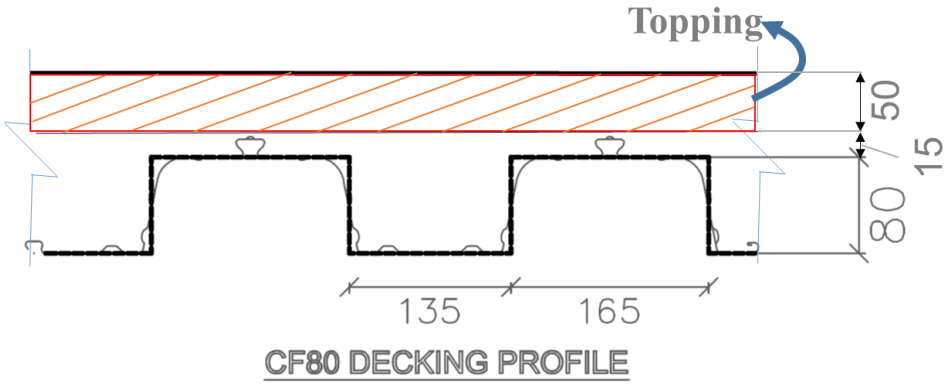

Figure M-5. Composite slab cross-section

❖ **Truss Model 2**

➢ Diagonal truss element properties, $a = 2000mm, t = 65mm, L = 1414mm$

$$A_D = at$$

$$= 130000mm^2$$

$$Axial\ stiffness\ (A_D) = {EA}/{L_D}$$

$$= 2298kN/mm$$

➢ Orthogonal element properties, $a = 2000mm, t = 65mm, L = 2000mm$

$$A_{OT} = at$$

$$= 130000mm^2$$

$$Axial\ stiffness\ (A_{OT}) = {EA}/{L_O}$$

$$= 1625kN/mm$$

$A_{OC} = 0.585at$

$$= 76050mm^2$$

$Axial\ stiffness\ (A_{OC}) = {EA}/{L_O}$

$$= 950kN/mm$$

❖ **Truss Model 3**

➢ Diagonal truss element properties, $a = 2000mm, t = 65mm, L = 1414mm$

$A_D = 0.725at$

$$= 94250mm^2$$

$Axial\ stiffness\ (A_D) = {EA}/{L_D}$

$$= 1667kN/mm$$

➢ Orthogonal element properties, $a = 2000mm, t = 65mm, L = 2000mm$ and $188mm^2/m$ reinforcement

$A_{OT} = A_s$

$$= 376mm^2$$

$Axial\ stiffness\ (A_{OT}) = {EA}/{L_O}$

$$= 37.6kN/mm$$

$A_{OC} = 0.97at$

$$= 126100mm^2$$

$Axial\ stiffness\ (A_{OC}) = {EA}/{L_O}$

$$= 1576kN/mm$$

M.3.5 Step 5, Applying diaphragm in-plane forces to the truss model

The diaphragm lateral forces obtained from the DESA method are distributed based on the tributary area of each node as shown in Figure M-6. VLFR system reactions are also applied at the corresponding nodes in the truss model in this Figure.

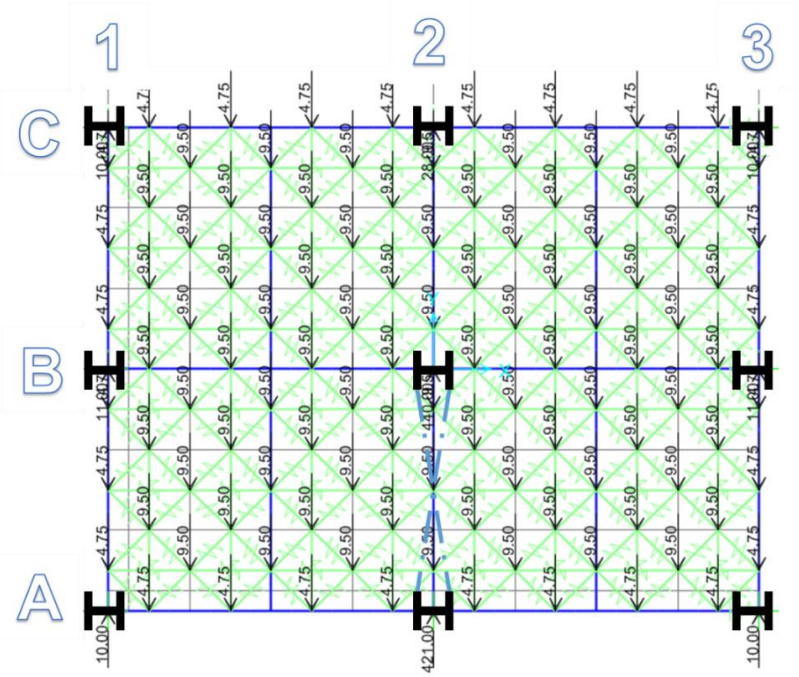

a) Elastic diaphragm

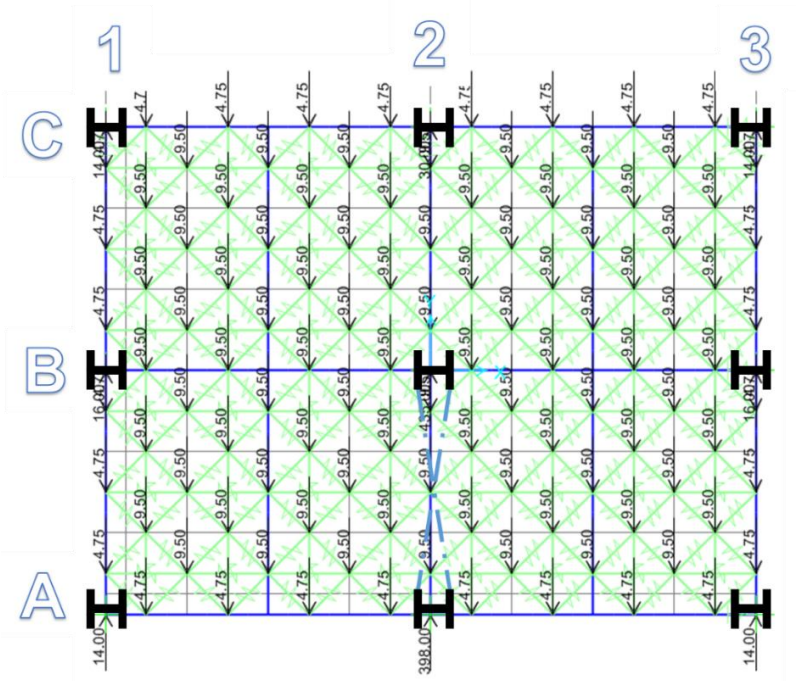

b) Cracked diaphragm

Figure M-6. Inertia forces and VLFR system forces imposed on the diaphragm in the Y-direction

M.3.6 Step 6, Obtaining diaphragm internal forces and load path to VLFR system

Figure M-7 shows the axial force diagram of truss elements for the elastic diaphragm.

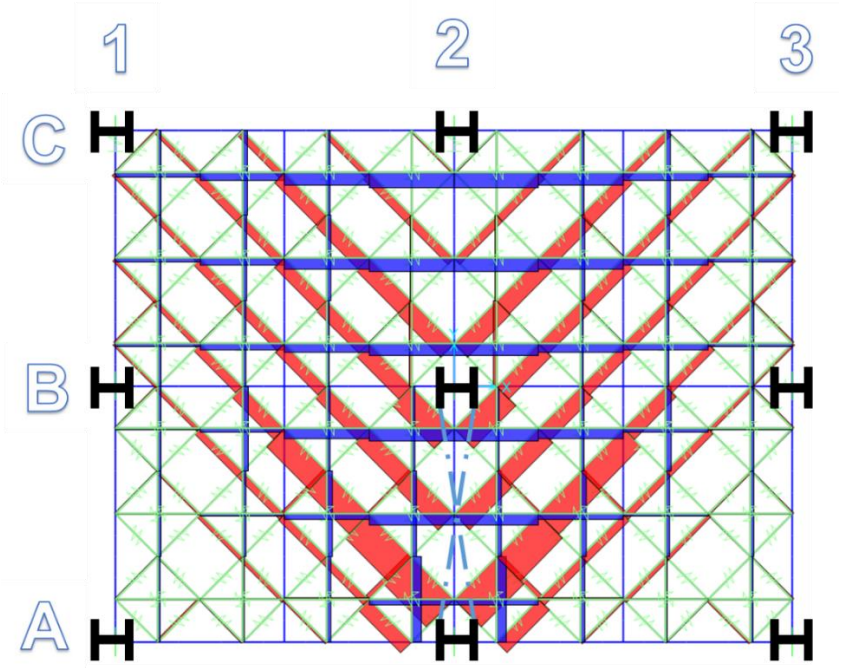

a) Lateral loading in the negative Y-direction

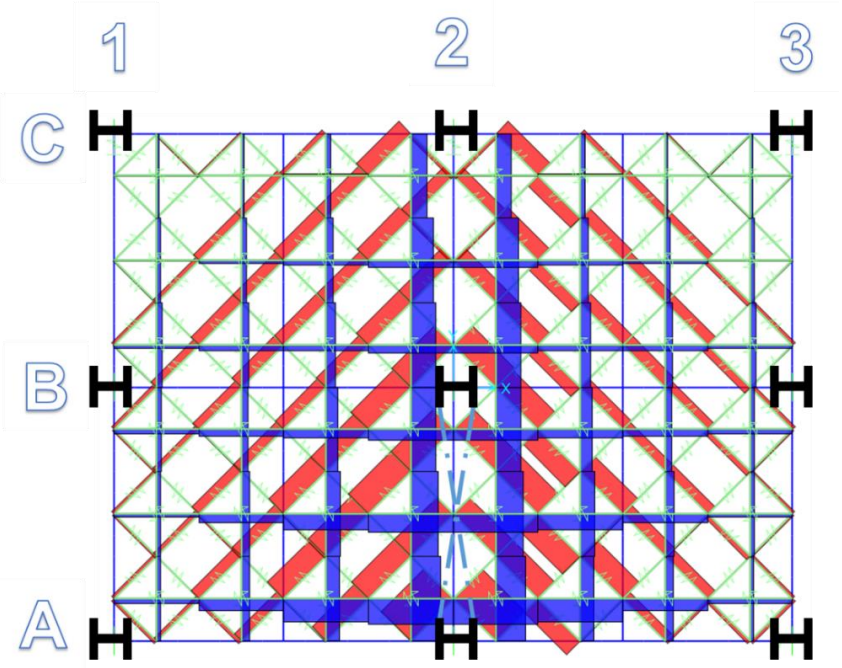

b) Lateral loading in the positive Y-direction

Figure M-7. Axial force diagram of truss elements

Maximum compression strut axial forces and tension tie axial forces of both elastic and cracked diaphragm models are presented in Table M-4.

Table M-4. Maximum strut and tie forces obtained from both elastic and cracked diaphragm analysis

	Maximum Strut compression force (kN)	**Maximum Tie tension force (kN)**
Elastic diaphragm model	-186	117
Cracked diaphragm model	-166	26

Figure M-8 shows the beam axial forces obtained from elastic and cracked diaphragm analysis. Maximum compression and tension forces at the beam-ends (beam-column connections) and the beam mid-span are presented in Table M-5.

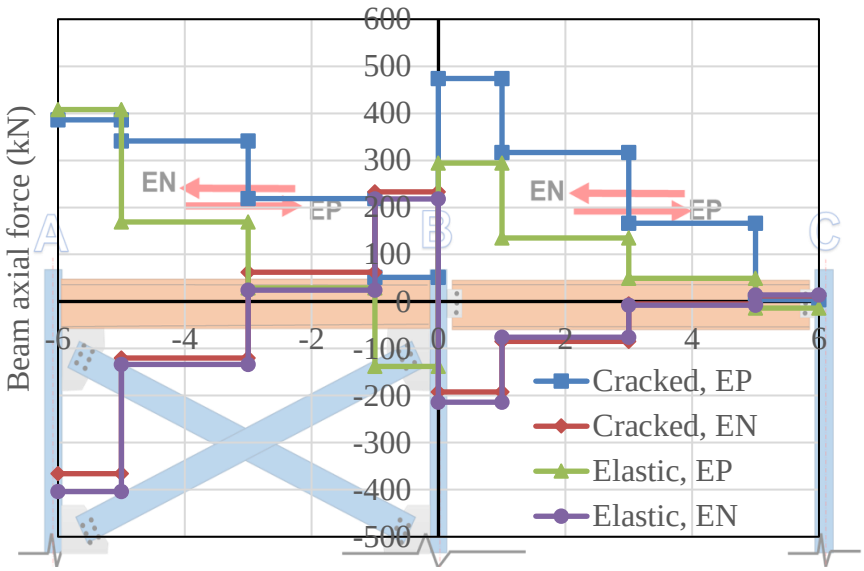

Figure M-8. Beam axial force diagram

Table M-5. Maximum beam axial demands at the beam-column connections and beam mid-span

Axis		**Left beam, braced bay (kN)**			**Right beam (kN)**		
		A	Mid-span	B	B	Mid-span	C
Elastic diaphragm model	EP	+408	+169	+218	+294	+135	+14
	EN	-404	-134	-138	-214	-76	-14
Cracked diaphragm model	EP	+386	+341	+233	+474	+317	+12
	EN	-386	-120	0	-192	-85	0

Shear stud demands can be calculated using the difference of the beam axial forces at the beam-ends. The maximum shear stud demands obtained from analyses are presented in Table M-6.

Table M-6. Maximum shear stud demands

	Left beam, braced bay (kN)	**Right beam (kN)**
Elastic diaphragm model	622	308
Cracked diaphragm model	599	470

M.3.7 Step 7, Beam design for axial forces

Beam axial forces should be considered in beam design. This may be performed by considering two critical sections along the beam length:

1. At the maximum axial force which is usually at the beam-ends and
2. At the maximum bending moment location to consider bending moment-axial force interaction.

The beam axial force diagrams plotted in Figure M-8 show that the maximum beam axial force at the beam-mid point (maximum bending moment) is about 317kN. The axial strength of the steel beam section considering 460UB67.1 is 2917kN. The maximum beam axial force is about 10% of the nominal section strength of the steel beam and axial force-bending moment interaction can be ignored.

Table M-7 presents the beam-column connection forces considering both gapped and no gap conditions. Here it is assumed the slab bearing force is transferred to the beam-column connection on the tension side.

Table M-7. Maximum beam axial forces at the beam-column connections considering gapped and no gap conditions

	Braced bay (kN)		**Pinned beam (kN)**	
Axis	A	B	B	C
Elastic diaphragm model	+408G, +1084NG	+218G, +894NG	+294G, +970NG	+14G, +690NG
Cracked diaphragm model	+386G, +1062NG	+233G, +909NG	+474G, +1150NG	+12G, +688NG
G→Gapped, NG→No Gap				

Cowie et al. (2014) recommended to use a bolted top flange connection that looks the same as the top flange connection in a Sliding Hinge Joint to carry axial forces in conjunction

with the flexible end plate (FE) or web side plate (WSP) connection to carry the vertical shear as shown in Figure M-9. The net effective tensile area was considered to be the top flange and half the beam web. The connection also has to be detailed to develop inelastic rotation without bolt or weld failure and so will handle the connection rotation due to the top flange pin. Also, the stiffener must be welded to the column to develop the full tension capacity of the top plate and transfer this into the column web.

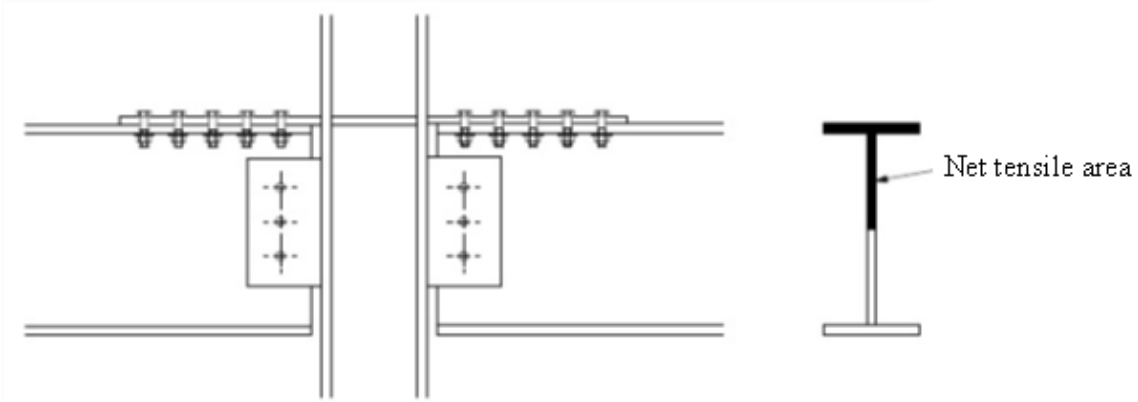

Figure M-9. Top plate connection to transfer collector beam axial forces, (Cowie et al., 2014)

Considering Cowie et al. (2014) recommendations, the beam tensile strength using the net tensile area is $\frac{8580}{2} \times 340 = 1458kN$, which is larger than the maximum of beam tensile forces, 1150kN, in Table M-8.

M.3.8 Step 8, Beam-column connection design

Figure M-10 shows a schematic view of the beam in the frame 2 (middle frame) and the applied gravity loads. The connection shear force demand using 1.2G+1.5Q load combination is 126kN.

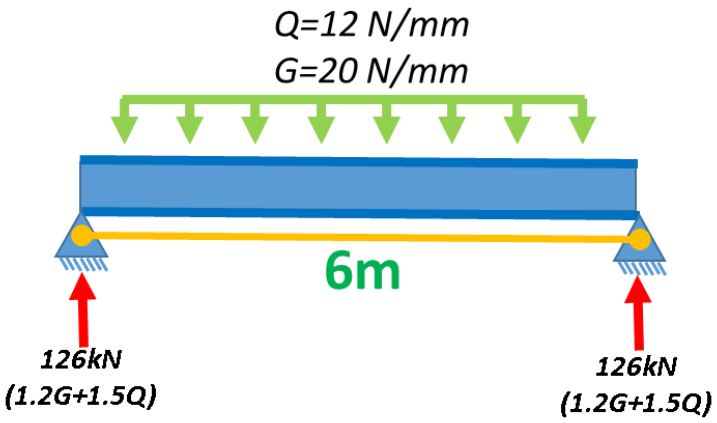

Figure M-10. Schematic view of pinned beam in frame 2 (middle frame)

The beam-column connection design to carry gravity loads was performed according to SCNZ report 14.1 (2007). Figure M-11 shows a snapshot of the spreadsheet developed to design these connections.

Units:
All measurments in mm
All forces in KN

Beam Properties:

w	190	mm
d	454	mm
t_f	12.7	mm
t_w/t_{wb}	8.50	mm
f_{yb}	0.34	kN/mm^2
f_{ub}	0.48	kN/mm^2

Bolt Properties:

n_p	4	no. bolts
l_{bolt}	55	mm
d_f	20	mm
ϕV_{fx}	129	kN
ϕV_{fn}	92.6	kN

Plate Properties:

b_i	100	mm
d_i	300	mm
t_i	6	mm
f_{yi}	0.32	kN/mm^2
f_{ui}	0.44	kN/mm^2
ϕ_s	0.9	

Connection Properties:

t_{ww}	8	mm
s_p	75	mm
s_{g1}	60	mm
a	60	mm
a_{e1}	40	mm

f_{uw} 0.48 KN/mm2 weld tensile strength

Beam span	6.00	m
Tributary area	4.00	m
G	5.00	kPa
Qu	3.00	kPa

Calculated Values:

a_c	132
a_{eyi}	38
a_{eyb}	64
a_{e3}	64
a_{e6}	37.5
a_{e7}	40
A_{ni}	1272
A_{gt}	340.0
A_{nt}	246.5
d_h	22
e	60
Z_b	2.89
Z_e	1.04
M_{drift}	21384.00
E_{drift}	4.71
V_{drift}	100.71
V*	126

Governing Criteria:

OK	General condition
OK	Beam/column seismic shear
OK	Beam/column seismic moment
OK	Beam/column seismic end gap
OK	Weld
OK	Plate/bolt thickness
OK	Plate depth
OK	Edge distances: Manual flame cut or crop
OK	Beam web edge distance
OK	end gap=>20mm

Design Actions:

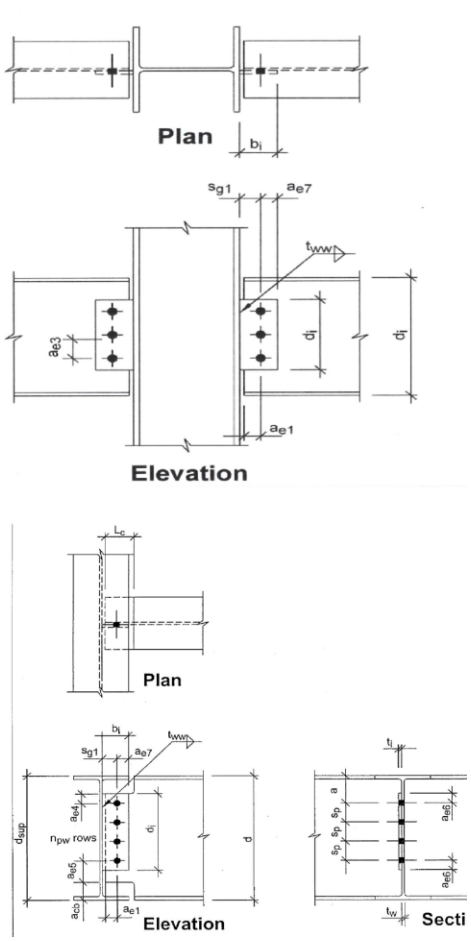

Connection Strength Limits:

ϕV_{con} 259.20 $[\phi V_b; \phi V_i; \phi V_{wb}]_{min}$

Bolt Group Strength Limits:

ϕV_b	372.24	
ϕM_b	32250.00	21384
ϕV_f	129.00	

Web Plate Strength Limits:

ϕV_i	259.20	$[\phi V_{bi}; \phi V_{tti}; \phi V_{lti}; \phi V_{gfi}; \phi V_{nfi}; \phi V_{gsi}; \phi V_{nsi}]_{min}$
ϕV_{bi}	438.79	
ϕV_{tti}	356.4	
ϕV_{lit}	396	
ϕV_{gfi}	648.00	
ϕV_{nfi}	535.19	
ϕV_{gsi}	259.2	
ϕV_{nsi}	302.23	
N_{gti}	518.4	
ss shear strength	345.6	0.3646

Section Web Strength Limits:

ϕV_{wb}	612.00	$[\phi V_{bw}; \phi V_{ttw}; \phi V_{ltw}; \phi V_{gsw}]_{min}$
ϕV_{bw}	678.13	
ϕV_{ttw}	940.03	
ϕV_{ltw}	612.00	
ϕV_{wb}	708.51	

Weld Strength Limits:

ϕN_{ww} 782.00

Pure tensile Strength:

Tensile strength 361.15 kN

Bolt Strength	516.00
Web block shear	708.70
Bolt tearout	558.14
Bolt bearing	940.03
Plate yielding	518.40
Platefracture net	428.16
Bolt tearout	361.15
Bolt bearing	608.26

Figure M-11. Spreadsheet developed according to SCNZ report 14.1 (2007)

Figure M-12 shows details of the connection designed to carry gravity loads. Connection shear capacity was calculated **259.2kN** and connection tensile capacity was calculated **361.15kN.**

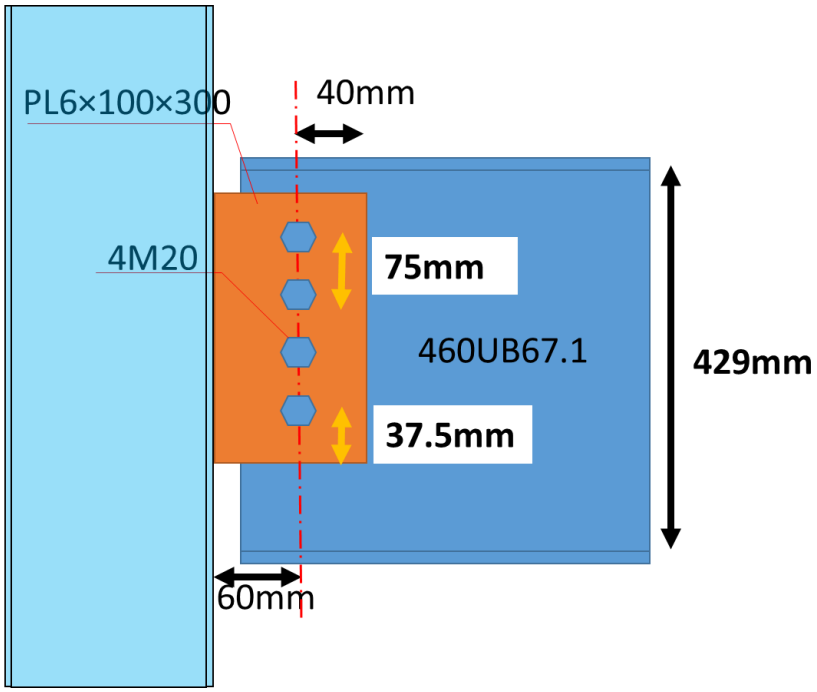

Figure M-12. Connection details

Applied shear force to the connection considering the reduced gravity load combination, 0.3Q+G, is **70.8kN**. This value should be used to calculate the axial compression capacity of the WSP connection considering axial-shear force interaction.

M.3.8.1WSP axial compression strength calculation

According to the proposed method in Chapter 4:

- **Case two, beam top flange restrained laterally**

Here it is assumed that the top flange is restrained laterally due to the presence of shear studs.

Checking the cleat plate axial strength:

1) Obtain h_{eff} according to Clause 6.2.4 of NZS 3404 (2007)

$$h_{eff} = min\begin{bmatrix} 16t_w\sqrt{\frac{250}{f_{yw}}} \\ h_w \end{bmatrix}$$

$$f_{yw} = 340MPa$$

$$h_{eff} = 116.7mm$$

- Note: if the beam top flange is retrained and the beam is coped, the h_{eff} should be modified using:

$$\frac{h_{ec}}{h_e} = 1 - 0.5\frac{L_c}{d}$$

2) Calculate h_1 and h_2

$$h_1 = h_{eff} + t_f - a + a_{e6}$$

$$h_1 = 116.7 + 12.7 - 60 + 37.5$$

$$= 106mm$$

$$h_2 = h_c - h_1$$

$$h_2 = 300 - 106$$

$$= 194mm$$

Note: a_{e6} is the vertical edge distance at top of the cleat plate

3) Calculate the cleat axial capacity at zone 1 (P_{c1}).

$$P_{c1} = h_1 t_c f_{yc}$$

$$= 205kN$$

4) Calculate P_2,

4.1) Obtain the effective length of the beam web (L_w)

$$\begin{cases} L_w = \frac{h_w}{5} + L_{cope} - a_{e1} \ \rightarrow for\ coped\ beam \\ L_w = \frac{h_w}{5} \ \rightarrow for\ un-coped\ beam \end{cases}$$

$$L_w = 85.8mm$$

4.2) Obtain contributing height of the beam web, $h_{we} = min[h_w, 1.5h_2]$

$$h_{we} = 289mm$$

4.3) Calculate the effective length factor for the cleat plate

$$\begin{cases} k_c = 1.05\frac{L_w}{L_c}\sqrt{\frac{EI_{c2}}{EI_w}} + 1.2 \;\; \rightarrow for \; \frac{L_w}{L_c}\sqrt{\frac{EI_{c2}}{EI_w}} < 2 \\ k_c = 0.9\frac{L_w}{L_c}\sqrt{\frac{EI_{c2}}{EI_w}} + 1.5 \;\; \rightarrow for \; \frac{L_w}{L_c}\sqrt{\frac{EI_{c2}}{EI_w}} \geq 2 \end{cases}$$

$$k_c = 1.92$$

- Note: I_w is calculated based on effective beam web height (h_{we}) and I_{c2} is calculated using h_2

4.4) Calculate the elastic buckling force for the cleat plate, $P_{cr} = \frac{\pi^2 EI_{c2}}{(k_c L_c)^2}$

$$P_{cr} = 512\text{kN}$$

4.5) Obtain P_u for the cleat plate based on Section 6 of NZS 3404 (2007) considering $\alpha_b = 0.5$

$$P_u = 238\text{kN}$$

4.6) Obtain M_{u3} (plastic moment) of the cleat plate about the weak axis (using h_2)

$$M_{u3} = 0.55kN.m$$

4.7) Calculate moment participation factor, $\alpha = \left(\frac{I_{c2}/L_c}{I_{c2}/L_c + I_w/L_w}\right)$

$$\alpha = 0.25$$

4.8) Calculate e (axial load eccentricity) using $e = \frac{t_c + t_w}{2}$

$$e = 7.25mm$$

4.9) Find M_{u2} (plastic moment) of the cleat plate about the strong axis

- Note: the plastic moment of cleat plate about the strong axis should be modified using shear-moment interaction relationship

$$\begin{cases} \frac{V}{V_v} + \frac{1.6M_{u2}}{\emptyset M_{s2}} \leq 2.2 \quad for \;\; V \geq 0.6V_v \\ M_{u2} = \emptyset M_{s2} \quad for \;\; V < 0.6V_v \end{cases}$$

$$for \;\; V < 0.6V_v \rightarrow \quad M_{u2} = 43kN.m$$

4.10) Calculate the cleat plate capacity at zone 2 (P_{c2})

$$\frac{P_{c2}}{P_u} + \frac{\alpha \times P_{c2} \times e}{M_{u3}(1-P/P_{cr})} + \frac{M_2}{M_{u2}} \leq 1$$

$$P_{c2} = 108kN$$

5) Calculate total cleat capacity

$$P_c = P_{c1} + P_{c2}$$

$$P_c = 313kN$$

M.3.8.2 Check the beam web axial strength

1) Calculate beam web strength at zone 1 (P_{w1})

$$P_{w1} = (h_{eff} - h_2)t_w f_{yw}$$

$$P_{w1} = 337kN$$

The process of calculating P_{w2} is similar to the cleat plate axial strength calculation, only the effective length factor and moment participation factor are different as:

$$k_w = k_c \frac{L_c}{L_w} \sqrt{\frac{EI_w}{EI_{c2}}}$$

$$\alpha = \left(\frac{{}^{I_w}/_{L_w}}{{}^{I_{c2}}/_{L_c} + {}^{I_w}/_{L_w}} \right)$$

$$\frac{P_{w2}}{P_u} + \frac{\alpha \times P_{w2} \times e}{M_{u3}(1-P/P_{cr})} + \frac{M_2}{M_{u2}} \leq 1$$

$$P_w = P_{w1} + P_{w2}$$

$$P_{w2} = 135kN$$

$$P_w = 472kN$$

Nominal compression strength of the WSP connection is equal to the minimum of $\{P_w, P_c\}$

- It is suggested that the calculated compression capacity is multiplied by a strength reduction factor of $\phi = 0.75$ to account for packing effects.

$$WSP\ compression\ strength\ = 0.75 \times minimum\ of\ \{472, 313\}$$

$$WSP\ compression\ strength\ = 234kN$$

Table M-5 presented the beam-end forces for gapped and no gap conditions. The WSP axial tension and compression strengths are equal to 361kN and 234kN respectively. Therefore the steel beams on axis B-C need the top-plate detail (Cowie et al. 2014) shown in Figure M-9.

The maximum tensile force demand on the beam-column connection was 1150kN (Beam on axis B-C). Here, 500×200×20mm Grade 350 steel plate is considered to transfer the beam axial forces to the columns.

$$Top\ plate\ strength = 20 \times 200 \times 340MPa = 1224kN$$

Figure M-13 shows the details of the top plate connection.

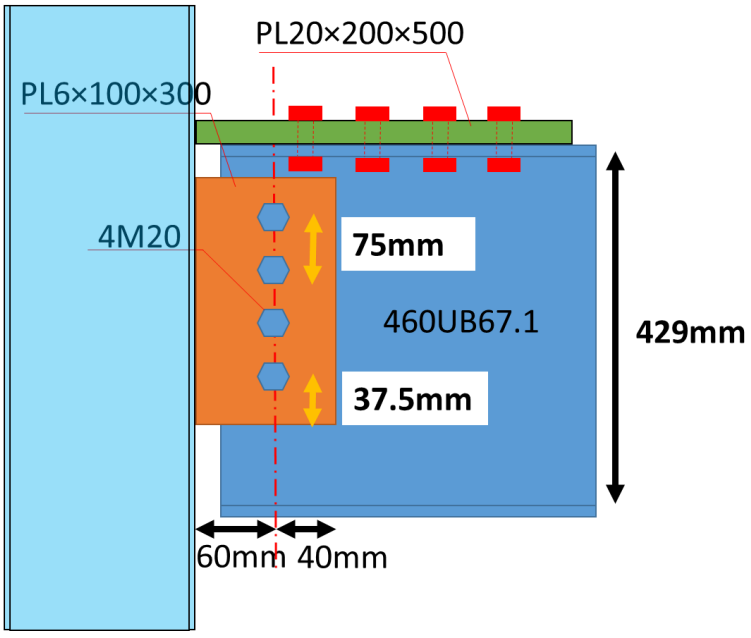

Figure M-13. Top plate connection detail

Note that this connection requires further research and development to investigate the axial force behaviour, possible failure modes and the amount of bending resistance that the top plate may add to the connection.

M.3.9 Step 9, Shear studs design

Shear stud demand on beams of the frame 2 can be obtained using the beam axial force diagrams provided in Figure M-5. The magnitude of shear stud demands was shown in Table M-6 for the gapped condition.

The slab bearing forces should be considered for shear stud design as well as beam axial and beam-column connection design where the gap is not provided around the column. The maximum bearing force may be calculated using Clause 12.10.2.4 of NZS3404 (2007):

$$N_{slab} = min\left\{1.3t_{ef}b_{sef}(f_c' + f_{cos}');\ \sum\left(A_g F_y\right)_i\right\}$$

$$N_{slab} = min\{1.3 \times 65mm \times 200mm \times (30 + 10)MPa;\ \sum\left(A_g F_y\right)_i\}$$

The bearing force depends on the slab area in contact with the column face. It can either be the concrete topping or total slab thickness (rib zone). Here only concrete topping is considered to be in contact with the column face.

$$N_{slab} = \mathbf{676kN}$$

The slab bearing force is considered to be distributed between shear studs uniformly.

Table M-8. Shear stud demands for gapped and no gap conditions

		Left beam, braced bay (kN)	**Right beam (kN)**
Elastic diaphragm model	Gapped	622	308
	No gap	1298	984
Cracked diaphragm model	Gapped	599	470
	No gap	1275	1146

M.3.9.1 Calculating shear stud strength considering gravity load and lateral force interaction

According to Chapter 5 findings:

- **Calculating S_{max} for propped beams**

The maximum shear stud slip, S_{max}, can be obtained for propped beams as

$$S_{max} = 1.6\frac{\Delta_v d}{L}$$

Where

Δ_v: is a mid-point vertical deflection of the bare steel beam under gravity loads ($\frac{5WL^4}{384EI}$).

d: is total beam height including the steel beam and the concrete slab.

L: is the beam span.

Note that Δ_v should be calculated using the bare steel beam stiffness without considering composite action.

$$W = 23.6\ kN/m\ or\ N/mm$$

$$I = 296e6\ mm^4$$

Δ_v=6.72mm

$$d = 454 + 80 + 65$$

$$= 599$$

$$S_{max} = 1.07mm$$

- **Calculating lateral force resistance**

Obtaining effective shear stud zone:

To obtain the effective shear stud zone the shear stud slip limit is required. Here the value of $S_u/3$ is recommended to be assumed as the shear stud slip limit. The maximum monotonic shear slip capacity, S_u, of 19mm shear studs is 7.2mm.

Lateral force resistance of shear studs on the beam is equal to the sum of the strengths of all shear studs, because the maximum calculated slip is less than 2.4mm ($S_u/3$) therefore all shear studs may be used to carry lateral forces.

Here 25% composite action is considered:

$$Composite\ force = 0.25 \times min\{65mm \times 1500mm \times 30MPa;\ 8580 \times 340\}$$

$$Composite\ force = 621kN$$

Total shear stud strength on the beam is $2 \times 621 = 1242kN$ based on 25% composite action.

Note that the composite action is not considered to carry gravity loads in this example. The minimum allowable composite action level to carry gravity loads is given by Clause 3.5.8.3 of NZS2327 (2017) equal to 40%.

M.3.10 Step 10, Diaphragm in-plane strength check

M.3.10.1 Compression strut and tension ties

According to NZS3101 (2006) Clause 13.3.9, the strength design of diaphragms for shear shall be based on strut and tie models in accordance with Appendix A of NZS3101 (2006). Here, the compression strength of struts and tensile strength of ties are calculated to compare with the analysis results presented in Table M-4.

Nominal compression strut strength may be calculated according to Clause A5.2 NZS3101 (2006). Here the concrete thickness is considered equal to the concrete topping as described in Section M.3.4.

- Strut strength:

$$f_{cu} = \beta_s \alpha_1 f_c'$$

$$= 0.6 \times 0.85 \times 30$$

$$= 15.3MPa$$

$$F_{ns} = 15.3 \times at$$

$$= 15.3 \times 50 \times 2000$$

$$= 554kN$$

Maximum strut force obtained from the analysis (Table M-4) was -186kN.

$$554kN > 186kN \quad OK$$

Nominal tension tie strength may be calculated according to Clause A6.1 NZS3101 (2006). It is assumed 664/188mesh is used in the concrete topping with $f_y = 460MPa$. This mesh provides $188mm^2/m$ steel cross-section.

- Tie strength:

$$F_{nt} = A_{st} f_y$$

$$= 188 \times 2 \times 460$$

$$= 86.5kN$$

Maximum tension force obtained from diaphragm analysis was 117kN (see Table M-4).

$$86.5kN \ngeq 117kN \quad NG$$

This shows that additional reinforcement is required to carry diaphragm tension tie forces.

M.3.10.2 Diaphragm buckling check

Diaphragm buckling check can be performed according to the finding of Chapter 6. The buckling strength of diaphragms is obtained for both elastic (un-cracked) and cracked (strut buckling) situations. Here, the diaphragm shear strength obtained according to Clause 13.4.10.2 of NZS3404 (2007) is considered as the upper bound of diaphragm shear strength to compare with the calculated buckling strengths. Also the maximum strut compression forces obtained from the analyses, Table M-4, are used to be compared with the strut buckling capacity.

According to NZS3404 (2007), Clause 13.4.10.2 the diaphragm shear strength may be calculated as

$$V_r = min\begin{cases} 0.8\emptyset A_{rt} f_{yr} + 2.76\emptyset_C A_{CV} \\ 0.5\emptyset_C f'_C A_{CV} \end{cases}$$

$$V_{rx} = min\begin{cases} 0.8 \times 0.9 \times 188 \times 460 \times 8 + 2.76 \times 0.6 \times 50 \times 8000 \\ 0.5 \times 0.6 \times 30 \times 50 \times 8000 \end{cases}$$

$$= 892kN$$

$$V_{ry} = min\begin{cases} 0.8 \times 0.9 \times 188 \times 460 \times 6 + 2.76 \times 0.6 \times 50 \times 6000 \\ 0.5 \times 0.6 \times 30 \times 50 \times 6000 \end{cases}$$

$$= 617\ kN$$

- **Diaphragm buckling mode 1, inter-rib (local) buckling**

The mode one buckling (local buckling) was shown that does not govern for ComFlor 80 and 60 for 50mm concrete topping thickness in Chapter 6.

The other buckling modes (intra-panel and intra-bay) are investigated in the following:

- Notations:

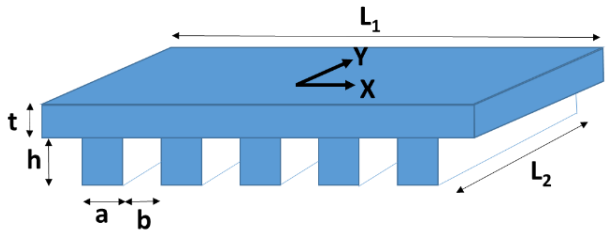

$\boldsymbol{N_{xy1}}$	Elastic critical shear stress (MPa)
$\boldsymbol{b}$	Plate width (distance between ribs) (mm)
$\boldsymbol{t}$	Concrete topping thickness (mm)
$\boldsymbol{E}$	Concrete elastic modulus (MPa)
$\boldsymbol{\nu}$	Concrete Poisson's ratio
$\boldsymbol{k_s}$	Plate shear buckling coefficient
$\boldsymbol{N_{cr}}$	Elastic critical axial stress (MPa)
$\boldsymbol{k}$	Plate axial buckling coefficient
$\boldsymbol{\tau_c}$ and $\boldsymbol{\partial_c}$	Imposed shear and axial stresses to the concrete topping (MPa)
$\boldsymbol{e_y}$	Distance between concrete topping centre line to the section neutral axis (mm)
$\boldsymbol{h}$	Steel deck height (mm)
$\boldsymbol{a}$	Steel deck rib width (mm)
$\boldsymbol{\beta}$	Ribs height modification factor
$\boldsymbol{G_{xy}}$	Elastic shear modulus of concrete (MPa)
$\boldsymbol{\eta}$	Numerical factor depending on the ribs aspect ratios

k_B	Reduction factor accounting for the decrease in the torsional stiffness of reinforced concrete beams due to concrete cracking
N_{xy2}	Elastic critical shear stress of intra-panel orthogonal plate (MPa)
D_x	Flexural stiffness of the steel deck slab in the direction perpendicular to ribs (N.mm)
D_y	Flexural stiffness of the steel deck slab in the ribs direction (N.mm)
L_2	Slab length parallel to the ribs (mm)
f'_c	Concrete compressive strength (MPa)
I_s	Moment of inertia of the concrete strut per unit width (mm^4)
I_r	Moment of inertia of the rib per unit width(mm^4)
L_s	Strut length (mm)
α	The angle between the concrete strut and the ribs
L_1	Slab length perpendicular to the ribs (mm)
L_2	Slab length parallel to the ribs (mm)
V_{SB2}	Slab shear buckling strength per unit length due to intra-panel buckling (N/mm)
V_{strut2}	Slab shear from strut buckling capacity per unit length (intra-panel buckling) (N/mm)
t_{eq}	Equivalent plate thickness to the steel deck slab in the X direction (mm)
e_x	Distance between equivalent slab centre line to the section neutral axis (mm)
E_s	Steel elastic modulus (MPa)
I_y	Moment of inertia of secondary beams (mm^4)
A_s	Cross section area of secondary beams (mm^2)
h_1	Steel beam height (secondary beam) (mm)
c_1	Distance between secondary beams (mm)
d_i	Width of steel beam flanges and web (mm)
t_i	Thickness of steel beam flanges and web (mm)
G_{xys}	Elastic shear modulus of steel (MPa)
N_{xy3}	Elastic critical shear stress of intra-bay orthogonal plate (MPa)
V_{SB3}	Slab shear buckling strength per unit length due to intra-bay buckling (N/mm)
I_{sb}	Is the secondary beam moment of inertia per unit width of the slab (I_y/c_1) (mm^3)
ψ	Buckling correction factor, 0.9 for a composite floor with one secondary beam, 1 for more than one
n	Number of secondary beams per bay
V_{strut3}	Slab shear from strut buckling capacity per unit length (intra-bay buckling) (N/mm)
P_{cr3}	Strut buckling capacity per unit length (intra-bay) (N/mm)
P_{cr2}	Strut buckling capacity per unit length (intra-panel buckling) (N/mm)
$N_{existing}$	Maximum imposed shear stress to intra-panel (MPa)

- **Diaphragm buckling mode 2, Intra-panel buckling**

1. ***Calculating critical shear buckling of the intra-panel subjected to pure shear, (pre-crack condition)***
   - Preliminary check:

If the equation below is satisfied, there is no need to check the critical shear buckling of the intra-panel subjected to pure shear:

$$0.3f_c' \leq 0.75 \times 3.5 \frac{\pi^2}{tL_2{}^2} \sqrt[4]{D_x D_y{}^3}$$

$$9 \leq 0.75 \times 3.5 \frac{\pi^2}{65 \times 4000^2} 9.6 \times 10^8$$

$$9 \leq 23.8 \quad OK \quad \text{This failure mode does not need to be checked}$$

Where $\sqrt[4]{D_x D_y{}^3}$ for different topping thickness is presented in plots shown in Figure M-14 for ComFlor 60 and 80 (these values are calculated using flexural stiffness reduction factor 0.35 based on Table C6.5 NZS 3101, 2006).

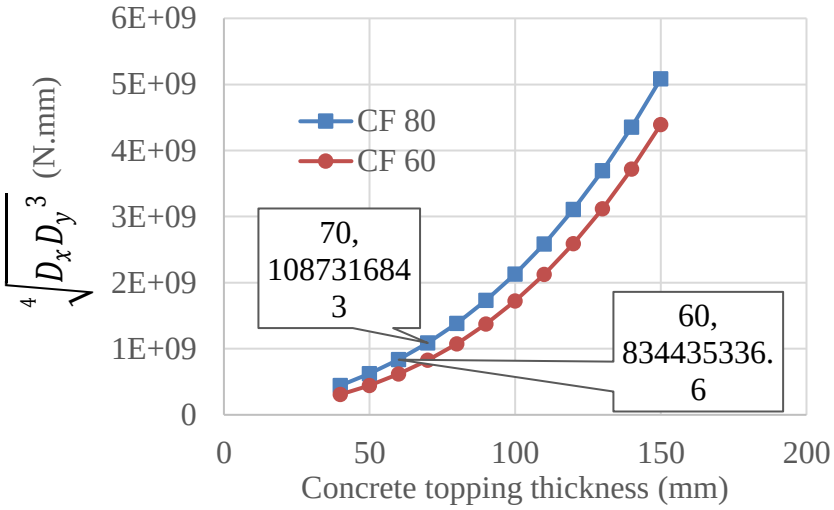

Figure M-14. Calculated values of $\sqrt[4]{D_x D_y{}^3}$ for ComFlor 60 and 80 against different concrete topping thickness

1. Intra-panel subjected to diagonal force (strut force), post-crack condition

The critical strut buckling load per unit width of the strut is calculated using:

$$P_{cr2} = 0.75 \frac{\pi^2 \left(EI_s + EI_r \left(\frac{L_s}{L_2} \right)^3 \right)}{L_s{}^2}$$

Where,

$$I_r = 0.35\frac{a(t+h)^3}{12(a+b)}$$

$$I_s = 0.8\frac{t^3 \sin\alpha}{12}$$

$$L_s = \frac{L_2}{\sin\alpha}$$

Considering $a = 135mm$, $b = 165mm$, $t = 65mm$, $h = 80mm$ and $L_2 = 4000mm$

$$I_r = 40013\ mm^3$$

$$\alpha = 45°$$

$$I_s = 12011\ mm^3$$

$$L_s = 5656mm$$

$$P_{cr2} = 0.75 \times \frac{\pi^2 \times 25000 \times 12011 \times sin^3(45) + \pi^2 \times 25000 \times 40013}{5656^2 \times sin^3(41)}$$

$= 743N/mm$ → capacity

$\frac{186000\ (Max\ struc\ force\ from\ Table\ M-4)}{2000} = 93N/mm$→ Demand

$743\ N/mm > 93\ N/mm\ \ OK$

- **Diaphragm buckling mode 3, Global buckling**

1. ***Calculating critical shear buckling of the intra-bay subjected to pure shear, (pre-crack condition)***
   - Preliminary check:

First, the effect of the secondary beam could be ignored and the same as the intra-bay the following equation could be used as a preliminary check. If the equation below is satisfied, there is no need to check the critical shear buckling of the intra-bay subjected to pure shear:

$$0.3f_c' \leq 0.75 \times 3.5\frac{\pi^2}{t{L_2}^2}\sqrt[4]{D_x{D_y}^3}$$

$$9 \nleq 0.75 \times 3.5\frac{\pi^2}{65 \times 8000^2}9.6 \times 10^8$$

$9 > 5.96 \quad NG$ This failure mode needs to be checked

First, the properties of the equivalent orthotropic plate need to be calculated:

Finding the flexural stiffness of the steel deck slab in the ribs direction (D_y) same as the intra-panel:

$$D_y = 0.35\left(\frac{Et^3}{12(1-\vartheta^2)} + \frac{Ete_y{}^2}{(1-\vartheta^2)} + \frac{Eah^3}{12(a+b)} + \frac{Eha\left(\frac{h}{2}+\frac{t}{2}-e_y\right)^2}{(a+b)}\right)$$

$$D_y = 1457977781\ N.mm$$

Finding the flexural stiffness of the steel deck slab in the direction perpendicular to the ribs (D_x):

First, the equivalent plate thickness to the steel deck slab should be calculated: (D_{xs} is the steel deck slab stiffness equal to D_x for the intra-panel)

Finding the flexural stiffness of the steel deck slab in the direction perpendicular to ribs (D_x):

$$\begin{cases} \beta = 0.9224e^{\left(\frac{-2.756h}{a}\right)} & for\ \frac{h}{a} \le 0.4 \\ \beta = \frac{a}{8h} & for\ \frac{h}{a} > 0.4 \end{cases}$$

$$\beta = 0.21$$

$$D_a = \frac{E(t+\beta h)^3}{12(1-\vartheta^2)}$$

$$= 1.19 \times 10^9 N.mm$$

$$D_b = \frac{Et^3}{12(1-\vartheta^2)}$$

$$= 5.96 \times 10^8 N.mm$$

$$D_{xs} = \frac{D_a D_b (a+b)}{(bD_a + aD_b)}$$

$$= 7.69 \times 10^8 N.mm$$

$$t_{eq} = \sqrt[3]{\frac{12(1-\vartheta^2)D_{xs}}{E}}$$

$$= 70.45mm$$

Then:

$$D_x = \frac{Et_{eq}{}^3}{12(1-\vartheta^2)} + \frac{Et_{eq}e_x{}^2}{(1-\vartheta^2)} + \frac{E_s I_y}{c_1} + \frac{E_s A_s \left(\frac{h_1}{2} + t + h - \frac{t_{eq}}{2} - e_x\right)^2}{c_1}$$

$$D_x = 7.69 \times 10^{10} \text{N. mm}$$

The torsional stiffness of the steel deck slab is calculated using:

$$B = \frac{Et_{eq}{}^3}{12(1-\vartheta^2)} + \frac{G_{xy}}{2}\frac{ha^3\eta}{(a+b)}k_B + \frac{G_{xy_s}}{6}\left(\frac{\sum d_i t_i{}^3}{c_1}\right)$$

$$= 601124761.3 \text{ N. mm}$$

Where k_B can be considered zero conservatively.

Elastic critical shear stress (buckling stress) is expressed as:

$$N_{xy3} = K_s \frac{\pi^2}{tL_2{}^2}\sqrt[4]{D_x D_y{}^3}$$

From Figure 6-22: $K_s = 3.75$

$$N_{xy3} = 254N/mm2$$

$$254 \times 65 \times \frac{6000}{1000} = 99060kN$$

$$N_{xy3} \gg V_{rx}$$

$$99060kN \gg 892kN \quad OK$$

2. Intra-bay subjected to diagonal force (strut force), post-crack

The strut critical buckling load per unit width of the strut is calculated using:

$$P_{cr3} = 0.75 \times min \begin{cases} \frac{\pi^2 EI_s}{{L_s}^2} + \frac{\pi^2 EI_r}{{L_2}^2 \sin\alpha} + \psi \frac{\pi^2 E_s I_{sb}}{{L_1}^2 \cos\alpha} \\ (n+1)^2 \left(\frac{\pi^2 EI_s}{{L_s}^2} + \frac{\pi^2 EI_r}{{L_2}^2 \sin\alpha} \right) \end{cases}$$

Considering $a = 135mm$, $b = 165mm$, $t = 65mm$, $h = 80mm$ and $L_2 = 4000mm$

$$I_r = 40013\ mm^3$$

$$I_s = 12011\ mm^3$$

$$L_2 = 8000mm$$

$$L_s = 11313mm$$

$$P_{cr3} = 0.75 \times$$

$$min \begin{cases} \frac{\pi^2 \times 25000 \times 12011}{11313^2} + \frac{\pi^2 \times 25000 \times 40013}{8000^2 \times sin\,41} + 0.9 \frac{\pi^2 \times 200000 \times 875000000/8000}{6000^2 \times cos\,41} \\ (1+1)^2 \left(\frac{\pi^2 \times 25000 \times 12011}{11313^2} + \frac{\pi^2 \times 25000 \times 40013}{8000^2 \times sin\,41} \right) \end{cases}$$

$P_{cr3} = 765N/mm \rightarrow$ Capacity

Same as the intra-panel strut buckling:

$$\frac{186000\ (struc\ force\ from\ Table\ M-4)}{2000} = 93N/mm \rightarrow \text{Demand}$$

$$765\ N/mm > 93\ N/mm\ \ OK$$

The calculated buckling strengths are multiplied by 0.75 to account for the out-of-straightness effect due to existing gravity forces.

References

[1] AS/NZS 2327 (2017). Composite structures, Composite steel-concrete construction in buildings.

[2] ComFlor Steel Composite Metal Deck Design software, Ver 9.0.33.0

[3] Cowie, K. A., Fussell, A. J., Clifton, G. C., MacRae, G. A., & Hicks, S. J. (2014, March). Seismic design of composite metal deck and concrete-filled diaphragms–A discussion paper. In NZSEE Conference.

[4] Hyland, C., Cowie, K., & Clifton, C. (2008). Structural Steelwork Connections Guide: Design Procedures, SCNZ 14.1 2007. Steel Construction New Zealand (Inc), Manukau City.

[5] NZS 1170.5 (2004). Structural Design Actions-Part, 5. Standards New Zealand, Wellington, New Zealand. Including Amendment 1, 2016.

[6] NZS 3101 (2006). Concrete structures standard. Standards New Zealand, Wellington, NZ.

[7] NZS 3404 (2007). Steel Structures Standard. Standards New Zealand, Wellington, New Zealand. Including Amendments 1 and 2, 2001/2007.

Appendix N: Glossary

Bay	Area of composite floor between primary beams	Chapter 6
Composite floor	Composite slabs plus supporting (secondary and/or primary) beams	Chapter 6
Composite slab	Decking, concrete and any reinforcement (without supporting beams)	Chapter 6
Decking (or steel decking, cold-formed steel decking)	The steel profile used to support the concrete (and any reinforcement) in a composite slab. The decking is usually cold-formed from steel sheets	Chapter 6
Floor diaphragm	Horizontal floor used to carry horizontal (as well as vertical) forces	Chapter 2 Chapter 3 Chapter 6
Inter	Between	Chapter 6
Intra	Within	Chapter 6
Panel	Area of composite slab between secondary beams	Chapter 6
Primary beams	Beams that transfer the floor forces to the secondary beams	Chapter 6
Secondary beams	Beams connecting columns in a normal building frame	Chapter 6
Strut-and-Tie model	A subset of truss model with a combination of compression-only diagonal members and compression/tension orthogonal members	Chapter 2 Chapter 3 Chapter 6
Topping	Concrete placed above highest point of decking	Chapter 2 Chapter 6 Chapter 8
Truss element	Orthogonal and diagonal axial members that form a truss model	Chapter 3
Truss framework	A number of truss mesh units placed together to represent floor slab in-plane behaviour	Chapter 3
Truss mesh unit	Square or rectangular block consists of several truss elements	Chapter 3
Truss model	A truss framework that may have different truss element properties such as elastic, tension-only, compression-only, or different stiffness in each direction	Chapter 3
Vertical lateral load resisting (VLFR) system	Vertical elements used to resist horizontal forces such as those coming from wind or earthquake	All Chapters